TU Clausthal
Clausthal University of Technology

Electro-Thermo-Mechanical Modeling of Field Assisted Sintering Technology: Experiments, Constitutive Modeling and Finite Element Analysis

Doctoral Thesis
(Dissertation)

to be awarded the degree of

Doctor in Mechanical Engineering (Dr.-Ing.)

submitted by

Dipl.-Ing. Steffen Rothe

from Kassel
(place of birth)

approved by the Faculty of
Mathematics/Computer Science and Mechanical Engineering,
Clausthal University of Technology

Date of oral examination
14.11.2014

Chairperson of the Board of Examiners
Prof. Dr.-Ing. Alfons Esderts

Chief Reviewer
Prof. Dr.-Ing. habil. Stefan Hartmann

Reviewer
Prof. Dr.-Ing. habil. Alexander Düster, Technische Universität Hamburg-Harburg

Vorwort und Danksagung

Die vorliegende Dissertation entstand während meiner Tätigkeit von 2010 bis 2014 als wissenschaftlicher Mitarbeiter am Institut für Technische Mechanik der TU Clausthal. Für die Finanzierung des Forschungsvorhabens danke ich der Deutschen Forschungsgemeinschaft.

Mein besonderer Dank gilt Prof. Stefan Hartmann für die mir gebotene Möglichkeit zur wissenschaftlichen Arbeit mit einer interessanten Aufgabenstellung sowie die engagierte Betreuung bis zur Promotion. Ich konnte in dieser Zeit viel lernen und für die Förderung bin ich ihm zu Dank verpflichtet.

Prof. Alexander Düster danke ich recht herzlich für die Übernahme des Korreferats und das Interesse an meiner Arbeit sowie die wissenschaftliche Zusammenarbeit im Projekt und bei Veröffentlichungen. Für die Übernahme des Prüfungsvorsitzes möchte ich mich bei Prof. Alfons Esderts bedanken.

Für die konstruktive und gute Zusammenarbeit möchte ich mich bei allen Beteiligten des Projekts, namentlich Prof. N. Frage, Prof. A. Düster, Prof. E. Rank, Prof. Z. Yosibash sowie P. Erbts, Dr. S. Kollmannsberger, N. Zander, Dr. S. Kalabukhov und Dr. V. Kasyan bedanken. Die Aufenthalte in Beer-Sheva, Israel, waren von großer Gastfreundschaft geprägt. Weiterhin möchte ich mich bei Prof. H. Steeb für das Interesse am Thema und die Unterstützung zur Bestimmung der elektrischen Kontaktwiderstände bedanken.

Außerdem möchte ich die angenehme Arbeitsatmosphäre mit allen Kollegen im Institut für Technische Mechanik hervorheben. Besonders meiner Zimmerkollegin Dr.-Ing. Carmen Sguazzo möchte ich für die fachlichen und nichtfachlichen Diskussionen, die gemeinsamen Kaffeerunden sowie die gute Zusammenarbeit danken. Weiterhin konnte ich von zahlreichen wissenschaftlichen Diskussionen mit Dipl.-Ing. Matthias Grafenhorst und Dipl.-Phys. Stephan Krämer profitieren. Bei Dr.-Ing. Raad Al-Kinani möchte ich mich für die Gesprächsbereitschaft bei Fragen zur Kontinuumsmechanik bedanken. Außerdem möchte ich Dr.-Ing. Karsten Jens Quint erwähnen, der mich im Studium hervorragend betreute und förderte. Während der Anfangszeit meiner Promotion war Dr.-Ing. Ahmad-Wahadj Hamkar eine große Unterstützung und ich konnte von seinem Wissen und seinen Erfahrungen profitieren.

Darüber hinaus haben einige Studenten meine Arbeit bereichert. Für die wissenschaftlichen Arbeiten von Dipl.-Ing. Jan Henrik Schmidt, Bsc. Sebastian Betz, Bsc. Thorben Ziemer, Dipl.-Ing. Maria Angeles Martinez Page, Dipl.-Ing. Jan Klinger und Dipl.-Ing. Zhijia Liu bin ich dankbar. Insbesondere Bsc. Sebastian

Betz zeigte großes Engagement im Bereich der Messtechnik und der Durchführung von Experimenten. Dipl.-Ing. Jan Henrik Schmidt zeigte hervorragende Leistungen, sowohl bei seinen Studienarbeiten, als auch bei seiner Tätigkeit als studentische Hilfskraft.

Nicht zuletzt möchte ich mich bei meinen Eltern für ihren Rückhalt sowie bei all meinen Freunden für die Unterstützung bedanken.

Abstract

In powder metallurgy, a common process is hot isostatic pressing (HIP). This process is characterized by the densification of powders using a liquid or a gas. Due to the indirect heating, such processes usually take several hours. A new and innovative production process for the sintering of powders is the Field Assisted Sintering Technology (FAST). Here, the powder is filled into a graphite die and compacted by a punch. At the same time, the powder and the graphite tool system are heated volumetrically by an electric current that induces Joule heating. With this technology at hand, it is possible to ensure faster heating and shorter cooling periods, leading to shorter production times and improved material properties. The shorter production times are also beneficial for the microstructure, since grain coarsening due to large dwell times can be avoided.

A major challenge of this new technology is to control the various process parameters in order to determine the desired material properties. In order to get a deeper insight into the process by means of simulations, a constitutive model is derived for the highly instationary, non-linear thermo-mechanical powder consolidation process on the basis of principal experiments. Additionally, the graphite tool system is modeled for the simulation of the entire process. The parameters of the developed model are identified with the concept of material parameter identification.

The finite element method proved to be a powerful tool for the numerical simulation of physical problems. For the numerical simulation of the sintering process, the underlying thermo-electro-mechanically coupled problem has to be solved together with temperature-dependent graphite material properties, the temperature and the relative density-dependent material properties for the powder material. This time-dependent non-linear multi-field problem is interpreted as a system of differential algebraic equations and its solution procedure by means of finite elements is explained.

The final stress algorithm is implemented into the commercial finite element program Abaqus, and a fully coupled monolithic simulation is performed in order to simulate a real FAST-process and to compare the temperature and stress distribution with experiments. Moreover, it is possible to make predictions concerning the powder densification and the temperature distribution, which leads to a better insight into the process. As a result, the numerical model for the simulation of the thermal, electrical and mechanical problems of sintering can be seen as a suitable tool to optimize the sintering process.

Contents

1 Introduction

Nowadays, numerical simulations are getting more and more important because, on the one hand, real experiments are costly and time consuming and, on the other hand, simulations can deliver a deeper insight into a real process. In this work, a new powder consolidation technology is investigated and simulated by means of finite elements. The following statement emphasizes the need for simulation to improve and understand the sintering process in its details.

> "*Modeling is not just a scholastic attachment marginally improving the understanding of the technological process; it becomes rather an essential part of the spark plasma sintering manufacturing approach.*" (Olevsky et al., 2012b)

This work is a part of an international collaborative research project between the universities TU Munich, TU Hamburg-Harburg, TU Clausthal in Germany and the Ben Gurion University (BGU) in Beer-Sheva, Israel, funded by the DFG (German Research Foundation). The title of the entire research topic is "Electro-thermo-mechanical modeling of Field Assisted Sintering Technology using high-order finite elements validated by experiments".

All the sintering experiments presented in this thesis were performed at the institute of Prof. Frage at the Ben Gurion University in Israel. The experiments were designed by Prof. Hartmann and me in order to develop a constitutive model for the powder material. In the group of Prof. Yosibash, the focus lies on the uncertainties quantification. The aim of the groups of Prof. Rank in Munich and Prof. Düster in Hamburg is the spatial discretization of the thermo-electro-mechanical coupled problem using the p-version of the finite element method. In particular, the group of Prof. Düster works on the partitioned solution of the three-field coupled problem, whereas the group of Prof. Rank uses and extends the Finite Cell Method. The FCM combines a fictitious domain approach with the high-order finite element method and simplifies the mesh generation drastically.

1.1 Field Assisted Sintering Process

Field Assisted Sintering Technology is a powder consolidation process. Within this process, the powder is filled into a graphite die and is simultaneously heated and pressed. The heat treatment is done by an electric current flowing through the graphite tool system and the powder (if the powder is a conducting material). The volumetric Joule heating ensures high heating rates and short production times. Due to the high heating and cooling rates, the sintering can be reduced to minutes instead of hours as in conventional methods.

A typical FAST-machine consists of a vacuum chamber with water-cooled walls. The electric current is applied through water-cooled electrodes. Different types can be used for the application in question: direct current (DC), alternating current (AC) or a pulsed DC. In this work, a current application with direct current is used. The whole process is force-controlled using a hydraulic system. The tool system, in which the powder is filled into, consists of graphite. During the process, the temperature is either controlled using a thermocouple or a pyrometer. A proportional-integral-derivative controller (PID controller) inside the machine is used to control the electric power in order to follow a prescribed temperature path. This means that, during the process, the temperature can be controlled only at one point within the graphite tool system – but not in the powder itself. Therefore, it is of interest to simulate the process and to get a better understanding of the entire technology.

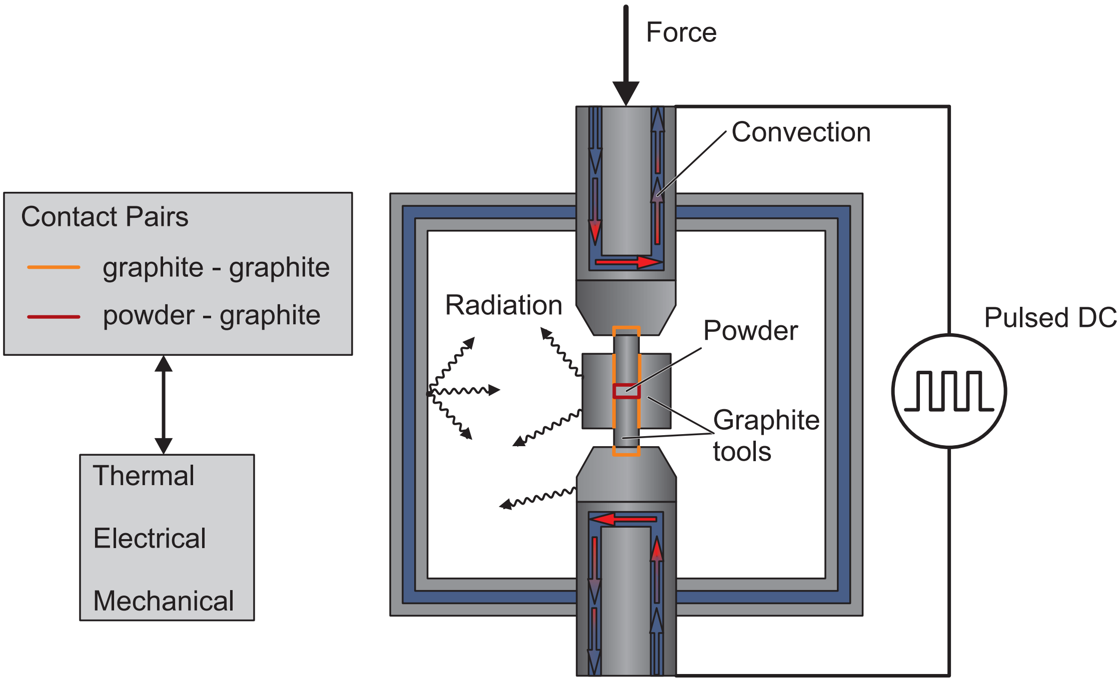

Figure 1.1: FAST conditions

1.2 Challenges in Modeling the FAST-process

Despite the worldwide popularity of the FAST-process, the possibility to predict and control the sintering parameters is still a challenging task and an ongoing field of research. For the numerical simulation of this process, it is necessary to solve the underlying thermo-electro-mechanically coupled problem including its large temperature changes and moving boundaries due to the compressible powder behavior. During the sintering process, the powder changes its thermal and electrical conductivity not only due to the temperature but also due to the compaction. Furthermore, it is necessary to treat the heat transfer by conduction, radiation and convection, see Fig. 1.1. Apart from the powder material, the graphite die and the graphite punch have to be investigated too, in order to determine the electrical, thermal and mechanical behavior in the tool system. Moreover, the contact conditions between the different parts play an essential role for the temperature as well as the electrical potential distribution. The occurring contacts are the imperfect contact between graphite and graphite as well as between the powder and graphite. Thus, the electrical contact resistance has to be determined. Since there are three fields – namely the electrical, thermal and the mechanical one, see Fig. 1.2 – coupled multi-field simulations have to be performed. Due to the large powder deformations, finite strain contact simulations have to be taken into account.

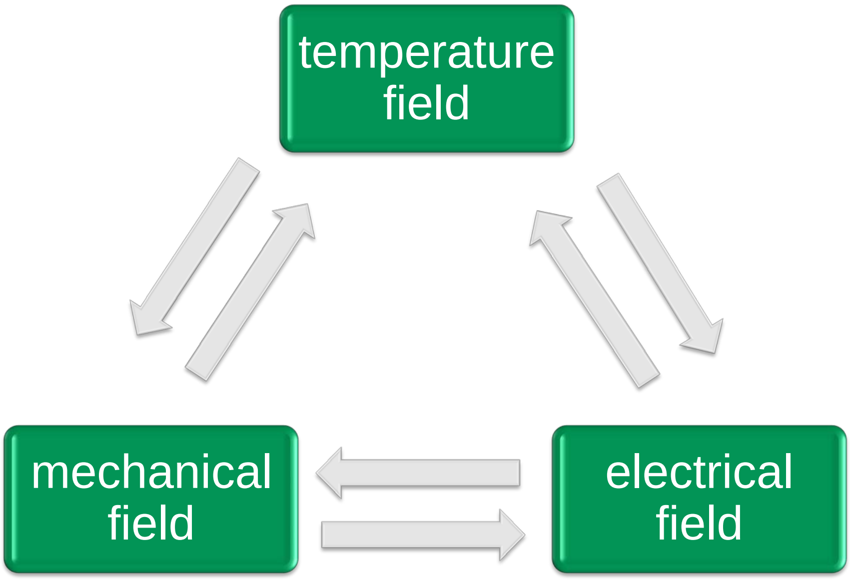

Figure 1.2: Thermo-electro-mechanical coupling

1.3 Literature Review

Sintering is a process technology to consolidate powders below the melting point of the powder material. The consolidation process is mainly driven by the thermal activation of local mass transport due to the reduction of surface and grain boundary energies, [Munir et al., 2011]. As conventional methods such as pressureless sintering and hot pressing (HP) lead to processing times of several hours, see [Garay, 2010], it is of high interest to find a possibility to enhance the mass transport. It turned out that the use of an electric current can accelerate the sintering process, providing a possibility to sinter powders in approximately 20 min or even shorter times, [Garay, 2010]. Furthermore, the heating rates in FAST are approximately $200\,°\mathrm{C}\,\mathrm{min}^{-1}$ to $300\,°\mathrm{C}\,\mathrm{min}^{-1}$, but can also reach $1000\,°\mathrm{C}\,\mathrm{min}^{-1}$, while typical heating rates in hot pressing are $1\,°\mathrm{C}\,\mathrm{min}^{-1}$ to $10\,°\mathrm{C}\,\mathrm{min}^{-1}$, [Quach et al., 2010]. In addition, there are a lot of benefits in comparison to conventional methods. These are higher heating and cooling rates, shorter dwell times, fewer processing steps, short processing times, no need of sintering aids as well as enhanced material properties by minimized grain growth.

There are several terms that refer to methods of sintering powder with a simultaneous use of electric current and pressure, such as Spark Plasma Sintering (SPS), the Field-Assisted Sintering Technique (FAST), Pulsed Electric-Current Sintering (PECS) and Electric Current Activated/Assisted Sintering (ECAS). A newly published review paper describing the mechanical, thermal and electrical effects in the FAST-process is presented in [Guillon et al., 2014], also featuring a description of successful material developments and a discussion of further technological aspects. The most important developments in the ECAS technology are summarized in the following by drawing on the review article by Grasso et al. [2009]. It is mentioned that Bloxam, who obtained a patent in 1906, can be seen as a pioneer in the use of electric current for the purpose of sintering. He used pure direct current resistance sintering for the production of incandescent lamps. In 1913, Weintraub and Rush invented a new method to simultaneously apply a pressure and a direct current. In 1966, Inoue in Japan used a pulsed electric current for the powder consolidation and thus inspired the development of the PECS method. But the high cost of equipment, the lack of repeatability and the low sintering efficiency prevented a widespread use of the ECAS production technology. In the late 1980s, when Inoue's patents expired, various companies started to produce PECS machines. The popularity of this process can be proved by 450 papers published in 2009 as reported in [Munir et al., 2011].

1.3.1 Thermo-Electrical Modeling

Zavaliangos et al. [2004] analyzed the temperature distribution during FAST-processes with Abaqus to identify thermal gradients in the sample and the tool system. A reliable thermal simulation enables a proper comparison between FAST and conventional sintering techniques as well as an optimization of the process parameters of large size specimens. Also, they were the first to mention the importance of the thermal and electrical contact resistance and to employ vertical and horizontal contacts especially designed to match the experimental data. The fact that the resistance is dependent on the temperature and on the pressure was neglected. A coupled thermo-electrical analysis using Ansys is presented by Vanmeensel et al. [2005]. They fitted horizontal and vertical contact resistances to minimize differences between measured and simulated temperatures. Anselmi-Tamburini et al. [2005] applied the commercial code CFD-ACE+ to investigate current and temperature distributions with a thermal conductive and a non-conductive sample material, copper and alumina. They considered ideal contact conditions and neglected any contact resistances. The temperature distribution for the sintering of a silicon nitride and tungsten carbide powder material is investigated by Räthel et al. [2009]. They observe a strong influence of the temperature measurement point on the sample temperature. Furthermore, the temperature distribution is influenced by the tool geometry, depending on whether a conductive or a non-conductive material is used, [Räthel et al., 2009]. Thermo-electrically coupled finite element simulations with Abaqus and Matlab can be found in [Tiwari et al., 2009]. Here, it is found that the temperature inside the powder compact is strongly influenced by the thermal conductivity and the power input. In the work of Muñoz and Anselmi-Tamburini [2012], the influence of various process parameters such as the die geometry, heating rate, material properties and the sintering temperature are investigated with respect to the temperature distribution. A study of the Joule heating effect for powder mixtures is given in [Zohdi, 2012a]. In addition, Zohdi [2010] simulated electrical, magnetic and thermal fields with the finite difference time domain method. An optimization of the temperature distribution in the specimen is performed in [Vanherck et al., 2013]. It is mentioned that the heterogeneity of the microstructure in the compact originates from the heterogeneity of the temperature field – and it is shown that this can be resolved by changing the die dimensions. In [Pavia et al., 2013], electro-thermal simulations are compared to actual measurements. It is pointed out that the graphite properties are important for the accuracy of the simulation. The root mean square values of the current and the voltage are found to be lower than the values reported by the machine.

The goal of all these simulations is to determine thermal gradients that affect the final material properties. Large thermal gradients can lead to an inhomogenous microstructure and to inhomogenous mechanical properties of the sintered parts.

1.3.2 Thermo-Electro-Mechanical Modeling

In the literature, there are only few attempts to model the whole thermo-electro-mechanical problem. In the work of Cincotti et al. [2007], the SPS-process is modeled without powder to study the thermal and the electrical field together with a small strain thermoelasticity relation for the tool system. Maizza et al. [2007] studied the influence of the moving punch on the temperature. He emphasizes that the reliability of the model predictions is highly dependent on the correct modeling of the contact resistances.

Wang et al. [2007] investigated the electrical, temperature and stress fields in order to evaluate stress gradients in the fully dense sample (copper and alumina). Thus, the densification process is not treated. The final stage of sintering with fully dense specimens is considered in [Antou et al., 2009] too. A staggered approach for the thermo-electro-mechanical simulation of a free sintering process without a die is performed in [McWilliams and Zavaliangos, 2008; McWilliams, 2008]. In this staggered approach, the specimen mesh is fixed for the thermo-electric simulation. The calculated temperature is used as an input for the mechanical simulation, where the new relative density is computed. Munoz and Anselmi-Tamburini [2010] computed stress distributions inside a fully dense specimen with a linear elastic material model. They performed an electro-thermo-mechanical simulation with Ansys for copper and alumina with a PID controller for the temperature. Wang et al. [2010] analyzed the effect of different die sizes, heating rates and pressures on the temperature and stress distribution inside an alumina sample, on the tool system and on the resulting microstructure. For the material relation, small strain elasticity is assumed. In [Hartmann et al., 2013], the temperature distribution inside graphite tools with fully dense copper and ceramic is studied using temperature-dependent heat capacity, thermal and electrical conductivities and a small strain thermoelasticity relation. For code verification purposes, analytical solutions for the thermo-electro-mechanical coupling are derived in [Rothe et al., 2014]. In addition, high-order time integration methods (which enable an efficient step-size control) and the Newton-Chord method in connection with an Aitken-relaxation are applied – leading to very efficient computations. A different approach to simulate electrically aided sintering is followed by Zohdi [2014], where a particle-based simulation is applied.

What all the mentioned investigations have in common is that they do not model the densification process occurring in the powder material during the FAST-process. The specimens are assumed to be fully dense and modeled by a small strain thermoelasticity material relation. In the FAST-machine, the powder material undergoes large plastic deformation. Recently, several articles were published that deal with the densification, see [Song et al., 2011; Olevsky et al., 2012a; Wolff et al., 2012]. In [Song et al., 2011], an additive decomposition of the strain rate tensor is used to separate the material model into an elastic, viscoplastic and a thermal part. The relative density is computed out of the mass balance. It is found that the electrical and thermal field are significantly affected by the mechanical field, due to the changing geometry and the contact conditions. Additionally, it is shown that greater pressures will decrease the temperature gradient and the sintering temperature.

Olevsky et al. [2012a] modeled the thermo-electro-mechanical problem using the commercial program COMSOL to analyze the scalability of Spark Plasma Sintering. Their work aims to study the influence of four different tool sizes and various temperature regimes on the grain growth and the densification behavior. In [Giuntini et al., 2013], this model is used to optimize the tool geometry to avoid overheating in the sample.

In [Mondalek et al., 2011], see also [Mondalek, 2012], the strain rate tensor is additively decomposed into a plastic diffusion part under load as well as a diffusion part by electro-migration and by surface tension. It is emphasized that, due to the motion of the upper punches, the temperature in the axial direction is not symmetric.

An electro-thermo-mechanical simulation with Abaqus is performed in [Wolff et al., 2012]. In their work, they develop a micro-mechanical thermo-viscoplastic model with a decomposition of the strain rate tensor into an elastic, thermal and viscoplastic part. The model serves to simulate spark plasma sintering of lead.

All these publications are based on an additive split of the strain rate tensor. In this work, a different approach is considered. The material model is developed on the basis of a multiplicative decomposition of the deformation gradient. In contrast to the mentioned publications, this work also addresses the thermodynamical consistency i.e. the fulfillment of the Clausius-Duhem inequality.

1.4 Scope of Thesis

The main topic of this thesis is the development of a new constitutive model describing the sintering behavior of copper powder. For this purpose, various experiments are performed to investigate the force and temperature-rate behavior as well as the creep behavior of the powder material. Furthermore, tension tests with sintered specimens are performed to gather information concerning the increasing tensile yield stress during sintering. Moreover, thermo-electrical properties such as the heat capacity as well as the thermal and electrical conductivity are measured. In particular, it is the temperature and relative density dependence of the conductivities of the copper powder material that is of interest. For the simulation of the entire process, the graphite tool system has to be modeled too. For this reason, the temperature-dependent thermo-electrical properties for graphite are measured as well. With all these experiments at hand, it is possible to develop a large strain compressible thermo-plasticity model to describe the essential material behavior. The model is constructed in such a way that it fulfills the Clausius-Duhem inequality. It contains a decomposition of the deformation gradient into four parts – precisely an elastic, a thermal, plastic and creep part – that is studied here for the first time.

The numerical solution of the multi-physical problem consisting of the thermal, electrical and mechanical field is done with the finite element method. The commercial finite element program Abaqus serves to perform the numerical simulation. Due to the fact that the documentation does not deliver a deep insight into the equations, the numerical solution procedure of the multi-field problem with the finite element method is described in its details. This offers a better understanding of the coupling between the fields and the discretized equations.

In the last chapter, all the information is brought together for the simulation of the FAST-process. With the developed material model, the sintering process can be simulated and is then compared to experimental data to verify the quality of the developed model.

1.5 Outline

This thesis is divided into eight chapters. Chapter 2 offers a description of the FAST-process, the experimental setup and the experiments to define the thermo-mechanical behavior of copper powder – as well as a description of uniaxial compression experiments for the development of a model to compute the radial stresses, which – together with the axial stresses – define the current stress state. For the heat equation as well as the stationary charge equation, the thermo-electrical properties have to be measured, which are: the heat capacity, the thermal and electrical conductivity. Within the FAST-process, the powder is inserted into a graphite die and heated by an electrical current. Therefore, one has to model the graphite material as well. Additionally, if two parts get in contact, an electrical resistance occurs due to the surface topology. To account for this non-perfect contact, measurements to determine the electrical contact resistance are performed.

Chapter 3 serves to summarize the fundamentals of Continuum Mechanics. This includes the kinematics of deformable bodies as well as the introduction of the stress tensor, the heat flux and the electric current density. Furthermore, the thermo-electro-mechanical balance equations are introduced, which are the balance of mass, linear and angular momentum, energy, entropy and the Maxwell equations. Moreover, the chapter contains a description of the concept of dual variables, which is important for the development of a material model.

The material model Chapter 4 starts with a summary of the essential material behavior of copper powder during sintering. Afterwards, the temperature-dependent yield function is introduced, followed by an explanation of the multiplicative decomposition motivated by the material behavior. For the development of the material model, a free energy function is postulated and additively separated into parts describing the different effects. On the basis of the Clausius-Duhem inequality, the material model is developed to consider thermodynamical consistency. With the help of this inequality, it is possible to derive the evolution equations for the internal variables. Finally, the constitutive equations for the heat flux and electrical current density are derived and the heat conduction equation is formulated.

The proposed material model has to be adapted to the experiments, which is done in Chapter 5. In a second step, the parameter identification procedure is explained briefly – and the three-dimensional material model is reduced to the one-dimensional case of constrained compression. Based on this algorithm, the large strain thermoplasticity model is adapted to the experiments in Chapter 2. The identified model serves to make predictions and to enable comparison with experiments, as it is of interest to investigate the model behavior beyond the experiments used for the identification. Afterwards, the thermo-electrical properties for copper as well as graphite are fitted to the experimental data. Based on the experimental data, it is possible to identify the electrical contact conductance of the graphite-graphite as well as the graphite-copper contact. Additionally, the thermal contact conductance for the copper-copper contact is fitted to data from literature.

The physical problem behind the FAST-process is a coupled multi-field problem that consists of the thermal, electrical and the mechanical field. This initial boundary value problem is stated in its local form in Chapter 6. For a better insight into the coupling and the discretized equations, which can not be found in detail in the Abaqus documentation, the solution procedure is explained in this chapter. The solution procedure using finite elements is based on variational formulations. The following numerical solution is explained with the h-version of finite elements and the monolithic approach, leading to a differential-algebraic equation system that has to be solved in the time domain. The time integration is done with the backward Euler method, leading to a system of nonlinear equations that has to be solved in each time step. Its solution is performed with the Multilevel-Newton algorithm (MLNA). On the local level of the MLNA, the stresses and the consistent tangent operator are calculated, which is explained in detail.

The numerical simulation of the FAST-process with the commercial program Abaqus can be found in Chapter 7. In a first step, the graphite tool system is studied without any powder, and the temperature distribution is compared to experimental data. Moreover, a PID-controller is introduced to allow temperature control at the thermocouple position. Subsequently, the whole thermo-electro-mechanical coupled sintering process is simulated. For this purpose, the finite strain compressible thermo-viscoplasticity is implemented into Abaqus via a user subroutine. The sintering process simulations allow to predict the temperature, stress, as well as the relative density distribution – and the values are compared to the experimental data.

Chapter 8 serves to summarize the main aspects of the thesis and to provide an outlook for future research work.

2 Experimental Observations

This chapter focuses on a detailed description of the various experiments designed for material model development. First of all, the FAST-process is described and the experimental setup is shown. As the radial stresses are required for the purpose of material parameter identification, the according measurement procedure is explained. A model for the computation of the radial stresses is developed with the help of these experiments, followed by a description of the different experiments performed in the FAST/SPS-machine at the BGU. In order to obtain the real powder deformation, calibration experiments serve to determine the machine behavior under mechanical and thermal loads. For the material characterization, different experiments are designed and performed in order to develop a constitutive model for the sintering process of the copper powder material. Due to the thermo-mechanical nature of this process, it is necessary to determine the thermal parameters of the powder. Furthermore, the thermo-electrical properties of the graphite tool system are investigated.

2.1 FAST-Process

The FAST-process is characterized by the simultaneous application of an electric current and an uniaxially applied pressure. During the FAST-process, a powder is inserted into a die (which is usually made out of graphite) and is then simultaneously compressed by a uniaxial force and heated by a high pulsed DC current with a relatively low voltage of approximately 10 V. The pulsing patterns of the DC current consist of a sequence of pulses with current and no current, see Fig. 2.1b. In this work, a non-pulsed DC is used, see Fig. 2.1a. The current flows directly through the graphite die and the graphite punches, thus inducing Joule heating. If a conducting powder material is used, the powder is intrinsically heated by the current, while a non-conducting powder – ceramics, for example – is heated by the surrounding graphite punches and the die. The maximum axial pressure is limited to the mechanical strength of the graphite die. This high-density graphite combines good mechanical strength with high temperature resistance and good electrical and thermal conductivity.

Although Field Assisted Sintering is also known as Spark Plasma Sintering, there are controversial discussions whether plasma is present. Experiments show the absence of plasma in the process, [Hulbert et al., 2009].

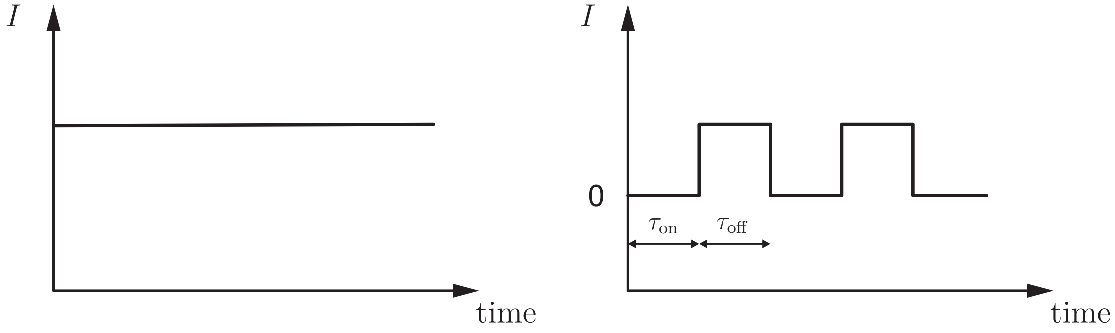

(a) Non-pulsed DC

(b) Pulsed DC, where τ_{on} denotes the time with current and τ_{off} is the time without any current.

Figure 2.1: Pulsed and non-pulsed DC current

In the early stages of the sintering process, in which the density is low, the electrical resistance of the powder is high because of the geometric constriction of the powder contacts (if the powder particles are conductive).

In [Frei et al., 2007], the sintering of copper spheres to copper plates is investigated. The experimental setup is developed in such a way that the current varies, while the temperature remains constant. It is observed that the electric current tends to enhance neck formation and neck growth. Furthermore, simulations show that the current density and the temperature reach a maximum around the neck because of the geometric constriction. Even if the overall temperature is constant due to the small necks in the early stages, the high current at these contacts leads to high temperatures in these areas.

Apart from the temperature, it is also the pressure that influences the powder consolidation. The applied uniaxial force leads to plastic deformations at the contacts between the powder particles and enhances the arising contacts, [Kieback and Trapp, 2011]. Additionally, the yield stress decreases with increasing temperature and leads to further plastic deformations and consolidation. Therefore, the simultaneously applied temperature and pressure lead to a faster compaction than diffusion-driven sintering. In summary, the FAST-process has several advantages, which are: higher heating and cooling rates, shorter hold times, fewer processing steps, short processing times, no need for sintering aids and enhanced material properties by minimized grain growth.

2.2 Experimental Setup

A typical FAST-machine, see Fig. 2.2a, consists of a vacuum chamber, water cooled electrodes for current and force loading as well as a power supply with high

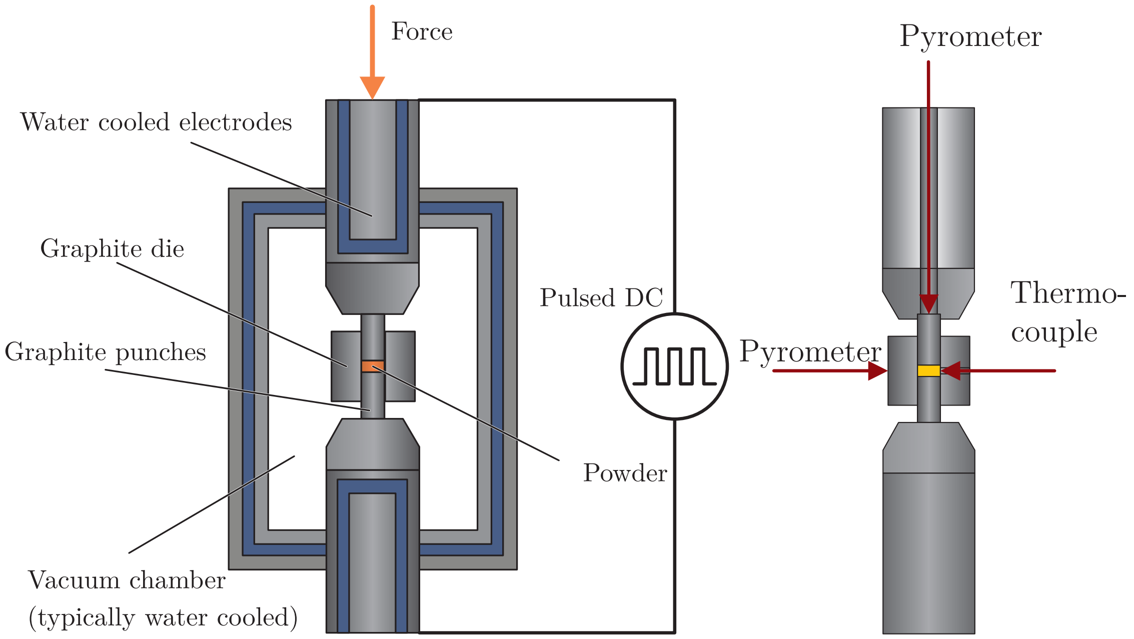

(a) Schematic of a typical FAST-machine (b) Measurement points of temperature control

Figure 2.2: FAST-machine

electrical current at low voltages. The die and punch are usually made out of graphite because of its high electrical and thermal conductivity and because of its temperature resistance even at temperatures above 3300 K. Oxidation takes place in air and limits the application to 800 K, [Jäger et al., 2000]. This is one of the reasons for the use of a vacuum chamber. In typical FAST-machines of the FCT group (a German manufacturer), the current ranges from 3000 A to 48 000 A at 8 V to 12 V. The maximum pressing force ranges from 12.5 kN to 4000 kN. The recorded data during an experiment are the time, force, temperature, current, voltage and displacement.

Fig. 2.3 shows the typical prescribed quantities, which are the temperature and the uniaxial force. The parameters to be defined are the (1) heating rate, (2) maximum/hold temperature, (3) cooling rate, (4) load rate, (5) maximum/hold force and (6) unloading rate. The temperature in the machine is controlled by a thermocouple in the die or by a pyrometer, see Fig. 2.2b. A PID-controller serves to change the power in order to follow a prescribed temperature path.

The displacement of the entire system is measured. This includes the graphite tool system, the electrodes and the powder itself. Due to the mechanical and thermal loads, it is necessary to characterize the thermal expansion and the machine compliance – while the real powder displacement is determined by calibration experiments without any powder. With these calibration data, the true powder

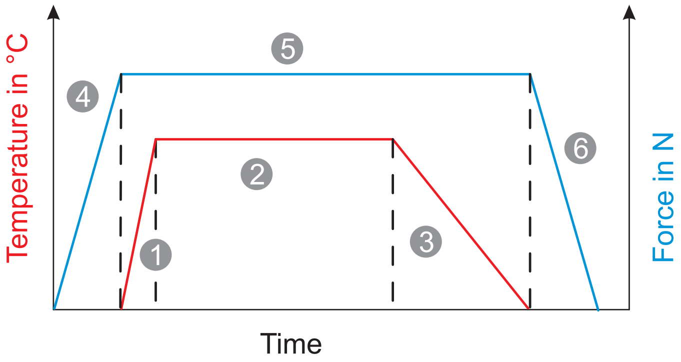

Figure 2.3: Prescribed quantities of a typical FAST-experiment

shrinkage curves can be computed.

Spark Plasma Sintering Furnace HP D 5/1


(a) FAST machine HP D5/1

(b) Vacuum chamber with graphite tool system

(c) Glowing die/punch system

Figure 2.4: Experimental setup

All sintering experiments are performed with the FAST-machine located at BGU in Israel. The FAST-machine was built by FCT-Systeme GmbH and its type is HP D5/1, see Fig. 2.4a. In Tab. 2.1, the main properties are listed. Fig. 2.4b shows the vacuum chamber with its electrodes and the graphite tool system. Fig. 2.4c shows how the heat treatment during the process causes the graphite die and punch to glow. The FAST-machine is force-controlled by a hydraulic cylinder. The working temperature ranges from room temperature (25 °C) to 2400 °C. There are two possibilities to control the temperature. Between 25 °C and 1000 °C, the

Table 2.1: Properties of FAST-Machine HP D5/1

Type	mould dimension mm	components dimension mm	max. force kN	max. voltage V	max. current A	power consumption kW
HP D 5	∅60 × 80	∅30	50	7.2	5500	45

temperature can be controlled by a thermocouple located in a borehole of the die near the powder. For a temperature control above 1000 °C the temperature is controlled by a pyrometer, which is able to measure the temperature above 400 °C. The exact temperature measurement positions are shown in Fig. 2.5b.

In this work, temperature control is governed by a thermocouple – due to the fact that the maximum temperatures are about 700 °C and that the measurement point is close to the powder. Thus, it is assumed that the measured temperature represents the temperature of the powder. The powder material under consideration is pure copper, see Sect. 2.3, which has a good thermal conductivity, see Fig. 2.50b. The graphite tool system consists of the die, the punch and the cone part, see Figs. 2.5a and 2.6a to 2.6c. All dimensions in the drawings are given in mm. For the computation of the stretch $\lambda = h/H_0$ and the initial relative density, the initial height H_0 is required. In the FAST-machine, the minimum applied force is

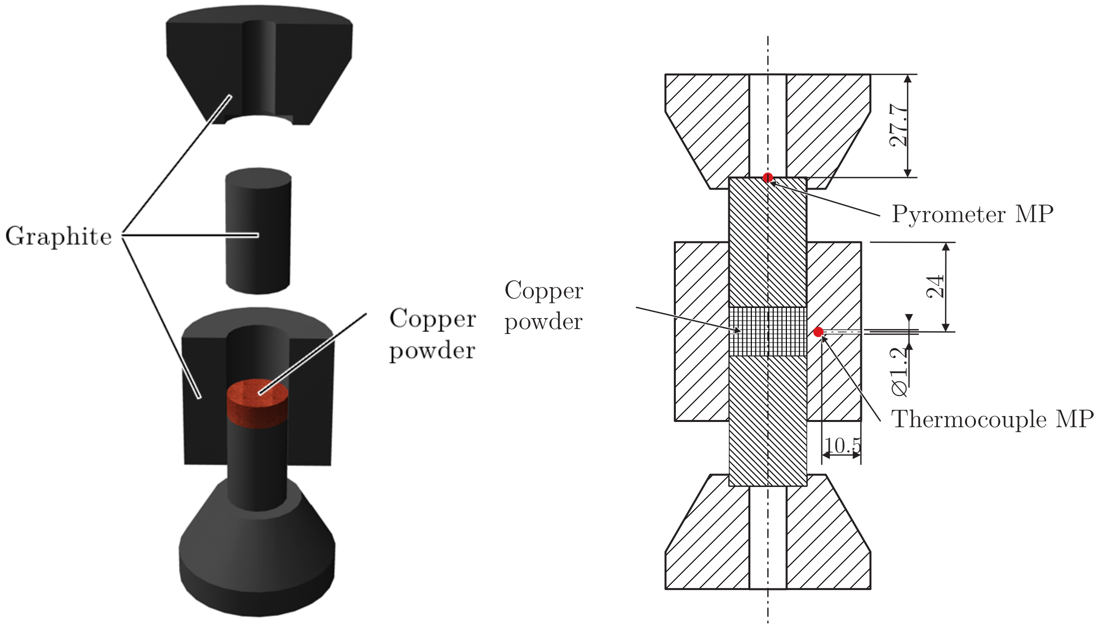

(a) Graphite tool system with copper powder (b) Temperature measurement positions

Figure 2.5: Tool system and temperature measurement points (MP)

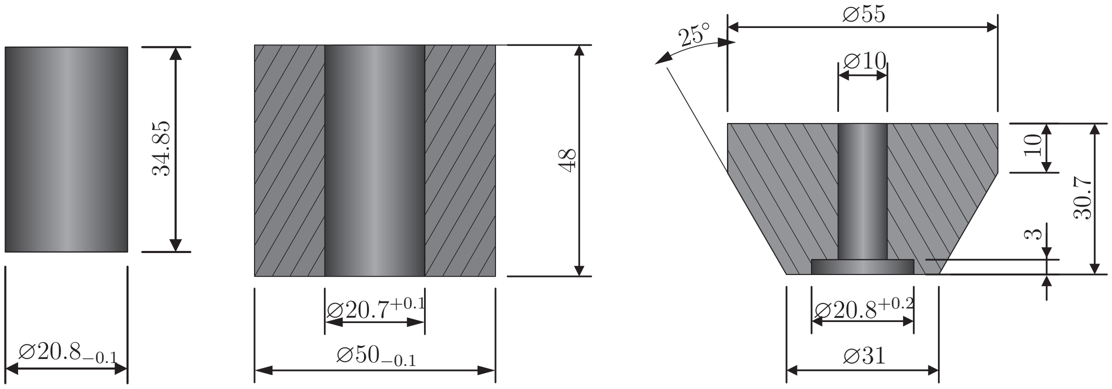

(a) Punch (b) Die (c) Cone part

Figure 2.6: Graphite tool system

approximately 2.5 kN. A reason for this is that all parts have to be in contact to be able to apply an electric current. All experiments performed in the FAST-machine concern the following sequence, as illustrated in Fig. 2.7. At first, the powder is filled into the die. Afterwards, the graphite tool system with the powder inside is placed into the machine and the minimum axial force of 2.5 kN is applied. Subsequently, after the unloading the initial height, H_0 is measured with a caliper. This height is used for the computation of the relative density and the stretch. Furthermore, the final height and the measured displacement are compared to the initial height for verification purposes.

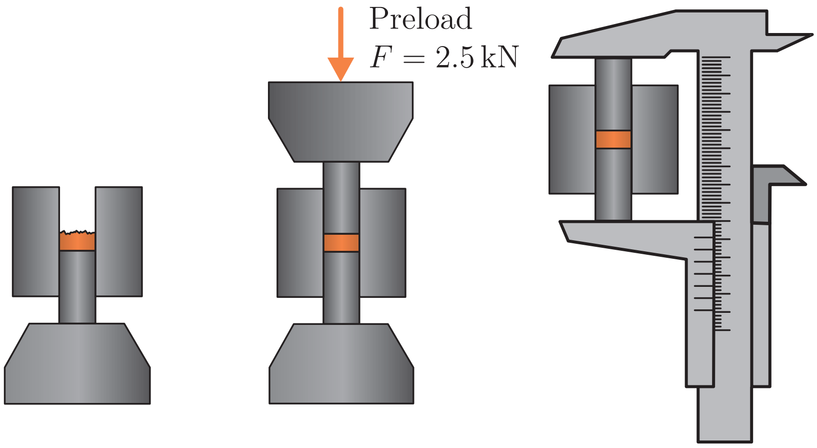

1. Powder fill-in **2.** Precompaction **3.** H_0 measurement

Figure 2.7: Precompaction in FAST-machine due to minimal force and measurement of initial height

2.3 Copper Powder

The investigated material in this project is a fine-grain copper powder. The density of the bulk material (Cu) is 8960 kg m^{-3}. Fig. 2.8a shows the copper powder – and Fig. 2.8b shows an optical image of the loose powder with irregular shaped particles and an average grain size of 4 µm. Fig. 2.9 provides optical images of the sintered specimen with different relative densities. As can be seen, there is a decrease in pores (the darker parts) with increasing relative density. The surface of a nearly fully dense specimen with a relative density of 0.99 is shown in Fig. 2.10a. The etched surface shows grains with an average size of 7 µm to 8 µm, see Fig. 2.10b.

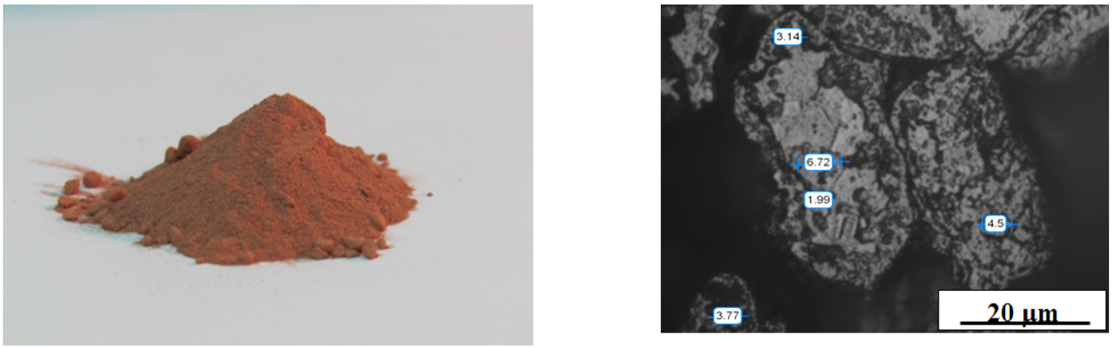

(a) Copper powder

(b) Irregular shaped copper particles with an average grain size of 4 µm provided by Prof. Frage

Figure 2.8: Loose copper powder images provided by Prof. Frage

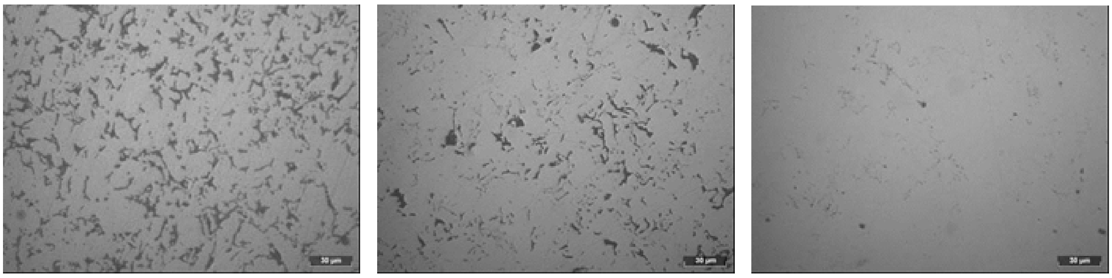

(a) Relative density of $\rho_{\text{rel}} = 0.70$

(b) Relative density of $\rho_{\text{rel}} = 0.80$

(c) Relative density of $\rho_{\text{rel}} = 0.90$

Figure 2.9: Optical images of sintered copper powder provided by Prof. Frage (resolution 30 µm)

(a) Relative density of $\rho_{\text{rel}} = 0.99$

(b) Etched surface of nearly fully dense specimen with $\rho_{\text{rel}} = 0.99$ and an average grain size of 7 µm to 8 µm

Figure 2.10: Optical images of sintered copper powder with $\rho_{\text{rel}} = 0.99$ provided by Prof. Frage (resolution 30 µm)

2.4 Uniaxial Compression Experiments for Determining the Radial Stresses

For the material parameter identification, not only the prescribed axial stress is required, but also the radial stress, see Chapter 5. Due to the laterally constrained compaction, an increase in axial force leads to radial stresses – as a result of the fact that radial expansion of the powder is restricted by the die, see Fig. 2.5a.

It is not possible to measure the radial stresses in the FAST-machine. Thus, the radial stresses are determined for cold compaction experiments. Based on this, it is possible to develop assumptions concerning the estimation of the radial stresses in the FAST-process.

These experiments are conducted with a Zwick testing machine Z100 in the Institute of Applied Mechanics at the Clausthal University of Technology, see Fig. 2.11a. For the circumferential strain measurement, four equally spaced strain gauges are applied around the graphite die, see Fig. 2.11c. The height of the strain gauges is chosen in such a way that – after the powder compaction with 25 kN – the strain gauges are in the middle of the resulting powder sample. Because the lower punch is fixed and the upper punch is moving, only one of the distance-values decreases. Fig. 2.11b illustrates the experimental setup including the graphite die and punch as well as the clamping. The idea is to measure the circumferential strains at the outer surface of the die. Assuming an elastic behavior of the graphite, the radial stresses can be computed inversely. A similar procedure is used in [Bier et al., 2007]. During the process, the Zwick software records force, displacement and time, while the circumferential strains of the four strain gauges are logged by an Autolog 3000.

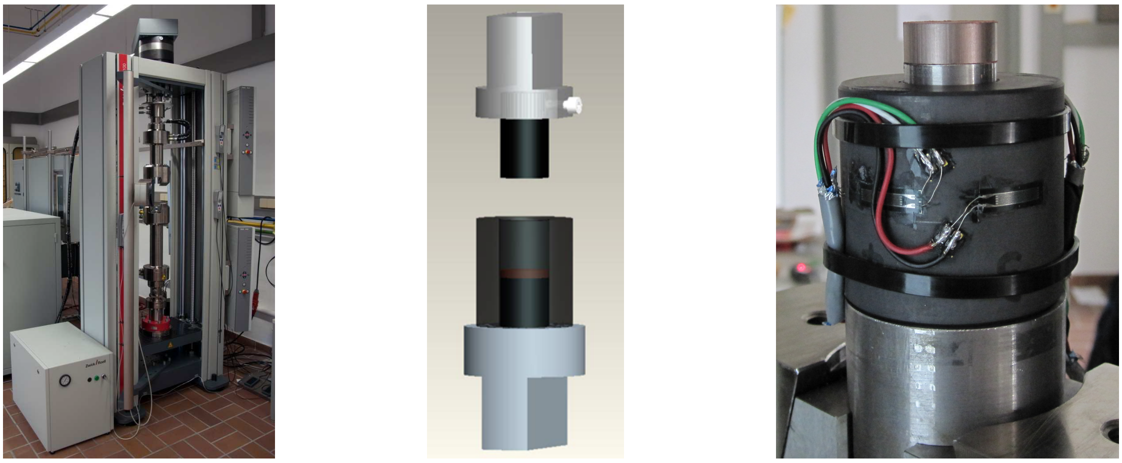

(a) Zwick testing machine (b) Sketch of experimental setup (c) Graphite die with strain gauges

Figure 2.11: Experimental setup

2.4.1 Calibration Experiments

As a consequence of the applied force on the one hand, the punches get radially in contact with the surrounding die and, on the other hand, the testing machine deforms elastically. These circumstances demand a calibration procedure for the circumferential strains and for the displacements in axial direction. The measured axial displacement u_{axial} is the sum of the change in the height of the powder $u_{\text{axial}}^{\text{powder}}$ and the machine compliance $u_{\text{axial}}^{\text{system}}$

$$u_{\text{axial}} = u_{\text{axial}}^{\text{powder}} + u_{\text{axial}}^{\text{system}} \quad \Leftrightarrow \quad u_{\text{axial}}^{\text{powder}} = u_{\text{axial}} - u_{\text{axial}}^{\text{system}}. \tag{2.1}$$

The elastic deformation of the machine including the graphite system is measured by an experiment without any powder. The measured displacement is used to calibrate the measured data and to determine the real powder displacement, see Fig. 2.12a. Thus, the overall measured displacement u_{axial} is subtracted by the system displacement $u_{\text{axial}}^{\text{system}}$ in dependence of the force in order to compute the powder displacement $u_{\text{axial}}^{\text{powder}}$.

The graphite punches do not only deform in axial direction, they deform in radial direction too, hence they also exert a pressure on the die in radial direction. For this reason, the circumferential strains $\varepsilon_{\varphi\varphi}$ can be decomposed into two parts, one part resulting from the pressure of the punch $\varepsilon_{\varphi\varphi}^{\text{punch}}$ and one from the powder pressure against the inner die surface $\varepsilon_{\varphi\varphi}^{\text{powder}}$

$$\varepsilon_{\varphi\varphi} = \varepsilon_{\varphi\varphi}^{\text{punch}} + \varepsilon_{\varphi\varphi}^{\text{powder}} \quad \Leftrightarrow \quad \varepsilon_{\varphi\varphi}^{\text{powder}} = \varepsilon_{\varphi\varphi} - \varepsilon_{\varphi\varphi}^{\text{punch}}. \tag{2.2}$$

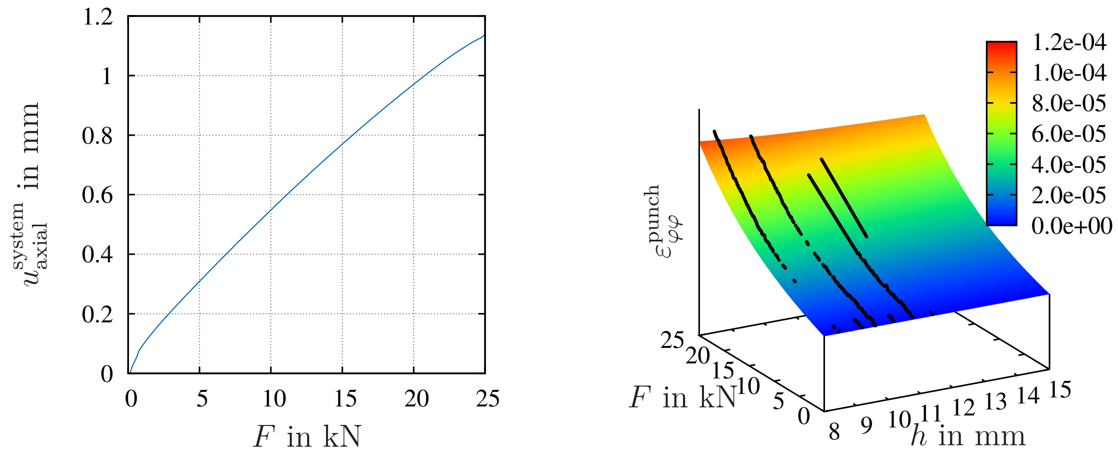

(a) Axial calibration data

(b) Radial calibration data

Figure 2.12: Calibration experiments

In order to compute powder induced radial stresses from the circumferential strains, one has to subtract the strains induced by the punches from the measured circumferential strains. In the experiment, it is necessary to consider that, during the process, the upper punch moves towards the strain gauge position, which is why the radial punch expansion leads to an increase of the measured strains. To account for this fact, steel samples with different heights (8.47 mm, 9.2 mm, 9.6 mm, 10.2 mm, 10.8 mm and 11.4 mm) were produced and loaded up to 25 kN. The measured circumferential strains are shown as black lines in Fig. 2.12b. The following function is fitted to the measured strains

$$\varepsilon_{\varphi\varphi}^{\text{punch}} = \tilde{\varepsilon}_{\varphi\varphi}^{\text{punch}}(F,h) = a_\varepsilon \exp(b_\varepsilon F) + c_\varepsilon \frac{F}{h} + d_\varepsilon \tag{2.3}$$

and the fitted parameters are specified in Tab. 2.2. This results in a scalar field for the punch-induced strains depending on the actual punch position (height) and the force, see Fig. 2.12b. These values are subtracted from the measured data in order to get the real circumferential strains caused by the powder expansion.

Table 2.2: Circumferential strain calibration function parameters

a_ε	b_ε	c_ε	d_ε
12.29	80.70×10^{-6}	9.51×10^{-3}	-12.29

2.4.2 Data Evaluation

For the data evaluation, the stretch λ is given by

$$\lambda = \frac{h}{H_0} = \frac{H_0 - u_{\text{axial}}^{\text{powder}}}{H_0} = 1 - \frac{u_{\text{axial}}^{\text{powder}}}{H_0} \tag{2.4}$$

with the current height h and the initial height of the powder H_0. In the literature on powder materials, the stresses, displacements and other quantities are often connected to the relative density, which is defined by

$$\rho_{\text{rel}} := \frac{\rho}{\rho_{\text{solid}}} \tag{2.5}$$

with ρ as the current density. The density of the pore-free bulk material is symbolized by ρ_{solid}. The porosity Φ is connected to the relative density and can be calculated by

$$\Phi = 1 - \rho_{\text{rel}}. \tag{2.6}$$

The copper powder used in the experiments has a density of $\rho_{\text{solid}} = 8960\,\text{kg}\,\text{m}^{-3}$. The initial relative density is approximately 0.35 and in the limit case of full compaction the relative density reaches $\rho_{\text{rel}} = 1$. In the case of an uniaxial laterally constrained compression, see Eq. (3.45) and Eq. (16) in the appendix, neglecting the die's expansion, the expression

$$\lambda\rho = \rho_0 \tag{2.7}$$

is valid.[1] The division of both sides by the bulk density ρ_{solid} yields

$$\frac{\rho}{\rho_{\text{solid}}} = \frac{\rho_0}{\lambda\rho_{\text{solid}}} \quad \Leftrightarrow \quad \rho_{\text{rel}} = \frac{\rho_{0,\text{rel}}}{\lambda}. \tag{2.8}$$

In the experiments, the relative density is computed by

$$\rho_{\text{rel}} = \frac{\rho_0}{\lambda\ \rho_{\text{solid}}} = \frac{m_{\text{powder}}}{\lambda V_0\ \rho_{\text{solid}}} = \frac{m_{\text{powder}}}{\lambda H_0 A_0\ \rho_{\text{solid}}} = \frac{m_{\text{powder}}}{h A_0\ \rho_{\text{solid}}} \tag{2.9}$$

$$= \frac{m_{\text{powder}}}{(H_0 - u_{\text{axial}}) A_0\ \rho_{\text{solid}}}, \tag{2.10}$$

where $m_{\text{powder}} = 15\,\text{g}$ is the amount of powder inserted in the die. The initial volume V_0 is given by the product of the initial height H_0 and the area of the punches, respectively of the powder A_0. The axial stress can be determined by the current prescribed force F and the constant area neglecting the die's expansion

$$\sigma_{\text{axial}} = \frac{F}{A_0}. \tag{2.11}$$

---

[1] In a more general case, the relation $\rho = \rho_0 / \det \mathbf{F}$, where $\mathbf{F}$ is the deformation gradient and $\det \mathbf{F} = \lambda$ holds for the uniaxial compression case, see Eq. (16) in the appendix.

The diameter of the punches is given by $d = 20.75\,\mathrm{mm}$.

For the data evaluation, the mean of the four circumferential strains is computed

$$\bar{\varepsilon}_{\varphi\varphi}^{\mathrm{powder}} = \frac{1}{n}\sum_{i=1}^{n} \varepsilon_{\varphi\varphi}^{\mathrm{powder}}. \tag{2.12}$$

2.4.3 Conversion Procedure of Circumferential Strains into Radial Stresses

A finite element simulation with Abaqus is performed to determine the conversion of the circumferential strains into radial stresses. The idea behind this simulation is that the die deforms only elastically. Thus, the radial stress can be converted with the help of the function $f(h)$, depending on the actual height of the powder

$$\sigma_{\mathrm{radial}} = f(h)\bar{\varepsilon}_{\varphi\varphi}^{\mathrm{powder}}. \tag{2.13}$$

The elastic properties of graphite are determined at the institute of Prof. Frage at the Ben Gurion University using ultrasonic measurements, [Workman et al., 2007; Krautkrämer and Krautkrämer, 1990], leading to the Young's modulus $E = 11\,500\,\mathrm{MPa}$, which is identical to the producer's specification, see [SGL Carbon GmbH, 2014], and the Poisson ratio $\nu = 0.2$. The geometry of the specimen is shown in Fig. 2.13. It consists of $n_{\mathrm{e}} = 17520$ eight-noded quadratic axisymmetric elements (CAX8). The total number of unknowns is $n_{\mathrm{eq}} = 106374$. The length h, where the pressure of $\sigma_{\mathrm{radial}} = 1\,\mathrm{MPa}$ is applied, see Fig. 2.13, is varied from 15 mm to 8 mm in 0.2 mm steps. This means that each point in Fig. 2.14 is the result of a finite element simulation, where the circumferential strain at the middle of the strain gauge at the outer surface of the die is calculated. The conversion factor is determined by $f(h) = \sigma_{\mathrm{radial}}/\varepsilon_{\varphi\varphi}^{\mathrm{powder}}$. For a smooth representation, the data points are fitted by a third order polynomial

$$f(h) = p_1 h^3 + p_2 h^2 + p_3 h + p_4 \tag{2.14}$$

with the parameter values specified in Tab. 2.3. With this function at hand, the circumferential strains are converted into radial stresses at the inner die surface by including the changing height of the powder during the compaction experiment.

Table 2.3: Parameters of conversion function

p_1 $\mathrm{MPa\,mm^{-3}}$	p_2 $\mathrm{MPa\,mm^{-2}}$	p_3 $\mathrm{MPa\,mm^{-1}}$	p_4 MPa
-46.29	2095	-3.39×10^4	2.41×10^5

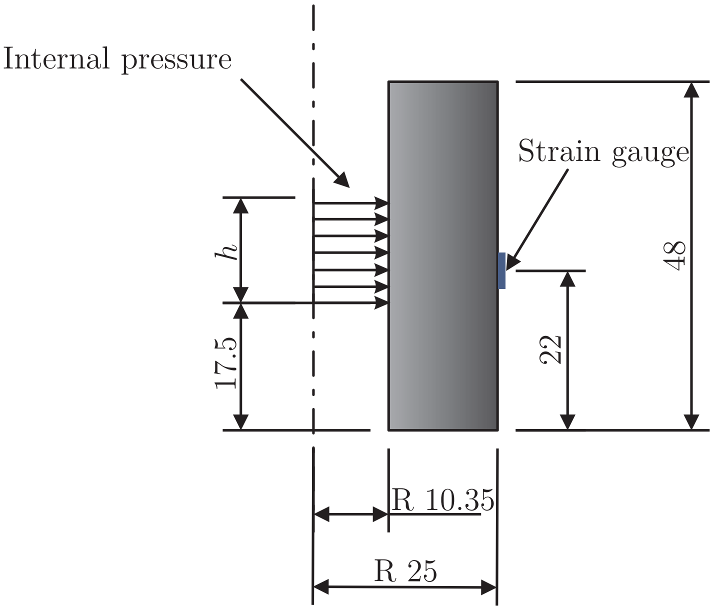

Figure 2.13: Geometry of FE-mesh in mm to determine the conversion function

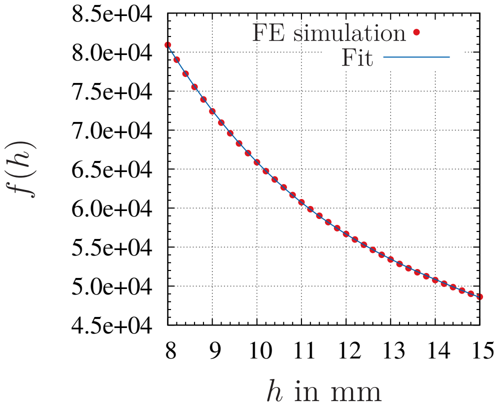

Figure 2.14: Determined conversion function with dependence of the actual height of the powder. A third order polynomial is used for the data fitting.

2.4.4 Uniaxial Powder Compaction Experiments

Fig. 2.15a shows the prescribed force. It is increased up to 25 kN with a velocity of $5\,\mathrm{kN\,min^{-1}}$. The measured quantity of the Zwick testing machine is the axial displacement. Additionally, the circumferential strains are measured by four strain gauges applied on the graphite die.

The experiments start with filling 15 g copper powder into the die. Then, the die is knocked onto the table five times to ensure an equal fill level of the graphite die. Subsequently, the assembly is put in the testing machine and a preforce of 100 N is applied. By applying the preforce, it is ensured that the punch is in contact with the powder, which is an important prerequisite for the measurement of the initial powder height.

After the preforce is raised, the program stops and the gap between the die and the upper clamping is measured by means of a video extensometer. With this information at hand, the initial height of the copper powder is computed. The circumferential strains at the outer surface of the graphite die are measured by the applied strain gauges and recorded by an Autolog 3000 measurement system built by Peekel. Subsequently, the force controlled experiment starts and the force is linearly increased up to 25 kN.

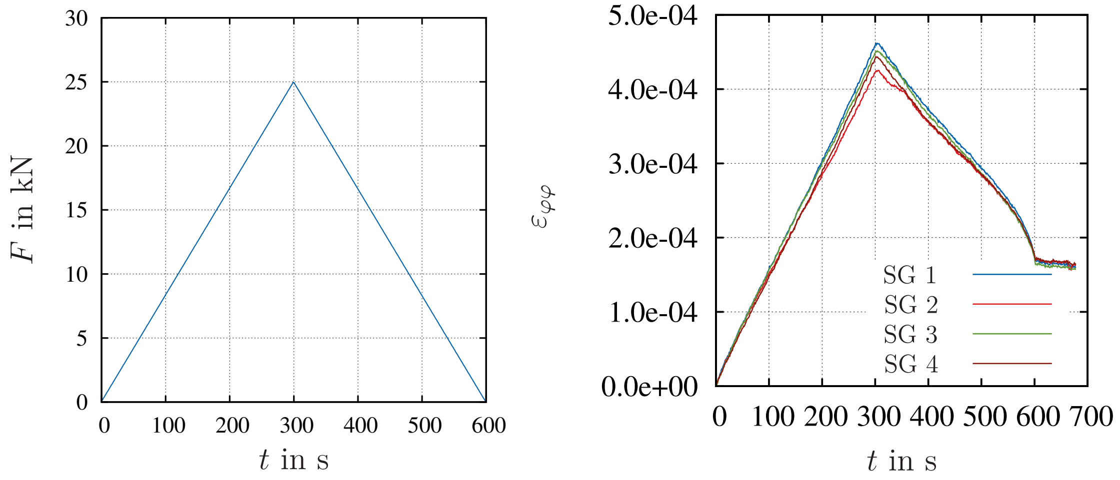

(a) Prescribed force

(b) Measured circumferential strains of one experiment

Figure 2.15: Uniaxial powder compaction

Fig. 2.15b shows the measured circumferential strains for the four strain gauges over the time. The different curves coincide very well – except at the maximum value, where a deviation of approximately 8% can be observed. Fig. 2.16a shows the measured and calibrated axial displacements. It can be seen that the uncalibrated displacement decreases in the unloading section. The actual powder displacement is obtained by subtracting the calibration curves. After the calibration, the powder displacement remains constant while the force decreases. The circumferential strain calibration reduces the maximum value and subtracts the punch-induced strain, see Fig. 2.16b. The uniaxial powder compaction experiment is repeated five times in order to prove the reproducibility. Fig. 2.17a shows the calibrated copper powder deformation.

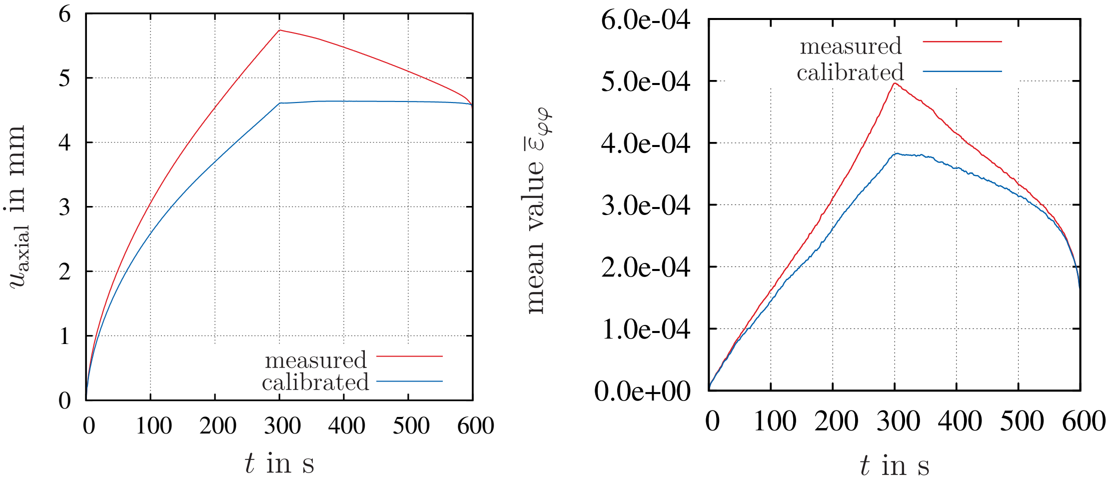

(a) Measured and calibrated axial displacements

(b) Measured and calibrated circumferential strains

Figure 2.16: Calibration of experimental data

A deviation of the final displacement between the different experiments can be observed. A reason for this deviation could be the different initial heights of the powder. The initial heights, as listed in Tab. 2.4, are measured after applying a preforce of 100 N. The initial height in the first experiment is the lowest height of all experiments. The displacement in this experiment is the lowest one as well. This means that the copper powder was more compacted at the beginning of the experiment than in the other experiments. The highest height and maximum displacement occurs in the third experiment. As a conclusion, it can be pointed out that the initial height is a uncertain quantity. The question is when the punch makes initial contact with the powder. In the FAST-process, the powder heights deviate less because of the applied preforce of 2.5 kN. In Fig. 2.17a, the displacement curves

Table 2.4: Measured initial heights of copper powder in mm

H_0^{M1}	H_0^{M2}	H_0^{M3}	H_0^{M4}	H_0^{M5}
13.105	13.670	14.420	14.170	14.310

M3, M4 and M5 are almost identical. The curves M1 and M2 show a large deviation and have lower displacements. Fig. 2.17b shows the mean strain over the four strain gauges for different materials. Curve M1 shows the largest strain. The curves M2, M3, M5 show little deviation, whereas curve M4 has the lowest strains. In terms of the material model, the stretch λ and the relative density ρ_{rel} are of greater interest than the measured displacements. In Fig. 2.18a, the stretch is plotted over the time for the 5 experiments. At the end of the experiment, the stretch varies from 0.61 to 0.65, which corresponds to a deviation of approximately 6%. The relative density in Fig. 2.18b shows an acceptable deviation of approximately 3.5%. The reason for this lower deviation in contrast to the measured displacement originates from the fact that the initial height, see Tab. 2.4, is taken into account for the computation of the relative density and the stretch according to Eq. (2.9) and Eq. (2.4). The final mean stresses of five experiments are computed according to

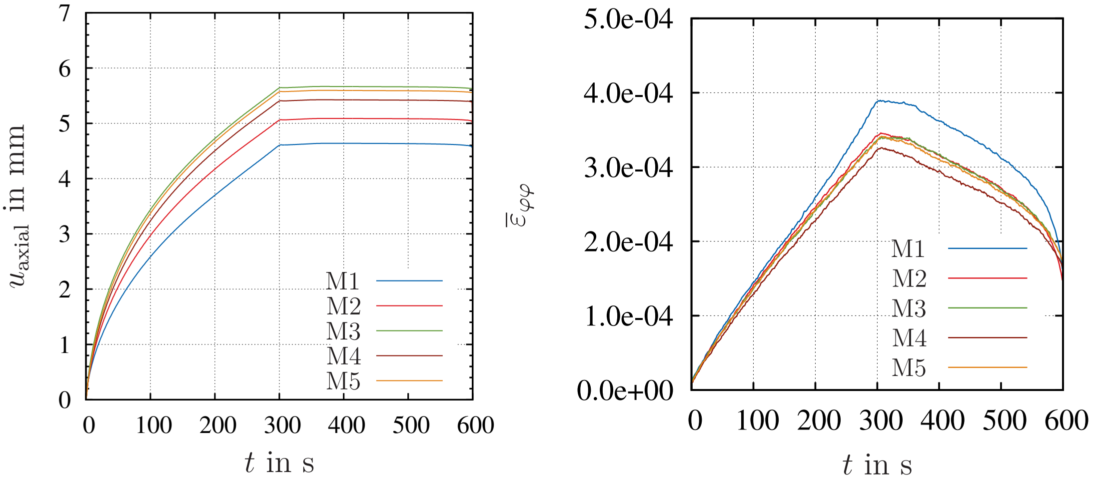

(a) Axial displacements over time

(b) Circumferential strains over time

Figure 2.17: Calibrated data of 5 experiments

$$\bar{\sigma}_{\mathrm{axial}} = \frac{1}{n}\sum_{i=1}^{n} \sigma_{\mathrm{axial}}, \qquad \bar{\sigma}_{\mathrm{radial}} = \frac{1}{n}\sum_{i=1}^{n} \sigma_{\mathrm{radial}}, \qquad n = 5 \tag{2.15}$$

and plotted over the relative density in Fig. 2.19a. The axial and radial stresses serve to determine the stress ratio $R_{\mathrm{Rad/Ax}}$. It can be seen that the ratio is nearly constant in the investigated range of relative density.

2.4.5 Multi-Step Loading/Unloading Experiments

In addition to the previous tests, multi-stage experiments are performed in order to investigate the evolution of the radial stresses for loading and unloading conditions.

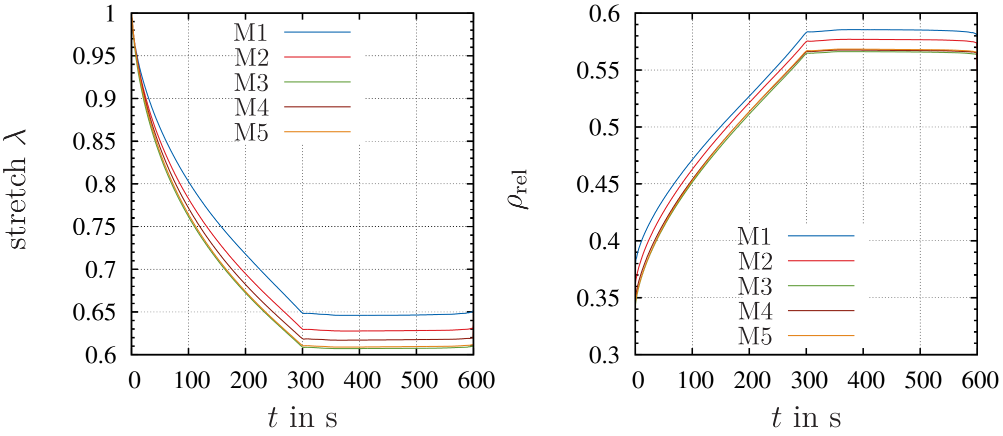

(a) Stretch vs. time (b) Relative density vs. time

Figure 2.18: Computed quantities plotted over the time

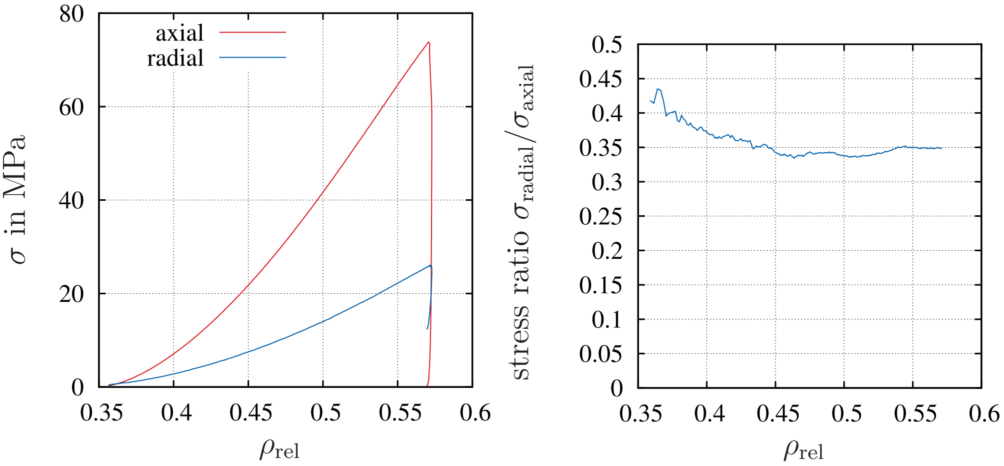

(a) Mean stresses over relative density (b) Radial-axial stress ratio over the relative density

Figure 2.19: Uniaxial powder compaction

This information will be utilized for the estimation of the radial stresses, see Sect. 2.4.6. Fig. 2.20a shows the prescribed force over the time. At first, the force is increased up to 2.5 kN and held constant for 3 min. Afterwards, the multi-stage loading up to 5 kN, 10 kN, 15 kN, 20 kN and 25 kN is carried out, followed by the unloading to 2.5 kN. Again, the circumferential strains are measured and shown in Fig. 2.20b. One can observe a remaining circumferential strain after each unloading, which increases over the time. The powder is axially compacted in the punch-die system and – as a result – the powder induces a pressure on the inner die surface, which is measured by the strain gauges. Fig. 2.21a lists the measured and calibrated axial displacements. In the unloading range, the uncalibrated displacements show a decrease that originates from the machine and the tool system compliance. The calibrated displacement shows a constant value in the unloading range. The circumferential strains are calibrated by subtracting the punch-induced strains according to the calibration data in Fig. 2.12b. In Fig. 2.21b and Fig. 2.21a, one can observe a change of the slope in the loading range at the height of the maximum value of the last loading regime. The experiments are repeated five times. For each experiment, the circumferential strains are recorded by the four strain gauges, and the mean value out of the four curves is computed. Then, Eq. (2.13) serves to compute the radial stresses, based on the strain values. The resulting axial and radial mean stresses over the relative density are shown in Fig. 2.22a while Fig. 2.22b represents the stresses plotted over the time. In the following, the performed experiments serve as a basis for the proposition of a model for the computation of the radial stresses in the FAST-machine.

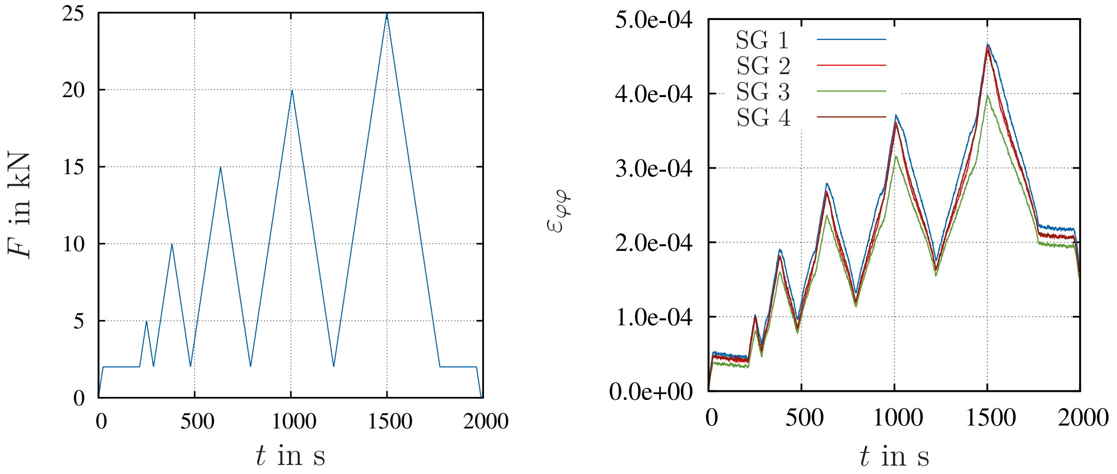

(a) Prescribed force

(b) Measured circumferential strains of one experiment

Figure 2.20: Multi-step loading/unloading experiments

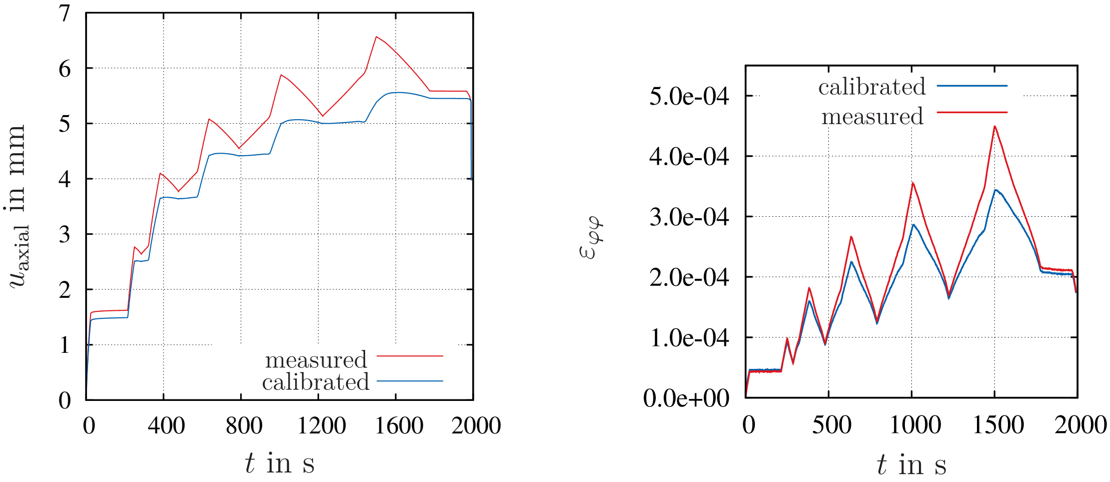

(a) Measured and calibrated axial displacements

(b) Measured and calibrated circumferential strains

Figure 2.21: Calibration of experimental data

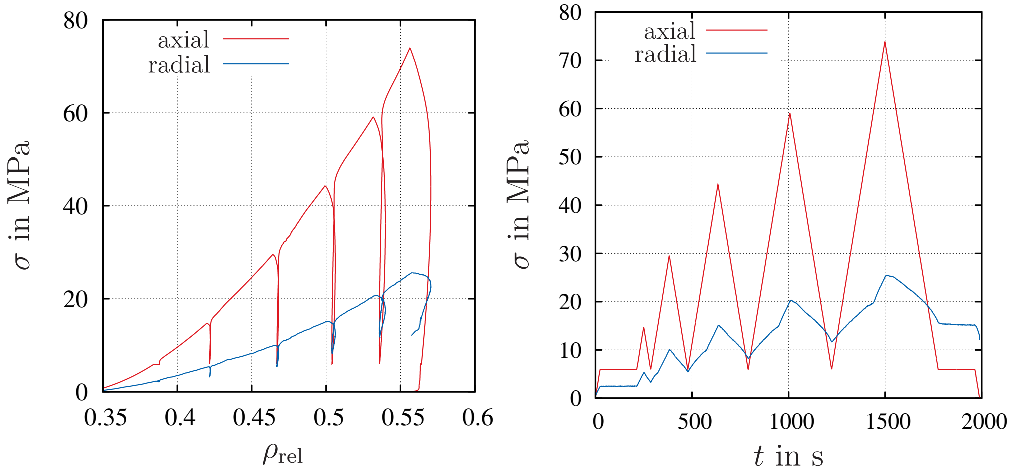

(a) Mean stresses over relative density

(b) Radial and axial stresses over the time

Figure 2.22: Multi-step loading/unloading powder compaction

2.4.6 A Model for the Radial Stress Computation

The axial stresses are prescribed in the sintering experiments. The radial stresses cannot be measured, which is due to the high temperatures and the closed vacuum chamber. In contrast, the radial stresses are required for the definition of the current state of stress. Therefore, the proposed model draws on the ratio between the axial and the radial stresses. Based on this model, it is possible to compute the radial stresses.

First, the measured stress ratio, see Fig. 2.19b, is compared to literature data. Fig. 2.23 shows the radial-axial stress ratio for different literature data. The ratio is computed using the measurement data of [Bier et al., 2007] for irregular-shaped copper powder. The same sort of powder is used in this project. In [Carnavas, 1996], the Poisson ratio was determined for spherical, irregular and dendritic shaped copper powder. This measurement data was fitted by Carnavas [1996] to the relationship suggested by Kuhn and Downey [1971],

$$\nu = k(\rho_{\mathrm{rel}})^n. \tag{2.16}$$

The parameters can be found in Tab. 2.5. Drawing on this data, the ratio can be computed by the formula in Eq. (2.17).

Table 2.5: Model parameters for irregular copper powder according to [Carnavas, 1996]

rel. density range	k	n
0.45 – 0.60	0.168	0.214
0.77 – 0.95	0.325	0.174

For a fully compacted material, the copper powder should behave like solid copper. Let us assume linear elasticity with $\mathbf{T} = E/(1+\nu)\,[\mathbf{E} + \nu/(1-2\nu)(\mathrm{tr}\,\mathbf{E})\mathbf{I}]$. In the die, the powder is axially compressed and the deformation in radial direction is assumed to be zero, which leads to the following strain vector $\mathbf{E}^T = \begin{Bmatrix} \varepsilon & 0 & 0 & 0 & 0 & 0 \end{Bmatrix}$ and to the stress state $\mathbf{T}^T = \begin{Bmatrix} \sigma_{\mathrm{axial}} & \sigma_{\mathrm{radial}} & \sigma_{\mathrm{radial}} & 0 & 0 & 0 \end{Bmatrix}$. Computing the radial-axial stress ratio leads to

$$R_{\mathrm{Rad/Ax}} = \frac{\sigma_{\mathrm{radial}}}{\sigma_{\mathrm{axial}}} = \frac{\nu}{1-\nu} = 0.5385 \tag{2.17}$$

As a result, the radial-axial stress ratio is only dependent on the Poisson ratio. According to [Carnavas, 1996], the Poisson ratio for pure copper is assumed to be $\nu = 0.35$. The resulting value in equation Eq. (2.17) is used as a limit case for the proposed model $R_{\mathrm{Rad/Ax}}(\rho_{\mathrm{rel}} = 1, \Theta = 25\,^{\circ}\mathrm{C}) = 0.5385$. As irregular-shaped copper powder is used for the experiments in this thesis, it is the data from [Bier et al.,

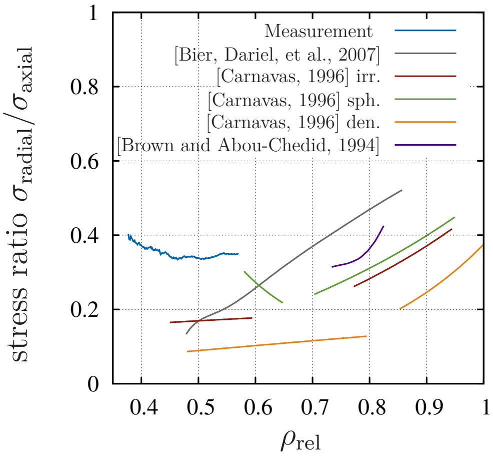

Figure 2.23: Comparison of measured radial-axial stress ratio to experimental data from [Bier et al., 2007] for copper powder, from [Carnavas, 1996] for irregular spherical and dendritic-shaped copper powder and from [Brown and Abou-Chedid, 1994] for spherical copper powder.

2007] and [Carnavas, 1996] as well as the measurement data of Sect. 2.4 that are relevant. An exponential function is assumed to fit the data and the limit case for $\rho_{\text{rel}} = 1$, see Fig. 2.24a. The model reads

$$R_{\text{Rad/Ax}}(\rho_{\text{rel}}, \Theta) = c_1 \exp(c_2 \rho_{\text{rel}}) + c_3 s_\Theta, \tag{2.18}$$

with the model parameters c_1, c_2 and c_3.

Additionally, the temperature has to be taken into account. Here, it is assumed that the ratio at the melting temperature of solid copper at 1085 °C is $R_{\text{Rad/Ax}}(\rho_{\text{rel}} = 1, \Theta = 1085\,°\text{C}) = 1$. Between room temperature and the melting temperature, a linear dependence of the ratio on the temperature is assumed, see Fig. 2.24b. Furthermore, it is proposed that the ratio is not directly dependent on the temperature, but instead on a temperature arclength defined by

$$s_\Theta = s_\Theta(t_0) + \int_{t_0}^{t} \langle \dot{\Theta}(\tau) \rangle \, \mathrm{d}\tau, \qquad s_\Theta(t_0) = \Theta(t_0) \tag{2.19}$$

This arclength evolves during positive temperature changes and stays constant for negative temperature rates due to the Macaulay brackets, $\langle x \rangle$. They have the property $\langle x \rangle = 0$ for $x \leq 0$ and $\langle x \rangle = x$ for $x > 0$. This prevents a decrease of the ratio in the case of a decreasing temperature while a constant force is applied. Later on, an example will be given to explain this in more detail. The radial stresses are computed by the proposed ratio Eq. (2.18) and a stress arclength with the following equation

$$\sigma_{\text{radial}} = \tilde{R}_{\text{Rad/Ax}}(\rho_{\text{rel}}, \Theta) \hat{\sigma}_{\text{axial}}(t) + C \varepsilon^{i}_{\text{radial}}(t). \tag{2.20}$$

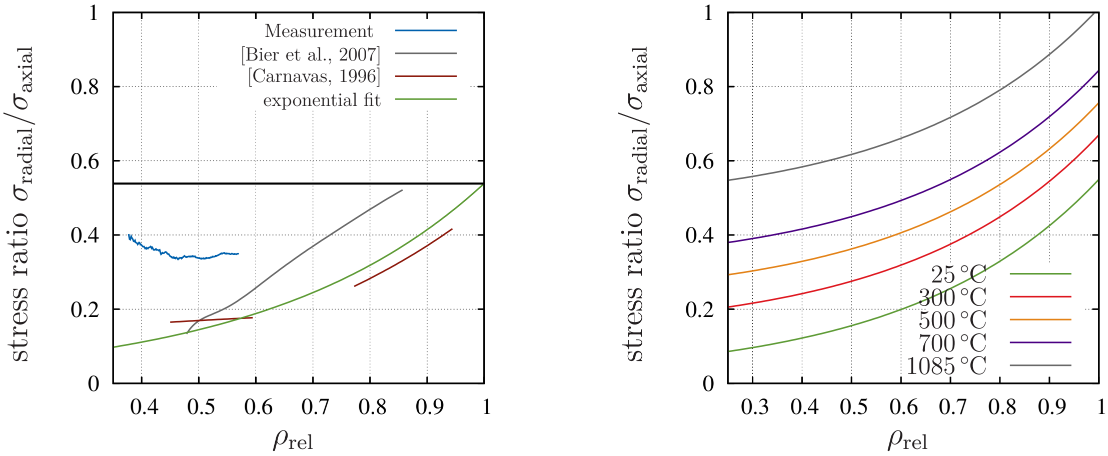

(a) Quadratic fit to different stress ratios from literature

(b) Temperature dependence of stress ratio

Figure 2.24: Radial-axial stress ratio at room temperature

The inelastic strain is taken into account to model the behavior in Fig. 2.22a. The radial stresses increase during the loading part in the multistep experiment, but they do not go back to zero in the unloading range. There are remaining radial stresses due to the constrained compaction by the die system. Thus, the inelastic strain is introduced. It evolves during the loading phase of the experiments and is constant during unloading

$$\dot{\varepsilon}^i_{\text{radial}} = \Lambda \operatorname{sgn}(\sigma_{\text{axial}}), \tag{2.21}$$

$$\dot{k} = \Lambda \alpha_k (k_\infty - k), \tag{2.22}$$

$$f(\sigma_{\text{axial}}, k) = |\sigma_{\text{axial}}| - k = 0, \tag{2.23}$$

with the model parameters α_k, k_∞ and C in Eq. (2.20). This differential-algebraic equation (DAE) system is solved by the backward Euler method. The initial yield stress is set to zero, $k(t_0) = 0$. The identified model parameters out of a least-square fit match the experiments in Fig. 2.25a, and the stress ratios in Fig. 2.24a are given in Tab. 2.6.

Table 2.6: Parameters for the radial stress computation model

c_1	c_2	c_3	C	k_∞	α_k
0.0388	2.6311	4.3541×10^{-4}	3213.6 MPa	257.6258 MPa	77.3402

Fig. 2.25a shows the measured and computed radial stresses with Eq. (2.20) over the time. The model represents the experimental data very well.

Additionally, the radial-axial stress ratios are compared. The measured ratio is computed by the measured axial and radial stresses and the model ratio is calculated by the measured axial and the computed radial stresses in Fig. 2.25b. Here, the modeled ratio shows a good agreement with the experimental one. The peaks in the ratio originate from the fact that the axial stress goes back to zero during unloading while the radial stresses are nonzero.

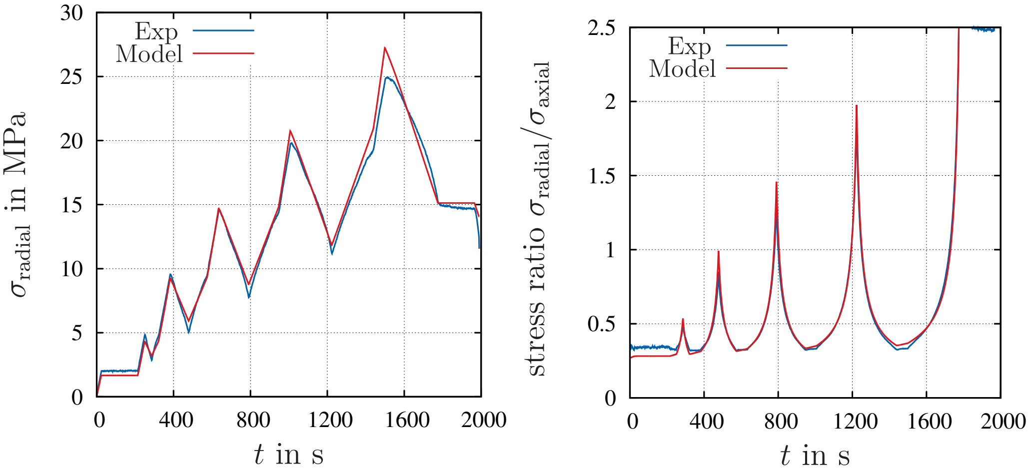

(a) Comparison between measured and computed radial stresses by Eq. (2.20)

(b) Radial-axial stress ratio over the time

Figure 2.25: Comparison of model behavior to measurement data

Fig. 2.26 shows a FAST-experiment. First, the axial stress is increased up to 44 MPa. Subsequently the temperature is increased up to 700 °C and then decreased again, see Fig. 2.26a. The computed radial stress is shown in Fig. 2.26a. Without the temperature arclength in Eq. (2.18), the radial stresses would decrease during the temperature unloading. In this period, the relative density Fig. 2.26b still increases slightly, and it is to be assumed that the radial stresses are not decreasing either, due to the applied axial stress.

Remark 1 *On the one hand, it would be desirable to measure the radial stresses from a viewpoint of material theory. The radial stresses are required to formulate the current stress state. On the other hand, a new machine has to be developed to measure the radial expansion of the graphite die – for example by a dilatometer – and to compute the inner radial stresses of the powder. Strain gauges are not applicable because of the high temperatures up to* 700 °C *and they cannot be welded due to the graphite tool system. Another possibility would be fibre bragg gratings, but as they commonly feature a polymer coating, they would only be suitable for low to medium temperatures. Moreover, discrete element simulations can provide hints concerning the axial radial stress ratio, see for example [Martin et al., 2003]*

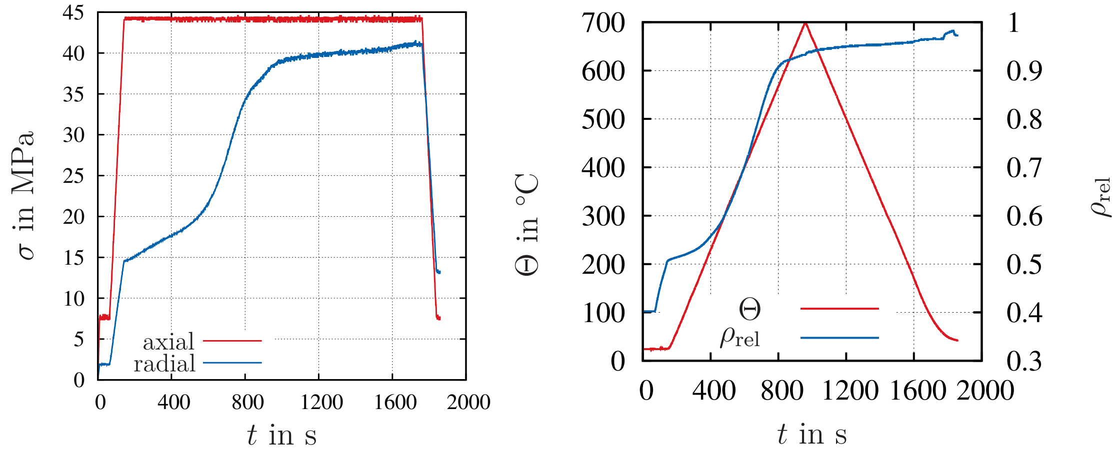

(a) Prescribed axial stress in a FAST-experiment and computed radial stress

(b) Prescribed temperature and measured relative density in a FAST-experiment

Figure 2.26: FAST-experiment and computed radial stresses for plausibility check

and [Pizette et al., 2010] for simulations at room temperature. The author is not aware of any discrete element simulations at higher temperatures that could serve to compute the stress ratio.

The radial stress measurement can be seen as a conflict of objectives between the material theory and a real process. In general, it is not always possible to get all the desired quantities in a real process. Additionally, the thermo-electro-mechanical nature of this production process in a closed vacuum chamber tends to complicate the measurement. Therefore, the proposed model will be used to compute the radial stresses.

2.5 Thermo-Mechanical Behavior of Copper Powder

In this section, all experiments for the characterization of the copper powder are explained. On the basis of the observed material behavior in these sintering experiments, a material model is developed in Chap. 4. All sintering experiments are performed in the FAST-machine at the BGU, as described in Sect. 2.2. For all experiments, 15 g of copper powder are inserted into the die, and the initial height is measured according to Fig. 2.7. Based on this information, the relative density is computed according to Eq. (2.9). Then, the force and the temperature in each of the experiments are prescribed and the displacements are measured. The power is changed by a PID-controller to follow a certain temperature path, which is measured by the thermocouple located in the die, Fig. 2.5b. In the powder metallurgy community, it is common to use the relative density to describe the state of compaction. The same approach is used here too. The relative density and the stretch can be converted into each other by Eq. (2.8). In the sintering experiments, the axial (compressive) stresses are always negative and the negative sign is omitted.

At first, the calibration experiments are described to get the real powder deformation. Subsequently, it is investigated whether the material shows a force-rate as well as a temperature-rate dependence. In common practice, dwell times are often used to fully sinter the material. Therefore, the creep behavior at different temperatures and axial forces is examined. Furthermore, dilatometer experiments serve to analyze the thermal deformation without any applied force due to the fact that there is always a minimal force of 2.5 kN present in FAST-experiments. During the sintering process, the powder turns into a bulk material. Thus, information about the dependence of the tensile yield stress evolution is gathered by tensile experiments.

2.5.1 Calibration Experiments

During a FAST-process, the machine and the tool systems deform due to the applied force and temperature. The resulting machine and tool deformation has to be taken into account to determine the real powder height. In order to determine the actual powder height, every experiment has to be performed twice: one experiment with powder and one calibration experiment without powder, but both based on the same loading path. Fig. 2.27 shows the measured displacement of a calibration experiment. At the beginning of every experiment, a minimum force of approximately 2.5 kN is applied, leading to a jump in the displacements. This preforce is necessary to ensure that all parts are in contact for the application of an electric current. During this precompaction period, the displacements and forces are not recorded in the

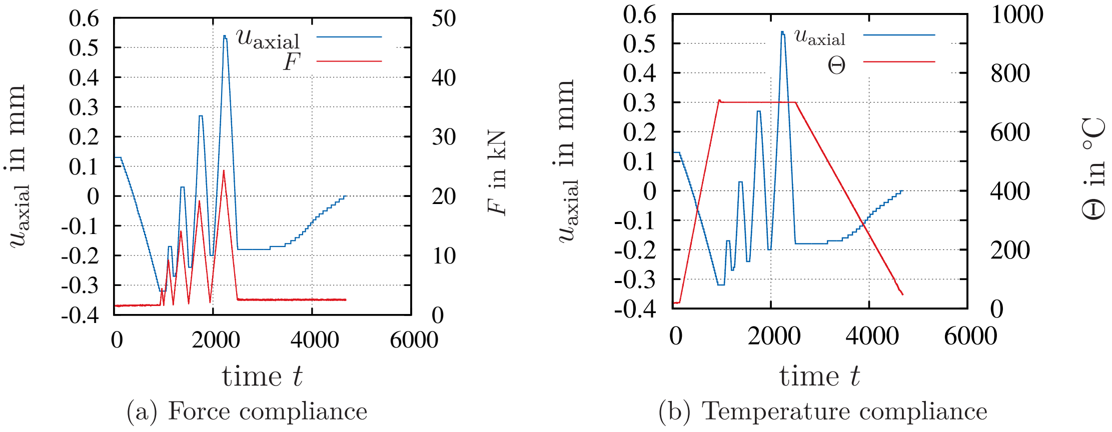

(a) Force compliance
(b) Temperature compliance

Figure 2.27: Calibration experiment

machine. The calibration experiment starts off with an increase in temperature, leading to an expansion of the tool system [2]. Upon reaching a temperature of 700 °C, a loading-unloading experiment is performed with increasing force values. In this case, the graphite punches are compressed and an increasing and a decreasing displacement is recorded. Following a decrease in temperature, the displacement turns out to be zero at the end of the experiment.

Another property of the machine can be observed in Fig. 2.27a by taking a look at the peaks of the force values. If the force is released, the displacement remains constant for a certain time. This hysteresis can be seen in the force-displacement plot in Fig. 2.28a and can be explained by dynamic and sticking friction in the hydraulic cylinder and the plunger guidance.

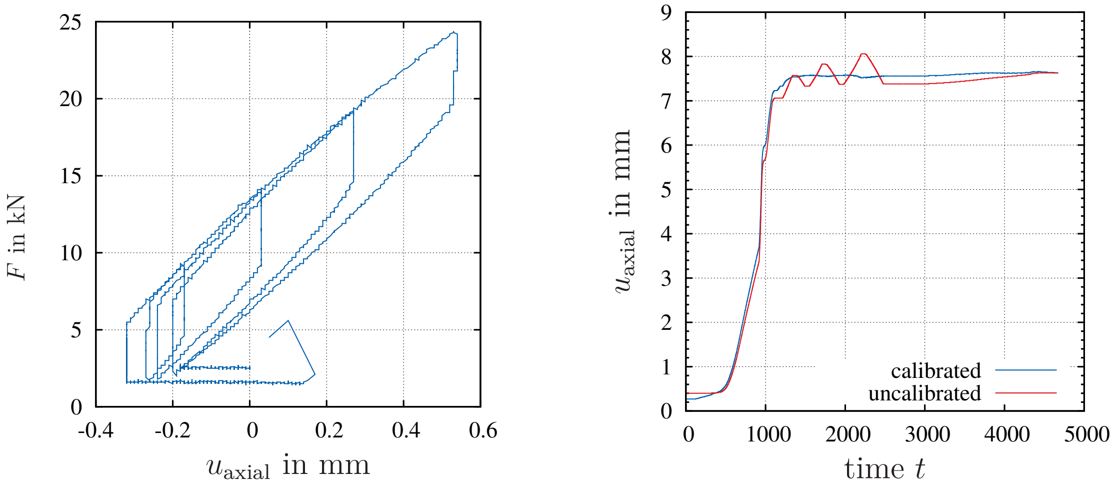

(a) Hysteresis behavior of FAST-machine

(b) Influence of the machine compliance on the measured displacement

Figure 2.28: Hysteresis behavior and influence of machine compliance

Fig. 2.28b illustrates the uncalibrated and calibrated displacement. The uncalibrated displacement shows an increasing and a decreasing displacement if the force is increased and decreased. The calibrated displacement curve shows the actual powder displacement, which will be used in the following for the computation of the relative density.

2.5.2 Force-Rate Experiments

First of all, uniaxial laterally constrained compaction experiments at different temperatures are performed. The goal of these experiments is to check whether

---

[2] In the experiments conducted during the FAST-process, a positive displacement indicates compression while a negative displacement indicates tension.

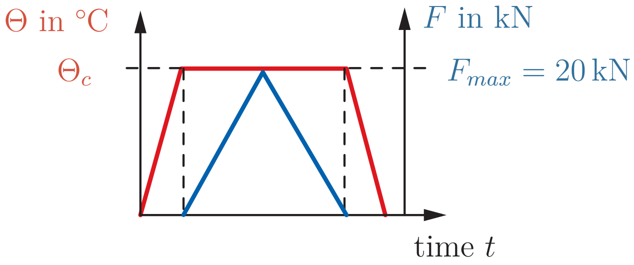

Figure 2.29: Loading paths of rate-experiments

the material shows a force-rate dependence or not. In Fig. 2.29, the prescribed force and temperature path is shown. First, the temperature is raised up to the constant temperature Θ_c with the temperature-rate $\dot{\Theta} = 50\,°\text{C}\,\text{min}^{-1}$, then the force is increased up to 20 kN with different force-rates. These force-rates are $1\,\text{kN}\,\text{min}^{-1}$, $5\,\text{kN}\,\text{min}^{-1}$, $10\,\text{kN}\,\text{min}^{-1}$, $15\,\text{kN}\,\text{min}^{-1}$ and are chosen according to the minimal and maximal machine velocities. Subsequently, the force and the temperature are decreased. Three different temperatures Θ_c are investigated: 25 °C, 300 °C and 700 °C. Fig. 2.30 shows the axial stress over the relative density at room temperature. The copper powder shows no rate-dependence for the chosen force-rates. During the cold compaction, the relative density increases from 0.39 up to 0.54.

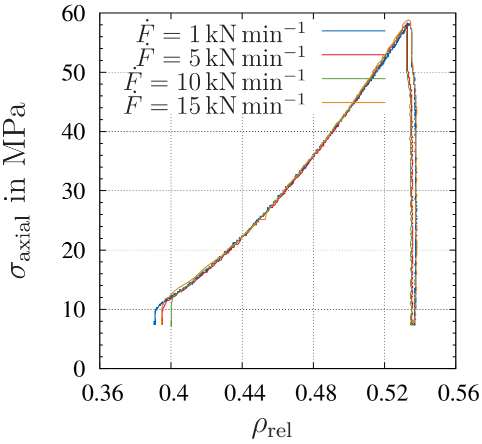

Figure 2.30: Stress over relative density for different force-rates at room temperature

Fig. 2.31a shows the stress over the relative density for experiments at 300 °C. In the experiment with the lowest velocity of $\dot{F} = 1\,\text{kN}\,\text{min}^{-1}$, the largest relative density is reached at the end of the experiment, which can be explained by a higher dwell time at this temperature due to the low force-rate. In contrast to the experiments at room temperature, one can observe a force-rate dependence above 300 °C. In Fig. 2.31b, the relative density over the temperature is plotted. The diagram also shows an increase of relative density due to the temperature, which is negligible in this experiment.

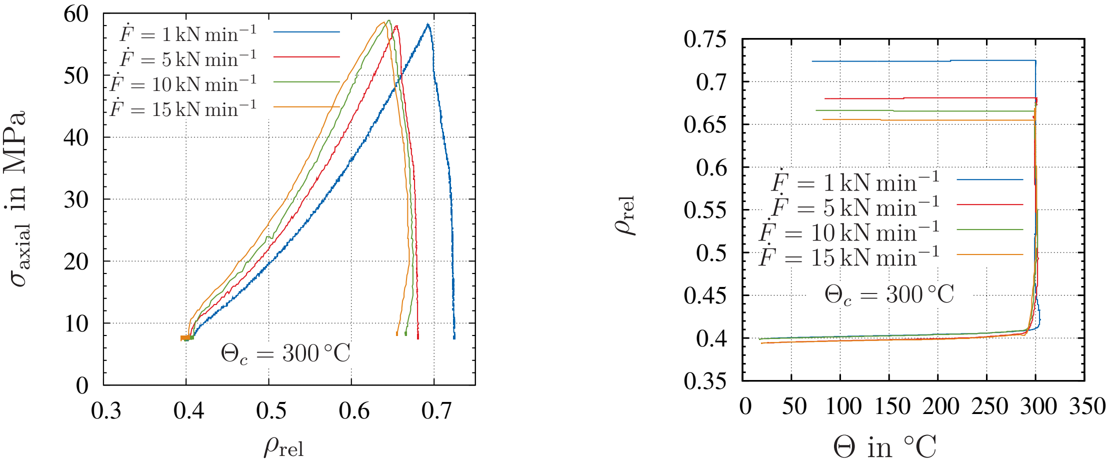

(a) Stress over relative density

(b) Relative density over temperature

Figure 2.31: Investigation of force rate dependence at 300 °C

Finally, the force-rate dependence at 700 °C is investigated. In Fig. 2.32b, the relative density increases from 0.4 up to approximately 0.6 due to the applied temperature. The applied force remains constant during the increase of temperature, as indicated by a horizontal line in Fig. 2.32a. The minimum applied force of 2.5 kN is present during the heating phase. Subsequently, the force is raised up to 20 kN following the different force-rates. It can be seen that all the experiments reach the same final relative density of approximately 0.98. An increasing force-rate leads to a higher stress response in Fig. 2.32a.

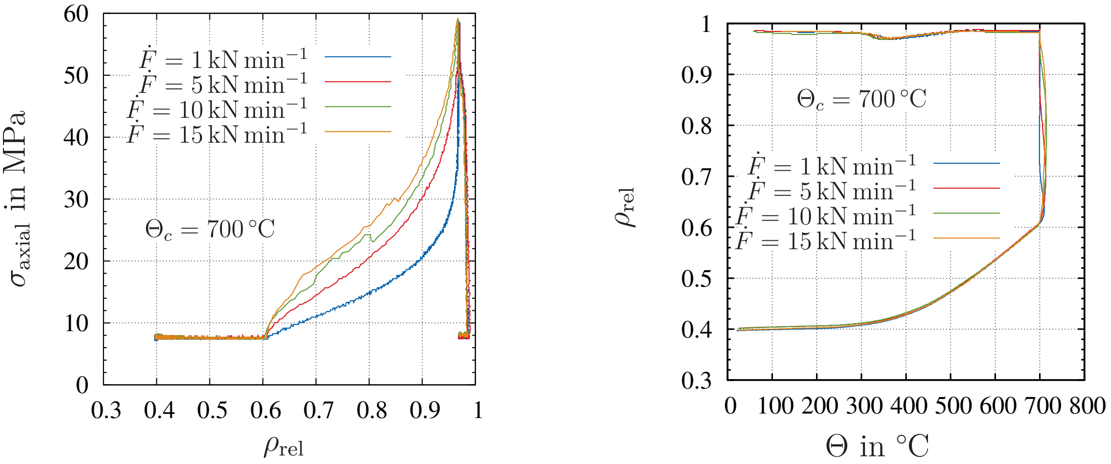

(a) Stress over relative density

(b) Relative density over temperature

Figure 2.32: Investigation of force rate dependence at 700 °C

The experiments reveal that an identical applied axial force at higher temperatures leads to a higher compaction, see Fig. 2.33. The material becomes weaker – and at 700 °C, the applied axial force of 20 kN leads to a state close to full compaction.

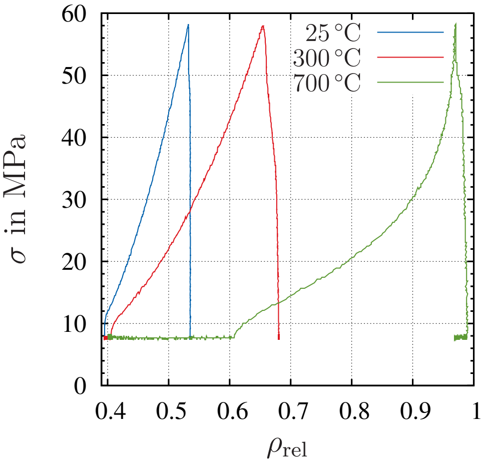

Figure 2.33: Uniaxial powder sintering at different temperatures with $\dot{F} = 5\,\text{kN}\,\text{min}^{-1}$

2.5.3 Temperature-Rate Experiments

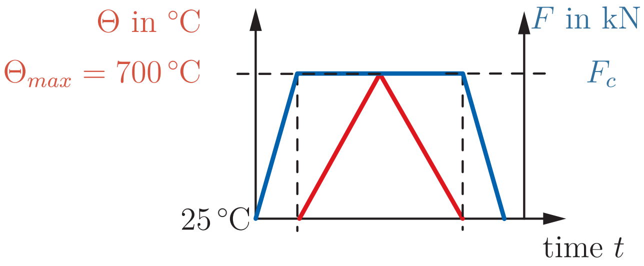

Figure 2.34: Loading paths of temperature rate experiments

The following considerations focus on an investigation of the temperature-rate dependence. In a first step, the force is thus raised to the constant value F_c and, accordingly, the temperature is raised up to 700 °C with the different temperature-rates: $25\,°\text{C}\,\text{min}^{-1}$, $50\,°\text{C}\,\text{min}^{-1}$, $100\,°\text{C}\,\text{min}^{-1}$ and $200\,°\text{C}\,\text{min}^{-1}$. After the cooling process, the force is decreased. Fig. 2.34 shows the loading paths.

At first, the force is raised, leading to an increase in the relative density. This can be seen in the Figs. 2.35 and 2.36, which appears as a vertical line in these diagrams. For an applied force of $F_c = 5\,\text{kN}$, the relative density increases about 0.02, whereas a force of $F_c = 15\,\text{kN}$ leads to an compaction and a change in the

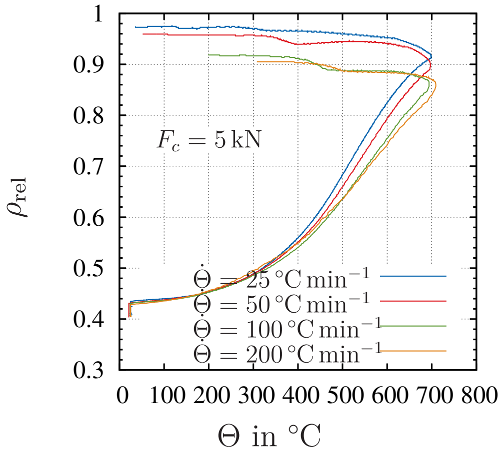

Figure 2.35: Relative density over the temperature with $F_c = 5\,\text{kN}$

relative density of 0.1. The highest increase in relative density is reached with the highest force of $F_c = 25\,\text{kN}$ of approximately 0.2. Afterwards, the temperature is raised up to 700 °C, leading to a large growth in relative density and to increased sintering of the copper powder. Experiments with 15 kN and 25 kN yield a fully sintered copper specimen with a relative density of approximately one. The change of the heating-rate has no significant influence on the progress of the relative density over the temperature, which can be seen in Figs. 2.35 and 2.36.

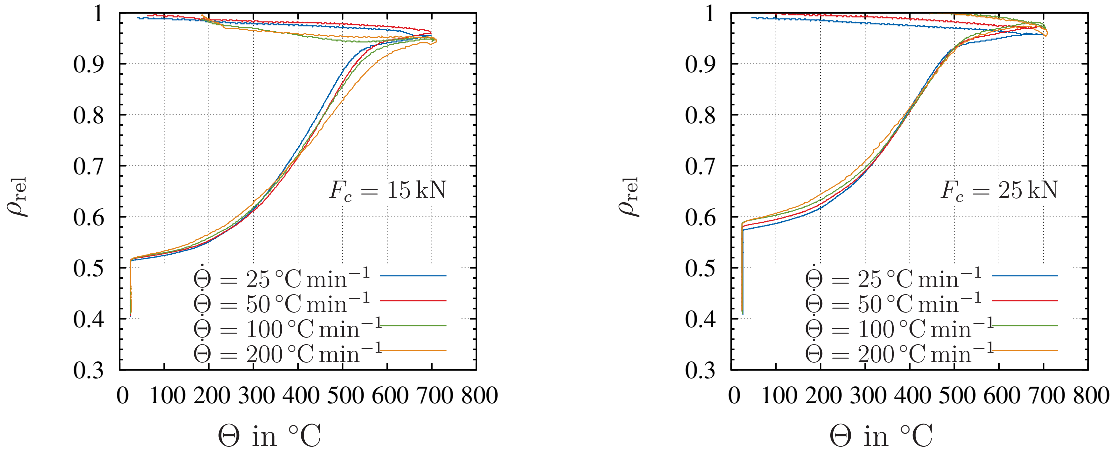

(a) Relative density over the temperature with $F_c = 15\,\text{kN}$

(b) Relative density over the temperature with $F_c = 25\,\text{kN}$

Figure 2.36: Relative density over the temperature for different heating rates.

The relative density over the time is shown in Fig. 2.37 for $F_c = 15\,\text{kN}$ and $F_c = 25\,\text{kN}$. In both figures, first the relative density increases due to the applied axial force. Afterwards, the temperature is raised with different velocities. It can be observed that a higher heating-rate leads to a faster sintering. The final relative density turns out almost the same in all experiments. Thus, higher heating rates can accelerate the production process and can reach the same final density in less time.

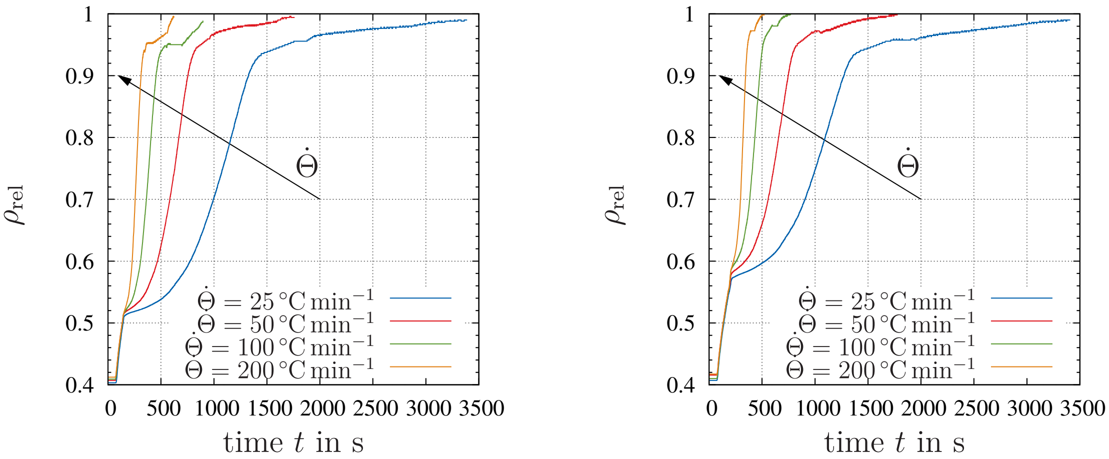

(a) Relative density over the time with $F_c = 15\,\mathrm{kN}$

(b) Relative density over the time with $F_c = 25\,\mathrm{kN}$

Figure 2.37: Relative density over the temperature for different heating rates.

2.5.4 Creep Experiments at Different Temperatures

The following section serves to describe the creep experiments. Often, dwell times help to ensure fully sintered powder in the FAST-experiments. Therefore, it is of interest to investigate the copper powder behavior at constant force and temperature. Fig. 2.38 shows the prescribed force and temperature path. Firstly, the temperature is raised up to the constant temperature Θ_c with the temperature rate $\dot{\Theta} = 50\,°\mathrm{C\,min^{-1}}$. Then, the force is raised up to the constant force F_c and held constant for the dwell time t_h. Finally, the force and the temperature are subsequently decreased. Three different constant force values at five different temperatures are investigated. These are $F_c = 5\,\mathrm{kN}$, 15 kN and 25 kN as well as the temperatures $\Theta_c = 25\,°\mathrm{C}$, 200 °C, 300 °C, 500 °C and 700 °C.

Fig. 2.39b shows the relative density over the time. The vertical dashed lines indicate the beginning of the force dwell time. During the dwell time, the relative density remains nearly constant for the different force values and, accordingly, almost no creep occurs at room temperature. Fig. 2.39a shows the axial stress over the relative density. In this figure, the relative density increases at constant axial stress. Due to the fact that no heating is applied, the overall increase in relative density stays low. At 200 °C, the increase in relative density at constant axial stress and temperature is higher than at room temperature. It reaches a maximum of approximately 9% in Fig. 2.39c.

The stress relative density curves in Fig. 2.39e show an even larger creep behavior. Under a constant force F_c, there is an increase in relative density over the time. It reaches a maximum of approximately 16%. The relative density reaches its limit at 500 °C for F_c =15 kN and 25 kN, see Fig. 2.39g. Thus, no creep occurs anymore. The relative density at $F_c = 5$ kN increases by about 23% at constant temperature and axial stress. The same behavior can be observed at 700 °C. In this case, the full densification is reached faster than at 500 °C and F_c =15 kN and 25 kN. In Fig. 2.39i, the increase in relative density from 0.4 up to 0.6 is related to the applied temperature while the minimum force of 2.5 kN is present.

In summary, the creep behavior is an important mechanism for the sintering of copper powder and has to be incorporated into the material model in Chap. 4.

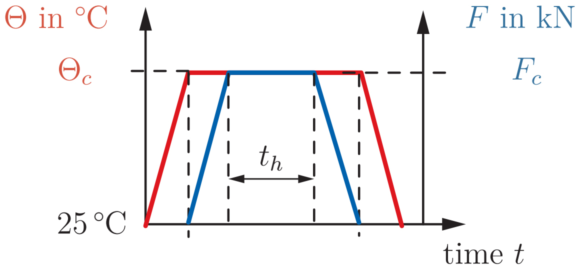

Figure 2.38: Loading paths of creep experiments

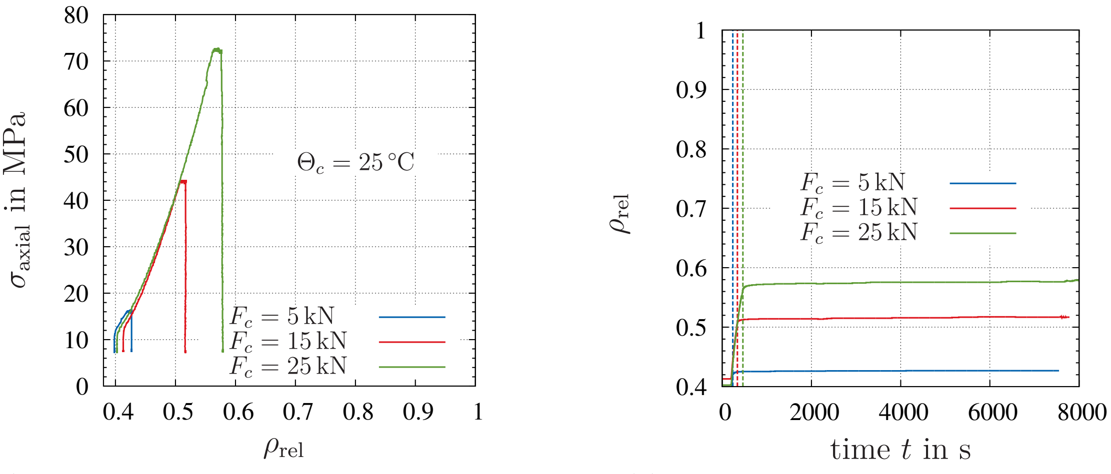

(a) Axial stress over relative density at 25 °C

(b) Relative density over time at 25 °C

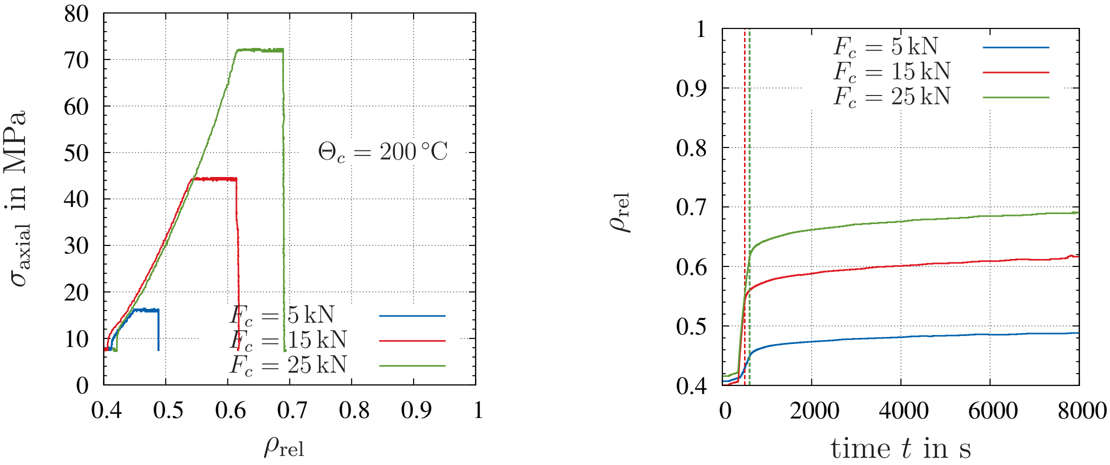

(c) Axial stress over relative density at 200 °C

(d) Relative density over time at 200 °C

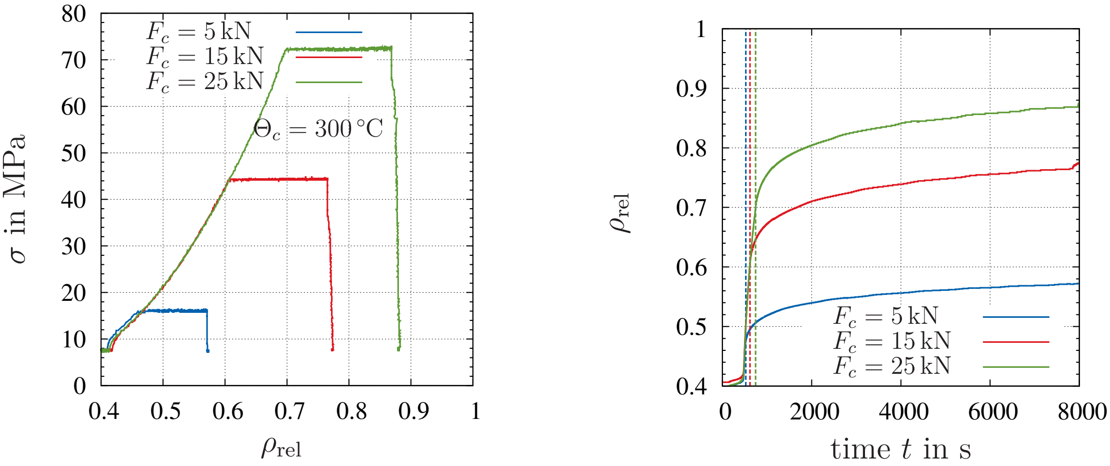

(e) Axial stress over relative density at 300 °C

(f) Relative density over time at 300 °C

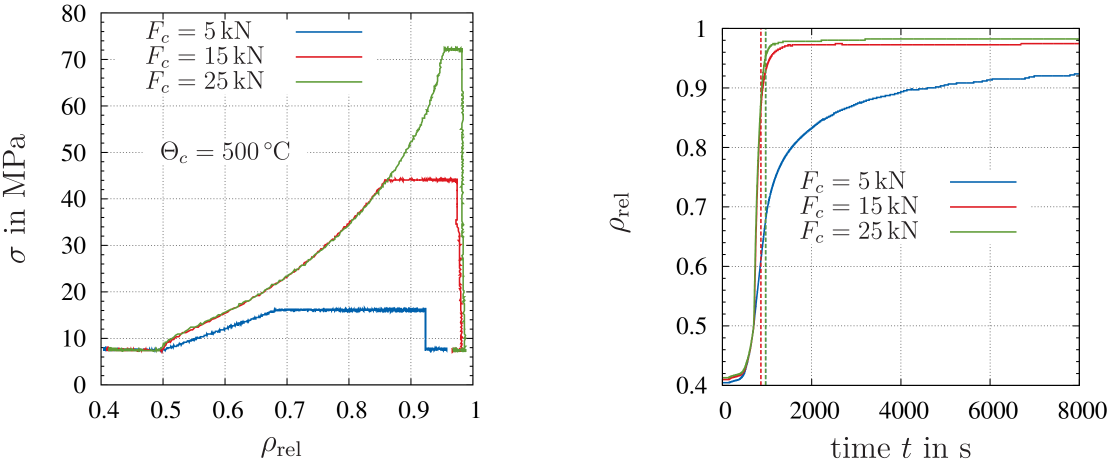

(g) Axial stress over relative density at 500 °C

(h) Relative density over time at 500 °C

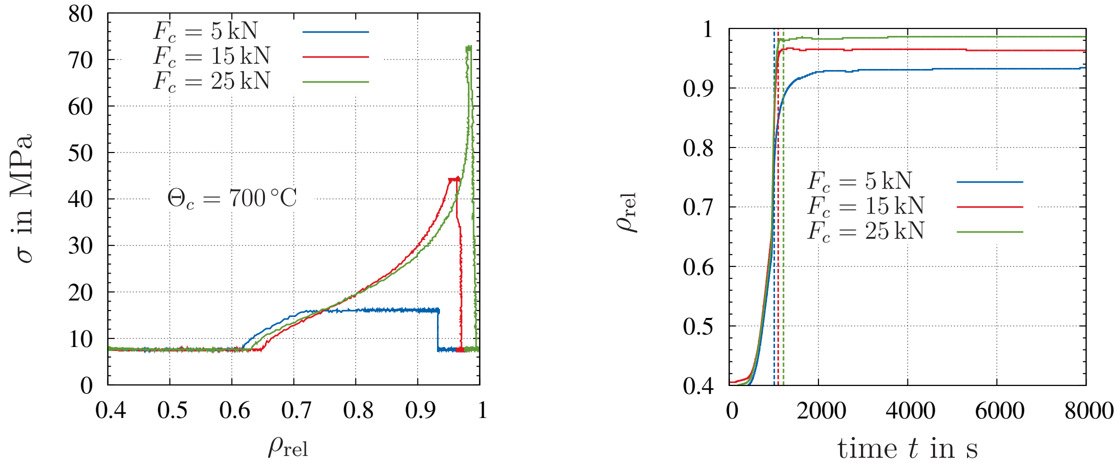

(i) Axial stress over relative density at 700 °C

(j) Relative density over time at 700 °C

Figure 2.39: Creep experiments at 25 °C, 200 °C, 300 °C, 500 °C and 700 °C

2.5.5 Dilatometer Experiments

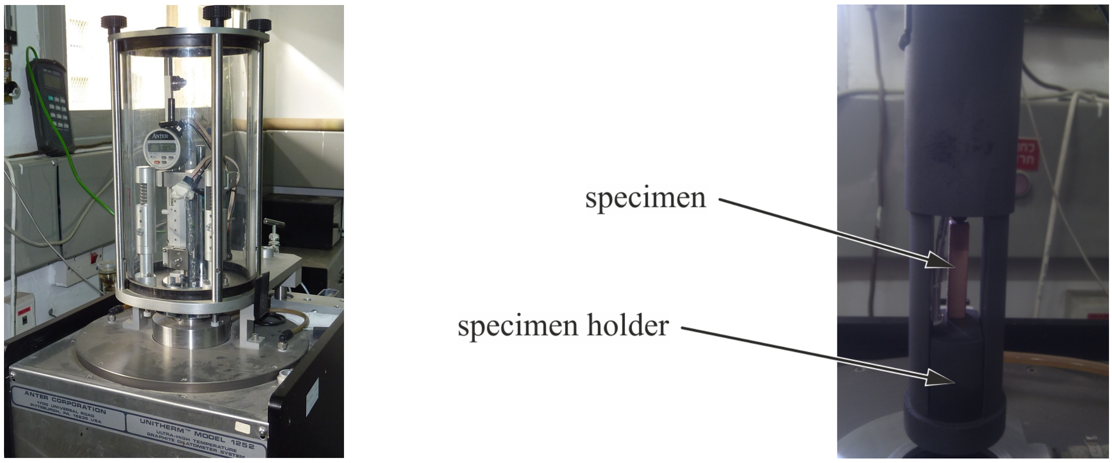

(a) Unitherm Model 1252 dilatometer

(b) Specimen holder

Figure 2.40: Dilatometer and specimen holder

The thermal expansion behavior is measured by a Unitherm (model 1252) dilatometer, Fig. 2.40a. In the machine, the copper specimens are placed into the specimen holder (which is made out of graphite), see Fig. 2.40b. The copper specimens are only cold-compacted with different relative densities, $\rho_{\mathrm{rel}} = 0.62$ and $\rho_{\mathrm{rel}} = 0.74$. In the furnace, the specimens are heated from room temperature to the constant temperature of Θ_c. The temperature values are: 300 °C, 400 °C, 500 °C and 600 °C. The heating rate is chosen to be $\dot{\Theta} = 2\,°\text{C}\,\text{min}^{-1}$ in order to ensure a homogeneous temperature in the specimen. Subsequently, the temperature Θ_c is held constant for 2 h, see Fig. 2.41. The main idea behind these experiments is to investigate the thermal behavior of the cold-compacted specimen without any applied stress. The dilatometer measures the change in length due to the applied temperature. The thermal strain ε_Θ can be computed due to the elongation $L(\Theta)$ by

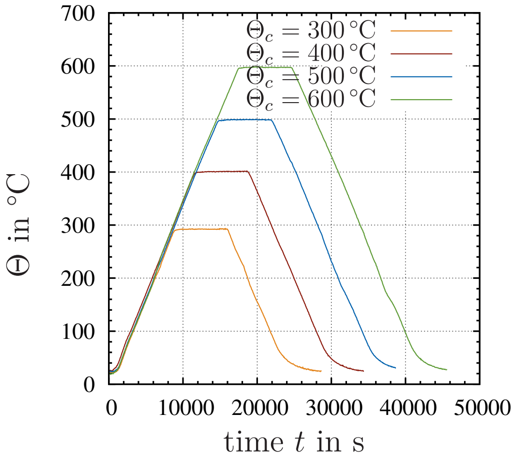

Figure 2.41: Prescribed temperature of dilatometer experiment

$$\varepsilon_\Theta = \frac{L(\Theta) - L(20\,°\text{C})}{L(20\,°\text{C})}. \tag{2.24}$$

Fig. 2.42 shows the thermal strain over the temperature for the two specimens. At first, the thermal strain, which is connected to a maximum temperature of 600 °C, grows linearly until the constant temperature is reached – as can be seen in Fig. 2.42b. The thermal strain decreases at the constant temperatue of 600 °C. After cooling to room temperature, the thermal strain is negative. This means that the specimen is shorter than before and that there are remaining inelastic strains. This might be due to sintering of the powder caused by the high temperature. Nevertheless, the magnitude of these strains are in the order of 10^{-3} and are assumed to have only little influence on the sintering process in the FAST-machine, where the overall strains reach values up to 0.6. Thus, the sintering behavior is assumed to be mainly driven by the applied axial force in connection with the high temperature, as seen in Fig. 2.33.

2.5.6 Tension Tests with Sintered Samples

The powder particles are compacted together in the sintering process, finally leading to a solid specimen. Thus, the tensile strength is assumed to increase due to the

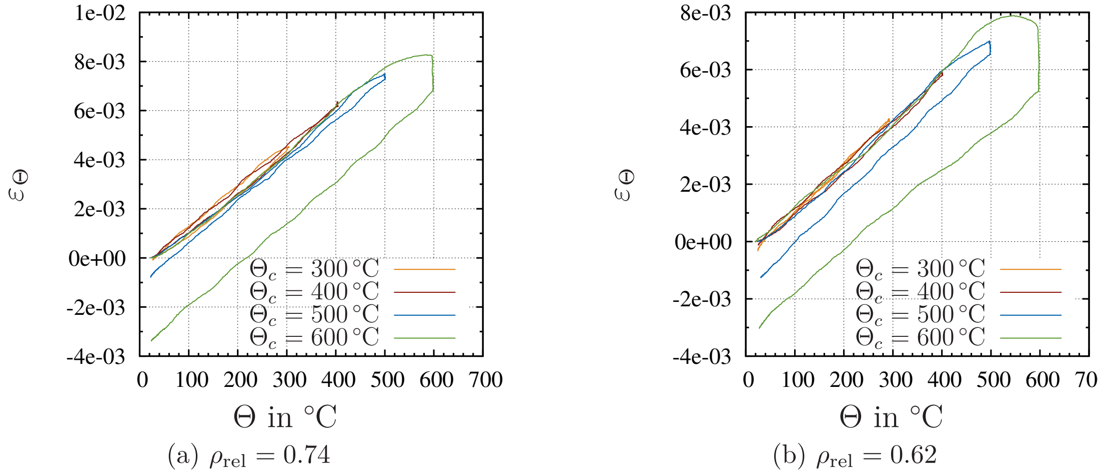

(a) $\rho_{\mathrm{rel}} = 0.74$ (b) $\rho_{\mathrm{rel}} = 0.62$

Figure 2.42: Thermal strain of cold-compacted specimens with different relative densities

sintering, which is to be investigated by tensile experiments in the following. In order to investigate the hardening behavior in the tensile range, sintered tensile specimens with different relative densities are produced, $\rho_{\mathrm{rel}} = 0.85, 0.92, 0.96$ and 0.97. The applied axial stress and temperature loading path for the specimen production sintering process are shown in Fig. 2.43. The maximum temperature in

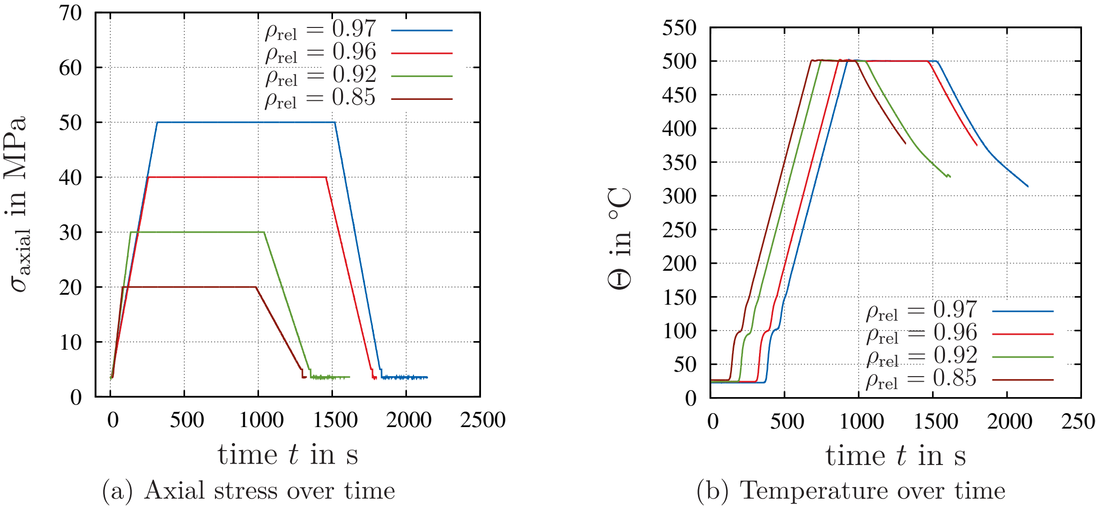

(a) Axial stress over time (b) Temperature over time

Figure 2.43: Loading paths for the production of sintered tensile specimens

all experiments remains the same – while the stress and the temperature dwell time are varied to yield specimens with different relative densities, see also Tab. 2.7. The produced specimens have a length of 50 mm and a square area of 4 mm × 4 mm.

For the tensile tests, they are glued into a steel clamp.[3] The geometry is shown in Fig. 2.44. The tensile experiments are performed in a Zwick testing machine with a clip gauge. For the calibration experiment, a steel specimen is used to subtract the machine compliance and the glue behavior. The resulting stress-strain curves are shown in Fig. 2.45a. It can be observed that for an increasing relative density, the yield stress increases too. For comparison, a solid copper specimen is tested in addition to the sintered specimen. Further, a cold-compacted specimen from Fig. 2.19a is investigated, see Fig. 2.45b. Due to the cold compaction, it is assumed that the tensile stress is low and no bonding between the particles occurred.

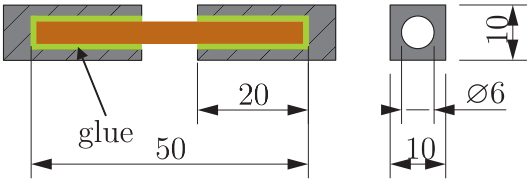

Figure 2.44: Geometry of tensile specimen in mm

Table 2.7: Sintering experiments for the production of tensile specimens

Relative density	Max. temperature	Temperature dwell time	Max. stress
0.97	500 °C	10 min	50 MPa
0.96	500 °C	10 min	40 MPa
0.92	500 °C	5 min	30 MPa
0.85	500 °C	5 min	20 MPa

The yield stress computation is done in two steps: at first, the identification of Young's modulus is computed, followed by the $R_{p0.02}$ which is defined as the yield stress. In order to determine the Young's modulus, linear elasticity $\sigma = E\varepsilon$ is fitted to the experimental data $\boldsymbol{\sigma}^{\text{Exp}} \in \mathbb{R}^{n_d}$ and $\boldsymbol{\varepsilon}^{\text{Exp}} \in \mathbb{R}^{n_d}$, which are given as discrete values $\boldsymbol{\sigma}^{\text{Exp}} = \{\sigma_1^{\text{Exp}}, \dots, \sigma_k^{\text{Exp}}, \dots, \sigma_{\text{end}}^{\text{Exp}}\}$ at the strains $\boldsymbol{\varepsilon}^{\text{Exp}} = \{\varepsilon_1^{\text{Exp}}, \dots, \varepsilon_k^{\text{Exp}}, \dots, \varepsilon_{\text{end}}^{\text{Exp}}\}$. n_d denotes the number of experimental data points. For the evaluation of the Young's modulus, the number of data points n_k respectively the strain $\varepsilon_{\min} \leq \varepsilon_k \leq \varepsilon_{\text{end}}$ is changed during the optimization process, $\boldsymbol{\varepsilon}_{\text{Cut}}^{\text{Exp}} = \{\varepsilon_1^{\text{Exp}}, \dots, \varepsilon_k^{\text{Exp}}\}$ resulting in $\boldsymbol{\sigma}_{\text{Cut}}^{\text{Exp}} = \{\sigma_1^{\text{Exp}}, \dots, \sigma_k^{\text{Exp}}\}$, $\boldsymbol{\sigma}_{\text{Cut}}^{\text{Exp}} \in \mathbb{R}^{n_k}$ and $\boldsymbol{\varepsilon}_{\text{Cut}}^{\text{Exp}} \in \mathbb{R}^{n_k}$. The goal of the optimization is to identify a linear curve that fits the curve of the experimental data with a change of the largest strain value. The quantity based on which the accuracy can be determined is related to the coefficient

---

[3] Here, the glue “Loctite Hysol 9497” is used.

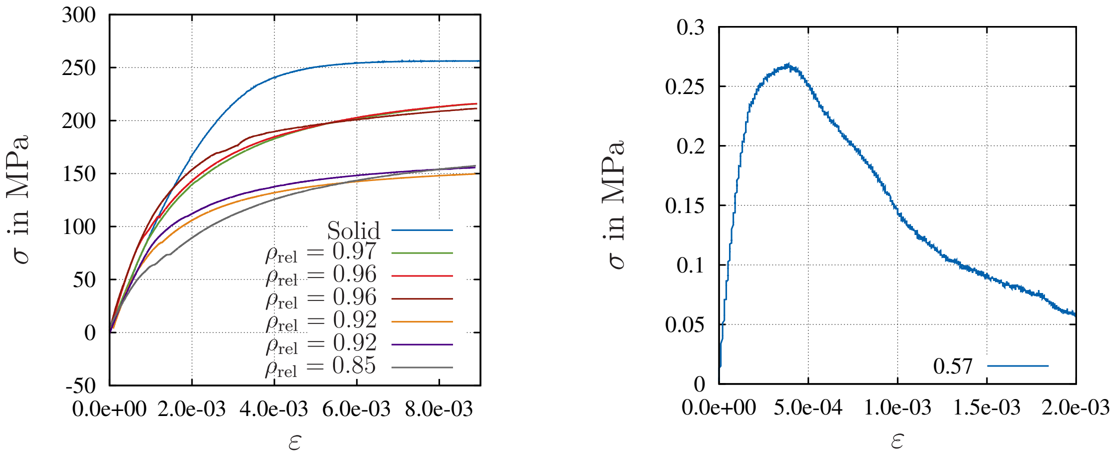

(a) Stress over strain

(b) Tensile test of a cold-compacted copper specimen from experiment Fig. 2.19a

Figure 2.45: Results of tensile test

of determination R^2. It can be defined as

$$R^2 = 1 - \frac{\sum_{i=1}^{n_d}(\sigma_i^{\text{Exp}} - E\varepsilon_i^{\text{Exp}})^2}{\sum_{i=1}^{n_d}(\sigma_i^{\text{Exp}} - \overline{\sigma}^{\text{Exp}})^2} \quad \text{with} \quad \overline{\sigma}^{\text{Exp}} = \frac{1}{n_d}\sum_{i=1}^{n_d}\sigma_i^{\text{Exp}} \tag{2.25}$$

The R^2-value shows how well the model corresponds to the underlying experimental data. The closer the value is to one, the better the fit. In the optimization process, the goal is to minimize the parameter $1 - R^2$ by changing the strain range. A Nelder-Mead algorithm serves to solve the minimization problem, see [Nelder and Mead, 1965; Lagarias et al., 1998]. The routines used in Matlab are taken from [Oldenhuis, 2009]. They allow the use of the Nelder-Mead algorithm for a constrained optimization algorithm. For the yield stress computation, the $R_{p0.02}$ is used. Thus, the elastic linear curve is shifted by 0.02% and the intersection point between this shifted curve and the experimental stress curve is used as the yield stress, see Fig. 2.47. The yield stress $R_{p0.02}$ represents the elastic limit at 0.02% plastic strains. The $R_{p0.01}$ value is called the elastic limit, see [Bergmann, 2003]. According to Lemaitre and Chaboche [2010], the yield stress or the elastic limit is defined by the stress for a fixed amount of permanent strain, $\varepsilon = 0.02\%$ or 0.05% or 0.2%. The question what amount of permanent strain might be appropriate for the elastic limit cannot be answered in general. Rather, it has to be defined according to the experimental data and the measurement accuracy. The whole Young's modulus identification procedure is shown in Fig. 2.46.

The identified Young's moduli from the stress-strain curve in Fig. 2.45a are shown in Fig. 2.48a. The values are compared to the relation of the Young's modulus proposed by Wang [1984]. This relation is used in [Carnavas, 1996] for a copper

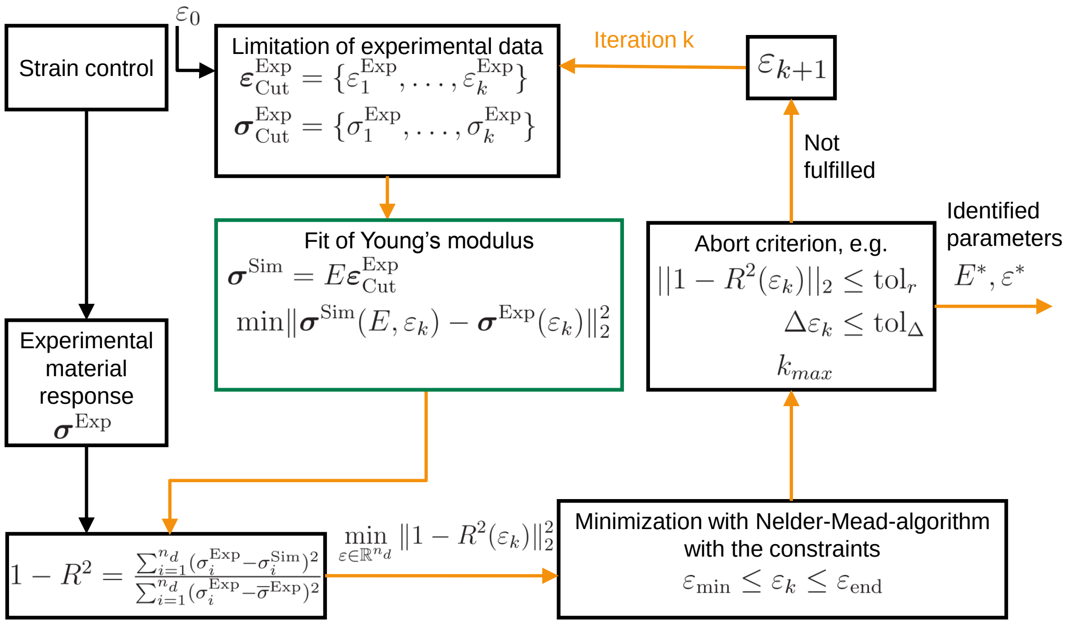

Figure 2.46: Young's modulus identification procedure

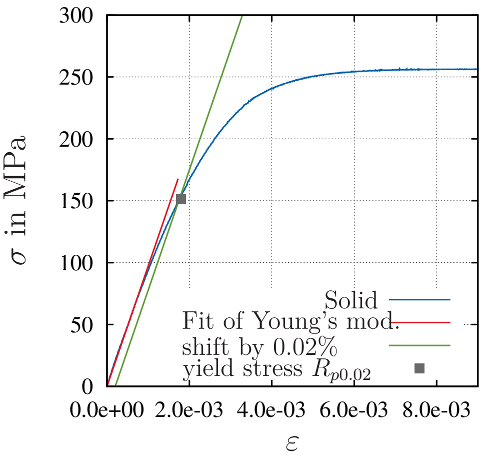

Figure 2.47: Visualization of yield stress computation

powder, and the identified model reads

$$E = E_0 \exp(-5.44(1-\rho_{\mathrm{rel}}) - 0.68(1-\rho_{\mathrm{rel}})^2), \tag{2.26}$$

where $E_0 = 120\,000\,\mathrm{MPa}$ represents the Young's modulus of solid copper. The relation offers a good description of the principle behavior of a higher Young's modulus while increasing the relative density. The computed yield stress shows an increasing behavior over the relative density, as can be seen in Fig. 2.48b. The yield stress at $\rho_{\mathrm{rel}} = 0.55$ is nearly zero, whereas the yield stress at $\rho_{\mathrm{rel}} = 1.0$ has a value of approximately 160 MPa. This information will be used in Chap. 5 to model the hardening behavior in the tensile range during the sintering process.

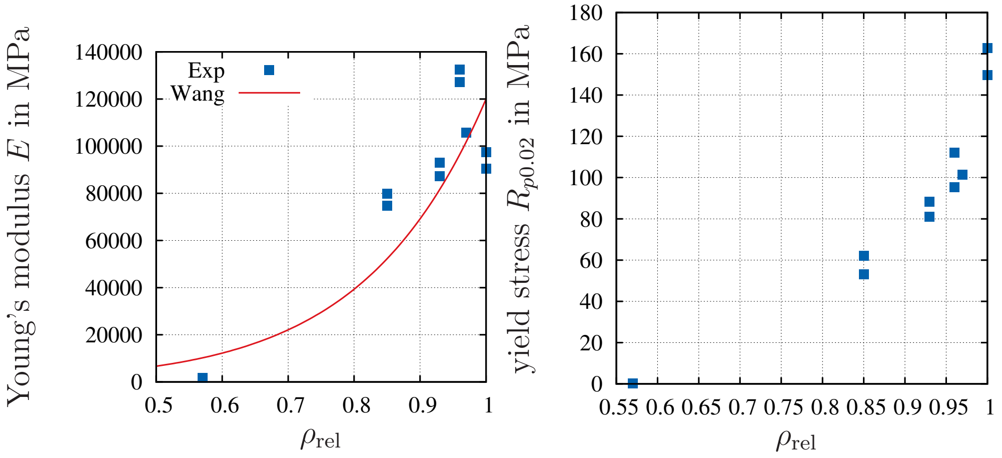

(a) Evaluated Young's modulus

(b) Computed yield stress at an elastic limit of 0.02% plastic strains

Figure 2.48: Computed Young's modulus and yield stress from the experimental stress-strain curve in Fig. 2.45a

2.6 Thermo-Electrical Properties of Copper Powder

For the characterization of the thermo-electrical behavior of the copper powder during the process, it is necessary to determine the material properties. The heat capacity, which is required in the heat equation, will be measured to define the heat absorption. The thermal conductivity occurring in Fourier's heat flux cannot be measured directly, so it will be derived from the density, the heat capacity and the thermal diffusivity. Further, the electrical conductivity, which is required for the use of Ohm's model, is measured.

2.6.1 Heat Capacity

The specific heat capacity c_p is a measure for the amount of heat Q necessary to increase the temperature of a body Θ with the mass m at constant pressure p by 1 K. The heat capacity C_p is given by

$$C_\mathrm{p} = \left(\frac{\partial Q}{\partial \Theta}\right)_{p=\mathrm{const.}} . \tag{2.27}$$

The heat capacity will be determined using a Differential Scanning Calorimeter. An overview of the method and further aspects of the differential scanning calorimetry (DSC) can be found in [Höhne et al., 2003].

The measurements are performed at the Institute of Particle Technology at the Clausthal University of Technology with a Netzsch DSC 204 F1 Phoenix. The maximum temperature is set to 500 °C. During the measurement, the temperature of the sample and the temperature difference between the sample and a reference sample is recorded. The sample and the reference sample are subjected to a controlled temperature path without any applied stress. The sample had a diameter of 5 mm and a mass of approximately 35 g. The sample is heated up to 500 °C with a heating rate of 50 K min^{-1}. The resulting specific heat capacity is shown in Fig. 2.49, showing a linear dependence on the temperature. It corresponds very well with the literature data from [Lide and Haynes, 2009] and [Touloukian, 1970].

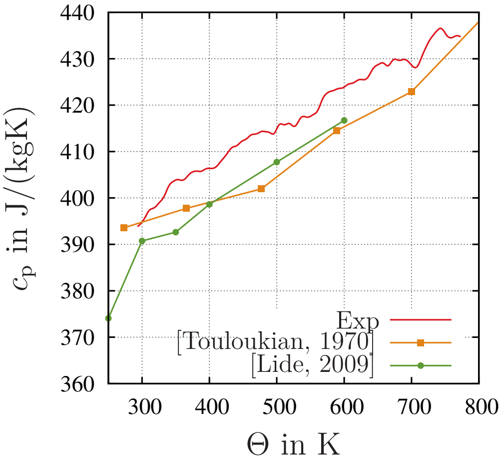

Figure 2.49: Specific heat capacity of copper

2.6.2 Thermal Conductivity

In this section, the measurements for the computation of the thermal conductivity κ_th are explained. The thermal conductivity, which describes the ability to conduct heat in a material, can be computed by

$$\kappa_{\text{th}}(\rho_{\text{rel}}, \Theta) = \alpha_T(\rho_{\text{rel}}, \Theta)\rho(\rho_{\text{rel}}, \Theta)c_{\text{p}}(\Theta). \tag{2.28}$$

The thermal diffusivity α_T is determined by a laser flash apparatus (LFA). The experiments are also performed at the Institute of Particle Technology at the Clausthal University of Technology with a Netzsch LFA 457. In the machine, sintered specimens with different relative densities are heated up to the maximum temperature of 500 °C in a furnace. These cylindrical specimens have a diameter of 12.7 mm and a height of 3 mm and were coated with graphite prior to the measurement in order to enhance their emissivity. During the measurement, a short laser pulse is applied at the bottom surface of the specimens at certain temperatures. This irradiation leads to a homogeneous heating of the bottom surface, to a heat conduction through the sample and thus to a temperature increase at the top surface. The rise of temperature at the top surface is measured by an infrared (IR) detector and the diffusivity is computed based on this information. Under the assumption of adiabatic conditions and a homogeneous temperature distribution over the sample radius, the diffusivity can be computed by $0.1388 l^2/t_{0.5}$, with a sample thickness of l. $t_{0.5}$ symbolizes the time for a temperature increase of 50%. Three single laser shots/measurements are performed for each of the temperature values.

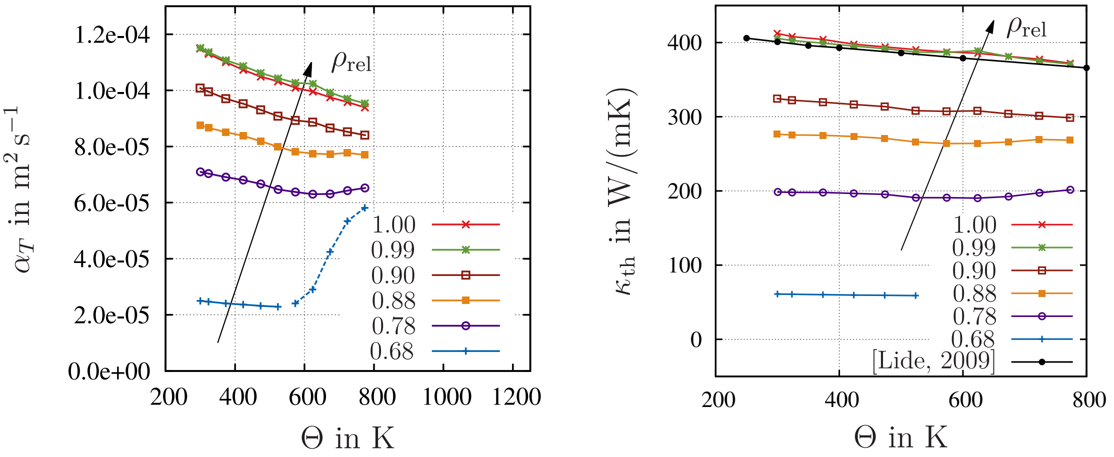

(a) Thermal diffusivity (b) Thermal conductivity

Figure 2.50: Thermal diffusivity and thermal conductivity of sintered copper specimens

The mean values of the thermal diffusivity are shown in Fig. 2.50a for sintered specimens with different relative densities. For the specimen with the lowest relative density, $\rho_{\text{rel}} = 0.68$, a large increase over the temperature is observed. This phenomenon could be connected to sintering effects during the measurement. Thus, the data is not used for the thermal conductivity computation, which is performed with the help of Eq. (2.28). The density is computed by

$$\rho = \frac{\rho_{\mathrm{Copper}} \rho_{\mathrm{rel}}}{(1 + \alpha_\Theta(\Theta - \Theta_0))^3} \approx \frac{\rho_{\mathrm{Copper}} \rho_{\mathrm{rel}}}{1 + 3\alpha_\Theta(\Theta - \Theta_0)} \tag{2.29}$$

with the density of copper, $\rho_{\mathrm{Copper}} = 8960\,\mathrm{kg\,m^{-3}}$ and the thermal expansion coefficient $\alpha_\Theta = 1.5 \times 10^{-5}$, see Chap. 5. It is assumed that the specimen shows an isotropic thermal expansion. The computed thermal conductivity is shown in Fig. 2.50b. For solid and nearly solid specimens with $\rho_{\mathrm{rel}} = 0.99$, the conductivity matches the literature data well, showing a decreasing behavior with increasing temperature. In general, the conductivity decreases with increasing temperature for the different relative densities. The conductivity for the specimen with $\rho_{\mathrm{rel}} = 0.78$ shows a minor increasing conductivity above 600 K. This data will be used in Chap. 5 for the definition of a copper powder conductivity relation.

2.6.3 Electrical Conductivity

The specific electrical conductivity[4] κ_{el} describes the material's ability to conduct an electric current. It connects the electrical field with the electric current density, see Sect. 4.6.6, and is the reciprocal to the electrical resistivity. In metals, electrons can be imagined to form a kind of cloud that allows the electrons to move freely, [Rösler et al., 2008]. At higher temperatures, lattice vibrations lead to a higher resistance and to a decreasing electrical conductivity, [Lindner, 1978]. The electrical conductivity measurement is performed drawing on the four-terminal sensing technique, also known as "Kelvin sensing". This measurement technique has the advantage that the wire resistances have no influence on the measurement. It is especially suitable for the measurement of low resistances, such as in copper.

If an electric potential difference is applied to a wire, this causes an electric current flow. Between the applied voltage U and the electric current I, the proportionality is given by the electric resistance R or the electric conductance G

$$U = RI, \qquad I = \frac{1}{R} U = GU \tag{2.30}$$

This relationship, which was discovered by Ohm, can be written in different forms as

$$R = \frac{U}{I} = \text{const.}, \qquad \vec{j} = \kappa_{\mathrm{el}} \vec{E} \tag{2.31}$$

with the electrical field $\vec{E}$ and the electric current density $\vec{j}$. For more information, see Sect. 3.3.4. The specific resistance can be computed for a constant current

---

[4] The unit of the electrical conductivity is Siemens per meter $\mathrm{S\,m^{-1}} = \mathrm{m^{-1}\,\Omega^{-1}} = \mathrm{A\,m^{-1}\,V^{-1}}$

density by

$$\rho_{\mathrm{el}} = R\frac{A}{l}, \qquad \kappa_{\mathrm{el}} = \frac{1}{\rho_{\mathrm{el}}} = \frac{l}{RA}. \tag{2.32}$$

with the cross section area A and the length l as well as the specific resistance ρ_{el} and the specific electrical conductivity κ_{el}.

Figure 2.51: Experimental setup of electrical conductivity measurement [Klinger, 2013]

The electrical resistance measurements described in the following were performed at the Chair of Continuum Mechanics at the Ruhr-Universität Bochum in collaboration with Prof. Steeb. They are a part of a diploma thesis, [Klinger, 2013]. The electrical resistance is measured by a Burster Resistomat 2304, which uses an improved four-terminal sensing technique. In the measurement process, the voltage drop at the specimen and at an internal reference resistor is recorded. The quotient of both voltage drops is computed and then multiplied with the characteristic value

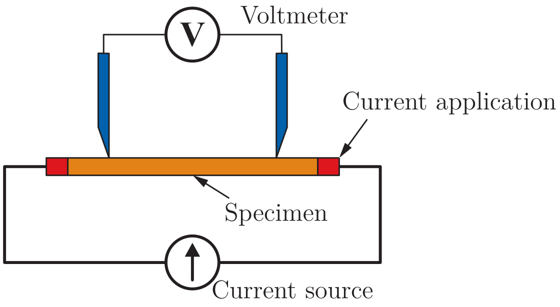

Figure 2.52: Sketch of the four-terminal sensing measurement technique

of the reference resistor – resulting in a sample resistance that is only dependent on the quality of the reference resistance. According to the manufacturer, the measuring error is $\leq 0.01\%$. The experimental setup – including the specimen – is shown in Fig. 2.51. Due to the small resistances, a current of 10 A is chosen for the measurement. The electrical resistance is measured between room temperature and 700 °C. A furnace is used to apply the temperature and the temperature is controlled by a thermocouple, which is applied to the specimen. In order to ensure a homogeneous temperature inside the specimen, a heating rate of $2\,°\mathrm{C\,min^{-1}}$ is chosen. The measured electrical conductivity for two specimens – one solid copper specimen and one sintered specimen with $\rho_{\mathrm{rel}} = 0.85$ – is shown in Fig. 2.53. Here, the electrical conductivity for the solid copper specimen and the literature data correspond very well. The electrical conductivity shows a decreasing behavior with increasing temperature, which can be explained by the temperature-activated lattice vibrations leading to collisions with phonons, [Lindner, 1978]. Due to the failure of the specimen contacting, the measurement data for the sintered specimen is limited to 850 K. These measurements can be seen as a first attempt to determine the electrical conductivity. In Sect. 4.6.6, a model from the literature is proposed.

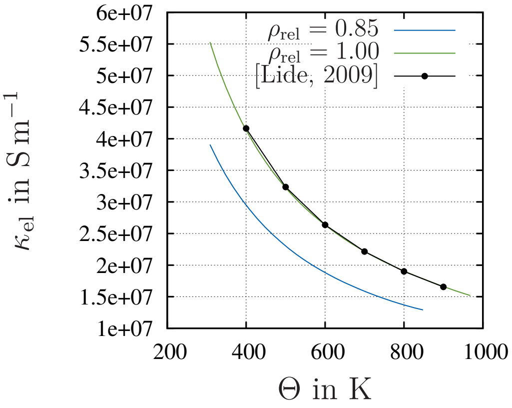

Figure 2.53: Electrical conductivity over the temperature, depending on the relative density

2.7 Thermo-Electrical Properties of Graphite

The tool system consists of the punch, the die and the cone part, see Fig. 2.5a. The temperature in the powder, – and, accordingly, the final material properties of the sintering process – are essentially influenced by the graphite tools. The punches compact the powder inside the die and, moreover, the temperature varies over a large range. In addition, the thermo-electrical parameters depend on the temperature itself. The graphite used for the tool system is a product of the SGL

Group, type R8510. Graphite has a remarkable electrical and thermal conductivity and is also known as “metallic carbon modification”, [Neumüller, 1972]. Generally, graphite is an anisotropic material, [Brandt et al., 2012]. The industrially produced graphite for the spark erosion is produced by isostatic pressing and sintering, which leads to an isotropic material, [SGL Carbon GmbH, 2014]. It is temperature resistant up to 3300 K in a vacuum. In air, however, oxidation takes place – limiting the application to 800 K, [Jäger et al., 2000].

As the finite element simulation requires the thermal expansion, the heat capacity, the thermal conductivity as well as the electrical conductivity, the respective measurements are described in the following.

2.7.1 Thermal Expansion

The thermal expansion is measured by the dilatometer in Fig. 2.40 at the Institute of Prof. Frage. The graphite specimen is heated from 20 °C up to 755 °C. The thermal strain is computed by Eq. (2.24) and plotted over the temperature difference $\Delta\Theta$ in Fig. 2.54. The graphite shows an almost linear thermal expansion behavior.

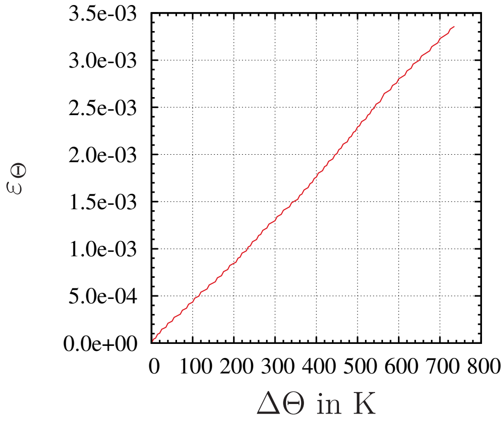

Figure 2.54: Thermal strain over the temperature for graphite

2.7.2 Heat Capacity

For the heat capacity measurement, cylindrical samples with a diameter of 5 mm and a height of 1 mm with an approximate mass of 35 mg are used. The measurements are performed by Netzsch Application Laboratories using a DSC 404 F1 Pegasus. The experiment is performed under an argon atmosphere, and the specimen is heated from room temperature up to 1200 °C with a heating rate of 20 K min^{-1}. The resulting curves of two specimens are shown in Fig. 2.55. The maximum deviation between the two curves is 4%. The literature data is limited to 600 K. In this range, the measured capacity matches the literature data well. For values above 1000 K, it is assumed that there is a reaction between the graphite and the crucible as well as the specimen holder (which is made out of PtRh and Al_2O_3). This is why only the values up to 1000 K are used, which is sufficient because the FAST-experiments cover a range of up to 1000 K.

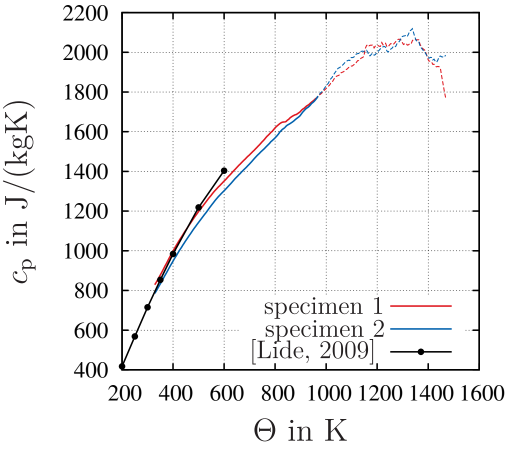

Figure 2.55: Heat capacity of graphite

2.7.3 Thermal Conductivity

The thermal diffusivity is measured by a Netzsch LFA 427 under argon atmosphere up to 1473 K at the Institute of Non-Metallic Materials (INW) at the Clausthal University of Technology. The cylindrical specimens have a diameter of 12.7 mm and a height of 3 mm and were coated with graphite prior to the measurement. The thermal diffusivity computation is described in Sect. 2.6.2. Two graphite specimens are measured and the resulting diffusivity is shown in Fig. 2.56a. The thermal diffusivity shows a decreasing behavior with increasing temperature. Its mean value is computed, and the thermal conductivity is derived with the help of

$$\kappa_{\mathrm{th}}(\Theta) = \alpha_T(\Theta)\rho(\Theta)c_{\mathrm{p}}(\Theta). \tag{2.33}$$

The measured heat capacity is given up to 1000 K, limiting the thermal conductivity computation. This temperature is sufficient because the FAST-experiments for copper powder are performed up to 1000 K. The measurements will be used for the material model definition.

2.7.4 Electrical Conductivity

The procedure described in Sect. 2.6.3 also serves as a basis for the electrical conductivity measurement. The graphite oxidation in air limits the measurement at

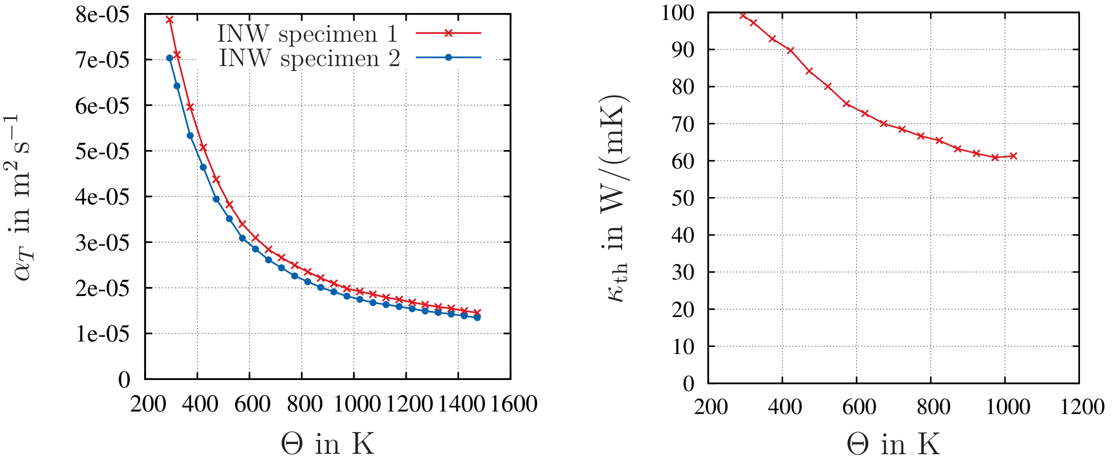

(a) Thermal diffusivity

(b) Thermal conductivity

Figure 2.56: Thermal diffusivity and thermal conductivity of graphite

800 K. At room temperature, the graphite specific resistance varies from 9.3 µΩ m to 14 µΩ m. The mean value out of 10 experiments is 11.9 µΩ m. The manufacturer's data sheet [SGL Carbon GmbH, 2014] lists a value of 13 µΩ m for graphite R8510. The measured electrical conductivity is shifted to the mean value at room temperature and is shown in Fig. 2.57. This data corresponds well with values provided by the manufacturer, which cannot be shown here due to copyright regulations.

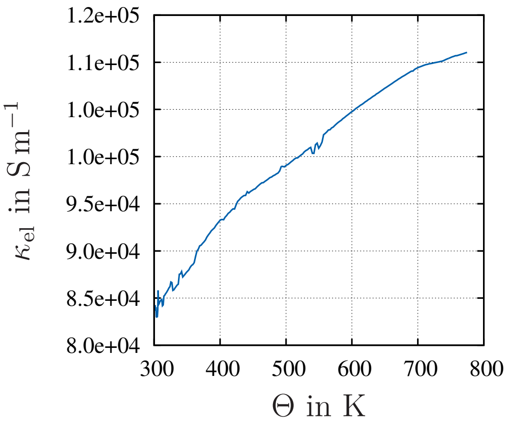

Figure 2.57: Electrical conductivity over the temperature for graphite

2.8 Electrical Contact Resistance

The graphite tool system of the FAST-machine consists of several parts. During the experiment, the electric current flows through the graphite parts, which are in contact due to the applied force. According to Holm [1999], an electric contact can be defined as follows: “The term *electric contact* means a releasable junction between two conductors which is apt to carry electric current.” In the ideal situation of rigid bodies, such a contact would occur at a maximum of three points. In reality, due to the presence of deformable bodies and due to the applied force, small contact areas tend to arise and enlarge – and the plastic deformations might even lead to further areas of contact. According to Holm [1999], three different types of contact areas can be distinguished. There is the load bearing area A_b, which carries the load through the contact spots, the true contact area A_c and the apparent contact area A_a, the punch diameter, for example.

If one measures the resistance of two bodies that are in contact, the resistance is higher than the resistance of a single body of the same size of the two bodies. The reason for this is the contact resistance, which can be divided into two parts, [Holm, 1999],

$$R_{\text{contact}} = R_c + R_f, \tag{2.34}$$

where one part is the constriction resistance and the other part is the film resistance. The constriction resistance originates from the constricted current flow through small conducting spots. Every real surface has a certain surface topology and roughness, see Fig. 2.58. If two real surfaces get in contact, the load bearing contact area is smaller than the apparent contact area. The two bodies appear to be in contact on a microscopical scale by small contact areas, see Fig. 2.59a. Another part of the contact resistance is the film resistance, which arises from tarnish films, for example, oxide layers. Therefore, the load bearing area can be divided into metallic and quasi-metallic contacts due to these impurity layers. Together, the metallic contact areas and the conducting impurity layers are defined as the true contact area A_c.

Figure 2.58: Surface roughness

In general, the contact resistance depends on the applied pressure and on the temperature, see [Holm, 1999]. The measurements described in the following were performed at the Chair of Continuum Mechanics at the Ruhr-Universität Bochum in collaboration with Prof. Steeb. They are a part of a diploma thesis, [Klinger, 2013]. For these measurements, the four-terminal sensing technique is used again in combination with a Burster Resistomat 2304, see Sect. 2.6.3. The contact resistance is measured for different material combinations, which are: graphite and graphite, copper and copper as well as copper and graphite. The diameter of the specimen is 20 mm and the height is 10 mm. For the measurement, two specimens are placed on top of each other. The contacting is in the middle of the specimen 5 mm far from the contact surface. The experimental setup is shown in Fig. 2.59b. During

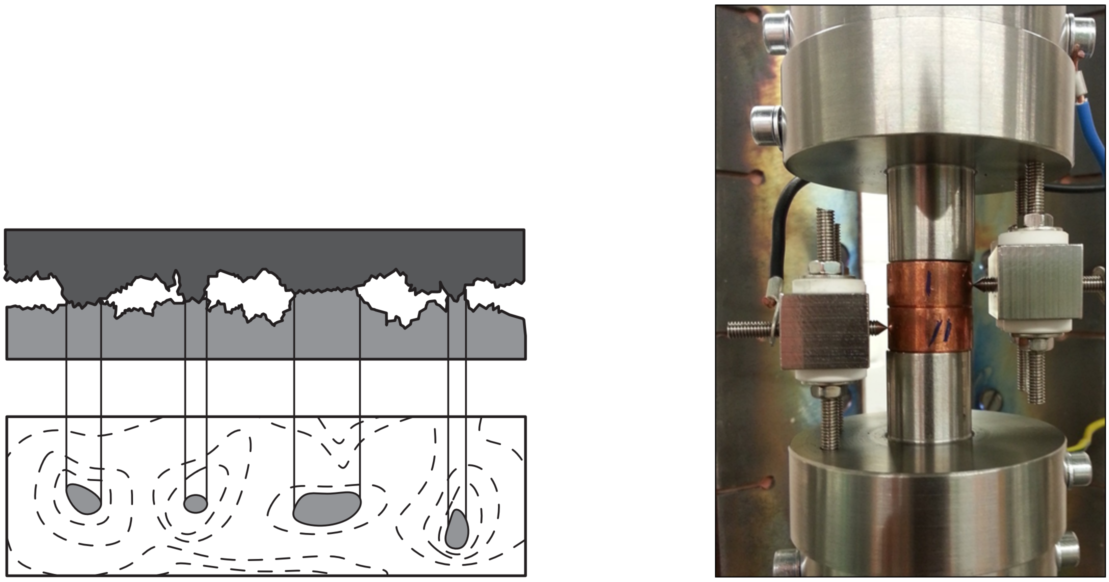

(a) Effective contact areas

(b) Experimental setup

Figure 2.59: Effective contact areas and experimental setup of contact resistance measurement

the measurement, the total resistance R_{total} is recorded and the force is increased from 2 kN to 25 kN according to the axial force in the sintering experiments. The contact resistance R_{contact} can be calculated by the ohmic resistance of the two bodies R_{B1} and R_{B2}

$$R_{\mathrm{total}} = R_{\mathrm{contact}} + R_{B1} + R_{B2} \quad \Leftrightarrow \quad R_{\mathrm{contact}} = R_{\mathrm{total}} - R_{B1} - R_{B2}. \qquad (2.35)$$

Fig. 2.60a shows the contact resistance for copper over the applied pressure. It can be seen that the contact resistance decreases with increasing pressure. Additionally, the standard deviation becomes smaller. The specific resistance for graphite measured at room temperature varies from $9.3\,\mu\Omega\,\mathrm{m}$ to $14\,\mu\Omega\,\mathrm{m}$, which is why the resulting total resistance for a copper-graphite and a graphite-graphite material combination are shown in Fig. 2.60b. In Chap. 5, the electrical contact conductance will be computed out of the contact resistance and will be used in Chap. 7 for the finite element simulations.

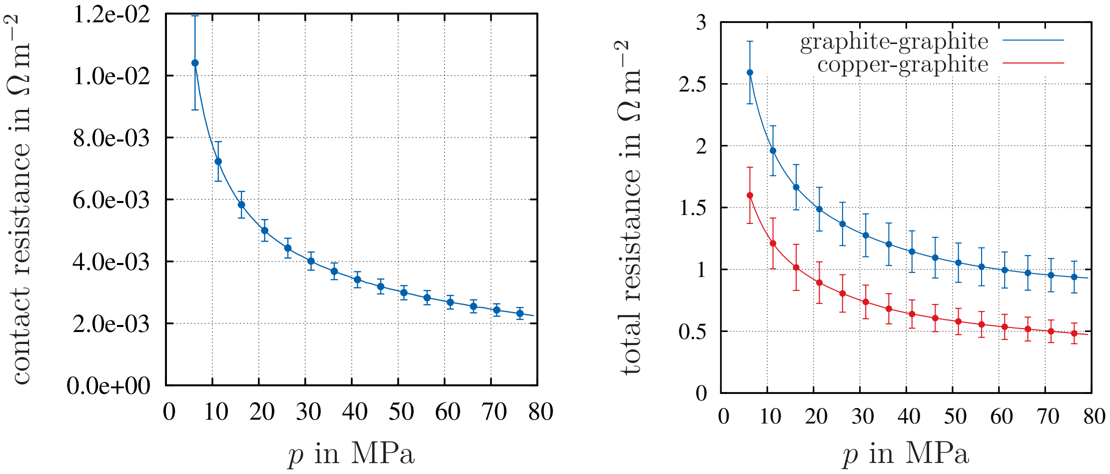

(a) Copper-copper material combination

(b) Total resistance over the pressure for copper-graphite and graphite-graphite material combinations

Figure 2.60: Electrical contact resistance, depending on the axial pressure for different material combinations

3 Fundamentals of Continuum Mechanics

After the experimental observations were illustrated and the thermo-electro-mechanical behavior of copper powder and graphite were investigated in the previous chapter, the present chapter focuses on an introduction of the fundamentals of Continuum Mechanics – in order to provide a mathematical basis for the underlying thermo-electro-mechanical problem. Later on, a material model for copper powder is formulated with the help of Continuum Mechanics and the balance equations for the multi-field problem are introduced. Therefore, it is of main importance to understand and describe the motion and the deformation which are caused by stresses in a material. Continuum Mechanics provide a theory to describe the complex physical nature without detailed knowledge about the micro-structure. In the framework of Continuum Mechanics, the discrete nature of matter, e.g. the grain structure in metals or any chains for a polymer material, is ignored. The microscopic model of matter is replaced by a macroscopic phenomenological model of matter called continuum. This assumption is valid if the assembly under consideration is much larger than these particles. As a consequence, predictions that are based on this kind of model are not exact – but sufficient for many engineering applications.

The theory presented in this chapter is based on the Continuum Mechanics books of Haupt [2002], Holzapfel [2000], Hutter and Jöhnk [2004], Altenbach and Altenbach [1994], and Eringen and Maugin [1990].

The assumption that matter is continuously distributed in space leads to the development of field theories, where the quantities are scalar-, vector- or tensor-valued functions of time and space, [Haupt, 2002]. Thus, liquids (such as water, for example) can be treated as a continuum with a mass density, a temperature and a velocity – depending on the space and the time, see [Holzapfel, 2000]. In fluid mechanics, it is rather the velocity, temperature and pressure of a fluid that are of interest, while solid mechanics focus on the state of stress, temperature and displacement of a solid body. Commonly, the field of Continuum Mechanics is divided into several subject areas:

- study of motion and deformation (kinematics)
- study of stress in a continuum

- fundamental laws of physics (balance equations)
- constitutive or material equations, which relate the deformation to the stress state

Kinematics describe the motion and deformation of a material body $\mathcal{B}$, whereas the balance equations provide the influence of the outside world on the material body. The constitutive equations connect the kinematic quantities, e.g. strains, with dynamic values such as stress or heat flux.

The following section serves to explain the motions and deformations that cause a change of shape and size.

3.1 Kinematics

Geometrical studies of motion without the driving forces are called kinematics. In this section, configurations and the motion of a material body are introduced. Furthermore, the deformation gradient will be introduced, which characterizes the local motion. Additionally, strain measures are constructed with the help of the deformation gradient.

3.1.1 Configuration and Motion

A material body, denoted by $\mathcal{B}$, continuously fills a region of the space with matter. The material body $\mathcal{B} = \{\mathcal{P}\}$ in $\mathbb{R}^3$ is – at least in the mathematical sense – a continuously filled set of material points or particles $\mathcal{P} \in \mathcal{B}$. Here, "particle" means a part of the material body which can be seen as a conglomeration of molecules, at the same time small enough to be treated as a particle. A material body $\mathcal{B} = \{\mathcal{P}\}$ has the property of a one-to-one mapping

$$\boldsymbol{\chi}\colon \begin{cases} \mathcal{B} & \to \boldsymbol{\chi}[\mathcal{B}] \subset \mathbb{R}^3 \\ \mathcal{P} & \mapsto \boldsymbol{\chi}(\mathcal{P}) = (x_1, x_2, x_3) \Longleftrightarrow \mathcal{P} = \boldsymbol{\chi}^{-1}(x_1, x_2, x_3). \end{cases} \tag{3.1}$$

where the mapping $\boldsymbol{\chi} \in \mathcal{K}$ is called configuration. Thus, every material point is uniquely connected to a number triplet. By definition, it is claimed that a composition of two configurations is continuously differentiable.[1]

The motion of a material body is defined by a sequence of configurations

---

[1] The uniqueness and the continuous differentiability ensures that a material point has a unique position in space and is not shared by any other point. Additionally, neighboring material points remain as neighbors.

parametrized with the time t.

$$t \mapsto \boldsymbol{\chi}_t\colon \begin{cases} \mathcal{B} & \to \boldsymbol{\chi}_t[\mathcal{B}] \subset \mathbb{R}^3 \\ \mathcal{P} & \mapsto \boldsymbol{\chi}_t(\mathcal{P}) = (x_1(t), x_2(t), x_3(t)) \Longleftrightarrow \mathcal{P} = \boldsymbol{\mathcal{R}}^{-1}(x_1(t), x_2(t), x_3(t)), \end{cases} \tag{3.2}$$

The time-dependent configuration $\boldsymbol{\chi}_t$ is called *current configuration*

$$\boldsymbol{\mathcal{R}}\colon \begin{cases} \mathcal{B} & \to \boldsymbol{\mathcal{R}}[\mathcal{B}] \subset \mathbb{R}^3 \\ \mathcal{P} & \mapsto \boldsymbol{\mathcal{R}}(\mathcal{P}) = (X_1, X_2, X_3) \Longleftrightarrow \mathcal{P} = \boldsymbol{\mathcal{R}}^{-1}(X_1, X_2, X_3). \end{cases} \tag{3.3}$$

Furthermore, it is convenient to introduce a fixed configuration that does not change over the time, called *reference configuration.*[2] With this configuration, the material points $\mathcal{P}$ can be identified by their number triplets (X_1, X_2, X_3). This triple can be interpreted as positions vectors by introducing an origin O and base vectors $\vec{e}_i$ for a frame of reference. In this work, a Cartesian coordinate system is used – which is not mandatory at all. Depending on the specific problem, other basis systems might be more appropriate. Thus, the vectors $\vec{X} = X_k \vec{E}_k$ and $\vec{x} = x_i \vec{e}_i$ are position vectors of the material point within the reference and the current configuration, see Fig. 3.1. Eliminating the material point in the description of the motion leads to

$$\vec{x} = \vec{\boldsymbol{\chi}}_t(\boldsymbol{\mathcal{R}}^{-1}(\vec{X})) = \vec{\boldsymbol{\chi}}_{\mathrm{R}}(\vec{X}, t). \tag{3.4}$$

The motion causes a general change of shape, position and orientation of the body. The orientation and the position can be changed by a rigid body motion whereas the shape changes if a deformable motion and body are present.

The number triplets (X_1, X_2, X_3) are called material (referential) coordinates and x_1, x_2, x_3 are called spatial (current) coordinates of the material point $\mathcal{P}$. In solid mechanics, the reference configuration is usually known – and the current configuration can be computed by the change of the material points. This is related to the Lagrangian description. In fluid mechanics, the velocity at a certain point is of interest and can be measured more easily, which refers to the Eulerian description. In general, the use of the Lagrange or Eulerian depends on the specific application.

The motion can be expressed by the displacement of a particle, which is defined by the difference between the position vectors in the current and the reference configuration.

$$\vec{u}(\vec{X}, t) = \vec{x} - \vec{X} = \vec{\boldsymbol{\chi}}_{\mathrm{R}}(\vec{X}, t) - \vec{X}. \tag{3.5}$$

---

[2] Often, another configuration is introduced: the initial configuration at the time t_0. In this work, it is assumed that the initial configuration and the reference configuration coincide. In dynamical problems, it is more appropriate to choose another configuration to be the reference configuration than the initial configuration, Holzapfel [2000].

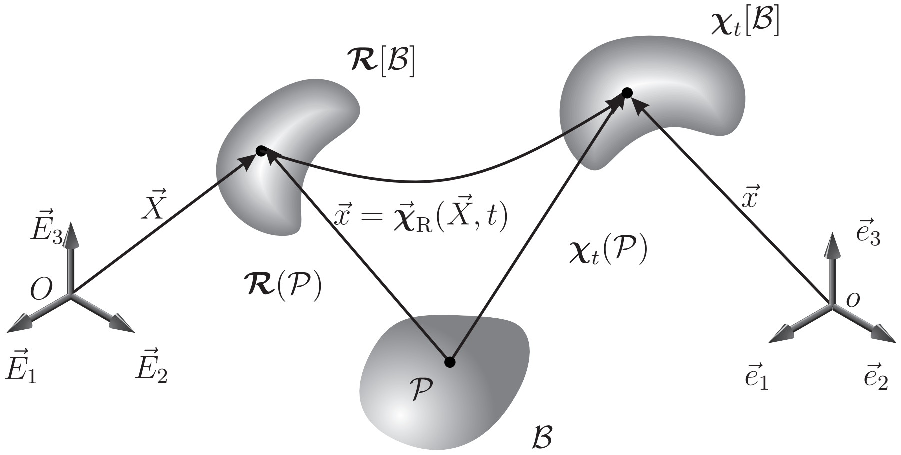

Figure 3.1: Configurations

3.1.2 Deformation Gradient

One crucial quantity in Continuum Mechanics is the deformation gradient, which characterizes the local behavior of motion around a material point. It is defined by[3]

$$\mathbf{F}(\vec{X}, t) = \operatorname{Grad} \vec{\boldsymbol{\chi}}_{\mathrm{R}}(\vec{X}, t). \tag{3.6}$$

It is of interest how a body deforms by moving from the reference configuration to the current configuration. Material line elements $\mathrm{d}\vec{X}$ transform according to

$$\mathrm{d}\vec{x} = \mathbf{F}\,\mathrm{d}\vec{X}, \tag{3.7}$$

see [Haupt, 2002, p. 25] for a mathematical derivation. Thus, the deformation gradient transforms the line element from the reference to the current configuration, see Fig. 3.2.

In addition to the transformation of material line elements, the deformation gradient also transforms surface elements

$$\mathrm{d}\vec{a} = (\det \mathbf{F})\,\mathbf{F}^{-\mathrm{T}}\,\mathrm{d}\vec{A} \tag{3.8}$$

from the reference to the current configuration as well as volume elements

$$\mathrm{d}v = (\det \mathbf{F})\,\mathrm{d}V. \tag{3.9}$$

The deformation gradient $\mathbf{F}$ is a second-order tensor and is generally unsymmetric, having nine different components. Due to the invertibility of the coordinate transformation Eq. (3.4), the relation $\det \mathbf{F} \neq 0$ holds. It is generally assumed that

---

[3] The operator Grad is related to the differentiation with respect to the material coordinates $\vec{X}$.

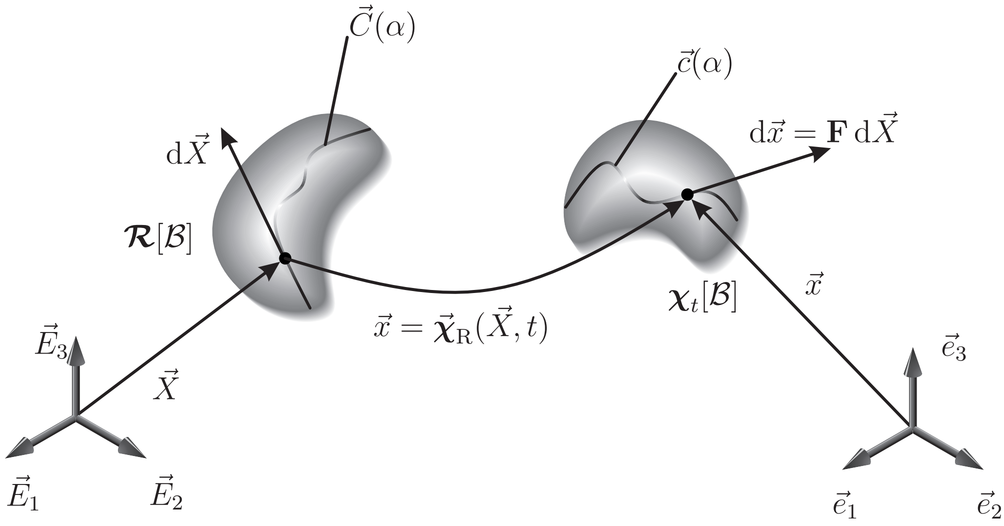

Figure 3.2: Transformation of material line elements by the deformation gradient modified from [Quint, 2012]

$\det \mathbf{F} > 0$. Introducing the displacement gradient tensor $\mathbf{H}(\vec{X}, t) := \operatorname{Grad} \vec{u}(\vec{X}, t)$ the deformation gradient can be expressed by $\mathbf{F} = \mathbf{1} + \mathbf{H}$, see [Haupt, 2002].

Even though the deformation gradient contains all the necessary information about the deformation, it is not primarily used as a strain measure in constitutive equations, due to the fact that the deformation gradient is not independent of rigid body motions. Instead, tensors are used which can be introduced by the polar decomposition of the deformation gradient $\mathbf{F}$, see Fig. 3.3. With this unique polar decomposition, $\mathbf{F}$ can be represented by the product of two tensors

$$\mathbf{F} = \mathbf{R}\mathbf{U} = \mathbf{V}\mathbf{R}. \tag{3.10}$$

$\mathbf{U}$ and $\mathbf{V}$ are positive definite[4] and symmetric second order tensors. They measure both the stretching or the contraction of material line elements. The right stretch tensor $\mathbf{U}$ operates on the reference configuration, whereas the left stretch tensor $\mathbf{V}$ is connected to the current configuration. The orthogonal tensor $\mathbf{R}$ is called *rotation tensor* and describes a pure rotation of a material line element with the properties $\mathbf{R}^{\mathrm{T}}\mathbf{R} = \mathbf{1}$ and $\det \mathbf{R} = +1$. By means of the two tensors, $\mathbf{U}$ and $\mathbf{V}$ it is possible to describe the deformation independently from rigid body motions. Subsequently, the right and left Cauchy-Green tensors are introduced, see [Haupt, 2002].

$$\mathbf{C} \;= \mathbf{F}^{\mathrm{T}}\mathbf{F} = \mathbf{U}^2, \tag{3.11}$$

$$\mathbf{B} \;= \mathbf{F}\mathbf{F}^{\mathrm{T}} = \mathbf{V}^2. \tag{3.12}$$

---

[4] A symmetric tensor $\mathbf{U} = \mathbf{U}^{\mathrm{T}}$ is positive definite if $\vec{v} \cdot \mathbf{U}\vec{v} > 0$ holds for any vector $\vec{v} \neq \vec{0}$.

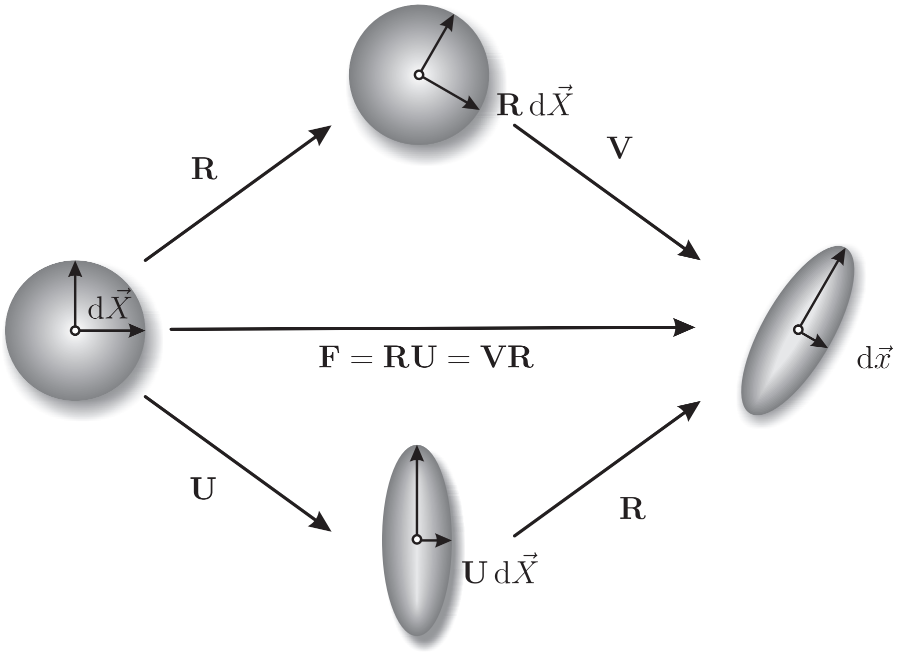

Figure 3.3: Polar decomposition of the deformation gradient

Therefore, one can avoid the calculation of roots, which has to be computed for the construction of $\mathbf{U}$ and $\mathbf{V}$.[5] In the following, these two tensors are used to define appropriate strain measures.

3.1.3 Strain Tensors

An appropriate strain measure should not be dependent on the rotational part of the polar decomposition. Thus, the Green strain tensor

$$\mathbf{E}(\vec{X},t) := \tfrac{1}{2}\left(\mathbf{C} - \mathbf{1}\right) = \tfrac{1}{2}\left(\mathbf{F}^{\mathrm{T}}\mathbf{F} - \mathbf{1}\right) \tag{3.13}$$

is introduced with the help of the right Cauchy-Green tensor.[6] It can be seen as a measure for the motion's deviation from a rigid body motion, [Haupt, 2002]. The tensor $\mathbf{1}$ represents a second-order unity tensor. The Green strain tensor $\mathbf{E}$ operates on the tangent space of the reference configuration and can also be introduced by the difference of the squares of material line elements and the help of Eq. (3.7)

$$|\,\mathrm{d}\vec{x}|^2 - |\,\mathrm{d}\vec{X}|^2 = \mathbf{F}\,\mathrm{d}\vec{X} \cdot \mathbf{F}\,\mathrm{d}\vec{X} - \mathrm{d}\vec{X} \cdot \mathrm{d}\vec{X} = \mathrm{d}\vec{X} \cdot \left(\mathbf{F}^{\mathrm{T}}\mathbf{F} - \mathbf{1}\right)\mathrm{d}\vec{X} \tag{3.14}$$

$$= \mathrm{d}\vec{X} \cdot 2\mathbf{E}\,\mathrm{d}\vec{X}. \tag{3.15}$$

---

[5] This generally includes the solution of an eigenvalue problem in order to obtain a diagonal structure for the calculation of roots, which can be numerically costly.

[6] The factor one-half is introduced for the connection to the small strain theory, see Eq. (3.17).

The Green tensor can also be expressed by the displacement gradient, yielding

$$\mathbf{E} = \tfrac{1}{2}(\mathbf{H} + \mathbf{H}^{\mathrm{T}} + \mathbf{H}^{\mathrm{T}}\mathbf{H}). \tag{3.16}$$

In the case of small strain theory, the quadratic term is neglected. This leads to the linear strain tensor

$$\boldsymbol{\varepsilon} := \tfrac{1}{2}(\mathbf{H} + \mathbf{H}^{\mathrm{T}}) = \tfrac{1}{2}(\operatorname{Grad}\vec{u} + \operatorname{Grad}^{T}\vec{u}). \tag{3.17}$$

Another important strain measure acting on the current configuration is the Almansi strain tensor

$$\mathbf{A} := \tfrac{1}{2}\left(\mathbf{1} - \mathbf{B}^{-1}\right) = \tfrac{1}{2}\left(\mathbf{1} - \mathbf{F}^{-\mathrm{T}}\mathbf{F}^{-1}\right). \tag{3.18}$$

Again, this tensor can be motivated by

$$\begin{aligned} |\,\mathrm{d}\vec{x}|^2 - |\,\mathrm{d}\vec{X}|^2 &= \mathrm{d}\vec{x}\cdot\mathrm{d}\vec{x} - \mathbf{F}^{-1}\,\mathrm{d}\vec{x}\cdot\mathbf{F}^{-1}\,\mathrm{d}\vec{x} = \mathrm{d}\vec{x}\cdot\left(\mathbf{1} - \mathbf{F}^{-\mathrm{T}}\mathbf{F}^{-1}\right)\mathrm{d}\vec{x} && (3.19)\\ &= \mathrm{d}\vec{x}\cdot 2\mathbf{A}\,\mathrm{d}\vec{x}. && (3.20)\end{aligned}$$

The two strain tensors are transferable into each other by

$$\mathbf{A} = \mathbf{F}^{-\mathrm{T}}\mathbf{E}\mathbf{F}^{-1} \quad\Leftrightarrow\quad \mathbf{E} = \mathbf{F}^{\mathrm{T}}\mathbf{A}\mathbf{F}. \tag{3.21}$$

3.1.4 Deformation Velocities

In Continuum Mechanics, it is also the rate of change that is of interest – in addition to the change of line, surface and volume elements. This is described by the spatial velocity gradient tensor, which can be motivated by the time derivative of Eq. (3.7)

$$\dot{\overline{\mathrm{d}\vec{x}}} = \dot{\mathbf{F}}\,\mathrm{d}\vec{X} = \dot{\mathbf{F}}\mathbf{F}^{-1}\,\mathrm{d}\vec{x} := \mathbf{L}\,\mathrm{d}\vec{x} \tag{3.22}$$

yielding the spatial velocity gradient tensor

$$\mathbf{L} = \dot{\mathbf{F}}\mathbf{F}^{-1} = \operatorname{grad}\vec{v}(\vec{x},t). \tag{3.23}$$

The dot denotes the material time derivative and $\vec{v}$ represents the velocity field. With $\mathbf{L}$, the rate of change for the line, surface and volume elements can be written as

$$\begin{aligned} \dot{\overline{\mathrm{d}\vec{x}}} &= \mathbf{L}\,\mathrm{d}\vec{x}, && (3.24)\\ \dot{\overline{\mathrm{d}\vec{a}}} &= \left[(\operatorname{tr}\mathbf{L})\mathbf{1} - \mathbf{L}^{\mathrm{T}}\right]\mathrm{d}\vec{a}, && (3.25)\\ \dot{\overline{\mathrm{d}v}} &= (\operatorname{tr}\mathbf{L})\,\mathrm{d}v, && (3.26)\end{aligned}$$

where $\operatorname{tr}\mathbf{L} = L_{kk}$ represents the trace operator. The spatial velocity gradient can be decomposed additively in a symmetric part $\mathbf{D}$ and a skew-symmetric part $\mathbf{W}$

$$\mathbf{L} = \mathbf{D} + \mathbf{W}. \tag{3.27}$$

The symmetric tensor $\mathbf{D}$ describes the rate at which material line elements change their length and angle (thus known as *stretching or strain-rate tensor*)

$$\mathbf{D} := \tfrac{1}{2}\left(\mathbf{L} + \mathbf{L}^{\mathrm{T}}\right), \quad \mathbf{D} = \mathbf{D}^{\mathrm{T}}. \tag{3.28}$$

The skew-symmetric part $\mathbf{W}$ is called *spin or vorticity tensor* and is defined by

$$\mathbf{W} := \tfrac{1}{2}\left(\mathbf{L} - \mathbf{L}^{\mathrm{T}}\right), \quad \mathbf{W} = -\mathbf{W}^{\mathrm{T}}. \tag{3.29}$$

It can be shown that the following relations

$$\dot{\mathbf{E}} = \mathbf{F}^{\mathrm{T}}\mathbf{D}\mathbf{F} \quad \Leftrightarrow \quad \mathbf{D} = \mathbf{F}^{-\mathrm{T}}\dot{\mathbf{E}}\mathbf{F}^{-1} \tag{3.30}$$

hold, see [Haupt, 2002]. With the help of Eq. (3.21) and Eq. (3.30), the following relation can be computed

$$\mathbf{D} = \mathbf{F}^{-\mathrm{T}}\dot{\mathbf{E}}\mathbf{F}^{-1} = \mathbf{F}^{-\mathrm{T}}\dot{\overline{\left(\mathbf{F}^{\mathrm{T}}\mathbf{A}\mathbf{F}\right)}}\mathbf{F}^{-1} = \dot{\mathbf{A}} + \mathbf{L}^{\mathrm{T}}\mathbf{A} + \mathbf{A}\mathbf{L} \equiv \overset{\vartriangle}{\mathbf{A}}, \tag{3.31}$$

where $\overset{\vartriangle}{\mathbf{A}}$ is the covariant Oldroyd derivative and is also equivalent to the strain rate tensor, see Eq. (3.115) for the definition of the covariant Oldroyd derivative and Eq. (3.129) for the connection to the concept of dual variables.

3.2 Stress Tensors, Heat Flux and Current Density

Due to the deformation inside a body, the occurring interactions result in stresses that have the unit force per area. The stresses are a crucial quantity in Continuum Mechanics, Holzapfel [2000]. Depending on the configuration, various stress tensors can be introduced and used for constitutive modeling. The following section serves to introduce stress tensors that are required in this work.

A traction is applied to the boundary of a material body. If the body is cut into two parts by a plane surface, see Fig. 3.4, this leads to forces on the surfaces on each part – in opposite direction. According to Fig. 3.4 it is claimed that, for every surface element,

$$\mathrm{d}\vec{f} = \vec{t}\,\mathrm{d}a = \mathbf{T}\,\mathrm{d}\vec{a}, \qquad \mathrm{d}\vec{a} = \vec{n}\,\mathrm{d}a. \tag{3.32}$$

The vector $\vec{t}$ represents the Cauchy stress vector and $\mathbf{T}$ is the Cauchy stress tensor, which is also called *true stress tensor* because it acts on surface elements in the current configuration. Cauchy's stress theorem connects the surface traction $\vec{t}$ with the stress tensor $\mathbf{T}$

$$\vec{t} = \mathbf{T}\vec{n} \tag{3.33}$$

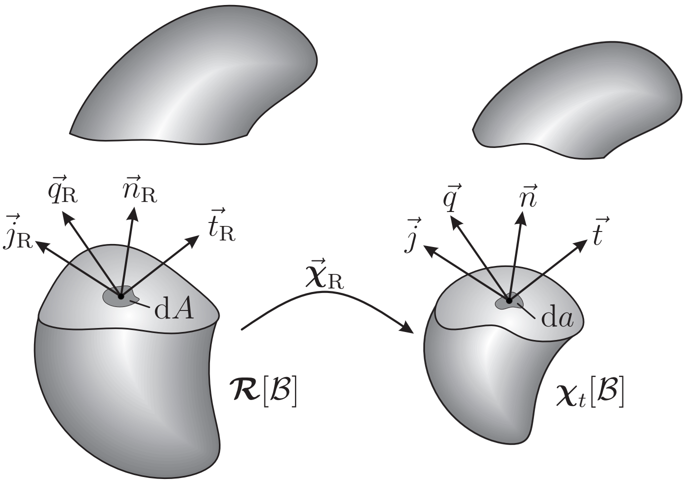

Figure 3.4: Stress, heat flux and current density vector

and states that the stress vector $\vec{t}$ depends linearly on the unit normal vectors $\vec{n}$.

With the force acting on the current configuration and the surface element in the reference configuration, the first Piola-Kirchhoff stress tensor $\mathbf{T}_\mathrm{R}$ can be introduced by

$$\mathrm{d}\vec{f} = \vec{t}_\mathrm{R}\,\mathrm{d}A = \mathbf{T}_\mathrm{R}\,\mathrm{d}\vec{A}, \qquad \mathrm{d}\vec{A} = \vec{n}_\mathrm{R}\,\mathrm{d}A. \tag{3.34}$$

Therefore, the first Piola-Kirchhoff tensor is a two-point tensor related to two configurations, due to the fact that the force acts in the current configuration and the surface elements refer to the reference configuration. The vector $\vec{n}_\mathrm{R}$ represents the unit normal vector in the reference configuration. Cauchy's theorem can also be defined in the reference configuration, yielding

$$\vec{t}_\mathrm{R} = \mathbf{T}_\mathrm{R}\vec{n}_\mathrm{R}. \tag{3.35}$$

With the transformation relation for surface element Eq. (3.8) the Cauchy and the first Piola-Kirchhoff stress tensors are connected by

$$\mathbf{T}_\mathrm{R} = \mathbf{T}(\det\mathbf{F})\mathbf{F}^{-\mathrm{T}}. \tag{3.36}$$

Another important stress tensor operating on the reference configuration is the second Piola-Kirchhoff tensor

$$\tilde{\mathbf{T}} := (\det\mathbf{F})\,\mathbf{F}^{-1}\mathbf{T}\mathbf{F}^{-\mathrm{T}}, \tag{3.37}$$

which is a symmetric tensor. In constitutive modeling often the Kirchhoff stress tensor is used, which is related to the Cauchy stress tensor and weighted with $\det\mathbf{F}$

$$\mathbf{S} := (\det\mathbf{F})\,\mathbf{T}. \tag{3.38}$$

Table 3.1: Stress tensor transformation table: first Piola-Kirchhoff stresses $\mathbf{T}_\mathrm{R}$, second Piola-Kirchhoff stresses $\tilde{\mathbf{T}}$, Kirchhoff stresses $\mathbf{S}$, Cauchy stresses $\mathbf{T}$

	$\mathbf{T}_\mathrm{R}$	$\tilde{\mathbf{T}}$	$\mathbf{S}$	$\mathbf{T}$
$\mathbf{T}_\mathrm{R}$		$\mathbf{F}\tilde{\mathbf{T}}$	$\mathbf{S}\mathbf{F}^{-\mathrm{T}}$	$(\det\mathbf{F})\mathbf{T}\mathbf{F}^{-\mathrm{T}}$
$\tilde{\mathbf{T}}$	$\mathbf{F}^{-1}\mathbf{T}_\mathrm{R}$		$\mathbf{F}^{-1}\mathbf{S}\mathbf{F}^{-\mathrm{T}}$	$(\det\mathbf{F})\mathbf{F}^{-1}\mathbf{T}\mathbf{F}^{-\mathrm{T}}$
$\mathbf{S}$	$\mathbf{T}_\mathrm{R}\mathbf{F}^\mathrm{T}$	$\mathbf{F}\tilde{\mathbf{T}}\mathbf{F}^\mathrm{T}$		$(\det\mathbf{F})\mathbf{T}$
$\mathbf{T}$	$\frac{1}{\det\mathbf{F}}\mathbf{T}_\mathrm{R}\mathbf{F}^\mathrm{T}$	$\frac{1}{\det\mathbf{F}}\mathbf{F}\tilde{\mathbf{T}}\mathbf{F}^\mathrm{T}$	$\frac{1}{\det\mathbf{F}}\mathbf{S}$	

The previously introduced stress tensors can be converted into each other as summarized in Tab. 3.1.

The equivalent quantities to the stress tensor are the heat flux[7] $\vec{q}$ and the electric current density[8] $\vec{j}$ over the surface of the body in the current configuration $\boldsymbol{\chi}_t$

$$q_\mathrm{n} = -\vec{q}\cdot\vec{n}, \qquad j_\mathrm{n} = -\vec{j}\cdot\vec{n}. \tag{3.39}$$

The time dependent vector field $\vec{q}$ is also known as *Cauchy heat flux or true heat flux* with the property $-\vec{q}\cdot\mathrm{d}\vec{a} = -\vec{q}\cdot\vec{n}\,\mathrm{d}a = q_\mathrm{n}\,\mathrm{d}a$, see [Haupt, 2002, p. 122]. The minus sign is due to the convention that a flow is defined to be positive if the material body absorbs energy. With help of Eq. (3.8), the heat flux and the current density in the reference configuration are given by

$$\vec{q}_\mathrm{R} = (\det\mathbf{F})\,\mathbf{F}^{-1}\vec{q}, \qquad \vec{j}_\mathrm{R} = (\det\mathbf{F})\,\mathbf{F}^{-1}\vec{j}. \tag{3.40}$$

3.3 Thermo-Electro-Mechanical Balance Equations

In this chapter, the classical balance principles are introduced and discussed. These are the conservation of mass, the momentum balance principles, the balance of energy and the Maxwell balance equations. Additionally, the entropy inequality is introduced – and is used later on to define a physically plausible material model.

3.3.1 Balance of Mass

The mass of a material body is a measure for the resistance against any change of velocity (inertial mass) and measures the effects of gravitational force. The mass is

---

[7] The heat flux has the unit W m^{-2}.

[8] The electric current density has the unit A m^{-2}.

defined over the volume integral of the mass density

$$m(t) = \int\limits_V \rho_0(\vec{X}, t)\,\mathrm{d}V = \int\limits_v \rho\,(\vec{x}, t)\,\mathrm{d}v, \tag{3.41}$$

where ρ and ρ_0 denote the mass densities in the current and the reference configuration. The mass conservation $\dot{m} = 0$ yields

$$\frac{\mathrm{d}m}{\mathrm{d}t} = \frac{\mathrm{d}}{\mathrm{d}t}\int\limits_V \rho_0(\vec{X}, t)\,\mathrm{d}V = \frac{\mathrm{d}}{\mathrm{d}t}\int\limits_v \rho(\vec{x}, t)\,\mathrm{d}v = 0. \tag{3.42}$$

The local form in the reference configuration can be computed by

$$\frac{\partial}{\partial t}\rho_0(\vec{X}, t) = 0 \Longleftrightarrow \rho_0(\vec{X}, t) = \rho_0(\vec{X}). \tag{3.43}$$

This relation states that the density is temporally constant in the reference configuration. Accordingly, the local form can be written in the current configuration as

$$\dot{\rho} + \rho \operatorname{div} \vec{v} = 0. \tag{3.44}$$

The mass densities of the current ρ and the reference configuration ρ_0 can be connected by means of Eq. (3.9)

$$\rho_0 = \rho \det \mathbf{F}. \tag{3.45}$$

3.3.2 Balance of Linear Momentum

The linear momentum of a material body is defined by the volume integral with the product of the mass density and the velocity. The balance of linear momentum states that the change of linear momentum with respect to the time is equal to the external forces, which can be separated in volume and surface distributed forces

$$\frac{\mathrm{d}}{\mathrm{d}t}\int\limits_v \vec{v}\rho\,\mathrm{d}v = \int\limits_a \vec{t}\,\mathrm{d}a + \int\limits_v \vec{k}\rho\,\mathrm{d}v. \tag{3.46}$$

Here, $\vec{k}$ represents the force density per unit mass and $\vec{t}$ is the stress vector exerting on the surface of the material body. By applying Gauss's theorem, the surface integral can be converted into a volume integral that – together with the mass balance and Cauchy's theorem Eq. (3.33) – leads to the local form of the balance of linear momentum, see [Haupt, 2002, p. 96],

$$\rho\dot{\vec{v}} = \operatorname{div} \mathbf{T} + \rho\vec{k}. \tag{3.47}$$

The equivalent integral and local representation in the reference (material) representation can be given with the transformation of the material surface element (3.8) and volume elements (3.9)

$$\frac{\mathrm{d}}{\mathrm{d}t}\int\limits_V \vec{v}\rho_0\,\mathrm{d}V = \int\limits_A \vec{t}_\mathrm{R}\,\mathrm{d}A + \int\limits_V \vec{k}\rho_0\,\mathrm{d}V, \qquad \rho_0\dot{\vec{v}} = \mathrm{Div}\,\mathbf{T}_\mathrm{R} + \rho_0\vec{k}. \tag{3.48}$$

3.3.3 Balance of Angular Momentum

The balance of angular momentum states that the change of rotational momentum with respect to the time is equal to the angular momentum exerted by forces acting on the material body. It is given by

$$\frac{\mathrm{d}}{\mathrm{d}t}\int\limits_v (\vec{x}-\vec{c})\times\vec{v}\rho\,\mathrm{d}v = \int\limits_a (\vec{x}-\vec{c})\times\vec{t}\,\mathrm{d}a + \int\limits_v (\vec{x}-\vec{c})\times\vec{k}\rho\,\mathrm{d}v, \tag{3.49}$$

related to $\vec{c}$ as a fixed point in space. The local form of the balance of rotational momentum is given by

$$\mathbf{T} = \mathbf{T}^\mathrm{T}, \tag{3.50}$$

which means that the Cauchy stress tensor is symmetric, see [Haupt, 2002, p. 99] for a proof.

3.3.4 Balance Equations of Electrodynamics - Maxwell Equations

The fundamental equations describing the theory of electrodynamics of continua are the Maxwell equations. In the following, the Maxwell equations will be introduced on the macroscopic level. The microscopic sources and equations are not discussed here and it is referred to the literature, see e.g. [Eringen and Maugin, 1990]. In this context, the particular focus lies on the explanation of the Joule heating effect and the connection to the Maxwell equations. The scope of this work does not cover any theories concerning piezoelectrics. These can be found, for example, in [Kamlah, 2000]. A comprehensive overview of the subject area of electrodynamics in general can be found in [Klingbeil, 2010; Griffiths, 2011; Landau et al., 2008]. An overview from the point of Continuum Mechanics can be found in [Eringen and Maugin, 1990].

Motivation - Coulomb Force

In the case of electrostatics, the interaction between charged particles can be described by Coulomb's model. The question is which force $\vec{F}_{12}$ is exerted on two particles with the distance $\vec{d}_{12} := (\vec{x}_{q_2} - \vec{x}_{q_1}) = d_{12}\vec{e}_{12}$. Coulomb showed by experiments that the following relation

$$\vec{F}_{12} = \frac{q_1 q_2}{4\pi\epsilon_0 d_{12}^2}\vec{e}_{12} \tag{3.51}$$

holds, see Fig. 3.5. The force between two charged particles is proportional to the charge product and inversely proportional to the square of the distance. In general, a charge[9] can be positive or negative. Equally charged particles repel each other and opposite charge particles attract each other. In Eq. (3.51), the constant ϵ_0 is

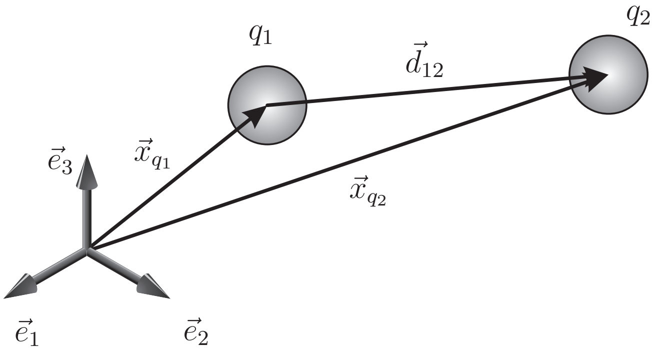

Figure 3.5: Two charged particles

called *vacuum permittivity* and is given by $\epsilon_0 = 8.854 \times 10^{-12}\,\mathrm{F\,m^{-1}}$.[10] In other media than vacuum, the permittivity is given by $\epsilon = \epsilon_r\epsilon_0$, where ϵ_r denotes the relative permittivity. In the case of multiple charges, the superposition principle holds and the resulting force, see [Griffiths, 2011, p. 100] and [Zohdi, 2012b, p. 14], can be computed by the sum of the electrical charges

$$\vec{F} = \sum_{k=2}^{N} \frac{q_1 q_k}{4\pi\epsilon_0 d_{1k}^2}\vec{e}_{1k}. \tag{3.52}$$

Electric Field

The force field on a test charge q_t and a charge q_{el} with the distance $\vec{e}_d$ is given by

$$\vec{F} = \frac{q_{\mathrm{el}} q_t}{4\pi\epsilon_0 d^2}\vec{e}_d. \tag{3.53}$$

The electric field[11] is defined by the force per unit charge q_t and reads

$$\vec{E} := \frac{\vec{F}}{q_t} = \frac{q_{\mathrm{el}}}{4\pi\epsilon_0 d^2}\vec{e}_d. \tag{3.54}$$

---

[9] The unit of electrical charge is given by Coulomb and derived from by the SI-units $\mathrm{C} = \mathrm{A\,s}$.

[10] Farad represents the electrical capacitance and is given in the SI-units $\mathrm{F} = \mathrm{A\,s\,V^{-1}}$.

[11] Also known as *electric field intensity*.

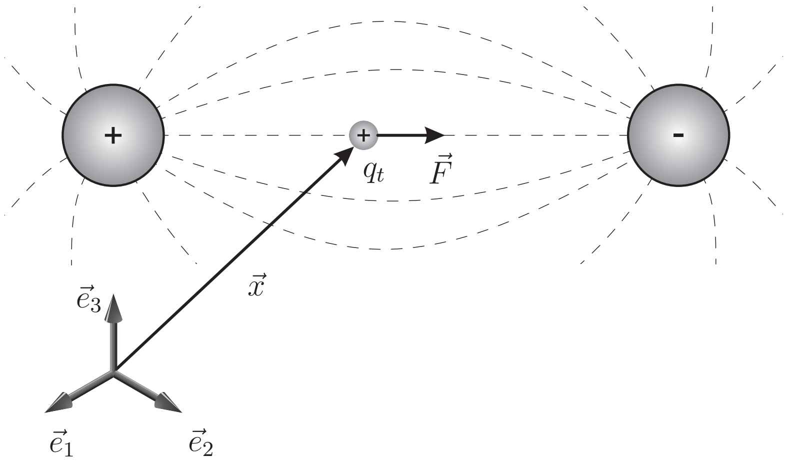

Figure 3.6: Electrical field

If the charge q_{el} is volumetrically distributed and can be expressed by the charge density ρ_φ, the electric field is represented by

$$\vec{E}(\vec{d}) = \int\limits_V \frac{\rho_\varphi}{4\pi\epsilon_0 d^2}\vec{e}_d \, \mathrm{d}V. \tag{3.55}$$

The total charge Q_{el} over the volume is given by

$$Q_{\text{el}} = \int\limits_V \rho_\varphi \, \mathrm{d}V. \tag{3.56}$$

Voltage

For the movement of a charge q_{el} along a curve c from one point to another, work W is required. The voltage U is defined as the work per unit charge, see [Zohdi, 2012b] and [Klingbeil, 2010],

$$U = \frac{W}{q_{\text{el}}} = \int\limits_C \vec{E} \cdot \mathrm{d}\vec{X}, \tag{3.57}$$

where $\mathrm{d}\vec{X}$ denotes the motion of the charge q_{el} under the influence of the force $\vec{F}$.

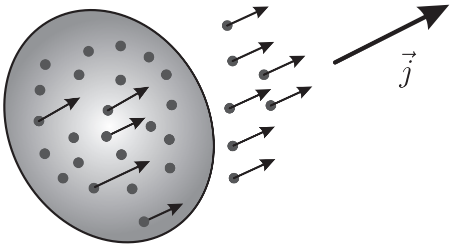

Figure 3.7: Electrical charge flow causes electric current density

Electric Current

An electric current[12] can be seen as a flow of electrical charge, see Fig. 3.7,

$$I = \frac{\mathrm{d}Q_{\mathrm{el}}}{\mathrm{d}t}. \tag{3.58}$$

Inserting the total charge Eq. (3.56) yields

$$I = \int\limits_V \dot{\rho}_\varphi \,\mathrm{d}V \tag{3.59}$$

Considering the charge conservation (3.72), the current has the following expression

$$I = -\int\limits_V \mathrm{Div}\,\vec{j}_{\mathrm{R}} \,\mathrm{d}V, \qquad \vec{j}_{\mathrm{R}} = n q_{\mathrm{el}} \vec{v}_{\mathrm{R}}. \tag{3.60}$$

The vector $\vec{j}_{\mathrm{R}}$ is called *electric current density* related to the reference configuration and is caused by a number of n charge particles q_{el} with the velocity $\vec{v}_{\mathrm{R}}$, see Fig. 3.7. With the help of the divergence theorem, the volume integral can be transformed into a surface integral with the electric current density

$$I = -\int\limits_a \vec{j}_{\mathrm{R}} \cdot \vec{n}_{\mathrm{R}} \,\mathrm{d}A = \int\limits_a j_{\mathrm{n}} \,\mathrm{d}A. \tag{3.61}$$

In the finite element simulations, see Chap. 7, the electric current is applied as a boundary condition.

Maxwell Equations

The fundamental equations describing the theory of electromagnetic fields are the Maxwell equations. They are a set of partial differential equations and characterize

---

[12] The unit of the electric current is Ampere $\mathrm{A{=}C\,s^{-1}}$.

the interaction between electric and magnetic fields as well as between charges and currents.

Ampere's law can be stated in integral form as

$$\oint\limits_{c} \vec{H} \cdot \mathrm{d}\vec{x} = \int\limits_{a} \vec{j} \cdot \mathrm{d}\vec{a} + \frac{\mathrm{d}}{\mathrm{d}t} \int\limits_{a} \vec{D} \cdot \mathrm{d}\vec{a}, \tag{3.62}$$

where $\vec{H}$ is the magnetic field intensity and $\vec{j}$ denotes the electric current density[13] whereas $\vec{D}$ is the electric displacement field. Ampere's law describes that a magnetic field can be generated by an electrical current or a changing electrical field. The transformation with the help of the Kelvin-Stokes theorem[14] leads to the local form

$$\operatorname{curl} \vec{H} = \vec{j} + \dot{\vec{D}}. \tag{3.63}$$

Faraday's law states that a time-varying magnetic field $\dot{\vec{B}}$ comes along with an electrical field $\vec{E}$

$$\oint\limits_{c} \vec{E} \cdot \mathrm{d}\vec{x} = -\frac{\mathrm{d}}{\mathrm{d}t} \int\limits_{a} \vec{B} \cdot \mathrm{d}\vec{a}. \tag{3.64}$$

The magnetic field $\vec{B}$ is also referred to as *magnetic field density* or *magnetic induction*. The local form of Faraday's law is given by

$$\operatorname{curl} \vec{E} = -\dot{\vec{B}}. \tag{3.65}$$

Gauss's law for magnetism in integral form reads

$$\oint\limits_{a} \vec{B} \cdot \mathrm{d}\vec{a} = 0. \tag{3.66}$$

The result of Gauss's law for magnetism is that there are no magnetic sources or, in other words, no magnetic monopoles. Its local form is given by

$$\operatorname{div} \vec{B} = 0. \tag{3.67}$$

Gauss's law is related to an electrical field caused by an electric charge

$$\oint\limits_{a} \vec{D} \cdot \mathrm{d}\vec{a} = \int\limits_{v} \rho_{\varphi} \, \mathrm{d}v \tag{3.68}$$

with the charge density ρ_{φ}. The local form reads

$$\operatorname{div} \vec{D} = \rho_{\varphi}. \tag{3.69}$$

---

[13] The current density has the unit $\mathrm{A\,m^{-2}}$.

[14] The Kelvin-Stokes or "curl" theorem connects the integral of the curl of a vector field over a surface to the line integral of the vector field over a surface boundary, $\oint_c \vec{V} \cdot \mathrm{d}\vec{x} = \int_a \operatorname{curl} \vec{V} \cdot \mathrm{d}\vec{a}$

Applying the divergence on Ampere's law Eq. (3.63) yields

$$\operatorname{div}(\vec{j} + \dot{\vec{D}}) = 0 \tag{3.70}$$

because $\operatorname{div}(\operatorname{curl}\vec{H}) = 0$ holds. The use of Gauss's law Eq. (3.69)

$$\operatorname{div}(\vec{j} + \dot{\vec{D}}) = \operatorname{div}\vec{j} + \frac{\mathrm{d}}{\mathrm{d}t}\operatorname{div}\vec{D} \tag{3.71}$$

$$\Rightarrow \operatorname{div}\vec{j} + \dot{\rho}_\varphi = 0 \tag{3.72}$$

leads to the charge conservation. It states that the change of electric charge is the difference between the charge flowing in and out of the volume. Thus, there are no charge sources or sinks in a volume.

Electromagnetic Energy

Considering the Poynting vector $\vec{S} = \vec{E} \times \vec{H}$,[15] the outward power transportation P over a surface can be written, see [Klingbeil, 2010], as

$$P = \int_a \vec{S} \cdot \mathrm{d}\vec{a} = \int_a \left(\vec{E} \times \vec{H}\right) \cdot \mathrm{d}\vec{a}. \tag{3.73}$$

By applying the Gauss theorem, the surface integral can be converted into a volume integral

$$P = \int_a \left(\vec{E} \times \vec{H}\right) \cdot \mathrm{d}\vec{a} = \int_v \operatorname{div}\left(\vec{E} \times \vec{H}\right) \mathrm{d}v. \tag{3.74}$$

With the help of the relation $\operatorname{div}(\vec{V}_1 \times \vec{V}_2) = \vec{V}_2 \cdot \operatorname{curl}\vec{V}_1 - \vec{V}_1 \cdot \operatorname{curl}\vec{V}_2$ the power can be formulated as

$$P = \int_v \left(\vec{H} \cdot \operatorname{curl}\vec{E} - \vec{E} \cdot \operatorname{curl}\vec{H}\right) \mathrm{d}v. \tag{3.75}$$

Inserting Faraday's law (3.65) and Ampere's law (3.63) leads to

$$P = \int_v \left(-\vec{H} \cdot \dot{\vec{B}} - \vec{E} \cdot \left(\vec{j} + \dot{\vec{D}}\right)\right) \mathrm{d}v \tag{3.76}$$

$$= -\int_v \vec{H} \cdot \dot{\vec{B}}\,\mathrm{d}v - \int_v \vec{E} \cdot \vec{j}\,\mathrm{d}v - \int_v \vec{E} \cdot \dot{\vec{D}}\,\mathrm{d}v. \tag{3.77}$$

App. 1 shows the connection to the magnetic and electric energy. The electric power will be used in the balance of energy (3.101a).

---

[15] × denotes the cross product.

Stationary Charge Equation

In this work, the Joule heating effect for the volumetric heating of the FAST-tool system and the powder is of main importance. In the following, a motivation for the stationary charge equation will be given.

App. 2 provides an estimation for the change of charge density with respect to the time. As a result, the change is negligible – which leads to the stationary charge equation

$$\operatorname{div} \vec{j} = 0 \tag{3.78}$$

All the sintering experiments shown in Chap. 2 feature a non-pulsed direct current. Due to this, and due to the arguments mentioned in App. 2, the Maxwell equations are assumed to be time-independent and reduce to

$$\operatorname{curl} \vec{H} = \vec{j} \tag{3.79}$$

$$\operatorname{curl} \vec{E} = 0 \tag{3.80}$$

$$\operatorname{div} \vec{B} = 0 \tag{3.81}$$

$$\operatorname{div} \vec{D} = \rho_\varphi \tag{3.82}$$

The first equation leads to the stationary charge equation as explained above. The second equation Eq. (3.80) can be fulfilled by a potential field

$$\vec{E} = -\operatorname{grad} \varphi \tag{3.83}$$

because $\operatorname{curl} \operatorname{grad} \varphi = 0$ holds. Eq. (3.80) can be written in integral form as

$$\oint_C \vec{E} \cdot \mathrm{d}\vec{x} = 0 \tag{3.84}$$

stating that the voltage is independent on the curve progression. This can be proved by assuming a voltage along a curve c_1 and another voltage along a different curve c_2 with the same initial and end points but different orientations, see [Klingbeil, 2010].

$$U_1 = \int_{c_1} \vec{E} \cdot \mathrm{d}\vec{x} \qquad U_2 = \int_{c_2} \vec{E} \cdot \mathrm{d}\vec{x} \tag{3.85}$$

Using Eq. (3.84), it is possible to write

$$\oint_C \vec{E} \cdot \mathrm{d}\vec{x} = \int_{c_1} \vec{E} \cdot \mathrm{d}\vec{x} - \int_{c_2} \vec{E} \cdot \mathrm{d}\vec{x} = U_1 - U_2 = 0 \quad \Rightarrow \quad U_1 = U_2. \tag{3.86}$$

In the following, the voltage between two points is computed. Therefore, Eq. (3.83) is inserted into Eq. (3.57) leading to

$$U = -\int_c (\operatorname{grad}\varphi) \cdot \mathrm{d}\vec{x}. \tag{3.87}$$

The curve integral is now parametrized with the parameter α and reads

$$U = -\int_a^b (\operatorname{grad}\varphi) \cdot \frac{\mathrm{d}\vec{x}}{\mathrm{d}\alpha}\,\mathrm{d}\alpha. \tag{3.88}$$

The gradient $\operatorname{grad}\varphi$ and the position vector $\vec{x}$ can be written as

$$\operatorname{grad}\varphi = \varphi_{,i}\vec{e}_i, \qquad \frac{\mathrm{d}\vec{x}}{\mathrm{d}\alpha} = x_{i,\alpha}\vec{e}_i. \tag{3.89}$$

Inserting these relations into Eq. (3.88) yields

$$U = -\int_a^b \varphi_{,i}\, x_{i,\alpha}\,\mathrm{d}\alpha = -\int_a^b \frac{\mathrm{d}\varphi}{\mathrm{d}\alpha}\,\mathrm{d}\alpha = \varphi(a) - \varphi(b). \tag{3.90}$$

Thus, in the electrostatics, the voltage can be seen as a potential difference. Here, $\varphi(a)$ denotes the electrical potential at the initial point of the curve and $\varphi(b)$ is the potential at the end point.

3.3.5 Energy Balance

Both the mechanical and electrical power as well as the heat supply to a material body lead to a change of the kinetic and internal energy given by the relation

$$\dot{K} + \dot{E} = P_{\mathrm{mech}} + P_{\mathrm{elec}} + Q, \tag{3.91}$$

see [Eringen and Maugin, 1990]. The kinetic energy of the material body is given by the volume integral

$$K = \int_v \tfrac{1}{2}\vec{v} \cdot \vec{v}\rho\,\mathrm{d}v. \tag{3.92}$$

The internal energy is given as the volume integral over the specific energy e

$$E = \int_v e\rho\,\mathrm{d}v. \tag{3.93}$$

The internal energy represents the total energy of the material body subtracted by the kinetic energy. A change in energy can be caused by the mechanical power and by the external forces exterted on the material body

$$P_{\mathrm{mech}} = \int\limits_a \vec{t} \cdot \vec{v} \,\mathrm{d}a + \int\limits_v \vec{k} \cdot \vec{v} \rho \,\mathrm{d}v. \tag{3.94}$$

Furthermore, the energy can be changed by the electrical field. Due to the stationary electrical field, Eq. (3.77) reduces to[16]

$$P_{\mathrm{elec}} = \int\limits_v \vec{E} \cdot \vec{j} \,\mathrm{d}v. \tag{3.95}$$

A change in the heat supply causes an energy change as well

$$Q = -\int\limits_a \vec{q} \cdot \vec{n} \,\mathrm{d}a + \int\limits_v r \rho \,\mathrm{d}v. \tag{3.96}$$

A volumetric heat source is given by the scalar r and can be caused by radiation or internal processes.

Inserting the definitions Eq. (3.92)-Eq. (3.96) in Eq. (3.91) yields

$$\frac{\mathrm{d}}{\mathrm{d}t} \int\limits_v \left(\tfrac{1}{2}\vec{v} \cdot \vec{v} + e\right) \rho \,\mathrm{d}v = \int\limits_a \mathbf{T}\vec{n} \cdot \vec{v} \,\mathrm{d}a + \int\limits_v \vec{k} \cdot \vec{v} \rho \,\mathrm{d}v + \int\limits_v \vec{E} \cdot \vec{j} \,\mathrm{d}v - \int\limits_a \vec{q} \cdot \vec{n} \,\mathrm{d}a + \int\limits_v r \rho \,\mathrm{d}v. \tag{3.97}$$

With the help of the divergence theorem, the surface integral can be transformed into a volume integral

$$\int\limits_v \left(\vec{v} \cdot \dot{\vec{v}} + \dot{e}\right) \rho \,\mathrm{d}v = \int\limits_v \left[\mathrm{div}\, \left(\mathbf{T}^{\mathrm{T}}\vec{v}\right) + \vec{k} \cdot \vec{v}\rho + \vec{E} \cdot \vec{j} - \mathrm{div}\,\vec{q} + r\rho\right] \mathrm{d}v. \tag{3.98}$$

After applying the identity $\mathrm{div}\,\left(\mathbf{T}^{\mathrm{T}}\vec{v}\right) = (\mathrm{div}\,\mathbf{T}) \cdot \vec{v} + \mathbf{T} \cdot \mathrm{grad}\,\vec{v}$ and the symmetry of the stress tensor $\mathbf{T} = \mathbf{T}^{\mathrm{T}}$, the energy balance reads

$$\int\limits_v \left(\dot{e} + \vec{v} \cdot \dot{\vec{v}}\right) \rho \,\mathrm{d}v = \int\limits_v \left(\mathbf{T} \cdot \mathbf{D} + \vec{E} \cdot \vec{j} - \mathrm{div}\,\vec{q} + r\rho\right) \mathrm{d}v + \int\limits_v \left(\mathrm{div}\,\mathbf{T} + \vec{k}\rho\right) \cdot \vec{v} \,\mathrm{d}v. \tag{3.99}$$

---

[16] In Eq. (3.77) the Poynting vector describes the power flowing out of the body. Here, it is assumed that the electrical power increases the energy of the material body. By definition, the absorbed energy by the material body is set to be positive.

Eliminating the balance of linear momentum Eq. (3.47) leads to the simplified equation

$$\int\limits_v \left(\dot{e} - \frac{1}{\rho}\mathbf{T}\cdot\mathbf{D} - \frac{1}{\rho}\vec{E}\cdot\vec{j} + \frac{1}{\rho}\operatorname{div}\vec{q} - r \right) \rho\,\mathrm{d}v = 0. \tag{3.100}$$

Accordingly, the local balance of energy can be written relative to the current configuration

$$\dot{e} = \frac{1}{\rho}\mathbf{T}\cdot\mathbf{D} + \frac{1}{\rho}\vec{E}\cdot\vec{j} - \frac{1}{\rho}\operatorname{div}\vec{q} + r \tag{3.101a}$$

and relative to the reference (material) configuration

$$\dot{e} = \frac{1}{\rho_0}\tilde{\mathbf{T}}\cdot\dot{\mathbf{E}} + \frac{1}{\rho_0}\vec{E}_\mathrm{R}\cdot\vec{j}_\mathrm{R} - \frac{1}{\rho_0}\operatorname{Div}\vec{q}_\mathrm{R} + r. \tag{3.101b}$$

3.3.6 Principle of Irreversibility

Generally, the entropy s can be seen as a measure of the microscopic randomness and disorder, [Holzapfel, 2000]. The principle of irreversibility states that the entropy production of a closed system can never decrease. The entropy can only increase or remain constant. Starting from the local form of the Clausius-Duhem inequality

$$\rho\dot{s} \geq -\operatorname{div}\left(\frac{\vec{q}}{\Theta}\right) + \rho\frac{r}{\Theta}, \tag{3.102}$$

the identity

$$\operatorname{div}\left(\frac{\vec{q}}{\Theta}\right) = \frac{1}{\Theta}\operatorname{div}\vec{q} - \frac{1}{\Theta^2}\operatorname{grad}\Theta\cdot\vec{q} \tag{3.103}$$

leads to an alternative representation

$$\rho\dot{s} \geq -\frac{1}{\Theta}\operatorname{div}\vec{q} + \frac{1}{\Theta^2}\operatorname{grad}\Theta\cdot\vec{q} + \rho\frac{r}{\Theta}. \tag{3.104}$$

By means of the definition of the Helmholtz free energy, [Haupt, 2002, p. 488], and its time derivative

$$\psi := e - \Theta s \quad \Rightarrow \quad \dot{\psi} = \dot{e} - \dot{\Theta}s - \Theta\dot{s}, \tag{3.105}$$

the entropy time derivative can be replaced. Then, inserting the energy balance Eq. (3.101a) leads to

$$-\rho\dot{\psi} - \rho s\dot{\Theta} + \mathbf{T}\cdot\mathbf{D} + \vec{E}\cdot\vec{j} - \frac{1}{\Theta}\operatorname{grad}\Theta\cdot\vec{q} \geq 0. \tag{3.106}$$

In the reference configuration, the Clausius-Duhem inequality reads

$$-\rho_0\dot{\psi} - \rho_0 s\dot{\Theta} + \tilde{\mathbf{T}}\cdot\dot{\mathbf{E}} + \vec{E}_\mathrm{R}\cdot\vec{j}_\mathrm{R} - \frac{1}{\Theta}\operatorname{Grad}\Theta\cdot\vec{q}_\mathrm{R} \geq 0. \tag{3.107}$$

This form of the Clausius-Duhem inequality will be used later to develop a thermodynamically consistent material model.

3.4 Issues of Constitutive Modeling

The previous sections served to introduce the balance equations. These balance principles are considered to be universal laws of nature.[17] This forms an initial boundary value problem, which can not be solved solely with the balance equations. This gap has to be filled by constitutive equations, which e.g. connect the heat flux with the temperature and the current density with the electrical potential as well as stresses with strains. Additionally, the internal energy and the entropy flux arise in this context.

The theory of materials is a branch of Continuum Mechanics and has been strongly influenced by Truesdell and Noll [2004] since the sixties of the last century. It provides systematic methods for the construction of constitutive models. In general, constitutive equations are relations that describe the response of a material element to a given input process. It is not the aim of material modeling to develop a single universal material model for all input processes under all circumstances. Rather, material models define the material behavior under specific conditions in a certain application range. There are some basic principles concerning the construction of such constitutive models. They are:

- **Determinism**
  The principle of determinism states that the material behavior is determined by the actual load and can only depend on processes that have already taken place, not on future processes.

- **Local action**
  The principle of local action demands that the stress state of a material point can only be influenced by its environment. Commonly, the local motion is described by a first order approximation, the deformation gradient, see [Haupt, 2002].

- **Equipresence**
  According to this principle, all material equations should depend on the same set of variables.

- **Material frame indifference**
  Material objectivity means that the material equations should be independent of a change of reference system. Thus, it is necessary to define variables that are invariant with respect to a change of frame. The concept of dual variables, which is introduced later, offers a guideline to define such quantities.

---

[17] These physical principles are conclusions from scientific experiments and observations and have been accepted within the scientific community. Thus, it is possible to use the term “principles” instead of “laws” – but it has become common to refer to the Clausius-Duhem inequality as the *second law of thermodynamics*.

- **Physical Consistency**
  The constitutive model should not contradict the second law of thermodynamics. The entropy inequality restricts the material relations in such a way that the second law should be fulfilled for any process. There are two possibilities to ensure the fulfillment of the Clausius-Duhem inequality. One possibility would be to check this issue after the construction of the material model – but this would turn out to be rather difficult. In this work, the Clausius-Duhem inequality is therefore used to develop a thermodynamically consistent material model.

Other recommendations concerning the material symmetry or kinematical constraints such as incompressibility are not addressed here. Instead, it is referred to the literature, see [Holzapfel, 2000; Haupt, 2002; Hutter and Jöhnk, 2004; Altenbach and Altenbach, 1994]. In general, the necessary and sufficient rules to construct a physically plausible and consistent material model are still an open question in material theory, [Haupt, 2002].

3.4.1 Objectivity

In the following, the term *objectivity* (which is related to certain transformation properties of physical quantities) is explained by introducing an Euclidean transformation Eq. (3.108), which represents a transformation between two reference systems

$$\vec{x}^* = \mathbf{Q}(t)\vec{x} + \vec{c}(t), \qquad t^* = t - a. \tag{3.108}$$

It consists of a time-dependent rotation, denoted by the orthogonal tensor $\mathbf{Q}(t)$ and a translation according to $\vec{c}(t)$. The constant $a \in \mathbb{R}$ describes a shift of time between the two systems. This Euclidean transformation describes a rigid body motion.

A scalar quantity φ, a vector quantity $\vec{v}$ and a tensor quantity $\mathbf{A}$ are to be seen as "objective" if – for every change of frame – the relations

$$\varphi^* = \varphi, \qquad \vec{v}^* = \mathbf{Q}(t)\vec{v}, \qquad \mathbf{A}^* = \mathbf{Q}\mathbf{A}\mathbf{Q}^{\mathrm{T}} \tag{3.109}$$

hold. In this case, another possible expression is "observer-independence". With the transformed position vector Eq. (3.108), the transformed line element is given by

$$\mathrm{d}\vec{x}^* = \mathbf{F}^*\,\mathrm{d}\vec{X} = \mathbf{Q}\mathbf{F}\,\mathrm{d}\vec{X} = \mathbf{Q}\,\mathrm{d}\vec{x}, \qquad \mathbf{F}^* = \mathbf{Q}\mathbf{F} \tag{3.110}$$

leading to the transformed deformation gradient $\mathbf{F}^*$, which is a non-objective tensor according to Eq. (3.109). From this it follows for the transformation of the right Cauchy-Green tensor

$$\mathbf{C}^* = \left(\mathbf{F}^*\right)^{\mathrm{T}} \mathbf{F}^* = \mathbf{F}^{\mathrm{T}}\mathbf{Q}^{\mathrm{T}}\mathbf{Q}\mathbf{F} = \mathbf{C} \tag{3.111}$$

Thus, the Cauchy-Green tensor is invariant under an Euclidean transformation but not objective with respect to Eq. (3.109). The objectivity is more related to quantities in the current or intermediate configurations, which are time-dependent.

The Cauchy stress tensor is an objective tensor that, accordingly, transforms to

$$\mathbf{T}^{*} = \mathbf{Q}\mathbf{T}\mathbf{Q}^{\mathrm{T}} \tag{3.112}$$

Many materials show a rate dependence. Therefore, it is of interest to investigate time rates of stresses and strains. Here, the time derivative of $\mathbf{T}^{*}$ is considered. The material time derivative reads

$$\frac{\mathrm{d}}{\mathrm{d}t}\left(\mathbf{T}^{*}\right) = \frac{\mathrm{d}}{\mathrm{d}t}\left(\mathbf{Q}\mathbf{T}\mathbf{Q}^{\mathrm{T}}\right) = \mathbf{Q}\dot{\mathbf{T}}\mathbf{Q}^{\mathrm{T}} + \dot{\mathbf{Q}}\mathbf{T}\mathbf{Q}^{\mathrm{T}} + \mathbf{Q}\mathbf{T}\dot{\mathbf{Q}}^{\mathrm{T}}. \tag{3.113}$$

According to the rule Eq. (3.109), this tensor is non-objective – and due to this, it is possible to introduce different tensor rates. Two of such objective rates are Oldroyd-rates, which are used in this work.[18] The covariant Oldroyd-rate is defined as

$$\overset{\triangle}{\mathbf{T}} = \dot{\mathbf{T}} + \mathbf{L}^{\mathrm{T}}\mathbf{T} + \mathbf{T}\mathbf{L}, \tag{3.114}$$

and the contravariant Oldroyd-rate reads

$$\overset{\triangledown}{\mathbf{T}} = \dot{\mathbf{T}} - \mathbf{L}\mathbf{T} - \mathbf{T}\mathbf{L}^{\mathrm{T}}. \tag{3.115}$$

The concept of dual variables offers a guideline for the choice of appropriate conjugated stress and strain tensors for the purpose of material modeling. This concept will be explained in the following.

3.4.2 Dual Variables

In constitutive modeling, strains and stress measures as well as their rates have to be connected to different configurations. In the Clausius-Duhem inequality, the stress power $\tilde{\mathbf{T}} \cdot \dot{\mathbf{E}}$ occurs, formulated with quantities relative to the reference configuration. Material models are often formulated with quantities that are neither relative to the current nor to the reference configuration. Rather, they are defined relative to an intermediate configuration. Thus, it is of importance to introduce dual variables to ensure that the stress power is invariant towards any change of the configuration. Haupt and Tsakmakis [1989] introduced the concept of dual variables, which is a guideline for the choice of appropriate stress and strain measures and

---

[18] There are also other rates that are frequently used in the formulation of constitutive equations, see [Haupt, 2002]. These objective rates are, for example, the Zaremba-Jaumann derivative and the Green and McInnis rate, among others.

their objective rates, see additionally [Haupt and Taskmakis, 1996; Haupt, 2002]. Stress and strain tensors are referred to as *dual to each other* if the scalar products

$$\tilde{\mathbf{T}} \cdot \dot{\mathbf{E}} \qquad \text{stress power} \tag{3.116}$$

$$\dot{\tilde{\mathbf{T}}} \cdot \mathbf{E} \qquad \text{complementary stress power} \tag{3.117}$$

$$\dot{\tilde{\mathbf{T}}} \cdot \dot{\mathbf{E}} \qquad \text{incremental stress power} \tag{3.118}$$

$$\tilde{\mathbf{T}} \cdot \mathbf{E} \qquad \text{accumulated work} \tag{3.119}$$

remain invariant against a transformation. By the definition of a tensor field

$$(\vec{X}, t) \mapsto \mathbf{\Psi}(\vec{X}, t), \quad \det \mathbf{\Psi} \neq 0, \tag{3.120}$$

the material line elements in the reference configuration $\mathrm{d}\vec{X}$ are transformed into material line elements $\mathrm{d}\vec{\xi}$ in the new configuration by

$$\mathrm{d}\vec{\xi} = \mathbf{\Psi}\, \mathrm{d}\vec{X}. \tag{3.121}$$

Analogously with the spatial velocity gradient Eq. (3.23), the relative rate of change can be written as

$$\overset{\cdot}{\overline{\mathrm{d}\vec{\xi}}} = \dot{\mathbf{\Psi}}\mathbf{\Psi}^{-1}\, \mathrm{d}\vec{\xi} = \mathbf{\Lambda}\, \mathrm{d}\vec{\xi}, \qquad \mathbf{\Lambda} := \dot{\mathbf{\Psi}}\mathbf{\Psi}^{-1}. \tag{3.122}$$

In the new configuration, $\mathbf{\Sigma}$ is defined as the new stress tensor and $\mathbf{\Lambda}$ as the new strain tensor. The transformation of the quantities from the reference to the new configuration yields

$$\mathbf{\Pi} = \mathbf{\Psi}^{-\mathrm{T}}\mathbf{E}\mathbf{\Psi}^{-1}, \tag{3.123}$$

$$\overset{\triangle}{\mathbf{\Pi}} = \mathbf{\Psi}^{-\mathrm{T}}\dot{\mathbf{E}}\mathbf{\Psi}^{-1} = \dot{\mathbf{\Pi}} + \mathbf{\Lambda}^{\mathrm{T}}\mathbf{\Pi} + \mathbf{\Pi}\mathbf{\Lambda}, \tag{3.124}$$

$$\mathbf{\Sigma} = \mathbf{\Psi}\tilde{\mathbf{T}}\mathbf{\Psi}^{\mathrm{T}}, \tag{3.125}$$

$$\overset{\triangledown}{\mathbf{\Sigma}} = \mathbf{\Psi}\dot{\tilde{\mathbf{T}}}\mathbf{\Psi}^{\mathrm{T}} = \dot{\mathbf{\Sigma}} - \mathbf{\Lambda}\mathbf{\Sigma} - \mathbf{\Sigma}\mathbf{\Lambda}^{\mathrm{T}}, \tag{3.126}$$

where $\overset{\triangledown}{\mathbf{\Sigma}}$ denotes the contravariant Oldroyd derivative and $\overset{\triangle}{\mathbf{\Pi}}$ is called covariant Oldroyd derivative. The transformation rules yield the frame-invariance of the scalar products

$$\tilde{\mathbf{T}} \cdot \dot{\mathbf{E}} = \mathbf{\Sigma} \cdot \overset{\triangle}{\mathbf{\Pi}}, \qquad \dot{\tilde{\mathbf{T}}} \cdot \mathbf{E} = \overset{\triangledown}{\mathbf{\Sigma}} \cdot \mathbf{\Pi}, \qquad \dot{\tilde{\mathbf{T}}} \cdot \dot{\mathbf{E}} = \overset{\triangledown}{\mathbf{\Sigma}} \cdot \overset{\triangle}{\mathbf{\Pi}}, \qquad \tilde{\mathbf{T}} \cdot \mathbf{E} = \mathbf{\Sigma} \cdot \mathbf{\Pi}. \tag{3.127}$$

With the aforementioned definitions, the scalar product of the corresponding stress and strain tensors are equal in every configuration

$$\tilde{\mathbf{T}} \cdot \mathbf{E} = \mathbf{\Psi}^{-1}\tilde{\mathbf{T}}\mathbf{\Psi}^{-\mathrm{T}} \cdot \mathbf{\Psi}^{\mathrm{T}}\mathbf{E}\mathbf{\Psi} = \mathbf{\Sigma} \cdot \hat{\mathbf{\Pi}} = \mathbf{S} \cdot \mathbf{A}. \tag{3.128}$$

The choice of $\boldsymbol{\Psi} \equiv \mathbf{F}$ is followed by $\boldsymbol{\Lambda} = \mathbf{L}$, so that the dual tensors on the current configuration can be obtained

$$\mathbf{A} = \mathbf{F}^{-\mathrm{T}}\mathbf{E}\mathbf{F}^{-1}, \tag{3.129}$$

$$\overset{\vartriangle}{\mathbf{A}} = \mathbf{F}^{-\mathrm{T}}\dot{\mathbf{E}}\mathbf{F}^{-1} = \dot{\mathbf{A}} + \mathbf{L}^{\mathrm{T}}\mathbf{A} + \mathbf{A}\mathbf{L}, \tag{3.130}$$

$$\mathbf{S} = \mathbf{F}\tilde{\mathbf{T}}\mathbf{F}^{\mathrm{T}}, \tag{3.131}$$

$$\overset{\triangledown}{\mathbf{S}} = \mathbf{F}\dot{\tilde{\mathbf{T}}}\mathbf{F}^{\mathrm{T}} = \dot{\mathbf{S}} - \mathbf{L}\mathbf{S} - \mathbf{S}\mathbf{L}^{\mathrm{T}}, \tag{3.132}$$

The dual variables that are introduced here are of the first family and define the connection between the Green strain tensor and the Almansi strain tensor as well as the connection between the second Piola-Kirchhoff stress tensor and the Kirchhoff stress tensor. The second family of dual variables, which is not used in this work, is related to the Piola and the Finger tensor, see [Haupt and Tsakmakis, 1989; Haupt, 2002] for further information.

The concept of dual variables connects conjugated stress and strain tensors in a natural way. Furthermore, it is possible to retrieve objective tensors such as the Oldroyd derivatives for the stress rate as well as strain rate tensors. This concept will be used in Chap. 4 to define appropriate stress and strain tensors in the intermediate configurations for the description of the material behavior.

4 Material Model

In the previous chapter, the fundamentals and the balance relations of Continuum Mechanics were introduced. This system of equations – formed by the balance of mass, linear and angular momentum, energy and entropy as well as the stationary electrical equation – can not be solved directly. It has to be closed by additional relations for the material behavior. The heat flux vector $\vec{q}$, for example, is connected to the temperature Θ by Fourier's model of heat transfer. The electric current is modeled by Ohm's model for the electrical conduction and connects the electrical potential with the current density. The entropy inequality (3.107) acts as a constraint for the formulation of the constitutive equations and should always be fulfilled. For this reason, the second law of thermodynamics in the form of the Clausius-Duhem inequality will be used to construct thermodynamically consistent material relations.

4.1 Overview about Constitutive Models for Sintering

In this work, a thermodynamically consistent thermo-viscoplasticity material model is developed. This model draws on the pressure-dependent yield function proposed by Bier and Hartmann [2006]. In general, very few attempts have been made to develop unified constitutive models for the whole process simulation of compaction and sintering in a thermodynamically consistent manner. In [Mähler et al., 2001], a thermo-hyperelastic-viscoplastic model for the simulation of porous materials is introduced. A different approach is followed by Mähler and Runesson [2000], whose mesomechanical approach serves to model the solid-phase sintering of hard metal. In the continuum model, the introduced sintering stress acts as a driving force for the powder consolidation. A similar sintering stress approach is used in [Reid and Oakberg, 1990]. A finite strain thermo-viscoplasticity model is developed and applied in [Mähler and Runesson, 2003] for the sintering of hard metal. This model is able to simulate free sintering – where no stress needs to be applied since the sintering stress is sufficient to consolidate the powder – and is derived from micro-mechanical considerations, see also [Mähler and Runesson, 2000]. This material model is adopted in [Frischkorn and Reese, 2011] for the simulation of a new production method called *process-integrated powder coating by radial axial rolling of rings*. In [Kebriaei et al., 2013], the focus lies on the process simulation and a new control method for the ring rolling finite element model. Khoei et al. [2013] computes hot isostatic pressing with a temperature-dependent cap plasticity model within a thermo-mechanical coupled finite element simulation. A unified plasticity model is used in [Jeong et al., 2012] for the simulation of compaction and sintering behavior. An FE-simulation of the compaction and solid-state sintering with a temperature-dependent cap model is performed in [Brandt, 1998]. Microscopic models are developed in [Shinagawa, 1996] for the study of the deformation behavior of powder particles during sintering. Another model for solid state sintering is presented in [Kraft and Riedel, 2004] and applied to an uniaxial die compaction simulation of a face seal made of SiC.

The modeling of liquid phase sintering is addressed in [Svoboda et al., 1996] as well as in [Öhman et al., 2012] and [Öhman et al., 2013]. In the latter two publications, the liquid phase sintering simulation is based on numerical homogenization.

Mondalek et al. [2011] provides a thermo-electro-mechanical simulation of a FAST-process with an experimental based material model to describe the powder densification. Wolff et al. [2012] proposes a modified micro-mechanical model that is extended for the representation of the behavior in the range of porosity between 0%-50%. This model is applied for the simulation of conventional hot compaction and spark plasma sintering.

The FAST-process is a complex thermo-electro-mechanical process for the sintering of powders. Due to the poor measurement possibilities, there is a strong need to understand and improve the process by simulations. In the following, a new constitutive model based on the multiplicative decomposition of the deformation gradient is developed. This model is constructed with the help of the Clausius-Duhem inequality in such a way that it is thermodynamically consistent. The literature shows frequent use of ellipse yield functions, see [Mähler and Runesson, 2003; Frischkorn and Reese, 2011], which evolve equally in tensile and compression range, but cold compacted powder shows no or little resistance to tensile loading.

The model developed in this work accounts for this effect by a single surface yield function with a drop-like shape. During the sintering process, the powder turns into a solid material and the evolution of the tensile yield stress is included in the model, which is motivated by tensile experiments in Sect. 2.5.6. As a limit case, the von Mises yield function is reached. The model also accounts for the creep consolidation, which is a main factor for the consolidation process. The creep behavior is mainly coupled to the change of relative density and, accordingly, to the change of volume. Hence, a new volumetric creep flow rule is proposed. Additionally, the experiments in Sect. 2.6 show a relative density dependence of the thermal and electrical conductivity. This is another important and new aspect included in the material model. As a result, the main effects of metal powder sintering will be incorporated into the material model. The most important effects that occur during the sintering experiments with copper powder are discussed in the following section.

4.2 General Material Behavior of Copper Powder during Sintering

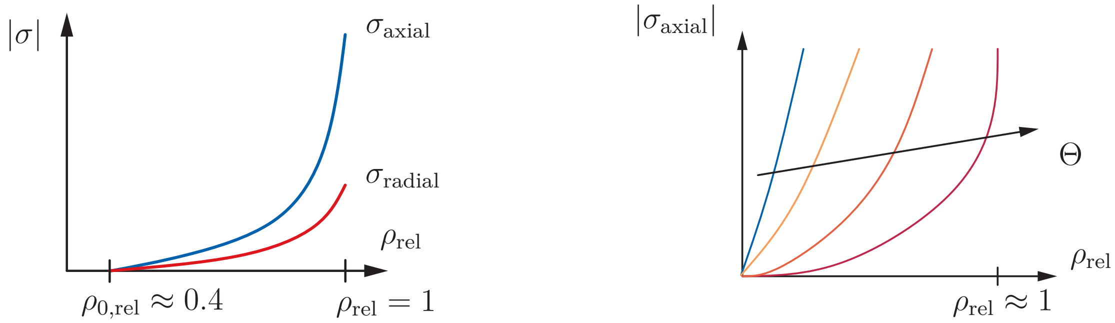

(a) Qualitative mechanical response in die compaction

(b) Compression behavior in dependence of temperature

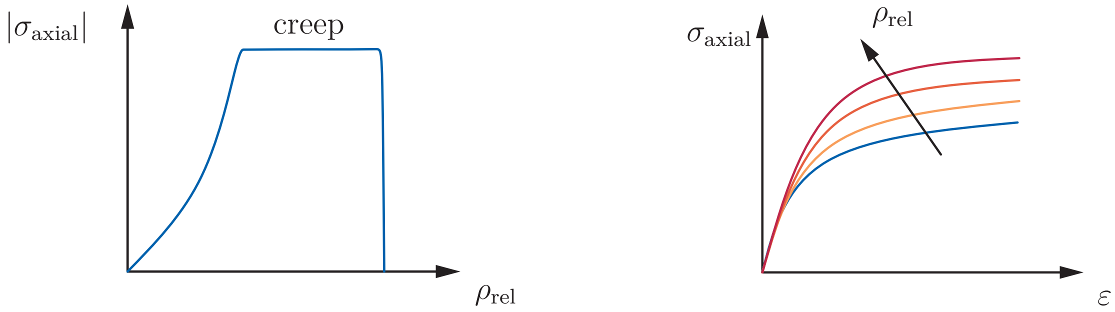

(c) Creep behavior at elevated temperatures

(d) Mechanical behavior of sintered specimen in tensile range

Figure 4.1: General material behavior of copper powder during sintering

The sintering experiments for the development of a constitutive model are described in Chap. 2. The model is to be conceived in such a way that it is able to represent the general behaviour and to capture the main effects. In the uniaxial constrained compression experiments, the initial relative density is approximately $\rho_{0,\text{rel}} = 0.4$. The axial stress is applied – and if the powder is fully compacted, the relative density reaches $\rho_{\text{rel}} \approx 1.0$. At this stage, it is assumed that no further compaction is possible and that the axial stress σ_{axial} tends towards infinity. Additionally, radial stresses occur due to the surrounding die, which are lower than the axial stresses. The qualitative material response in die compaction is shown in Fig. 4.1a.

In principle, it can be stated that metals show nearly no volume deformation, see [Lubliner, 2008, p. 75]. Hence, it is assumed that the main volume change due to the compaction of metal powders can be connected to the change of the pore size. This inelastic deformation is shown schematically in Fig. 4.2. In the FAST-process,

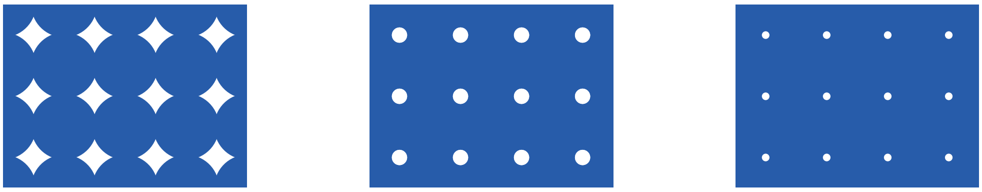

Figure 4.2: Schematic representation of vanishing pores during the sintering process

the powder is volumetrically heated by the electric current. The material becomes weaker due to the temperature, and a higher relative density is reached at the same level of applied axial force, as shown in Fig. 4.1b.

As can be seen in Fig. 4.1c, creep occurs at elevated temperatures, and the relative density increases at constant axial stress and temperature. Accordingly, the volume decreases at the same time. This effect is connected to the inelastic creep deformation. After the sintering process, the final specimen can be compared to a solid material. The tensile experiments with sintered specimens in Sect. 2.5.6 show an increasing yield stress with increasing relative density, see Fig. 4.1d. Therefore, the yield stress in tensile direction has to evolve according to the value of relative density. In Fig. 2.45b, a cold compacted specimen has a very low tensile stress. Due to this reason, it is assumed that the temperature plays an important role and the yield stress evolution is also dependent on the temperature.

4.3 Motivation

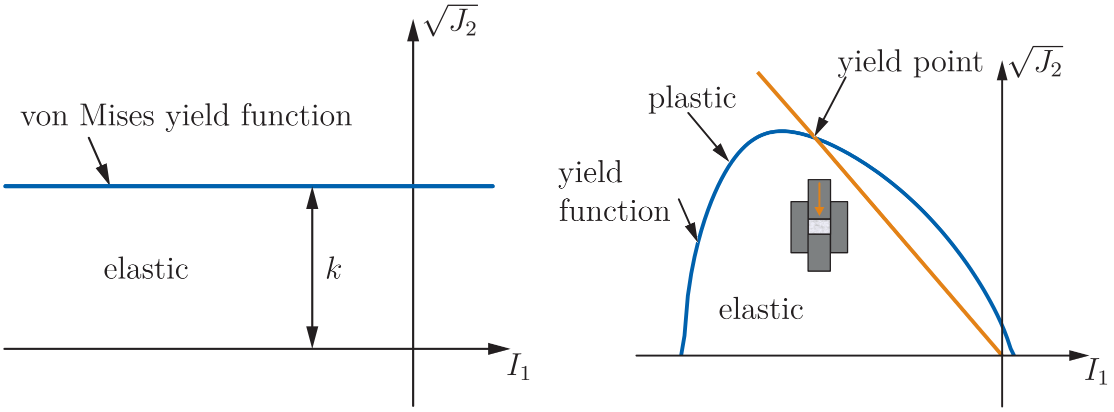

(a) Von Mises yield function

(b) Yield function for pressure-dependent materials

Figure 4.3: Yield functions

In the stress-relative density curve in Fig. 2.30, the powder material after unloading shows remaining deformations. Also, the increase in stress leads to no significant deformation. It is only after the stress reaches a certain point that larger deformations appear again. Accordingly, these observations suppose a separation into an elastic and an inelastic part. In an elastoplasticity model, the yield function separates the elastic from the plastic region. The yield surface is of main importance for the definition of the elastoplastic material model.

An overview about different plasticity models for cold powder compaction can be found in [Cocks and Sinka, 2007] and [Sinka, 2007]. The investigated models in [Cocks and Sinka, 2007] are calibrated to experimental data in the accompanying paper, [Sinka and Cocks, 2007]. A micro-mechanical based model is developed in [Fleck, 1995]. A Drucker-Prager-cap model is implemented in Abaqus for the finite element simulation of cold isostatic pressing and sintering in [Riedel et al., 2003]. Oliver et al. [1996] developed a finite strain plasticity model for industrial powder compaction. A model accounting for the cold compaction of metal powders is developed in [Bier and Hartmann, 2006], consisting of a compressible viscoplasticity model with a pressure-dependent yield surface.

Inside the yield function $F < 0$, the material behaves elastic and on the yield function $F = 0$, the plastic evolution equations evolve during loading. The evolution equations determine the change of the internal variables, e.g. plastic strains or hardening variables. These equations describe the internal material behavior and are also called *history* or *state variables.* They describe the hardening behavior and the model has to account for a vanishing deformation at a relative density of one. Mathematically, the evolution equations are ordinary differential equations of first order.

The yield function describes the shape and size of the elastic region and is dependent on the current state of stress, which is described in the I_1-J_2-plane. These invariants are calculated by the current stress state $\mathbf{T}$. The invariants are defined by

$$\mathrm{I}_1 = \operatorname{tr}\mathbf{T}, \qquad \mathrm{I}_2 = \frac{1}{2}\left((\operatorname{tr}\mathbf{T})^2 - \operatorname{tr}\mathbf{T}^2\right), \qquad \mathrm{I}_3 = \det\mathbf{T}. \tag{4.1}$$

Additionally, the invariants of the stress deviator

$$\mathbf{T}^{\mathrm{D}} = \mathbf{T} - \frac{1}{3}(\operatorname{tr}\mathbf{T})\mathbf{1} \tag{4.2}$$

are defined by

$$\mathrm{J}_1 = \operatorname{tr}\mathbf{T}^{\mathrm{D}} = 0, \qquad \mathrm{J}_2 = \frac{1}{2}\mathbf{T}^{\mathrm{D}} \cdot \mathbf{T}^{\mathrm{D}}, \qquad \mathrm{J}_3 = \det\mathbf{T}^{\mathrm{D}}. \tag{4.3}$$

Alternatively, the principal stresses can be used for the definition of the yield function, which is not investigated in this work. For an overview of different yield functions for pressure-dependent materials, see [Bier, 2008].

The simplest and well known von Mises yield function is shown in Fig. 4.3a. It represents a horizontal line parallel to the hydrostatic axis I_1 with the distance k,[1] which is the yield stress,

$$F = \sqrt{\mathrm{J}_2} - k. \tag{4.4}$$

Thus, the von Mises yield function assumes no difference between the yield stress in the compression and the tensile range. For example, if the stress state reaches the plastic region, which means $F = 0 \wedge \dot{F}|_{\dot{k}=0} \geq 0$, the evolution equation for the yield stress grows (isotropic hardening) and this implies the growth of the elastic region. In the deviatoric plane, the von Mises yield function can be illustrated by a circle – and in the principal stress space, it can be represented by an infinite long cylinder, see Fig. 4.4a.

For pressure-dependent materials, the general shape of a yield function is shown in Fig. 4.3b. Due to the fact that pressure-dependent materials like powders or soils show no or only little resistance against tensile-loading, the yield function has a drop-like shape. This means that in tensile direction (positive values of I_1), the intersection with the hydrostatic axis I_1 is at a small value. The yield function will be defined by uniaxial laterally constrained compression tests performed in the FAST-machine. In all these experiments, the axial stress σ_{axial} is prescribed and radial stresses occur due to the surrounding die. The stress state, see App. 4, is given by

$$\mathbf{T} = \begin{bmatrix} \sigma_{\text{radial}} & 0 & 0 \\ 0 & \sigma_{\text{radial}} & 0 \\ 0 & 0 & \sigma_{\text{axial}} \end{bmatrix} \vec{e}_i \otimes \vec{e}_j. \tag{4.5}$$

The invariants for this stress state read

$$\mathrm{I}_1 = \operatorname{tr}\mathbf{T} = \sigma_{\text{axial}} + 2\sigma_{\text{radial}} \tag{18}$$

$$\mathrm{J}_2 = \frac{1}{2}\mathbf{T}^{\mathrm{D}} \cdot \mathbf{T}^{\mathrm{D}} = \frac{1}{3}\left(\sigma_{\text{axial}} - \sigma_{\text{radial}}\right)^2. \tag{4.6}$$

In this work, the yield surface is defined by the first invariant I_1 and the second invariant of the stress deviator J_2. Any dependence on the third invariant J_3 is neglected. This assumption leads to a rotational symmetry of the yield function around the hydrostatic axis, and the yield surface has a drop-like shape as shown in Fig. 4.4b. A reason for neglecting the dependence on the third invariant is the lack of experimental data. One would need to perform additional experiments to define the yield function in the deviatoric plane. In this work, the simulation of the FAST-process is of main importance, which is a uniaxial laterally constrained compaction process.

---

[1] The connection between the parameter k and the uniaxial yield stress σ_y is given by $k = \sigma_y/\sqrt{3}$, see also Eq. (15).

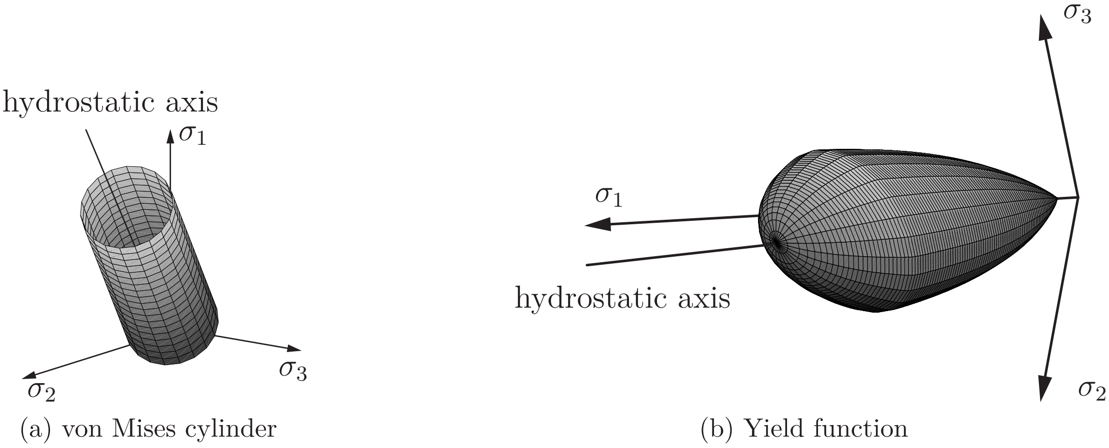

(a) von Mises cylinder

(b) Yield function

Figure 4.4: Yield functions in the principal stress space

In Fig. 4.5, other possible stress states are shown, see App. 3 for their definition. In general, triaxial experiments are best suited to define the yield function. In this case, the ratio between axial and radial stresses can be chosen arbitrarily.[2]

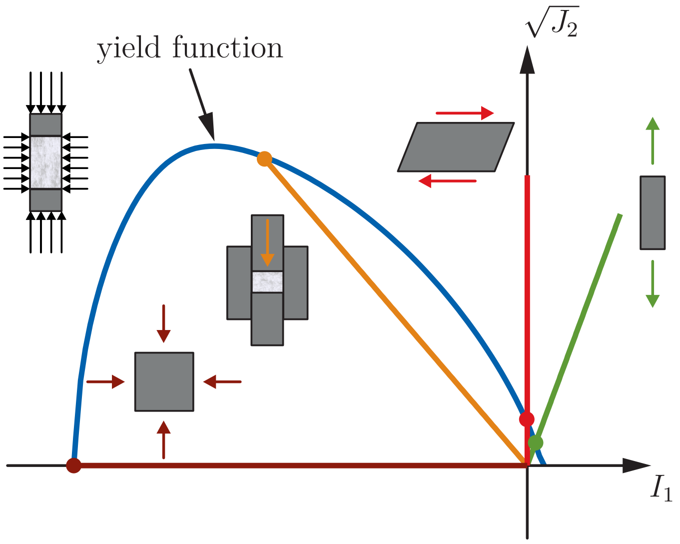

Figure 4.5: Load cases for determining the yield function

---

[2] From the point of material modeling, triaxial experiments are optimal to characterize the yield function. It must however be kept in mind that it is necessary to develop a completely new machine that allows to apply electro-thermo-mechanical loads.

4.3.1 Temperature-Dependence

According to the experiments, the powder turns out to become weaker at higher temperatures, i.e. it deforms plastically at lower applied axial stresses. Thus, the yield stress decreases with increasing temperature. For the model, this means that the plastic deformations start at lower stresses at higher temperatures. This can be incorporated into the model by a shrinkage of the yield function with the temperature.

The creep experiments also show that higher temperatures lead to thermal creep, which is to be described by an additional part of the deformation gradient. Another possibility would be to incorporate the viscous effects into the plastic multiplier, which is not followed here, see [Chaboche, 2008] for an overview of different plasticity models and different possibilities for the creep modeling. The introduction of an additional part of the deformation gradient helps to identify the creep behavior. The experiments in Sect. 2.5.4 show that the creep behavior leads to an increase of the relative density which is coupled to a decrease of the volume. Thus, volumetric thermal creep is assumed.

4.4 Temperature-Dependent Yield Function

First of all, the yield function proposed by Bier and Hartmann [2006] is recapitulated. This yield function serves as a basis for the yield function in this work. Two simple yield functions, namely an exponential and an ellipse function, are combined by a log-interpolation, which is taken from Kreisselmeier and Steinhauser [1979] and Arnold and Frischmuth [1998]. An ellipse yield function is used in [Kuhn and Downey, 1971], [Shima and Oyane, 1976] and [Abou-Chedid, 1993]. The use of an exponential yield function goes back to DiMaggio and Sandler [1971].

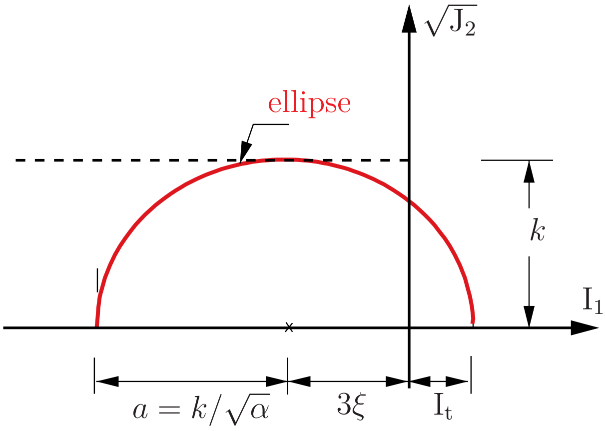

Figure 4.6: Ellipse function

The general form for an ellipse is given by

$$\frac{(\mathrm{I}_1 - \mathrm{I}_M)^2}{a^2} + \frac{\sqrt{\mathrm{J}_2}^2}{k^2} = 1 \tag{4.7}$$

The parameter k describes the height of the ellipse, whereas a is related to half of the width of the function. The middle point is assumed to be at $(-3\xi|0)$. The variable ξ is used later on to describe the kinematic hardening in the negative hydrostatic direction I_1, meaning in the compression range. The hydrostatic pressure is defined by $p = -\mathrm{I}_1/3$. By its definition, the hydrostatic kinematic hardening variable ξ can be connected to the hydrostatic pressure by $p \mathrel{\hat{=}} \xi$. Geometrically, ξ describes the position of the ellipse center on the I_1-axis. With the definition of the middle point, the ellipse equation reads

$$\frac{(\mathrm{I}_1 + 3\xi)^2}{a^2} + \frac{\sqrt{\mathrm{J}_2}^2}{k^2} = 1. \tag{4.8}$$

In order to get a function $\sqrt{\mathrm{J}_2} = f_1(\mathrm{I}_1)$, the ellipse is reformulated

$$\sqrt{\mathrm{J}_2} = \sqrt{k^2 - \frac{k^2}{a^2}(\mathrm{I}_1 + 3\xi)^2} =: f_1(\mathrm{I}_1). \tag{4.9}$$

The aspect ratio between the height and the width of the ellipse is defined by the parameter α

$$\sqrt{\alpha} := \frac{k}{a}. \tag{4.10}$$

The intersection point with the hydrostatic axis is chosen to be at

$$f_1(\mathrm{I}_\mathrm{t}) = 0 \quad \rightarrow \quad k^2 = \alpha(\mathrm{I}_\mathrm{t} + 3\xi)^2. \tag{4.11}$$

Accordingly, the final ellipse yield function reads

$$f_1(\mathrm{I}_1) = \sqrt{k^2 - \alpha(\mathrm{I}_1 + 3\xi)^2}. \tag{4.12}$$

This function has three independent variables. In [Bier and Hartmann, 2006], the parameters α, ξ and I_t are used to describe the ellipse function. Instead of α, the yield stress k will be used to characterize the yield function in this work. A reason for the use of k is the connection to the classical von Mises plasticity, where the yield function in the $\mathrm{I}_1 - \sqrt{\mathrm{J}_2}$–plane is a horizontal line described by the parameter k. It is assumed that after the sintering process, the powder is fully dense and the von Mises plasticity is reached as a limit case. Thus, in this work, the ratio α is the dependent parameter of the yield function, which can be calculated by

$$\alpha = \frac{k^2}{(\mathrm{I}_\mathrm{t} + 3\xi)^2}. \tag{4.13}$$

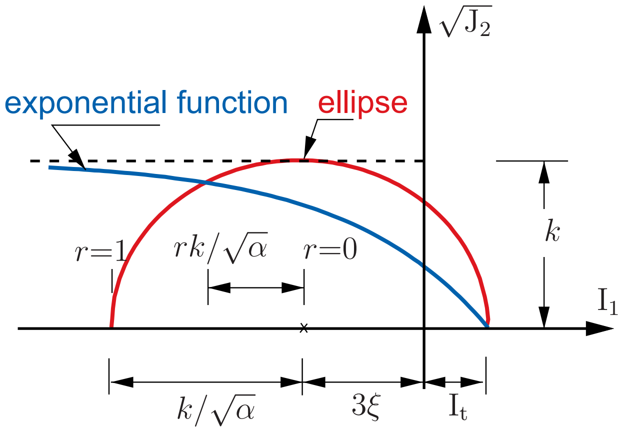

Figure 4.7: Exponential and ellipse function

The second function is an exponential function

$$f_2(\mathrm{I}_1) = A_1 - A_2 \exp^{A_3 \mathrm{I}_1}. \tag{4.14}$$

This function is determined by the three parameters A_1, A_2 and A_3. The limit value is defined by A_1 and should be the same as for the ellipse function

$$A_1 = \lim_{\mathrm{I}_1 \to -\infty} f_2(\mathrm{I}_1) = k. \tag{4.15}$$

It is supposed that the intersection point with the hydrostatic axis coincides with that of the ellipse function – which leads to

$$f_2(\mathrm{I}_\mathrm{t}) = 0 \quad \to \quad A_3 = \frac{1}{\mathrm{I}_\mathrm{t}} \ln\left(\frac{k}{A_2}\right). \tag{4.16}$$

The remaining parameter A_2 is determined by the intersection point between the ellipse and exponential function. The intersection point should be between 3ξ and $3\xi - rk/\sqrt{\alpha} = 3\xi - r(\mathrm{I}_\mathrm{t} + 3\xi)$, see Fig. 4.7, depending on the parameter $r \in [0, 1]$. The parameter A_2 can now be computed by

$$f_1(-3\xi - \frac{rk}{\sqrt{\alpha}}) = f_2(-3\xi - \frac{rk}{\sqrt{\alpha}}) \quad \to \quad A_2 = \frac{k}{(1 - \sqrt{1 - r^2})^{I_0/((-3\xi - \mathrm{I}_\mathrm{t})(1+r))}}. \tag{4.17}$$

According to Bier and Hartmann [2006], the parameter r is set to 0.3.

The interpolation concept of Kreisselmeier and Steinhauser [1979] and Arnold and Frischmuth [1998] is used to combine the ellipse and the exponential function. The interpolation formula (weighted mean) of two scalar functions $y_1 = f_1(x)$ and $y_2 = f_2(x)$ is given by

$$f(x) = -c \ln\left(\frac{e^{-\frac{f_1(x)}{c}} + e^{-\frac{f_2(x)}{c}}}{2}\right) \tag{4.18}$$

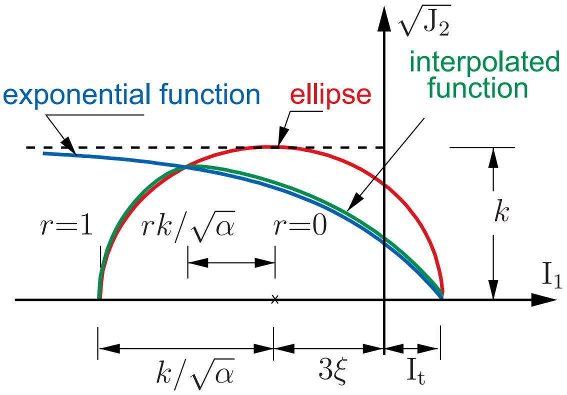

Figure 4.8: Interpolation of ellipse and exponential function

with the property that for $c > 0$, $f(x)$ tends towards the function with the smaller value. In addition, $f(x_0) = f_1(x_0) = f_2(x_0)$ holds at the intersection point x_0 of both functions. The parameter c controls the sharpness at the intersection point x_0 as well as the closeness of $f(x)$ to the function $f_1(x), x \leq x_0$ and $f_2(x), x \geq x_0$. The result is shown in Fig. 4.8. More information concerning this interpolation concept and its properties can be found in [Bier and Hartmann, 2006].

A yield function can be built if the interpolated function is subtracted by $\sqrt{J_2}$, meaning that the yield function is negative for values below the curve – and only on the curve $F = 0$ holds.

$$F(I_1, \sqrt{J_2}) = \sqrt{J_2} - f(I_1) = \sqrt{J_2} + c \ln \left(\frac{e^{-\frac{f_1(I_1)}{c}} + e^{-\frac{f_2(I_1)}{c}}}{2} \right) \tag{4.19}$$

As the ellipse and the exponential function are convex, the interpolated single yield surface is convex too. A proof of the convexity can be found in [Bier and Hartmann, 2006].

One drawback of this formulation is that the ellipse yield function is not defined for values outside of the curve. In a numerical implementation such as the elastic predictor and plastic corrector scheme, values outside the ellipse yield function can occur. In this case, the term in the square root would be negative. Hence, $f_1(I_1)$ is not defined, leaving $f(I_1)$ undefined too. Due to this reason, both functions are reformulated by

$$\sqrt{J_2} - f_1(I_1) = 0 \quad \Rightarrow \quad g_1(I_1, \sqrt{J_2}) = \sqrt{J_2 + \alpha\,(I_1 + 3\xi)^2} - k. \tag{4.20}$$

$$\sqrt{J_2} - f_2(I_1) = 0 \quad \Rightarrow \quad g_2(I_1, \sqrt{J_2}) = \sqrt{J_2} - A_1 + A_2 e^{A_3 I_1}. \tag{4.21}$$

If the interpolation concept is once again applied to the two curves, this leads to the single yield surface

$$\tilde{F}(\mathrm{I}_1, \mathrm{J}_2, k, \xi, \mathrm{I}_\mathrm{t}, \Theta) := F(\mathrm{I}_1, \sqrt{\mathrm{J}_2}) = ck \ln \left(\frac{e^{g_1(\mathrm{I}_1, \sqrt{\mathrm{J}_2})/(ck)} + e^{g_2(\mathrm{I}_1, \sqrt{\mathrm{J}_2})/(ck)}}{2} \right). \tag{4.22}$$

Fig. 4.9 shows the yield function for $\tilde{F}(\mathrm{I}_1, \sqrt{\mathrm{J}_2}) \geq 0$.[3] One can observe that the yield function has positive values on the outside, due to the reformulation in Eq. (4.20)-Eq. (4.21), and can be used in a predictor-corrector scheme. If the stress state lies inside the curve, the yield function is negative. On the outside of the curve, its value is positive – and on the curve, $F = 0$ holds. Due to this new formulation there is one corner at $\mathrm{I}_1 = \mathrm{I}_\mathrm{t}$, which can lead to numerical problems. Here, according to Bier and Hartmann [2006] and Abbo and Sloan [1995], a rounding off by the parameter δ is introduced

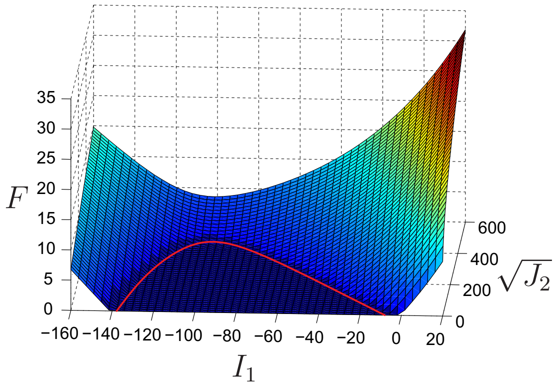

Figure 4.9: Yield function $\hat{F}(\mathrm{I}_1, \sqrt{\mathrm{J}_2}) \geq 0$. The red curve represents the yield function curve shown in Fig. 4.8.

$$g_2(\mathrm{I}_1, \sqrt{\mathrm{J}_2}) = \sqrt{\mathrm{J}_2 + \delta} - A_1 + A_2 e^{A_3 I_1}, \qquad \delta > 0 \tag{4.23}$$

In this work, the parameter is set to $\delta = 0.1$. As a result, a single surface convex yield function is given. In [Bier and Hartmann, 2006], it is shown that this yield function is flexible and can be adapted to many different materials, including metal powders, soils and granular materials. Additionally, the yield function is unique and does not have solutions for $F = 0$ outside the elastic domain, see Fig. 4.10 and [Bier, 2008]. The yield function temperature-dependence will be introduced in the next chapter.

4.4.1 Temperature-Dependence

For metals, it is well known that the yield stress decreases at higher temperatures, see [Lubliner, 2008, p. 85] and [Rösler et al., 2008, p. 209]. The material becomes

---

[3] The negative function values in the elastic domain are not shown here.

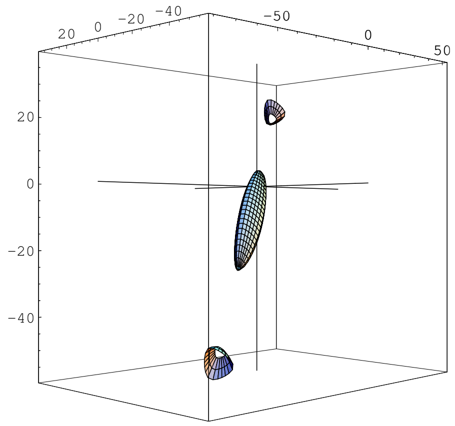

Figure 4.10: Non-uniqueness of yield surface proposed by Ehlers [1995] in stress space. $F = 0$ occurs also for regions away from the elastic domain. The figure is taken from [Bier, 2008].

weaker and plastic deformations occur at lower stresses. This behavior is connected to the diffusivity of atoms due to thermal activation, which can be explained by the Arrhenius equation, see [Rösler et al., 2008, p. 194]. The Arrhenius equation assumes an exponential temperature dependence, $\exp(-\Delta E/(k_\mathrm{B}\Theta))$, where ΔE is the activation energy, k_B is the Boltzmann constant and Θ is the absolute temperature. Furthermore, Mähler and Runesson [2003] assumed an exponential decrease of the yield stress with the temperature. Motivated by this publication and the Arrhenius equation, an exponential dependence will be used in this work too. It is assumed that the yield stress k is multiplicatively decomposed into the mechanical part k_M and the temperature-dependent part f_k. For the function f_k, an exponential dependence on the temperature with the material parameter m_k and Θ_S is assumed

$$k = \tilde{k}(\Theta, k_\mathrm{M}) = f_k(\Theta) k_\mathrm{M}, \qquad f_k(\Theta) = e^{-m_k \langle \Theta - \Theta_S \rangle}, \tag{4.24}$$

with the Macaulay brackets $\langle \cdot \rangle$. They have the property $\langle x \rangle = 0$ for $x \leq 0$ and $\langle x \rangle = x$ for $x > 0$. As a result, there is no decrease of the yield stress below the sintering temperature Θ_S. The temperature-dependence for the yield stress is depicted in Fig. 4.11a. The same exponential temperature-dependence is assumed for the ellipse middle point ξ. Again, ξ consists of a mechanical part ξ_M and is weighted with the temperature function $f_\xi(\Theta)$,

$$\xi = \tilde{\xi}(\Theta, \xi_\mathrm{M}, \mathrm{I_t}) = f_\xi(\Theta)\xi_\mathrm{M} + f_t(\mathrm{I_t}), \qquad f_\xi(\Theta) = e^{-m_\xi \langle \Theta - \Theta_S \rangle}. \tag{4.25}$$

Additionally, a function $f_t(\mathrm{I_t})$ is added – as defined in the following section. The material parameter m_ξ controls the exponential decrease of the center, see Fig. 4.11b. Fig. 4.12 shows the shape of the yield function due to an exponential decrease of ξ and k that is caused by the temperature.

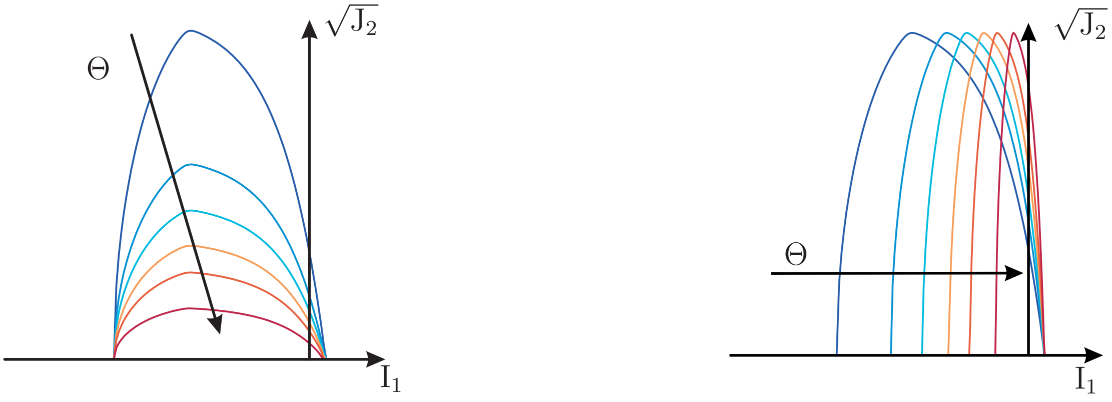

(a) Shape of yield function for increasing Θ and exponential decrease of k

(b) Shape of yield function for increasing Θ and exponential decrease of ξ

Figure 4.11: Change of yield function shape while increasing the temperature

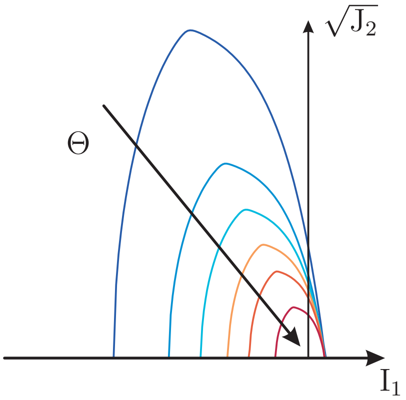

Figure 4.12: Change of yield function shape while the temperature increases and k and ξ decreases exponentially. I_t, ξ_M and k_M are fixed.

4.4.2 Hydrostatic Yield Stress Evolution

In practice, it can be observed that after a cold compaction experiment, the densified powder specimen shows little or no resistance against tensile loading, see Fig. 2.45b. This means that, due to cold compaction, the yield stress in tensile direction does not increase. Thus, the main increase of the yield stress in tensile direction originates from the heat treatment during the sintering process. The drop-like yield surface describes well the powder behavior for cold compaction, when the tensile yield stress is very low. During the sintering process, the powder transforms into a bulk material. This fact can be observed in the tensile experiments for sintered specimens with different relative densities, see Fig. 2.45a. This means that the drop-like yield surface has to transform into a von Mises-like yield surface during the sintering process, see Fig. 4.13. The basic idea to reach a horizontal line in the I_1-J_2-plane is to stretch the ellipse function by holding k constant. The sintering process leads to an increase of the yield stress of the final specimen. Thus, the parameter I_t has to grow during the process. If the parameter I_t is increased, the distance x changes, see Fig. 4.15 and Fig. 4.14a. In general, it is of interest to separate different effects. Therefore, it is proposed to decouple the kinematic hardening described by ξ and the tensile hardening represented by I_t. Accordingly, the evolution of ξ is reformulated in such a way that a change of I_t does not change the compression range, see Fig. 4.14b. Therefore, the function

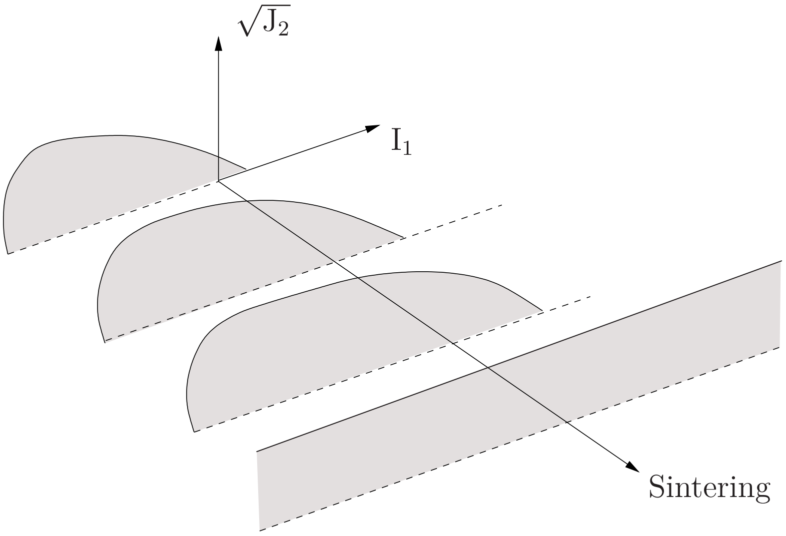

Figure 4.13: Conversion of drop-like yield surface into von Mises yield surface due to the sintering process

$$f_t(I_t) = mI_t + b \tag{4.26}$$

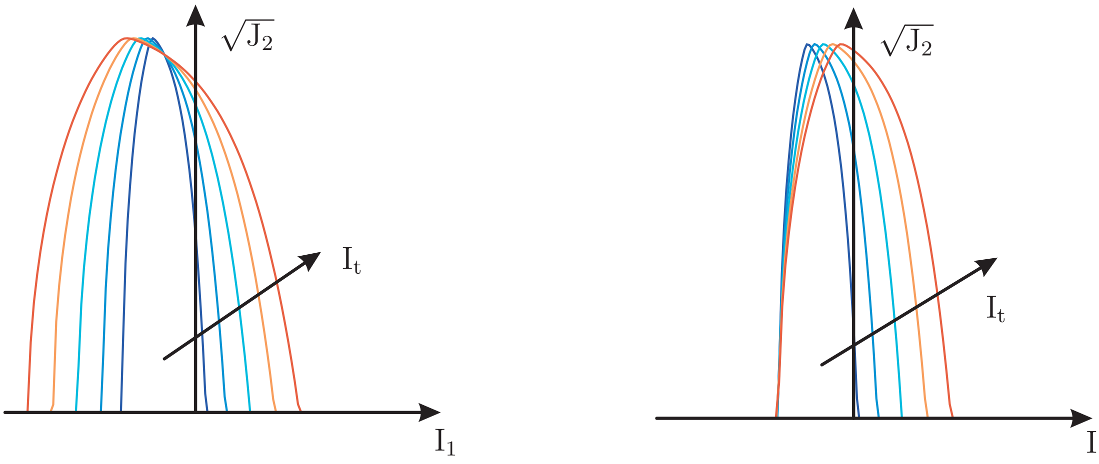

(a) Shape of yield function if I_t increases without $f_t(I_t)$

(b) Decoupling between kinematic and tensile hardening with the function $f_t(I_t)$

Figure 4.14: Difference between the yield function shape with and without the decoupling function $f_t(I_t)$

is introduced. It is assumed that the left point x of the yield function is constant for changing I_t, meaning that the ellipse middle point ξ will move. As a result, the evolution of the yield function is described by the variables k and ξ in the compression range. The distance x is given by

$$x = I_t + 6\xi = I_t + 6 f_\xi(\Theta)\xi_M + 6(m I_t + b) \overset{!}{=} \text{const}, \tag{4.27}$$

where Eq. (4.25) and Eq. (4.26) are inserted. This distance should be constant for a changing I_t. This can be achieved if the derivative vanishes

$$x'(I_t) = 0 \tag{4.28}$$

$$1 + 6m = 0 \quad \rightarrow \quad m = -\frac{1}{6} \tag{4.29}$$

The initial point should be at $f(I_t = I_0) = 0$, leading to the final function

$$f_t(I_t) = -\frac{1}{6}I_t + \frac{1}{6}I_0 \tag{4.30}$$

The decoupling function is fully determined and can be inserted into Eq. (4.25). As a result, the yield function does not change in the compression range if I_t increases, see Fig. 4.14b. The equations for the temperature-dependent yield function are summarized in Tab. 4.1. The evolution of the mechanical parameters in the yield function k_M, ξ_M and I_t are defined by the constitutive model.

Table 4.1: Summary of yield function

Ellipse function

$$g_1(\mathrm{I}_1, \sqrt{\mathrm{J}_2}, \Theta) = \sqrt{\mathrm{J}_2 + \alpha\left(\mathrm{I}_1 + 3\xi\right)^2} - k \tag{4.20}$$

Exponential function

$$g_2(\mathrm{I}_1, \sqrt{\mathrm{J}_2}, \Theta) = \sqrt{\mathrm{J}_2 + \delta} - k + \mathrm{A}_2 e^{\mathrm{A}_3 \mathrm{I}_1} \tag{4.21}$$

Interpolated single surface convex yield function

$$\tilde{F}(\mathrm{I}_1, \mathrm{J}_2, k, \xi, \mathrm{I}_\mathrm{t}, \Theta) = ck \ln\left(\frac{e^{g_1(\mathrm{I}_1, \sqrt{\mathrm{J}_2})/(ck)} + e^{g_2(\mathrm{I}_1, \sqrt{\mathrm{J}_2})/(ck)}}{2}\right) \tag{4.22}$$

Evolution and temperature dependence of ellipse height k

$$k = \tilde{k}(\Theta, k_\mathrm{M}) = f_k(\Theta) k_\mathrm{M}, \qquad f_k(\Theta) = e^{-m_k \langle \Theta - \Theta_S \rangle} \tag{4.24}$$

Evolution and temperature dependence of ellipse center ξ

$$\xi = \tilde{\xi}(\Theta, \xi_\mathrm{M}, \mathrm{I}_\mathrm{t}) = f_\xi(\Theta)\xi_\mathrm{M} + f_t(\mathrm{I}_\mathrm{t}), \qquad f_\xi(\Theta) = e^{-m_\xi \langle \Theta - \Theta_S \rangle} \tag{4.25}$$

Decoupling between kinematic and tensile hardening

$$f_t(\mathrm{I}_\mathrm{t}) = -\frac{1}{6}\mathrm{I}_\mathrm{t} + \frac{1}{6} \tag{4.30}$$

Abbreviations

$$\mathrm{I}_1 = \operatorname{tr}\mathbf{T}, \qquad \mathrm{J}_2 = \frac{1}{2}\mathbf{T}^\mathrm{D} \cdot \mathbf{T}^\mathrm{D}, \qquad \alpha = \frac{k^2}{(\mathrm{I}_\mathrm{t} + 3\xi)^2} \tag{4.1, 4.2, 4.13}$$

$$A_2 = \frac{k}{(1 - \sqrt{1 - r^2})^{I_0/((-3\xi - I_0)(1+r))}}, \qquad A_3 = \frac{1}{\mathrm{I}_\mathrm{t}} \ln\left(\frac{k}{A_2}\right) \tag{4.17, 4.16}$$

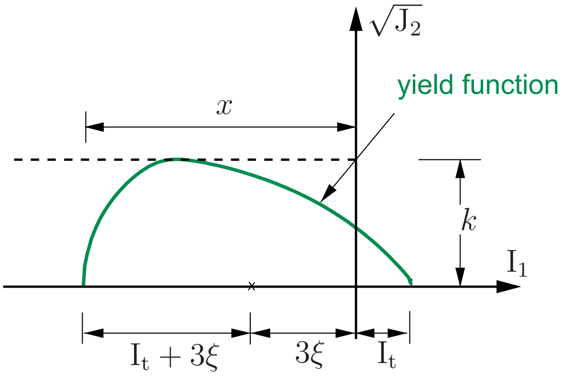

Figure 4.15: Decoupling between kinematic and tensile hardening. The distance x should remain constant if $\mathrm{I_t}$ changes. Therefore the middle point at 3ξ changes.

4.5 Multiplicative Decomposition

In the case of small strains, the additive strain decomposition is a common method, whereas for finite deformations the multiplicative decomposition according to Lee [1969] is used frequently. The multiplicative decomposition for thermoelastic deformations was developed by Lu and Pister [1975]. The main idea behind this decomposition is to separate the different partial effects by a kinematic assumption. The following multiplicative decomposition into a reversible $\mathbf{F}_\mathrm{r}$ and an inelastic part $\mathbf{F}_\mathrm{i}$ is chosen:

$$\mathbf{F} = \mathbf{F}_\mathrm{r}\mathbf{F}_\mathrm{i} = \breve{\mathbf{F}}_\mathrm{e}\hat{\mathbf{F}}_\Theta\mathbf{F}_\mathrm{i} = \breve{\mathbf{F}}_\mathrm{e}\hat{\mathbf{F}}_\Theta\check{\mathbf{F}}_\mathrm{p}\mathbf{F}_\mathrm{c}. \tag{4.31}$$

The reversible part decomposes into an elastic and a thermal part, whereas the inelastic part is given by the multiplicative decomposition into a plastic and a creep part

$$\mathbf{F}_\mathrm{r} :=\breve{\mathbf{F}}_\mathrm{e}\hat{\mathbf{F}}_\Theta, \qquad \mathbf{F}_\mathrm{i} := \check{\mathbf{F}}_\mathrm{p}\mathbf{F}_\mathrm{c}. \tag{4.32}$$

Due to the chosen decomposition, three intermediate configurations, $\check{\boldsymbol{\chi}}_t$, $\hat{\boldsymbol{\chi}}_t$ and $\breve{\boldsymbol{\chi}}_t$ arise, see Fig. 4.16. With the decomposition Eq. (4.31), the determinant decomposes into

$$\det\mathbf{F} =(\det\breve{\mathbf{F}}_\mathrm{e})(\det\hat{\mathbf{F}}_\Theta)(\det\check{\mathbf{F}}_\mathrm{p})(\det\mathbf{F}_\mathrm{c}) \qquad \Leftrightarrow \qquad J = J_\mathrm{e}J_\Theta J_\mathrm{p}J_\mathrm{c}. \tag{4.33}$$

With the decomposition Eq. (4.31), the following material line elements arise

$$\mathrm{d}\check{\vec{x}} = \mathbf{F}_\mathrm{c}\,\mathrm{d}\vec{X}, \quad \mathrm{d}\hat{\vec{x}} = \check{\mathbf{F}}_\mathrm{p}\,\mathrm{d}\check{\vec{x}}, \quad \mathrm{d}\breve{\vec{x}} = \hat{\mathbf{F}}_\Theta\,\mathrm{d}\hat{\vec{x}}, \quad \mathrm{d}\vec{x} = \breve{\mathbf{F}}_\mathrm{e}\,\mathrm{d}\breve{\vec{x}}$$

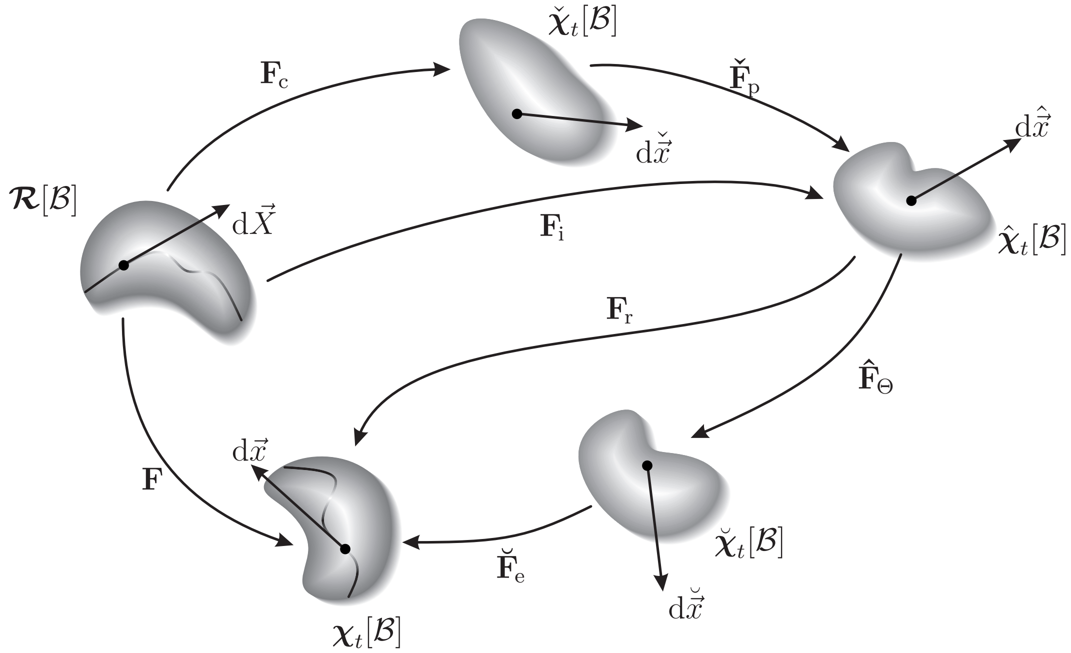

Figure 4.16: Configurations implied by the multiplicative split of the deformation gradient

On the basis of the difference between the squared material line elements[4], the Green strain tensor can be additively decomposed, see Eq. (3.14),

$$
\begin{aligned}
\mathrm{d}\vec{x}\cdot\mathrm{d}\vec{x}-\mathrm{d}\vec{X}\cdot\mathrm{d}\vec{X} &= \mathrm{d}\vec{X}\cdot 2\mathbf{E}\,\mathrm{d}\vec{X} && (4.34)\\
&= \mathrm{d}\check{\vec{x}}^2-\mathrm{d}\vec{X}^2+\mathrm{d}\hat{\vec{x}}^2-\mathrm{d}\check{\vec{x}}^2+\mathrm{d}\breve{\vec{x}}^2-\mathrm{d}\hat{\vec{x}}^2+\mathrm{d}\vec{x}^2-\mathrm{d}\breve{\vec{x}}^2 && (4.35)\\
&= \mathrm{d}\vec{X}\cdot(\mathbf{F}_\mathrm{c}^\mathrm{T}\mathbf{F}_\mathrm{c}-\mathbf{1})\,\mathrm{d}\vec{X}+\mathrm{d}\vec{X}\cdot(\mathbf{F}_\mathrm{pc}^\mathrm{T}\mathbf{F}_\mathrm{pc}-\mathbf{F}_\mathrm{c}^\mathrm{T}\mathbf{F}_\mathrm{c})\,\mathrm{d}\vec{X} && (4.36)\\
&+\mathrm{d}\vec{X}\cdot(\mathbf{F}_{\Theta\mathrm{pc}}^\mathrm{T}\mathbf{F}_{\Theta\mathrm{pc}}-\mathbf{F}_\mathrm{pc}^\mathrm{T}\mathbf{F}_\mathrm{pc})\,\mathrm{d}\vec{X} && (4.37)\\
&+\mathrm{d}\vec{X}\cdot(\mathbf{F}^\mathrm{T}\mathbf{F}-\mathbf{F}_{\Theta\mathrm{pc}}^\mathrm{T}\mathbf{F}_{\Theta\mathrm{pc}})\,\mathrm{d}\vec{X} && (4.38)\\
&= \mathrm{d}\vec{X}\cdot 2(\mathbf{E}_\mathrm{c}+\mathbf{E}_\mathrm{p}+\mathbf{E}_\Theta+\mathbf{E}_\mathrm{e})\,\mathrm{d}\vec{X} && (4.39)
\end{aligned}
$$

where the following abbreviations are used

$$
\mathbf{F}_\mathrm{i}=\mathbf{F}_\mathrm{pc}:=\check{\mathbf{F}}_\mathrm{p}\mathbf{F}_\mathrm{c},\qquad \mathbf{F}_{\Theta\mathrm{pc}}:=\hat{\mathbf{F}}_\Theta\check{\mathbf{F}}_\mathrm{p}\mathbf{F}_\mathrm{c}. \tag{4.40}
$$

Thus, the additive decomposition holds

$$
\mathbf{E}=\mathbf{E}_\mathrm{c}+\mathbf{E}_\mathrm{p}+\mathbf{E}_\Theta+\mathbf{E}_\mathrm{e} \tag{4.41}
$$

---

[4] In this case, the square of a vector $\vec{v}$ is defined as $\vec{v}^2=\vec{v}\cdot\vec{v}$.

with the Green strain tensors

$$\mathbf{E}_\mathrm{c} = \frac{1}{2}(\mathbf{F}_\mathrm{c}^\mathrm{T}\mathbf{F}_\mathrm{c} - \mathbf{1}) = \frac{1}{2}(\mathbf{C}_\mathrm{c} - \mathbf{1}), \quad \mathbf{C}_\mathrm{c} := \mathbf{F}_\mathrm{c}^\mathrm{T}\mathbf{F}_\mathrm{c} \tag{4.42}$$

$$\mathbf{E}_\mathrm{p} = \frac{1}{2}(\mathbf{F}_\mathrm{pc}^\mathrm{T}\mathbf{F}_\mathrm{pc} - \mathbf{F}_\mathrm{c}^\mathrm{T}\mathbf{F}_\mathrm{c}) = \frac{1}{2}(\mathbf{C}_\mathrm{pc} - \mathbf{C}_\mathrm{c}), \quad \mathbf{C}_\mathrm{i} = \mathbf{F}_\mathrm{i}^\mathrm{T}\mathbf{F}_\mathrm{i} = \mathbf{C}_\mathrm{pc} := \mathbf{F}_\mathrm{pc}^\mathrm{T}\mathbf{F}_\mathrm{pc} \tag{4.43}$$

$$\mathbf{E}_\Theta = \frac{1}{2}(\mathbf{F}_{\Theta\mathrm{pc}}^\mathrm{T}\mathbf{F}_{\Theta\mathrm{pc}} - \mathbf{F}_\mathrm{pc}^\mathrm{T}\mathbf{F}_\mathrm{pc}) = \frac{1}{2}(\mathbf{C}_{\Theta\mathrm{pc}} - \mathbf{C}_\mathrm{pc}), \quad \mathbf{C}_{\Theta\mathrm{pc}} := \mathbf{F}_{\Theta\mathrm{pc}}^\mathrm{T}\mathbf{F}_{\Theta\mathrm{pc}} \tag{4.44}$$

$$\mathbf{E}_\mathrm{e} = \frac{1}{2}(\mathbf{F}^\mathrm{T}\mathbf{F} - \mathbf{F}_{\Theta\mathrm{pc}}^\mathrm{T}\mathbf{F}_{\Theta\mathrm{pc}}) = \frac{1}{2}(\mathbf{C} - \mathbf{C}_{\Theta\mathrm{pc}}) \tag{4.45}$$

$\mathbf{E}_\mathrm{c}$ is the only quantity that depends solely on the creep deformation. All other strain tensors are also dependent on other partial deformations, which is the reason why they are not suitable for the formulation of a material relation. The concept of dual variables delivers appropriate strain measures in intermediate configurations, which will be used to define material relations. These strain tensors in the intermediate configurations are solely dependent on the partial deformations and are suitable for the formulation of constitutive equations.

Remark 2 *One has to mention that the decomposition in Eq.* (4.31) *is not the only possible multiplicative decomposition. Another possibility would be* $\mathbf{F} = \mathbf{F}_c\mathbf{F}_e\mathbf{F}_\Theta\mathbf{F}_p$ *– but in this case, the elastic deformations cannot be defined as the whole deformation minus the mechanical deformation. A further decomposition is given by* $\mathbf{F} = \mathbf{F}_\Theta\mathbf{F}_M = \mathbf{F}_\Theta\mathbf{F}_e\mathbf{F}_c\mathbf{F}_p$*, which leads to the same problem of identifying the elastic deformations. Moreover, the decomposition* $\mathbf{F} = \mathbf{F}_e\mathbf{F}_\Theta\mathbf{F}_c\mathbf{F}_p$ *can be chosen. In this case, the plastic intermediate configuration would be the first configuration and would also influence the creep deformation. Due to this reason, the creep flow-rule could not be assumed to be purely volumetric, as it is assumed in this work. Therefore, the proposed decomposition in Eq.* (4.31) *is used.*

Miehe [1988], for example, used the decomposition $\mathbf{F} = \mathbf{F}_\Theta\mathbf{F}_\mathrm{e}\mathbf{F}_\mathrm{p}$, whereas Lion [2000] proposed $\mathbf{F} = \mathbf{F}_\mathrm{e}\mathbf{F}_\mathrm{p}\mathbf{F}_\Theta$. Mähler et al. [2001] and Quint [2012] used the decomposition $\mathbf{F} = \mathbf{F}_\mathrm{e}\mathbf{F}_\Theta\mathbf{F}_\mathrm{p}$. In the case of isotropic thermoelasticity with purely volumetric thermal expansion, Hartmann [2012] showed the equivalence of $\mathbf{F} = \mathbf{F}_\mathrm{M}\mathbf{F}_\Theta$ and $\mathbf{F} = \mathbf{F}_\Theta\mathbf{F}_\mathrm{M}$.

The transformation of the Green strain tensor by means of the concept of dual variables, see Sect. 3.4.2, into the intermediate creep configuration $\check{\boldsymbol{\chi}}_t$ leads to

$$\check{\boldsymbol{\Gamma}} = \mathbf{F}_\mathrm{c}^{-\mathrm{T}}\mathbf{E}\mathbf{F}_\mathrm{c}^{-1} = \check{\boldsymbol{\Gamma}}_\mathrm{p} + \check{\boldsymbol{\Gamma}}_\mathrm{c} + \check{\boldsymbol{\Gamma}}_\Theta + \check{\boldsymbol{\Gamma}}_\mathrm{e} = \check{\boldsymbol{\Gamma}}_\mathrm{p} + \check{\boldsymbol{\Gamma}}_\mathrm{c} + \check{\boldsymbol{\Gamma}}_{\mathrm{e}\Theta}. \tag{4.46}$$

The strain tensor $\check{\boldsymbol{\Gamma}}$ decomposes additively into a thermo-elastic part $\check{\boldsymbol{\Gamma}}_{\mathrm{e}\Theta} := \check{\boldsymbol{\Gamma}}_\Theta + \check{\boldsymbol{\Gamma}}_\mathrm{e}$ and a pure plastic part $\check{\boldsymbol{\Gamma}}_\mathrm{p}$ as well as a pure creep part $\check{\boldsymbol{\Gamma}}_\mathrm{c}$. The reversible part of

$$\begin{tikzcd}
\begin{array}{l}\mathcal{R}\\ \boxed{\begin{array}{l}
\mathbf{E}=\frac{1}{2}(\mathbf{F}^{\mathrm{T}}\mathbf{F}-\mathbf{1})\\
\mathbf{E}_{\mathrm{c}}=\frac{1}{2}(\mathbf{F}_{\mathrm{c}}^{\mathrm{T}}\mathbf{F}_{\mathrm{c}}-\mathbf{1})\\
\mathbf{E}_{\mathrm{p}}=\frac{1}{2}(\mathbf{F}_{\mathrm{pc}}^{\mathrm{T}}\mathbf{F}_{\mathrm{pc}}-\mathbf{F}_{\mathrm{c}}^{\mathrm{T}}\mathbf{F}_{\mathrm{c}})\\
\mathbf{E}_{\Theta}=\frac{1}{2}(\mathbf{F}_{\Theta\mathrm{pc}}^{\mathrm{T}}\mathbf{F}_{\Theta\mathrm{pc}}-\mathbf{F}_{\mathrm{pc}}^{\mathrm{T}}\mathbf{F}_{\mathrm{pc}})\\
\mathbf{E}_{\mathrm{e}}=\frac{1}{2}(\mathbf{F}^{\mathrm{T}}\mathbf{F}-\mathbf{F}_{\Theta\mathrm{pc}}^{\mathrm{T}}\mathbf{F}_{\Theta\mathrm{pc}})\\
\mathbf{E}=\mathbf{E}_{\mathrm{c}}+\mathbf{E}_{\mathrm{p}}+\mathbf{E}_{\Theta}+\mathbf{E}_{\mathrm{e}}
\end{array}}\end{array}
\arrow[rr, "\mathbf{F}^{-\mathrm{T}}(\cdot)\mathbf{F}^{-1}"]
\arrow[d, "\mathbf{F}_{\mathrm{c}}^{-\mathrm{T}}(\cdot)\mathbf{F}_{\mathrm{c}}^{-1}"']
\arrow[drr, "\mathbf{F}_{\Theta\mathrm{pc}}^{-\mathrm{T}}(\cdot)\mathbf{F}_{\Theta\mathrm{pc}}^{-1}"]
& &
\begin{array}{l}\chi_t\\ \boxed{\begin{array}{l}
\mathbf{A}=\frac{1}{2}(\mathbf{1}-\mathbf{F}^{-\mathrm{T}}\mathbf{F}^{-1})\\
\mathbf{A}_{\mathrm{c}}=\frac{1}{2}(\mathbf{F}_{\mathrm{e}\Theta\mathrm{p}}^{-\mathrm{T}}\mathbf{F}_{\mathrm{e}\Theta\mathrm{p}}^{-1}-\mathbf{F}^{-\mathrm{T}}\mathbf{F}^{-1})\\
\mathbf{A}_{\mathrm{p}}=\frac{1}{2}(\mathbf{F}_{\mathrm{e}\Theta}^{-\mathrm{T}}\mathbf{F}_{\mathrm{e}\Theta}^{-1}-\mathbf{F}_{\mathrm{e}\Theta\mathrm{p}}^{-\mathrm{T}}\mathbf{F}_{\mathrm{e}\Theta\mathrm{p}}^{-1})\\
\mathbf{A}_{\Theta}=\frac{1}{2}(\breve{\mathbf{F}}_{\mathrm{e}}^{-\mathrm{T}}\breve{\mathbf{F}}_{\mathrm{e}}^{-1}-\mathbf{F}_{\mathrm{e}\Theta}^{-\mathrm{T}}\mathbf{F}_{\mathrm{e}\Theta}^{-1})\\
\mathbf{A}_{\mathrm{e}}=\frac{1}{2}(\mathbf{1}-\breve{\mathbf{F}}_{\mathrm{e}}^{-\mathrm{T}}\breve{\mathbf{F}}_{\mathrm{e}}^{-1})\\
\mathbf{A}=\mathbf{A}_{\mathrm{c}}+\mathbf{A}_{\mathrm{p}}+\mathbf{A}_{\Theta}+\mathbf{A}_{\mathrm{e}}
\end{array}}\end{array}
\\
\begin{array}{l}\breve{\chi}_t\\ \boxed{\begin{array}{l}
\breve{\boldsymbol{\Gamma}}=\frac{1}{2}(\mathbf{F}_{\mathrm{e}\Theta\mathrm{p}}^{\mathrm{T}}\mathbf{F}_{\mathrm{e}\Theta\mathrm{p}}-\mathbf{F}_{\mathrm{c}}^{-\mathrm{T}}\mathbf{F}_{\mathrm{c}}^{-1})\\
\breve{\boldsymbol{\Gamma}}_{\mathrm{c}}=\frac{1}{2}(\mathbf{1}-\mathbf{F}_{\mathrm{c}}^{-\mathrm{T}}\mathbf{F}_{\mathrm{c}}^{-1})\\
\breve{\boldsymbol{\Gamma}}_{\mathrm{p}}=\frac{1}{2}(\breve{\mathbf{F}}_{\mathrm{p}}^{\mathrm{T}}\breve{\mathbf{F}}_{\mathrm{p}}-\mathbf{1})\\
\breve{\boldsymbol{\Gamma}}_{\Theta}=\frac{1}{2}(\mathbf{F}_{\Theta\mathrm{p}}^{\mathrm{T}}\mathbf{F}_{\Theta\mathrm{p}}-\breve{\mathbf{F}}_{\mathrm{p}}^{\mathrm{T}}\breve{\mathbf{F}}_{\mathrm{p}})\\
\breve{\boldsymbol{\Gamma}}_{\mathrm{e}}=\frac{1}{2}(\mathbf{F}_{\mathrm{e}\Theta\mathrm{p}}^{\mathrm{T}}\mathbf{F}_{\mathrm{e}\Theta\mathrm{p}}-\mathbf{F}_{\Theta\mathrm{p}}^{\mathrm{T}}\mathbf{F}_{\Theta\mathrm{p}})\\
\breve{\boldsymbol{\Gamma}}=\breve{\boldsymbol{\Gamma}}_{\mathrm{c}}+\breve{\boldsymbol{\Gamma}}_{\mathrm{p}}+\breve{\boldsymbol{\Gamma}}_{\Theta}+\breve{\boldsymbol{\Gamma}}_{\mathrm{e}}
\end{array}}\end{array}
\arrow[urr, "\mathbf{F}_{\mathrm{e}\Theta\mathrm{p}}^{-\mathrm{T}}(\cdot)\mathbf{F}_{\mathrm{e}\Theta\mathrm{p}}^{-1}"']
\arrow[rr, "\mathbf{F}_{\Theta\mathrm{p}}^{-\mathrm{T}}(\cdot)\mathbf{F}_{\Theta\mathrm{p}}^{-1}"]
\arrow[dr, "\breve{\mathbf{F}}_{\mathrm{p}}^{-\mathrm{T}}(\cdot)\breve{\mathbf{F}}_{\mathrm{p}}^{-1}"']
& &
\begin{array}{l}\breve{\chi}_t\\ \boxed{\begin{array}{l}
\breve{\boldsymbol{\gamma}}=\frac{1}{2}(\breve{\mathbf{F}}_{\mathrm{e}}^{\mathrm{T}}\breve{\mathbf{F}}_{\mathrm{e}}-\mathbf{F}_{\Theta\mathrm{pc}}^{-\mathrm{T}}\mathbf{F}_{\Theta\mathrm{pc}}^{-1})\\
\breve{\boldsymbol{\gamma}}_{\mathrm{c}}=\frac{1}{2}(\mathbf{F}_{\Theta\mathrm{p}}^{-\mathrm{T}}\mathbf{F}_{\Theta\mathrm{p}}^{-1}-\mathbf{F}_{\Theta\mathrm{pc}}^{-\mathrm{T}}\mathbf{F}_{\Theta\mathrm{pc}}^{-1})\\
\breve{\boldsymbol{\gamma}}_{\mathrm{p}}=\frac{1}{2}(\hat{\mathbf{F}}_{\Theta}^{-\mathrm{T}}\hat{\mathbf{F}}_{\Theta}^{-1}-\mathbf{F}_{\Theta\mathrm{p}}^{-\mathrm{T}}\mathbf{F}_{\Theta\mathrm{p}}^{-1})\\
\breve{\boldsymbol{\gamma}}_{\Theta}=\frac{1}{2}(\mathbf{1}-\hat{\mathbf{F}}_{\Theta}^{-\mathrm{T}}\hat{\mathbf{F}}_{\Theta}^{-1})\\
\breve{\boldsymbol{\gamma}}_{\mathrm{e}}=\frac{1}{2}(\breve{\mathbf{F}}_{\mathrm{e}}^{\mathrm{T}}\breve{\mathbf{F}}_{\mathrm{e}}-\mathbf{1})\\
\breve{\boldsymbol{\gamma}}=\breve{\boldsymbol{\gamma}}_{\mathrm{c}}+\breve{\boldsymbol{\gamma}}_{\mathrm{p}}+\breve{\boldsymbol{\gamma}}_{\Theta}+\breve{\boldsymbol{\gamma}}_{\mathrm{e}}
\end{array}}\end{array}
\arrow[uu, phantom]
\arrow[u, "\breve{\mathbf{F}}_{\mathrm{e}}^{-\mathrm{T}}(\cdot)\breve{\mathbf{F}}_{\mathrm{e}}^{-1}"']
\\
&
\begin{array}{l}\hat{\chi}_t\\ \boxed{\begin{array}{l}
\hat{\boldsymbol{\varepsilon}}=\frac{1}{2}(\mathbf{F}_{\mathrm{e}\Theta}^{\mathrm{T}}\mathbf{F}_{\mathrm{e}\Theta}-\mathbf{F}_{\mathrm{pc}}^{-\mathrm{T}}\mathbf{F}_{\mathrm{pc}}^{-1})\\
\hat{\boldsymbol{\varepsilon}}_{\mathrm{c}}=\frac{1}{2}(\breve{\mathbf{F}}_{\mathrm{p}}^{-\mathrm{T}}\breve{\mathbf{F}}_{\mathrm{p}}^{-1}-\mathbf{F}_{\mathrm{pc}}^{-\mathrm{T}}\mathbf{F}_{\mathrm{pc}}^{-1})\\
\hat{\boldsymbol{\varepsilon}}_{\mathrm{p}}=\frac{1}{2}(\mathbf{1}-\breve{\mathbf{F}}_{\mathrm{p}}^{-\mathrm{T}}\breve{\mathbf{F}}_{\mathrm{p}}^{-1})\\
\hat{\boldsymbol{\varepsilon}}_{\Theta}=\frac{1}{2}(\hat{\mathbf{F}}_{\Theta}^{\mathrm{T}}\hat{\mathbf{F}}_{\Theta}-\mathbf{1})\\
\hat{\boldsymbol{\varepsilon}}_{\mathrm{e}}=\frac{1}{2}(\mathbf{F}_{\mathrm{e}\Theta}^{\mathrm{T}}\mathbf{F}_{\mathrm{e}\Theta}-\hat{\mathbf{F}}_{\Theta}^{\mathrm{T}}\hat{\mathbf{F}}_{\Theta})\\
\hat{\boldsymbol{\varepsilon}}=\hat{\boldsymbol{\varepsilon}}_{\mathrm{c}}+\hat{\boldsymbol{\varepsilon}}_{\mathrm{p}}+\hat{\boldsymbol{\varepsilon}}_{\Theta}+\hat{\boldsymbol{\varepsilon}}_{\mathrm{e}}
\end{array}}\end{array}
\arrow[ur, "\hat{\mathbf{F}}_{\Theta}^{-\mathrm{T}}(\cdot)\hat{\mathbf{F}}_{\Theta}^{-1}"']
&
\end{tikzcd}$$

Figure 4.17: Transformation of strain tensors

$$\begin{tikzcd}[column sep=large, row sep=large]
\begin{array}{l} \mathcal{R} \\ \boxed{\begin{array}{l}
\dot{\mathbf{E}} = \frac{1}{2}\dot{\mathbf{C}} \\
\dot{\mathbf{E}}_{\mathrm{c}} = \frac{1}{2}\dot{\mathbf{C}}_{\mathrm{c}} \\
\dot{\mathbf{E}}_{\mathrm{p}} = \frac{1}{2}(\dot{\mathbf{C}}_{\mathrm{pc}} - \dot{\mathbf{C}}_{\mathrm{c}}) \\
\dot{\mathbf{E}}_{\Theta} = \frac{1}{2}(\dot{\mathbf{C}}_{\Theta\mathrm{pc}} - \dot{\mathbf{C}}_{\mathrm{pc}}) \\
\dot{\mathbf{E}}_{\mathrm{e}} = \frac{1}{2}(\dot{\mathbf{C}} - \dot{\mathbf{C}}_{\Theta\mathrm{pc}}) \\
\dot{\mathbf{E}} = \dot{\mathbf{E}}_{\mathrm{c}} + \dot{\mathbf{E}}_{\mathrm{p}} + \dot{\mathbf{E}}_{\Theta} + \dot{\mathbf{E}}_{\mathrm{e}}
\end{array}} \end{array}
\arrow[rr, "\mathbf{F}^{-\mathrm{T}}(\cdot)\mathbf{F}^{-1}"]
\arrow[d, "\mathbf{F}_{\mathrm{c}}^{-\mathrm{T}}(\cdot)\mathbf{F}_{\mathrm{c}}^{-1}"']
\arrow[drr, "\mathbf{F}_{\Theta\mathrm{pc}}^{-\mathrm{T}}(\cdot)\mathbf{F}_{\Theta\mathrm{pc}}^{-1}"]
& &
\begin{array}{l} \chi_t \\ \boxed{\begin{array}{l}
\overset{\vartriangle}{\mathbf{A}} = \dot{\mathbf{A}} + \mathbf{L}^{\mathrm{T}}\mathbf{A} + \mathbf{A}\mathbf{L} = \mathbf{D} \\
\overset{\vartriangle}{\mathbf{A}}_{\mathrm{p}} = \dot{\mathbf{A}}_{\mathrm{p}} + \mathbf{L}^{\mathrm{T}}\mathbf{A}_{\mathrm{p}} + \mathbf{A}_{\mathrm{p}}\mathbf{L} \\
\overset{\vartriangle}{\mathbf{A}}_{\mathrm{c}} = \dot{\mathbf{A}}_{\mathrm{c}} + \mathbf{L}^{\mathrm{T}}\mathbf{A}_{\mathrm{c}} + \mathbf{A}_{\mathrm{c}}\mathbf{L} \\
\overset{\vartriangle}{\mathbf{A}}_{\Theta} = \dot{\mathbf{A}}_{\Theta} + \mathbf{L}^{\mathrm{T}}\mathbf{A}_{\Theta} + \mathbf{A}_{\Theta}\mathbf{L} \\
\overset{\vartriangle}{\mathbf{A}}_{\mathrm{e}} = \dot{\mathbf{A}}_{\mathrm{e}} + \mathbf{L}^{\mathrm{T}}\mathbf{A}_{\mathrm{e}} + \mathbf{A}_{\mathrm{e}}\mathbf{L} \\
\overset{\vartriangle}{\mathbf{A}} = \overset{\vartriangle}{\mathbf{A}}_{\mathrm{p}} + \overset{\vartriangle}{\mathbf{A}}_{\mathrm{c}} + \overset{\vartriangle}{\mathbf{A}}_{\Theta} + \overset{\vartriangle}{\mathbf{A}}_{\mathrm{e}}
\end{array}} \end{array}
\\
\begin{array}{l} \breve{\chi}_t \\ \boxed{\begin{array}{l}
\overset{\vartriangle}{\breve{\boldsymbol{\Gamma}}} = \dot{\breve{\boldsymbol{\Gamma}}} + \mathbf{L}_{\mathrm{c}}^{\mathrm{T}}\breve{\boldsymbol{\Gamma}} + \breve{\boldsymbol{\Gamma}}\mathbf{L}_{\mathrm{c}} \\
\overset{\vartriangle}{\breve{\boldsymbol{\Gamma}}}_{\mathrm{c}} = \dot{\breve{\boldsymbol{\Gamma}}}_{\mathrm{c}} + \mathbf{L}_{\mathrm{c}}^{\mathrm{T}}\breve{\boldsymbol{\Gamma}}_{\mathrm{c}} + \breve{\boldsymbol{\Gamma}}_{\mathrm{c}}\mathbf{L}_{\mathrm{c}} = \mathbf{D}_{\mathrm{c}} \\
\overset{\vartriangle}{\breve{\boldsymbol{\Gamma}}}_{\mathrm{p}} = \dot{\breve{\boldsymbol{\Gamma}}}_{\mathrm{p}} + \mathbf{L}_{\mathrm{c}}^{\mathrm{T}}\breve{\boldsymbol{\Gamma}}_{\mathrm{p}} + \breve{\boldsymbol{\Gamma}}_{\mathrm{p}}\mathbf{L}_{\mathrm{c}} \\
\overset{\vartriangle}{\breve{\boldsymbol{\Gamma}}}_{\Theta} = \dot{\breve{\boldsymbol{\Gamma}}}_{\Theta} + \mathbf{L}_{\mathrm{c}}^{\mathrm{T}}\breve{\boldsymbol{\Gamma}}_{\Theta} + \breve{\boldsymbol{\Gamma}}_{\Theta}\mathbf{L}_{\mathrm{c}} \\
\overset{\vartriangle}{\breve{\boldsymbol{\Gamma}}}_{\mathrm{e}} = \dot{\breve{\boldsymbol{\Gamma}}}_{\mathrm{e}} + \mathbf{L}_{\mathrm{c}}^{\mathrm{T}}\breve{\boldsymbol{\Gamma}}_{\mathrm{e}} + \breve{\boldsymbol{\Gamma}}_{\mathrm{e}}\mathbf{L}_{\mathrm{c}} \\
\overset{\vartriangle}{\breve{\boldsymbol{\Gamma}}} = \overset{\vartriangle}{\breve{\boldsymbol{\Gamma}}}_{\mathrm{p}} + \overset{\vartriangle}{\breve{\boldsymbol{\Gamma}}}_{\mathrm{c}} + \overset{\vartriangle}{\breve{\boldsymbol{\Gamma}}}_{\Theta} + \overset{\vartriangle}{\breve{\boldsymbol{\Gamma}}}_{\mathrm{e}}
\end{array}} \end{array}
\arrow[urr, "\mathbf{F}_{\mathrm{e}\Theta\mathrm{p}}^{-\mathrm{T}}(\cdot)\mathbf{F}_{\mathrm{e}\Theta\mathrm{p}}^{-1}"']
\arrow[rr, "\mathbf{F}_{\Theta\mathrm{p}}^{-\mathrm{T}}(\cdot)\mathbf{F}_{\Theta\mathrm{p}}^{-1}"]
\arrow[dr, "\breve{\mathbf{F}}_{\mathrm{p}}^{-\mathrm{T}}(\cdot)\breve{\mathbf{F}}_{\mathrm{p}}^{-1}"']
& &
\begin{array}{l} \breve{\chi}_t \\ \boxed{\begin{array}{l}
\overset{\vartriangle}{\breve{\gamma}} = \dot{\breve{\gamma}} + \mathbf{L}_{\Theta\mathrm{pc}}^{\mathrm{T}}\breve{\gamma} + \breve{\gamma}\mathbf{L}_{\Theta\mathrm{pc}} \\
\overset{\vartriangle}{\breve{\gamma}}_{\mathrm{c}} = \dot{\breve{\gamma}}_{\mathrm{c}} + \mathbf{L}_{\Theta\mathrm{pc}}^{\mathrm{T}}\breve{\gamma}_{\mathrm{c}} + \breve{\gamma}_{\mathrm{c}}\mathbf{L}_{\Theta\mathrm{pc}} \\
\overset{\vartriangle}{\breve{\gamma}}_{\mathrm{p}} = \dot{\breve{\gamma}}_{\mathrm{p}} + \mathbf{L}_{\Theta\mathrm{pc}}^{\mathrm{T}}\breve{\gamma}_{\mathrm{p}} + \breve{\gamma}_{\mathrm{p}}\mathbf{L}_{\Theta\mathrm{pc}} \\
\overset{\vartriangle}{\breve{\gamma}}_{\Theta} = \dot{\breve{\gamma}}_{\Theta} + \mathbf{L}_{\Theta\mathrm{pc}}^{\mathrm{T}}\breve{\gamma}_{\Theta} + \breve{\gamma}_{\Theta}\mathbf{L}_{\Theta\mathrm{pc}} \\
\overset{\vartriangle}{\breve{\gamma}}_{\mathrm{e}} = \dot{\breve{\gamma}}_{\mathrm{e}} + \mathbf{L}_{\Theta\mathrm{pc}}^{\mathrm{T}}\breve{\gamma}_{\mathrm{e}} + \breve{\gamma}_{\mathrm{e}}\mathbf{L}_{\Theta\mathrm{pc}} \\
\overset{\vartriangle}{\breve{\gamma}} = \overset{\vartriangle}{\breve{\gamma}}_{\mathrm{p}} + \overset{\vartriangle}{\breve{\gamma}}_{\mathrm{c}} + \overset{\vartriangle}{\breve{\gamma}}_{\Theta} + \overset{\vartriangle}{\breve{\gamma}}_{\mathrm{e}}
\end{array}} \end{array}
\arrow[u, "\breve{\mathbf{F}}_{\mathrm{e}}^{-\mathrm{T}}(\cdot)\breve{\mathbf{F}}_{\mathrm{e}}^{-1}"']
\\
&
\begin{array}{l} \hat{\chi}_t \\ \boxed{\begin{array}{l}
\overset{\vartriangle}{\hat{\boldsymbol{\varepsilon}}} = \dot{\hat{\boldsymbol{\varepsilon}}} + \mathbf{L}_{\mathrm{pc}}^{\mathrm{T}}\hat{\boldsymbol{\varepsilon}} + \hat{\boldsymbol{\varepsilon}}\mathbf{L}_{\mathrm{pc}} \\
\overset{\vartriangle}{\hat{\boldsymbol{\varepsilon}}}_{\mathrm{c}} = \dot{\hat{\boldsymbol{\varepsilon}}}_{\mathrm{c}} + \mathbf{L}_{\mathrm{pc}}^{\mathrm{T}}\hat{\boldsymbol{\varepsilon}}_{\mathrm{c}} + \hat{\boldsymbol{\varepsilon}}_{\mathrm{c}}\mathbf{L}_{\mathrm{pc}} \\
\overset{\vartriangle}{\hat{\boldsymbol{\varepsilon}}}_{\mathrm{p}} = \dot{\hat{\boldsymbol{\varepsilon}}}_{\mathrm{p}} + \mathbf{L}_{\mathrm{pc}}^{\mathrm{T}}\hat{\boldsymbol{\varepsilon}}_{\mathrm{p}} + \hat{\boldsymbol{\varepsilon}}_{\mathrm{p}}\mathbf{L}_{\mathrm{pc}} \\
\overset{\vartriangle}{\hat{\boldsymbol{\varepsilon}}}_{\Theta} = \dot{\hat{\boldsymbol{\varepsilon}}}_{\Theta} + \mathbf{L}_{\mathrm{pc}}^{\mathrm{T}}\hat{\boldsymbol{\varepsilon}}_{\Theta} + \hat{\boldsymbol{\varepsilon}}_{\Theta}\mathbf{L}_{\mathrm{pc}} \\
\overset{\vartriangle}{\hat{\boldsymbol{\varepsilon}}}_{\mathrm{e}} = \dot{\hat{\boldsymbol{\varepsilon}}}_{\mathrm{e}} + \mathbf{L}_{\mathrm{pc}}^{\mathrm{T}}\hat{\boldsymbol{\varepsilon}}_{\mathrm{e}} + \hat{\boldsymbol{\varepsilon}}_{\mathrm{e}}\mathbf{L}_{\mathrm{pc}} \\
\overset{\vartriangle}{\hat{\boldsymbol{\varepsilon}}} = \overset{\vartriangle}{\hat{\boldsymbol{\varepsilon}}}_{\mathrm{p}} + \overset{\vartriangle}{\hat{\boldsymbol{\varepsilon}}}_{\mathrm{c}} + \overset{\vartriangle}{\hat{\boldsymbol{\varepsilon}}}_{\Theta} + \overset{\vartriangle}{\hat{\boldsymbol{\varepsilon}}}_{\mathrm{e}}
\end{array}} \end{array}
\arrow[ur, "\hat{\mathbf{F}}_{\Theta}^{-\mathrm{T}}(\cdot)\hat{\mathbf{F}}_{\Theta}^{-1}"']
&
\end{tikzcd}$$

Figure 4.18: Transformation of strain rate tensors

$$\begin{tikzcd}
\overset{\mathcal{R}}{\boxed{\begin{array}{l} \tilde{\mathbf{T}} = J\mathbf{F}^{-1}\mathbf{T}\mathbf{F}^{-\mathrm{T}} \\ \dot{\tilde{\mathbf{T}}} \end{array}}} \arrow[rr, "\mathbf{F}(\cdot)\mathbf{F}^{\mathrm{T}}"] \arrow[d, "\mathbf{F}_{\mathrm{c}}(\cdot)\mathbf{F}_{\mathrm{c}}^{\mathrm{T}}"'] \arrow[drr, "\mathbf{F}_{\Theta\mathrm{pc}}(\cdot)\mathbf{F}_{\Theta\mathrm{pc}}^{\mathrm{T}}" near start] & & \overset{\chi_t}{\boxed{\begin{array}{l} \mathbf{S} = \mathbf{F}\tilde{\mathbf{T}}\mathbf{F}^{\mathrm{T}} = J\mathbf{T} \\ \overset{\triangledown}{\mathbf{S}} = \dot{\mathbf{S}} - \mathbf{L}\mathbf{S} - \mathbf{S}\mathbf{L}^{\mathrm{T}} \end{array}}} \\
\overset{\check{\chi}_t}{\boxed{\begin{array}{l} \check{\mathbf{S}} = \mathbf{F}_{\mathrm{c}}\tilde{\mathbf{T}}\mathbf{F}_{\mathrm{c}}^{\mathrm{T}} \\ \overset{\triangledown}{\check{\mathbf{S}}} = \dot{\hat{\mathbf{S}}} - \mathbf{L}_{\mathrm{c}}\check{\mathbf{S}} - \check{\mathbf{S}}\mathbf{L}_{\mathrm{c}}^{\mathrm{T}} \end{array}}} \arrow[rr, "\mathbf{F}_{\Theta\mathrm{p}}(\cdot)\mathbf{F}_{\Theta\mathrm{p}}^{\mathrm{T}}"] \arrow[urr, "\mathbf{F}_{\mathrm{e}\Theta\mathrm{p}}(\cdot)\mathbf{F}_{\mathrm{e}\Theta\mathrm{p}}^{\mathrm{T}}"' near start] \arrow[dr, "\check{\mathbf{F}}_{\mathrm{p}}(\cdot)\check{\mathbf{F}}_{\mathrm{p}}^{\mathrm{T}}"'] & & \overset{\breve{\chi}_t}{\boxed{\begin{array}{l} \breve{\mathbf{S}} = \hat{\mathbf{F}}_{\Theta}\hat{\mathbf{S}}\hat{\mathbf{F}}_{\Theta}^{\mathrm{T}} \\ \overset{\triangledown}{\breve{\mathbf{S}}} = \dot{\breve{\mathbf{S}}} - \mathbf{L}_{\Theta\mathrm{pc}}\breve{\mathbf{S}} - \breve{\mathbf{S}}\mathbf{L}_{\Theta\mathrm{pc}}^{\mathrm{T}} \end{array}}} \arrow[u, "\breve{\mathbf{F}}_{\mathrm{e}}(\cdot)\breve{\mathbf{F}}_{\mathrm{e}}^{\mathrm{T}}"'] \\
& \overset{\hat{\chi}_t}{\boxed{\begin{array}{l} \hat{\mathbf{S}} = \check{\mathbf{F}}_{\mathrm{p}}\check{\mathbf{S}}\check{\mathbf{F}}_{\mathrm{p}}^{\mathrm{T}} \\ \overset{\triangledown}{\hat{\mathbf{S}}} = \dot{\hat{\mathbf{S}}} - \mathbf{L}_{\mathrm{pc}}\hat{\mathbf{S}} - \hat{\mathbf{S}}\mathbf{L}_{\mathrm{pc}}^{\mathrm{T}} \end{array}}} \arrow[ur, "\hat{\mathbf{F}}_{\Theta}(\cdot)\hat{\mathbf{F}}_{\Theta}^{\mathrm{T}}"'] &
\end{tikzcd}$$

Figure 4.19: Transformation of stress tensors

the strain tensors can be expressed by

$$\check{\boldsymbol{\Gamma}}_\Theta = \frac{1}{2}(\mathbf{F}_{\Theta\mathrm{p}}^{\mathrm{T}}\mathbf{F}_{\Theta\mathrm{p}} - \check{\mathbf{F}}_{\mathrm{p}}^{\mathrm{T}}\check{\mathbf{F}}_{\mathrm{p}}), \qquad \check{\boldsymbol{\Gamma}}_{\mathrm{e}} = \frac{1}{2}(\mathbf{F}_{\mathrm{e}\Theta\mathrm{p}}^{\mathrm{T}}\mathbf{F}_{\mathrm{e}\Theta\mathrm{p}} - \mathbf{F}_{\Theta\mathrm{p}}^{\mathrm{T}}\mathbf{F}_{\Theta\mathrm{p}}) \tag{4.47}$$

$$\check{\boldsymbol{\Gamma}}_{\mathrm{e}\Theta} = \check{\boldsymbol{\Gamma}}_\Theta + \check{\boldsymbol{\Gamma}}_{\mathrm{e}} = \frac{1}{2}(\mathbf{F}_{\mathrm{e}\Theta\mathrm{p}}^{\mathrm{T}}\mathbf{F}_{\mathrm{e}\Theta\mathrm{p}} - \check{\mathbf{F}}_{\mathrm{p}}^{\mathrm{T}}\check{\mathbf{F}}_{\mathrm{p}}) \tag{4.48}$$

The plastic part reads

$$\check{\boldsymbol{\Gamma}}_{\mathrm{p}} = \frac{1}{2}(\check{\mathbf{F}}_{\mathrm{p}}^{\mathrm{T}}\check{\mathbf{F}}_{\mathrm{p}} - \mathbf{1}) = \frac{1}{2}(\mathbf{C}_{\mathrm{p}} - \mathbf{1}), \qquad \mathbf{C}_{\mathrm{p}} := \check{\mathbf{F}}_{\mathrm{p}}^{\mathrm{T}}\check{\mathbf{F}}_{\mathrm{p}} \tag{4.49}$$

and the creep part, which solely depends on the creep deformation, is given by

$$\check{\boldsymbol{\Gamma}}_{\mathrm{c}} = \frac{1}{2}(\mathbf{1} - \mathbf{F}_{\mathrm{c}}^{-\mathrm{T}}\mathbf{F}_{\mathrm{c}}^{-1}) \tag{4.50}$$

The inelastic deformation is described by

$$\mathbf{E}_{\mathrm{i}} = \mathbf{E}_{\mathrm{p}} + \mathbf{E}_{\mathrm{c}} = \frac{1}{2}(\mathbf{F}_{\mathrm{pc}}^{\mathrm{T}}\mathbf{F}_{\mathrm{pc}} - \mathbf{1}) = \frac{1}{2}(\mathbf{F}_{\mathrm{i}}^{\mathrm{T}}\mathbf{F}_{\mathrm{i}} - \mathbf{1}) = \frac{1}{2}(\mathbf{C}_{\mathrm{i}} - \mathbf{1}). \tag{4.51}$$

The transformation to the intermediate creep configuration reads

$$\check{\boldsymbol{\Gamma}}_{\mathrm{i}} = \mathbf{F}_{\mathrm{c}}^{-\mathrm{T}}\mathbf{E}_{\mathrm{i}}\mathbf{F}_{\mathrm{c}}^{-1} = \frac{1}{2}(\check{\mathbf{F}}_{\mathrm{p}}^{\mathrm{T}}\check{\mathbf{F}}_{\mathrm{p}} - \mathbf{F}_{\mathrm{c}}^{-\mathrm{T}}\mathbf{F}_{\mathrm{c}}^{-1}). \tag{4.52}$$

Due to the concept of dual variables, the Green strain rate tensors are transformed into objective time derivatives in form of the covariant Oldroyd derivative for the creep intermediate configuration $\check{\boldsymbol{\chi}}_t$

$$\overset{\triangle}{\check{(\cdot)}} = \dot{\check{(\cdot)}} + \mathbf{L}_{\mathrm{c}}^{\mathrm{T}}(\cdot) + (\cdot)\mathbf{L}_{\mathrm{c}}, \qquad \mathbf{L}_{\mathrm{c}} := \dot{\mathbf{F}}_{\mathrm{c}}\mathbf{F}_{\mathrm{c}}^{-1}, \tag{4.53}$$

with the creep velocity gradient $\mathbf{L}_{\mathrm{c}}$. The strain decomposition in Eq. (4.39) implies also the strain rate decomposition in the intermediate configuration $\check{\boldsymbol{\chi}}_t$

$$\overset{\triangle}{\check{\boldsymbol{\Gamma}}} = \mathbf{F}_{\mathrm{c}}^{-\mathrm{T}}\dot{\mathbf{E}}\mathbf{F}_{\mathrm{c}}^{-1} = \dot{\check{\boldsymbol{\Gamma}}} + \mathbf{L}_{\mathrm{c}}^{\mathrm{T}}\check{\boldsymbol{\Gamma}} + \check{\boldsymbol{\Gamma}}\mathbf{L}_{\mathrm{c}} = \overset{\triangle}{\check{\boldsymbol{\Gamma}}}_{\mathrm{p}} + \overset{\triangle}{\check{\boldsymbol{\Gamma}}}_{\mathrm{c}} + \overset{\triangle}{\check{\boldsymbol{\Gamma}}}_\Theta + \overset{\triangle}{\check{\boldsymbol{\Gamma}}}_{\mathrm{e}} \tag{4.54}$$

The covariant Oldroyd derivative of the creep strain tensor $\check{\boldsymbol{\Gamma}}_{\mathrm{c}}$ leads to the symmetric part of the creep velocity gradient $\mathbf{L}_{\mathrm{c}}$

$$\overset{\triangle}{\check{\boldsymbol{\Gamma}}}_{\mathrm{c}} = \mathbf{D}_{\mathrm{c}} = \frac{1}{2}(\mathbf{L}_{\mathrm{c}}^{\mathrm{T}} + \mathbf{L}_{\mathrm{c}}) \tag{4.55}$$

This creep strain rate tensor will be used later to define the creep flow-rule.

In the plastic intermediate configuration, the strain tensor additively decomposes into

$$\hat{\boldsymbol{\varepsilon}} = \mathbf{F}_{\mathrm{i}}^{-\mathrm{T}}\mathbf{E}\mathbf{F}_{\mathrm{i}}^{-1} = \check{\mathbf{F}}_{\mathrm{p}}^{-\mathrm{T}}\check{\boldsymbol{\Gamma}}\check{\mathbf{F}}_{\mathrm{p}}^{-1} = \hat{\boldsymbol{\varepsilon}}_{\mathrm{p}} + \hat{\boldsymbol{\varepsilon}}_{\mathrm{c}} + \hat{\boldsymbol{\varepsilon}}_\Theta + \hat{\boldsymbol{\varepsilon}}_{\mathrm{e}}. \tag{4.56}$$

In this configuration, the plastic strain tensor is solely dependent on the plastic deformation – and serves to define the plastic flow-rule

$$\hat{\boldsymbol{\varepsilon}}_\mathrm{p} = \frac{1}{2}(\mathbf{1} - \check{\mathbf{F}}_\mathrm{p}^{-\mathrm{T}} \check{\mathbf{F}}_\mathrm{p}^{-1}). \tag{4.57}$$

The inelastic strain tensor in this configuration reads

$$\hat{\boldsymbol{\varepsilon}}_\mathrm{i} = \hat{\boldsymbol{\varepsilon}}_\mathrm{p} + \hat{\boldsymbol{\varepsilon}}_\mathrm{c} = \frac{1}{2}(\mathbf{1} - \mathbf{F}_\mathrm{i}^{-\mathrm{T}} \mathbf{F}_\mathrm{i}^{-1}). \tag{4.58}$$

The covariant Oldroyd derivative of the inelastic strain tensor is given by

$$\overset{\triangle}{\hat{\boldsymbol{\varepsilon}}}_\mathrm{i} = \overset{\triangle}{\hat{\boldsymbol{\varepsilon}}}_\mathrm{p} + \overset{\triangle}{\hat{\boldsymbol{\varepsilon}}}_\mathrm{c} = \dot{\hat{\boldsymbol{\varepsilon}}}_\mathrm{i} + \mathbf{L}_\mathrm{i}^\mathrm{T} \hat{\boldsymbol{\varepsilon}}_\mathrm{i} + \hat{\boldsymbol{\varepsilon}}_\mathrm{i} \mathbf{L}_\mathrm{i}, \qquad \mathbf{L}_\mathrm{i} := \mathbf{L}_\mathrm{pc} = \dot{\mathbf{F}}_\mathrm{i} \mathbf{F}_\mathrm{i}^{-1}. \tag{4.59}$$

Computing the material time derivative of the tensor $\hat{\boldsymbol{\varepsilon}}_\mathrm{i}$ in the reference configuration and transferring the result back to the intermediate configuration leads to

$$\overset{\triangle}{\hat{\boldsymbol{\varepsilon}}}_\mathrm{i} = \hat{\mathbf{D}}_\mathrm{i} = \frac{1}{2}(\mathbf{L}_\mathrm{i}^\mathrm{T} + \mathbf{L}_\mathrm{i}). \tag{4.60}$$

Another possibility is to formulate the material behavior in the thermal intermediate configuration $\breve{\boldsymbol{\chi}}_t$. The Green strain tensor in this configuration can be computed by

$$\breve{\boldsymbol{\gamma}} = \mathbf{F}_{\Theta\mathrm{pc}}^{-\mathrm{T}} \mathbf{E} \mathbf{F}_{\Theta\mathrm{pc}}^{-1} = \mathbf{F}_{\Theta\mathrm{p}}^{-\mathrm{T}} \check{\boldsymbol{\Gamma}} \mathbf{F}_{\Theta\mathrm{p}}^{-1} = \hat{\mathbf{F}}_\Theta^{-\mathrm{T}} \hat{\boldsymbol{\varepsilon}} \hat{\mathbf{F}}_\Theta^{-1} = \breve{\boldsymbol{\gamma}}_\mathrm{p} + \breve{\boldsymbol{\gamma}}_\mathrm{c} + \breve{\boldsymbol{\gamma}}_\Theta + \breve{\boldsymbol{\gamma}}_\mathrm{e} \tag{4.61}$$

The elastic part of the strain tensor is given by

$$\breve{\boldsymbol{\gamma}}_\mathrm{e} = \frac{1}{2}(\breve{\mathbf{F}}_\mathrm{e}^\mathrm{T} \breve{\mathbf{F}}_\mathrm{e} - \mathbf{1}) = \frac{1}{2}(\breve{\mathbf{C}}_\mathrm{e} - \mathbf{1}), \qquad \breve{\mathbf{C}}_\mathrm{e} := \breve{\mathbf{F}}_\mathrm{e}^\mathrm{T} \breve{\mathbf{F}}_\mathrm{e}. \tag{4.62}$$

The elastic right Cauchy-Green tensor $\breve{\mathbf{C}}_\mathrm{e}$ in this configuration will be used in the formulation of the elasticity relation. The thermal symmetric strain tensor reads

$$\breve{\boldsymbol{\gamma}}_\Theta = \frac{1}{2}(\mathbf{1} - \hat{\mathbf{F}}_\Theta^{-\mathrm{T}} \hat{\mathbf{F}}_\Theta^{-1}) = \frac{1}{2}(\mathbf{1} - \check{\mathbf{B}}_\Theta^{-1}), \qquad \hat{\mathbf{B}}_\Theta := \hat{\mathbf{F}}_\Theta \hat{\mathbf{F}}_\Theta^\mathrm{T} \tag{4.63}$$

The covariant Oldroyd derivative can be stated as

$$\overset{\triangle}{\breve{(\cdot)}} = \dot{\breve{(\cdot)}} + \mathbf{L}_{\Theta\mathrm{pc}}^\mathrm{T} (\cdot) + (\cdot) \mathbf{L}_{\Theta\mathrm{pc}}, \tag{4.64}$$

with the thermal-inelastic velocity gradient defined by

$$\mathbf{L}_{\Theta\mathrm{pc}} := \dot{\mathbf{F}}_{\Theta\mathrm{pc}} \mathbf{F}_{\Theta\mathrm{pc}}^{-1} = \frac{\mathrm{d}(\hat{\mathbf{F}}_\Theta \check{\mathbf{F}}_\mathrm{p} \mathbf{F}_\mathrm{c})}{\mathrm{d}t} (\hat{\mathbf{F}}_\Theta \check{\mathbf{F}}_\mathrm{p} \mathbf{F}_\mathrm{c})^{-1}. \tag{4.65}$$

The thermal expansion is assumed to be purely volumetric. Thus, the thermal deformation gradient reads

$$\hat{\mathbf{F}}_\Theta = \phi(\Theta) \mathbf{1}, \qquad \phi(\Theta) := 1 + \alpha_\Theta (\Theta - \Theta_0) = 1 + \alpha_\Theta \vartheta \tag{4.66}$$

with the temperature difference $\vartheta := \Theta - \Theta_0$. Θ_0 denotes the initial temperature at time $t = t_0$. With the special form of the thermal deformation gradient and the relations

$$\dot{\hat{\mathbf{F}}}_\Theta = \phi'(\Theta)\dot{\Theta}\mathbf{1}, \qquad \hat{\mathbf{F}}_\Theta^{-1} = 1/\phi\,\mathbf{1} \tag{4.67}$$

the thermal-inelastic velocity gradient can be expressed as

$$\begin{aligned} \mathbf{L}_{\Theta\mathrm{pc}} &= \dot{\mathbf{F}}_{\Theta\mathrm{pc}}\mathbf{F}_{\Theta\mathrm{pc}}^{-1} = (\dot{\hat{\mathbf{F}}}_\Theta\mathbf{F}_{\mathrm{pc}} + \hat{\mathbf{F}}_\Theta\dot{\mathbf{F}}_{\mathrm{pc}})(\mathbf{F}_{\mathrm{pc}}^{-1}\hat{\mathbf{F}}_\Theta^{-1}) & (4.68)\\ &= \dot{\hat{\mathbf{F}}}_\Theta\hat{\mathbf{F}}_\Theta^{-1} + \hat{\mathbf{F}}_\Theta\mathbf{L}_{\mathrm{i}}\hat{\mathbf{F}}_\Theta^{-1} = \dot{\hat{\mathbf{F}}}_\Theta\hat{\mathbf{F}}_\Theta^{-1} + \mathbf{L}_{\mathrm{i}} = \frac{\phi'(\Theta)}{\phi}\dot{\Theta}\mathbf{1} + \mathbf{L}_{\mathrm{i}} & (4.69) \end{aligned}$$

Drawing on the concept of dual variables, see Sect. 3.4.2, the dual stress tensors can be derived, see Fig. 4.19. As a result, the stress power is invariant to any change of the configuration and reads with quantities relative to the configuration $\check{\boldsymbol{\chi}}_t$

$$\tilde{\mathbf{T}} \cdot \dot{\mathbf{E}} = \tilde{\mathbf{T}} \cdot \mathbf{F}_{\mathrm{c}}^{\mathrm{T}}\overset{\triangle}{\check{\boldsymbol{\Gamma}}}\mathbf{F}_{\mathrm{c}} = \mathbf{F}_{\mathrm{c}}\tilde{\mathbf{T}}\mathbf{F}_{\mathrm{c}}^{\mathrm{T}} \cdot \overset{\triangle}{\check{\boldsymbol{\Gamma}}} = \check{\mathbf{S}} \cdot \overset{\triangle}{\check{\boldsymbol{\Gamma}}} \tag{4.70}$$

with the stress tensor $\check{\mathbf{S}} := \mathbf{F}_{\mathrm{pc}}\tilde{\mathbf{T}}\mathbf{F}_{\mathrm{pc}}^{\mathrm{T}}$, which is dual to the strain tensor $\check{\boldsymbol{\Gamma}}$. In the plastic intermediate configuration $\hat{\boldsymbol{\chi}}_t$, the stress power is given by

$$\tilde{\mathbf{T}} \cdot \dot{\mathbf{E}} = \tilde{\mathbf{T}} \cdot \mathbf{F}_{\mathrm{pc}}^{\mathrm{T}}\overset{\triangle}{\hat{\boldsymbol{\varepsilon}}}\mathbf{F}_{\mathrm{pc}} = \mathbf{F}_{\mathrm{pc}}\tilde{\mathbf{T}}\mathbf{F}_{\mathrm{pc}}^{\mathrm{T}} \cdot \overset{\triangle}{\hat{\boldsymbol{\varepsilon}}} = \hat{\mathbf{S}} \cdot \overset{\triangle}{\hat{\boldsymbol{\varepsilon}}} \tag{4.71}$$

with the stress tensor $\hat{\mathbf{S}} := \mathbf{F}_{\mathrm{pc}}\tilde{\mathbf{T}}\mathbf{F}_{\mathrm{pc}}^{\mathrm{T}}$ dual to the strain tensor $\hat{\boldsymbol{\varepsilon}}$. In the thermal intermediate configuration $\breve{\boldsymbol{\chi}}_t$, the stress power is obtained analogously

$$\tilde{\mathbf{T}} \cdot \dot{\mathbf{E}} = \tilde{\mathbf{T}} \cdot \mathbf{F}_{\Theta\mathrm{pc}}^{\mathrm{T}}\overset{\triangle}{\breve{\boldsymbol{\gamma}}}\mathbf{F}_{\Theta\mathrm{pc}} = \mathbf{F}_{\Theta\mathrm{pc}}\tilde{\mathbf{T}}\mathbf{F}_{\Theta\mathrm{pc}}^{\mathrm{T}} \cdot \overset{\triangle}{\breve{\boldsymbol{\gamma}}} = \breve{\mathbf{S}} \cdot \overset{\triangle}{\breve{\boldsymbol{\gamma}}} \tag{4.72}$$

with the dual stress tensor $\breve{\mathbf{S}} = \mathbf{F}_{\Theta\mathrm{pc}}\tilde{\mathbf{T}}\mathbf{F}_{\Theta\mathrm{pc}}^{\mathrm{T}}$. The stress power with the decomposition of the strain tensor Eq. (4.61) can be written as

$$\breve{\mathbf{S}} \cdot \overset{\triangle}{\breve{\boldsymbol{\gamma}}} = \breve{\mathbf{S}} \cdot (\overset{\triangle}{\breve{\boldsymbol{\gamma}}}_{\mathrm{p}} + \overset{\triangle}{\breve{\boldsymbol{\gamma}}}_{\mathrm{c}} + \overset{\triangle}{\breve{\boldsymbol{\gamma}}}_{\Theta} + \overset{\triangle}{\breve{\boldsymbol{\gamma}}}_{\mathrm{e}}). \tag{4.73}$$

The thermal strain tensor and its time derivative in the thermal intermediate configuration $\breve{\boldsymbol{\chi}}_t$ can be expressed as

$$\breve{\boldsymbol{\gamma}}_\Theta = \frac{1}{2}(1 - 1/\phi^2)\mathbf{1}. \tag{4.74}$$

With the identity of $\breve{\boldsymbol{\gamma}}_\Theta$, the covariant Oldroyd derivative $\overset{\triangle}{\breve{\boldsymbol{\gamma}}}_\Theta$ can be simplified to

$$\begin{aligned} \overset{\triangle}{\breve{\boldsymbol{\gamma}}}_\Theta &= \dot{\breve{\boldsymbol{\gamma}}}_\Theta + \mathbf{L}_{\Theta\mathrm{pc}}^{\mathrm{T}}\breve{\boldsymbol{\gamma}}_\Theta + \breve{\boldsymbol{\gamma}}_\Theta\mathbf{L}_{\Theta\mathrm{pc}} = \frac{\phi'(\Theta)\dot{\Theta}}{\phi^3}\mathbf{1} + 2\frac{\phi'(\Theta)\dot{\Theta}}{\phi}\breve{\boldsymbol{\gamma}}_\Theta + \breve{\boldsymbol{\gamma}}_\Theta(\mathbf{L}_{\mathrm{i}}^{\mathrm{T}} + \mathbf{L}_{\mathrm{i}}) & (4.75)\\ &= \frac{\phi'(\Theta)\dot{\Theta}}{\phi^3}\mathbf{1} + 2\frac{\phi'(\Theta)\dot{\Theta}}{\phi}\breve{\boldsymbol{\gamma}}_\Theta + 2\breve{\boldsymbol{\gamma}}_\Theta\overset{\triangle}{\check{\boldsymbol{\Gamma}}}_{\mathrm{i}} & (4.76) \end{aligned}$$

Inserting this equation into the partial stress power

$$\breve{\mathbf{S}} \cdot \overset{\triangle}{\breve{\boldsymbol{\gamma}}}_\Theta = \frac{\phi'(\Theta)\dot{\Theta}}{\phi^3}\,\mathrm{tr}(\breve{\mathbf{S}}) + \left(\frac{\phi'(\Theta)\dot{\Theta}}{\phi}\right)\left(1 - \frac{1}{\phi^2}\right)\mathrm{tr}(\breve{\mathbf{S}}) + 2\breve{\mathbf{S}} \cdot \breve{\boldsymbol{\gamma}}_\Theta \overset{\triangle}{\check{\mathbf{\Gamma}}}_\mathrm{i} \tag{4.77}$$

$$= \frac{\phi'(\Theta)\dot{\Theta}}{\phi}\,\mathrm{tr}(\breve{\mathbf{S}}) + 2\breve{\boldsymbol{\gamma}}_\Theta \breve{\mathbf{S}} \cdot \overset{\triangle}{\check{\mathbf{\Gamma}}}_\mathrm{i} \tag{4.78}$$

leads to a simplified equation that is used in the entropy inequality.

4.6 Large Strain Thermo-viscoplasticity for Copper Powder

Together with the temperature-dependent yield function, see Tab. 4.1, a finite strain thermo-viscoplasticity model for sintering of metal powders is derived. The basis for this model is the isothermal rate-independent model for the cold compaction of metal powders developed by Bier [2008], see [Bier and Hartmann, 2006] as well.

First, the structure of the free energy is introduced. Subsequently, the evaluation of the entropy inequality in the form of the Clausius-Duhem inequality is performed, leading to evolution equations for the internal variables. All these derived equations will be transformed into the reference configuration where the time integration is performed. Additionally, the constitutive equations for the heat flux and current density vector as well as the heat conduction equation are formulated.

4.6.1 Structure of Free-Energy

The Helmholtz free-energy function – also called *strain-energy function* – is a scalar valued function ψ, which is the basis for the formulation of a constitutive model. It is assumed that the free-energy additively decomposes into an elastic, inelastic and a thermal part

$$\psi = \psi\big(\breve{\boldsymbol{\gamma}}_\mathrm{e}, r_\mathrm{i}, r_\mathrm{v}, \Theta\big) = \psi_\mathrm{e}\big(\breve{\boldsymbol{\gamma}}_\mathrm{e}\big) + \psi_\mathrm{i}\big(r_\mathrm{i}, r_\mathrm{v}, J_\mathrm{i}, \Theta\big) + \psi_\Theta(\Theta). \tag{4.79}$$

The elastic part depends on the elastic Green strain tensor $\breve{\boldsymbol{\gamma}}_\mathrm{e}$, whereas the thermal part depends solely on the temperature Θ. Furthermore, the inelastic part decomposes into three parts, where ψ_k is connected to the hydrostatic kinematic hardening, ψ_i describes the isotropic hardening and ψ_t specifies the hydrostatic tensile hardening

$$\psi_\mathrm{i}\big(r_\mathrm{i}, r_\mathrm{v}, J_\mathrm{i}, \Theta\big) = \psi_\mathrm{k}\big(r_\mathrm{v}\big) + \psi_\mathrm{i}\big(r_\mathrm{i}\big) + \psi_\mathrm{t}(J_\mathrm{i}, \Theta). \tag{4.80}$$

The kinematic part depends on the internal variable r_v, which is coupled to the inelastic volume change

$$r_\mathrm{v} := \frac{1}{2}\ln(\det \mathbf{C}_\mathrm{i}) = \ln(\det \mathbf{F}_\mathrm{i}) = \ln(\det \check{\mathbf{F}}_\mathrm{p}) + \ln(\det \mathbf{F}_\mathrm{c}). \tag{4.81}$$

The same definition is used in [Bier and Hartmann, 2006] and [Bier, 2008]. Computing the material time derivative leads to

$$\dot{r}_\mathrm{v} = \frac{\dot{\overline{\ln(\det \mathbf{C}_\mathrm{i})}}}{2} = \frac{1}{2}\frac{(\det \mathbf{C}_\mathrm{i})\mathbf{C}_\mathrm{i}^{-1}}{(\det \mathbf{C}_\mathrm{i})} \cdot \dot{\mathbf{C}}_\mathrm{i} = \frac{1}{2}\dot{\mathbf{C}}_\mathrm{i} \cdot \mathbf{C}_\mathrm{i}^{-1}. \tag{4.82}$$

This scalar variable can be expressed by the relations Eq. (4.59) and Eq. (4.60)

$$\mathbf{F}_\mathrm{i}^{-\mathrm{T}}\dot{\mathbf{C}}_\mathrm{i}\mathbf{F}_\mathrm{i}^{-1} = \mathbf{F}_\mathrm{i}^{-\mathrm{T}}\dot{\mathbf{F}}_\mathrm{i}^{\mathrm{T}}\mathbf{F}_\mathrm{i}\mathbf{F}_\mathrm{i}^{-1} + \mathbf{F}_\mathrm{i}^{-\mathrm{T}}\mathbf{F}_\mathrm{i}^{\mathrm{T}}\dot{\mathbf{F}}_\mathrm{i}\mathbf{F}_\mathrm{i}^{-1} = \mathbf{L}_\mathrm{i}^{\mathrm{T}} + \mathbf{L}_\mathrm{i} = 2\hat{\mathbf{D}}_\mathrm{i} = 2\overset{\triangle}{\hat{\boldsymbol{\varepsilon}}}_\mathrm{i} \tag{4.83}$$

in the inelastic intermediate configuration

$$\dot{r}_\mathrm{v} = \frac{1}{2}\dot{\mathbf{C}}_\mathrm{i} \cdot \mathbf{C}_\mathrm{i}^{-1} = \frac{1}{2}\left(\mathbf{F}_\mathrm{i}^{-\mathrm{T}}\dot{\mathbf{C}}_\mathrm{i}\mathbf{F}_\mathrm{i}^{-1}\right) \cdot \mathbf{1} = \operatorname{tr}\overset{\triangle}{\hat{\boldsymbol{\varepsilon}}}_\mathrm{i}. \tag{4.84}$$

This internal variable describes the inelastic volume change $\dot{r}_\mathrm{v} = \operatorname{tr}\overset{\triangle}{\hat{\boldsymbol{\varepsilon}}}_\mathrm{i}$.

For the isotropic hardening part of the free energy, the strain-like variable r_i is used, while the tensile hardening part depends on the determinant of the inelastic deformation gradient $J_\mathrm{i} := \det \mathbf{F}_\mathrm{i}$ and the temperature Θ.

4.6.2 Evaluation of Dissipation Inequality

On the basis of the multiplicative decomposition and the derived kinematical quantities together with the free-energy, a structure for the material model can be derived by inserting these relations into the Clausius-Duhem inequality (3.107)

$$-\dot{\psi} - s\dot{\Theta} + \frac{1}{\rho_0}\tilde{\mathbf{T}} \cdot \dot{\mathbf{E}} - \frac{1}{\Theta\rho_0}\operatorname{Grad}\Theta \cdot \vec{q}_\mathrm{R} - \frac{1}{\rho_0}\operatorname{Grad}\varphi \cdot \vec{j}_\mathrm{R} \geq 0 \tag{4.85}$$

and separated into the internal dissipation inequality

$$\delta = -\dot{\psi} - s\dot{\Theta} + \frac{1}{\rho_0}\tilde{\mathbf{T}} \cdot \dot{\mathbf{E}} \geq 0 \tag{4.86}$$

and the heat conduction inequality

$$-\frac{1}{\Theta\rho_0}\operatorname{Grad}\Theta \cdot \vec{q}_\mathrm{R} \geq 0 \tag{4.87}$$

as well as the electrical conduction inequality

$$-\frac{1}{\rho_0}\operatorname{Grad}\varphi \cdot \vec{j}_\mathrm{R} \geq 0. \tag{4.88}$$

The heat flux and the current density material relations are treated in Sect. 4.6.6.

Taking the material time derivative of the free-energy Eq. (4.79) yields

$$\dot{\psi} = \frac{\partial \psi_{\mathrm{e}}}{\partial \breve{\boldsymbol{\gamma}}_{\mathrm{e}}} \cdot \dot{\breve{\boldsymbol{\gamma}}}_{\mathrm{e}} + \frac{\partial \psi}{\partial \Theta} \dot{\Theta} + \dot{\psi}_{\mathrm{i}}. \tag{4.89}$$

Inserting this result and the stress power decomposition Eq. (4.73) in the internal dissipation inequality Eq. (4.86) results in

$$\delta = -\frac{\partial \psi_{\mathrm{e}}}{\partial \breve{\boldsymbol{\gamma}}_{\mathrm{e}}} \cdot \dot{\breve{\boldsymbol{\gamma}}}_{\mathrm{e}} - s\dot{\Theta} + \frac{1}{\rho_0} \breve{\mathbf{S}} \cdot \overset{\vartriangle}{\breve{\boldsymbol{\gamma}}}_{\mathrm{i}} + \frac{1}{\rho_0} \breve{\mathbf{S}} \cdot \overset{\vartriangle}{\breve{\boldsymbol{\gamma}}}_{\Theta} + \frac{1}{\rho_0} \breve{\mathbf{S}} \cdot \overset{\vartriangle}{\breve{\boldsymbol{\gamma}}}_{\mathrm{e}} - \frac{\partial \psi}{\partial \Theta} \dot{\Theta} - \dot{\psi}_{\mathrm{i}} \geq 0. \tag{4.90}$$

The material time derivative of the elastic strain tensor $\dot{\breve{\boldsymbol{\gamma}}}_{\mathrm{e}}$ can be expressed by Eq. (4.69) as

$$\dot{\breve{\boldsymbol{\gamma}}}_{\mathrm{e}} = \overset{\vartriangle}{\breve{\boldsymbol{\gamma}}}_{\mathrm{e}} - \mathbf{L}_{\Theta\mathrm{pc}}^{\mathrm{T}} \breve{\boldsymbol{\gamma}}_{\mathrm{e}} - \breve{\boldsymbol{\gamma}}_{\mathrm{e}} \mathbf{L}_{\Theta\mathrm{pc}} = \overset{\vartriangle}{\breve{\boldsymbol{\gamma}}}_{\mathrm{e}} - 2\frac{\phi'(\Theta)\dot{\Theta}}{\phi} \breve{\boldsymbol{\gamma}}_{\mathrm{e}} - \mathbf{L}_{\mathrm{i}}^{\mathrm{T}} \breve{\boldsymbol{\gamma}}_{\mathrm{e}} - \breve{\boldsymbol{\gamma}}_{\mathrm{e}} \mathbf{L}_{\mathrm{i}}. \tag{4.91}$$

Inserting this relation and the simplified thermal part of the stress power (4.77) into Eq. (4.90) yields

$$\begin{aligned} \delta = &-\frac{\partial \psi_{\mathrm{e}}}{\partial \breve{\boldsymbol{\gamma}}_{\mathrm{e}}} \cdot \overset{\vartriangle}{\breve{\boldsymbol{\gamma}}}_{\mathrm{e}} + \frac{\partial \psi_{\mathrm{e}}}{\partial \breve{\boldsymbol{\gamma}}_{\mathrm{e}}} \cdot (\mathbf{L}_{\mathrm{i}}^{\mathrm{T}} \breve{\boldsymbol{\gamma}}_{\mathrm{e}} + \breve{\boldsymbol{\gamma}}_{\mathrm{e}} \mathbf{L}_{\mathrm{i}}) - s\dot{\Theta} + \frac{1}{\rho_0} \breve{\mathbf{S}} \cdot \overset{\vartriangle}{\breve{\boldsymbol{\gamma}}}_{\mathrm{i}} + \frac{\phi'(\Theta)\dot{\Theta}}{\phi} \operatorname{tr}(\breve{\mathbf{S}}) \\ &+ 2\breve{\boldsymbol{\gamma}}_{\Theta} \breve{\mathbf{S}} \cdot \overset{\vartriangle}{\breve{\boldsymbol{\Gamma}}}_{\mathrm{i}} + \frac{1}{\rho_0} \breve{\mathbf{S}} \cdot \overset{\vartriangle}{\breve{\boldsymbol{\gamma}}}_{\mathrm{e}} + 2\frac{\phi'(\Theta)\dot{\Theta}}{\phi} \breve{\boldsymbol{\gamma}}_{\mathrm{e}} \cdot \frac{\partial \psi_{\mathrm{e}}}{\partial \breve{\boldsymbol{\gamma}}_{\mathrm{e}}} - \frac{\partial \psi}{\partial \Theta} \dot{\Theta} - \dot{\psi}_{\mathrm{i}} \geq 0. \end{aligned} \tag{4.92}$$

By rearranging this inequality, one obtains

$$\begin{aligned} \delta = &\left(\frac{1}{\rho_0} \breve{\mathbf{S}} - \frac{\partial \psi_{\mathrm{e}}}{\partial \breve{\boldsymbol{\gamma}}_{\mathrm{e}}} \right) \cdot \overset{\vartriangle}{\breve{\boldsymbol{\gamma}}}_{\mathrm{e}} - \left(s + \frac{\partial \psi}{\partial \Theta} - 2\frac{\phi'(\Theta)}{\phi} \breve{\boldsymbol{\gamma}}_{\mathrm{e}} \cdot \frac{\partial \psi_{\mathrm{e}}}{\partial \breve{\boldsymbol{\gamma}}_{\mathrm{e}}} - \frac{1}{\rho_0} \frac{\phi'(\Theta)}{\phi} \operatorname{tr}(\breve{\mathbf{S}}) \right) \dot{\Theta} \\ &+ \frac{\partial \psi_{\mathrm{e}}}{\partial \breve{\boldsymbol{\gamma}}_{\mathrm{e}}} \cdot (\mathbf{L}_{\mathrm{i}}^{\mathrm{T}} \breve{\boldsymbol{\gamma}}_{\mathrm{e}} + \breve{\boldsymbol{\gamma}}_{\mathrm{e}} \mathbf{L}_{\mathrm{i}}) + 2\frac{1}{\rho_0} \breve{\mathbf{S}} \cdot \breve{\boldsymbol{\gamma}}_{\Theta} \overset{\vartriangle}{\hat{\boldsymbol{\varepsilon}}}_{\mathrm{i}} + \frac{1}{\rho_0} \breve{\mathbf{S}} \cdot \overset{\vartriangle}{\breve{\boldsymbol{\gamma}}}_{\mathrm{i}} - \dot{\psi}_{\mathrm{i}} \geq 0. \end{aligned} \tag{4.93}$$

This inequality has to be fulfilled for arbitrary thermodynamic processes. Therefore, the terms in the parentheses are assumed to be zero. As a result, one obtains the potential relation for the stresses $\breve{\mathbf{S}}$ and the specific entropy s

$$\breve{\mathbf{S}} = \rho_0 \frac{\partial \psi_{\mathrm{e}}}{\partial \breve{\boldsymbol{\gamma}}_{\mathrm{e}}} \quad \text{and} \quad s = -\frac{\partial \psi}{\partial \Theta} + \frac{\phi'}{\rho_0} \left(\frac{1}{\phi} \operatorname{tr} \breve{\mathbf{S}} + \frac{2}{\phi} \breve{\boldsymbol{\gamma}}_{\mathrm{e}} \cdot \breve{\mathbf{S}} \right). \tag{4.94}$$

The remaining part is given by

$$\frac{\partial \psi_{\mathrm{e}}}{\partial \breve{\boldsymbol{\gamma}}_{\mathrm{e}}} \cdot (\mathbf{L}_{\mathrm{i}}^{\mathrm{T}} \breve{\boldsymbol{\gamma}}_{\mathrm{e}} + \breve{\boldsymbol{\gamma}}_{\mathrm{e}} \mathbf{L}_{\mathrm{i}}) + 2\frac{1}{\rho_0} \breve{\mathbf{S}} \cdot \breve{\boldsymbol{\gamma}}_{\Theta} \overset{\vartriangle}{\hat{\boldsymbol{\varepsilon}}}_{\mathrm{i}} + \frac{1}{\rho_0} \breve{\mathbf{S}} \cdot \overset{\vartriangle}{\breve{\boldsymbol{\gamma}}}_{\mathrm{i}} - \dot{\psi}_{\mathrm{i}} \geq 0. \tag{4.95}$$

Due to the symmetry of the elastic strain tensor $\breve{\boldsymbol{\gamma}}_{\mathrm{e}} = \frac{1}{2}(\breve{\mathbf{C}}_{\mathrm{e}} - \mathbf{1})$ and the property of the scalar product $\mathbf{A} \cdot (\mathbf{B}\mathbf{C}) = (\mathbf{B}^{\mathrm{T}}\mathbf{A}) \cdot \mathbf{C}$ and due to the assumption of isotropic elasticity, which implies $\breve{\boldsymbol{\gamma}}_{\mathrm{e}}(\partial\psi_{\mathrm{e}}/\partial\breve{\boldsymbol{\gamma}}_{\mathrm{e}}) = (\partial\psi_{\mathrm{e}}/\partial\breve{\boldsymbol{\gamma}}_{\mathrm{e}})\breve{\boldsymbol{\gamma}}_{\mathrm{e}}$, the first part in the remaining dissipation inequality can be replaced

$$\mathcal{D}_i = 2\frac{1}{\rho_0}\breve{\boldsymbol{\gamma}}_{\mathrm{e}}\breve{\mathbf{S}} \cdot \overset{\vartriangle}{\hat{\boldsymbol{\varepsilon}}}_{\mathrm{i}} + 2\frac{1}{\rho_0}\breve{\boldsymbol{\gamma}}_{\Theta}\breve{\mathbf{S}} \cdot \overset{\vartriangle}{\hat{\boldsymbol{\varepsilon}}}_{\mathrm{i}} + \frac{1}{\rho_0}\breve{\mathbf{S}} \cdot \overset{\vartriangle}{\breve{\boldsymbol{\gamma}}}_{\mathrm{i}} - \dot{\psi}_{\mathrm{i}} \geq 0. \tag{4.96}$$

All quantities in the remaining inequality are transferred to the plastic intermediate configuration $\hat{\boldsymbol{\chi}}_t$. The stress power $\breve{\mathbf{S}} \cdot \overset{\vartriangle}{\breve{\boldsymbol{\gamma}}}_{\mathrm{i}}$ can be transferred with the help of the relations

$$\breve{\mathbf{S}} = \hat{\mathbf{F}}_{\Theta}\hat{\mathbf{S}}\hat{\mathbf{F}}_{\Theta}^{\mathrm{T}}, \qquad \overset{\vartriangle}{\breve{\boldsymbol{\gamma}}}_{\mathrm{i}} = \hat{\mathbf{F}}_{\Theta}^{-\mathrm{T}}\overset{\vartriangle}{\hat{\boldsymbol{\varepsilon}}}_{\mathrm{i}}\hat{\mathbf{F}}_{\Theta}^{-1} \tag{4.97}$$

into the plastic intermediate configuration

$$\breve{\mathbf{S}} \cdot \overset{\vartriangle}{\breve{\boldsymbol{\gamma}}}_{\mathrm{i}} = (\hat{\mathbf{F}}_{\Theta}\hat{\mathbf{S}}\hat{\mathbf{F}}_{\Theta}^{\mathrm{T}}) \cdot (\hat{\mathbf{F}}_{\Theta}^{-\mathrm{T}}\overset{\vartriangle}{\hat{\boldsymbol{\varepsilon}}}_{\mathrm{i}}\hat{\mathbf{F}}_{\Theta}^{-1}) = (\phi\mathbf{1}\hat{\mathbf{S}}\phi\mathbf{1}) \cdot (\phi^{-1}\mathbf{1}\overset{\vartriangle}{\hat{\boldsymbol{\varepsilon}}}_{\mathrm{i}}\phi^{-1}\mathbf{1}) = \hat{\mathbf{S}} \cdot \overset{\vartriangle}{\hat{\boldsymbol{\varepsilon}}}_{\mathrm{i}}. \tag{4.98}$$

The two expressions $\breve{\boldsymbol{\gamma}}_{\mathrm{e}}\breve{\mathbf{S}}$ and $\breve{\boldsymbol{\gamma}}_{\Theta}\breve{\mathbf{S}}$ read in the plastic intermediate configuration $\hat{\boldsymbol{\chi}}_t$

$$\breve{\boldsymbol{\gamma}}_{\mathrm{e}} = \hat{\mathbf{F}}_{\Theta}^{-\mathrm{T}}\hat{\boldsymbol{\varepsilon}}_{\mathrm{e}}\hat{\mathbf{F}}_{\Theta}^{-1}, \quad \breve{\boldsymbol{\gamma}}_{\mathrm{e}}\breve{\mathbf{S}} = \hat{\mathbf{F}}_{\Theta}^{-\mathrm{T}}\hat{\boldsymbol{\varepsilon}}_{\mathrm{e}}\hat{\mathbf{F}}_{\Theta}^{-1}\hat{\mathbf{F}}_{\Theta}\hat{\mathbf{S}}\hat{\mathbf{F}}_{\Theta}^{\mathrm{T}} = \phi^{-1}\mathbf{1}\hat{\boldsymbol{\varepsilon}}_{\mathrm{e}}\hat{\mathbf{S}}\phi\mathbf{1} = \hat{\boldsymbol{\varepsilon}}_{\mathrm{e}}\hat{\mathbf{S}} \tag{4.99}$$

$$\breve{\boldsymbol{\gamma}}_{\Theta} = \hat{\mathbf{F}}_{\Theta}^{-\mathrm{T}}\hat{\boldsymbol{\varepsilon}}_{\Theta}\hat{\mathbf{F}}_{\Theta}^{-1}, \quad \breve{\boldsymbol{\gamma}}_{\Theta}\breve{\mathbf{S}} = \hat{\mathbf{F}}_{\Theta}^{-\mathrm{T}}\hat{\boldsymbol{\varepsilon}}_{\Theta}\hat{\mathbf{F}}_{\Theta}^{-1}\hat{\mathbf{F}}_{\Theta}\hat{\mathbf{S}}\hat{\mathbf{F}}_{\Theta}^{\mathrm{T}} = \hat{\boldsymbol{\varepsilon}}_{\Theta}\hat{\mathbf{S}} \tag{4.100}$$

Inserting these transferred quantities into the remaining inequality yields

$$\mathcal{D}_i = (\mathbf{1} + 2\hat{\boldsymbol{\varepsilon}}_{\mathrm{e}} + 2\hat{\boldsymbol{\varepsilon}}_{\Theta})\,\hat{\mathbf{S}} \cdot \overset{\vartriangle}{\hat{\boldsymbol{\varepsilon}}}_{\mathrm{i}} - \rho_0\dot{\psi}_{\mathrm{i}} \geq 0. \tag{4.101}$$

This expression can be further simplified with the relation

$$\hat{\boldsymbol{\varepsilon}}_{\mathrm{e}\Theta} = \hat{\boldsymbol{\varepsilon}}_{\Theta} + \hat{\boldsymbol{\varepsilon}}_{\mathrm{e}} = \frac{1}{2}(\mathbf{F}_{\mathrm{e}\Theta}^{\mathrm{T}}\mathbf{F}_{\mathrm{e}\Theta} - \mathbf{1}) = \frac{1}{2}(\hat{\mathbf{C}}_{\mathrm{e}\Theta} - \mathbf{1}) \tag{4.102}$$

$$\hat{\mathbf{C}}_{\mathrm{e}\Theta} := \mathbf{F}_{\mathrm{e}\Theta}^{\mathrm{T}}\mathbf{F}_{\mathrm{e}\Theta}, \qquad \mathbf{F}_{\mathrm{e}\Theta} := \breve{\mathbf{F}}_{\mathrm{e}}\hat{\mathbf{F}}_{\Theta} \tag{4.103}$$

and the definition of the Mandel stress tensor

$$\hat{\mathbf{P}} := (\mathbf{1} + 2\hat{\boldsymbol{\varepsilon}}_{\mathrm{e}\Theta})\hat{\mathbf{S}} = \hat{\mathbf{C}}_{\mathrm{e}\Theta}\hat{\mathbf{S}}, \tag{4.104}$$

leading to

$$\mathcal{D}_i = \hat{\mathbf{P}} \cdot \overset{\vartriangle}{\hat{\boldsymbol{\varepsilon}}}_{\mathrm{i}} - \dot{\psi}_{\mathrm{i}} \geq 0. \tag{4.105}$$

If the inelastic part of the free energy (4.80) is inserted into Eq. (4.105), one obtains

$$\mathcal{D}_i = (\hat{\mathbf{P}} + \xi_{\mathrm{M}}\mathbf{1}) \cdot \overset{\vartriangle}{\hat{\boldsymbol{\varepsilon}}}_{\mathrm{i}} - \xi_{\mathrm{M}}\mathbf{1} \cdot \overset{\vartriangle}{\hat{\boldsymbol{\varepsilon}}}_{\mathrm{i}} - \rho_0\frac{\partial\psi_{\mathrm{k}}}{\partial r_{\mathrm{v}}}\dot{r}_{\mathrm{v}} - \rho_0\frac{\partial\psi_{\mathrm{i}}}{\partial r_{\mathrm{i}}}\dot{r}_{\mathrm{i}} - \rho_0\frac{\partial\psi_{\mathrm{t}}}{\partial J_{\mathrm{i}}}\dot{J}_{\mathrm{i}} \geq 0. \tag{4.106}$$

Additionally, a stress-like internal variable ξ_{M} is introduced, separating a hydrostatic stress part, see [Bier and Hartmann, 2006] and [Bier, 2008]. The inequality is decomposed into a creep, a kinematic, an isotropic and a tensile hardening part

$$\mathcal{D}_i = \mathcal{D}_c + \mathcal{D}_K + \mathcal{D}_I + \mathcal{D}_{\mathrm{t}} \geq 0. \tag{4.107}$$

These parts are defined by

$$\begin{aligned} &\mathcal{D}_c = \hat{\mathbf{P}} \cdot \overset{\triangle}{\hat{\boldsymbol{\varepsilon}}}_{\mathrm{c}} \geq 0, \quad \mathcal{D}_K = (\hat{\mathbf{P}} - \xi_{\mathrm{M}}\mathbf{1}) \cdot \overset{\triangle}{\hat{\boldsymbol{\varepsilon}}}_{\mathrm{i}} + \xi_{\mathrm{M}}\mathbf{1} \cdot \overset{\triangle}{\hat{\boldsymbol{\varepsilon}}}_{\mathrm{i}} - \rho_0 \frac{\partial \psi_{\mathrm{k}}}{\partial r_{\mathrm{v}}} \dot{r}_{\mathrm{v}} \geq 0 \\ &\mathcal{D}_I = \hat{\mathbf{P}} \cdot \overset{\triangle}{\hat{\boldsymbol{\varepsilon}}}_{\mathrm{i}} - \rho_0 \frac{\partial \psi_{\mathrm{i}}}{\partial r_{\mathrm{i}}} \dot{r}_{\mathrm{i}} \geq 0, \quad \mathcal{D}_{\mathrm{t}} = \hat{\mathbf{P}} \cdot \overset{\triangle}{\hat{\boldsymbol{\varepsilon}}}_{\mathrm{i}} - \rho_0 \frac{\partial \psi_{\mathrm{t}}}{\partial J_{\mathrm{i}}} \dot{J}_{\mathrm{i}} \geq 0. \end{aligned} \tag{4.108}$$

4.6.3 Formulation of Evolution Equations

In the following, the evolution equations for the internal variables are derived. First, the connection between the inelastic volume change and the relative density is shown. Here, the assumption of small elastic strains leads to simplified transformations. Subsequently, the plastic and the creep flow-rules are proposed, followed by an introduction of the evolution equations for the characterization of the yield function – namely the yield function parameters, which are the height of the function k_{M}, the center of the ellipse function ξ_{M} and the hardening in tensile direction I_{t}.

Connection between the Inelastic Volume Change and the Relative Density

The balance of mass (3.45) is divided by the density of the solid material ρ_{solid},

$$\frac{\rho}{\rho_{\mathrm{solid}}} \det \mathbf{F} = \frac{\rho_0}{\rho_{\mathrm{solid}}} \quad \Leftrightarrow \quad \rho_{\mathrm{rel}} \det \mathbf{F} = \rho_{0,\mathrm{rel}}. \tag{4.109}$$

In this relation, $\rho_{0,\mathrm{rel}} := \rho_0/\rho_{\mathrm{solid}}$ is the initial relative density at the beginning of the experiment. In the limit case of full compaction, ρ_{rel} – which is the actual relative density – reaches $\rho_{\mathrm{rel}} = 1$. Computing the material time derivative leads to

$$\left(\frac{\mathrm{d}}{\mathrm{d}t}\rho_{\mathrm{rel}}\right) \det \mathbf{F} + \rho_{\mathrm{rel}} \frac{\mathrm{d}}{\mathrm{d}t} \det \mathbf{F} = 0. \tag{4.110}$$

Using the property

$$\frac{\mathrm{d}}{\mathrm{d}t} \det \mathbf{F} = (\det \mathbf{F})\mathbf{F}^{-\mathrm{T}} \cdot \dot{\mathbf{F}}\mathbf{1} = (\det \mathbf{F}) \operatorname{tr} \mathbf{L} = (\det \mathbf{F}) \operatorname{tr} \mathbf{D} \tag{4.111}$$

with the spatial velocity gradient $\mathbf{L} = \dot{\mathbf{F}}\mathbf{F}^{-1}$ and its symmetric part $\mathbf{D}$ one obtains

$$\dot{\rho}_{\mathrm{rel}} = -\rho_{\mathrm{rel}} \operatorname{tr} \mathbf{D}. \tag{4.112}$$

In the powder experiments, the volume change is mostly coupled to the inelastic volume change and can be decomposed into the creep and plastic parts. For small elastic and thermal deformations one can assume

$$\det \mathbf{F} \approx \det \mathbf{F}_\mathrm{i} = (\det \mathbf{F}_\mathrm{c})(\det \check{\mathbf{F}}_\mathrm{p}) \qquad \mathbf{D} \approx \hat{\mathbf{D}}_\mathrm{i} \tag{4.113}$$

The following equation is used as an evolution equation for the relative density, see, for example, in the work of Mähler and Runesson [2000] and Mähler and Runesson [2003] and Frischkorn and Reese [2011] as well as Kebriaei et al. [2013]

$$\dot{\rho}_\mathrm{rel} \approx -\rho_\mathrm{rel} \operatorname{tr} \hat{\mathbf{D}}_\mathrm{i} = -\rho_\mathrm{rel} \operatorname{tr} \overset{\triangle}{\hat{\boldsymbol{\varepsilon}}}_\mathrm{i}. \tag{4.114}$$

This concept is not followed here. The author's opinion is that the density is directly given by the mass balance, meaning that the deformation gradient determines the relative density based on the density in the reference configuration, see Eq. (4.109). In this work, the internal variable r_v is used to describe the plastic volume change, which is connected to the relative density. The equivalence can be seen by computing its time derivative

$$\dot{r}_\mathrm{v} = \frac{\dot{\overline{\ln(\det \mathbf{C}_\mathrm{i})}}}{2} = \frac{1}{2} \frac{(\det \mathbf{C}_\mathrm{i}) \mathbf{C}_\mathrm{i}^{-1}}{(\det \mathbf{C}_\mathrm{i})} \cdot \dot{\mathbf{C}}_\mathrm{i} = \frac{1}{2} \dot{\mathbf{C}}_\mathrm{i} \cdot \mathbf{C}_\mathrm{i}^{-1} = \operatorname{tr} \overset{\triangle}{\hat{\boldsymbol{\varepsilon}}}_\mathrm{i}, \tag{4.115}$$

see Eq. (4.84). In the powder metallurgy community, the relative density plays an important role. Hence, the connection between ρ_rel and the internal variable r_v is of interest. With the help of the property – once again neglecting the elastic and the thermal deformation – one obtains

$$\rho_\mathrm{rel} \det \mathbf{F} = \rho_{0,\mathrm{rel}} \quad \Leftrightarrow \quad \det \mathbf{F} \approx \det \mathbf{F}_\mathrm{i} = (\det \mathbf{F}_\mathrm{c})(\det \check{\mathbf{F}}_\mathrm{p}) = \frac{\rho_{0,\mathrm{rel}}}{\rho_\mathrm{rel}}. \tag{4.116}$$

Inserting Eq. (4.116) into Eq. (4.81) leads to

$$r_\mathrm{v} = \ln(\det \mathbf{F}_\mathrm{i}) = \ln\left(\frac{\rho_{0,\mathrm{rel}}}{\rho_\mathrm{rel}}\right) \quad \Rightarrow \quad \rho_\mathrm{rel} = \rho_{0,\mathrm{rel}}\, e^{-r_\mathrm{v}} = \frac{\rho_{0,\mathrm{rel}}}{(\det \mathbf{F}_\mathrm{c})(\det \check{\mathbf{F}}_\mathrm{p})}. \tag{4.117}$$

This equation is only valid if the elastic and thermal strains are negligible or have minor influence on the volume change.

Assumption of Small Elastic Strains

In the investigated sintering process, the overall deformation is dominated by the inelastic effects. The elastic strains are of the order of 10^{-3}, whereas the inelastic strains are of the order of 10^{-1}. Therefore, the elastic strains can be assumed to be negligible, which leads to a simplified theory, see [Lubliner, 2008, p. 490] and [Casey, 1985]. Hence, the elastic Cauchy-Green tensor can be assumed to be close to unity, $\breve{\mathbf{C}}_{\mathrm{e}} \approx \mathbf{1}$. The same concept is also used in [Quint, 2012]. According to [Haupt, 2002, p. 473], the assumption of small elastic strains leads to simplified transformations. The elastic deformation gradient can be represented with the polar decomposition, Eq. (3.10), $\breve{\mathbf{F}}_{\mathrm{e}} = \mathbf{R}_{\mathrm{e}}\mathbf{U}_{\mathrm{e}}$. The stretch tensor is close to unity $\mathbf{U}_{\mathrm{e}} \approx \mathbf{1}$ and the elastic deformation gradient is equal to the elastic rotational tensor $\breve{\mathbf{F}}_{\mathrm{e}} \approx \mathbf{R}_{\mathrm{e}}$. This means that there are small elastic strains and arbitrary rotations, [Haupt, 2002, p. 473].

Based on this assumption, the Mandel stress tensor Eq. (4.104) can be simplified. First, the Mandel stress tensor is transformed into the thermal intermediate configuration, see Eq. (4.103),

$$\hat{\mathbf{C}}_{\mathrm{e}\Theta}\hat{\mathbf{S}} = \hat{\mathbf{C}}_{\mathrm{e}\Theta}\hat{\mathbf{F}}_{\Theta}^{-1}\breve{\mathbf{S}}\hat{\mathbf{F}}_{\Theta}^{-\mathrm{T}} = \mathbf{F}_{\mathrm{e}\Theta}^{\mathrm{T}}\mathbf{F}_{\mathrm{e}\Theta}\hat{\mathbf{F}}_{\Theta}^{-1}\breve{\mathbf{S}}\hat{\mathbf{F}}_{\Theta}^{-\mathrm{T}} = \breve{\mathbf{F}}_{\mathrm{e}}^{\mathrm{T}}\breve{\mathbf{F}}_{\mathrm{e}}\breve{\mathbf{S}} = \breve{\mathbf{C}}_{\mathrm{e}}\breve{\mathbf{S}}. \tag{4.118}$$

With the assumption of small elastic strains, the Mandel stress tensor is equal to the stress tensor in the thermal configuration

$$\breve{\mathbf{C}}_{\mathrm{e}}\breve{\mathbf{S}} \approx \breve{\mathbf{S}}. \tag{4.119}$$

Plastic Flow-Rule

The inelastic flow-rule is additively decomposed into a creep flow rule and a plastic associative flow-rule, see Eq. (4.59),

$$\overset{\triangle}{\hat{\boldsymbol{\varepsilon}}}_{\mathrm{i}} = \overset{\triangle}{\hat{\boldsymbol{\varepsilon}}}_{\mathrm{p}} + \overset{\triangle}{\hat{\boldsymbol{\varepsilon}}}_{\mathrm{c}}. \tag{4.120}$$

In the stress power, the Mandel stress tensor can be simplified by assuming small elastic strains, leading to

$$\hat{\mathbf{P}} \cdot \overset{\triangle}{\hat{\boldsymbol{\varepsilon}}}_{\mathrm{i}} \approx \hat{\mathbf{S}} \cdot \overset{\triangle}{\hat{\boldsymbol{\varepsilon}}}_{\mathrm{i}} = \hat{\mathbf{S}} \cdot \overset{\triangle}{\hat{\boldsymbol{\varepsilon}}}_{\mathrm{p}} + \hat{\mathbf{S}} \cdot \overset{\triangle}{\hat{\boldsymbol{\varepsilon}}}_{\mathrm{c}}. \tag{4.121}$$

The creep flow-rule is defined in the next section. Since an associative flow-rule is successfully applied to model powder compaction in the works of [Mähler and Runesson, 2003; Mähler and Runesson, 2000; Oliver et al., 2010; Frischkorn and Reese, 2011], an associative rule for the plastic flow is considered here too:

$$\overset{\triangle}{\hat{\boldsymbol{\varepsilon}}}_{\mathrm{p}} = \Lambda \frac{\partial \tilde{F}}{\partial \hat{\mathbf{S}}} = \Lambda \left(\frac{\partial \tilde{F}}{\partial \hat{\mathrm{I}}_{1\mathrm{i}}} \mathbf{1} + \frac{\partial \tilde{F}}{\partial \hat{\mathrm{J}}_{2\mathrm{i}}} \hat{\mathbf{S}}^{\mathrm{D}} \right). \tag{4.122}$$

The first stress invariant and second stress deviator invariant are given by

$$\hat{\mathrm{I}}_{1\mathrm{i}} = \operatorname{tr} \hat{\mathbf{S}}, \qquad \hat{\mathrm{J}}_{2\mathrm{i}} = \frac{1}{2} \hat{\mathbf{S}}^{\mathrm{D}} \cdot \hat{\mathbf{S}}^{\mathrm{D}}. \tag{4.123}$$

The derivatives of the yield function $\tilde{F}$ with respect to the invariants can be computed by

$$\frac{\partial \tilde{F}}{\partial \hat{\mathrm{I}}_{1\mathrm{i}}} = \frac{\partial F}{\partial \hat{\mathrm{I}}_{1\mathrm{i}}} = \frac{\partial F}{\partial g_1}\frac{\partial \tilde{g}_1}{\partial \hat{\mathrm{I}}_{1\mathrm{i}}} + \frac{\partial F}{\partial g_2}\frac{\partial \tilde{g}_2}{\partial \hat{\mathrm{I}}_{1\mathrm{i}}}, \tag{4.124}$$

$$\frac{\partial \tilde{F}}{\partial \hat{\mathrm{J}}_{2\mathrm{i}}} = \frac{1}{2\sqrt{\hat{\mathrm{J}}_{2\mathrm{i}}}}\frac{\partial F}{\partial \sqrt{\hat{\mathrm{J}}_{2\mathrm{i}}}} = \frac{1}{2\sqrt{\hat{\mathrm{J}}_{2\mathrm{i}}}}\left(\frac{\partial F}{\partial g_1}\frac{\partial \tilde{g}_1}{\partial \sqrt{\hat{\mathrm{J}}_{2\mathrm{i}}}} + \frac{\partial F}{\partial g_2}\frac{\partial \tilde{g}_2}{\partial \sqrt{\hat{\mathrm{J}}_{2\mathrm{i}}}}\right) \tag{4.125}$$

and the additional derivatives read

$$\frac{\partial F}{\partial g_1} = \frac{e^{g_1/(ck)}}{e^{g_1/(ck)} + e^{g_2/(ck)}}, \qquad \frac{\partial F}{\partial g_2} = \frac{e^{g_2/(ck)}}{e^{g_1/(ck)} + e^{g_2/(ck)}} \tag{4.126}$$

$$\frac{\partial \tilde{g}_1}{\partial \hat{\mathrm{I}}_{1\mathrm{i}}} = \frac{\alpha(\hat{\mathrm{I}}_{1\mathrm{i}} + 3\xi)}{\sqrt{\hat{\mathrm{J}}_{2\mathrm{i}} + \alpha(\hat{\mathrm{I}}_{1\mathrm{i}} + 3\xi)^2}}, \qquad \frac{\partial \tilde{g}_2}{\partial \hat{\mathrm{I}}_{1\mathrm{i}}} = \mathrm{A}_2\mathrm{A}_3 e^{\mathrm{A}_3\hat{\mathrm{I}}_{1\mathrm{i}}} \tag{4.127}$$

$$\frac{\partial \tilde{g}_1}{\partial \sqrt{\hat{\mathrm{J}}_{2\mathrm{i}}}} = \frac{\sqrt{\hat{\mathrm{J}}_{2\mathrm{i}}}}{\sqrt{\hat{\mathrm{J}}_{2\mathrm{i}} + \alpha(\hat{\mathrm{I}}_{1\mathrm{i}} + 3\xi)^2}}, \qquad \frac{\partial \tilde{g}_2}{\partial \sqrt{\hat{\mathrm{J}}_{2\mathrm{i}}}} = 1. \tag{4.128}$$

The plastic arclength is defined by

$$\dot{s} = \sqrt{\overset{\triangle}{\hat{\boldsymbol{\varepsilon}}}_{\mathrm{p}} \cdot \overset{\triangle}{\hat{\boldsymbol{\varepsilon}}}_{\mathrm{p}}} = \Lambda\sqrt{\left(\frac{\partial \tilde{F}}{\partial \hat{\mathrm{I}}_{1\mathrm{i}}}\mathbf{1} + \frac{\partial \tilde{F}}{\partial \hat{\mathrm{J}}_{2\mathrm{i}}}\hat{\mathbf{S}}^{\mathrm{D}}\right) \cdot \left(\frac{\partial \tilde{F}}{\partial \hat{\mathrm{I}}_{1\mathrm{i}}}\mathbf{1} + \frac{\partial \tilde{F}}{\partial \hat{\mathrm{J}}_{2\mathrm{i}}}\hat{\mathbf{S}}^{\mathrm{D}}\right)} \tag{4.129}$$

$$= \Lambda\sqrt{3\left(\frac{\partial \tilde{F}}{\partial \hat{\mathrm{I}}_{1\mathrm{i}}}\right)^2 + 2\hat{\mathrm{J}}_{2\mathrm{i}}\left(\frac{\partial \tilde{F}}{\partial \hat{\mathrm{J}}_{2\mathrm{i}}}\right)^2} = \Lambda\chi \tag{4.130}$$

with

$$\chi = \tilde{\chi}(\hat{\mathrm{I}}_{1\mathrm{i}}, \hat{\mathrm{J}}_{2\mathrm{i}}, \xi, k, \mathrm{I}_{\mathrm{t}}) := \sqrt{3\left(\frac{\partial \tilde{F}}{\partial \hat{\mathrm{I}}_{1\mathrm{i}}}\right)^2 + 2\hat{\mathrm{J}}_{2\mathrm{i}}\left(\frac{\partial \tilde{F}}{\partial \hat{\mathrm{J}}_{2\mathrm{i}}}\right)^2}. \tag{4.131}$$

Creep Flow-Rule

The creep flow-rule will be defined in the creep intermediate configuration $\check{\boldsymbol{\chi}}_t$. Due to negligible elastic strains, the Mandel stress tensor can be simplified. Therefore, the stress power can be easily transformed to the intermediate creep configuration

$$\breve{\mathbf{P}} \approx \breve{\mathbf{S}} \quad \Rightarrow \quad \breve{\mathbf{S}} \cdot \overset{\triangle}{\breve{\gamma}}_{\mathrm{c}} = \hat{\mathbf{S}} \cdot \overset{\triangle}{\hat{\boldsymbol{\varepsilon}}}_{\mathrm{c}} = \check{\mathbf{S}} \cdot \overset{\triangle}{\check{\boldsymbol{\Gamma}}}_{\mathrm{c}} \tag{4.132}$$

The creep inequality equation reads

$$\mathcal{D}_c = \check{\mathbf{S}} \cdot \overset{\triangle}{\check{\boldsymbol{\Gamma}}}_{\mathrm{c}} \geq 0 \tag{4.133}$$

The creep strain rate tensor as well as the stress tensor can be decomposed into a volumetric and a deviatoric part

$$\check{\mathbf{S}} = \frac{1}{3}(\operatorname{tr}\check{\mathbf{S}})\mathbf{1} + \check{\mathbf{S}}^{\mathrm{D}}, \qquad \overset{\vartriangle}{\check{\mathbf{\Gamma}}}_{\mathrm{c}} = g_{\mathrm{v}}\frac{1}{3}(\operatorname{tr}\check{\mathbf{S}})\mathbf{1} + g_{\mathrm{d}}\check{\mathbf{S}}^{\mathrm{D}}. \tag{4.134}$$

The scalar functions g_{v} and g_{d} define the creep evolution. Inserting the decomposition into the creep inequality leads to

$$\mathcal{D}_c = \check{\mathbf{S}} \cdot \overset{\vartriangle}{\check{\mathbf{\Gamma}}}_{\mathrm{c}} = g_{\mathrm{v}}\frac{1}{3}(\operatorname{tr}\check{\mathbf{S}})^2 + g_{\mathrm{d}}\check{\mathbf{S}}^{\mathrm{D}} \cdot \check{\mathbf{S}}^{\mathrm{D}} \geq 0. \tag{4.135}$$

The inequality can be fulfilled by assuming $g_{\mathrm{v}} \geq 0$ and $g_{\mathrm{d}} \geq 0$. In metals, the creep mechanisms are connected to the second invariant of the stress deviator, see [Naumenko et al., 2009] and [Naumenko, 2006]. The experiments in Sect. 2.5.4 show that consolidation creep is present. The relative density increases at a constant temperature and axial force, which is connected to a decrease of the volume. Accordingly, the function g_{d} is set to zero to assure that it is not assumed to be dependent on the deviatoric stress state. As the creep process is a volumetric phenomenon, a similar approach as in the work of Hofer and Kamlah [2005], Gan and Kamlah [2007] and Gan [2008] is followed. In these works, a Drucker-Prager cap model is used for the description of pebble beds in fusion blankets. Here, the creep depends on the hydrostatic pressure p.

To fulfill the inequality requirement, the function g_{v} has to be greater or equal to zero. The creep behavior is mainly influenced by the temperature, whereas the applied stress plays a minor role according to the experiments, see Sect. 2.5.4. For this reason, the following creep flow-rule is proposed

$$\overset{\vartriangle}{\check{\mathbf{\Gamma}}}_{\mathrm{c}} = g_{\mathrm{v}}\frac{1}{3}\left\langle \operatorname{tr}\check{\mathbf{S}} \right\rangle_* \mathbf{1} = \frac{1}{3}g_{\mathrm{v}}\left\langle \check{\mathrm{I}}_{1\mathrm{c}} \right\rangle_* \mathbf{1}, \qquad \check{\mathrm{I}}_{1\mathrm{c}} := \operatorname{tr}\check{\mathbf{S}}, \tag{4.136}$$

where the brackets $\langle\cdot\rangle_*$ ensure that the creep deformation vanishes in the case of tensile loading. The function is defined as

$$\langle x\rangle_* = \begin{cases} 0, & x \geq 0 \\ -1, & x < 0 \end{cases} \tag{4.137}$$

Hydrostatic Kinematic Hardening

The hydrostatic kinematic hardening is described by the internal variable ξ_{M}, i.e. the ellipse center can evolve, see Eq. (4.12) and Eq. (4.25). The dissipation inequality in the case of kinematic hardening reads

$$\mathcal{D}_K = (\hat{\mathbf{S}} - \xi_{\mathrm{M}}\mathbf{1}) \cdot \overset{\vartriangle}{\hat{\boldsymbol{\varepsilon}}}_{\mathrm{i}} + \xi_{\mathrm{M}}\mathbf{1} \cdot \overset{\vartriangle}{\hat{\boldsymbol{\varepsilon}}}_{\mathrm{i}} - \rho_0\frac{\partial\psi_{\mathrm{k}}}{\partial r_{\mathrm{v}}}\dot{r}_{\mathrm{v}} \geq 0. \tag{4.138}$$

For the free energy ψ_{k}, the following ansatz is chosen

$$\rho_0 \psi_{\mathrm{k}}\big(r_{\mathrm{v}}\big) = \frac{a_\xi}{b_\xi} e^{-b_\xi r_{\mathrm{v}}} - \frac{c_\xi}{2} r_{\mathrm{v}}^2 + \ln(e^{r_{\mathrm{v}}} - \rho_{\mathrm{rel}}) \tag{4.139}$$

Here, a_ξ, b_ξ and c_ξ denote non-negative material parameters and $\rho_{0,\mathrm{rel}}$ is the initial relative density. The kinematic hardening variable ξ_{M} is defined by

$$\xi_{\mathrm{M}} := \rho_0 \frac{\partial \psi_{\mathrm{k}}}{\partial r_{\mathrm{v}}} = a_\xi e^{-b_\xi r_{\mathrm{v}}} - c_\xi r_{\mathrm{v}} + \frac{1}{1 - \underbrace{\rho_{0,\mathrm{rel}} e^{-r_{\mathrm{v}}}}_{\rho_{\mathrm{rel}}}} \tag{4.140}$$

Using relation Eq. (4.117), the last term can be simplified to

$$\xi_{\mathrm{M}} = a_\xi e^{-b_\xi r_{\mathrm{v}}} - c_\xi r_{\mathrm{v}} + \frac{1}{1 - \frac{\rho_{0,\mathrm{rel}}}{\det \mathbf{F}_{\mathrm{i}}}} \tag{4.141}$$

The hardening variable ξ_{M} describes the evolution of the ellipse center point on the hydrostatic axis I_1. With positive material parameters, the value of ξ_{M} will be always positive. The last term in the evolution equation can be seen as a limiting term. If the determinant of $\mathbf{F}_{\mathrm{i}}$ reaches the initial density $\rho_{0,\mathrm{rel}}$, ξ_{M} will tend to infinity and the ellipse center will tend to minus infinity. Inserting ξ_{M} into the dissipation inequality yields

$$\mathcal{D}_K = (\hat{\mathbf{S}} - \xi_{\mathrm{M}} \mathbf{1}) \cdot \overset{\triangle}{\hat{\boldsymbol{\varepsilon}}}_{\mathrm{i}} + \xi_{\mathrm{M}} \mathbf{1} \cdot \overset{\triangle}{\hat{\boldsymbol{\varepsilon}}}_{\mathrm{i}} - \xi_{\mathrm{M}} \dot{r}_{\mathrm{v}} \geq 0. \tag{4.142}$$

Rearranging and decomposing the flow rules Eq. (4.120) yields

$$\mathcal{D}_K = \Big(\hat{\mathbf{S}} - \xi_{\mathrm{M}} \mathbf{1}\Big) \cdot \overset{\triangle}{\hat{\boldsymbol{\varepsilon}}}_{\mathrm{p}} + \Big(\hat{\mathbf{S}} - \xi_{\mathrm{M}} \mathbf{1}\Big) \cdot \overset{\triangle}{\hat{\boldsymbol{\varepsilon}}}_{\mathrm{c}} + \xi_{\mathrm{M}} \Big(\operatorname{tr} \overset{\triangle}{\hat{\boldsymbol{\varepsilon}}}_{\mathrm{i}} - \dot{r}_{\mathrm{v}}\Big) \geq 0. \tag{4.143}$$

The first part is connected to the convexity of the yield function. According to [Luenberger and Ye, 2008], a yield function is convex if

$$f(\mathbf{y}) \geq f(\mathbf{x}) + \left\{\frac{\partial f(\mathbf{x})}{\partial \mathbf{x}}\right\} \{\mathbf{y} - \mathbf{x}\} \tag{4.144}$$

holds. The stress state is defined by $\mathbf{x} \hat{=} \hat{\mathbf{S}}$, and in the case of elastoplasticity, $F(\hat{\mathbf{S}}) = 0$ holds. The hydrostatic kinematic hardening represents $\mathbf{y} \hat{=} \xi_{\mathrm{M}} \mathbf{1}$. Thus, the invariants for $\mathbf{y}$ are given by $\hat{\mathrm{I}}_{1\mathrm{i}} = 3\xi_{\mathrm{M}}$ and $\hat{\mathrm{J}}_{2\mathrm{i}} = 0$. The yield function reads $F = \tilde{F}(\hat{\mathrm{I}}_{1\mathrm{i}}, \hat{\mathrm{J}}_{2\mathrm{i}}, k_{\mathrm{M}}, \xi_{\mathrm{M}}, \mathrm{I}_{\mathrm{t}}, \Theta)$. Inserting these quantities into Eq. (4.144) leads to

$$\tilde{F}(3\xi_{\mathrm{M}}, 0, k_{\mathrm{M}}, \xi_{\mathrm{M}}, \mathrm{I}_{\mathrm{t}}, \Theta) \geq \frac{\partial \tilde{F}}{\partial \hat{\mathbf{S}}} \cdot \Big(\xi_{\mathrm{M}} \mathbf{1} - \hat{\mathbf{S}}\Big) \tag{4.145}$$

In the case of elastoplasticity, $\tilde{F}(3\xi_{\mathrm{M}}, 0, k_{\mathrm{M}}, \xi_{\mathrm{M}}, \mathrm{I}_{\mathrm{t}}, \Theta) \leq 0$ is valid – and one obtains

$$\frac{\partial \tilde{F}}{\partial \hat{\mathbf{S}}} \cdot \left(\hat{\mathbf{S}} - \xi_{\mathrm{M}} \mathbf{1}\right) = \left(\frac{\partial \tilde{F}}{\partial \hat{\mathrm{I}}_{1\mathrm{i}}} \mathbf{1} + \frac{\partial \tilde{F}}{\partial \hat{\mathrm{J}}_{2\mathrm{i}}} \hat{\mathbf{S}}^{\mathrm{D}}\right) \cdot \left(\hat{\mathbf{S}} - \xi_{\mathrm{M}} \mathbf{1}\right) \tag{4.146}$$

$$= \left(\hat{\mathrm{I}}_{1\mathrm{i}} - 3\xi_{\mathrm{M}}\right) \frac{\partial \tilde{F}}{\partial \hat{\mathrm{I}}_{1\mathrm{i}}} + 2\hat{\mathrm{J}}_{2\mathrm{i}} \frac{\partial \tilde{F}}{\partial \hat{\mathrm{J}}_{2\mathrm{i}}} \geq 0. \tag{4.147}$$

Consequently, the first part of the inequality is fulfilled. The second term can be expressed by the relation

$$\operatorname{tr} \overset{\triangle}{\hat{\boldsymbol{\varepsilon}}}_{\mathrm{c}} = \operatorname{tr}(\check{\mathbf{F}}_{\mathrm{p}}^{-\mathrm{T}} \overset{\triangle}{\check{\mathbf{\Gamma}}}_{\mathrm{c}} \check{\mathbf{F}}_{\mathrm{p}}^{-1}) = \operatorname{tr}(\mathbf{C}_{\mathrm{p}}^{-1} \overset{\triangle}{\check{\mathbf{\Gamma}}}_{\mathrm{c}}) = \frac{1}{3} g_{\mathrm{v}} \check{\mathrm{I}}_{1\mathrm{c}} \operatorname{tr} \mathbf{C}_{\mathrm{p}}^{-1} \tag{4.148}$$

as

$$\left(\hat{\mathbf{S}} - \xi_{\mathrm{M}} \mathbf{1}\right) \cdot \overset{\triangle}{\hat{\boldsymbol{\varepsilon}}}_{\mathrm{c}} = \hat{\mathbf{S}} \cdot \overset{\triangle}{\hat{\boldsymbol{\varepsilon}}}_{\mathrm{c}} - \xi_{\mathrm{M}} \operatorname{tr} \overset{\triangle}{\hat{\boldsymbol{\varepsilon}}}_{\mathrm{c}} = \check{\mathbf{S}} \cdot \overset{\triangle}{\check{\mathbf{\Gamma}}}_{\mathrm{c}} - \xi_{\mathrm{M}} \frac{1}{3} g_{\mathrm{v}} \check{\mathrm{I}}_{1\mathrm{c}} \operatorname{tr} \mathbf{C}_{\mathrm{p}}^{-1} \geq 0. \tag{4.149}$$

The stress power is larger or equal zero according to Eq. (4.135) and the definition of g_{v}, which is always positive, see Eq. (4.196). In the second part, the hydrostatic kinematic hardening variable ξ_{M} is always positive, Eq. (4.141). The first invariant $\check{\mathrm{I}}_{1\mathrm{c}}$ is negative. If the trace is positive, the whole term will be zero due to the Macaulay brackets in g_{v}, see Eq. (4.196). The plastic Cauchy Green tensor is positive definite. Therefore, its inverse is positive definite – and the trace is positive too. As a result, the inequality is fulfilled.

The last term in Eq. (4.143) is fulfilled with the definition Eq. (4.82) and Eq. (4.84).

Isotropic Hardening

The isotropic hardening describes the evolution of the yield stress in J_2-direction and will be connected to the height of the ellipse function k, see Eq. (4.12) and Eq. (4.24). The inequality reads

$$\mathcal{D}_I = \hat{\mathbf{S}} \cdot \overset{\triangle}{\hat{\boldsymbol{\varepsilon}}}_{\mathrm{i}} - \rho_0 \frac{\partial \psi_{\mathrm{i}}}{\partial r_{\mathrm{i}}} \dot{r}_{\mathrm{i}} \geq 0. \tag{4.150}$$

For the isotropic hardening, a quadratic approach is chosen

$$\rho_0 \psi_{\mathrm{i}}(r_{\mathrm{i}}) = \frac{1}{2} \gamma_k r_{\mathrm{i}}^2. \tag{4.151}$$

The yield stress k_{M} is defined by

$$k_{\mathrm{M}} := \rho_0 \frac{\partial \psi_{\mathrm{i}}}{\partial r_{\mathrm{i}}}. \tag{4.152}$$

By computing the time-derivative of the internal variable $\dot{r}_{\mathrm{i}}$, one obtains

$$\dot{r}_{\mathrm{i}} = \frac{\dot{k}_{\mathrm{M}}}{\gamma_k}. \tag{4.153}$$

Inserting the yield stress k_{M} and $\dot{r}_{\mathrm{i}}$ into the inequality (4.150) yields

$$\mathcal{D}_I = \hat{\mathbf{S}} \cdot \overset{\triangle}{\hat{\boldsymbol{\varepsilon}}}_{\mathrm{i}} - \frac{k_{\mathrm{M}} \dot{k}_{\mathrm{M}}}{\gamma_k} \geq 0. \tag{4.154}$$

Decomposing the inelastic flow yields

$$\mathcal{D}_I = k_{\mathrm{M}} \left(\frac{1}{k_{\mathrm{M}}} \hat{\mathbf{S}} \cdot \left(\overset{\triangle}{\hat{\boldsymbol{\varepsilon}}}_{\mathrm{p}} + \overset{\triangle}{\hat{\boldsymbol{\varepsilon}}}_{\mathrm{c}} \right) - \frac{\dot{k}_{\mathrm{M}}}{\gamma_k} \right) \geq 0. \tag{4.155}$$

The creep flow-rule (4.136) can be transferred into the plastic intermediate configuration by

$$\overset{\triangle}{\hat{\boldsymbol{\varepsilon}}}_{\mathrm{c}} = \check{\mathbf{F}}_{\mathrm{p}}^{-\mathrm{T}} \overset{\triangle}{\check{\boldsymbol{\Gamma}}}_{\mathrm{c}} \check{\mathbf{F}}_{\mathrm{p}}^{-1} = \frac{1}{3} g_{\mathrm{v}} \left\langle \check{\mathrm{I}}_{1\mathrm{c}} \right\rangle_{*} \check{\mathbf{F}}_{\mathrm{p}}^{-\mathrm{T}} \check{\mathbf{F}}_{\mathrm{p}}^{-1} \tag{4.156}$$

Inserting the flow-rules and using the property $\Lambda = \dot{s}/\chi$ leads to

$$\mathcal{D}_I = k_{\mathrm{M}} \left(\frac{\dot{s}}{k_{\mathrm{M}} \chi} \hat{\mathbf{S}} \cdot \frac{\partial F}{\partial \hat{\mathbf{S}}} + \frac{1}{k_{\mathrm{M}}} \hat{\mathbf{S}} \cdot \left(\frac{1}{3} g_{\mathrm{v}} \left\langle \check{\mathrm{I}}_{1\mathrm{c}} \right\rangle_{*} \check{\mathbf{F}}_{\mathrm{p}}^{-\mathrm{T}} \check{\mathbf{F}}_{\mathrm{p}}^{-1} \right) - \frac{\dot{k}_{\mathrm{M}}}{\gamma_k} \right) \geq 0. \tag{4.157}$$

With the relation

$$\frac{1}{3} g_{\mathrm{v}} \left\langle \check{\mathrm{I}}_{1\mathrm{c}} \right\rangle_{*} \hat{\mathbf{S}} \cdot (\check{\mathbf{F}}_{\mathrm{p}}^{-\mathrm{T}} \check{\mathbf{F}}_{\mathrm{p}}^{-1}) = \frac{1}{3} g_{\mathrm{v}} \left\langle \check{\mathrm{I}}_{1\mathrm{c}} \right\rangle_{*} (\check{\mathbf{F}}_{\mathrm{p}}^{-1} \hat{\mathbf{S}} \check{\mathbf{F}}_{\mathrm{p}}^{-\mathrm{T}}) \cdot \mathbf{1} = \frac{1}{3} g_{\mathrm{v}} \left\langle \check{\mathrm{I}}_{1\mathrm{c}} \right\rangle_{*} \operatorname{tr} \check{\mathbf{S}} \tag{4.158}$$

$$= \frac{1}{3} g_{\mathrm{v}} \left\langle \check{\mathrm{I}}_{1\mathrm{c}} \right\rangle_{*} \check{\mathrm{I}}_{1\mathrm{c}} \tag{4.159}$$

the inequality can be reduced to

$$\mathcal{D}_I = k_{\mathrm{M}} \left(\frac{\dot{s}}{k_{\mathrm{M}} \chi} \hat{\mathbf{S}} \cdot \frac{\partial F}{\partial \hat{\mathbf{S}}} + \frac{1}{3 k_{\mathrm{M}}} g_{\mathrm{v}} \left\langle \check{\mathrm{I}}_{1\mathrm{c}} \right\rangle_{*} \check{\mathrm{I}}_{1\mathrm{c}} - \frac{\dot{k}_{\mathrm{M}}}{\gamma_k} \right) \geq 0. \tag{4.160}$$

This expression can be fulfilled if the bracket term is proportional to k_{M} with the proportional factor β_k

$$\frac{\dot{s}}{k_{\mathrm{M}} \chi} \hat{\mathbf{S}} \cdot \frac{\partial F}{\partial \hat{\mathbf{S}}} + \frac{1}{3 k_{\mathrm{M}}} g_{\mathrm{v}} \left\langle \check{\mathrm{I}}_{1\mathrm{c}} \right\rangle_{*} \check{\mathrm{I}}_{1\mathrm{c}} - \frac{\dot{k}_{\mathrm{M}}}{\gamma_k} = k_{\mathrm{M}} \frac{\beta_k}{\gamma_k} \dot{s}. \tag{4.161}$$

The part connected to the creep on the left side will always be greater or equal to zero because $g_{\mathrm{v}} \geq 0$ holds by its definition Eq. (4.196) and $\left\langle \check{\mathrm{I}}_{1\mathrm{c}} \right\rangle_{*} \check{\mathrm{I}}_{1\mathrm{c}}$ is positive or equal to zero. The evolution equation is now given by

$$\dot{k}_{\mathrm{M}} = \frac{\gamma_k \dot{s}}{k_{\mathrm{M}} \chi} \hat{\mathbf{S}} \cdot \frac{\partial F}{\partial \hat{\mathbf{S}}} + \frac{\gamma_k}{3 k_{\mathrm{M}}} g_{\mathrm{v}} \left\langle \check{\mathrm{I}}_{1\mathrm{c}} \right\rangle_{*} \check{\mathrm{I}}_{1\mathrm{c}} - \dot{s} \beta_k k_{\mathrm{M}} \tag{4.162}$$

with the material parameters γ_k and β_k.

Hydrostatic Tensile Stress Hardening

During the sintering process, the powder material transforms into a solid material. Due to this reason, the yield stress in tensile direction grows, which is proven by the tensile experiments in Fig. 2.45a. The inequality reads

$$\mathcal{D}_\mathrm{t} = \hat{\mathbf{S}} \cdot \overset{\triangle}{\hat{\boldsymbol{\varepsilon}}}_\mathrm{i} - \rho_0 \frac{\partial \psi_\mathrm{t}}{\partial J_\mathrm{i}} \dot{J}_\mathrm{i} \geq 0. \tag{4.163}$$

The hydrostatic yield stress in tensile direction I_t is defined by

$$\mathrm{I}_\mathrm{t} := \rho_0 \frac{\partial \psi_\mathrm{t}}{\partial J_\mathrm{i}}. \tag{4.164}$$

This value defines the intersection of the yield function with the I_1-axis, see Eq. (4.11). For the strain energy function, the following approach is considered

$$\rho_0 \psi_\mathrm{t}(J_\mathrm{i}) = -\beta_\mathrm{t}(\Theta) \frac{\rho_\mathrm{rel}}{b_\mathrm{t}} e^{b_\mathrm{t} \rho_{0,\mathrm{rel}}/J_\mathrm{i}} + \mathrm{I}_0 J_\mathrm{i} \tag{4.165}$$

with an exponential dependence on J_i and a linear part. The hydrostatic tensile stress hardening can be derived by

$$\mathrm{I}_\mathrm{t} = \beta_\mathrm{t}(\Theta) \frac{\rho_{0,\mathrm{rel}}^2}{J_\mathrm{i}^2} e^{b_\mathrm{t} \rho_{0,\mathrm{rel}}/J_\mathrm{i}} + \mathrm{I}_0 \tag{4.166}$$

In the evolution equation, $\beta_\mathrm{t}(\Theta)$ is a temperature dependent material function and b_t is a constant material parameter. For β_t, the following ordinary differential equation (ODE) is proposed

$$\dot{\beta}_\mathrm{t} = c_\beta (1 - \beta_\mathrm{t}) \langle \Theta - \Theta_S \rangle \quad \Leftrightarrow \quad \dot{\beta}_\mathrm{t}(t) + c_\beta \langle \Theta - \Theta_S \rangle \beta_\mathrm{t}(t) = c_\beta \langle \Theta - \Theta_S \rangle. \tag{4.167}$$

Here, Θ_S is the sintering temperature below which there is no increase in the tensile yield stress. Equation Eq. (4.167) is a first-order ODE and its solution is given by

$$\beta_\mathrm{t}(t, \Theta) = 1 - \exp\left(-c_\beta \langle \Theta - \Theta_S \rangle t\right). \tag{4.168}$$

The parameter c_β defines the slope of the curve. At its limit, β_t reaches one. The determinant of the inelastic deformation gradient reads

$$J_\mathrm{i} = \det \mathbf{F}_\mathrm{i} = (\det \mathbf{C}_\mathrm{i})^{1/2}. \tag{4.169}$$

The material time derivative can be computed by

$$\dot{J}_\mathrm{i} = \frac{1}{2} \frac{1}{(\det \mathbf{C}_\mathrm{i})^{1/2}} (\det \mathbf{C}_\mathrm{i}) \mathbf{C}_\mathrm{i}^{-1} \cdot \dot{\mathbf{C}}_\mathrm{i} = \frac{1}{2} (\det \mathbf{C}_\mathrm{i})^{1/2} \mathbf{C}_\mathrm{i}^{-1} \cdot \dot{\mathbf{C}}_\mathrm{i} \tag{4.170}$$

This expression can be transferred to the inelastic intermediate configuration, see Eq. (4.83), and the results are given by

$$\dot{J}_\mathrm{i} = \frac{1}{2} J_\mathrm{i} \, \mathrm{tr} \, \overset{\vartriangle}{\hat{\boldsymbol{\varepsilon}}}_\mathrm{i} \tag{4.171}$$

By inserting this result into the inequality (4.163) – and with the help of the flow-rule decomposition Eq. (4.120) and Eq. (4.121) – one obtains

$$\begin{aligned} \mathcal{D}_\mathrm{t} &= \hat{\mathbf{S}} \cdot \overset{\vartriangle}{\hat{\boldsymbol{\varepsilon}}}_\mathrm{i} - \mathrm{I}_\mathrm{t} \dot{J}_\mathrm{i} = \hat{\mathbf{S}} \cdot \overset{\vartriangle}{\hat{\boldsymbol{\varepsilon}}}_\mathrm{i} - \frac{1}{2} \mathrm{I}_\mathrm{t} J_\mathrm{i} \overset{\vartriangle}{\hat{\boldsymbol{\varepsilon}}}_\mathrm{i} \cdot \mathbf{1} && (4.172) \\ &= \left(\hat{\mathbf{S}} - \frac{1}{2} \mathrm{I}_\mathrm{t} J_\mathrm{i} \mathbf{1} \right) \cdot \overset{\vartriangle}{\hat{\boldsymbol{\varepsilon}}}_\mathrm{p} + \left(\hat{\mathbf{S}} - \frac{1}{2} \mathrm{I}_\mathrm{t} J_\mathrm{i} \mathbf{1} \right) \cdot \overset{\vartriangle}{\hat{\boldsymbol{\varepsilon}}}_\mathrm{c} \geq 0. && (4.173) \end{aligned}$$

The first summand of this inequality can be proved with the help of Eq. (4.144). With the stress state $\mathbf{x} \widehat{=} \hat{\mathbf{S}}$, the yield condition $F(\hat{\mathbf{S}}) = 0$ and $\mathbf{y} \widehat{=} (1/2) \mathrm{I}_\mathrm{t} J_\mathrm{i} \mathbf{1}$ condition (4.144) reads

$$\tilde{F}(\mathrm{I}_1, 0, k_\mathrm{M}, \xi_\mathrm{M}, \mathrm{I}_\mathrm{t}, \Theta) \geq \frac{\partial \tilde{F}}{\partial \hat{\mathbf{S}}} \cdot \left(\frac{1}{2} \mathrm{I}_\mathrm{t} J_\mathrm{i} \mathbf{1} - \hat{\mathbf{S}} \right) \tag{4.174}$$

In elastoplasticity, the yield function is always smaller or equal to zero, $\tilde{F} \leq 0$. As a result, one obtains

$$\frac{\partial \tilde{F}}{\partial \hat{\mathbf{S}}} \cdot \left(\hat{\mathbf{S}} - \frac{1}{2} \mathrm{I}_\mathrm{t} J_\mathrm{i} \mathbf{1} \right) = \left(\hat{\mathrm{I}}_{1\mathrm{i}} - \frac{3}{2} \mathrm{I}_\mathrm{t} J_\mathrm{i} \right) \frac{\partial \tilde{F}}{\partial \hat{\mathrm{I}}_{1\mathrm{i}}} + 2 \hat{\mathrm{J}}_{2\mathrm{i}} \frac{\partial \tilde{F}}{\partial \hat{\mathrm{J}}_{2\mathrm{i}}} \geq 0. \tag{4.175}$$

Hence, this part of the inequality is fulfilled. The second term can be written with the help of Eq. (4.148) and Eq. (4.136) as

$$\left(\hat{\mathbf{S}} - \frac{1}{2} \mathrm{I}_\mathrm{t} J_\mathrm{i} \mathbf{1} \right) \cdot \overset{\vartriangle}{\hat{\boldsymbol{\varepsilon}}}_\mathrm{c} = \check{\mathbf{S}} \cdot \overset{\vartriangle}{\check{\boldsymbol{\Gamma}}}_\mathrm{c} - \frac{1}{6} \mathrm{I}_\mathrm{t} J_\mathrm{i} g_\mathrm{v} \left\langle \check{\mathrm{I}}_{1\mathrm{c}} \right\rangle_* \mathrm{tr} \, \mathbf{C}_\mathrm{p}^{-1} \geq 0 \tag{4.176}$$

The stress power is positive or zero due to the flow rule, see Eq. (4.135) and Eq. (4.136). The determinant J_i is always larger than zero. The hydrostatic tensile hardening variable I_t is positive by its definition, see Eq. (4.166). The part $g_\mathrm{v} \left\langle \check{\mathrm{I}}_{1\mathrm{c}} \right\rangle_*$ is negative or zero due to the brackets, see Eq. (4.137). Due to the positive definiteness of the tensor $\mathbf{C}_\mathrm{p}$, the trace of its inverse is positive. Therefore, the inequality is satisfied.

4.6.4 Elasticity Relation

For the evaluation of the potential relation for the stress tensor, Eq. (4.94), the definition of the elastic strain energy is required. It is defined by

$$\rho_0 \psi_\mathrm{e}(\overline{\check{\mathbf{C}}}_\mathrm{e}) = U(J_\mathrm{e}) + v(\mathrm{I}_{\bar{\mathrm{e}}}) \tag{4.177}$$

with the volumetric and isochoric parts

$$U(J_\mathrm{e}) = \frac{K}{50}\left(J_\mathrm{e}^5 + J_\mathrm{e}^{-5} - 2\right), \quad \text{and} \quad v(\mathrm{I}_{\bar{\mathrm{e}}}) = \frac{G}{2}\left(\mathrm{I}_{\bar{\mathrm{e}}} - 3\right), \tag{4.178}$$

where K is the bulk modulus and G the shear modulus. $\mathrm{I}_{\bar{\mathrm{e}}}$ is the first invariant of the unimodular elastic right Cauchy-Green tensor $\overline{\breve{\mathbf{C}}}_\mathrm{e}$

$$\mathrm{I}_{\bar{\mathrm{e}}} := \operatorname{tr} \overline{\breve{\mathbf{C}}}_\mathrm{e}, \qquad \overline{\breve{\mathbf{C}}}_\mathrm{e} := \left(\det \breve{\mathbf{C}}_\mathrm{e}\right)^{-1/3} \breve{\mathbf{C}}_\mathrm{e}. \tag{4.179}$$

For the isochoric part $v(\mathrm{I}_{\bar{\mathrm{e}}})$ of the elastic free energy, a Neo-Hookean type is chosen. For the dilatory part $U(J_\mathrm{e})$, the relation proposed by Hartmann and Neff [2003] is used, which depends on the elastic deformation gradient $J_\mathrm{e} := \det \breve{\mathbf{F}}_\mathrm{e}$. The stresses on the thermal intermediate configuration can be computed by

$$\breve{\mathbf{S}} = 2\rho_0 \frac{\partial \psi_\mathrm{e}}{\partial \breve{\mathbf{C}}_\mathrm{e}} = J_\mathrm{e} U'(J_\mathrm{e}) \breve{\mathbf{C}}_\mathrm{e}^{-1} + J_\mathrm{e}^{-2/3} G \left(\mathbf{1} - \tfrac{1}{3}\left(\operatorname{tr} \breve{\mathbf{C}}_\mathrm{e}\right) \breve{\mathbf{C}}_\mathrm{e}^{-1}\right) \tag{4.180}$$

$$= \frac{K}{10}\left(J_\mathrm{e}^5 - J_\mathrm{e}^{-5}\right) \breve{\mathbf{C}}_\mathrm{e}^{-1} + J_\mathrm{e}^{-2/3} G \left(\breve{\mathbf{C}}_\mathrm{e}^\mathrm{D} \breve{\mathbf{C}}_\mathrm{e}^{-1}\right), \tag{4.181}$$

where $\breve{\mathbf{C}}_\mathrm{e}^\mathrm{D} := \breve{\mathbf{C}}_\mathrm{e} - 1/3(\operatorname{tr} \breve{\mathbf{C}}_\mathrm{e})\mathbf{1}$ is the deviator of the elastic right Cauchy-Green tensor. The Mandel stress tensor in the intermediate configuration reads

$$\mathbf{P} = \hat{\mathbf{C}}_{\mathrm{e}\Theta} \hat{\mathbf{S}} = \breve{\mathbf{C}}_\mathrm{e} \breve{\mathbf{S}} = \frac{K}{10}\left(J_\mathrm{e}^5 - J_\mathrm{e}^{-5}\right) \mathbf{1} + G J_\mathrm{e}^{-2/3} \left(\breve{\mathbf{C}}_\mathrm{e} - \tfrac{1}{3}\left(\operatorname{tr} \breve{\mathbf{C}}_\mathrm{e}\right) \mathbf{1}\right). \tag{4.182}$$

Due to the assumption of small elastic strains, the stress tensor is linearized at $\breve{\mathbf{C}}_\mathrm{e} = \mathbf{1}$, leading to

$$\breve{\mathbf{S}} = \frac{K}{2}\left(\operatorname{tr} \breve{\mathbf{C}}_\mathrm{e} - 3\right) \mathbf{1} + G \breve{\mathbf{C}}_\mathrm{e}^\mathrm{D}. \tag{4.183}$$

The back-transformation to the inelastic configuration results in

$$\hat{\mathbf{S}} = \hat{\mathbf{F}}_\Theta^{-1} \breve{\mathbf{S}} \hat{\mathbf{F}}_\Theta^{-\mathrm{T}} = \frac{K}{2\phi^2}\left(\operatorname{tr} \breve{\mathbf{C}}_\mathrm{e} - 3\right) \mathbf{1} + \frac{G}{\phi^2} \breve{\mathbf{C}}_\mathrm{e}^\mathrm{D}, \tag{4.184}$$

with K as the bulk and G as the shear modulus. ϕ originates from the linear thermal expansion, see Eq. (4.66).

4.6.5 Transformation into Reference Configuration

In general, the material can be evaluated and integrated in any configuration. The time integration and the numerical computation of the constitutive model should maintain the material frame-indifference, see [Simo and Hughes, 2000, p. 276]. The reference configuration has the advantage that it is fixed. For this reason, all constitutive equations are transformed into the reference configuration in which the time integration is performed.

Elasticity Relation

The elasticity relation Eq. (4.183) can be expressed by the relations

$$\operatorname{tr}\breve{\mathbf{C}}_{\mathrm{e}} = \operatorname{tr}(\mathbf{F}_{\Theta\mathrm{pc}}^{-\mathrm{T}}\mathbf{C}\mathbf{F}_{\Theta\mathrm{pc}}^{-1}) = \frac{1}{\phi^2}\operatorname{tr}(\mathbf{C}_{\mathrm{i}}^{-1}\mathbf{C}) \tag{4.185}$$

$$\mathbf{F}_{\Theta\mathrm{pc}}^{-1}\breve{\mathbf{C}}_{\mathrm{e}}\mathbf{F}_{\Theta\mathrm{pc}}^{-\mathrm{T}} = \frac{1}{\phi^4}\mathbf{F}_{\mathrm{pc}}^{-1}\mathbf{F}_{\mathrm{pc}}^{-\mathrm{T}}\mathbf{F}^{\mathrm{T}}\mathbf{F}\mathbf{F}_{\mathrm{pc}}^{-1}\mathbf{F}_{\mathrm{pc}}^{-\mathrm{T}} = \frac{1}{\phi^4}\mathbf{C}_{\mathrm{i}}^{-1}\mathbf{C}\mathbf{C}_{\mathrm{i}}^{-1} \tag{4.186}$$

in the reference configuration. Consequently, the second Piola-Kirchhoff stress tensor reads

$$\tilde{\mathbf{T}} = \frac{K}{2\phi^2}\left(\frac{\operatorname{tr}(\mathbf{C}\mathbf{C}_{\mathrm{i}}^{-1})}{\phi^2} - 3\right)\mathbf{C}_{\mathrm{i}}^{-1} + \frac{G}{\phi^4}\left(\mathbf{C}_{\mathrm{i}}^{-1}\mathbf{C}\mathbf{C}_{\mathrm{i}}^{-1} - \tfrac{1}{3}\operatorname{tr}(\mathbf{C}\mathbf{C}_{\mathrm{i}}^{-1})\mathbf{C}_{\mathrm{i}}^{-1}\right). \tag{4.187}$$

Applying the relation $\mathbf{A}\mathbf{C}\mathbf{B}^{\mathrm{T}} = [\mathbf{A}\otimes\mathbf{B}]^{T_{23}}\,\mathbf{C}$, the stress tensor can be rewritten

$$\begin{aligned}\tilde{\mathbf{T}} = \frac{1}{\phi^2}\left(\frac{K}{2\phi^2}\operatorname{tr}(\mathbf{C}\mathbf{C}_{\mathrm{i}}^{-1}) - \frac{3K}{2} - \frac{G}{3\phi^2}\operatorname{tr}(\mathbf{C}\mathbf{C}_{\mathrm{i}}^{-1})\right)\mathbf{C}_{\mathrm{i}}^{-1}&\\ + \frac{G}{\phi^4}\left[\mathbf{C}_{\mathrm{i}}^{-1}\otimes\mathbf{C}_{\mathrm{i}}^{-1}\right]^{T_{23}}\mathbf{C}.&\end{aligned} \tag{4.188}$$

With the relation $(\mathbf{B}\cdot\mathbf{C})\mathbf{A} = (\mathbf{A}\otimes\mathbf{B})\mathbf{C}$, the elasticity is given by

$$\begin{aligned}\tilde{\mathbf{T}} = \frac{G}{\phi^4}\left(\left[\mathbf{C}_{\mathrm{i}}^{-1}\otimes\mathbf{C}_{\mathrm{i}}^{-1}\right]^{T_{23}} - \frac{1}{3}[\mathbf{C}_{\mathrm{i}}^{-1}\otimes\mathbf{C}_{\mathrm{i}}^{-1}]\right)\mathbf{C}&\\ + \frac{K}{2\phi^2}\left(\frac{1}{\phi^2}[\mathbf{C}_{\mathrm{i}}^{-1}\otimes\mathbf{C}_{\mathrm{i}}^{-1}]\mathbf{C} - 3\mathbf{C}_{\mathrm{i}}^{-1}\right).&\end{aligned} \tag{4.189}$$

Creep Flow-Rule

The creep flow-rule in the reference configuration can be derived by

$$\dot{\mathbf{C}}_{\mathrm{c}} = 2\dot{\mathbf{E}}_{\mathrm{c}} = 2\mathbf{F}_{\mathrm{c}}^{\mathrm{T}}\overset{\triangle}{\breve{\mathbf{\Gamma}}}_{\mathrm{c}}\mathbf{F}_{\mathrm{c}} = \frac{2}{3}g_{\mathrm{v}}\left\langle \breve{\mathrm{I}}_{1\mathrm{c}}\right\rangle_{*}\mathbf{C}_{\mathrm{c}}. \tag{4.190}$$

The first stress invariant expressed with quantities in the reference configuration reads

$$\breve{\mathrm{I}}_{1\mathrm{c}} = \operatorname{tr}\breve{\mathbf{S}} = \operatorname{tr}(\mathbf{F}_{\mathrm{c}}\tilde{\mathbf{T}}\mathbf{F}_{\mathrm{c}}^{\mathrm{T}}) = \operatorname{tr}(\mathbf{C}_{\mathrm{c}}\tilde{\mathbf{T}}). \tag{4.191}$$

By definition, the creep Cauchy-Green tensor $\mathbf{C}_{\mathrm{c}}$ is assumed to be an identity tensor at $t = t_0$

$$\mathbf{C}_{\mathrm{c}}(t = t_0) = \mathbf{1}. \tag{4.192}$$

As a result, the creep Cauchy-Green tensor is an identity tensor times a scalar. It can be written as

$$\mathbf{C}_{\mathrm{c}} = f_{\mathrm{c}}\mathbf{1}, \qquad \dot{\mathbf{C}}_{\mathrm{c}} = \dot{f}_{\mathrm{c}}\mathbf{1}. \tag{4.193}$$

Computing the trace of Eq. (4.190) yields

$$\operatorname{tr} \dot{\mathbf{C}}_\mathrm{c} = \frac{2}{3} g_\mathrm{v} \left\langle \check{\mathrm{I}}_{1\mathrm{c}} \right\rangle_* \operatorname{tr} \mathbf{C}_\mathrm{c}. \tag{4.194}$$

Inserting f_c and its time derivative $\dot{f}_\mathrm{c} = 1/3 \operatorname{tr} \dot{\mathbf{C}}_\mathrm{c}$ leads to

$$\dot{f}_\mathrm{c} = \frac{2}{3} g_\mathrm{v} \left\langle \check{\mathrm{I}}_{1\mathrm{c}} \right\rangle_* f_\mathrm{c}. \tag{4.195}$$

According to the experiments, the following creep equation is proposed

$$g_\mathrm{v} = A_c (\Theta - \Theta_0) \left(1 - \frac{c_\infty}{f_\mathrm{c}} \right). \tag{4.196}$$

A linear temperature dependence is assumed with the creep material parameters $A_c \geq 0$ and $c_\infty > 0$.

Replacing the first invariant by $\check{\mathrm{I}}_{1\mathrm{c}} = \operatorname{tr}(\mathbf{C}_\mathrm{c} \tilde{\mathbf{T}}) = f_\mathrm{c} \operatorname{tr} \tilde{\mathbf{T}}$ and inserting g_v into (4.195) leads to

$$\dot{f}_c = \frac{2}{3} A_c (\Theta - \Theta_0) \left(f_\mathrm{c} - c_\infty \right) \left\langle f_\mathrm{c} \operatorname{tr} \tilde{\mathbf{T}} \right\rangle_* \tag{4.197}$$

This equation can be reformulated as

$$\dot{f}_\mathrm{c} + a f_\mathrm{c} = b, \qquad a := \frac{2}{3} A_c (\Theta - \Theta_0) \left\langle f_\mathrm{c} \operatorname{tr} \tilde{\mathbf{T}} \right\rangle_*, \qquad b := a c_\infty \tag{4.198}$$

As this is an ordinary differential equation, it can be solved based on the assumption that the coefficients a and b are constant. This differential equation of first order can be solved analytically with the initial value $f_\mathrm{c}(t_0) = 1$ and the solution is given by

$$f_\mathrm{c}(t) = e^{a(t-t_0)} + \frac{b}{a} \left(1 - e^{a(t-t_0)} \right), \qquad \dot{f}_\mathrm{c}(t) = a e^{a(t-t_0)} - b e^{a(t-t_0)}. \tag{4.199}$$

The initial slope of the creep variable f_c is given by $a - b = a(1 - c_\infty)$ and can be controlled by the material parameter A_c. The coefficient a can be negative or zero due to the brackets $\langle x \rangle_*$. Due to the structure of the ODE, the function reaches a saturation value, which is given by $b/a = c_\infty$, see Fig. 4.20.

Plastic Flow-Rule

The plastic flow-rule can be transformed into the reference configuration by

$$\dot{\mathbf{E}}_\mathrm{p} = \frac{1}{2} (\dot{\mathbf{C}}_\mathrm{pc} - \dot{\mathbf{C}}_\mathrm{c}) = \frac{1}{2} (\dot{\overline{f_\mathrm{c} \mathbf{C}_\mathrm{p}}} - \dot{f}_\mathrm{c} \mathbf{1}) = \frac{1}{2} (\dot{f}_\mathrm{c} \mathbf{C}_\mathrm{p} + f_\mathrm{c} \dot{\mathbf{C}}_\mathrm{p} - \dot{f}_\mathrm{c} \mathbf{1}) \tag{4.200}$$

$$\Rightarrow \dot{\mathbf{C}}_\mathrm{p} = \frac{1}{f_\mathrm{c}} (2 \dot{\mathbf{E}}_\mathrm{p} - \dot{f}_\mathrm{c} \mathbf{C}_\mathrm{p} + \dot{f}_\mathrm{c} \mathbf{1}) = \frac{1}{f_\mathrm{c}} (2 \mathbf{F}_\mathrm{pc}^\mathrm{T} \overset{\vartriangle}{\hat{\boldsymbol{\varepsilon}}}_\mathrm{p} \mathbf{F}_\mathrm{pc} - \dot{f}_\mathrm{c} \mathbf{C}_\mathrm{p} + \dot{f}_\mathrm{c} \mathbf{1}). \tag{4.201}$$

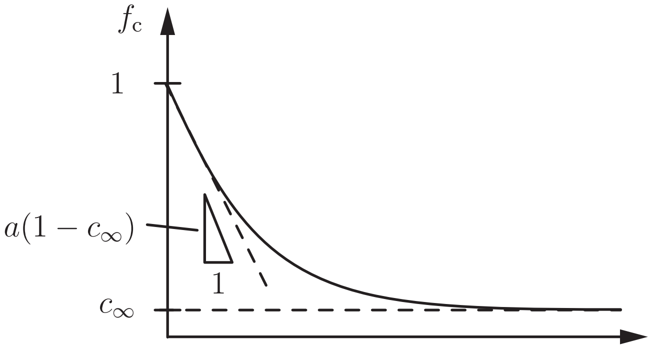

Figure 4.20: Evolution of creep variable f_c

Accordingly, the plastic flow-rule is given by

$$\dot{\mathbf{C}}_\mathrm{p} = \frac{2}{f_\mathrm{c}}\Lambda\left(\frac{\partial F}{\partial \hat{\mathrm{I}}_{1\mathrm{i}}} f_\mathrm{c}\mathbf{C}_\mathrm{p} + \frac{\partial F}{\partial \hat{\mathrm{J}}_{2\mathrm{i}}}\mathbf{F}_\mathrm{pc}^\mathrm{T}\hat{\mathbf{S}}^\mathrm{D}\mathbf{F}_\mathrm{pc}\right) + \frac{\dot{f}_\mathrm{c}}{f_\mathrm{c}}(\mathbf{1}-\mathbf{C}_\mathrm{p}). \tag{4.202}$$

The deviatoric part of the stress tensor Eq. (4.184) reads

$$\hat{\mathbf{S}}^\mathrm{D} = \frac{G}{\phi^2}\breve{\mathbf{C}}_\mathrm{e}^\mathrm{D} = \frac{G}{\phi^2}\left(\breve{\mathbf{C}}_\mathrm{e} - \tfrac{1}{3}\left(\mathrm{tr}\,\breve{\mathbf{C}}_\mathrm{e}\right)\mathbf{1}\right). \tag{4.203}$$

With the relations

$$\mathbf{F}_\mathrm{pc}^\mathrm{T}\mathbf{F}_\mathrm{pc} = \mathbf{C}_\mathrm{i} = f_\mathrm{c}\mathbf{C}_\mathrm{p}, \qquad \mathbf{F}_\mathrm{pc}^\mathrm{T}\breve{\mathbf{C}}_\mathrm{e}\mathbf{F}_\mathrm{pc} = \mathbf{F}_\mathrm{pc}^\mathrm{T}(\mathbf{F}_{\Theta\mathrm{pc}}^{-\mathrm{T}}\mathbf{C}\mathbf{F}_{\Theta\mathrm{pc}}^{-1})\mathbf{F}_\mathrm{pc} = 1/\phi^2\mathbf{C} \tag{4.204}$$

together with the expression Eq. (4.185), the deviatoric part of the stress tensor in the reference configuration is obtained

$$\mathbf{F}_\mathrm{pc}^\mathrm{T}\hat{\mathbf{S}}^\mathrm{D}\mathbf{F}_\mathrm{pc} = \frac{G}{\phi^2}\left(\frac{1}{\phi^2}\mathbf{C} - \frac{1}{3}\frac{f_\mathrm{c}}{f_\mathrm{c}\phi^2}\,\mathrm{tr}(\mathbf{C}_\mathrm{p}^{-1}\mathbf{C})\mathbf{C}_\mathrm{p}\right) = \frac{G}{\phi^4}\left(\mathbf{C} - \frac{1}{3}\,\mathrm{tr}(\mathbf{C}_\mathrm{p}^{-1}\mathbf{C})\mathbf{C}_\mathrm{p}\right). \tag{4.205}$$

Inserting this equation into the evolution equation for the plastic strains yields

$$\dot{\mathbf{C}}_\mathrm{p} = \frac{2}{f_\mathrm{c}}\Lambda\left(\frac{\partial F}{\partial \hat{\mathrm{I}}_{1\mathrm{i}}} f_\mathrm{c}\mathbf{1} + \frac{\partial F}{\partial \hat{\mathrm{J}}_{2\mathrm{i}}}\frac{G}{\phi^4}\left(\mathbf{C}\mathbf{C}_\mathrm{p}^{-1} - \frac{1}{3}\,\mathrm{tr}(\mathbf{C}_\mathrm{p}^{-1}\mathbf{C})\mathbf{1}\right)\right)\mathbf{C}_\mathrm{p} + \frac{\dot{f}_\mathrm{c}}{f_\mathrm{c}}(\mathbf{1}-\mathbf{C}_\mathrm{p}). \tag{4.206}$$

Rearranging leads to

$$\dot{\mathbf{C}}_\mathrm{p} = \frac{2}{f_\mathrm{c}}\Lambda\frac{\partial F}{\partial \hat{\mathrm{J}}_{2\mathrm{i}}}\frac{G}{\phi^4}\mathbf{C} + \frac{2}{f_\mathrm{c}}\Lambda\left(\frac{\partial F}{\partial \hat{\mathrm{I}}_{1\mathrm{i}}} f_\mathrm{c}\mathbf{1} - \frac{1}{3}\frac{\partial F}{\partial \hat{\mathrm{J}}_{2\mathrm{i}}}\frac{G}{\phi^4}\,\mathrm{tr}(\mathbf{C}_\mathrm{p}^{-1}\mathbf{C})\mathbf{1}\right)\mathbf{C}_\mathrm{p} + \frac{\dot{f}_\mathrm{c}}{f_\mathrm{c}}(\mathbf{1}-\mathbf{C}_\mathrm{p}) \tag{4.207}$$

Hence, the plastic flow depends on the temperature, on the right Cauchy-Green tensor and also on the creep deformation.

Isotropic Hardening

First, the flow-rule in the evolution equation is evaluated

$$\hat{\mathbf{S}} \cdot \frac{\partial F}{\partial \hat{\mathbf{S}}} = \hat{\mathbf{S}} \cdot \left(\frac{\partial F}{\partial \hat{\mathrm{I}}_{1\mathrm{i}}} \mathbf{1} + \frac{\partial F}{\partial \hat{\mathrm{J}}_{2\mathrm{i}}} \hat{\mathbf{S}}^{\mathrm{D}} \right) = \frac{\partial F}{\partial \hat{\mathrm{I}}_{1\mathrm{i}}} \operatorname{tr} \hat{\mathbf{S}} + \frac{\partial F}{\partial \hat{\mathrm{J}}_{2\mathrm{i}}} \hat{\mathbf{S}} \cdot \hat{\mathbf{S}}^{\mathrm{D}}. \tag{4.208}$$

With the identity $\hat{\mathbf{S}} \cdot \hat{\mathbf{S}}^{\mathrm{D}} = \hat{\mathbf{S}}^{\mathrm{D}} \cdot \hat{\mathbf{S}}^{\mathrm{D}}$ and the definition of the invariants, this equation simplifies to

$$\hat{\mathbf{S}} \cdot \frac{\partial F}{\partial \hat{\mathbf{S}}} = \frac{\partial F}{\partial \hat{\mathrm{I}}_{1\mathrm{i}}} \hat{\mathrm{I}}_{1\mathrm{i}} + 2 \frac{\partial F}{\partial \hat{\mathrm{J}}_{2\mathrm{i}}} \hat{\mathrm{J}}_{2\mathrm{i}}. \tag{4.209}$$

This leads to the evolution equation for the yield stress in the reference configuration

$$\dot{k}_{\mathrm{M}} = \Lambda \frac{\gamma_k}{k_{\mathrm{M}}} \left(\frac{\partial F}{\partial \hat{\mathrm{I}}_{1\mathrm{i}}} \hat{\mathrm{I}}_{1\mathrm{i}} + 2 \frac{\partial F}{\partial \hat{\mathrm{J}}_{2\mathrm{i}}} \hat{\mathrm{J}}_{2\mathrm{i}} \right) + \frac{\gamma_k}{3 k_{\mathrm{M}}} g_{\mathrm{v}} \check{\mathrm{I}}_{1\mathrm{c}}^2 - \Lambda \chi \beta_k k_{\mathrm{M}}. \tag{4.210}$$

Here, the invariants have to be expressed in the reference configuration. The first invariant $\hat{\mathrm{I}}_{1\mathrm{i}}$ can be transferred according to

$$\hat{\mathrm{I}}_{1\mathrm{i}} = \operatorname{tr} \hat{\mathbf{S}} = \operatorname{tr}(\mathbf{F}_{\mathrm{i}} \tilde{\mathbf{T}} \mathbf{F}_{\mathrm{i}}^{\mathrm{T}}) = \operatorname{tr}(\mathbf{C}_{\mathrm{i}} \tilde{\mathbf{T}}). \tag{4.211}$$

The first invariant $\check{\mathrm{I}}_{1\mathrm{c}}$ is given by Eq. (4.191). The second invariant of the stress deviator can be expressed by

$$\hat{\mathrm{J}}_{2\mathrm{i}} = \frac{1}{2} \hat{\mathbf{S}}^{\mathrm{D}} \cdot \hat{\mathbf{S}}^{\mathrm{D}} = \frac{1}{2} \left(\hat{\mathbf{S}} \cdot \hat{\mathbf{S}} - \frac{1}{3} \hat{\mathrm{I}}_{1\mathrm{i}}^2 \right) = \frac{1}{2} \left(\mathbf{C}_{\mathrm{i}} \tilde{\mathbf{T}} \cdot \tilde{\mathbf{T}} \mathbf{C}_{\mathrm{i}} - \frac{1}{3} \hat{\mathrm{I}}_{1\mathrm{i}}^2 \right). \tag{4.212}$$

Hydrostatic Kinematic Hardening and Tensile Stress Hardening

Both in the evolution equation for the hydrostatic kinematic and for the tensile stress hardening, there are only scalar values. The internal variable r_{v} is given by

$$r_{\mathrm{v}} = \ln(\det \mathbf{F}_{\mathrm{i}}) = \frac{1}{2} \ln(\det \mathbf{C}_{\mathrm{i}}) = \frac{1}{2} \ln(f_{\mathrm{c}}^3 \det \mathbf{C}_{\mathrm{p}}), \tag{4.213}$$

i.e. the determinant J_{i} reads

$$J_{\mathrm{i}} = \det \mathbf{F}_{\mathrm{i}} = (\det \mathbf{C}_{\mathrm{i}})^{\frac{1}{2}} = f_c^{\frac{3}{2}} (\det \mathbf{C}_{\mathrm{p}})^{\frac{1}{2}}. \tag{4.214}$$

4.6.6 Constitutive Equation for Heat Flux and Current Density Vector

The inequality (4.85) has to be fulfilled by constitutive relations. A well-established equation for the connection between the heat flux vector and the temperature is Fourier's model

$$\vec{q} = -\kappa_{\mathrm{th}}(\Theta, \rho_{\mathrm{rel}}) \operatorname{grad} \Theta. \tag{4.215}$$

Table 4.2: Summary of constitutive model formulated with quantities relative to intermediate configurations

Elasticity Relation defined on $\breve{\chi}_t$

$$\breve{\mathbf{S}} = \frac{K}{2}\left(\operatorname{tr}\breve{\mathbf{C}}_{\mathrm{e}} - 3\right)\mathbf{1} + G\breve{\mathbf{C}}_{\mathrm{e}}^{\mathrm{D}} \tag{4.183}$$

Plastic Flow-Rule on $\hat{\chi}_t$, Elasticity ($\tilde{F} < 0$), Plasticity ($\tilde{F} = 0 \wedge \dot{\tilde{F}} \geq 0$), see Tab. 4.1

$$\overset{\triangle}{\hat{\boldsymbol{\varepsilon}}}_{\mathrm{p}} = \begin{cases} \mathbf{0}, & \tilde{F} \leq 0 \\ \Lambda \dfrac{\partial \tilde{F}}{\partial \hat{\mathbf{S}}} = \Lambda\left(\dfrac{\partial \tilde{F}}{\partial \hat{\mathrm{I}}_{1\mathrm{i}}}\mathbf{1} + \dfrac{\partial \tilde{F}}{\partial \hat{\mathrm{J}}_{2\mathrm{i}}}\hat{\mathbf{S}}^{\mathrm{D}}\right), & \tilde{F} = 0 \wedge \dot{\tilde{F}} \geq 0 \end{cases} \tag{4.122}$$

Creep Flow-Rule on $\breve{\chi}_t$

$$\overset{\triangle}{\breve{\boldsymbol{\Gamma}}}_{\mathrm{c}} = \frac{1}{3} g_{\mathrm{v}} \left\langle \breve{\mathrm{I}}_{1\mathrm{c}} \right\rangle_{*} \mathbf{1}, \qquad \breve{\mathrm{I}}_{1\mathrm{c}} := \operatorname{tr}\breve{\mathbf{S}}, \qquad g_{\mathrm{v}} = A_c(\Theta - \Theta_0)\left(1 - \frac{c_\infty}{f_{\mathrm{c}}}\right) \tag{4.136, 4.196}$$

Isotropic Hardening on $\hat{\chi}_t$

$$\dot{k}_{\mathrm{M}} = \begin{cases} \dfrac{\gamma_k}{3k_{\mathrm{M}}} g_{\mathrm{v}} \left\langle \breve{\mathrm{I}}_{1\mathrm{c}} \right\rangle_{*} \breve{\mathrm{I}}_{1\mathrm{c}}, & \tilde{F} \leq 0 \\ \dfrac{\gamma_k \dot{s}}{k_{\mathrm{M}}\chi} \hat{\mathbf{S}} \cdot \dfrac{\partial F}{\partial \hat{\mathbf{S}}} + \dfrac{\gamma_k}{3k_{\mathrm{M}}} g_{\mathrm{v}} \left\langle \breve{\mathrm{I}}_{1\mathrm{c}} \right\rangle_{*} \breve{\mathrm{I}}_{1\mathrm{c}} - \dot{s}\beta_k k_{\mathrm{M}}, & \tilde{F} = 0 \wedge \dot{\tilde{F}} \geq 0 \end{cases} \tag{4.162}$$

Hydrostatic Kinematic Hardening on $\hat{\chi}_t$

$$\xi_{\mathrm{M}} = a_\xi e^{-b_\xi r_{\mathrm{v}}} - c_\xi r_{\mathrm{v}} + \frac{1}{1 - \frac{\rho_{0,\mathrm{rel}}}{(\det \mathbf{C}_{\mathrm{i}})})^{\frac{1}{2}}} \tag{4.141}$$

Hydrostatic Tensile Hardening on $\hat{\chi}_t$

$$\mathrm{I}_{\mathrm{t}} = \beta_{\mathrm{t}}(\Theta)\frac{\rho_{0,\mathrm{rel}}^2}{J_{\mathrm{i}}^2} e^{b_{\mathrm{t}}\rho_{0,\mathrm{rel}}/J_{\mathrm{i}}} + \mathrm{I}_0, \qquad \dot{\beta}_{\mathrm{t}} = c_\beta(1 - \beta_{\mathrm{t}})\langle \Theta - \Theta_S \rangle \tag{4.166, 4.167}$$

Abbreviations

$$\hat{\mathrm{I}}_{1\mathrm{i}} = \operatorname{tr}\hat{\mathbf{S}}, \qquad \hat{\mathrm{J}}_{2\mathrm{i}} = \frac{1}{2}\breve{\mathbf{S}}^{\mathrm{D}} \cdot \breve{\mathbf{S}}^{\mathrm{D}}, \qquad \chi = \sqrt{3\left(\frac{\partial F}{\partial \hat{\mathrm{I}}_{1\mathrm{i}}}\right)^2 + 2\hat{\mathrm{J}}_{2\mathrm{i}}\left(\frac{\partial F}{\partial \hat{\mathrm{J}}_{2\mathrm{i}}}\right)^2} \tag{4.123, 4.131}$$

Table 4.3: Summary of constitutive model formulated with quantities relative to the reference configuration

Elasticity relation

$$\tilde{\mathbf{T}} = \frac{K}{2\phi^2}\left(\frac{\mathrm{tr}(\mathbf{C}\mathbf{C}_{\mathrm{i}}^{-1})}{\phi^2} - 3\right)\mathbf{C}_{\mathrm{i}}^{-1} + \frac{G}{\phi^4}\left(\mathbf{C}_{\mathrm{i}}^{-1}\mathbf{C}\mathbf{C}_{\mathrm{i}}^{-1} - \tfrac{1}{3}\,\mathrm{tr}(\mathbf{C}\mathbf{C}_{\mathrm{i}}^{-1})\mathbf{C}_{\mathrm{i}}^{-1}\right) \qquad (4.187)$$

Plastic Flow-Rule, Elasticity ($\tilde{F} < 0$), Plasticity ($\tilde{F} = 0 \wedge \dot{\tilde{F}} \geq 0$)

$$\dot{\mathbf{C}}_{\mathrm{p}} = \begin{cases} \dfrac{\dot{f}_{\mathrm{c}}}{f_{\mathrm{c}}}(\mathbf{1} - \mathbf{C}_{\mathrm{p}}), & \tilde{F} < 0 \\ \dfrac{2}{f_{\mathrm{c}}}\Lambda\dfrac{\partial F}{\partial \hat{\mathrm{J}}_{2\mathrm{i}}}\dfrac{G}{\phi^4}\mathbf{C} + \dfrac{2}{f_{\mathrm{c}}}\Lambda\left(\dfrac{\partial F}{\partial \hat{\mathrm{I}}_{1\mathrm{i}}}f_{\mathrm{c}}\mathbf{1} - \dfrac{1}{3}\dfrac{\partial F}{\partial \hat{\mathrm{J}}_{2\mathrm{i}}}\dfrac{G}{\phi^4}\,\mathrm{tr}(\mathbf{C}_{\mathrm{p}}^{-1}\mathbf{C})\mathbf{1}\right)\mathbf{C}_{\mathrm{p}} + \\ \quad + \dfrac{\dot{f}_{\mathrm{c}}}{f_{\mathrm{c}}}(\mathbf{1} - \mathbf{C}_{\mathrm{p}}), & \tilde{F} = 0 \wedge \dot{\tilde{F}} \geq 0 \end{cases}$$

Creep Flow-Rule

$$\dot{\mathbf{C}}_{\mathrm{c}} = \frac{2}{3}g_{\mathrm{v}}\left\langle \check{\mathrm{I}}_{1\mathrm{c}}\right\rangle_{*}\mathbf{C}_{\mathrm{c}}, \quad g_{\mathrm{v}} = A_c(\Theta - \Theta_0)\left(1 - \frac{c_\infty}{f_{\mathrm{c}}}\right) \qquad (4.190,\ 4.196)$$

$$\mathbf{C}_{\mathrm{c}} = f_{\mathrm{c}}\mathbf{1}, \quad \dot{f}_{\mathrm{c}}(t) = \frac{2}{3}A_c(\Theta - \Theta_0)\,(f_{\mathrm{c}} - c_\infty)\left\langle \check{\mathrm{I}}_{1\mathrm{c}}\right\rangle_{*}, \quad \check{\mathrm{I}}_{1\mathrm{c}} = f_{\mathrm{c}}\,\mathrm{tr}\,\tilde{\mathbf{T}} \qquad (4.193,\ 4.197)$$

Isotropic Hardening

$$\dot{k}_{\mathrm{M}} = \begin{cases} \dfrac{\gamma_k}{3k_{\mathrm{M}}}g_{\mathrm{v}}\left\langle \check{\mathrm{I}}_{1\mathrm{c}}\right\rangle_{*}\check{\mathrm{I}}_{1\mathrm{c}}, & \tilde{F} < 0 \\ \Lambda\dfrac{\gamma_k}{k_{\mathrm{M}}}\left(\dfrac{\partial F}{\partial \hat{\mathrm{I}}_{1\mathrm{i}}}(\hat{\mathrm{I}}_{1\mathrm{i}} + 3\xi_{\mathrm{M}}) + 2\dfrac{\partial F}{\partial \hat{\mathrm{J}}_{2\mathrm{i}}}\hat{\mathrm{J}}_{2\mathrm{i}}\right) - \\ \quad - \Lambda\chi\beta_k k_{\mathrm{M}} + \dfrac{\gamma_k}{3k_{\mathrm{M}}}g_{\mathrm{v}}\left\langle \check{\mathrm{I}}_{1\mathrm{c}}\right\rangle_{*}\check{\mathrm{I}}_{1\mathrm{c}}, & \tilde{F} = 0 \wedge \dot{\tilde{F}} \geq 0 \end{cases} \qquad (4.210)$$

Hydrostatic Kinematic Hardening

$$\xi_{\mathrm{M}} = a_\xi e^{-b_\xi r_{\mathrm{v}}} - c_\xi r_{\mathrm{v}} + \frac{1}{1 - \frac{\rho_{0,\mathrm{rel}}}{(\det \mathbf{C}_{\mathrm{i}})^{\frac{1}{2}}}}, \qquad r_{\mathrm{v}} = \frac{1}{2}\ln(\det \mathbf{C}_{\mathrm{i}}) \qquad (4.141,\ 4.81)$$

Hydrostatic Tensile Hardening

$$\mathrm{I}_{\mathrm{t}} = \beta_{\mathrm{t}}(\Theta)\rho_{\mathrm{rel}}^2 e^{b_{\mathrm{t}}\rho_{\mathrm{rel}}} + \mathrm{I}_0, \quad \dot{\beta}_{\mathrm{t}} = c_\beta(1 - \beta_{\mathrm{t}})\langle\Theta - \Theta_S\rangle \qquad (4.166,\ 4.167)$$

Abbreviations

$$\hat{\mathrm{I}}_{1\mathrm{i}} = \mathrm{tr}(\mathbf{C}_{\mathrm{i}}\tilde{\mathbf{T}}), \quad \hat{\mathrm{J}}_{2\mathrm{i}} = \frac{1}{2}\left(\mathbf{C}_{\mathrm{i}}\tilde{\mathbf{T}}\cdot\tilde{\mathbf{T}}\mathbf{C}_{\mathrm{i}} - \frac{1}{3}\hat{\mathrm{I}}_{1\mathrm{i}}^2\right), \quad \mathbf{C}_{\mathrm{i}} = f_{\mathrm{c}}\mathbf{C}_{\mathrm{p}} \qquad (4.211,\ 4.212,\ 4.204)$$

Here, κ_{th} represents the thermal conductivity[5], which has to be positive to fulfil the inequality provision. There exist also other models for the heat flux vector, but it is possible to use Fourier's model for technically relevant time and length scales in metals, see [Helm, 2001, p. 62] and the discussion therein.

The heat flux vector in the reference configuration can be obtained with the relation $\operatorname{grad}\Theta = \mathbf{F}^{-\mathrm{T}} \operatorname{Grad}\Theta$ and the help of Eq. (3.40) by

$$\vec{q}_{\mathrm{R}} = -\boldsymbol{\kappa}_{\mathrm{th}}^{\mathrm{R}} \operatorname{Grad}\Theta = -\kappa_{\mathrm{th}}(\Theta, \rho_{\mathrm{rel}})(\det \mathbf{F})\mathbf{C}^{-1} \operatorname{Grad}\Theta \tag{4.216}$$

where the heat conductivity in the reference configuration is a positive definite tensor of second order for $\kappa_{\mathrm{th}} > 0$

$$\boldsymbol{\kappa}_{\mathrm{th}}^{\mathrm{R}} = \kappa_{\mathrm{th}}(\Theta, \rho_{\mathrm{rel}})(\det \mathbf{F})\mathbf{C}^{-1}, \tag{4.217}$$

The experiments in Sect. 2.6.2 show that the thermal conductivity depends on the relative density and on the temperature. According to the measurements, a linear dependence on the temperature and a tanh-dependence on the relative density are assumed

$$\kappa_{\mathrm{th}}(\rho_{\mathrm{rel}}, \Theta) = a_\Theta \Theta + b_\Theta \tanh\left(\frac{\rho_{\mathrm{rel}} - c_\Theta}{d_\Theta}\right) + e_\Theta \tag{4.218}$$

with the material parameters a_Θ, b_Θ, c_Θ, d_Θ and e_Θ.

For the connection between the electric current density $\vec{j}$ and the electrical field $\vec{E} = -\operatorname{grad}\varphi$, Ohm's model is chosen

$$\vec{j} = \kappa_{\mathrm{el}}(\Theta, \rho_{\mathrm{rel}})\vec{E} = -\kappa_{\mathrm{el}}(\Theta, \rho_{\mathrm{rel}}) \operatorname{grad}\varphi. \tag{4.219}$$

In the measurements of electrical conductivity, a dependence on the temperature and the relative density can be observed. According to [Montes et al., 2003], a quadratic dependence of the relative density on the electrical conductivity is chosen

$$\kappa_{\mathrm{el}}(\Theta, \rho_{\mathrm{rel}}) = \rho_{\mathrm{rel}}^2 \tilde{\kappa}_{\mathrm{el}}(\Theta) = \rho_{\mathrm{rel}}^2 (a_\varphi \Theta^{-b_\varphi} - c_\varphi). \tag{4.220}$$

A power-law dependence is assumed for the temperature-dependence. The material parameters to be identified, are a_φ, b_φ and c_φ.

In order to prove the inequality (4.88), the current density is expressed in the reference configuration with $\operatorname{grad}\varphi = \mathbf{F}^{-\mathrm{T}} \operatorname{Grad}\varphi$ and the help of Eq. (3.40) by

$$\vec{j}_{\mathrm{R}} = \boldsymbol{\kappa}_{\mathrm{el}}^{\mathrm{R}} \vec{E}_{\mathrm{R}} = -\boldsymbol{\kappa}_{\mathrm{el}}^{\mathrm{R}} \operatorname{Grad}\varphi = -\kappa_{\mathrm{el}}(\Theta, \rho_{\mathrm{rel}})(\det \mathbf{F})\mathbf{C}^{-1} \operatorname{Grad}\varphi, \tag{4.221}$$

with the electrical conductivity tensor $\boldsymbol{\kappa}_{\mathrm{el}}^{\mathrm{R}}$ denoted by

$$\boldsymbol{\kappa}_{\mathrm{el}}^{\mathrm{R}} = \kappa_{\mathrm{el}}(\Theta, \rho_{\mathrm{rel}})(\det \mathbf{F})\mathbf{C}^{-1}. \tag{4.222}$$

---

[5] It has the unit W/(mK)

4.7 Derivation of Heat Conduction Equation

The local form of the balance of energy describes the transfer of thermal energy within a body. This relation connects the mechanical and electrical power with the internal and kinetic energy of a body. The flow of thermal energy in a body is known as *heat conduction*. Fourier's model describes the heat transport from hot temperature regions to cold areas by the heat flux vector. Additionally, the heat can be transferred due to convection, which describes the transport by the movement of fluids. Another transport phenomenon is radiation, which can be seen as energy emitted by matter as electromagnetic waves. In solids, convection and radiation are surface phenomena, which are incorporated by the heat flux over the boundary.

The heat conduction equation can be derived by the local form of the balance of energy (3.101b), where the internal energy is replaced by $e = \psi + s\Theta$, Eq. (3.105), and the result is given by

$$\dot{\psi} + \dot{s}\Theta + s\dot{\Theta} = \frac{1}{\rho_0}\tilde{\mathbf{T}} \cdot \dot{\mathbf{E}} + \frac{1}{\rho_0}\vec{E}_{\mathrm{R}} \cdot \vec{j}_{\mathrm{R}} - \frac{1}{\rho_0}\operatorname{Div}\vec{q}_{\mathrm{R}} + r. \tag{4.223}$$

Taking into account the internal dissipation Eq. (4.86), the equation can be simplified to

$$\Theta\dot{s} = \frac{1}{\rho_0}\vec{E}_{\mathrm{R}} \cdot \vec{j}_{\mathrm{R}} - \frac{1}{\rho_0}\operatorname{Div}\vec{q}_{\mathrm{R}} + r + \delta. \tag{4.224}$$

The entropy is given by Eq. (4.94) and depends on the elastic right Cauchy-Green tensor $\breve{\mathbf{C}}_{\mathrm{e}}$, the internal variables r_{i} and r_{v} as well as on the inelastic determinant J_{i} and the temperature Θ. Accordingly, the entropy time derivative reads

$$\dot{s} = \frac{\partial s}{\partial r_{\mathrm{i}}}\dot{r}_{\mathrm{i}} + \frac{\partial s}{\partial r_{\mathrm{v}}}\dot{r}_{\mathrm{v}} + \frac{\partial s}{\partial J_{\mathrm{i}}}\dot{J}_{\mathrm{i}} + \frac{\partial s}{\partial \breve{\mathbf{C}}_{\mathrm{e}}}\dot{\breve{\mathbf{C}}}_{\mathrm{e}} + \frac{\partial s}{\partial \Theta}\dot{\Theta}. \tag{4.225}$$

Inserting this equation into Eq. (4.224) yields

$$\Theta\frac{\partial s}{\partial \Theta}\dot{\Theta} = \delta - \Theta\left(\frac{\partial s}{\partial r_{\mathrm{i}}}\dot{r}_{\mathrm{i}} + \frac{\partial s}{\partial r_{\mathrm{v}}}\dot{r}_{\mathrm{v}} + \frac{\partial s}{\partial J_{\mathrm{i}}}\dot{J}_{\mathrm{i}} + \frac{\partial s}{\partial \breve{\mathbf{C}}_{\mathrm{e}}}\dot{\breve{\mathbf{C}}}_{\mathrm{e}}\right) + \frac{1}{\rho_0}\vec{E}_{\mathrm{R}} \cdot \vec{j}_{\mathrm{R}} - \frac{1}{\rho_0}\operatorname{Div}\vec{q}_{\mathrm{R}} + r. \tag{4.226}$$

With the heat production due to internal dissipation

$$w := \delta - \Theta\left(\frac{\partial s}{\partial r_{\mathrm{i}}}\dot{r}_{\mathrm{i}} + \frac{\partial s}{\partial r_{\mathrm{v}}}\dot{r}_{\mathrm{v}} + \frac{\partial s}{\partial J_{\mathrm{i}}}\dot{J}_{\mathrm{i}} + \frac{\partial s}{\partial \breve{\mathbf{C}}_{\mathrm{e}}}\dot{\breve{\mathbf{C}}}_{\mathrm{e}}\right) \tag{4.227}$$

and the heat capacity at constant deformation, see [Haupt, 2002, p. 535],

$$c_{\mathrm{p}} := \Theta\frac{\partial s}{\partial \Theta} \tag{4.228}$$

the heat conduction equation can be written as

$$c_\mathrm{p}\dot{\Theta} = w + \frac{1}{\rho_0}\vec{E}_\mathrm{R} \cdot \vec{j}_\mathrm{R} - \frac{1}{\rho_0} \operatorname{Div} \vec{q}_\mathrm{R} + r. \tag{4.229}$$

A common approximation in the literature is given by

$$c_\mathrm{p} \approx -\Theta \frac{\partial^2 \psi_\Theta}{\partial \Theta^2}, \tag{4.230}$$

see also [Jansohn, 1997, p. 33]. The thermal part of the free energy ψ_Θ is proposed to represent the thermal behavior of the DSC-measurements in Sect. 2.6.1. In these experiments, a linear dependence of the heat capacity is observed, and the following approach for the thermal free energy according to [Heimes, 2005]

$$\psi_\Theta = \rho_0 c_{\mathrm{p}0} \left(\left((\Theta - \Theta_0) - \Theta \ln \tfrac{\Theta}{\Theta_0} \right) (1 - c_{\mathrm{p}S}\Theta_0) - \frac{1}{2} c_{\mathrm{p}S} (\Theta^2 - \Theta_0^2) \right), \tag{4.231}$$

is chosen. This leads to the linear temperature-dependence

$$c_\mathrm{p}(\Theta) = c_{\mathrm{p}0} \left(1 + c_{\mathrm{p}S}(\Theta - \Theta_0)\right) \tag{4.232}$$

with the material parameters $c_{\mathrm{p}S}$ and $c_{\mathrm{p}0}$. The heat capacity at room temperature is represented by $c_{\mathrm{p}0}$ as long as $\Theta = \Theta_0$ holds. Inserting the electrical field $\vec{E}_\mathrm{R} = -\operatorname{Grad} \varphi$ and Fourier's model (4.216) into the heat conduction equation (4.229) yields

$$c_\mathrm{p}(\Theta)\dot{\Theta} = w - \frac{1}{\rho_0} \operatorname{Grad} \varphi \cdot \vec{j}_\mathrm{R} - \frac{1}{\rho_0} \operatorname{Div}(-\boldsymbol{\kappa}_\mathrm{th}^\mathrm{R} \operatorname{Grad} \Theta) + r. \tag{4.233}$$

In the FAST-experiments, no further volumetric heat sources are present. Hence, the volumetric heat source r can be neglected. By inserting Ohm's model into the heat equation, one obtains

$$c_\mathrm{p}(\Theta)\dot{\Theta} = -\frac{1}{\rho_0} \operatorname{Div} \left(-\boldsymbol{\kappa}_\mathrm{th}^\mathrm{R} \operatorname{Grad} \Theta\right) + r_\mathrm{el}. \tag{4.234}$$

The term r_el, the volumetric heat source originating from the electrical field, is known as *Joule heating*, see [Landau et al., 2008]. The source of Joule heating originates from charged particles moving through a medium. Due to collisions, their kinetic energy is transferred to heat, [Zohdi, 2012b],

$$r_\mathrm{el} := -\frac{1}{\rho_0} \operatorname{Grad} \varphi \cdot \vec{j}_\mathrm{R} = \frac{1}{\rho_0} \boldsymbol{\kappa}_\mathrm{el}^\mathrm{R} \operatorname{Grad} \varphi \cdot \operatorname{Grad} \varphi. \tag{4.235}$$

This represents the electrical energy that is converted into heat. It is assumed that the heating of the FAST tool system and the powder is caused mainly by this effect, so that the mechanical dissipation δ can be neglected.

5 Material Parameter Identification

In this chapter, the parameters for the constitutive model developed in Chap. 4 will be identified from the experiments of Chap. 2. On the one hand, the thermo-mechanical behavior has to be identified. On the other hand, it is necessary to determine the thermo-electrical properties such as heat capacity, the thermal and the electrical conductivity. This will be done for the copper powder material as well as the graphite material. Furthermore, the thermal as well as the electric contact conductance are obtained from experiments and data from the literature.

First of all, the parameter identification procedure is described. Within this procedure, the three-dimensional material model is reduced to a homogeneous constrained compression case, and a least-square method is used to minimize the residuals between the material model response and the experimental data leading to the identified parameters. It is not possible to measure the radial stress in the sintering experiments. With the help of the proposed model, see Sect. 2.4.6, the radial stresses can be derived, and the parameters for the material model are determined together with the identification algorithm.

5.1 Identification Procedure

For the identification procedure, it is advantageous to use the stress algorithm developed for three-dimensional finite element programs. In the case of homogeneous deformations such as tension/compression or plane stress conditions, the boundary conditions lead to constraints like zero stresses or strains in a specific direction. For constitutive models of evolutionary type, these constraints – together with the evolution equations, which are first order ordinary differential equations – yield a differential-algebraic equation system (DAE-system). This will be solved by diagonally implicit Runge-Kutta methods and the Multilevel-Newton algorithm.

In the sintering experiments in Chap. 2, the axial stress is prescribed. Due to the surrounding die, the radial strains are zero and lead to radial stresses. The deformation gradient $\mathbf{F}$, together with the Green strain tensor $\mathbf{E} = (1/2)\,(\mathbf{C} - \mathbf{1})$ and the stress state, are given by

$$\mathbf{F} = \begin{bmatrix} \lambda & 0 & 0 \\ 0 & 1 & 0 \\ 0 & 0 & 1 \end{bmatrix} \quad \mathbf{E} = \frac{1}{2} \begin{bmatrix} \lambda^2 - 1 & 0 & 0 \\ 0 & 0 & 0 \\ 0 & 0 & 0 \end{bmatrix} \quad \mathbf{T} = \begin{bmatrix} \sigma_{\text{axial}} & 0 & 0 \\ 0 & \sigma_{\text{radial}} & 0 \\ 0 & 0 & \sigma_{\text{radial}} \end{bmatrix}. \qquad (5.1)$$

The tensor **T** represents the Cauchy stress tensor. The reduction of a three-dimensional material model to this laterally constrained compaction loading path will not be explained here. A detailed description can be found in [Krämer et al., 2015], where it is shown that so-called filter matrices can be introduced for the reduction – and that various stress-strain states can be applied easily. As a result, one is able to verify a material model without the overhead of a full finite element program. Additionally, the same three-dimensional material routines can be used for all programs.

In this work, the material model reduction is used in combination with the material parameter identification. Furthermore, measures to ensure the quality of the identification are investigated.

The following statements are summarized from the work of Haupt [2002]. A constitutive model can be seen as a set of mathematical equations describing the essential material behavior. It is not the aim of the theory to develop a universal material model for all observable phenomena. Instead, the aim is to develop a model for a certain range of applications in order to represent the most important phenomena. In general, a material model should not only reproduce the material behavior of specific tests, moreover it should be able to represent general three-dimensional deformation processes beyond the specific behavior in the laboratory experiments. The material parameters of a constitutive model have to be identified by practicable experiments. In this sense, the test specimen can be seen as an operator, Fig. 5.1. The input can be stresses and the temperature and the output are strains for the experiments in Chap. 2. Here, some idealizations need to be performed. It is assumed that the sintering experiments lead to a homogeneous stress strain state, see App. 4. The question is how the material parameters can be identified from the experiments in Chap. 2. The response of the material model for a prescribed axial stress and temperature is fitted to the experimental data by means of identifying the material parameters. In practice, a least-square method is applied to minimize the sum of the squares of the residuals between the material

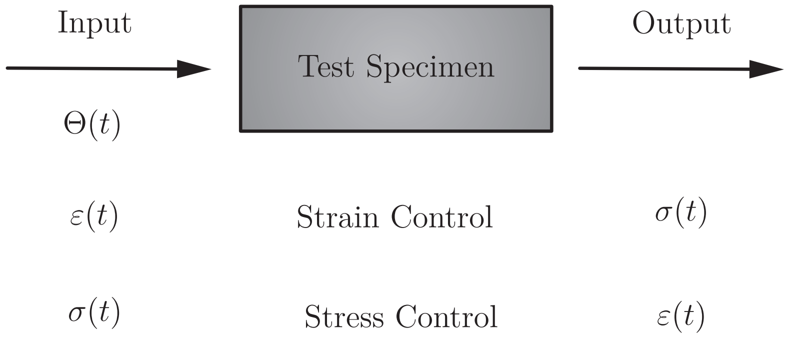

Figure 5.1: Specimen as operator according to [Haupt, 2002]

model response and the experimental data, see Fig. 5.2. The result can be seen as a least-square fit.

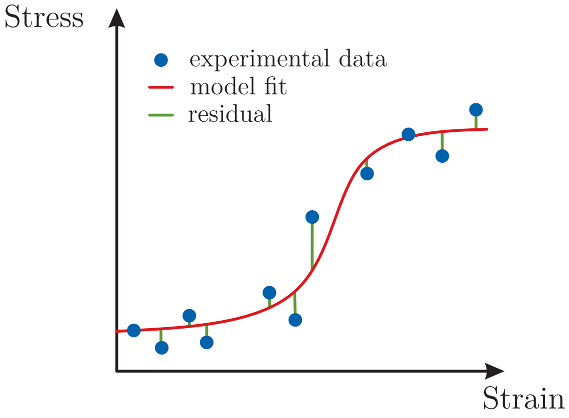

Figure 5.2: Schematic fit of material model to experimental data

In the following, the material parameter identification procedure is described for completeness. For a detailed description, it is referred to [Krämer et al., 2015]. The whole identification procedure is shown in Fig. 5.3. The experimental data is assembled in the vector $\mathbf{d} \in \mathbb{R}^{n_\mathrm{d}}$, $\hat{d}_i$, with the number of experimental data n_d from one or several experiments. The material model responses $\hat{\mathbf{s}} = \mathbf{s}(\boldsymbol{\kappa}, t), \quad \hat{s}_i = s(\boldsymbol{\kappa}, t_i)$ are given by the solution of the DAE-system, see Fig. 5.3, at discrete time values t_i, depending on the vector of material parameters $\boldsymbol{\kappa} \in \mathbb{R}^{n_{\boldsymbol{\kappa}}}$. $n_{\boldsymbol{\kappa}}$ is the number of parameters and $\boldsymbol{\kappa}_0$ are the initial parameters estimated by the user. The vectors $\mathbf{s}$ and $\mathbf{d}$ contain the axial stretch as well as the radial stresses. The residual vector $\mathbf{r}(\boldsymbol{\kappa})$ is defined as the difference between the material model response and the experimental data

$$r_i(\boldsymbol{\kappa}, t_i) = s(\boldsymbol{\kappa}, t_i) - d_i \quad \rightarrow \quad \mathbf{r}(\boldsymbol{\kappa}) = \mathbf{s}(\boldsymbol{\kappa}) - \mathbf{d}, \tag{5.2}$$

where a linear interpolation of the model data to the experimental data at the given time t_i is performed. As a result, the difference over the time is calculated. The goal is now to reduce the residual vector by means of modifying the material parameters $\boldsymbol{\kappa}$. In this sense, a trust-region-reflective algorithm from Matlab is used to reduce the L_2-norm of the residual

$$\min_{\boldsymbol{\kappa} \in \mathbb{R}^n} \|\mathbf{r}(\boldsymbol{\kappa})\|_2^2 = \min_{\boldsymbol{\kappa} \in \mathbb{R}^n} (\mathbf{r}^T(\boldsymbol{\kappa})\mathbf{r}(\boldsymbol{\kappa})) = \min_{\boldsymbol{\kappa} \in \mathbb{R}^n} (\{\mathbf{s}(\boldsymbol{\kappa}) - \mathbf{d}\}^T \{\mathbf{s}(\boldsymbol{\kappa}) - \mathbf{d}\}) \quad \rightsquigarrow \boldsymbol{\kappa}^* \tag{5.3}$$

The material parameters are changed until a certain abort criterion is fulfilled, e.g. $\|\mathbf{r}(\boldsymbol{\kappa}_k)\|_2 \leq \mathrm{tol}_r$ or $\Delta\boldsymbol{\kappa}_k \leq \mathrm{tol}_\Delta$. The optimization loop is marked in Fig. 5.3 by the orange arrows. As a result, one obtains the identified material parameters $\boldsymbol{\kappa}^*$.

For example, some of the material parameters should be positive. Therefore, constraints are introduced for the minimum κ_{min_i} and maximum value κ_{max_i},$i =$

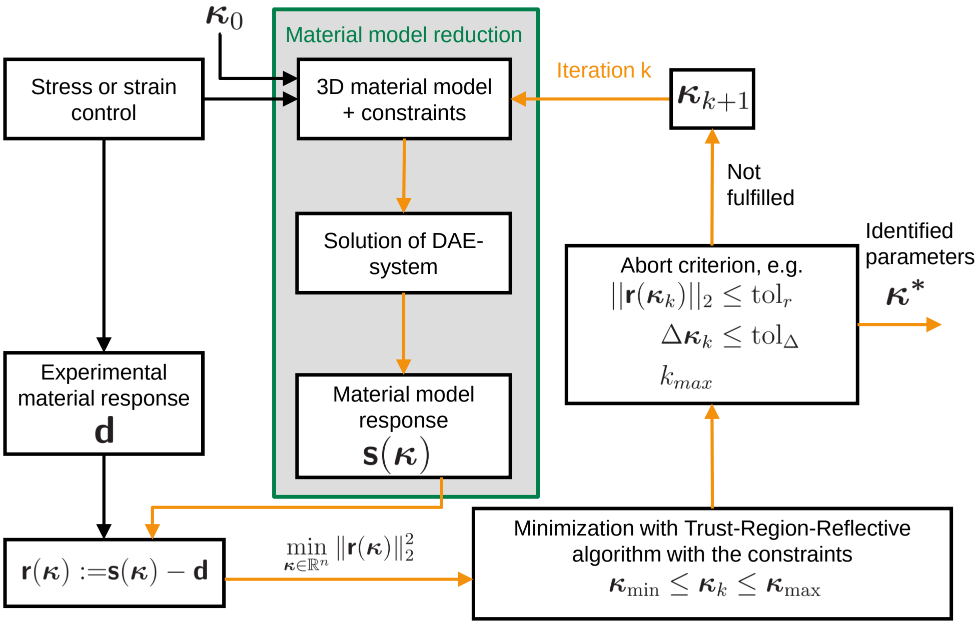

Figure 5.3: Material parameter identification procedure

$1, \ldots, n_{\boldsymbol{\kappa}}$, of each parameter. The optimization problem reads

$$\min_{\boldsymbol{\kappa} \in \mathbb{R}^{n_{\boldsymbol{\kappa}}}} \|\mathbf{r}(\boldsymbol{\kappa})\|_2^2 \quad \text{subject to} \quad \kappa_{\min_i} \leq \kappa_i \leq \kappa_{\max_i}, i = 1, \ldots, n_{\boldsymbol{\kappa}}. \tag{5.4}$$

With the identified parameters at hand, the question is how well the material model responds to the experimental data. In the field of linear least-square problems, there exist measures for the optimization quality. The measures used in this work are: the confidence interval, the correlation coefficient and the coefficient of determination. It should be mentioned that all these quantities are derived from a linear theory – but it is assumed that they can give an indication for the quality of the fit. These measures are introduced in the following.

Confidence Interval

Based on the nonlinear model, a linearization around the identified parameters $\boldsymbol{\kappa}^*$ is performed

$$\mathbf{r}(\boldsymbol{\kappa}^*) = \mathbf{r}(\boldsymbol{\kappa}) + \mathbf{J}(\boldsymbol{\kappa}^*)(\boldsymbol{\kappa}^* - \boldsymbol{\kappa}), \tag{5.5}$$

$\mathbf{J}(\boldsymbol{\kappa}) = \mathrm{d}\mathbf{r}(\boldsymbol{\kappa})/\,\mathrm{d}\boldsymbol{\kappa} \in \mathbb{R}^{n_\mathrm{d} \times n_{\boldsymbol{\kappa}}}$ represents the Jacobian. The covariance matrix $\mathbf{P}$ can be approximated by

$$\mathbf{P} \approx \sigma^2 \left[\mathbf{J}^\mathrm{T}(\boldsymbol{\kappa}^*)\mathbf{J}(\boldsymbol{\kappa}^*)\right]^{-1}, \qquad \sigma^2 = \frac{\mathbf{r}^T(\boldsymbol{\kappa})\mathbf{r}(\boldsymbol{\kappa})}{n_\mathrm{d} - 1}, \tag{5.6}$$

see [Brandt, 1999]. σ is the standard deviation and σ^2 the variance. The covariance measures the dependence of two material parameters on each other. With the covariance matrix, the confidence interval of the material parameter κ_i is given by the square root of the diagonal element $\sqrt{P_{ii}}$, see [Kreißig et al., 2001]. Thus, one obtains

$$\boldsymbol{\kappa}^\mathrm{conf} = \boldsymbol{\kappa}^* \pm \Delta\boldsymbol{\kappa}^*, \qquad \Delta\kappa_i^* = \sqrt{P_{ii}}, \qquad i = 1, \ldots, n_{\boldsymbol{\kappa}}. \tag{5.7}$$

Correlation Matrix

Another measure is the correlation coefficient, which describes the dependence of the parameter κ_i on the parameter κ_j. The correlation coefficient ranges from -1 to 1. If two parameters are strongly correlated, this means that the optimization did not serve to identify these parameters independently – and that a linear combination takes places, see [Tarantola, 2005]. The correlation matrix $\mathbf{R}$ can be computed with the help of the covariance matrix by

$$\mathbf{R} = r_{ij} = \left[\frac{P_{ij}}{\sqrt{P_{ii}P_{jj}}}\right], \qquad \mathbf{R} \in \mathbb{R}^{n_{\boldsymbol{\kappa}} \times n_{\boldsymbol{\kappa}}}. \tag{5.8}$$

Coefficient of Determination

The R^2-value measures how well the model fit corresponds to the experimental data. The value lies in the interval $[0, 1]$. If the R^2-value were to reach one, this would resemble a perfect fit and could also be seen as an indicator for the quality of the fit. It is a statistical quantity and can be defined as

$$R^2 = 1 - \frac{\sum_{i=1}^{n_\mathrm{d}} (d_i - s_i)^2}{\sum_{i=1}^{n_\mathrm{d}} (d_i - \bar{d})^2}, \quad \text{with } \bar{d} = \frac{1}{n_\mathrm{d}} \sum_{i=1}^{n_\mathrm{d}} d_i. \tag{5.9}$$

The numerator is the sum of the squared residuals and the denominator is the sum of the squared difference between the experimental data d_i and its mean value $\bar{d}$.

5.2 Parameter Identification of the Thermo-Mechanical Behavior of Copper Powder

The parameters of the material model, see Tab. 4.3 and Tab. 4.1, have to be identified by the sintering experiments in Sect. 2.5 and are described in Tab. 5.2. The experiments, which are used for the parameter identification, are shown in Tab. 5.1. The identified parameters from the particular experiment have a gray background, whereas the previously identified and fixed parameters are denoted by an asterisk.

Table 5.1: Material parameter identification procedure

Experiments	Identified parameters										
[Carnavas, 1996]	E	ν									
Cold compaction	E^*	ν^*	γ_k	a_ξ	b_ξ	c_ξ					
Monotonic loading at different temperatures	E^*	ν^*	γ_k^*	a_ξ^*	b_ξ^*	c_ξ^*	m_k	m_ξ	Θ_S		
Creep experiments	E^*	ν^*	γ_k^*	a_ξ^*	b_ξ^*	c_ξ^*	m_k^*	m_ξ^*	Θ_S^*	A_c	c_∞

5.2.1 Elasticity Parameters

In the elasticity relation, Eq. (4.187), the bulk and shear modulus have to be determined. In the work of Carnavas [1996], the Young's modulus and the Poisson

Table 5.2: List of material parameters

Parameters	Group	Description
K, G	Elasticity Relation	In the elasticity relation, Eq. (4.187), the bulk K and shear modulus G have to be determined.
α_Θ, Θ_0	Thermal Expansion	The parameter α_Θ describes the linear thermal expansion behavior with the initial temperature Θ_0.
A_c, c_∞	Creep Flow-Rule	The material parameter A_c describes the general creep behavior, Eq. (4.196), and is connected to the linear temperature dependence. c_∞ denotes the saturation value for the creep deformation.
β_k, γ_k	Isotropic Hardening	The material parameters describing the isotropic hardening variable k_M are β_k and γ_k, Eq. (4.210).
a_ξ, b_ξ, c_ξ	Hydrostatic Kinematic Hardening	The hydrostatic kinematic hardening variable ξ_M, Eq. (4.141), is connected to the middle point of the ellipse yield function and its evolution is described by a_ξ, b_ξ and c_ξ.
b_t, I_0, Θ_S, c_β	Hydrostatic Tensile Hardening	Below the sintering temperature Θ_S, no increase in the tensile yield stress occurs, which is controlled by the parameter β_t, Eq. (4.167). This parameter is between 0 and 1 and the slope in the evolution equation is controlled by c_β. The evolution of the yield stress, Eq. (4.166), depends on the parameter b_t.
m_k, Θ_S	Yield Function	Due to the temperature, the yield function shrinks exponentially, which is described for the yield stress k by the material parameter m_k, Eq. (4.24).
m_ξ, Θ_S	Yield Function	The exponential yield function shrinkage is described for the hydrostatic kinematic hardening variable ξ by the parameter m_ξ, Eq. (4.25).
r	Yield Function	The intersection between the elliptic and the exponential part of the yield function is defined by r, see Fig. 4.8 and Eq. (4.17).
c	Yield Function	For the interpolation concept, Eq. (4.18), between the elliptic and the exponential part of the yield function, the parameter c controls the sharpness at the intersection point.
$\rho_{0,\mathrm{rel}}$		The initial relative density has to be prescribed and can be taken from the experiments.
ρ_solid		In the heat equation, the density of the material occurs and is computed by $\rho = \rho_\mathrm{rel}\rho_\mathrm{solid}$. The density of bulk copper is given by $\rho_\mathrm{solid} = 8920\,\mathrm{kg\,m^{-3}}$.

ratio for spherical, dendritic and irregular shaped copper powder are determined, as shown in Fig. 5.4a and Fig. 5.4b. Additionally, the values for bulk copper, $E = 1.2 \times 10^5$ MPa and $\nu = 0.35$ reported in [Carnavas, 1996] are shown. Bier [2008] used the constant values $E = 1.98 \times 10^4$ MPa and $\nu = 0.1949$.

The Young's modulus and the Poisson ratio both show an increasing behavior with increasing relative density. Since the sintering experiments show that only a small elastic region is present and the main part is inelastic, constant values are used in this work. Furthermore, it is not common to perform cyclic experiments in sintering. If necessary, it is possible to incorporate the change of the elastic parameters due to the process by a dependence of K and G on $\det \mathbf{F}$. In this work, the parameters are chosen to be constant and are given by $E = 6 \times 10^4$ MPa and $\nu = 0.25$. The bulk and shear modulus can be calculated from the Young's modulus and the Poisson ratio by

$$K = \frac{E}{3(1-2\nu)} = 4 \times 10^4\,\text{MPa}, \qquad G = \frac{E}{2(1+\nu)} = 2.4 \times 10^4\,\text{MPa}. \tag{5.10}$$

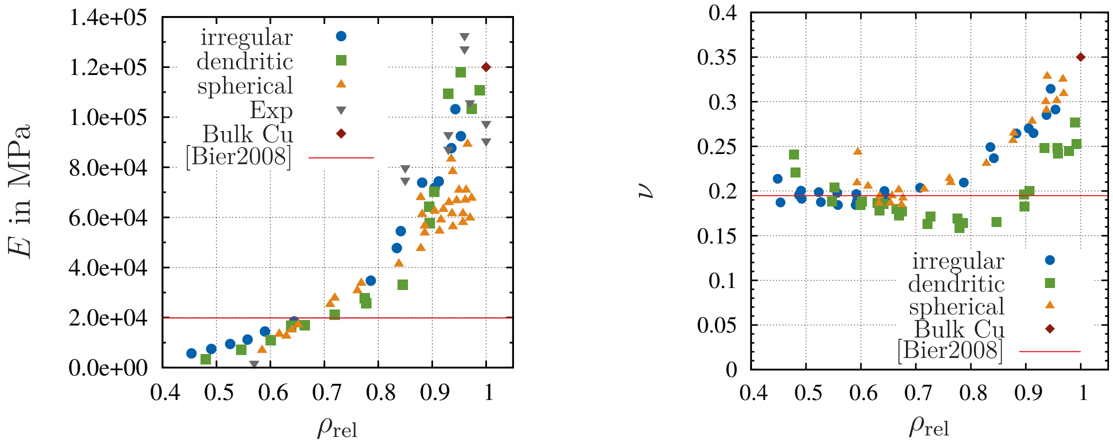

(a) Young's modulus over relative density

(b) Poisson ratio over relative density

Figure 5.4: Young's modulus and Poisson ratio for spherical, dendritic and irregular shaped copper powder particles, taken from [Carnavas, 1996].

5.2.2 Thermal Expansion

It is necessary to determine the thermal expansion coefficient for the linear thermal expansion behaviour. This can be achieved by the dilatometer experiments reported in Sect. 2.5.5. The identified thermal expansion coefficient reads $\alpha_\Theta = 1.5 \times 10^{-5}\,\text{K}^{-1}$, see Fig. 5.5.

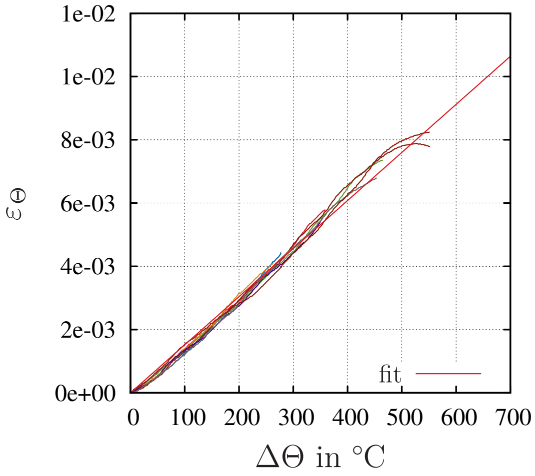

Figure 5.5: Measured thermal expansion behavior of copper powder and fitted linear thermal expansion from dilatometer experiments reported in Sect. 2.5.5

5.2.3 Inelastic Parameters for Cold Compaction

The inelastic parameters describing the shape of the yield function are the kinematic hardening parameters a_ξ, b_ξ and c_ξ as well as the isotropic hardening parameters β_k and γ_k. These parameters are identified by a monotonic compaction experiment at room temperature. The axial stress over the time is prescribed and shown in Fig. 5.6a. Since in the sintering experiments the axial stress (compressive pressure) is always negative, the negative sign is omitted. Because a strong correlation between the parameters γ_k and β_k is observed during the identification process, the parameter β_k is excluded and set a priori to $\beta_k = 0.01$. Each of the experiments is modified, due to the fact a precompaction with a force of approximately 2.5 kN is applied in the FAST-machine – and because no force and displacement data is recorded during the precompaction. In order to obtain a continuous loading path, the data is modified to reach an axial force of 2.5 kN in 10 s. The precompaction and the initial height measurement is described in Sect. 2.2 and illustrated in Fig. 2.7. The initial yield stress due to the precompaction is chosen to be $k_M(t_0) = 5\,\mathrm{MPa}$. During the parameter identification, the difference between the experimental axial stretch as well as the radial stress and the model response is minimized. The results are shown in Fig. 5.7a. The experiments are denoted by dots and the material model is indicated by solid lines. In the following, the stress over the relative density is shown – since the relative density is the main quantity to describe the sintering experiments. The axial and radial stresses over the relative density are shown in Fig. 5.7b. With a correlation coefficient of $R^2 = 0.9989$, the model appears to fit the experiments very well. The identified values with their confidence intervals are reported in Tab. 5.3.

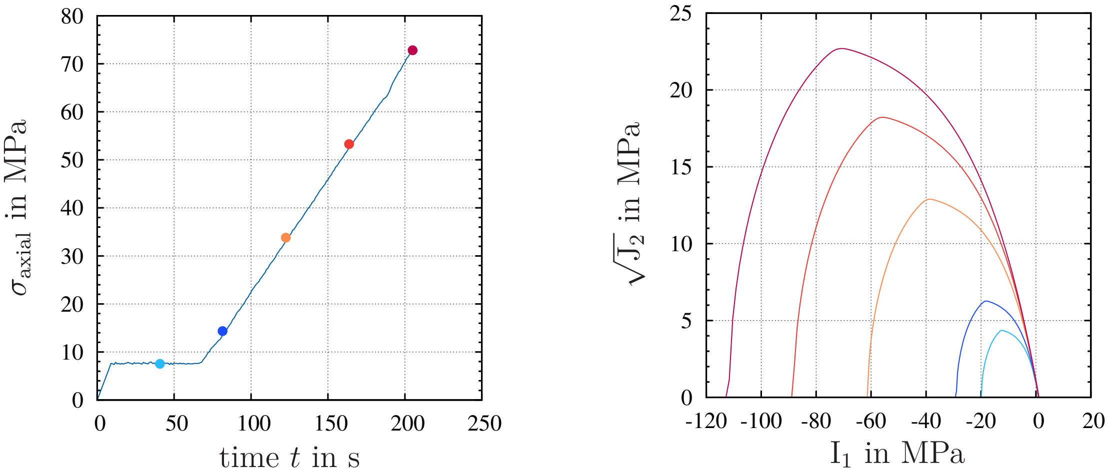

(a) Axial stress over time

(b) Shape of yield function. The lines show the yield function $F = 0$ at different axial stresses.

Figure 5.6: Loading path and identified shape of yield function

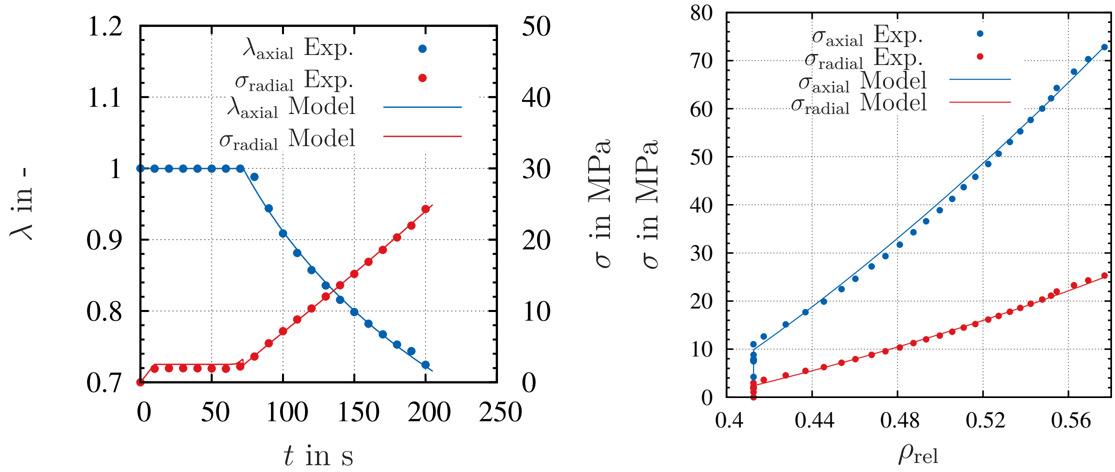

(a) Comparison of radial stresses and axial stretch between the experimental values and the material model

(b) Stresses over relative density

Figure 5.7: Adapted material model to cold compaction experiment

Table 5.3: Identified inelastic parameters

	γ_k MPa^{-1}	a_ξ MPa	b_ξ –	c_ξ MPa
initial	50	2	1	20
identified	26.7	1.41	2.45	38.9
conf. interval	4.54	0.469	3.82	13.1

The correlation matrix reads

$$\mathbf{R} = \left[\begin{array}{lrrrr} & \gamma_k & a_\xi & b_\xi & c_\xi \\ \gamma_k & 1.00 & -0.06 & 0.23 & 0.42 \\ a_\xi & & 1.00 & 0.23 & -0.45 \\ b_\xi & & & 1.00 & -0.75 \\ c_\xi & & & & 1.00 \end{array}\right]$$

It can be observed that the parameters b_ξ and c_ξ are inversely correlated to each other on the basis of the experiments used for the parameter identification process. Apart from that, there seem to be no other strong correlations between the other parameters.

5.2.4 Yield Function Temperature-Dependence

The yield function shrinkage with increasing temperature is described by an exponential dependence. The ellipse height decreases with increasing temperature, see Fig. 4.12. The slope of the exponential decrease is described by the parameter m_k. The parameter m_ξ is connected to the decrease of the ellipse center ξ for increasing temperature. Below the sintering temperature Θ_S, no temperature shrinkage occurs. These three parameters are identified by monotonic loading experiments at the different temperatures Θ_c =200 °C, 300 °C, 500 °C and 700 °C. In these experiments, the temperature is applied at first, see Fig. 5.8a. Subsequently, the axial stress is monotonically prescribed, Fig. 5.8b. The elasticity parameters and the inelastic parameters are used for parameter identification, see Tab. 5.1. The difference between the four experiments and the material model response is minimized, and the resulting material parameters are given in Tab. 5.4. The material model fitted to the experimental data is shown in Fig. 5.9. With the coefficient given by $R^2 = 0.9972$, it represents the experimental data well. The radial stresses over the relative density – which show a good agreement too – are shown in Fig. 5.10.

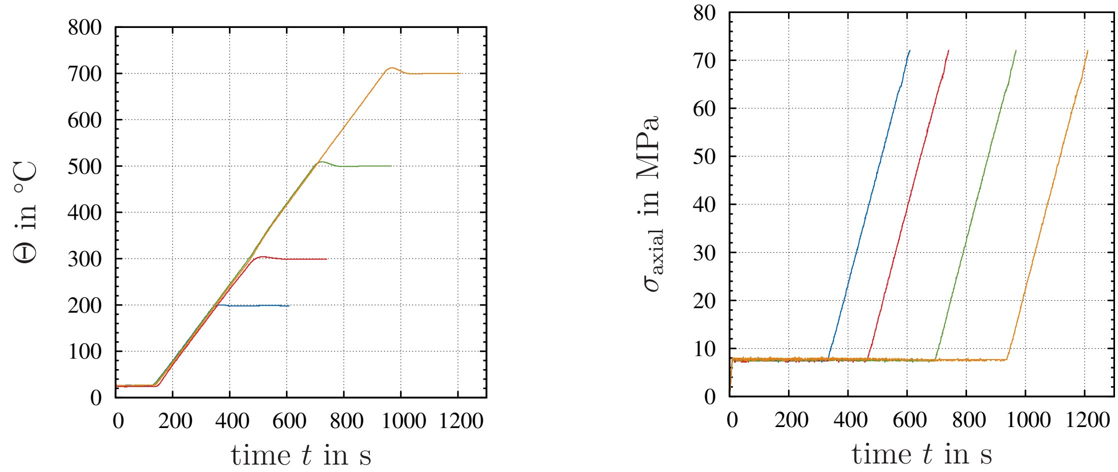

(a) Prescribed temperature in the experiments

(b) Prescribed axial stress

Figure 5.8: Loading path of experiments for the identification of the temperature-dependent yield function

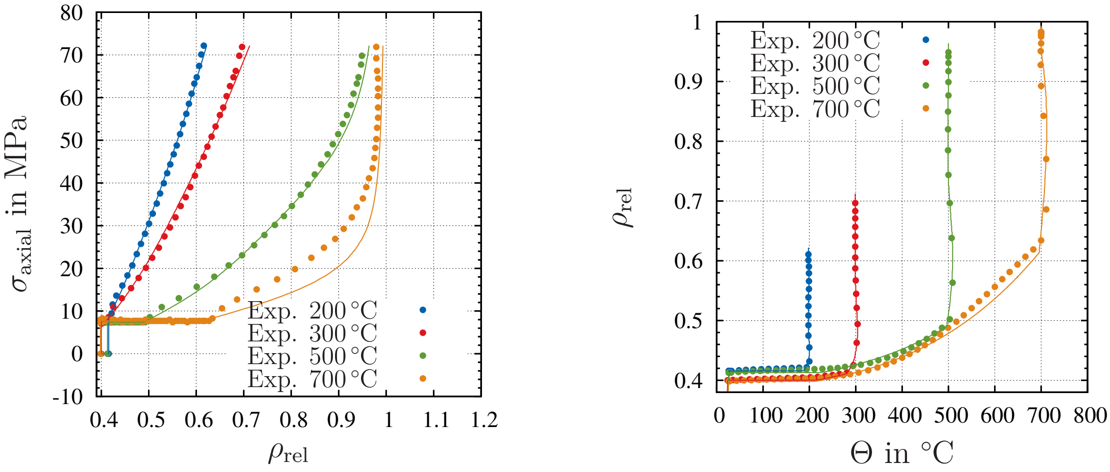

(a) Axial stress over relative density

(b) Relative density over temperature

Figure 5.9: Fit of material model (solid lines) to the experimental data (points)

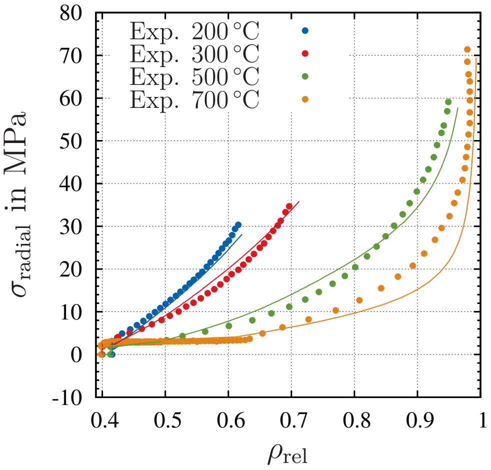

Figure 5.10: Fitted material model to the radial stresses computed by the proposed model Eq. (2.20)

Table 5.4: Identified yield function parameters

	m_k °C^{-1}	m_ξ °C^{-1}	Θ_S °C
initial	3.00×10^{-3}	5.00×10^{-3}	180
identified	3.55×10^{-3}	4.65×10^{-3}	151
conf. interval	1.43×10^{-5}	2.22×10^{-5}	0.713

The correlation matrix is given by

$$\mathbf{R} = \begin{bmatrix} & m_k & m_\xi & \Theta_S \\ m_k & 1.00 & -0.50 & -0.29 \\ m_\xi & & 1.00 & -0.23 \\ \Theta_S & & & 1.00 \end{bmatrix}$$

5.2.5 Creep Parameters

First of all, the general creep behavior is studied for a creep experiment at 300 °C and a dwell force of 25 kN. In the first step, the temperature is increased. Then, the force is applied and kept constant for 2 h, see Fig. 5.11. With the creep evolution equations, the experimental data can be very well represented for the axial stress over the relative density as well as the relative density over the time, Fig. 5.12. The radial stress computed by the material model and the radial stresses computed by Eq. (2.20) show a deviation, see Fig. 5.13a. The radial stress from the material model increases during loading and decreases during the creep period. This can be explained by the creep variable f_c shown in Fig. 5.13b. The creep volumetric deformation can be computed by

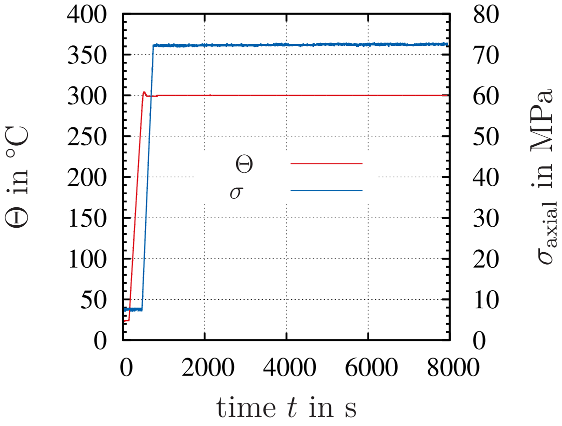

Figure 5.11: Loading path of creep experiment for $F_c = 25\,\text{kN}$ and $\Theta_c = 300\,°\text{C}$

$$\mathbf{C}_\mathrm{c} = f_\mathrm{c}\mathbf{1} \qquad \Rightarrow \qquad \mathbf{F}_\mathrm{c} = \sqrt{f_\mathrm{c}}\mathbf{1}. \tag{5.11}$$

Since a volumetric creep phenomenon is assumed, the powder shrinks in all directions and the radial stresses decrease. The computed radial stress increases, but this cannot be validated by experimental measurements. It is also possible that the radial stresses decrease due to the temperature. Nevertheless, it is possible to give a good description of the axial deformation behavior and the relative density.

The creep parameters A_c and c_∞ are determined by creep experiments at the different temperatures 25 °C, 200 °C and 300 °C and the consistent axial dwell force

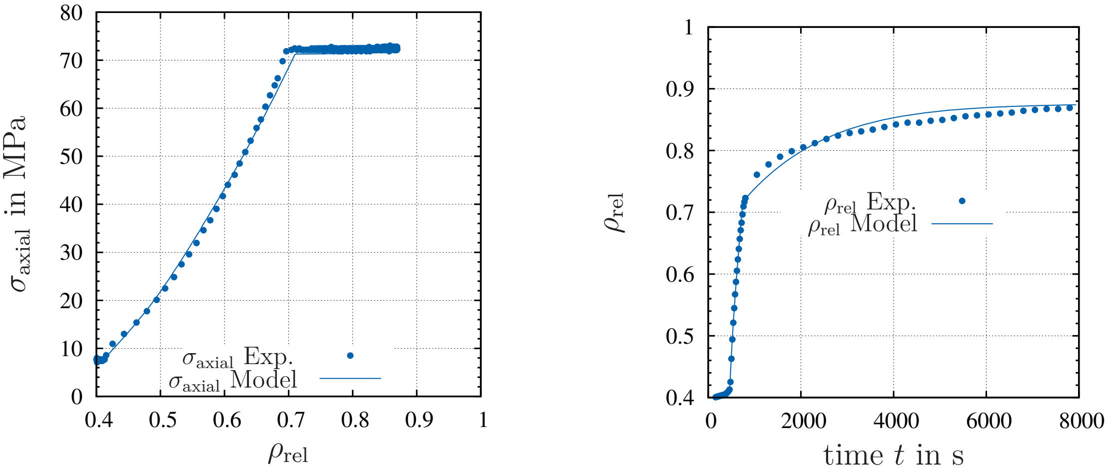

(a) Axial stress over relative density

(b) Relative density over time

Figure 5.12: Comparison between material model response and the experimental data

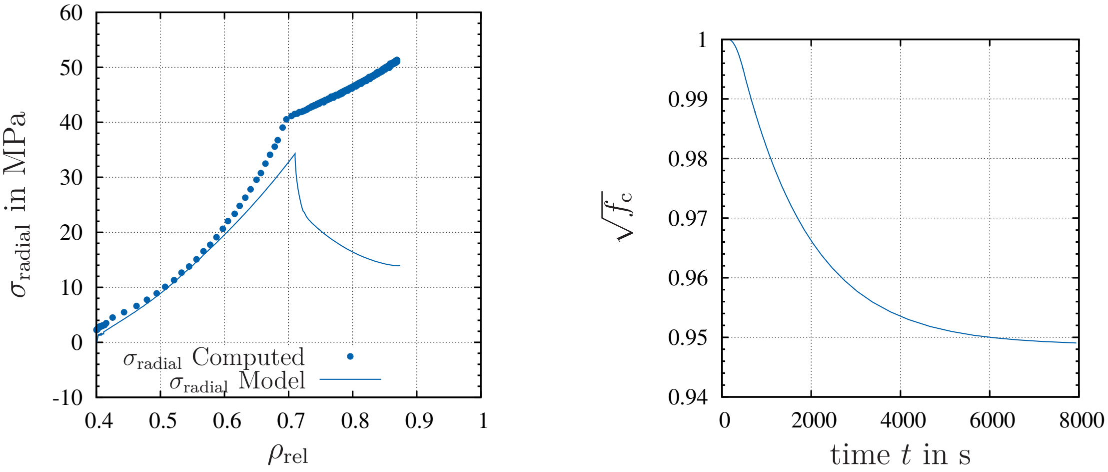

(a) Radial stress over relative density

(b) Creep variable over time

Figure 5.13: Comparison of radial stresses and the evolution of the sintering variable

of 25 kN. The results of the fit are shown in Fig. 5.14 with the fitted parameters $A_c = 2 \times 10^{-6}$ MPa and $c_\infty = 0.9$.

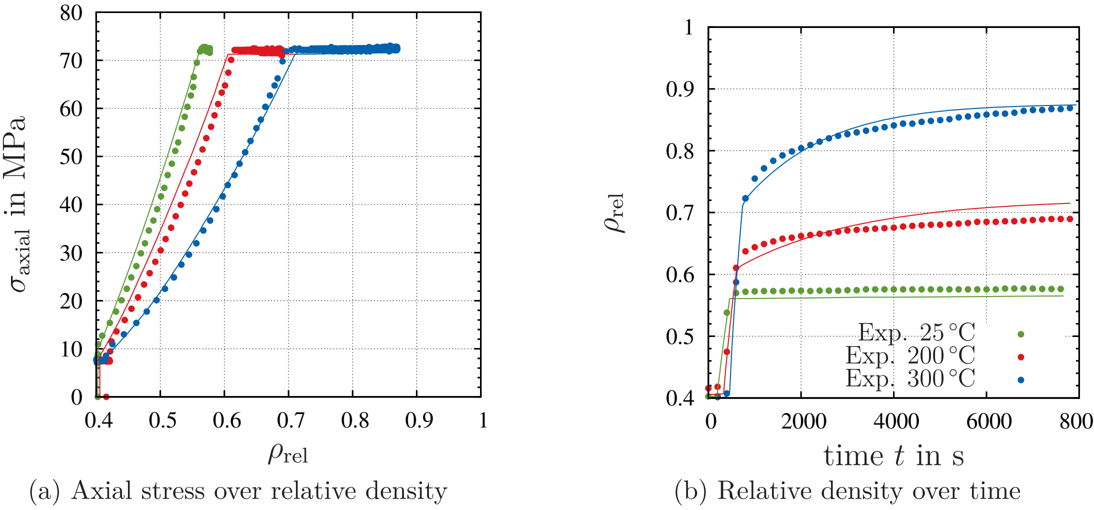

Figure 5.14: Comparison of creep experiments at Θ_c=25 °C, 200 °C and 300 °C and $F_c = 25$ kN with fitted material model (solid lines)

5.2.6 Tensile Stress Evolution

As a result of the sintering, the yield stress in tensile direction grows as reported in Sect. 2.5.6. Cold compacted specimens show a low resistance/yield stress in tensile direction and the parameter I_0 is set to 1 MPa. In the tensile yield stress hardening, Eq. (4.166), the parameter b_{t} has to be identified. This parameter is fitted with the help of the tensile experiments, and the fit is shown in Fig. 5.15 with $b_{\mathrm{t}} = 5.01$. The parameter c_β defines the slope of the sintering variable β_{t}. This sintering variable controls the tensile stress evolution and ranges from 0 to 1. Below the sintering temperature Θ_S, there is no evolution of β_{t}. The tensile specimens were produced at a dwell temperature of 500 °C. Due to this reason, the parameter c_β cannot be identified and is set to a small value of $7 \times 10^{-5}\,\mathrm{K}^{-1}$. Future research work could focus on investigating the yield stress for specimens produced under the same axial force but with different dwell temperatures. A summary of all identified parameters is given in Tab. 5.5.

5.3 Predictions

It is of interest to investigate the material model behavior beyond the experiments used for the parameter identification. For this reason, the material model is

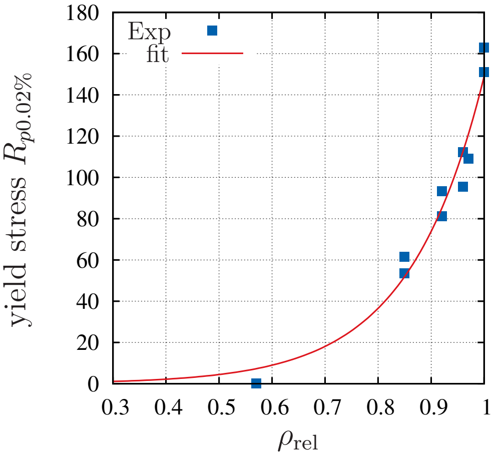

Figure 5.15: Fit of tensile hardening to experiments

Table 5.5: Identified parameter for the thermo-mechanical behavior of copper

K MPa	G MPa	α_Θ K^{-1}	β_k -	γ_k -	a_ξ MPa
4.00×10^4	2.40×10^4	1.51×10^{-5}	0.01	26.71	1.41
b_ξ -	c_ξ MPa	b_t -	I_0 MPa	Θ_S K	c_β K^{-1}
2.45	38.91	5.01	1.00	151.36	7.00×10^{-5}
m_k K^{-1}	m_ξ K^{-1}	A_c MPa	c_∞ -	ρ_solid $\mathrm{kg\,m^{-3}}$	
3.55×10^{-3}	4.65×10^{-3}	3.50×10^{-6}	0.90	8920	

compared to different experiments. First, the force-rate dependence is investigated. In a second step, the instationary creep experiments are compared, where first the force and then the temperature is applied. Furthermore, creep experiments at 500 °C and 700 °C are investigated.

5.3.1 Force-Rate Dependence

The force-rate experiments are described in Sect. 2.5.2. In Fig. 5.16a, the experiments at $\Theta_c = 300\,°\mathrm{C}$ show a larger force-rate dependence than the material model. At $\Theta_c = 700\,°\mathrm{C}$, the material model shows a smaller force-rate dependence than in the experiments. A possibility to improve the material model would be a Perzyna-type viscoplasticity model, where $F > 0$ is admissible and the plastic multiplier is calculated by $\Lambda = 1/\eta\langle F/\sigma_0\rangle^r$. The drawback in this case would be the separation between the rate effects given by the creep deformation and the viscous effects. Therefore, this approach is not followed here.

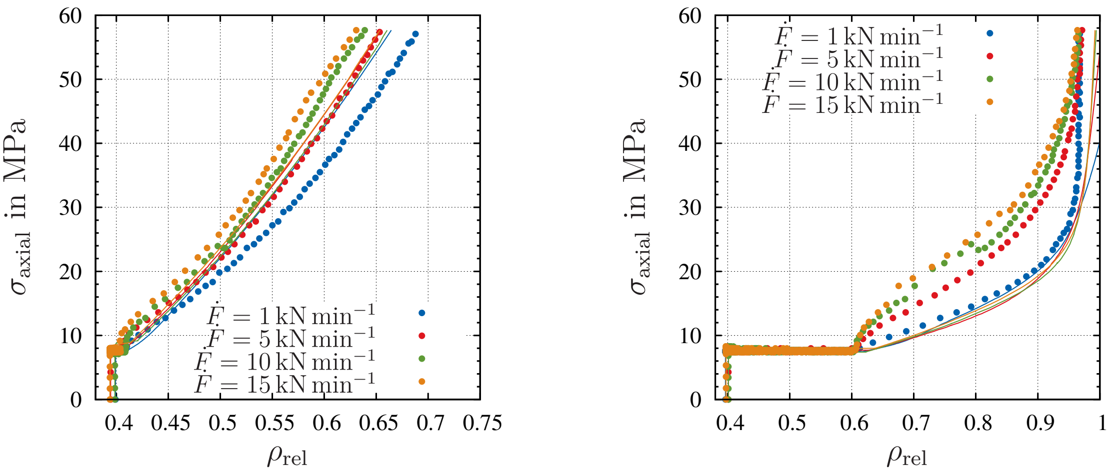

(a) Axial stress over relative density at $\Theta_c = 300\,°\mathrm{C}$

(b) Axial stress over relative density at $\Theta_c = 700\,°\mathrm{C}$

Figure 5.16: Force-rate experiments at different temperatures

5.3.2 Instationary Creep

In these experiments, the force is increased first – followed by an increase in temperature with a temperature rate of $\dot{\Theta} = 50\,°\mathrm{C\,min^{-1}}$, Fig. 5.17. Four different force levels are investigated: 2.5 kN, 5 kN, 15 kN and 25 kN. Here 2.5 kN is the lowest possible axial force in the FAST-machine. Fig. 5.18 shows the predictions of the material model. The prediction for the experiment with $F_c = 2.5\,\mathrm{kN}$ shows an overestimation of the relative density in Fig. 5.18b. In contrast, the prediction of

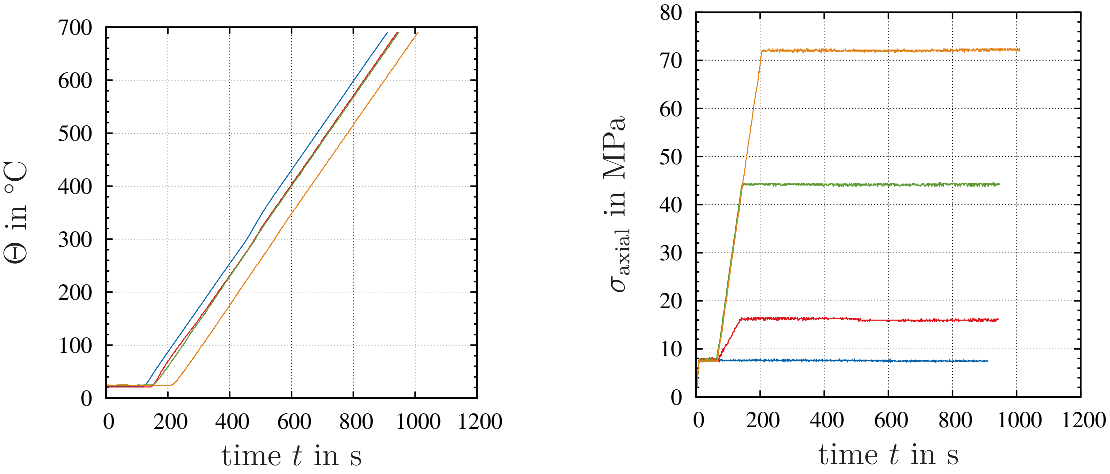

(a) Prescribed temperature in the experiments

(b) Prescribed axial stress

Figure 5.17: Loading path of experiments for the identification of the temperature dependent yield function

the material model for the experiment with $F_c = 5\,\text{kN}$ shows an underestimation. In general, the predictions indicate a good agreement – especially at the higher forces $F_c = 15\,\text{kN}$ and $F_c = 25\,\text{kN}$. The cold compaction part of the experiment and prediction is shown in Fig. 5.18a, also with a very good agreement.

5.3.3 Creep

The creep evolution equations are fitted to experiments for temperatures between $\Theta_c = 25\,°\text{C}$ and $\Theta_c = 300\,°\text{C}$ with a dwell force of 25 kN. For prediction, creep experiments at $\Theta_c = 300\,°\text{C}$ and different dwell force values are used, F_c=5 kN and 15 kN. The loading conditions are the same as shown in Fig. 5.11. First, the temperature is raised, followed by applying the axial force. The material model underestimates the creep behavior for these experiments, which is shown in Fig. 5.19. For further predictions, creep experiments at $\Theta_c = 500\,°\text{C}$ and $\Theta_c = 700\,°\text{C}$ are used at different force levels. The loading path for these experiments is shown in Fig. 5.20. First, the temperature is raised and kept constant, while the force is increased up to its constant level where it is held for 2 h. The predictions of the material model show a good agreement for the axial stress over the relative density in Fig. 5.21a. The relative density is underestimated for $F_c = 5\,\text{kN}$ in Fig. 5.21b. For higher force values, the material model shows a very good agreement with the experiments. For the same axial stress, the material model predictions of the creep experiments at $\Theta_c = 700\,°\text{C}$ show a higher relative density than the experiment in Fig. 5.21c.

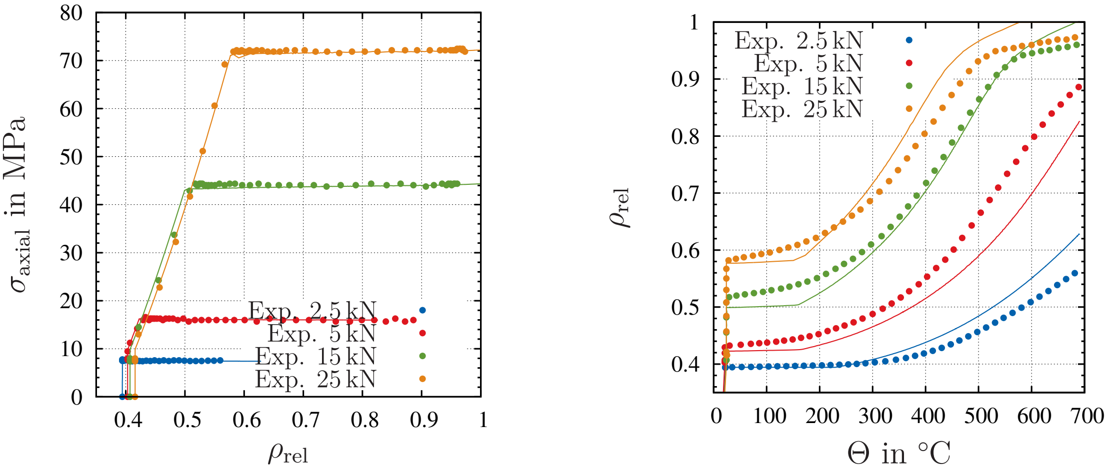

(a) Axial stress vs. relative density (b) Relative density vs. temperature

Figure 5.18: Prediction of instationary creep experiments by material model

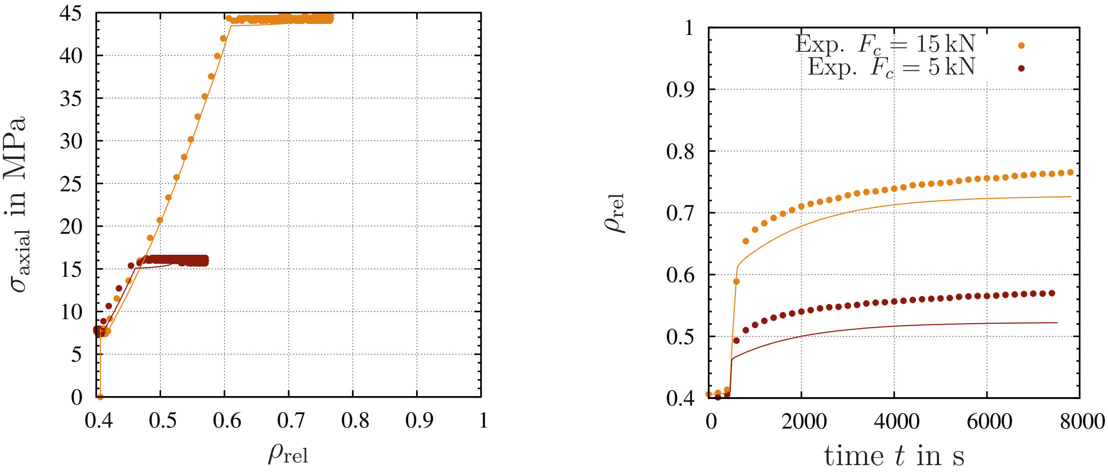

(a) Axial stress over relative density (b) Relative density over time

Figure 5.19: Comparison of creep experiments at $\Theta_c = 300\,°\text{C}$ and F_c=5 kN, 15 kN and 25 kN with material model response (solid lines)

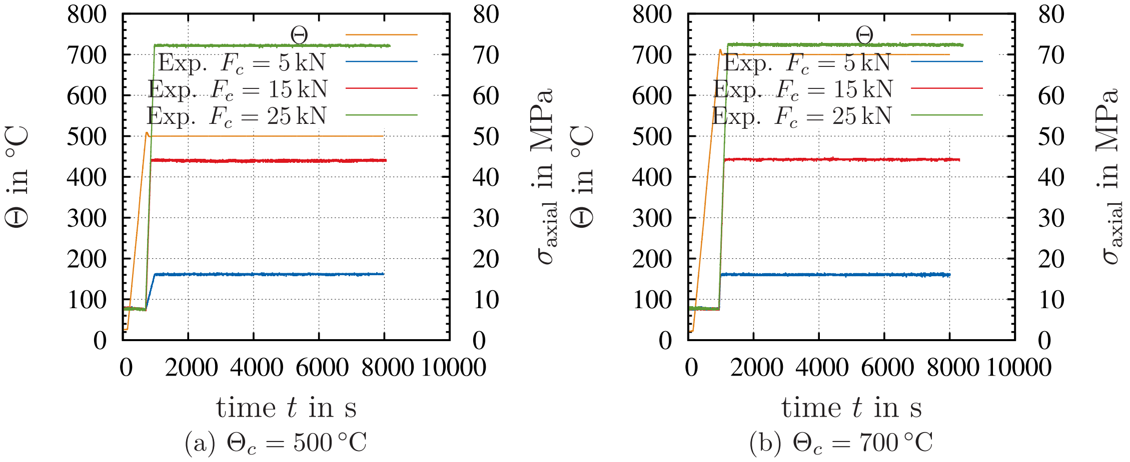

(a) $\Theta_c = 500\,°\text{C}$ (b) $\Theta_c = 700\,°\text{C}$

Figure 5.20: Loading path for creep experiments at $\Theta_c = 500\,°\text{C}$ and $\Theta_c = 700\,°\text{C}$

The predicted relative density for all different force values reaches a maximum value of one. In the experiments, the relative density lies between 0.94 and 0.99 and, thus, also shows a good agreement.

5.4 Summary

In general, the parameter identification shows that the material model is able to give a very good representation of the material behavior of the copper powder during sintering. The elasticity parameters are identified by experiments described in Carnavas [1996] and are assumed to be constant. Process-dependent elasticity parameters can be a further improvement for the model – but for the investigated sintering experiments, the constant parameters are sufficient. The linear thermal expansion behavior is identified with the help of the dilatometer experiments, see Fig. 5.5. The cold compaction experiments are used to identify the inelastic parameters, which describes the evolution of the yield surface. The model represents the experiments very well, see Fig. 5.7. The shrinkage behavior of the yield function with increasing temperature is adapted to sintering experiments at different temperatures. The material model also offers a good description of this specific behavior and of the vanishing deformation at $\rho_{\text{rel}} \approx 1$, Fig. 5.9.

The material model can be conveniently adapted to the creep experiments at different temperatures and the same axial force, see Fig. 5.12. Further improvements can be made for the radial stress identification, see Fig. 5.13a. It should be mentioned that the radial stresses cannot be measured and are thus computed by a model. Besides, the tensile stress hardening is identified by tensile tests with sintered specimens, and the model is able to represent the experiments very well.

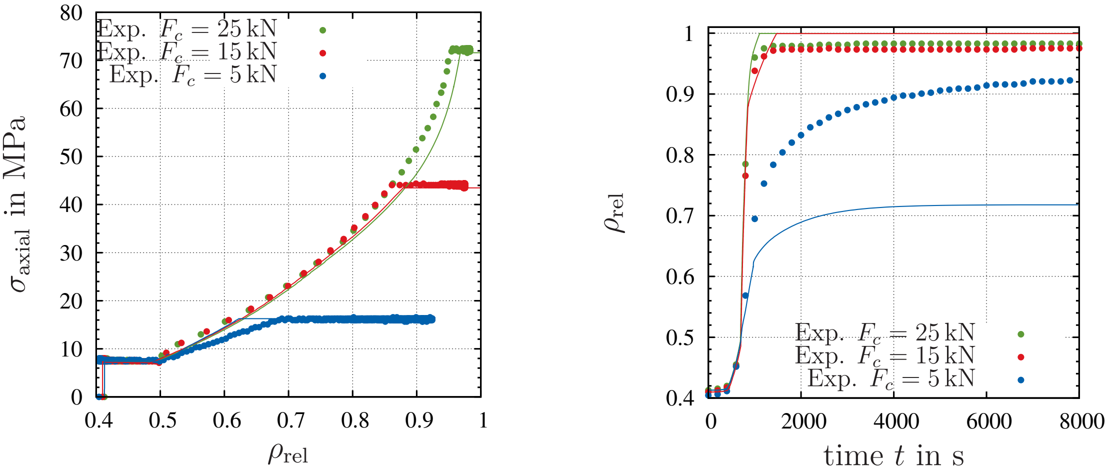

(a) Axial stress over relative density at $\Theta_c = 500\,°\text{C}$

(b) Relative density over at $\Theta_c = 500\,°\text{C}$

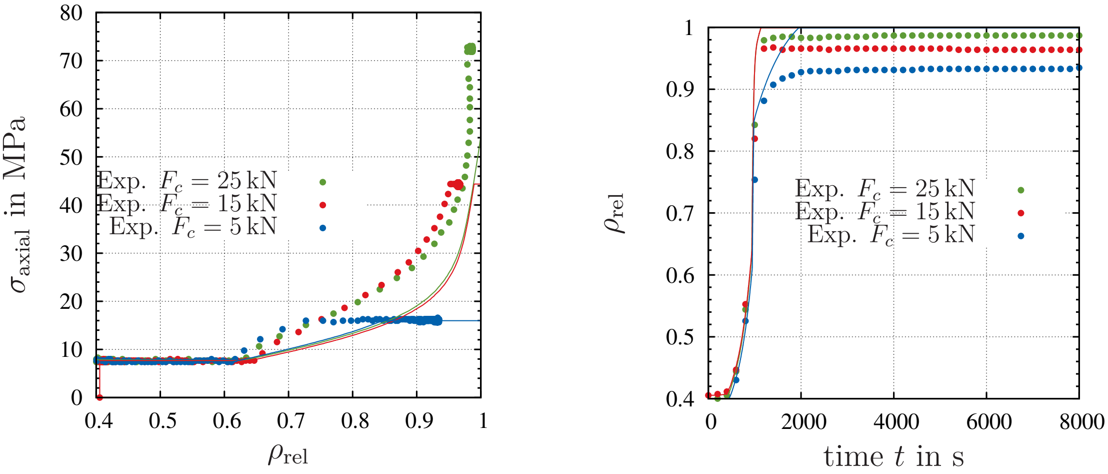

(c) Axial stress over relative density at $\Theta_c = 700\,°\text{C}$

(d) Relative density over at $\Theta_c = 700\,°\text{C}$

Figure 5.21: Prediction of creep experiments at $\Theta_c = 500\,°\text{C}$ and $\Theta_c = 700\,°\text{C}$

The predictions show how the material model behaves beyond the experiments used for the parameter identification. As the force-rate experiments cannot be represented by the model very well, this would be a point for further improvement of the model. Instead, the instationary creep experiments can be represented in an acceptable manner by the material model. Moreover, the model shows a good agreement with the creep experiments at 500 °C and 700 °C. Except for low forces with $F_c = 5\,\mathrm{kN}$ and $\Theta_c = 500\,^\circ\mathrm{C}$, the model behavior can be improved.

Keeping in mind the complex nature of the thermo-electro-mechanical sintering process, the material model generally reflects the experimental data very well.

5.5 Parameter Identification of Thermo-Electrical Properties

On the one hand, the information about the thermo-electrical properties of the copper powder is required for the simulation of the FAST-process. On the other hand, the tool system, which is made out of graphite, has to be considered. The required quantities are the heat capacity as well as the thermal and electrical conductivity. For the copper powder, the last two quantities depend not only on the temperature but also on the relative density as reported in Sect. 2.6.

5.5.1 Copper Powder

For the heat capacity, a linear dependence on the temperature is given in Sect. 4.7, and the equation reads

$$c_\mathrm{p}(\Theta) = c_{\mathrm{p}0}\left(1 + c_{\mathrm{p}S}(\Theta - \Theta_0)\right), \tag{4.232}$$

where the material parameters $c_{\mathrm{p}S}$, $c_{\mathrm{p}0}$ and the initial temperature Θ_0 have to be determined. $c_{\mathrm{p}0}$ describes the heat capacity at room temperature. The final fit is shown in Fig. 5.22a, and the parameters are specified in Tab. 5.6.

The thermal conductivity defined by the parameters a_Θ, b_Θ, c_Θ, d_Θ and e_Θ is given by

$$\kappa_\mathrm{th}(\rho_\mathrm{rel}, \Theta) = -a_\Theta\Theta + b_\Theta \tanh\left(\frac{\rho_\mathrm{rel} - c_\Theta}{d_\Theta}\right) + e_\Theta. \tag{4.218}$$

Fig. 5.22c shows the thermal conductivity over the relative density and the fit – also with a good agreement to the experimental data.[1] The thermal conductivity

---

[1] At lower relative densities, the thermal conductivity is assumed to be nearly constant. This ensures positive thermal conductivity values at higher temperatures. The thermal conductivity decreases, but should remain positive.

decreases at higher temperatures, and the surface fit is shown in Fig. 5.22d while the identified parameters are listed in Tab. 5.6.

The constitutive equation for the electrical conductivity is proposed in Sect. 4.6.6 and reads

$$\kappa_{\mathrm{el}}(\Theta, \rho_{\mathrm{rel}}) = \rho_{\mathrm{rel}}^2 \tilde{\kappa}_{\mathrm{el}}(\Theta) = \rho_{\mathrm{rel}}^2 (a_\varphi \Theta^{-b_\varphi} - c_\varphi). \tag{4.220}$$

The material parameters to be identified are a_φ, b_φ and c_φ. The model is fitted to the measured electrical conductivity for $\rho_{\mathrm{rel}} = 1.0$ with the parameters specified in Tab. 5.7. For the prediction at $\rho_{\mathrm{rel}} = 0.85$, the model shows an excellent agreement with the experimental curve. The model predicition is also shown for relative density values of 0.7 and 0.5, where no further measurements are available.

Table 5.6: Identified copper powder material parameters Eq. (4.232) and Eq. (4.218)

c_{p}		κ_{th}				
c_{p0} $\mathrm{J\,kg^{-1}\,K^{-1}}$	$c_{\mathrm{p}S}$ $\mathrm{K^{-1}}$	a_Θ $\mathrm{W\,m^{-1}\,K^{-2}}$	b_Θ $\mathrm{W\,m^{-1}\,K^{-1}}$	c_Θ -	d_Θ -	e_Θ $\mathrm{W\,m^{-1}\,K^{-1}}$
397.83	2.07×10^{-4}	0.05	214.60	0.83	0.17	259.80

Table 5.7: Identified copper powder material parameters for Eq. (4.220)

κ_{el}		
a_φ $\mathrm{S\,m^{-1}}$	b_φ -	c_φ $\mathrm{S\,m^{-1}}$
2.69×10^{10}	1.08	1.21×10^{6}

5.5.2 Graphite

As the powder is surrounded by the graphite tool system, the simulation of the temperature distribution as well as the electrical field distribution requires the heat capacity as well as the thermal and electrical conductivity. Additionally, the thermal expansion coefficient is determined. The tool system consists of graphite named R8510, produced by the SGL Carbon GmbH. For the heat capacity, again, the same linear dependence as for copper is assumed. For the thermal and electrical conductivity, a power-law dependence is proposed

$$c_{\mathrm{p}}(\Theta) = c_{\mathrm{p0}}\left(1 + c_{\mathrm{p}S}(\Theta - \Theta_0)\right), \qquad \kappa_{\mathrm{th}}(\Theta) = a_\Theta \Theta^{b_\Theta}, \qquad \kappa_{\mathrm{el}}(\Theta) = a_\varphi \Theta^{b_\varphi}. \tag{5.12}$$

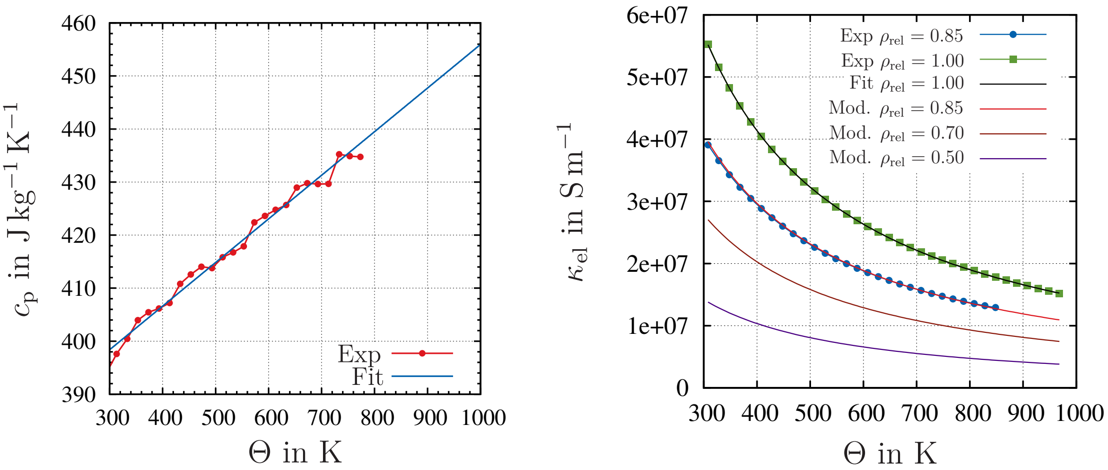

(a) Heat capacity

(b) Electrical conductivity

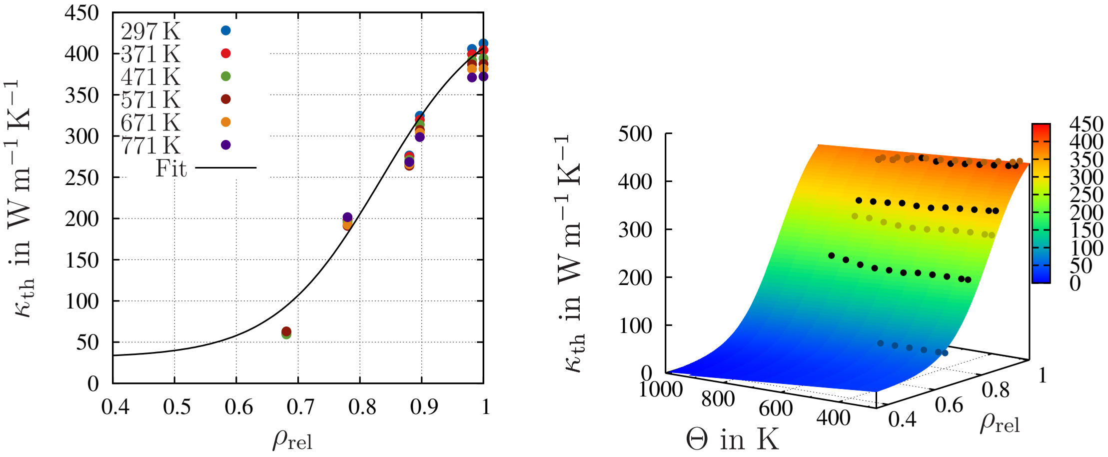

(c) Thermal conductivity over relative density

(d) Thermal conductivity

Figure 5.22: Fit of thermo-electrical properties of sintered copper

The parameters c_{p0}, $c_{\text{p}S}$, Θ_0, a_Θ, b_Θ, a_φ and b_φ have to be identified from the experiments in Sect. 2.7. The identified parameters are specified in Tab. 5.8 and Fig. 5.23 shows the fit as well as the experimental data. The fit of the thermal expansion behavior leads to $\alpha_\Theta = 4.554\,56 \times 10^{-6}\,\text{K}^{-1}$ – and the function that is fitted to the experimental data shows a good agreement.

Table 5.8: Identified graphite material parameters for Eq. (5.12)

c_{p}		κ_{th}		κ_{el}	
c_{p0} $\text{J}\,\text{kg}^{-1}\,\text{K}^{-1}$	$c_{\text{p}S}$ K^{-1}	a_Θ $\text{W}\,\text{m}^{-1}\,\text{K}^{-1}$	b_Θ -	a_φ $\text{S}\,\text{m}^{-1}$	b_φ -
8.96×10^{2}	1.62×10^{-3}	1.13×10^{3}	-4.25×10^{-1}	1.49×10^{4}	3.04×10^{-1}

5.5.3 Electrical Contact Conductance

If two parts are in contact, the electric potential shows a drop across the interface. This effect, which is known as *electric contact resistance*, is measured for graphite-copper and graphite-graphite contact in Sect. 2.8. The resistance originates from the surface roughness of the two parts in contact and depends on the contact pressure between the parts. The measured electrical contact resistance has to be converted to the contact conductance for the use in Abaqus. The total resistance is shown in Fig. 2.60b, and the contact resistance has to be computed. Due to the scatter of the specific resistance for graphite at room temperature, different resistance values are subtracted. These are $0\,\mu\Omega\,\text{m}$, $2\,\mu\Omega\,\text{m}$, $4\,\mu\Omega\,\text{m}$ and $6\,\mu\Omega\,\text{m}$. Higher values would lead to unphysical negative contact resistances. Fig. 5.24a lists the computed values of electrical contact conductance of the experiments. In addition, the electrical contact conductance is compared to data from the literature. In [Zavaliangos et al., 2004], the resistance is separated into an vertical and horizontal part, where the values are given by $\kappa^{\text{H}}_{C,\text{el,GG}} = 7.5 \times 10^{6}\,\text{S}\,\text{m}^{-2}$ as the horizontal and $\kappa^{\text{V}}_{C,\text{el,GG}} = 1.25 \times 10^{7}\,\text{S}\,\text{m}^{-2}$ as the vertical electrical contact conductance.

For the fit of the contact conductance of graphite-graphite, $\kappa_{C,\text{el,GG}}$ (in dependence of the pressure), the following function is proposed

$$\kappa_{C,\text{el}}(p) = \alpha_\varphi p^{\gamma_\varphi}, \tag{5.13}$$

with the material parameters α_φ and γ_φ. The identified parameters for the different curves are listed in Tab. 5.9, while Fig. 5.24b shows the fit together with the experimental data. A good agreement can be observed.

The same function, (5.13), is used for the fit of the contact conductance $\kappa_{C,\text{el,GC}}$ between graphite and copper. The identified parameters are reported in Tab. 5.10. The fit of the function (5.13), which is shown in Fig. 5.25, coincides well with the experimental data.

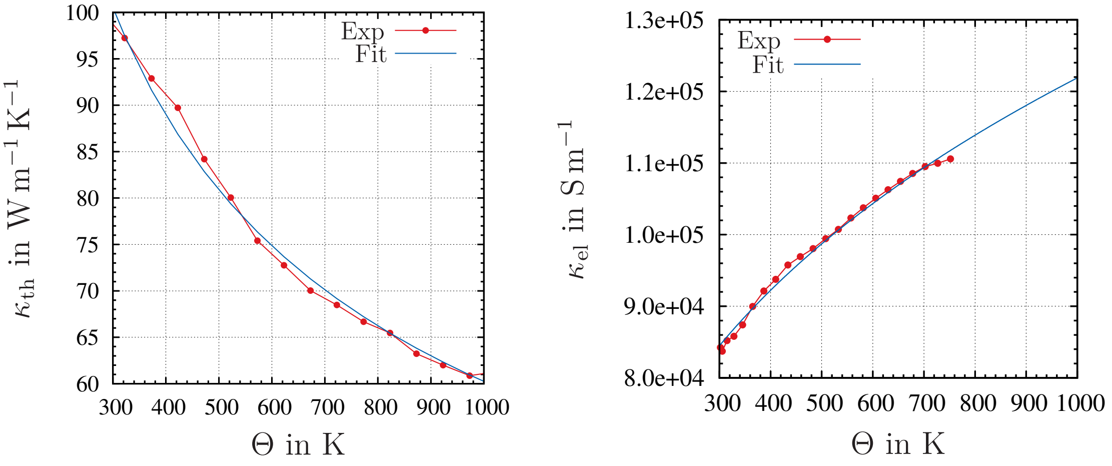

(a) Thermal conductivity

(b) Electrical conductivity

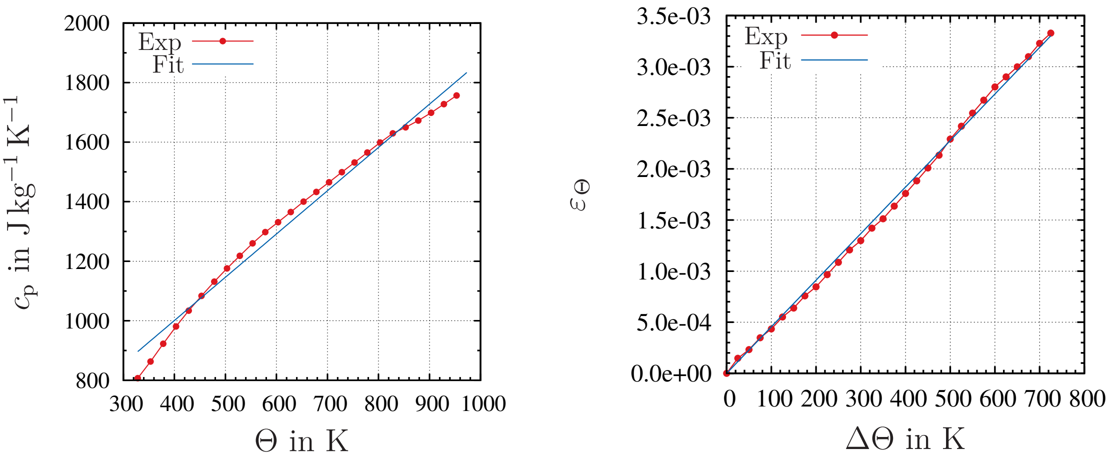

(c) Heat capacity

(d) Thermal expansion

Figure 5.23: Fit of thermo-electrical properties of graphite

Table 5.9: Identified graphite material parameters for Eq. (5.12) with graphite-graphite contact

	$\kappa_{C,\mathrm{el,GG0}}(p)$	$\kappa_{C,\mathrm{el,GG2}}(p)$	$\kappa_{C,\mathrm{el,GG4}}(p)$	$\kappa_{C,\mathrm{el,GG6}}(p)$
μΩ m	0	2	4	6
α_φ in S m^{-2}	2.07×10^6	1.92×10^6	1.58×10^6	7.99×10^5
γ_φ	0.39	0.46	0.58	0.87

Table 5.10: Identified graphite material parameters for Eq. (5.12) with graphite-copper contact

$\mu\Omega\,\mathrm{m}$	$\kappa_{C,\mathrm{el,GC0}}(p)$ 0	$\kappa_{C,\mathrm{el,GC2}}(p)$ 2	$\kappa_{C,\mathrm{el,GC4}}(p)$ 4	$\kappa_{C,\mathrm{el,GC6}}(p)$ 6
α_φ in $\mathrm{S\,m^{-2}}$	2.83×10^6	2.56×10^6	2.12×10^6	1.42×10^6
γ_φ	0.43	0.50	0.60	0.77

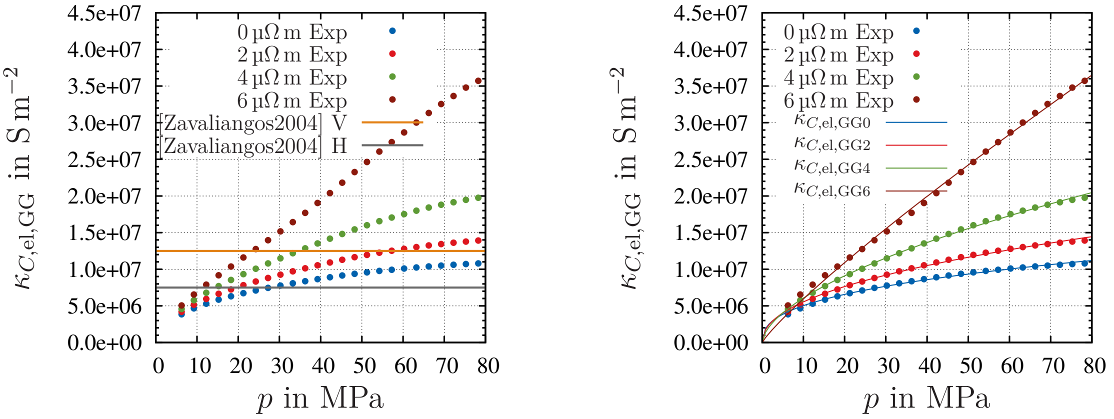

(a) Electrical contact conductance for graphite-graphite contact

(b) Electrical conductance for graphite-graphite contact

Figure 5.24: Fit of electric contact conductance (solid lines) to experimental data (points) for graphite-graphite contact

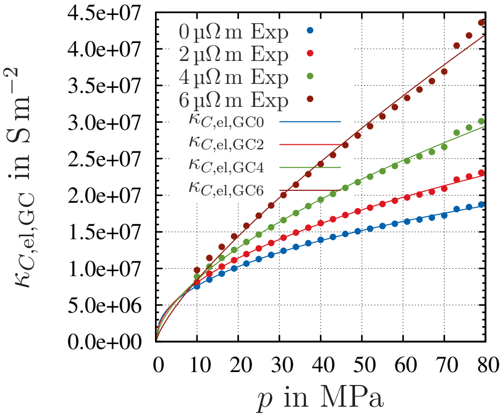

Figure 5.25: Fit of electric contact conductance for graphite-copper contact

5.5.4 Thermal Contact Conductance

Thermal contact resistance represents another kind of contact resistance. If two parts are in contact, a temperature drop across the interface due to the surface roughness of the two parts is possible. Due to the lack of experimental data for graphite-copper contact, the values for copper-copper contact are used. The thermal contact conductance of oxygen-free high conductivity (OFHC) copper in dependence of the contact pressure is measured in [Rao et al., 2004] and compared to the data of Fried and Kelley [1966]. Again, a power function is used for the fit of the thermal contact conductance to the experimental data from Rao et al. [2004]

$$\kappa_{C,\mathrm{th,CC}}(p) = \beta_\Theta p^{\gamma_\Theta}. \tag{5.14}$$

The final fit with the identified parameters $\beta_\Theta = 63.14 \times 10^3\,\mathrm{W\,m^{-2}\,K^{-1}}$ and $\gamma_\Theta = 1.62$, as can be seen in Fig. 5.26, shows a good agreement to the experimental data.

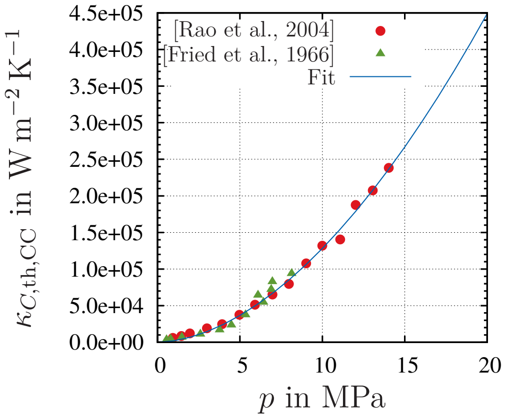

Figure 5.26: Fit of thermal contact conductance of OFHC copper contacts in dependence of the contact pressure in vacuum, data taken from [Rao et al., 2004]

6 Numerical Solution of Initial Boundary Value Problems

The aim of this chapter is to solve the initial boundary value problem, which consists of the balance relations of thermo-electro-mechanics together with constitutive relations, initial values and boundary conditions. Thus, the first step is to recap the thermo-electro-mechanical equations that form a system of partial differential equations together with the constitutive model. The solution strategy includes a clear application of the vertical method of lines (MOL). In this sense, this chapter offers the mathematical description of the thermo-electro-mechanical problem and its solution procedure. Starting from the variational forms of the balance relations, the spatial discretization with the finite element method is treated in a second step, leading to a system of differential-algebraic equations (DAE). This DAE-system is solved with the backward Euler method in the temporal domain. The resulting nonlinear equation systems are solved with the Multilevel-Newton algorithm in each time step. The MLNA is commonly applied in the finite element context with constitutive equations of evolutionary type. On the local level of the MLNA, a nonlinear system of equations originating from the material model has to be solved to compute the internal variables at the next time step. This nonlinear system is commonly solved with the Newton-Raphson method. Furthermore, the consistent tangent operator has to be calculated on the local level. This so-called stress algorithm is also explained in this chapter.

6.1 Local Form of Initial Boundary Value Problem

The three-field coupled problem consists of the equilibrium condition, Eq. (3.48),

$$\vec{0} = \operatorname{Div} \mathbf{T}_{\mathrm{R}} + \rho_0 \vec{k}$$

the heat conduction equation, Eq. (4.234),

$$c_{\mathrm{p}} \dot{\Theta} = -\frac{1}{\rho_0} \operatorname{Div} \vec{q}_{\mathrm{R}} + r_{\mathrm{el}}, \qquad r_{\mathrm{el}} = -\frac{1}{\rho_0} \operatorname{Grad} \varphi \cdot \vec{j}_{\mathrm{R}}$$

and the stationary charge equation, Eq. (3.78),

$$\vec{0} = \operatorname{Div} \vec{j}_{\mathrm{R}}.$$

Constitutive equations are required to complete these balance relations. The stress state is given by the elasticity relation

$$\tilde{\mathbf{T}}(\vec{X},t) = \mathbf{h}(\mathbf{C}(\vec{X},t), \Theta(\vec{X},t), \mathbf{q}(\vec{X},t)), \tag{6.1}$$

described by the second Piola-Kirchhoff stress tensor $\tilde{\mathbf{T}}$, depending on the displacement field, the temperature field and on internal variables. The internal variables characterizing the model in Chap. 4 are the plastic strains, the yield stress, the sintering variable and the creep deformation $\mathbf{q} = \{\mathbf{C}_\mathrm{p}, k_\mathrm{M}, \beta_\mathrm{t}, f_\mathrm{c}\}$, see Tab. 4.3. These evolution equations are ordinary differential equations of first order. They can be written in the general form as

$$\mathbf{A}\dot{\mathbf{q}}(\vec{X},t) = \tilde{\mathbf{r}}(\mathbf{C}(\vec{X},t), \Theta(\vec{X},t), \mathbf{q}(\vec{X},t)). \tag{6.2}$$

The material model proposed in Chap. 4 is a compressible thermo-elastoplasticity model, featuring a case distinction between an elastic and a plastic part. The model is based on a yield function, and the internal variables evolve according to ordinary differential equations under the constraint of the yield function. The yield condition $\tilde{F} = 0$ is an algebraic constraint acting on the evolution equations.

In order to complete the problem, initial values and boundary conditions are required. This means that the temperature, the electric potential and the motion have to be specified in the material body $\mathcal{B}$.

In this work, the influence of inertia is neglected. This means that the acceleration term in the balance of momentum is omitted and that quasistatic conditions are assumed. In this case, the problem still depends on the time due to transient boundary conditions and time-dependent internal processes, resulting in time-dependent partial differential equations, [Fritzen, 1997].

Since a DAE-system is present and the fields are coupled with each other, the initial values for the displacement, temperature, electrical field as well as for the internal variables have to be prescribed

$$\vec{u}(\vec{X},t_0) = \vec{u}_0(\vec{X}), \qquad \forall \vec{X} \in \boldsymbol{\mathcal{R}}\left[\mathcal{B}\right], \tag{6.3}$$

$$\Theta(\vec{X},t_0) = \Theta_0(\vec{X}), \qquad \forall \vec{X} \in \boldsymbol{\mathcal{R}}\left[\mathcal{B}\right], \tag{6.4}$$

$$\varphi(\vec{X},t_0) = \varphi_0(\vec{X}), \qquad \forall \vec{X} \in \boldsymbol{\mathcal{R}}\left[\mathcal{B}\right], \tag{6.5}$$

$$\mathbf{q}(\vec{X},t_0) = \mathbf{q}_0(\vec{X}), \qquad \forall \vec{X} \in \boldsymbol{\mathcal{R}}\left[\mathcal{B}\right], \tag{6.6}$$

expressed in material representation.

For the application of the boundary conditions, three different kinds can be classified. The Dirichlet boundary condition[1] $\partial_D \boldsymbol{\mathcal{R}}\left[\mathcal{B}\right]$ describes the actual field variables, which are the displacement, temperature and the electric potential. The

---

[1] Also known as *geometric boundary condition.*

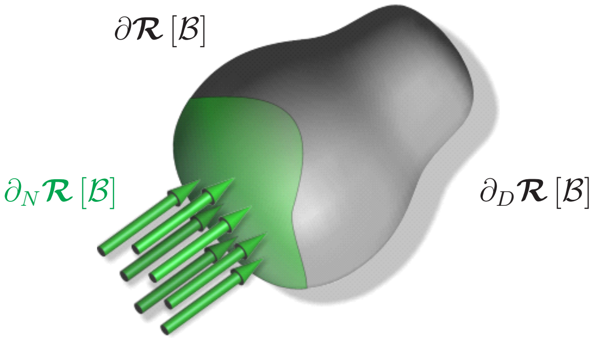

Figure 6.1: Dirichlet and Neumann boundary conditions

Neumann boundary condition[2] $\partial_N\boldsymbol{\mathcal{R}}\,[\mathcal{B}]$ describes the directional derivative of the field variable. The third kind of boundary condition is a combination of the first two. Convective heating or cooling are examples for this kind of boundary condition, see [Incropera et al., 2007, p. 78].

The material surface is split into subsets for the application of the prescribed Dirichlet and Neumann boundary conditions, see Fig. 6.1. In summary, the conditions for the subsets read

$$\partial\boldsymbol{\mathcal{R}}\,[\mathcal{B}] = \partial_{\mathrm{u}}\boldsymbol{\mathcal{R}}\,[\mathcal{B}] \cup \partial_{\mathrm{s}}\boldsymbol{\mathcal{R}}\,[\mathcal{B}] = \partial_{\Theta}\boldsymbol{\mathcal{R}}\,[\mathcal{B}] \cup \partial_{\mathrm{q}}\boldsymbol{\mathcal{R}}\,[\mathcal{B}] = \partial_{\varphi}\boldsymbol{\mathcal{R}}\,[\mathcal{B}] \cup \partial_{\mathrm{j}}\boldsymbol{\mathcal{R}}\,[\mathcal{B}] \tag{6.7}$$

with

$$\partial_{\mathrm{u}}\boldsymbol{\mathcal{R}}\,[\mathcal{B}] \cap \partial_{\mathrm{s}}\boldsymbol{\mathcal{R}}\,[\mathcal{B}] = \varnothing, \quad \partial_{\Theta}\boldsymbol{\mathcal{R}}\,[\mathcal{B}] \cap \partial_{\mathrm{q}}\boldsymbol{\mathcal{R}}\,[\mathcal{B}] = \varnothing, \quad \partial_{\varphi}\boldsymbol{\mathcal{R}}\,[\mathcal{B}] \cap \partial_{\mathrm{j}}\boldsymbol{\mathcal{R}}\,[\mathcal{B}] = \varnothing. \tag{6.8}$$

This means that it is possible to apply either a Dirichlet boundary condition for example displacements or the Neumann boundary condition-like tractions, but not both at the same position and with the same direction. For example, a combination of Dirichlet and Neumann boundary conditions occurs for convection or displacement-dependent surface tractions at the surface. In this case, the boundary reads

$$\partial_N\boldsymbol{\mathcal{R}}\,[\mathcal{B}] = \partial_{\Theta}\boldsymbol{\mathcal{R}}\,[\mathcal{B}] \cup \partial_{\mathrm{q}}\boldsymbol{\mathcal{R}}\,[\mathcal{B}] \cup \partial_{\Theta\mathrm{q}}\boldsymbol{\mathcal{R}}\,[\mathcal{B}]\,, \quad \partial_{\Theta}\boldsymbol{\mathcal{R}}\,[\mathcal{B}] \cap \partial_{\mathrm{q}}\boldsymbol{\mathcal{R}}\,[\mathcal{B}] \cap \partial_{\Theta\mathrm{q}}\boldsymbol{\mathcal{R}}\,[\mathcal{B}] = \varnothing \tag{6.9}$$

The Dirichlet boundary conditions over a certain time interval with $t \in \mathbb{R}^+$ and $t \in \,]t_0, t_e[$ can be defined on the subsets as

$$\vec{u}(\vec{X}, t) = \bar{\vec{u}}(\vec{X}, t), \qquad \forall \vec{X} \in \partial_{\mathrm{u}}\boldsymbol{\mathcal{R}}\,[\mathcal{B}] \tag{6.10}$$

$$\Theta(\vec{X}, t) = \bar{\Theta}(\vec{X}, t), \qquad \forall \vec{X} \in \partial_{\Theta}\boldsymbol{\mathcal{R}}\,[\mathcal{B}] \tag{6.11}$$

$$\varphi(\vec{X}, t) = \bar{\varphi}(\vec{X}, t), \qquad \forall \vec{X} \in \partial_{\varphi}\boldsymbol{\mathcal{R}}\,[\mathcal{B}] \tag{6.12}$$

---

[2] Also called *natural* or *dynamic boundary condition*.

The prescribed Neumann boundary conditions over the time are given by

$$\vec{t}_{\mathrm{R}} = \mathbf{T}_{\mathrm{R}}\vec{n}_{\mathrm{R}} = \vec{s}(\vec{X},t), \qquad \forall\vec{X} \in \partial_{\mathrm{s}}\boldsymbol{\mathcal{R}}\,[\mathcal{B}] \tag{6.13}$$

$$q_{\mathrm{R}} = \vec{q}_{\mathrm{R}} \cdot \vec{n}_{\mathrm{R}} = f_q(\vec{X},t), \qquad \forall\vec{X} \in \partial_{\mathrm{q}}\boldsymbol{\mathcal{R}}\,[\mathcal{B}] \tag{6.14}$$

$$j_{\mathrm{R}} = \vec{j}_{\mathrm{R}} \cdot \vec{n}_{\mathrm{R}} = f_j(\vec{X},t), \qquad \forall\vec{X} \in \partial_{\mathrm{j}}\boldsymbol{\mathcal{R}}\,[\mathcal{B}] \tag{6.15}$$

and in the case of mixed boundary conditions, the prescribed heat flux reads

$$q_{\mathrm{R}} = \vec{q}_{\mathrm{R}} \cdot \vec{n}_{\mathrm{R}} = f_c(\vec{X},\Theta,t), \qquad \forall\Theta,\vec{X} \in \partial_{\Theta\mathrm{q}}\boldsymbol{\mathcal{R}}\,[\mathcal{B}]\,. \tag{6.16}$$

The water cooling system in the FAST-machine will be modeled by convective cooling. In this case, mixed boundary conditions are present and the linear temperature dependence is assumed

$$\overline{q}_{\mathrm{con}} = h_{\mathrm{c}}(\Theta(\vec{x}) - \Theta_{\mathrm{f}}), \qquad \text{for } \vec{x} \in \partial_{\Theta\mathrm{q}}\boldsymbol{\chi}_t\,[\mathcal{B}] \text{ and } t \in\,]t_{\mathrm{i}}, t_{\mathrm{e}}[, \tag{6.17}$$

with the heat transfer coefficient h_{c} and the absolute temperature of the surrounding fluid Θ_{f} (in K). Another possibility would be to use fluid-structure interaction to determine the heat flux, see [Hartmann et al., 2009b; Birken et al., 2010].

Radiation occurs inside the vacuum chamber, meaning that the graphite die system emits energy. This radiative heat flux can be described by

$$\overline{q}_{\mathrm{rad}} = \epsilon\sigma(\Theta^4(\vec{x}) - \Theta_\infty^4), \qquad \text{for } \vec{x} \in \partial_{\Theta\mathrm{q}}\boldsymbol{\chi}_t\,[\mathcal{B}] \text{ and } t \in\,]t_{\mathrm{i}}, t_{\mathrm{e}}[, \tag{6.18}$$

where σ is the Stefan-Boltzmann constant ($\sigma = 5.67 \times 10^{-8}\,\mathrm{W\,m^{-2}\,K^{-4}}$), and Θ_∞ is the absolute temperature of the surroundings. The emissivity ϵ depends on the surface material and is between zero and one.

The boundary conditions Eq. (6.13), Eq. (6.14) and Eq. (6.15) are deformation dependent because the surface changes due to the deformation. This can be shown by the definition of the stress vector Eq. (3.35), the heat flux and the current density vector Eq. (3.39)

$$\mathbf{T}_{\mathrm{R}}\vec{n}_{\mathrm{R}}\,\mathrm{d}A = \mathbf{T}\vec{n}\,\mathrm{d}a, \qquad \vec{q}_{\mathrm{R}} \cdot \vec{n}_{\mathrm{R}}\,\mathrm{d}A = \vec{q} \cdot \vec{n}\,\mathrm{d}a, \qquad \vec{j}_{\mathrm{R}} \cdot \vec{n}_{\mathrm{R}}\,\mathrm{d}A = \vec{j} \cdot \vec{n}\,\mathrm{d}a, \tag{6.19}$$

and with the help of Eq. (3.8) leading to

$$\mathrm{d}a = \sqrt{\mathrm{d}\vec{a} \cdot \mathrm{d}\vec{a}} = (\det\mathbf{F})\sqrt{\vec{n}_{\mathrm{R}} \cdot (\mathbf{F}^{-1}\mathbf{F}^{-\mathrm{T}}\vec{n}_{\mathrm{R}})}\,\mathrm{d}A. \tag{6.20}$$

With the definition of the initial values and boundary conditions, the IBVP is completed. The equations describing the thermo-electro-mechanical problem are summarized in Tab. 6.1. In general, this nonlinear IBVP cannot be solved analytically. Thus, it is necessary to perform a solution based on variational principles and to apply the finite element method.

Table 6.1: Local form of initial boundary value problem

On the region $\boldsymbol{\mathcal{R}}\,[\mathcal{B}]\times\,]t_0, t_e[$ the displacement field $\vec{u}(\vec{X}, t)$, the temperature field $\Theta(\vec{X}, t)$ as well as the electric potential field $\varphi(\vec{X}, t)$ have to be determined by

$$\vec{0} = \operatorname{Div} \mathbf{T}_{\mathrm{R}} + \rho_0 \vec{k}, \tag{3.48}$$

$$c_{\mathrm{p}}\dot{\Theta} = -\frac{1}{\rho_0} \operatorname{Div} \vec{q}_{\mathrm{R}} + r_{\mathrm{el}}, \qquad r_{\mathrm{el}} = -\frac{1}{\rho_0} \operatorname{Grad} \varphi \cdot \vec{j}_{\mathrm{R}} \tag{4.234, 4.235}$$

$$\vec{0} = \operatorname{Div} \vec{j}_{\mathrm{R}}, \tag{3.78}$$

$$\boldsymbol{\mathsf{A}}\dot{\boldsymbol{\mathsf{q}}} = \tilde{\boldsymbol{\mathsf{r}}}(\mathbf{C}, \Theta, \boldsymbol{\mathsf{q}}) \tag{6.2}$$

with the constitutive relations

$$\tilde{\mathbf{T}} = \mathbf{h}(\mathbf{C}, \Theta, \boldsymbol{\mathsf{q}}), \qquad \tilde{\mathbf{T}} = \mathbf{F}^{-1}\mathbf{T}_{\mathrm{R}} \tag{6.1}$$

$$\vec{q}_{\mathrm{R}} = -\boldsymbol{\kappa}_{\mathrm{th}}^{\mathrm{R}} \operatorname{Grad} \Theta, \qquad \boldsymbol{\kappa}_{\mathrm{th}}^{\mathrm{R}} = \kappa_{\mathrm{th}}(\Theta, \rho_{\mathrm{rel}})(\det \mathbf{F})\mathbf{C}^{-1} \tag{4.216, 4.217}$$

$$\vec{j}_{\mathrm{R}} = -\boldsymbol{\kappa}_{\mathrm{el}}^{\mathrm{R}} \operatorname{Grad} \varphi, \qquad \boldsymbol{\kappa}_{\mathrm{el}}^{\mathrm{R}} = \kappa_{\mathrm{el}}(\Theta, \rho_{\mathrm{rel}})(\det \mathbf{F})\mathbf{C}^{-1} \tag{4.221, 4.222}$$

as well as the initial values and the boundary conditions

$$\vec{u}(\vec{X}, t_0) = \vec{u}_0(\vec{X}), \quad \Theta(\vec{X}, t_0) = \Theta_0(\vec{X}), \tag{6.3,6.4}$$

$$\varphi(\vec{X}, t_0) = \varphi_0(\vec{X}), \quad \boldsymbol{\mathsf{q}}(\vec{X}, t_0) = \boldsymbol{\mathsf{q}}_0(\vec{X}), \tag{6.5,6.6}$$

$$\vec{u}(\vec{X}, t) = \bar{\vec{u}}(\vec{X}, t), \quad \mathbf{T}_{\mathrm{R}}\vec{n}_{\mathrm{R}} = \vec{s}(\vec{X}, t), \tag{6.10, 6.13}$$

$$\Theta(\vec{X}, t) = \bar{\Theta}(\vec{X}, t), \quad \vec{q}_{\mathrm{R}} \cdot \vec{n}_{\mathrm{R}} = f_q(\vec{X}, t) + f_c(\vec{X}, \Theta, t), \tag{6.11, 6.14, 6.16}$$

$$\varphi(\vec{X}, t) = \bar{\varphi}(\vec{X}, t), \quad \vec{j}_{\mathrm{R}} \cdot \vec{n}_{\mathrm{R}} = f_j(\vec{X}, t). \tag{6.12, 6.15}$$

The balance relations consisting of the balance of momentum, the heat conduction equation and the steady-state charge equation are coupled with each other, see Fig. 6.2. The temperature field and the mechanical field are coupled by the thermal expansion and the temperature dependence of the mechanical behavior – the temperature-dependent yield function, for example. The mechanical field is coupled to the temperature field by the relative density dependence of the thermal conductivity, see Fig. 5.22c. The heat due to the mechanical work will be neglected because it is assumed that the main heating comes from the electrical field due to Joule heating. The electrical field is coupled to the temperature field by the temperature-dependent electrical conductivity, see Fig. 5.22b. Between the mechanical and the electrical field, a one-way coupling exists. All other fields are connected by a two-way coupling. The mechanical field influences the electrical field by the relative density dependence of the electrical conductivity and the deformation dependence of the current flow over surfaces. The deformation dependence also holds for the heat flux over surfaces.

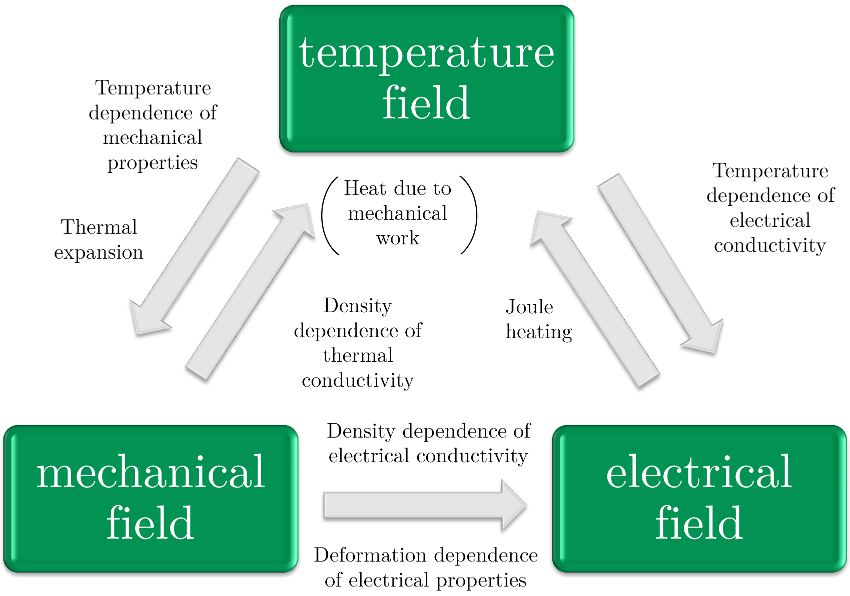

Figure 6.2: Thermo-Electro-Mechanical coupling

6.2 Variational Form of Initial Boundary Value Problem

The finite element method is based on a variational formulation of the IBVP, which will be derived from the local form of the thermo-electro-mechanical problem stated in Tab. 6.1 in the following. The variational formulation is also known as the weak form. In order to derive this form, the equations are multiplied with test functions and integrated over the whole domain. Additionally, the divergence theorem is applied to reduce the derivative by one order and to enlarge the space of admissible functions.

6.2.1 Weak Form of the Balance of Momentum

For the transformation of the local balance of momentum into its weak form, a test function out of the set

$$\boldsymbol{\mathcal{V}}_u := \left\{ \delta\vec{u}\colon \boldsymbol{\mathcal{R}}\,[\mathcal{B}] \to \mathbb{R}^3 \;\middle|\; \delta\vec{u}(\vec{X}) = \vec{0} \text{ for } \vec{X} \in \partial_{\mathrm{u}}\boldsymbol{\mathcal{R}}\,[\mathcal{B}] \right\} \tag{6.21}$$

is defined, where $\delta\vec{u}(\vec{X}) \in \boldsymbol{\mathcal{V}}_u$ are the virtual displacements, which vanish for Dirichlet boundary conditions. The Neumann boundary conditions are automatically satisfied by the weak form, see [Jeltsch-Fricker, 2007, p. 209] and the literature cited therein.

The multiplication with the virtual displacements and the integration over the volume results in

$$\int\limits_{\boldsymbol{\mathcal{R}}[\mathcal{B}]} \operatorname{Div} \mathbf{T}_{\mathrm{R}}(\vec{X},t) \cdot \delta\vec{u}(\vec{X})\,\mathrm{d}V + \int\limits_{\boldsymbol{\mathcal{R}}[\mathcal{B}]} \rho_0(\vec{X})\vec{k}(\vec{X},t) \cdot \delta\vec{u}(\vec{X})\,\mathrm{d}V = 0. \tag{6.22}$$

With the help of the relation

$$\operatorname{Div} \mathbf{T}_{\mathrm{R}} \cdot \delta\vec{u} = \operatorname{Div}(\mathbf{T}_{\mathrm{R}}^{\mathrm{T}}\delta\vec{u}) - \mathbf{T}_{\mathrm{R}} \cdot \operatorname{Grad}\delta\vec{u}, \tag{6.23}$$

the divergence theorem[3] and the Cauchy-theorem (3.35) $\vec{t}_{\mathrm{R}} = \mathbf{T}_{\mathrm{R}}\vec{n}_{\mathrm{R}}$, one obtains

$$\int\limits_{\boldsymbol{\mathcal{R}}[\mathcal{B}]} \mathbf{T}_{\mathrm{R}} \cdot \operatorname{Grad}\delta\vec{u}\,\mathrm{d}V = \int\limits_{\boldsymbol{\mathcal{R}}[\mathcal{B}]} \rho_0\vec{k} \cdot \delta\vec{u}\,\mathrm{d}V + \int\limits_{\partial_{\mathrm{s}}\boldsymbol{\mathcal{R}}[\mathcal{B}]} \vec{t}_{\mathrm{R}} \cdot \delta\vec{u}\,\mathrm{d}A. \tag{6.24}$$

Due to the relation between the first and the second Piola Kirchhoff stress tensor, $\mathbf{T}_{\mathrm{R}} = \mathbf{F}\tilde{\mathbf{T}}$, and the symmetry of the second Piola Kirchhoff stress tensor, the identity

$$\tilde{\mathbf{T}} \cdot \left(\mathbf{F}^{\mathrm{T}}\operatorname{Grad}\delta\vec{u}\right) = \tilde{\mathbf{T}} \cdot \frac{1}{2}\left[\mathbf{F}^{\mathrm{T}}\operatorname{Grad}\delta\vec{u} + (\operatorname{Grad}\delta\vec{u})^{\mathrm{T}}\,\mathbf{F}\right] = \tilde{\mathbf{T}} \cdot \delta\mathbf{E} \tag{6.25}$$

holds – leading to

$$\int\limits_{\boldsymbol{\mathcal{R}}[\mathcal{B}]} \tilde{\mathbf{T}} \cdot \delta\mathbf{E}\,\mathrm{d}V = \int\limits_{\boldsymbol{\mathcal{R}}[\mathcal{B}]} \rho_0\vec{k} \cdot \delta\vec{u}\,\mathrm{d}V + \int\limits_{\partial_{\mathrm{s}}\boldsymbol{\mathcal{R}}[\mathcal{B}]} \vec{t}_{\mathrm{R}} \cdot \delta\vec{u}\,\mathrm{d}A, \tag{6.26}$$

---

[3] The divergence theorem relates surface integrals with volume integrals: $\int \operatorname{Div}(\mathbf{T}_{\mathrm{R}}^{\mathrm{T}}\delta\vec{u})\,\mathrm{d}V = \int (\mathbf{T}_{\mathrm{R}}^{\mathrm{T}}\delta\vec{u}) \cdot \vec{n}_{\mathrm{R}}\,\mathrm{d}A$

where the virtual work can be derived with the definition of the Green strain tensor Eq. (3.13) and the Gateaux derivative

$$\delta\mathbf{E} := \mathrm{D}_{\vec{u}}\,\mathbf{E}(\vec{u})[\delta\vec{u}] = \frac{1}{2}\left(\mathbf{F}^{\mathrm{T}}\,\mathrm{Grad}\,\delta\vec{u} + (\mathrm{Grad}\,\delta\vec{u})^{T}\mathbf{F}\right). \tag{6.27}$$

The weak form of the balance of momentum in the current configuration reads

$$\int\limits_{\chi_t[\mathcal{B}]} \mathbf{T}\,(\vec{x},t)\cdot\mathrm{grad}\,\delta\vec{u}\,\mathrm{d}v = \int\limits_{\chi_t[\mathcal{B}]} \rho\,(\vec{x},t)\,\vec{k}\,(\vec{x},t)\cdot\delta\vec{u}\,\mathrm{d}v + \int\limits_{\partial_{\mathrm{s}}\chi_t[\mathcal{B}]} \vec{t}\,(\vec{x},t)\cdot\delta\vec{u}\,\mathrm{d}a \tag{6.28}$$

with the Cauchy stress tensor $\mathbf{T} = (\det\mathbf{F})^{-1}\mathbf{F}\tilde{\mathbf{T}}\mathbf{F}^{\mathrm{T}}$ and the relation $\mathrm{Grad}\,\delta\vec{u} = (\mathrm{grad}\,\delta\vec{u})\mathbf{F}$.

6.2.2 Weak Form of the Heat Conduction Equation

Again, test functions $\delta\Theta \in \mathcal{V}_\Theta$ are introduced, which can be interpreted as virtual temperatures that automatically fulfill the Dirichlet boundary conditions

$$\mathcal{V}_\Theta := \left\{ \delta\Theta\colon \boldsymbol{\mathcal{R}}\,[\mathcal{B}] \to \mathbb{R} \;\middle|\; \delta\Theta\left(\vec{X}\right) = 0 \text{ for } \vec{X} \in \partial_\Theta\boldsymbol{\mathcal{R}}\,[\mathcal{B}] \right\}. \tag{6.29}$$

The multiplication with the test functions and the application of the divergence theorem to the heat conduction Eq. (4.234) yields

$$\int\limits_{\boldsymbol{\mathcal{R}}[\mathcal{B}]} \rho_0 c_{\mathrm{p}}\dot{\Theta}\delta\Theta\,\mathrm{d}V - \int\limits_{\boldsymbol{\mathcal{R}}[\mathcal{B}]} \vec{q}_{\mathrm{R}}\cdot\mathrm{Grad}\,\delta\Theta\,\mathrm{d}V = -\int\limits_{\partial_{\mathrm{q}}\boldsymbol{\mathcal{R}}[\mathcal{B}]} \vec{q}_{\mathrm{R}}\cdot\vec{n}_{\mathrm{R}}\delta\Theta\,\mathrm{d}A + \int\limits_{\boldsymbol{\mathcal{R}}[\mathcal{B}]} \rho_0 r_{\mathrm{el}}\delta\Theta\,\mathrm{d}V. \tag{6.30}$$

By inserting the material relation for the heat flux (4.216), one obtains

$$\begin{aligned} \int\limits_{\boldsymbol{\mathcal{R}}[\mathcal{B}]} \rho_0 c_{\mathrm{p}}\dot{\Theta}\delta\Theta\,\mathrm{d}V + \int\limits_{\boldsymbol{\mathcal{R}}[\mathcal{B}]} \boldsymbol{\kappa}^{\mathrm{R}}_{\mathrm{th}}\,\mathrm{Grad}\,\Theta\cdot\mathrm{Grad}\,\delta\Theta\,\mathrm{d}V = \\ -\int\limits_{\partial_{\mathrm{q}}\boldsymbol{\mathcal{R}}[\mathcal{B}]} \vec{q}_{\mathrm{R}}\cdot\vec{n}_{\mathrm{R}}\,\delta\Theta\,\mathrm{d}A + \int\limits_{\boldsymbol{\mathcal{R}}[\mathcal{B}]} \rho_0 r_{\mathrm{el}}\delta\Theta\,\mathrm{d}V. \end{aligned} \tag{6.31}$$

The weak form in the current configuration reads

$$\begin{aligned} \int\limits_{\chi_t[\mathcal{B}]} \rho c_{\mathrm{p}}\dot{\Theta}\delta\Theta\,\mathrm{d}v + \int\limits_{\chi_t[\mathcal{B}]} \kappa_{\mathrm{th}}\,\mathrm{grad}\,\Theta\cdot\mathrm{grad}\,\delta\Theta\,\mathrm{d}v = \\ -\int\limits_{\partial_{\mathrm{q}}\chi_t[\mathcal{B}]} \vec{q}\cdot\vec{n}\delta\Theta\,\mathrm{d}a + \int\limits_{\chi_t[\mathcal{B}]} \rho r_{\mathrm{el}}\delta\Theta\,\mathrm{d}v. \end{aligned} \tag{6.32}$$

6.2.3 Weak Form of the Electrical Equation

Based on the conservation of charge,

$$\operatorname{Div} \vec{j}_{\mathrm{R}} = \vec{0}, \tag{3.78}$$

again, the equation is multiplied with virtual electric potentials $\delta\varphi$ and integrated over the volume. If Gauss's theorem is applied, this leads to

$$\int\limits_{\boldsymbol{\mathcal{R}}[\mathcal{B}]} \vec{j}_{\mathrm{R}} \cdot \operatorname{Grad} \delta\varphi \ \mathrm{d}V = \int\limits_{\partial_{\mathrm{j}}\boldsymbol{\mathcal{R}}[\mathcal{B}]} \vec{j}_{\mathrm{R}} \cdot \vec{n}_{\mathrm{R}} \delta\varphi \ \mathrm{d}A, \tag{6.33}$$

where the test functions are given by

$$\mathcal{V}_{\varphi} := \left\{ \delta\varphi \colon \boldsymbol{\mathcal{R}}\,[\mathcal{B}] \to \mathbb{R} \ \middle| \ \delta\varphi(\vec{X}) = 0 \text{ for } \vec{X} \in \partial_{\varphi}\boldsymbol{\mathcal{R}}\,[\mathcal{B}] \right\}. \tag{6.34}$$

Inserting Ohm's model (4.221) leads to the weak formulation

$$\int\limits_{\boldsymbol{\mathcal{R}}[\mathcal{B}]} \boldsymbol{\kappa}_{\mathrm{el}}^{\mathrm{R}} \operatorname{Grad} \varphi \cdot \operatorname{Grad} \delta\varphi \ \mathrm{d}V + \int\limits_{\partial_{\mathrm{j}}\boldsymbol{\mathcal{R}}[\mathcal{B}]} \vec{j}_{\mathrm{R}} \cdot \vec{n}_{\mathrm{R}} \delta\varphi \ \mathrm{d}A. \tag{6.35}$$

The weak formulations of the thermo-electro-mechanical problem are summarized in Tab. 6.2.

6.3 Numerical Solution Procedure

The weak form of the initial boundary value problem stated in Tab. 6.2 cannot be solved analytically in general. Therefore, a numerical solution with the method of lines is performed. The method of lines is a solution technique for partial differential equations where, for example, the spatial discretization is performed first, leaving the time undiscretized, see [Schiesser, 1991] and [Schiesser and Griffiths, 2009]. Commonly, the spatial discretization is performed in the first step and the discretization of the time domain is done in the second step, which is known as the vertical method of lines. The spatial discretization in Abaqus, which will be used in the following, draws on the h-version of the finite element method. Another possibility would be the p-version of finite elements, whereas hierarchical ansatz functions and Legendre-polynominals are used, leading to a high-order element formulation, see [Szabó and Babuška, 1991]. For high-order finite elements, see also [Szabo et al., 2004; Düster, 2001; Düster et al., 2003; Düster et al., 2001]. For elastoplasticity, see [Düster et al., 2002; Düster and Rank, 2002; Düster and Rank, 2001] and for powder compaction, see [Heisserer et al., 2008]. Finite hyperelasticity is considered in [Düster et al., 2003]. A comparison between low-order mixed elements and high-order finite elements can be found in [Netz et al., 2013a] and for the case of finite strain thermo-viscoelasticity, see [Netz, 2013].

Table 6.2: Summary of the weak form of the coupled problem

Determining the displacement field $\vec{u}(\vec{X},t)$, temperature field $\Theta(\vec{X},t)$ and the electric potential field $\varphi(\vec{X},t)$ such that for any $t \in [t_{\mathbf{i}}, t_{\mathbf{e}}]$

$$\begin{aligned}\pi_{\mathrm{u}}\big(\vec{u},\Theta,\boldsymbol{\mathsf{q}},\delta\vec{u}\big) &= \int\limits_{\boldsymbol{\mathcal{R}}[\mathcal{B}]} \tilde{\mathbf{T}}\cdot\delta\mathbf{E}\,\mathrm{d}V - \int\limits_{\partial_{\mathrm{s}}\boldsymbol{\mathcal{R}}[\mathcal{B}]} \vec{s}\cdot\delta\vec{u}\,\mathrm{d}A \\ &\quad - \int\limits_{\boldsymbol{\mathcal{R}}[\mathcal{B}]} \rho_0\vec{k}\cdot\delta\vec{u}\,\mathrm{d}V = 0, \quad \text{for all } \delta\vec{u}\in\boldsymbol{\mathcal{V}}_u \qquad (6.36)\end{aligned}$$

$$\begin{aligned}\pi_{\Theta}(\vec{u},\Theta,\boldsymbol{\mathsf{q}},\delta\Theta) &= \int\limits_{\boldsymbol{\mathcal{R}}[\mathcal{B}]} \rho_0\left(c_{\mathrm{p}}\dot{\Theta}-r_{\mathrm{el}}\right)\delta\Theta\,\mathrm{d}V - \int\limits_{\boldsymbol{\mathcal{R}}[\mathcal{B}]} \vec{q}_{\mathrm{R}}\cdot\operatorname{Grad}\delta\Theta\,\mathrm{d}V \qquad (6.37) \\ &\quad + \int\limits_{\partial_{\mathrm{q}}\boldsymbol{\mathcal{R}}[\mathcal{B}]} f_q\delta\Theta\,\mathrm{d}A + \int\limits_{\partial_{\Theta\mathrm{q}}\boldsymbol{\mathcal{R}}[\mathcal{B}]} f_c\delta\Theta\,\mathrm{d}A = 0, \quad \text{for all } \delta\Theta\in\mathcal{V}_{\Theta}\end{aligned}$$

$$\pi_{\varphi}(\varphi,\Theta,\delta\varphi) = -\int\limits_{\boldsymbol{\mathcal{R}}[\mathcal{B}]} \vec{j}_{\mathrm{R}}\cdot\operatorname{Grad}\delta\varphi\,\mathrm{d}V + \int\limits_{\partial_{\mathrm{j}}\boldsymbol{\mathcal{R}}[\mathcal{B}]} f_j\delta\varphi\,\mathrm{d}A, \quad \text{for all } \delta\varphi\in\mathcal{V}_{\varphi} \qquad (6.38)$$

with the prescribed initial values and boundary conditions

$$\begin{aligned}
\vec{u}(\vec{X},t_0) &= \vec{u}_0(\vec{X}), & \Theta(\vec{X},t_0) &= \Theta_0(\vec{X}), && (6.3, 6.4)\\
\varphi(\vec{X},t_0) &= \varphi_0(\vec{X}), & \boldsymbol{\mathsf{q}}(\vec{X},t_0) &= \boldsymbol{\mathsf{q}}_0(\vec{X}), && (6.5, 6.6)\\
\vec{u}(\vec{X},t) &= \bar{\vec{u}}(\vec{X},t), & \vec{t}_{\mathrm{R}} &= \mathbf{T}_{\mathrm{R}}\vec{n}_{\mathrm{R}} = \vec{s}(\vec{X},t), && (6.10, 6.13)\\
\Theta(\vec{X},t) &= \bar{\Theta}(\vec{X},t), & q_{\mathrm{R}} &= \vec{q}_{\mathrm{R}}\cdot\vec{n}_{\mathrm{R}} = f_q(\vec{X},t)+f_c(\vec{X},\Theta,t), && (6.11, 6.14, 6.16)\\
\varphi(\vec{X},t) &= \bar{\varphi}(\vec{X},t), & j_{\mathrm{R}} &= \vec{j}_{\mathrm{R}}\cdot\vec{n}_{\mathrm{R}} = f_j(\vec{X},t), && (6.12, 6.15)
\end{aligned}$$

and the constitutive relations

$$\begin{aligned}
\vec{q}_{\mathrm{R}} &= -\boldsymbol{\kappa}^{\mathrm{R}}_{\mathrm{th}}\operatorname{Grad}\Theta, & \vec{j}_{\mathrm{R}} &= -\boldsymbol{\kappa}^{\mathrm{R}}_{\mathrm{el}}\operatorname{Grad}\Theta, && (4.216, 4.221)\\
\tilde{\mathbf{T}} &= \mathbf{h}(\mathbf{C},\Theta,\boldsymbol{\mathsf{q}}), & \boldsymbol{\mathsf{A}}\dot{\boldsymbol{\mathsf{q}}} &= \tilde{\boldsymbol{\mathsf{r}}}(\mathbf{C},\Theta,\boldsymbol{\mathsf{q}}). && (6.1, 6.2)
\end{aligned}$$

are fulfilled.

6.3.1 Monolithic Solution

In the case of a monolithic solution procedure, the fully coupled system of equations is solved simultaneously at each time-step. Due to the full coupling, the tangent matrix is unsymmetric – and it can be quite costly to calculate all derivatives. The main advantage of this solution technique lies in the superior stability properties and the good convergence. If the Newton-Raphson method is applied, the convergence rate is quadratic close to the solution. For strongly coupled problems, the monolithic solution technique is recommended.

The monolithic finite element solution of the nonlinear transient heat conduction can be found in [Quint et al., 2011], while the thermo-electrical coupling within finite elements is considered in [Pérez-Aparicio et al., 2006; Palma et al., 2012; Pérez-Aparicio et al., 2012]. For the solution of Maxwell problems with hp-adaptive finite elements, see the work of Demkowicz [2006] concerning one or two dimensions. For the three-dimensional case, see [Demkowicz, 2008]. The monolithic solution of the electro-thermo-mechanical coupling at small strains compared to analytical solutions can be found in [Rothe et al., 2014].

6.3.2 Partitioned Solution

Another possibility for solving the equation system is the partitioned approach, which divides the problem into an iteration of coupled single field problems, see [Farhat et al., 1991], [Simo et al., 1991], [Armero and Simo, 1992], [Miehe, 1995b], [Miehe, 1995a]. The main advantage of this method is its flexibility to couple different programs or solvers. This method is widely used in the field of fluid structure interaction, for example to couple a fluid and a solid solver. Furthermore, different spatial discretizations, time increments and different solvers can be utilized for each single field. Generally, it is possible to differentiate between two different coupling schemes. If a loosely coupled problem exists, an explicit (single staggered) coupling scheme can be applied. Here, only one iteration is performed, assuming that the tolerance is then fulfilled. Strongly coupled problems require an implicit (multiple staggered) procedure with several iterations between the separate fields to achieve a sufficient accuracy. In the case of strong coupling, numerical instabilities can occur resulting from the isothermal split. In [Erbts and Düster, 2012] and [Erbts et al., 2012], these stabilization problems can be solved by dynamic relaxation and Quasi-Newton methods. Additionally, the convergence rate can be improved by these numerical acceleration procedures, thus reducing the number of iterations. Different spatial discretizations can lead to greater efficiency – but it is important to consider the interpolation of field or internal variables from one mesh to another. The partitioned solution of the thermo-electro-mechanical coupled problem is shown in [Erbts et al., 2014].

6.3.3 Spatial Discretization using Finite Elements

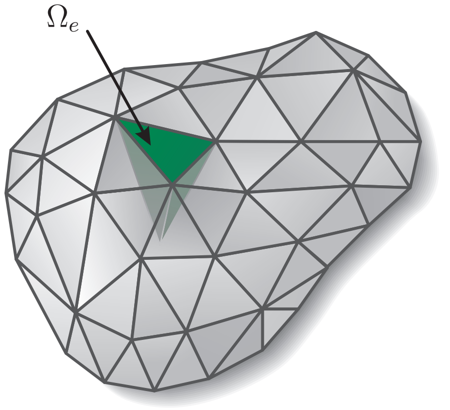

(a) Mesh of complete domain V consisting of elements with domain Ω_e

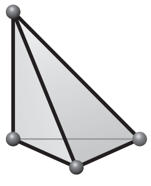

(b) Linear tetrahedron

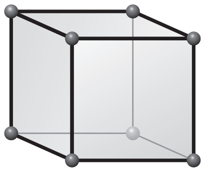

(d) Linear hexahedron

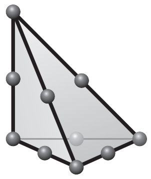

(c) Quadratic tetrahedron

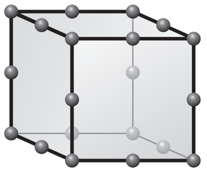

(e) Quadratic hexahedron

Figure 6.3: Spatial discretization with finite elements, taken from [Quint, 2012]

Within the finite element method, the body $\mathcal{B}$ is discretized into a region $\mathcal{B}^h$, which consists of n_e subsets $\Omega_e \subset \mathcal{B}^h$ called finite elements, see Fig. 6.3a. Typical shapes of three-dimensional finite elements are tetrahedra and hexahedra, see Figs. 6.3b to 6.3e. The terms *linear* or *quadratic* for the element are connected to the order of the shape functions. If linear shape functions are used, the element is called linear. For more information about the finite element method, see the standard textbooks of Hughes [2000], Wriggers [2009], Bathe [1996] and Zienkiewicz and Taylor [2005]. In Abaqus, there exist different element formulations. On the one hand, it is possible to use isoparametric finite elements – while, on the other hand, there are also mixed finite elements available. Additionally, one can decide between "full" spatial integration and "reduced" integration. In the case of full integration, the Gauss integration is used.[4] The following passage gives a description of the spatial discretization with isoparametric finite elements.

For the finite element discretization, all field variables have to be discretized. These are scalar variables $v \mathrel{\hat{=}} \{\Theta, \varphi\}$ or the displacements $\vec{u}$. The approximation – with the help of the shape functions N_a connected to the node a – is given by

$$v \approx v^h(\mathbf{x}, t) = \sum_{a=1}^{n_\mathrm{en}} N_a(\boldsymbol{\xi}) v_a^e(t), \qquad \vec{u}(\mathbf{x}, t) \approx \mathbf{u}^h(\boldsymbol{\xi}, t) = \sum_{a=1}^{n_\mathrm{en}} N_a(\boldsymbol{\xi}) \mathbf{u}_a^e(t). \tag{6.39}$$

---

[4] For second-order elements with reduced integration, the so-called *Barlow points* are used if the coordinate lines remain orthogonal. For first-order elements with reduced integration, the uniform strain formulation is to be chosen. For more information, see the Abaqus manual.

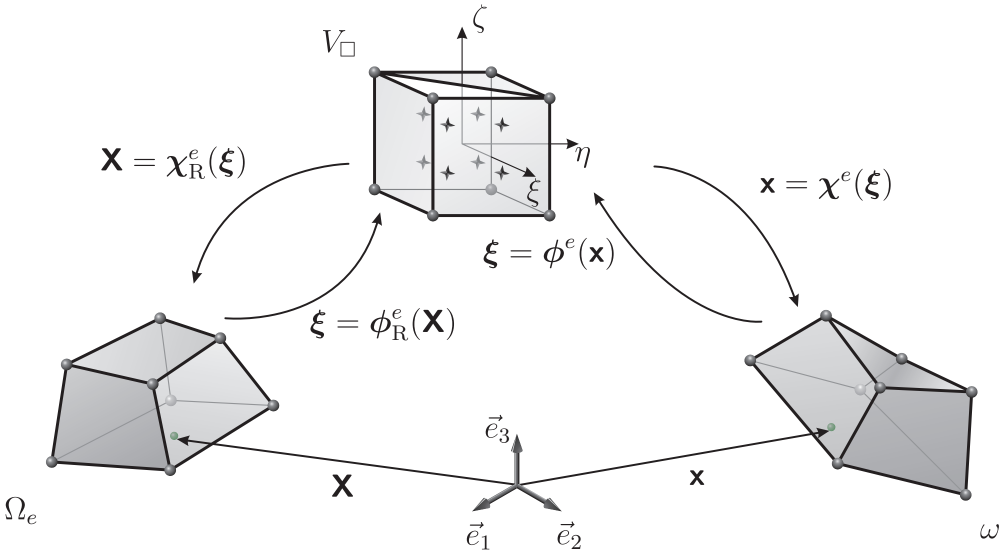

Figure 6.4: Transformation of linear hexahedral element e from the normed parameter space $V_\square$ into the reference Ω_e and the current ω_e configurations, modified from [Quint, 2012]. The stars symbolize the Gauss-points.

The transformation of a linear hexahedral element from the normed parameter space $V_\square$ into the reference Ω_e and current configuration ω_e is shown in Fig. 6.4. The connection between the coordinates $\mathbf{x}$ and the local coordinates $\boldsymbol{\xi} = \{\xi, \eta, \zeta\}^T$ with $\xi \in [-1, 1]$, $\eta \in [-1, 1]$ and $\zeta \in [-1, 1]$ is given by the mapping

$$\mathbf{x} = \boldsymbol{\chi}^e(\boldsymbol{\xi}) \Leftrightarrow \boldsymbol{\xi} = \boldsymbol{\phi}^e(\mathbf{x}), \qquad \mathbf{X} = \boldsymbol{\chi}^e_{\mathrm{R}}(\boldsymbol{\xi}) \Leftrightarrow \boldsymbol{\xi} = \boldsymbol{\phi}^e_{\mathrm{R}}(\mathbf{X}) \tag{6.40}$$

The coordinates in the reference and the current configuration can be directly defined by the ansatz Eq. (6.46)

$$\mathbf{x} = \boldsymbol{\chi}^e(\boldsymbol{\xi}) = \mathbf{x}^h(\boldsymbol{\xi}, t), \qquad \mathbf{X} = \boldsymbol{\chi}^e_{\mathrm{R}}(\boldsymbol{\xi}) = \mathbf{X}^h(\boldsymbol{\xi}) \tag{6.41}$$

The discretized equations are transferred to the normed parameter space $\boldsymbol{\xi}$. For this purpose, a transformation of the line elements is performed

$$\mathrm{d}\mathbf{x} = \mathbf{j}^e\,\mathrm{d}\boldsymbol{\xi}, \qquad \mathrm{d}\mathbf{X} = \mathbf{J}^e\,\mathrm{d}\boldsymbol{\xi}, \qquad \mathrm{d}\mathbf{x} = \mathbf{F}^e\,\mathrm{d}\mathbf{X} \quad \text{with} \quad \mathbf{F}^e = \mathbf{j}^e\mathbf{J}^{e-1}, \tag{6.42}$$

where the Jacobians are given by

$$\mathbf{j}_e = \left[\frac{\partial \mathbf{x}}{\partial \boldsymbol{\xi}}\right] = \mathrm{Grad}_\xi\,\mathbf{x}, \qquad \mathbf{J}_e = \left[\frac{\partial \mathbf{X}}{\partial \boldsymbol{\xi}}\right] = \mathrm{Grad}_\xi\,\mathbf{X}. \tag{6.43}$$

The transformation between the normed element space and the reference configuration is given by the Jacobian matrix $\mathbf{J}^e$ and its determinant $\det \mathbf{J}^e > 0$. The transformation to the current configuration can be obtained by $\mathbf{j}^e$ and $\det \mathbf{j}^e > 0$. As a result, the transformation between the volume elements reads

$$\mathrm{d}\omega_e = (\det \mathbf{F}_e)\,\mathrm{d}\Omega_e, \qquad \mathrm{d}\omega_e = (\det \mathbf{j}^e)\,\mathrm{d}V_\square, \qquad \mathrm{d}\Omega_e = (\det \mathbf{J}^e)\,\mathrm{d}V_\square. \tag{6.44}$$

The shape function N_a has the property to be 1 at the node a and 0 for the other nodes, which means that at a specific node a, only one shape function has the value one. Additionally, the sum of the shape function within an element is one, see [Schwarz and Köckler, 2004]. These properties are known as *partition of unity.* The shape functions for a linear hexahedral element (also known as a *brick element* consisting of eight nodes), see Fig. 6.3d, are given by

$$N_a(\boldsymbol{\xi}) = \tfrac{1}{8}(1+\xi_a\xi)(1+\eta_a\eta)(1+\zeta_a\zeta), \tag{6.45}$$

Here, $\boldsymbol{\xi}_a$ denotes the nodal coordinates in the $\boldsymbol{\xi}$ -space.

Due to the isoparametric element concept, the same shape functions are used for the discretizations of the geometry in the reference configuration and in the current configuration

$$\vec{X} = \mathbf{X}^h(\boldsymbol{\xi}) = \sum_{a=1}^{n_{\mathrm{en}}} N_a(\boldsymbol{\xi})\mathbf{X}_a^e, \qquad \vec{x}(t) = \mathbf{x}^h(\boldsymbol{\xi},t) = \sum_{a=1}^{n_{\mathrm{en}}} N_a(\boldsymbol{\xi})\mathbf{x}_a^e(t). \tag{6.46}$$

Accordingly, the shape functions for the displacements $\vec{u}$, virtual displacements $\delta\vec{u}$, temperatures Θ, virtual temperatures $\delta\Theta$, electrical potential φ and the virtual electrical potential $\delta\varphi$ are introduced within the element e for $\mathbf{x} \in \omega_e$

$$\mathbf{u}^h(\mathbf{x},t) = \mathbf{N}_{\mathrm{u}}^e(\boldsymbol{\phi}^e(\mathbf{x}))\mathbf{u}^e(t) = \mathbf{N}_{\mathrm{u}}^e(\boldsymbol{\phi}^e(\mathbf{x}))\boldsymbol{Z}_{\mathrm{ua}}^{\,e}\boldsymbol{u}_{\mathrm{a}} = \mathbf{N}_{\mathrm{u}}^e(\boldsymbol{\phi}^e(\mathbf{x}))\left\{\boldsymbol{Z}_{\mathrm{u}}^{\mathrm{e}}\boldsymbol{u} + \overline{\boldsymbol{Z}}_{\mathrm{u}}^{\mathrm{e}}\overline{\boldsymbol{u}}(t)\right\} \tag{6.47}$$

$$\delta\mathbf{u}^h(\mathbf{x}) = \mathbf{N}_{\mathrm{u}}^e(\boldsymbol{\phi}^e(\mathbf{x}))\delta\mathbf{u}^e = \mathbf{N}_{\mathrm{u}}^e(\boldsymbol{\phi}^e(\mathbf{x}))\boldsymbol{Z}_{\mathrm{ua}}^{\,e}\delta\boldsymbol{u}_{\mathrm{a}} = \mathbf{N}_{\mathrm{u}}^e(\boldsymbol{\phi}^e(\mathbf{x}))\boldsymbol{Z}_{\mathrm{u}}^{\mathrm{e}}\delta\boldsymbol{u} \tag{6.48}$$

$$\Theta^h(\mathbf{x},t) = \mathbf{N}_{\Theta}^{eT}(\boldsymbol{\phi}^e(\mathbf{x}))\boldsymbol{\Theta}^e(t) = \mathbf{N}_{\Theta}^{eT}(\boldsymbol{\phi}^e(\mathbf{x}))\boldsymbol{Z}_{\Theta\mathrm{a}}^{\,e}\boldsymbol{\Theta}_{\mathrm{a}} = \mathbf{N}_{\Theta}^{eT}(\boldsymbol{\phi}^e(\mathbf{x}))\left\{\boldsymbol{Z}_{\Theta}^{\mathrm{e}}\boldsymbol{\Theta} + \overline{\boldsymbol{Z}}_{\Theta}^{\mathrm{e}}\overline{\boldsymbol{\Theta}}(t)\right\} \tag{6.49}$$

$$\dot{\Theta}^h(\mathbf{x},t) = \mathbf{N}_{\Theta}^{eT}(\boldsymbol{\phi}^e(\mathbf{x}))\dot{\boldsymbol{\Theta}}^e(t) = \mathbf{N}_{\Theta}^{eT}(\boldsymbol{\phi}^e(\mathbf{x}))\boldsymbol{Z}_{\Theta\mathrm{a}}^{\,e}\dot{\boldsymbol{\Theta}}_{\mathrm{a}} = \mathbf{N}_{\Theta}^{eT}(\boldsymbol{\phi}^e(\mathbf{x}))\left\{\boldsymbol{Z}_{\Theta}^{\mathrm{e}}\dot{\boldsymbol{\Theta}} + \overline{\boldsymbol{Z}}_{\Theta}^{\mathrm{e}}\dot{\overline{\boldsymbol{\Theta}}}(t)\right\} \tag{6.50}$$

$$\delta\Theta^h(\mathbf{x}) = \mathbf{N}_{\Theta}^{eT}(\boldsymbol{\phi}^e(\mathbf{x}))\delta\boldsymbol{\Theta}^e = \mathbf{N}_{\Theta}^{eT}(\boldsymbol{\phi}^e(\mathbf{x}))\boldsymbol{Z}_{\Theta\mathrm{a}}^{\,e}\delta\boldsymbol{\Theta}_{\mathrm{a}} = \mathbf{N}_{\Theta}^{eT}(\boldsymbol{\phi}^e(\mathbf{x}))\boldsymbol{Z}_{\Theta}^{\mathrm{e}}\delta\boldsymbol{\Theta} \tag{6.51}$$

$$\varphi^h(\mathbf{x},t) = \mathbf{N}_{\varphi}^{eT}(\boldsymbol{\phi}^e(\mathbf{x}))\boldsymbol{\Phi}^e(t) = \mathbf{N}_{\varphi}^{eT}(\boldsymbol{\phi}^e(\mathbf{x}))\boldsymbol{Z}_{\varphi\mathrm{a}}^{\,e}\boldsymbol{\Phi}_{\mathrm{a}} = \mathbf{N}_{\varphi}^{eT}(\boldsymbol{\phi}^e(\mathbf{x}))\left\{\boldsymbol{Z}_{\varphi}^{\mathrm{e}}\boldsymbol{\Phi} + \overline{\boldsymbol{Z}}_{\varphi}^{\mathrm{e}}\overline{\boldsymbol{\Phi}}(t)\right\} \tag{6.52}$$

$$\delta\varphi^h(\mathbf{x}) = \mathbf{N}_{\varphi}^{eT}(\boldsymbol{\phi}^e(\mathbf{x}))\delta\boldsymbol{\Phi}^e = \mathbf{N}_{\varphi}^{eT}(\boldsymbol{\phi}^e(\mathbf{x}))\boldsymbol{Z}_{\varphi\mathrm{a}}^{\,e}\delta\boldsymbol{\Phi}_{\mathrm{a}} = \mathbf{N}_{\varphi}^{eT}(\boldsymbol{\phi}^e(\mathbf{x}))\boldsymbol{Z}_{\varphi}^{\mathrm{e}}\delta\boldsymbol{\Phi} \tag{6.53}$$

Here, $\mathbf{u}^h \in \mathbb{R}^3$ and $\delta\mathbf{u}^h \in \mathbb{R}^3$ hold for the three-dimensional case. Accordingly, the matrix and vector of the shape functions are given as $\mathbf{N}^e_{\mathrm{u}} \in \mathbb{R}^{3\times n^e_{\mathrm{u}}}$, $\mathbf{N}^e_{\Theta} \in \mathbb{R}^{n^e_{\Theta}}$, and $\mathbf{N}^e_{\varphi} \in \mathbb{R}^{n^e_{\varphi}}$, where n^e_{u}, n^e_{Θ}, and n^e_{φ} are the displacement, temperature, and electrical potential element degrees of freedom (DOF). $\mathbf{u}^e \in \mathbb{R}^{n^e_{\mathrm{u}}}$, $\boldsymbol{\Theta}^e \in \mathbb{R}^{n^e_{\Theta}}$ and $\boldsymbol{\Phi}^e \in \mathbb{R}^{n^e_{\varphi}}$ are element DOF concerned, whereas $\boldsymbol{u}_{\mathrm{a}} \in \mathbb{R}^{n_{\mathrm{ua}}}$, $\boldsymbol{\Theta}_{\mathrm{a}} \in \mathbb{R}^{n_{\Theta\mathrm{a}}}$ and $\boldsymbol{\Phi}_{\mathrm{a}} \in \mathbb{R}^{n_{\varphi\mathrm{a}}}$ are all displacement, temperature and electrical potential DOF of the entire mesh. Each is decomposed into unknown and known DOF, where the known, i.e. prescribed quantities are overlined. $\boldsymbol{u} \in \mathbb{R}^{n_{\mathrm{uu}}}$, $\boldsymbol{\Theta} \in \mathbb{R}^{n_{\Theta\mathrm{u}}}$, and $\boldsymbol{\Phi} \in \mathbb{R}^{n_{\varphi\mathrm{u}}}$ are the unknowns and $\overline{\boldsymbol{u}} \in \mathbb{R}^{n_{\mathrm{up}}}$, $\overline{\boldsymbol{\Theta}} \in \mathbb{R}^{n_{\Theta\mathrm{p}}}$, and $\overline{\boldsymbol{\Phi}} \in \mathbb{R}^{n_{\varphi\mathrm{p}}}$ are the prescribed DOF. Obviously, $n_{\mathrm{ua}} = n_{\mathrm{uu}} + n_{\mathrm{up}}$ for $\boldsymbol{u}^{\mathrm{T}}_{\mathrm{a}} = \{\boldsymbol{u}^{\mathrm{T}}\overline{\boldsymbol{u}}^{T}\}$ holds. The same decomposition can be carried out for the temperature and electrical potential DOF, $\boldsymbol{\Theta}^T_{\mathrm{a}} = \{\boldsymbol{\Theta}^T\overline{\boldsymbol{\Theta}}^T\}$ with $n_{\Theta\mathrm{a}} = n_{\Theta\mathrm{u}} + n_{\Theta\mathrm{p}}$, and $\boldsymbol{\Phi}^T_{\mathrm{a}} = \{\boldsymbol{\Phi}^T\overline{\boldsymbol{\Phi}}^T\}$ with $n_{\varphi\mathrm{a}} = n_{\varphi\mathrm{u}} + n_{\varphi\mathrm{p}}$.

The incidence matrices of global and local degrees of freedom $\boldsymbol{Z}^{\mathrm{e}}_{\mathrm{u}} \in \mathbb{R}^{n^e_{\mathrm{u}}\times n_{\mathrm{uu}}}$, $\overline{\boldsymbol{Z}}^{\mathrm{e}}_{\mathrm{u}} \in \mathbb{R}^{n^e_{\mathrm{u}}\times n_{\mathrm{up}}}$, $\boldsymbol{Z}^{\mathrm{e}}_{\Theta} \in \mathbb{R}^{n^e_{\Theta}\times n_{\Theta\mathrm{u}}}$, $\overline{\boldsymbol{Z}}^{\mathrm{e}}_{\Theta} \in \mathbb{R}^{n^e_{\Theta}\times n_{\Theta\mathrm{p}}}$, $\boldsymbol{Z}^{\mathrm{e}}_{\varphi} \in \mathbb{R}^{n^e_{\varphi}\times n_{\varphi\mathrm{u}}}$, and $\overline{\boldsymbol{Z}}^{\mathrm{e}}_{\mathrm{u}} \in \mathbb{R}^{n^e_{\varphi}\times n_{\varphi\mathrm{p}}}$ represent the assemblage procedure, which is frequently symbolized by $\bigcup_{e=1}^{n_{\mathrm{e}}}$ or $\mathbf{A}_{e=1}^{n_{\mathrm{e}}}$ in [Wriggers, 2009] and [Hughes, 2000]. Of course, the incidence matrices themselves are not programmed. However, the notation provides the possibility to develop new finite element schemes, see [Hartmann, 2005] or [Hartmann and Hamkar, 2010].

The second Piola Kirchhoff stress tensor reads in Voigt notation

$$\tilde{\mathbf{T}} = \left\{\tilde{T}_{11} \quad \tilde{T}_{22} \quad \tilde{T}_{33} \quad \tilde{T}_{12} \quad \tilde{T}_{23} \quad \tilde{T}_{31}\right\}^{\mathrm{T}}. \tag{6.54}$$

The virtual strain tensor can be expressed as

$$\delta\mathbf{E} = \left\{\delta E_{11} \quad \delta E_{22} \quad \delta E_{33} \quad 2\delta E_{12} \quad 2\delta E_{23} \quad 2\delta E_{31}\right\}^{\mathrm{T}} = \sum_{a=1}^{n_{\mathrm{en}}} \tilde{\mathbf{B}}_{\mathrm{u}a}\delta\mathbf{u}^e_a, \tag{6.55}$$

with n_{en} as the number of nodes per element. The reason for the factor two in the shear components is to be seen in the scalar product $\tilde{\mathbf{T}} \cdot \delta\mathbf{E}$. Based on this definition, the scalar product in tensor and vector notation is equal, $\tilde{\mathbf{T}} \cdot \delta\mathbf{E} = \delta\mathbf{E}^{\mathrm{T}}\tilde{\mathbf{T}}$. The matrix $\tilde{\mathbf{B}}_{\mathrm{u}a}$ is called strain-displacement matrix for each node a and is given by Eq. (36) in the appendix. The matrix contains the derivative of the shape functions with respect to the material (referential) coordinates. The discretized weak form of Eq. (6.28) can be obtained with the ansatz for the displacements (6.47) and for the virtual displacements (6.48) leading to

$$\tilde{\pi}^h_{\mathrm{M}}(\boldsymbol{u}, \Theta, \boldsymbol{q}, \delta\vec{u}, t) =$$

$$\delta\boldsymbol{u}^{\mathrm{T}} \sum_{e=1}^{n_{\mathrm{e}}} \boldsymbol{Z}^{\mathrm{eT}}_{\mathrm{u}} \left\{ \int_{\Omega_e} \tilde{\mathbf{B}}^{\mathrm{eT}}_{\mathrm{u}}(\mathbf{u}^e(t), \mathbf{X})\, \underbrace{\mathbf{h}^{\mathrm{e}}(\mathbf{C}^{\mathrm{e}}(\mathbf{X}, t), \boldsymbol{\Theta}^{\mathrm{e}}(\mathbf{X}, t), \mathbf{q}^{\mathrm{e}}(\mathbf{X}, t))}_{\tilde{\mathbf{T}}^{\mathrm{e}}}\, \mathrm{d}\Omega_e - \overline{\boldsymbol{p}}(\mathbf{X}, t) \right\} = 0 \tag{6.56}$$

with the strain displacement matrix $\tilde{\mathbf{B}}^{\mathrm{e}}_{\mathrm{u}}(\mathbf{u}^e(t),\mathbf{X}) = \left[\tilde{\mathbf{B}}^{\mathrm{e}}_{\mathrm{u}1}(\mathbf{u}^e(t),\mathbf{X}) \dots \tilde{\mathbf{B}}^{\mathrm{e}}_{\mathrm{u}n_{\mathrm{en}}}(\mathbf{u}^e(t),\mathbf{X})\right]$ $\in \mathbb{R}^{6\times 3n^{\mathrm{e}}_{\mathrm{u}}}$ and the vector containing the volume distributed loads and the tractions acting on the surface

$$\bar{\boldsymbol{p}}(\mathbf{X},t) := \int\limits_{\Omega_e} \mathbf{N}^{\mathrm{eT}}(\mathbf{X})\rho(\mathbf{X})\mathbf{k}^{\mathrm{e}}\,\mathrm{d}\Omega_e + \int\limits_{\Gamma_{\mathrm{e}}} \mathbf{N}^{\mathrm{eT}}(\mathbf{X})\mathbf{s}(\mathbf{X},t)\,\mathrm{d}\Gamma_{\mathrm{e}}. \tag{6.57}$$

Since the virtual displacements, $\delta\vec{u}$, are arbitrary, the discretized principle of virtual displacements, Eq. (6.56), yields a system of nonlinear equations

$$\tilde{\boldsymbol{g}}_{\mathrm{u}}(\boldsymbol{u},\Theta,\boldsymbol{q},t) = \sum_{e=1}^{n_{\mathrm{e}}} \boldsymbol{Z}^{\mathrm{eT}}_{\mathrm{u}} \int\limits_{\Omega_e} \tilde{\mathbf{B}}^{\mathrm{eT}}_{\mathrm{u}}(\mathbf{u}^e(t),\mathbf{X})\tilde{\mathbf{T}}^{\mathrm{e}}(\mathbf{X},t)\,\mathrm{d}\Omega_e - \bar{\boldsymbol{p}}(\mathbf{X},t) = \boldsymbol{0}. \tag{6.58}$$

The discretized principle of virtual displacements related to the current configuration can be found in [Hartmann, 2003] as well as [Hamkar, 2013] and is given by

$$\boldsymbol{g}_{\mathrm{u}}(\boldsymbol{u},\Theta,\boldsymbol{q},t) = \sum_{e=1}^{n_{\mathrm{e}}} \boldsymbol{Z}^{\mathrm{eT}}_{\mathrm{u}} \int\limits_{\Omega_e} \mathbf{B}^{\mathrm{eT}}_{\mathrm{u}}(\mathbf{x})\mathbf{S}^{\mathrm{e}}(\mathbf{x},t)\,\mathrm{d}\Omega_e - \bar{\boldsymbol{p}}(\mathbf{x},t) = \boldsymbol{0}, \tag{6.59}$$

with $\mathbf{S}^{\mathrm{e}}$ as the weighted Cauchy stress, which can be computed by the second Piola Kirchhoff stress by $\mathbf{S}^{\mathrm{e}} = \mathbf{F}^{\mathrm{e}}_{23}\tilde{\mathbf{T}}^{\mathrm{e}}$. The push-forward operator in matrix notation $\mathbf{F}^{\mathrm{e}}_{23}$ is given by Eq. (37) in the appendix. Inserting this relation into Eq. (6.59) yields

$$\boldsymbol{g}_{\mathrm{u}}(\boldsymbol{u},\Theta,\boldsymbol{q},t) = \sum_{e=1}^{n_{\mathrm{e}}} \boldsymbol{Z}^{\mathrm{eT}}_{\mathrm{u}} \int\limits_{\Omega_e} \mathbf{B}^{\mathrm{eT}}_{\mathrm{u}}(\mathbf{X})\mathbf{F}^{\mathrm{e}}_{23}\tilde{\mathbf{T}}^{\mathrm{e}}(\mathbf{X},t)\,\mathrm{d}\Omega_e - \bar{\boldsymbol{p}}(\mathbf{X},t) = \boldsymbol{0}, \tag{6.60}$$

The strain displacement matrix $\mathbf{B}^{\mathrm{e}}_{\mathrm{u}}$ consists of the shape function derivatives with respect to the spatial (current) coordinates and is given in the three-dimensional case by

$$\mathbf{B}^{\mathrm{e}}_{\mathrm{u}}(\boldsymbol{\phi}^e(\mathbf{x})) = \left[\mathbf{B}^{\mathrm{e}}_{\mathrm{u}1} \dots \mathbf{B}^{\mathrm{e}}_{\mathrm{u}n^{\mathrm{e}}_{\mathrm{u}}}\right] \in \mathbb{R}^{6\times 3n^{\mathrm{e}}_{\mathrm{u}}} \tag{6.61}$$

with

$$\mathbf{B}^{\mathrm{e}}_{\mathrm{u}a}(\boldsymbol{\phi}^e(\mathbf{x})) = \begin{bmatrix} N^e_{\mathrm{u}a,x} & 0 & 0 \\ 0 & N^e_{\mathrm{u}a,y} & 0 \\ 0 & 0 & N^e_{\mathrm{u}a,z} \\ N^e_{\mathrm{u}a,y} & N^e_{\mathrm{u}a,x} & 0 \\ 0 & N^e_{\mathrm{u}a,z} & N^e_{\mathrm{u}a,y} \\ N^e_{\mathrm{u}a,z} & 0 & N^e_{\mathrm{u}a,x} \end{bmatrix}, \qquad a = 1,\dots,n^e_{\mathrm{u}} \tag{6.62}$$

with the shape funcion $N^e_a(\boldsymbol{\xi})$ defined at the node a within the domain $V_{\Box}$ with the local coordinates $\boldsymbol{\xi}$. n^e_{u} represents the displacement degree of freedom, which – in this formulation – is equal to the number of nodes per element n_{en}.

Within the finite element discretization, a volume integral is approximated by an integral over the volume V^h and split in a sum of integrals over the elements. This is followed by a coordinate transformation into the local coordinate space $\boldsymbol{\xi} = \{\xi, \eta, \zeta\}^T$ with $\xi \in [-1, 1]$, $\eta \in [-1, 1]$ and $\zeta \in [-1, 1]$.

$$\begin{aligned}
\int\limits_V f(\mathbf{X})\,\mathrm{d}V \approx \int\limits_{V^h} f(\mathbf{X})\,\mathrm{d}V &= \sum_{e=1}^{n_\mathrm{e}} \int\limits_{\Omega_e} f(\mathbf{X})\,\mathrm{d}V \\
&= \sum_{e=1}^{n_\mathrm{e}} \int\limits_{V_\square} f(\boldsymbol{\xi}) \det \mathbf{J}^e(\boldsymbol{\xi})\,\mathrm{d}V_\square = \sum_{e=1}^{n_\mathrm{e}} \int\limits_{-1}^{+1}\int\limits_{-1}^{+1}\int\limits_{-1}^{+1} f(\boldsymbol{\xi}) J^e(\boldsymbol{\xi})\,\mathrm{d}\xi\,\mathrm{d}\eta\,\mathrm{d}\zeta \qquad (6.63) \\
&\approx \sum_{e=1}^{n_\mathrm{e}} \sum_{i,j,k=1}^{n_\mathrm{GP}} w_{ijk} f(\boldsymbol{\xi}_{ijk}) J^e(\boldsymbol{\xi}_{ijk}) = \sum_{e=1}^{n_\mathrm{e}} \sum_{l=1}^{n_\mathrm{GP}} w_l f(\boldsymbol{\xi}_l) J^e(\boldsymbol{\xi}_l) \qquad (6.64)
\end{aligned}$$

Additionally, the Gauss quadrature, see [Dhatt and Touzot, 1985] and [Schwarz and Köckler, 2004], is applied with the Gauss coordinates $\boldsymbol{\xi}_l = \{\xi, \eta, \zeta\}_l^T$. The weighting factors in the different directions are combined in $w_l \mathrel{\hat{=}} w_{ijk}$.

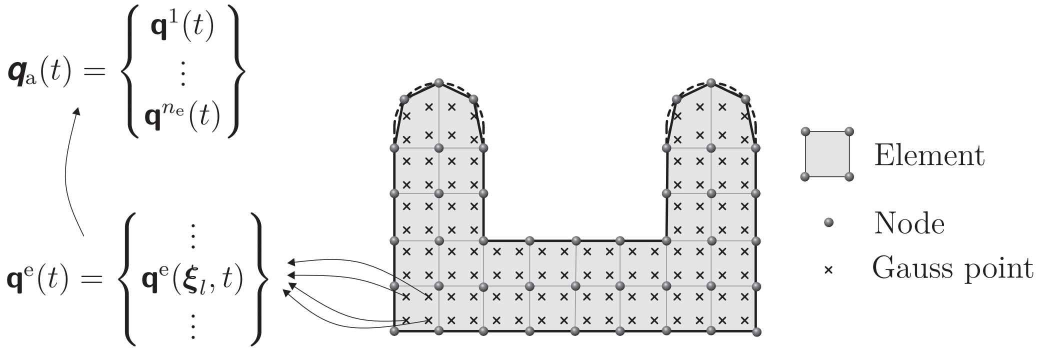

Figure 6.5: Assembly of internal variables element vector $\mathbf{q}^\mathrm{e}(\boldsymbol{\xi}_l, t)$ into global vector $\boldsymbol{q}(t)$ for a two-dimensional finite element mesh

The internal variables are computed by the evolution equations Eq. (6.2), which are calculated at the spatial integration points $\boldsymbol{\xi}_l$

$$\mathbf{A}\dot{\mathbf{q}}^\mathrm{e}(\boldsymbol{\xi}_l, t) = \tilde{\mathbf{r}}^\mathrm{e}\left(\mathbf{C}^\mathrm{e}(\boldsymbol{\xi}_l, t), \boldsymbol{\Theta}^\mathrm{e}(\boldsymbol{\xi}_l, t), \mathbf{q}^\mathrm{e}(\boldsymbol{\xi}_l, t), t\right), \qquad \mathbf{q}^\mathrm{e} \in \mathbb{R}^{n_\mathrm{q}}. \qquad (6.65)$$

These internal variables can be assembled formally into a global vector $\boldsymbol{q}(t)$ with the length n_Q, $\boldsymbol{q}(t) \in \mathbb{R}^{n_\mathrm{Q}}$. The number of internal variables is given by the product between the integration points of the entire mesh $n_\mathrm{e} \times n_\mathrm{GP}$ with the number of internal variables per Gauss point n_q, leading to $n_\mathrm{Q} = n_\mathrm{e} \times n_\mathrm{GP} \times n_\mathrm{q}$. The assembly procedure is illustrated in Fig. 6.5.

According to [Hartmann, 2005], see also [Hamkar, 2013], a coincidence matrix $\boldsymbol{Z}^{\mathrm{e}}_{\mathrm{q}l} \in \mathbb{R}^{n_{\mathrm{q}} \times n_{\mathrm{Q}}}$ for the internal variables can be introduced, which selects the internal variables $\mathbf{q}$ at the Gauss point $\boldsymbol{\xi}_l$ for the element e out of the global vector $\boldsymbol{q}$.

$$\mathbf{q}^{\mathrm{e}}(\boldsymbol{\xi}_l, t) = \boldsymbol{Z}^{\mathrm{e}}_{\mathrm{q}l}\, \boldsymbol{q}(t), \qquad \mathbf{q}^{\mathrm{e}}(\boldsymbol{\xi}_l, t) \in \mathbb{R}^{n_{\mathrm{q}}}. \tag{6.66}$$

The assembly in the global vector is possible because the internal variables and their evolution equations are decoupled point-wise, see [Hartmann, 2005] and [Hartmann, 2003]

$$\boldsymbol{q}(t) = \sum_{e=1}^{n_{\mathrm{e}}} \sum_{l=1}^{n_{\mathrm{GP}}} \boldsymbol{Z}^{\mathrm{eT}}_{\mathrm{q}l}\, \mathbf{q}^{\mathrm{e}}(\boldsymbol{\xi}_l, t). \tag{6.67}$$

As a result, the evolution equations are formally assembled into a global system of ordinary differential equations

$$\boldsymbol{A}\dot{\boldsymbol{q}}(t) - \boldsymbol{r}_{\mathrm{q}}(t, \boldsymbol{u}(t), \Theta(t), \boldsymbol{q}(t)) = \boldsymbol{0}, \qquad \boldsymbol{q}(t) \in \mathbb{R}^{n_{\mathrm{Q}}}. \tag{6.68}$$

In the following, the discretization of the heat equation is performed. The temperature field is determined with the discretization of the weak form (6.37)

$$\begin{aligned}
&\pi^h_\Theta(\boldsymbol{u}, \boldsymbol{\Theta}, \dot{\boldsymbol{\Theta}}, \boldsymbol{\Phi}, \delta\boldsymbol{\Theta}, t) = \\
&\quad \delta\boldsymbol{\Theta}^{\mathrm{T}} \left\{ \sum_{e=1}^{n_{\mathrm{e}}} \boldsymbol{Z}^{\mathrm{eT}}_{\Theta} \left\{ \int\limits_{\Omega_e} \rho(\mathbf{x}) c^h_{\mathrm{p}} \mathbf{N}^{\mathrm{e}}_{\Theta}(\mathbf{x}) \mathbf{N}^{\mathrm{eT}}_{\Theta}(\mathbf{x})\, \mathrm{d}\Omega_e\, \dot{\boldsymbol{\Theta}}^{\mathrm{e}} + \int\limits_{\Omega_e} \mathbf{B}^{\mathrm{eT}}_{\Theta}(\mathbf{x}) \kappa^h_{\mathrm{th}} \mathbf{B}^{\mathrm{e}}_{\Theta}(\mathbf{x})\, \mathrm{d}\Omega_e\, \boldsymbol{\Theta}^{\mathrm{e}} \right.\right. \\
&\qquad \left.\left. + \int\limits_{\Gamma_{\mathrm{e}}} f_q \mathbf{N}^{\mathrm{e}}_{\Theta}\, \mathrm{d}\Gamma_{\mathrm{e}} + \int\limits_{\Gamma_{\mathrm{e}}} f_c \mathbf{N}^{\mathrm{e}}_{\Theta}\, \mathrm{d}\Gamma_{\mathrm{e}} - \int\limits_{\Omega_e} \rho(\mathbf{x}) r^h_{\mathrm{el}} \mathbf{N}^{\mathrm{e}}_{\Theta}\, \mathrm{d}\Omega_e \right\} \right\} = 0.
\end{aligned} \tag{6.69}$$

The gradient of the temperature and the virtual temperature are approximated within the element e by

$$\operatorname{grad} \Theta^h = \mathbf{B}^{\mathrm{e}}_{\Theta}(\boldsymbol{\phi}^e(\mathbf{x}))\boldsymbol{\Theta}^e(t) = \mathbf{B}^{\mathrm{e}}_{\Theta}(\boldsymbol{\phi}^e(\mathbf{x})) \left\{ \boldsymbol{Z}^{\mathrm{e}}_{\Theta}\boldsymbol{\Theta} + \overline{\boldsymbol{Z}}^{\mathrm{e}}_{\Theta}\overline{\boldsymbol{\Theta}}(t) \right\} \tag{6.70}$$

$$\operatorname{grad} \delta\Theta^h = \mathbf{B}^{\mathrm{e}}_{\Theta}(\boldsymbol{\phi}^e(\mathbf{x}))\delta\boldsymbol{\Theta}^e = \mathbf{B}^{\mathrm{e}}_{\Theta}(\boldsymbol{\phi}^e(\mathbf{x}))\boldsymbol{Z}^{\mathrm{e}}_{\Theta}\delta\boldsymbol{\Theta} \tag{6.71}$$

The temperature-gradient matrix is given by

$$\mathbf{B}^{\mathrm{e}}_{\Theta}(\boldsymbol{\phi}^e(\mathbf{x})) = \left[\mathbf{B}^{\mathrm{e}}_{\Theta 1} \dots \mathbf{B}^{\mathrm{e}}_{\Theta n^e_\Theta} \right] \in \mathbb{R}^{3 \times n^e_\Theta} \tag{6.72}$$

In this matrix, the derivatives of the shape functions with respect to the spatial (current) coordinates at the node a are arranged

$$\mathbf{B}^{\mathrm{e}}_{\Theta a}(\boldsymbol{\phi}^e(\mathbf{x})) = \begin{Bmatrix} N^e_{\Theta a,x} \\ N^e_{\Theta a,y} \\ N^e_{\Theta a,z} \end{Bmatrix}, \qquad a = 1, \dots, n^e_\Theta \tag{6.73}$$

The heat capacity is discretized by $c_{\mathrm{p}}^h = \tilde{c}_p^h(t, \boldsymbol{\Theta}^{\mathrm{e}}(t))$ and depends on the temperature. The thermal conductivity $\kappa_{\mathrm{th}}^h = \tilde{\kappa}_{\mathrm{th}}^h(t, \boldsymbol{u}^{\mathrm{e}}(t), \boldsymbol{\Theta}^{\mathrm{e}}(t))$ is a function of the temperature and the deformation by the relative density dependence. The volumetric heat source given by the Joule heating $r_{\mathrm{el}}^h = \tilde{r}_{\mathrm{el}}^h(t, \boldsymbol{u}^{\mathrm{e}}(t), \boldsymbol{\Theta}^{\mathrm{e}}(t), \boldsymbol{\Phi}^{\mathrm{e}}(t))$ depends on the electrical potential and on the temperature as well as on the deformation by the electrical conductivity, which is affected by the relative density and the temperature.

Since the virtual temperatures are arbitrary, one obtains a system of ordinary differential equations of first order

$$\boldsymbol{C}_{\mathrm{p}}\left(t, \boldsymbol{u}(t), \boldsymbol{\Theta}(t)\right) \dot{\boldsymbol{\Theta}}(t) = \boldsymbol{r}_{\Theta}(t, \boldsymbol{u}(t), \boldsymbol{\Theta}(t), \boldsymbol{\Phi}(t)), \tag{6.74}$$

with the heat capacity matrices

$$\boldsymbol{C}_{\mathrm{p}}\left(t, \boldsymbol{u}(t), \boldsymbol{\Theta}(t)\right) := \sum_{e=1}^{n_{\mathrm{e}}} \boldsymbol{Z}_{\Theta}^{\mathrm{eT}} \left[\int_{\Omega_e} \rho\, c_{\mathrm{p}}^h\, \mathbf{N}_{\Theta}^{\mathrm{e}} \mathbf{N}_{\Theta}^{\mathrm{eT}} \,\mathrm{d}\Omega_e \right] \boldsymbol{Z}_{\Theta}^{\mathrm{e}} \quad \in \mathbb{R}^{n_{\Theta\mathrm{u}} \times n_{\Theta\mathrm{u}}} \tag{6.75}$$

$$\overline{\boldsymbol{C}}_{\mathrm{p}}\left(t, \boldsymbol{u}(t), \boldsymbol{\Theta}(t)\right) := \sum_{e=1}^{n_{\mathrm{e}}} \boldsymbol{Z}_{\Theta}^{\mathrm{eT}} \left[\int_{\Omega_e} \rho\, c_{\mathrm{p}}^h\, \mathbf{N}_{\Theta}^{\mathrm{e}} \mathbf{N}_{\Theta}^{\mathrm{eT}} \,\mathrm{d}\Omega_e \right] \overline{\boldsymbol{Z}}_{\Theta}^{\mathrm{e}} \quad \in \mathbb{R}^{n_{\Theta\mathrm{u}} \times n_{\Theta\mathrm{p}}}. \tag{6.76}$$

The right hand side in Eq. (6.74) is given by the integrals in Eq. (6.69)

$$\boldsymbol{r}_{\Theta}\left(t, \boldsymbol{u}(t), \dot{\boldsymbol{u}}(t), \boldsymbol{\Theta}(t)\right) := -\boldsymbol{C}_{\kappa}\boldsymbol{\Theta} + \boldsymbol{p}_{\Theta}^{\mathrm{vol}} - \boldsymbol{p}_{\Theta}^{\mathrm{ext}} - \overline{\boldsymbol{p}}_{\Theta}, \tag{6.77}$$

with the thermal conductivity matrix

$$\boldsymbol{C}_{\kappa}\left(t, \boldsymbol{u}(t), \boldsymbol{\Theta}(t)\right) := \sum_{e=1}^{n_{\mathrm{e}}} \boldsymbol{Z}_{\Theta}^{\mathrm{eT}} \int_{\Omega_e} \kappa_{\mathrm{th}}^h \mathbf{B}_{\Theta}^{\mathrm{eT}} \mathbf{B}_{\Theta}^{\mathrm{e}} \,\mathrm{d}\Omega_e, \tag{6.78}$$

and the volumetric heat source $\boldsymbol{p}_{\Theta}^{\mathrm{vol}}$ as well as the heat flux over the surface denoted by $\boldsymbol{p}_{\Theta}^{\mathrm{ext}}$

$$\boldsymbol{p}_{\Theta}^{\mathrm{vol}}\left(t, \boldsymbol{u}(t), \boldsymbol{\Theta}(t), \boldsymbol{\Phi}(t)\right) := \sum_{e=1}^{n_{\mathrm{e}}} \boldsymbol{Z}_{\Theta}^{\mathrm{eT}} \int_{\Omega_e} \rho r_{\mathrm{el}}^h \mathbf{N}_{\Theta}^{\mathrm{e}} \,\mathrm{d}\Omega_e, \tag{6.79}$$

$$\boldsymbol{p}_{\Theta}^{\mathrm{ext}}\left(t, \boldsymbol{u}(t), \boldsymbol{\Theta}(t)\right) := \sum_{e=1}^{n_{\mathrm{e}}} \boldsymbol{Z}_{\Theta}^{\mathrm{eT}} \int_{\Gamma_{\mathrm{e}}} (f_q + f_c) \mathbf{N}_{\Theta}^{\mathrm{e}} \,\mathrm{d}\Gamma_{\mathrm{e}}. \tag{6.80}$$

The surface heat flux also depends on the deformation by the geometrical nonlinearity, which means that the surface changes due to the large deformations and influences the heat flux per unit surface. The discretized Joule heating term reads

$$r_{\mathrm{el}}^h = \tilde{r}_{\mathrm{el}}^h(\boldsymbol{u}^{\mathrm{e}}(t), \boldsymbol{\Theta}^{\mathrm{e}}(t), \boldsymbol{\Phi}^{\mathrm{e}}(t)) = \frac{1}{\rho}\kappa_{\varphi}(\boldsymbol{\Theta}^{\mathrm{e}}, \boldsymbol{u}^{\mathrm{e}}) \boldsymbol{\Phi}^{eT} \mathbf{B}_{\varphi}^{\mathrm{eT}} \mathbf{B}_{\varphi}^{\mathrm{e}} \boldsymbol{\Phi}^{e} \tag{6.81}$$

The known and prescribed temperatures are abbreviated by

$$\overline{\boldsymbol{p}}_\Theta(t,\boldsymbol{u}(t),\boldsymbol{\Theta}(t)) = -\overline{\boldsymbol{C}}_\mathrm{p}\left(t,\boldsymbol{u}(t),\boldsymbol{\Theta}(t)\right)\dot{\overline{\boldsymbol{\Theta}}}(t). \tag{6.82}$$

The electrical field is now discretized from its weak formulation (6.38)

$$\pi_\varphi^h(\boldsymbol{u},\boldsymbol{\Theta},\boldsymbol{\Phi},\delta\boldsymbol{\Phi},t) = \\ \delta\boldsymbol{\Phi}^\mathrm{T}\left\{\sum_{e=1}^{n_\mathrm{e}}\boldsymbol{Z}_\varphi^{\mathrm{eT}}\left\{\int\limits_{\Omega_e}\mathbf{B}_\varphi^{\mathrm{eT}}(\mathbf{x})\kappa_\mathrm{el}^h\,\mathbf{B}_\varphi^\mathrm{e}(\mathbf{x})\,\mathrm{d}\Omega_e\,\boldsymbol{\Phi} + \int\limits_{\Gamma_\mathrm{e}} f_j\mathbf{N}_\varphi^\mathrm{e}\,\mathrm{d}\Gamma_\mathrm{e}\right\}\right\} = 0. \tag{6.83}$$

The gradient of the electrical potential and the virtual electrical potential are approximated within the element e by

$$\operatorname{grad}\varphi^h = \mathbf{B}_\varphi^\mathrm{e}(\boldsymbol{\phi}^e(\mathbf{x}))\boldsymbol{\Phi}^e(t) = \mathbf{B}_\varphi^\mathrm{e}(\boldsymbol{\phi}^e(\mathbf{x}))\left\{\boldsymbol{Z}_\varphi^\mathrm{e}\boldsymbol{\Phi} + \overline{\boldsymbol{Z}}_\varphi^\mathrm{e}\overline{\boldsymbol{\Phi}}(t)\right\} \tag{6.84}$$

$$\operatorname{grad}\delta\varphi^h = \mathbf{B}_\varphi^\mathrm{e}(\boldsymbol{\phi}^e(\mathbf{x}))\delta\boldsymbol{\Phi}^e = \mathbf{B}_\varphi^\mathrm{e}(\boldsymbol{\phi}^e(\mathbf{x}))\boldsymbol{Z}_\varphi^\mathrm{e}\delta\boldsymbol{\Phi} \tag{6.85}$$

The potential-gradient matrix decomposes into the submatrices

$$\mathbf{B}_\varphi^\mathrm{e}(\boldsymbol{\phi}^e(\mathbf{x})) = \left[\mathbf{B}_{\varphi 1}^\mathrm{e}\ldots\mathbf{B}_{\varphi n_\varphi^e}^\mathrm{e}\right] \in \mathbb{R}^{3\times n_\varphi^e}. \tag{6.86}$$

In this matrix, the derivatives of the shape functions with respect to the spatial (current) coordinates at the node a are arranged

$$\mathbf{B}_{\varphi_a}^\mathrm{e}(\boldsymbol{\phi}^e(\mathbf{x})) = \begin{Bmatrix} N_{\varphi a,x}^e \\ N_{\varphi a,y}^e \\ N_{\varphi a,z}^e \end{Bmatrix}, \qquad a = 1,\ldots,n_\varphi^e \tag{6.87}$$

The virtual electrical potentials are arbitrary and, accordingly, the discretized stationary electrical charge equation yields a system of non-linear equations

$$\boldsymbol{g}_\varphi(t,\boldsymbol{u},\boldsymbol{\Theta},\boldsymbol{\Phi}) = \boldsymbol{0} \tag{6.88}$$

with

$$\boldsymbol{g}_\varphi(t,\boldsymbol{u},\boldsymbol{\Theta},\boldsymbol{\Phi}) := \boldsymbol{K}_\varphi(t,\boldsymbol{\Theta},\boldsymbol{u})\boldsymbol{\Phi}(t) + \overline{\boldsymbol{p}}_\varphi(t,\boldsymbol{u}) + \overline{\boldsymbol{K}}_\varphi(t,\boldsymbol{\Theta},\boldsymbol{u})\overline{\boldsymbol{\Phi}}(t). \tag{6.89}$$

Here, the electrical conductivity matrices

$$\boldsymbol{K}_\varphi(t,\boldsymbol{\Theta},\boldsymbol{u}) := \sum_{e=1}^{n_\mathrm{e}}\boldsymbol{Z}_\varphi^{\mathrm{eT}}\left[\int\limits_{\Omega_e}\kappa_\mathrm{el}^h\,\mathbf{B}_\varphi^{\mathrm{eT}}(\mathbf{x})\mathbf{B}_\varphi^\mathrm{e}(\mathbf{x})\,\mathrm{d}\Omega_e\right]\boldsymbol{Z}_\varphi^\mathrm{e} \quad \in \mathbb{R}^{n_{\varphi\mathrm{u}}\times n_{\varphi\mathrm{u}}} \tag{6.90}$$

$$\overline{\boldsymbol{K}}_\varphi(t,\boldsymbol{\Theta},\boldsymbol{u}) := \sum_{e=1}^{n_\mathrm{e}}\boldsymbol{Z}_\varphi^{\mathrm{eT}}\left[\int\limits_{\Omega_e}\kappa_\mathrm{el}^h\,\mathbf{B}_\varphi^{\mathrm{eT}}(\mathbf{x})\mathbf{B}_\varphi^\mathrm{e}(\mathbf{x})\,\mathrm{d}\Omega_e\right]\overline{\boldsymbol{Z}}_\varphi^\mathrm{e} \quad \in \mathbb{R}^{n_{\varphi\mathrm{u}}\times n_{\varphi\mathrm{p}}} \tag{6.91}$$

and the prescribed electrical density over the surface

$$\overline{\boldsymbol{p}}_{\varphi}(t,\boldsymbol{u}) := \sum_{e=1}^{n_\mathrm{e}} \boldsymbol{Z}_{\varphi}^{\mathrm{eT}} \int\limits_{\Gamma_\mathrm{e}} f_j \mathbf{N}_{\varphi}^{\mathrm{e}} \,\mathrm{d}\Gamma_\mathrm{e} \tag{6.92}$$

are introduced. The last term in Eq. (6.88) stems from the prescribed known electrical potentials $\overline{\mathbf{\Phi}}$. The electrical conductivity $\kappa_{\mathrm{el}}^{h} = \tilde{\kappa}_{\mathrm{el}}(t, \boldsymbol{u}^{\mathrm{e}}(t), \mathbf{\Theta}^{\mathrm{e}}(t))$ in Eqns. (6.90) and (6.91) depends on the relative density and on the temperature. In summary, this leads to a DAE-system consisting of the balance of momentum, the evolutionary equations, the heat conduction equation and the electrical field equation in its discretized form, see Tab. 6.3.

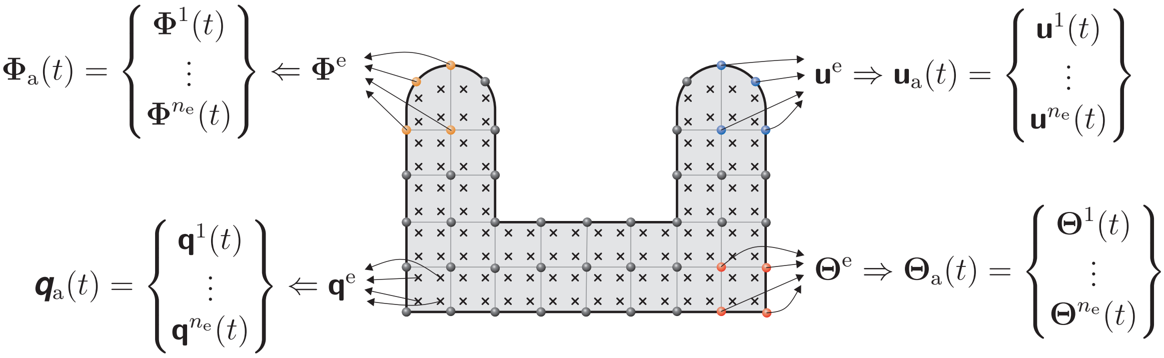

Figure 6.6: Assembly of the element degree of freedom into global vectors for the electrical potential $\mathbf{\Phi}$, the displacement $\mathbf{u}$, the internal variables $\mathbf{q}$ and the temperatures $\mathbf{\Theta}$

Remark 3 *The idea of interpreting non-linear finite element procedures as differential-algebraic equations goes back to Wittekindt [1991], Fritzen [1997] and Ellsiepen and Hartmann [2001]. The global DAE-system can be derived by arranging the nodal degrees of freedom as well as the internal variables into global vectors, see Fig. 6.6. The advantage of this interpretation is the application of efficient time integration schemes developed in Numerical Mathematics. These can be diagonally implicit Runge-Kutta (DIRK) methods with efficient time step-size control, see [Hartmann et al., 2008a; Hartmann et al., 2008b; Hartmann and Bier, 2008]. For thermal problems, see [Quint et al., 2011], while thermo-mechanically coupling with DIRK-methods is investigated in [Quint, 2012; Birken et al., 2010; Hartmann et al., 2009a; Hartmann and Rothe, 2013]. Rosenbrock methods, which yield an iteration-free procedure, are applied within the finite element context in [Hamkar, 2013; Hartmann and Hamkar, 2010; Hamkar et al., 2012; Netz et al., 2013b]. High-order space and time discretization can be found in [Netz, 2013; Netz et al., 2013b]. For a comparison of different time integration methods, see [Rothe et al.,* *2012]. The classical finite element implementations are based on the Multilevel Newton algorithm, [Rabbat et al., 1979]. Based on insight into the global structure of current finite elements, the Newton-Raphson method can be applied too – as shown in [Hartmann, 2005].*

Table 6.3: Semi-discretized system of the thermo-electro-mechanical coupled problem

For the computation of $\boldsymbol{u}(t)$, $\Theta(t)$, $\Phi(t)$ and $\boldsymbol{q}(t)$ in the interval $t \in [t_0, t_e]$ it is necessary to solve the semi-discretized DAE-system

$$\begin{aligned} \boldsymbol{A}\dot{\boldsymbol{q}}(t) &= \boldsymbol{r}_{\mathrm{q}}(t, \boldsymbol{u}(t), \Theta(t), \boldsymbol{q}(t)), & \boldsymbol{q}(t_0) &= \boldsymbol{q}_0 & (6.68)\\ \boldsymbol{C}_{\mathrm{p}}\,\dot{\Theta}(t) &= \boldsymbol{r}_{\Theta}(t, \boldsymbol{u}(t), \Theta(t), \Phi(t)), & \Theta(t_0) &= \Theta_0 & (6.74)\\ \boldsymbol{0} &= \boldsymbol{g}_{\varphi}(t, \boldsymbol{u}(t), \Theta(t), \Phi(t)), & \Phi(t_0) &= \Phi_0 & (6.88)\\ \boldsymbol{0} &= \boldsymbol{g}_{\mathrm{u}}(t, \boldsymbol{u}(t), \Theta(t), \boldsymbol{q}(t)), & \boldsymbol{u}(t_0) &= \boldsymbol{u}_0 & (6.59) \end{aligned}$$

The semi-discretized DAE-system in Tab. 6.3 has to be discretized in the time according to the vertical method of lines, which will be done in the following.

6.3.4 Temporal Discretization using Backward Euler Method

The temporal discretization in Abaqus Implicit is performed with the backward Euler method – here applied to the DAE-system. According to Hairer and Wanner [2002], the ε-embedded method can be applied to DAE-systems. This procedure serves to transform the DAE-system assembled in Tab. 6.3 into an ODE-system in order to apply the backward Euler method. By introducing a small parameter $0 < \varepsilon \ll 1$, one obtains

$$\boldsymbol{A}\dot{\boldsymbol{q}}(t) = \boldsymbol{r}_{\mathrm{q}}(t, \boldsymbol{u}(t), \Theta(t), \boldsymbol{q}(t)) \tag{6.93}$$

$$\boldsymbol{C}_{\mathrm{p}}\,\dot{\Theta}(t) = \boldsymbol{r}_{\Theta}(t, \boldsymbol{u}(t), \Theta(t), \Phi(t)) \tag{6.94}$$

$$\varepsilon\dot{\boldsymbol{\Phi}} = \boldsymbol{g}_{\varphi}(t, \boldsymbol{u}(t), \Theta(t), \Phi(t)) \tag{6.95}$$

$$\varepsilon\dot{\boldsymbol{u}} = \boldsymbol{g}_{\mathrm{u}}(t, \boldsymbol{u}(t), \Theta(t), \boldsymbol{q}(t)) \tag{6.96}$$

The application of the backward Euler method yields

$$\boldsymbol{A}\boldsymbol{q}_{n+1} = \boldsymbol{A}\boldsymbol{q}_n + \Delta t\boldsymbol{r}_{\mathrm{q}}(t_{n+1}, \boldsymbol{u}_{n+1}, \Theta_{n+1}, \boldsymbol{q}_{n+1}) \tag{6.97}$$

$$\boldsymbol{C}_{\mathrm{p}}\,\Theta_{n+1} = \boldsymbol{C}_{\mathrm{p}}\,\Theta_n + \Delta t\boldsymbol{r}_{\Theta}(t_{n+1}, \boldsymbol{u}_{n+1}, \Theta_{n+1}, \Phi_{n+1}) \tag{6.98}$$

$$\varepsilon\boldsymbol{\Phi}_{n+1} = \varepsilon\boldsymbol{\Phi}_n + \Delta t\boldsymbol{g}_{\varphi}(t_{n+1}, \boldsymbol{u}_{n+1}, \Theta_{n+1}, \Phi_{n+1}) \tag{6.99}$$

$$\varepsilon\mathbf{u}_{n+1} = \varepsilon\mathbf{u}_n + \Delta t\boldsymbol{g}_{\mathrm{u}}(t_{n+1}, \boldsymbol{u}_{n+1}, \Theta_{n+1}, \boldsymbol{q}_{n+1}) \tag{6.100}$$

where $\boldsymbol{v}_{n+1} = \boldsymbol{v}(t_{n+1})$ denotes the value at the next time t_{n+1}, whereas $\boldsymbol{v}_n = \boldsymbol{v}(t_n)$ represents the value at the last time t_n. With the limit $\varepsilon \to 0$, one obtains

$$\boldsymbol{0} = \boldsymbol{A}\frac{\boldsymbol{q}_{n+1} - \boldsymbol{q}_n}{\Delta t} - \boldsymbol{r}_{\mathrm{q}}(t_{n+1}, \boldsymbol{u}_{n+1}, \Theta_{n+1}, \boldsymbol{q}_{n+1}) \tag{6.101}$$

$$\boldsymbol{0} = \boldsymbol{C}_{\mathrm{p}}\frac{\Theta_{n+1} - \Theta_n}{\Delta t} - \boldsymbol{r}_{\Theta}(t_{n+1}, \boldsymbol{u}_{n+1}, \Theta_{n+1}, \Phi_{n+1}) \tag{6.102}$$

$$\boldsymbol{0} = \boldsymbol{g}_{\varphi}(t_{n+1}, \boldsymbol{u}_{n+1}, \Theta_{n+1}, \Phi_{n+1}) \tag{6.103}$$

$$\boldsymbol{0} = \boldsymbol{g}_{\mathrm{u}}(t_{n+1}, \boldsymbol{u}_{n+1}, \Theta_{n+1}, \boldsymbol{q}_{n+1}) \tag{6.104}$$

This means that for every time-step t_{n+1}, it is required to solve a system of non-linear equations for the unknown nodal displacements, nodal temperatures, nodal electrical potentials as well as the unknown internal variables

$$\boldsymbol{L}_{\mathrm{q}}(\boldsymbol{u}, \Theta, \boldsymbol{q}) := \boldsymbol{A}\frac{\boldsymbol{q}_{n+1} - \boldsymbol{q}_n}{\Delta t} - \boldsymbol{r}_{\mathrm{q}}(t_{n+1}, \boldsymbol{u}_{n+1}, \Theta_{n+1}, \boldsymbol{q}_{n+1}) = \boldsymbol{0} \tag{6.105}$$

$$\boldsymbol{G}_{\Theta}(\boldsymbol{u}, \Theta, \Phi) := \boldsymbol{C}_{\mathrm{p}}\frac{\Theta_{n+1} - \Theta_n}{\Delta t} - \boldsymbol{r}_{\Theta}(t_{n+1}, \boldsymbol{u}_{n+1}, \Theta_{n+1}, \Phi_{n+1}) = \boldsymbol{0} \tag{6.106}$$

$$\boldsymbol{G}_{\varphi}(\boldsymbol{u}, \Theta, \Phi) := \boldsymbol{g}_{\varphi}(t_{n+1}, \boldsymbol{u}_{n+1}, \Theta_{n+1}, \Phi_{n+1}) = \boldsymbol{0} \tag{6.107}$$

$$\boldsymbol{G}_{\mathrm{u}}(\boldsymbol{u}, \Theta, \boldsymbol{q}) := \boldsymbol{g}_{\mathrm{u}}(t_{n+1}, \boldsymbol{u}_{n+1}, \Theta_{n+1}, \boldsymbol{q}_{n+1}) = \boldsymbol{0} \tag{6.108}$$

The temperature and the internal variables' time derivatives are given by

$$\dot{\boldsymbol{q}}_{n+1} := \frac{\boldsymbol{q}_{n+1} - \boldsymbol{q}_n}{\Delta t}, \qquad \dot{\Theta}_{n+1} := \frac{\Theta_{n+1} - \Theta_n}{\Delta t}. \tag{6.109}$$

6.3.5 Solution of Nonlinear Systems by Means of the Multilevel-Newton Algorithm

In the finite element method, the iterative solution of internal variables is connected to the Multilevel-Newton algorithm (MLNA), which has the advantage of local quadratic convergence. The solution of the non-linear system (6.105) - (6.108) in Abaqus can also be interpreted as the solution with the MLNA, which is investigated in [Hartmann, 2005] for isothermal problems. Concerning the mathematical basis of the MLNA, see [Rabbat et al., 1979; Hoyer and Schmidt, 1984]. The Newton-Raphson method (NRM) is applied, for example, in the case of hyperelasticity if no iterations occur on Gauss-point level. Due to the evolution equations for the internal variables arranged in Eq. (6.105), the MLNA is used instead, as described in the following. In general, it is also possible to use an NRM-implementation in the context of finite elements by the formulation of a Newton-Schur scheme, see [Hartmann, 2005]. A similar approach is to be found in [Kulkarni et al., 2007], but this line of thought is not followed here.

Instead, the MLNA is decomposed into a global level – where the equilibrium condition, the heat equation and the electrical equation are solved – and a local level (Gauss-point level), where the internal variables are computed iteratively. According to Quint [2012], the "global" equations $\boldsymbol{G}^T = \{\boldsymbol{G}_\mathrm{u}^\mathrm{T}\,\boldsymbol{G}_\Theta^\mathrm{T}\,\boldsymbol{G}_\varphi^\mathrm{T}\}$ and the global variables $\boldsymbol{v}^\mathrm{T} = \{\boldsymbol{u}^\mathrm{T}\,\Theta^T\,\Phi^T\}$ are decomposed. In this case, the system of equations (6.105) - (6.108) reads

$$\boldsymbol{G}(\boldsymbol{v},\boldsymbol{q}) = \left\{\begin{array}{c} \boldsymbol{G}_\mathrm{u}(\boldsymbol{u},\Theta,\boldsymbol{q}) \\ \boldsymbol{G}_\Theta(\boldsymbol{u},\Theta,\Phi) \\ \boldsymbol{G}_\varphi(\boldsymbol{u},\Theta,\Phi) \end{array}\right\} = \boldsymbol{0} \tag{6.110}$$

$$\boldsymbol{L}(\boldsymbol{v},\boldsymbol{q}) = \boldsymbol{L}_\mathrm{q}(\boldsymbol{u},\Theta,\boldsymbol{q}) = \boldsymbol{0} \tag{6.111}$$

The MLNA is based on the implicit function theorem, i.e. there exists a solution $\boldsymbol{q} = \hat{\boldsymbol{q}}(\boldsymbol{v})$. This solution is inserted into Eq. (6.110),

$$\boldsymbol{G}(\boldsymbol{v},\hat{\boldsymbol{q}}(\boldsymbol{v})) = \boldsymbol{0}. \tag{6.112}$$

If the classical Newton-Raphson scheme is applied to this equation, a linear system within the iteration step (m) is obtained

$$\left[\frac{\partial\boldsymbol{G}}{\partial\boldsymbol{v}} + \frac{\partial\boldsymbol{G}}{\partial\boldsymbol{q}}\frac{\mathrm{d}\hat{\boldsymbol{q}}}{\mathrm{d}\boldsymbol{v}}\right]_{\boldsymbol{y}^{(m)}} \Delta\boldsymbol{v}^{(m)} = -\boldsymbol{G}(\boldsymbol{v}^{(m)},\boldsymbol{q}^{(m+1)}). \tag{6.113}$$

The matrix on the left-hand side can be interpreted as the consistent tangent operator for the coupled thermo-electro-mechanical system, see also [Simo and Taylor, 1985]. In Eq. (6.113), two quantities are unknown. First, $\boldsymbol{q}^{(m+1)} = \hat{\boldsymbol{q}}(\boldsymbol{v})$ must be provided. Secondly, the derivative $\mathrm{d}\hat{\boldsymbol{q}}/\,\mathrm{d}\boldsymbol{v}$ is not known – due to the fact that the function $\hat{\boldsymbol{q}}(\boldsymbol{v})$ exists – but its representation is unknown. In the first step, the internal variables are computed by Eq. (6.111) for given displacement, temperature and electric potential DOF $\boldsymbol{v}^{(m)}$

$$\boldsymbol{L}(\boldsymbol{v}^{(m)},\boldsymbol{q}^{(m+1)}) = \boldsymbol{0} \qquad \rightsquigarrow \qquad \boldsymbol{q}^{(m+1)}. \tag{6.114}$$

This can be done on element level, see for details Sect. 6.3.6 and [Hartmann, 2005]. The iteration number (m) is omitted for brevity in the following. The derivative $\mathrm{d}\hat{\boldsymbol{q}}/\,\mathrm{d}\boldsymbol{v}$ is computed in the second step by the chain-rule applied to Eq. (6.111) if the unknown function $\hat{\boldsymbol{q}}(\boldsymbol{v})$ is inserted

$$\boldsymbol{L}(\boldsymbol{v},\hat{\boldsymbol{q}}(\boldsymbol{v})) = \boldsymbol{0} \quad\longrightarrow\quad \frac{\partial\boldsymbol{L}}{\partial\boldsymbol{v}} + \frac{\partial\boldsymbol{L}}{\partial\boldsymbol{q}}\frac{\mathrm{d}\hat{\boldsymbol{q}}}{\mathrm{d}\boldsymbol{v}} = \boldsymbol{0}. \tag{6.115}$$

This represents a linear system of equations with several right-hand sides

$$\left[\frac{\partial\boldsymbol{L}}{\partial\boldsymbol{q}}\right]\left[\frac{\mathrm{d}\hat{\boldsymbol{q}}}{\mathrm{d}\boldsymbol{v}}\right] = -\left[\frac{\partial\boldsymbol{L}}{\partial\boldsymbol{v}}\right]. \tag{6.116}$$

Table 6.4: Multilevel-Newton algorithm

```
Given: starting vector estimation $\boldsymbol{v}^{(0)}$, $\boldsymbol{q}^{(0)}$ and $\Delta t_n$, $t_{n+1}$
Repeat   $m = 0, \ldots$
    local (Gauss-point) level
    given: $\boldsymbol{v}^{(m)}$, $\boldsymbol{y} = \left(\boldsymbol{u}^{(m)}, \Theta^{(m)}, \Phi^{(m)}, \boldsymbol{q}^{(m)}\right)$
    local integration step
        $\boldsymbol{L}(\boldsymbol{v}^{(m)}, \boldsymbol{q}^{(m+1)}) = \boldsymbol{0}$        $\rightsquigarrow \boldsymbol{q}^{(m+1)}$
    consistent linearization ($\boldsymbol{y} = \left(\boldsymbol{u}^{(m)}, \Theta^{(m)}, \Phi^{(m)}, \boldsymbol{q}^{(m+1)}\right)$)
        $\left.\frac{\partial \boldsymbol{L}}{\partial \boldsymbol{q}}\right|_{\boldsymbol{y}} \left.\frac{\mathrm{d}\hat{\boldsymbol{q}}}{\mathrm{d}\boldsymbol{v}}\right|_{\boldsymbol{y}} = -\left.\frac{\partial \boldsymbol{L}}{\partial \boldsymbol{v}}\right|_{\boldsymbol{y}}$        $\rightsquigarrow \left.\frac{\mathrm{d}\boldsymbol{q}}{\mathrm{d}\boldsymbol{v}}\right|_{\boldsymbol{y}}$
    global level
    solve linear system of equations
        $\left[\left.\frac{\partial \boldsymbol{G}}{\partial \boldsymbol{v}}\right|_{\boldsymbol{y}} + \left.\frac{\partial \boldsymbol{G}}{\partial \boldsymbol{q}}\right|_{\boldsymbol{y}} \left.\frac{\mathrm{d}\hat{\boldsymbol{q}}}{\mathrm{d}\boldsymbol{v}}\right|_{\boldsymbol{y}}\right] \Delta\boldsymbol{v} = -\boldsymbol{G}(\boldsymbol{v}^{(m)}, \boldsymbol{q}^{(m+1)})$        $\rightsquigarrow \Delta\boldsymbol{v}$
    update of global variables
        $\boldsymbol{v}^{(m+1)} \leftarrow \boldsymbol{v}^{(m)} + \Delta\boldsymbol{v}$        $\rightsquigarrow \boldsymbol{v}^{(m+1)}$
until   the convergence criterion is fulfilled
```

The matrices $\partial\boldsymbol{L}/\partial\boldsymbol{v}$ and $\partial\boldsymbol{L}/\boldsymbol{q}$ are known. The entire procedure is compiled in Tab. 6.4. The functional matrix in component form is given by

$$\left[\frac{\partial \boldsymbol{G}}{\partial \boldsymbol{v}} + \frac{\partial \boldsymbol{G}}{\partial \boldsymbol{q}}\frac{\mathrm{d}\hat{\boldsymbol{q}}}{\mathrm{d}\boldsymbol{v}}\right] = \begin{bmatrix} \frac{\partial \boldsymbol{G}_{\mathrm{u}}}{\partial \boldsymbol{u}} + \frac{\partial \boldsymbol{G}_{\mathrm{u}}}{\partial \boldsymbol{q}}\frac{\partial \hat{\boldsymbol{q}}}{\partial \boldsymbol{u}} & \frac{\partial \boldsymbol{G}_{\mathrm{u}}}{\partial \Theta} + \frac{\partial \boldsymbol{G}_{\mathrm{u}}}{\partial \boldsymbol{q}}\frac{\partial \hat{\boldsymbol{q}}}{\partial \Theta} & \boldsymbol{0} \\ \frac{\partial \boldsymbol{G}_{\Theta}}{\partial \boldsymbol{u}} & \frac{\partial \boldsymbol{G}_{\Theta}}{\partial \Theta} & \frac{\partial \boldsymbol{G}_{\Theta}}{\partial \Phi} \\ \frac{\partial \boldsymbol{G}_{\varphi}}{\partial \boldsymbol{u}} & \frac{\partial \boldsymbol{G}_{\varphi}}{\partial \Theta} & \frac{\partial \boldsymbol{G}_{\varphi}}{\partial \Phi} \end{bmatrix} \tag{6.117}$$

For the coupling between the three fields, see Fig. 6.2. In more detail, the system of equations (6.113) reads

$$\begin{bmatrix} \dfrac{\partial \boldsymbol{G}_{\mathrm{u}}}{\partial \boldsymbol{u}} + \dfrac{\partial \boldsymbol{G}_{\mathrm{u}}}{\partial \boldsymbol{q}} \dfrac{\partial \hat{\boldsymbol{q}}}{\partial \boldsymbol{u}} & \dfrac{\partial \boldsymbol{G}_{\mathrm{u}}}{\partial \Theta} + \dfrac{\partial \boldsymbol{G}_{\mathrm{u}}}{\partial \boldsymbol{q}} \dfrac{\partial \hat{\boldsymbol{q}}}{\partial \Theta} & \boldsymbol{0} \\ \dfrac{\partial \boldsymbol{G}_{\Theta}}{\partial \boldsymbol{u}} & \dfrac{\partial \boldsymbol{G}_{\Theta}}{\partial \Theta} & \dfrac{\partial \boldsymbol{G}_{\Theta}}{\partial \Phi} \\ \dfrac{\partial \boldsymbol{G}_{\varphi}}{\partial \boldsymbol{u}} & \dfrac{\partial \boldsymbol{G}_{\varphi}}{\partial \Theta} & \dfrac{\partial \boldsymbol{G}_{\varphi}}{\partial \Phi} \end{bmatrix} \begin{Bmatrix} \Delta \boldsymbol{u} \\ \Delta \Theta \\ \Delta \Phi \end{Bmatrix} = - \begin{Bmatrix} \boldsymbol{G}_{\mathrm{u}}(\boldsymbol{u}, \Theta, \boldsymbol{q}) \\ \boldsymbol{G}_{\Theta}(\boldsymbol{u}, \Theta, \Phi) \\ \boldsymbol{G}_{\varphi}(\boldsymbol{u}, \Theta, \Phi) \end{Bmatrix} \tag{6.118}$$

and Eq. (6.116) reads

$$\begin{bmatrix} \dfrac{\partial \boldsymbol{L}}{\partial \boldsymbol{q}} \end{bmatrix} \begin{bmatrix} \dfrac{\partial \hat{\boldsymbol{q}}}{\partial \boldsymbol{u}} & \dfrac{\partial \hat{\boldsymbol{q}}}{\partial \Theta} \end{bmatrix} = - \begin{bmatrix} \dfrac{\partial \boldsymbol{L}}{\partial \boldsymbol{u}} & \dfrac{\partial \boldsymbol{L}}{\partial \Theta} \end{bmatrix}, \tag{6.119}$$

for which the concrete representations are required.

6.3.6 Stress Algorithm

It is necessary to perform the local integration step for the computation of the internal variables for the Multilevel-Newton algorithm on local level. Furthermore, a consistent linearization has to be addressed.

In the following, the connection to the material model from Chap. 4 is described. The non-linear system $\boldsymbol{L}$ contains all evolution equations for the internal variables, which will be shown in detail. The vector of internal variables reads $\mathbf{q} = \{\mathbf{C}_{\mathrm{p}}, k_{\mathrm{M}}, \beta_{\mathrm{t}}, f_{\mathrm{c}}\}$. $\mathbf{C}_{\mathrm{p}} \in \mathbb{R}^6$ is the plastic Cauchy-Green tensor, k_{M} represents the isotropic hardening variable, β_{t} describes the sintering effect and is connected to the hydrostatic tensile hardening I_{t}, while f_{c} indicates the creep behavior.

Within the element, the temperatures Θ_{n+1}, the electrical potentials φ_{n+1} and the Cauchy-Green tensor components $\mathbf{C}_{n+1}$ are given at each Gauss-point, see Eq. (6.114). In order to determine the stress state Eq. (4.187), which is required in Eq. (6.58), the internal variables have to be computed by Eq. (6.105). With the computed internal variables, it is possible to evaluate the elasticity relation and to compute the new stress values. Therefore, this procedure is known as *stress algorithm*, although the scheme describes the computation of the internal variables. The elasticity relation for the material model in Chap. 4 reads

$$\begin{aligned} \tilde{\mathbf{T}} &:= \mathbf{h}(\mathbf{C}, \mathbf{C}_{\mathrm{p}}, \Theta, f_{\mathrm{c}}) \\ &= \frac{K}{2\phi^2} \left(\frac{\operatorname{tr}(\mathbf{C}\mathbf{C}_{\mathrm{i}}^{-1})}{\phi^2} - 3 \right) \mathbf{C}_{\mathrm{i}}^{-1} + \frac{G}{\phi^4} \left(\mathbf{C}_{\mathrm{i}}^{-1}\mathbf{C}\mathbf{C}_{\mathrm{i}}^{-1} - \tfrac{1}{3} \operatorname{tr}(\mathbf{C}\mathbf{C}_{\mathrm{i}}^{-1})\mathbf{C}_{\mathrm{i}}^{-1} \right). \end{aligned} \tag{4.187}$$

The constitutive model consists of four evolution equations. The creep variable f_{c} evolves continuously, whereas the sintering variable emerges only above the sintering temperature Θ_S. The evolution equations for these two internal variables read

$$\dot{\beta}_{\mathrm{t}} = h_\beta(\beta_{\mathrm{t}}, \Theta) = c_\beta(1 - \beta_{\mathrm{t}})\langle\Theta - \Theta_S\rangle \tag{4.167}$$

$$\dot{f}_{\mathrm{c}}(t) = h_c(f_{\mathrm{c}}, \Theta) = \frac{2}{3}A_c(\Theta - \Theta_0)\,(f_{\mathrm{c}} - c_\infty)\left\langle \check{\mathrm{I}}_{1\mathrm{c}} \right\rangle_*, \quad \check{\mathrm{I}}_{1\mathrm{c}} = f_{\mathrm{c}}\,\mathrm{tr}\,\tilde{\mathbf{T}} \tag{4.197,4.196}$$

with the material parameters c_β, Θ_S, A_c and c_∞.

The evolution equation for the plastic Cauchy-Green tensor $\mathbf{C}_{\mathrm{p}}$, (4.207) and the isotropic hardening variable k_{M}, (4.210) are subjected to a case distinction due to the yield function. Thus, the evolution equations are given by

---

$\tilde{F} < 0$

$$\dot{\mathbf{C}}_{\mathrm{p}} := \mathbf{h}_{\mathrm{p}}(\mathbf{C}, \mathbf{C}_{\mathrm{p}}, \Theta, f_{\mathrm{c}}) = \frac{\dot{f}_{\mathrm{c}}}{f_{\mathrm{c}}}(\mathbf{1} - \mathbf{C}_{\mathrm{p}})$$

$$\dot{k}_{\mathrm{M}} := h_{\mathrm{k}}(\mathbf{C}, \mathbf{C}_{\mathrm{p}}, k_{\mathrm{M}}, \Theta, f_{\mathrm{c}}) = \frac{\gamma_k}{3k_{\mathrm{M}}}g_{\mathrm{v}}\left\langle \check{\mathrm{I}}_{1\mathrm{c}} \right\rangle_* \check{\mathrm{I}}_{1\mathrm{c}}$$

$\tilde{F} = 0$

$$\dot{\mathbf{C}}_{\mathrm{p}} = \frac{2}{f_{\mathrm{c}}}\Lambda\frac{\partial F}{\partial\hat{\mathrm{J}}_{2\mathrm{i}}}\frac{G}{\phi^4}\mathbf{C} + \frac{2}{f_{\mathrm{c}}}\Lambda\left(\frac{\partial F}{\partial\hat{\mathrm{I}}_{1\mathrm{i}}}f_{\mathrm{c}}\mathbf{1} - \frac{1}{3}\frac{\partial F}{\partial\hat{\mathrm{J}}_{2\mathrm{i}}}\frac{G}{\phi^4}\,\mathrm{tr}(\mathbf{C}_{\mathrm{p}}^{-1}\mathbf{C})\mathbf{1}\right)\mathbf{C}_{\mathrm{p}} + \frac{\dot{f}_{\mathrm{c}}}{f_{\mathrm{c}}}(\mathbf{1} - \mathbf{C}_{\mathrm{p}})$$

$$\dot{k}_{\mathrm{M}} = \Lambda\frac{\gamma_k}{k_{\mathrm{M}}}\left(\frac{\partial F}{\partial\hat{\mathrm{I}}_{1\mathrm{i}}}(\hat{\mathrm{I}}_{1\mathrm{i}} + 3\xi_{\mathrm{M}}) + 2\frac{\partial F}{\partial\hat{\mathrm{J}}_{2\mathrm{i}}}\hat{\mathrm{J}}_{2\mathrm{i}}\right) - \Lambda\chi\beta_k k_{\mathrm{M}} + \frac{\gamma_k}{3k_{\mathrm{M}}}g_{\mathrm{v}}\left\langle \check{\mathrm{I}}_{1\mathrm{c}} \right\rangle_* \check{\mathrm{I}}_{1\mathrm{c}}$$

These evolution equations change depending on the yield function. If the stress state reaches the yield function, the plastic multiplier can be computed out of the yield condition $\tilde{F} = 0$. Otherwise, the plastic multiplier is zero – and $\mathbf{C}_{\mathrm{p}}$ as well as k_{M} evolve due to the influence of the creep variable f_{c}.

To incorporate the case distinctions in the numerical algorithm, the elastic-predictor/plastic-corrector scheme is applied, which is described in detail in the work of Simo and Hughes [2000]. The use of the elastic predictor scheme means that the yield function is evaluated with the new strains $\mathbf{C}_{n+1}$ and internal variables $\boldsymbol{q}_n$ from the last time-step. If the yield function $\tilde{F}(\mathbf{C}_{n+1}, \Theta_{n+1}, \boldsymbol{q}_n) \geq 0$ is greater or equal to zero, the plastic corrector scheme has to be applied and the new internal variables $\boldsymbol{q}_{n+1}$ are computed in such a way that $\tilde{F} = 0$ holds. The plastic multiplier Λ is computed by $\tilde{F} = 0$. For an elastoplasticity model with nonlinear kinematic hardening, the work of Hartmann and Haupt [1993] offers a possibility to reduce the computational effort by analytical considerations. This implies a reduction to one equation with one unknown, called problem-adapted stress-algorithm, see [Lührs et al., 1997] as well as [Hartmann et al., 1997] for details.

The time integration is performed with the backward Euler method, see Sect. 6.3.4, leading for Eqns. (4.167), (4.197), (4.207) and (4.210) to

$$\mathbf{0} = \mathbf{C}_\mathrm{p}^{n+1} - \mathbf{C}_\mathrm{p}^{n} - \Delta t\; \mathbf{h}_\mathrm{p}(\mathbf{C}, \mathbf{C}_\mathrm{p}^{n+1}, k_\mathrm{M}^{n+1}, \Theta^{n+1}, f_\mathrm{c}^{n+1}, \Lambda^{n+1}) \tag{6.120}$$

$$0 = k_\mathrm{M}^{n+1} - k_\mathrm{M}^{n} - \Delta t\; h_\mathrm{k}(\mathbf{C}, \mathbf{C}_\mathrm{p}^{n+1}, k_\mathrm{M}^{n+1}, \Theta^{n+1}, f_\mathrm{c}^{n+1}, \Lambda^{n+1}) \tag{6.121}$$

$$0 = \beta_\mathrm{t}^{n+1} - \beta_\mathrm{t}^{n} - \Delta t\; h_\beta(\beta_\mathrm{t}^{n+1}, \Theta^{n+1}) \tag{6.122}$$

$$0 = f_\mathrm{c}^{n+1} - f_\mathrm{c}^{n} - \Delta t\; h_c(\mathbf{C}, \Theta^{n+1}, \mathbf{C}_\mathrm{p}^{n+1}, f_\mathrm{c}^{n+1}) \tag{6.123}$$

$$0 = \tilde{F}^{n+1}(\mathbf{C}, \mathbf{C}_\mathrm{p}^{n+1}, k_\mathrm{M}^{n+1}, \Theta^{n+1}, \Lambda^{n+1}, \mathrm{I}_\mathrm{t}(\beta_\mathrm{t})) \tag{6.124}$$

Due to the symmetry of $\mathbf{C}$ and $\mathbf{C}_\mathrm{p}$, they are arranged as vectors in the finite element program, see [Hartmann, 2003] for more details about the matrix notation. These discretized equations form a non-linear system of equations

$$\mathbf{L}_\mathrm{p}(\mathbf{C}, \Theta, \mathbf{C}_\mathrm{p}, k_\mathrm{M}, f_\mathrm{c}, \Lambda) = \mathbf{0} \tag{6.125}$$

$$\mathsf{L}_\mathrm{k}(\mathbf{C}, \Theta, \mathbf{C}_\mathrm{p}, k_\mathrm{M}, f_\mathrm{c}, \Lambda) = 0 \tag{6.126}$$

$$\mathsf{L}_\beta(\Theta, \beta_\mathrm{t}) = 0 \tag{6.127}$$

$$\mathsf{L}_c(\mathbf{C}, \Theta, \mathbf{C}_\mathrm{p}, f_\mathrm{c}) = 0 \tag{6.128}$$

$$\mathsf{L}_f(\mathbf{C}, \Theta, \mathbf{C}_\mathrm{p}, k_\mathrm{M}, f_\mathrm{c}, \Lambda) = 0 \tag{6.129}$$

where the time index $n+1$ is omitted. All these equations can be formally written as a single equation system, leading to

$$\mathbf{L}(\mathbf{C}, \Theta, \mathbf{q}) = \mathbf{0} \tag{6.130}$$

By applying the Newton-Raphson method to these equation systems, one obtains

$$\left[\frac{\mathrm{d}\mathbf{L}}{\mathrm{d}\mathbf{q}}\right]\Bigg|_{\mathbf{q}=\mathbf{q}^{(k)}} \Delta\mathbf{q}^{(k)} = -\mathbf{L}(\mathbf{C}, \Theta, \mathbf{q}^{(k)}) \tag{6.131}$$

with the iteration index k. If the solution $\Delta\mathbf{q}^{(k)}$ of this linear system is computed, the internal variables for the next iteration read

$$\mathbf{q}^{(k+1)} = \mathbf{q}^{(k)} + \Delta\mathbf{q}^{(k)}. \tag{6.132}$$

This iterative procedure is continued until a certain convergence criterion is fulfilled, for example

$$\|\mathbf{L}(\mathbf{C}, \Theta, \boldsymbol{q}^{(k)})\| < \mathrm{tol}_\mathbf{L} \quad \text{and} \quad \|\Delta\boldsymbol{q}^{(k)}\| < \mathrm{tol}_{\boldsymbol{q}} \tag{6.133}$$

with the abort tolerance $\mathrm{tol}_\mathbf{L}$ and $\mathrm{tol}_{\boldsymbol{q}}$. In [Hartmann and Bier, 2008], it turned out that a Newton method with line-search can stabilize the numerical algorithm – which is the reason for the use of this approach in this work instead of the classical Newton-Raphson method. For more information about the line-search algorithm, see [Hartmann and Bier, 2008], [Pérez-Foguet and Armero, 2002] as well as [Armero and Perez-Foguet, 2002].

The follwing passage focuses on a detailed description of the equation systems that are required for the computation of the new internal variables and the consistent tangent matrix on the local level.

If the yield function is negative, β_{t} can be computed by

$$\frac{\partial \mathsf{L}_\beta}{\partial \beta_{\mathrm{t}}} \Delta\beta_{\mathrm{t}} = -\mathsf{L}_\beta(\Theta, \beta_{\mathrm{t}}). \tag{6.134}$$

For the other variables, the equation system has to be solved

$$\begin{bmatrix} \dfrac{\partial \boldsymbol{\mathsf{L}}_{\mathrm{p}}}{\partial \boldsymbol{\mathsf{C}}_{\mathrm{p}}} & \dfrac{\partial \boldsymbol{\mathsf{L}}_{\mathrm{p}}}{\partial k_{\mathrm{M}}} & \dfrac{\partial \boldsymbol{\mathsf{L}}_{\mathrm{p}}}{\partial f_{\mathrm{c}}} \\ \left\{ \dfrac{\partial \mathsf{L}_{\mathrm{k}}}{\partial \boldsymbol{\mathsf{C}}_{\mathrm{p}}} \right\}^{\mathrm{T}} & \dfrac{\partial \mathsf{L}_{\mathrm{k}}}{\partial k_{\mathrm{M}}} & \dfrac{\partial \mathsf{L}_{\mathrm{k}}}{\partial f_{\mathrm{c}}} \\ \left\{ \dfrac{\partial \mathsf{L}_c}{\partial \boldsymbol{\mathsf{C}}_{\mathrm{p}}} \right\}^{\mathrm{T}} & 0 & \dfrac{\partial \mathsf{L}_c}{\partial f_{\mathrm{c}}} \end{bmatrix} \begin{Bmatrix} \Delta \boldsymbol{\mathsf{C}}_{\mathrm{p}} \\ \Delta k_{\mathrm{M}} \\ \Delta f_{\mathrm{c}} \end{Bmatrix} = - \begin{Bmatrix} \boldsymbol{\mathsf{L}}_{\mathrm{p}}(\boldsymbol{\mathsf{C}}, \Theta, \boldsymbol{\mathsf{C}}_{\mathrm{p}}, k_{\mathrm{M}}, f_{\mathrm{c}}, \Lambda) \\ \mathsf{L}_{\mathrm{k}}(\boldsymbol{\mathsf{C}}, \Theta, \boldsymbol{\mathsf{C}}_{\mathrm{p}}, k_{\mathrm{M}}, f_{\mathrm{c}}, \Lambda) \\ \mathsf{L}_c(\boldsymbol{\mathsf{C}}, \Theta, \boldsymbol{\mathsf{C}}_{\mathrm{p}}, f_{\mathrm{c}}) \end{Bmatrix}. \tag{6.135}$$

If $\tilde{F} \geq 0$ holds, the equation system

$$\begin{bmatrix} \dfrac{\partial \boldsymbol{\mathsf{L}}_{\mathrm{p}}}{\partial \boldsymbol{\mathsf{C}}_{\mathrm{p}}} & \dfrac{\partial \boldsymbol{\mathsf{L}}_{\mathrm{p}}}{\partial k_{\mathrm{M}}} & \dfrac{\partial \boldsymbol{\mathsf{L}}_{\mathrm{p}}}{\partial f_{\mathrm{c}}} & \dfrac{\partial \boldsymbol{\mathsf{L}}_{\mathrm{p}}}{\partial \Lambda} & 0 \\ \left\{ \dfrac{\partial \mathsf{L}_{\mathrm{k}}}{\partial \boldsymbol{\mathsf{C}}_{\mathrm{p}}} \right\}^{\mathrm{T}} & \dfrac{\partial \mathsf{L}_{\mathrm{k}}}{\partial k_{\mathrm{M}}} & \dfrac{\partial \mathsf{L}_{\mathrm{k}}}{\partial f_{\mathrm{c}}} & \dfrac{\partial \mathsf{L}_{\mathrm{k}}}{\partial \Lambda} & 0 \\ \left\{ \dfrac{\partial \mathsf{L}_c}{\partial \boldsymbol{\mathsf{C}}_{\mathrm{p}}} \right\}^{\mathrm{T}} & 0 & \dfrac{\partial \mathsf{L}_c}{\partial f_{\mathrm{c}}} & 0 & 0 \\ \left\{ \dfrac{\partial \mathsf{L}_f}{\partial \boldsymbol{\mathsf{C}}_{\mathrm{p}}} \right\}^{\mathrm{T}} & \dfrac{\partial \mathsf{L}_f}{\partial k_{\mathrm{M}}} & \dfrac{\partial \mathsf{L}_f}{\partial f_{\mathrm{c}}} & \dfrac{\partial \mathsf{L}_f}{\partial \Lambda} & \dfrac{\partial \mathsf{L}_f}{\partial \beta_{\mathrm{t}}} \\ 0 & 0 & 0 & 0 & \dfrac{\partial \mathsf{L}_\beta}{\partial \beta_{\mathrm{t}}} \end{bmatrix} \begin{Bmatrix} \Delta \boldsymbol{\mathsf{C}}_{\mathrm{p}} \\ \Delta k_{\mathrm{M}} \\ \Delta f_{\mathrm{c}} \\ \Delta \Lambda \\ \Delta \beta_{\mathrm{t}} \end{Bmatrix} = - \begin{Bmatrix} \boldsymbol{\mathsf{L}}_{\mathrm{p}}(\boldsymbol{\mathsf{C}}, \Theta, \boldsymbol{\mathsf{C}}_{\mathrm{p}}, k_{\mathrm{M}}, f_{\mathrm{c}}, \Lambda) \\ \mathsf{L}_{\mathrm{k}}(\boldsymbol{\mathsf{C}}, \Theta, \boldsymbol{\mathsf{C}}_{\mathrm{p}}, k_{\mathrm{M}}, f_{\mathrm{c}}, \Lambda) \\ \mathsf{L}_c(\boldsymbol{\mathsf{C}}, \Theta, \boldsymbol{\mathsf{C}}_{\mathrm{p}}, f_{\mathrm{c}}) \\ \mathsf{L}_f(\boldsymbol{\mathsf{C}}, \Theta, \boldsymbol{\mathsf{C}}_{\mathrm{p}}, k_{\mathrm{M}}, f_{\mathrm{c}}, \Lambda, \beta_{\mathrm{t}}) \\ \mathsf{L}_\beta(\Theta, \beta_{\mathrm{t}}) \end{Bmatrix} \tag{6.136}$$

has to be solved in every iteration k to obtain the new internal variables. This system can be reduced by static condensation. Therefore, the system is written with the remaining nonlinear equations $\boldsymbol{\mathsf{L}}_r = \{\boldsymbol{\mathsf{L}}_{\mathrm{p}}\ \mathsf{L}_{\mathrm{k}}\ \mathsf{L}_c\ \mathsf{L}_f\}$ and the remaining internal variables $\boldsymbol{\mathsf{q}}_r = \{\boldsymbol{\mathsf{C}}_{\mathrm{p}}\ k_{\mathrm{M}}\ f_{\mathrm{c}}\ \Lambda\}$ as

$$\begin{bmatrix} \dfrac{\partial \boldsymbol{\mathsf{L}}_r}{\partial \boldsymbol{\mathsf{q}}_r} & \dfrac{\partial \boldsymbol{\mathsf{L}}_r}{\partial \beta_{\mathrm{t}}} \\ \boldsymbol{0} & \dfrac{\partial \mathsf{L}_\beta}{\partial \beta_{\mathrm{t}}} \end{bmatrix} \begin{Bmatrix} \Delta \beta_{\mathrm{t}} \\ \Delta \boldsymbol{\mathsf{q}}_r \end{Bmatrix} = - \begin{Bmatrix} \boldsymbol{\mathsf{L}}_r \\ \mathsf{L}_\beta \end{Bmatrix}. \tag{6.137}$$

The second equation can be written as

$$\frac{\partial \mathsf{L}_\beta}{\partial \beta_{\mathrm{t}}} \Delta\beta_{\mathrm{t}} = -\mathsf{L}_\beta \quad \Rightarrow \quad \Delta\beta_{\mathrm{t}} = -\left(\frac{\partial \mathsf{L}_\beta}{\partial \beta_{\mathrm{t}}} \right)^{-1} \mathsf{L}_\beta. \tag{6.138}$$

The first equation reads

$$\frac{\partial \boldsymbol{\mathsf{L}}_r}{\partial \boldsymbol{\mathsf{q}}_r}\Delta \boldsymbol{\mathsf{q}}_r + \frac{\partial \boldsymbol{\mathsf{L}}_r}{\partial \beta_\mathrm{t}}\Delta\beta_\mathrm{t} = -\boldsymbol{\mathsf{L}}_r. \tag{6.139}$$

Inserting $\Delta\beta_\mathrm{t}$ yields

$$\frac{\partial \boldsymbol{\mathsf{L}}_r}{\partial \boldsymbol{\mathsf{q}}_r}\Delta \boldsymbol{\mathsf{q}}_r + \frac{\partial \boldsymbol{\mathsf{L}}_r}{\partial \beta_\mathrm{t}}\left(-\left(\frac{\partial \mathsf{L}_\beta}{\partial \beta_\mathrm{t}}\right)^{-1}\mathsf{L}_\beta\right) = -\boldsymbol{\mathsf{L}}_r. \tag{6.140}$$

Then, the equation system is reduced

$$\frac{\partial \boldsymbol{\mathsf{L}}_r}{\partial \boldsymbol{\mathsf{q}}_r}\Delta \boldsymbol{\mathsf{q}}_r = -\left(\boldsymbol{\mathsf{L}}_r - \frac{\partial \boldsymbol{\mathsf{L}}_r}{\partial \beta_\mathrm{t}}\left(\frac{\partial \mathsf{L}_\beta}{\partial \beta_\mathrm{t}}\right)^{-1}\mathsf{L}_\beta\right), \qquad \frac{\partial \boldsymbol{\mathsf{L}}_r}{\partial \beta_\mathrm{t}} \to \frac{\partial \mathsf{L}_f}{\partial \beta_\mathrm{t}} \tag{6.141}$$

and the unknowns are $\Delta \boldsymbol{\mathsf{q}}_r$. The only non-linear equation depending on the variable β_t out of the remaining equations $\boldsymbol{\mathsf{L}}_r$ is L_f, which stems from the yield condition. In more detail, the reduced system now reads

$$\begin{bmatrix} \dfrac{\partial \boldsymbol{\mathsf{L}}_\mathrm{p}}{\partial \boldsymbol{\mathsf{C}}_\mathrm{p}} & \dfrac{\partial \boldsymbol{\mathsf{L}}_\mathrm{p}}{\partial k_\mathrm{M}} & \dfrac{\partial \boldsymbol{\mathsf{L}}_\mathrm{p}}{\partial f_\mathrm{c}} & \dfrac{\partial \boldsymbol{\mathsf{L}}_\mathrm{p}}{\partial \Lambda} \\ \left\{\dfrac{\partial \mathsf{L}_\mathrm{k}}{\partial \boldsymbol{\mathsf{C}}_\mathrm{p}}\right\}^\mathrm{T} & \dfrac{\partial \mathsf{L}_\mathrm{k}}{\partial k_\mathrm{M}} & \dfrac{\partial \mathsf{L}_\mathrm{k}}{\partial f_\mathrm{c}} & \dfrac{\partial \mathsf{L}_\mathrm{k}}{\partial \Lambda} \\ \left\{\dfrac{\partial \mathsf{L}_c}{\partial \boldsymbol{\mathsf{C}}_\mathrm{p}}\right\}^\mathrm{T} & 0 & \dfrac{\partial \mathsf{L}_c}{\partial f_\mathrm{c}} & 0 \\ \left\{\dfrac{\partial \mathsf{L}_f}{\partial \boldsymbol{\mathsf{C}}_\mathrm{p}}\right\}^\mathrm{T} & \dfrac{\partial \mathsf{L}_f}{\partial k_\mathrm{M}} & \dfrac{\partial \mathsf{L}_f}{\partial f_\mathrm{c}} & \dfrac{\partial \mathsf{L}_f}{\partial \Lambda} \end{bmatrix} \begin{Bmatrix} \Delta \boldsymbol{\mathsf{C}}_\mathrm{p} \\ \Delta k_\mathrm{M} \\ \Delta f_\mathrm{c} \\ \Delta \Lambda \end{Bmatrix} = -\begin{Bmatrix} \boldsymbol{\mathsf{L}}_\mathrm{p}(\boldsymbol{\mathsf{C}}, \Theta, \boldsymbol{\mathsf{C}}_\mathrm{p}, k_\mathrm{M}, f_\mathrm{c}, \Lambda) \\ \mathsf{L}_\mathrm{k}(\boldsymbol{\mathsf{C}}, \Theta, \boldsymbol{\mathsf{C}}_\mathrm{p}, k_\mathrm{M}, f_\mathrm{c}, \Lambda) \\ \mathsf{L}_c(\boldsymbol{\mathsf{C}}, \Theta, \boldsymbol{\mathsf{C}}_\mathrm{p}, f_\mathrm{c}) \\ \mathsf{L}_f - \dfrac{\partial \mathsf{L}_f}{\partial \beta_\mathrm{t}}\left(\dfrac{\partial \mathsf{L}_\beta}{\partial \beta_\mathrm{t}}\right)^{-1}\mathsf{L}_\beta \end{Bmatrix} \tag{6.142}$$

Consistent Tangent Matrix

For the consistent linearization, the derivatives of the elasticity relation Eq. (4.187) with respect to $\mathbf{C}$ and Θ are required. They can be derived by applying the chain rule

$$\frac{\mathrm{d}\mathbf{h}}{\mathrm{d}\mathbf{C}} = \frac{\partial \mathbf{h}}{\partial \mathbf{C}} + \frac{\partial \mathbf{h}}{\partial \mathbf{C}_\mathrm{p}}\frac{\mathrm{d}\mathbf{C}_\mathrm{p}}{\mathrm{d}\mathbf{C}} + \frac{\partial \mathbf{h}}{\partial f_\mathrm{c}}\frac{\mathrm{d}f_\mathrm{c}}{\mathrm{d}\mathbf{C}} \tag{6.143}$$

$$\frac{\mathrm{d}\mathbf{h}}{\mathrm{d}\Theta} = \frac{\partial \mathbf{h}}{\partial \Theta} + \frac{\partial \mathbf{h}}{\partial \mathbf{C}_\mathrm{p}}\frac{\mathrm{d}\mathbf{C}_\mathrm{p}}{\mathrm{d}\Theta} + \frac{\partial \mathbf{h}}{\partial f_\mathrm{c}}\frac{\mathrm{d}f_\mathrm{c}}{\mathrm{d}\Theta} \tag{6.144}$$

Here, the derivative of $\mathbf{h}$ with respect to the internal variables $\mathbf{C}_\mathrm{p}$, f_c and the temperature Θ can be computed directly by the elasticity relation Eq. (4.187). For the derivative of the internal variables with respect to the right Cauchy-Green tensor and the temperature, the system of non-linear equations (6.125) - (6.129) is used. At local level, the strains and the temperature are known – and with the implicit function theorem, see Eq. (6.112), the equation system can be written as

$$
\boldsymbol{\mathsf{L}}(\boldsymbol{\mathsf{C}},\Theta,\hat{\boldsymbol{\mathsf{q}}}(\boldsymbol{\mathsf{C}},\Theta)) \Leftrightarrow
\begin{aligned}
&\boldsymbol{\mathsf{L}}_\mathrm{p}(\boldsymbol{\mathsf{C}},\Theta,\boldsymbol{\mathsf{C}}_\mathrm{p}(\boldsymbol{\mathsf{C}},\Theta),k_\mathrm{M}(\boldsymbol{\mathsf{C}},\Theta),f_\mathrm{c}(\boldsymbol{\mathsf{C}},\Theta),\Lambda(\boldsymbol{\mathsf{C}},\Theta)) = \boldsymbol{\mathsf{0}} && (6.145)\\
&\mathsf{L}_\mathrm{k}(\boldsymbol{\mathsf{C}},\Theta,\boldsymbol{\mathsf{C}}_\mathrm{p}(\boldsymbol{\mathsf{C}},\Theta),k_\mathrm{M}(\boldsymbol{\mathsf{C}},\Theta),f_\mathrm{c}(\boldsymbol{\mathsf{C}},\Theta),\Lambda(\boldsymbol{\mathsf{C}},\Theta)) = 0 && (6.146)\\
&\mathsf{L}_\beta(\Theta,\beta_\mathrm{t}(\Theta)) = 0 && (6.147)\\
&\mathsf{L}_c(f_\mathrm{c}(\boldsymbol{\mathsf{C}},\Theta),\Theta) = 0 && (6.148)\\
&\mathsf{L}_f(\boldsymbol{\mathsf{C}},\Theta,\boldsymbol{\mathsf{C}}_\mathrm{p}(\boldsymbol{\mathsf{C}},\Theta),k_\mathrm{M}(\boldsymbol{\mathsf{C}},\Theta),f_\mathrm{c}(\boldsymbol{\mathsf{C}},\Theta),\Lambda(\boldsymbol{\mathsf{C}},\Theta),\beta_\mathrm{t}(\Theta)) = 0 && (6.149)
\end{aligned}
$$

With the chain rule, see Eq. (6.115), one obtains

$$
\frac{\mathrm{d}\boldsymbol{\mathsf{L}}}{\mathrm{d}\boldsymbol{\mathsf{u}}} \rightarrow \frac{\mathrm{d}\boldsymbol{\mathsf{L}}}{\mathrm{d}\boldsymbol{\mathsf{C}}} = \frac{\partial\boldsymbol{\mathsf{L}}}{\partial\boldsymbol{\mathsf{C}}} + \frac{\partial\boldsymbol{\mathsf{L}}}{\partial\boldsymbol{\mathsf{q}}}\frac{\mathrm{d}\hat{\boldsymbol{\mathsf{q}}}}{\mathrm{d}\boldsymbol{\mathsf{C}}} = \boldsymbol{\mathsf{0}} \qquad \Rightarrow \qquad \left[\frac{\partial\boldsymbol{\mathsf{L}}}{\partial\boldsymbol{\mathsf{q}}}\right]\left[\frac{\mathrm{d}\hat{\boldsymbol{\mathsf{q}}}}{\mathrm{d}\boldsymbol{\mathsf{C}}}\right] = -\frac{\partial\boldsymbol{\mathsf{L}}}{\partial\boldsymbol{\mathsf{C}}} \tag{6.150}
$$

$$
\frac{\mathrm{d}\boldsymbol{\mathsf{L}}}{\mathrm{d}\Theta} = \frac{\partial\boldsymbol{\mathsf{L}}}{\partial\Theta} + \frac{\partial\boldsymbol{\mathsf{L}}}{\partial\boldsymbol{\mathsf{q}}}\frac{\mathrm{d}\hat{\boldsymbol{\mathsf{q}}}}{\mathrm{d}\Theta} = \boldsymbol{\mathsf{0}} \qquad \Rightarrow \qquad \left[\frac{\partial\boldsymbol{\mathsf{L}}}{\partial\boldsymbol{\mathsf{q}}}\right]\left[\frac{\mathrm{d}\hat{\boldsymbol{\mathsf{q}}}}{\mathrm{d}\Theta}\right] = -\frac{\partial\boldsymbol{\mathsf{L}}}{\partial\Theta} \tag{6.151}
$$

In detail, this linear equation system reads for the case of $\tilde{F} < 0$

$$
\begin{bmatrix}
\dfrac{\partial\boldsymbol{\mathsf{L}}_\mathrm{p}}{\partial\boldsymbol{\mathsf{C}}_\mathrm{p}} & \dfrac{\partial\boldsymbol{\mathsf{L}}_\mathrm{p}}{\partial k_\mathrm{M}} & \dfrac{\partial\boldsymbol{\mathsf{L}}_\mathrm{p}}{\partial f_\mathrm{c}}\\[2ex]
\left\{\dfrac{\partial\mathsf{L}_\mathrm{k}}{\partial\boldsymbol{\mathsf{C}}_\mathrm{p}}\right\}^\mathrm{T} & \dfrac{\partial\mathsf{L}_\mathrm{k}}{\partial k_\mathrm{M}} & \dfrac{\partial\mathsf{L}_\mathrm{k}}{\partial f_\mathrm{c}}\\[2ex]
\left\{\dfrac{\partial\mathsf{L}_c}{\partial\boldsymbol{\mathsf{C}}_\mathrm{p}}\right\}^\mathrm{T} & 0 & \dfrac{\partial\mathsf{L}_c}{\partial f_\mathrm{c}}
\end{bmatrix}
\begin{bmatrix}
\dfrac{\mathrm{d}\boldsymbol{\mathsf{C}}_\mathrm{p}}{\mathrm{d}\boldsymbol{\mathsf{C}}}\\[2ex]
\left\{\dfrac{\mathrm{d}k_\mathrm{M}}{\mathrm{d}\boldsymbol{\mathsf{C}}}\right\}^\mathrm{T}\\[2ex]
\left\{\dfrac{\mathrm{d}f_\mathrm{c}}{\mathrm{d}\boldsymbol{\mathsf{C}}}\right\}^\mathrm{T}
\end{bmatrix}
= -
\begin{bmatrix}
\dfrac{\mathrm{d}\boldsymbol{\mathsf{L}}_\mathrm{p}}{\mathrm{d}\boldsymbol{\mathsf{C}}}\\[2ex]
\left\{\dfrac{\mathrm{d}\mathsf{L}_\mathrm{k}}{\mathrm{d}\boldsymbol{\mathsf{C}}}\right\}^\mathrm{T}\\[2ex]
\left\{\dfrac{\mathrm{d}\mathsf{L}_c}{\mathrm{d}\boldsymbol{\mathsf{C}}}\right\}^\mathrm{T}
\end{bmatrix}
\tag{6.152}
$$

and for $\tilde{F} \geq 0$, the linear system of equation is given by

$$
\begin{bmatrix}
\dfrac{\partial\boldsymbol{\mathsf{L}}_\mathrm{p}}{\partial\boldsymbol{\mathsf{C}}_\mathrm{p}} & \dfrac{\partial\boldsymbol{\mathsf{L}}_\mathrm{p}}{\partial k_\mathrm{M}} & \dfrac{\partial\boldsymbol{\mathsf{L}}_\mathrm{p}}{\partial f_\mathrm{c}} & \dfrac{\partial\boldsymbol{\mathsf{L}}_\mathrm{p}}{\partial\Lambda}\\[2ex]
\left\{\dfrac{\partial\mathsf{L}_\mathrm{k}}{\partial\boldsymbol{\mathsf{C}}_\mathrm{p}}\right\}^\mathrm{T} & \dfrac{\partial\mathsf{L}_\mathrm{k}}{\partial k_\mathrm{M}} & \dfrac{\partial\mathsf{L}_\mathrm{k}}{\partial f_\mathrm{c}} & \dfrac{\partial\mathsf{L}_\mathrm{k}}{\partial\Lambda}\\[2ex]
\left\{\dfrac{\partial\mathsf{L}_c}{\partial\boldsymbol{\mathsf{C}}_\mathrm{p}}\right\}^\mathrm{T} & 0 & \dfrac{\partial\mathsf{L}_c}{\partial f_\mathrm{c}} & 0\\[2ex]
\left\{\dfrac{\partial\mathsf{L}_f}{\partial\boldsymbol{\mathsf{C}}_\mathrm{p}}\right\}^\mathrm{T} & \dfrac{\partial\mathsf{L}_f}{\partial k_\mathrm{M}} & \dfrac{\partial\mathsf{L}_f}{\partial f_\mathrm{c}} & \dfrac{\partial\mathsf{L}_f}{\partial\Lambda}
\end{bmatrix}
\begin{bmatrix}
\dfrac{\mathrm{d}\boldsymbol{\mathsf{C}}_\mathrm{p}}{\mathrm{d}\boldsymbol{\mathsf{C}}}\\[2ex]
\left\{\dfrac{\mathrm{d}k_\mathrm{M}}{\mathrm{d}\boldsymbol{\mathsf{C}}}\right\}^\mathrm{T}\\[2ex]
\left\{\dfrac{\mathrm{d}f_\mathrm{c}}{\mathrm{d}\boldsymbol{\mathsf{C}}}\right\}^\mathrm{T}\\[2ex]
\left\{\dfrac{\mathrm{d}\Lambda}{\mathrm{d}\boldsymbol{\mathsf{C}}}\right\}^\mathrm{T}
\end{bmatrix}
= -
\begin{bmatrix}
\dfrac{\mathrm{d}\boldsymbol{\mathsf{L}}_\mathrm{p}}{\mathrm{d}\boldsymbol{\mathsf{C}}}\\[2ex]
\left\{\dfrac{\mathrm{d}\mathsf{L}_\mathrm{k}}{\mathrm{d}\boldsymbol{\mathsf{C}}}\right\}^\mathrm{T}\\[2ex]
\left\{\dfrac{\mathrm{d}\mathsf{L}_c}{\mathrm{d}\boldsymbol{\mathsf{C}}}\right\}^\mathrm{T}\\[2ex]
\left\{\dfrac{\mathrm{d}\mathsf{L}_f}{\mathrm{d}\boldsymbol{\mathsf{C}}}\right\}^\mathrm{T}
\end{bmatrix}
\tag{6.153}
$$

for the computation of the derivatives with respect to the right Cauchy-Green tensor. The same system with a different right-hand side has to be solved to determine the derivatives of the internal variables with respect to the temperature for $\tilde{F} < 0$

$$\begin{bmatrix} \dfrac{\partial \boldsymbol{\mathsf{L}}_\mathrm{p}}{\partial \boldsymbol{\mathsf{C}}_\mathrm{p}} & \dfrac{\partial \boldsymbol{\mathsf{L}}_\mathrm{p}}{\partial k_\mathrm{M}} & \dfrac{\partial \boldsymbol{\mathsf{L}}_\mathrm{p}}{\partial f_\mathrm{c}} \\ \left\{\dfrac{\partial \mathsf{L}_\mathrm{k}}{\partial \boldsymbol{\mathsf{C}}_\mathrm{p}}\right\}^\mathrm{T} & \dfrac{\partial \mathsf{L}_\mathrm{k}}{\partial k_\mathrm{M}} & \dfrac{\partial \mathsf{L}_\mathrm{k}}{\partial f_\mathrm{c}} \\ \left\{\dfrac{\partial \mathsf{L}_c}{\partial \boldsymbol{\mathsf{C}}_\mathrm{p}}\right\}^\mathrm{T} & 0 & \dfrac{\partial \mathsf{L}_c}{\partial f_\mathrm{c}} \end{bmatrix} \begin{Bmatrix} \dfrac{\mathrm{d}\boldsymbol{\mathsf{C}}_\mathrm{p}}{\mathrm{d}\Theta} \\ \dfrac{\mathrm{d}k_\mathrm{M}}{\mathrm{d}\Theta} \\ \dfrac{\mathrm{d}f_\mathrm{c}}{\mathrm{d}\Theta} \end{Bmatrix} = - \begin{Bmatrix} \dfrac{\mathrm{d}\boldsymbol{\mathsf{L}}_\mathrm{p}}{\mathrm{d}\Theta} \\ \dfrac{\mathrm{d}\mathsf{L}_\mathrm{k}}{\mathrm{d}\Theta} \\ \dfrac{\mathrm{d}\mathsf{L}_c}{\mathrm{d}\Theta} \end{Bmatrix} \quad \text{and} \quad \frac{\partial \mathsf{L}_\beta}{\partial \beta_\mathrm{t}} \frac{\mathrm{d}\beta_\mathrm{t}}{\mathrm{d}\Theta} = -\frac{\mathrm{d}\mathsf{L}_\beta}{\mathrm{d}\Theta} \tag{6.154}$$

and in the case of $\tilde{F} \geq 0$, the system reads

$$\begin{bmatrix} \dfrac{\partial \boldsymbol{\mathsf{L}}_\mathrm{p}}{\partial \boldsymbol{\mathsf{C}}_\mathrm{p}} & \dfrac{\partial \boldsymbol{\mathsf{L}}_\mathrm{p}}{\partial k_\mathrm{M}} & \dfrac{\partial \boldsymbol{\mathsf{L}}_\mathrm{p}}{\partial f_\mathrm{c}} & \dfrac{\partial \boldsymbol{\mathsf{L}}_\mathrm{p}}{\partial \Lambda} \\ \left\{\dfrac{\partial \mathsf{L}_\mathrm{k}}{\partial \boldsymbol{\mathsf{C}}_\mathrm{p}}\right\}^\mathrm{T} & \dfrac{\partial \mathsf{L}_\mathrm{k}}{\partial k_\mathrm{M}} & \dfrac{\partial \mathsf{L}_\mathrm{k}}{\partial f_\mathrm{c}} & \dfrac{\partial \mathsf{L}_\mathrm{k}}{\partial \Lambda} \\ \left\{\dfrac{\partial \mathsf{L}_c}{\partial \boldsymbol{\mathsf{C}}_\mathrm{p}}\right\}^\mathrm{T} & 0 & \dfrac{\partial \mathsf{L}_c}{\partial f_\mathrm{c}} & 0 \\ \left\{\dfrac{\partial \mathsf{L}_f}{\partial \boldsymbol{\mathsf{C}}_\mathrm{p}}\right\}^\mathrm{T} & \dfrac{\partial \mathsf{L}_f}{\partial k_\mathrm{M}} & \dfrac{\partial \mathsf{L}_f}{\partial f_\mathrm{c}} & \dfrac{\partial \mathsf{L}_f}{\partial \Lambda} \end{bmatrix} \begin{Bmatrix} \dfrac{\mathrm{d}\boldsymbol{\mathsf{C}}_\mathrm{p}}{\mathrm{d}\Theta} \\ \dfrac{\mathrm{d}k_\mathrm{M}}{\mathrm{d}\Theta} \\ \dfrac{\mathrm{d}f_\mathrm{c}}{\mathrm{d}\Theta} \\ \dfrac{\mathrm{d}\Lambda}{\mathrm{d}\Theta} \end{Bmatrix} = - \begin{Bmatrix} \dfrac{\mathrm{d}\boldsymbol{\mathsf{L}}_\mathrm{p}}{\mathrm{d}\Theta} \\ \dfrac{\mathrm{d}\mathsf{L}_\mathrm{k}}{\mathrm{d}\Theta} \\ \dfrac{\mathrm{d}\mathsf{L}_c}{\mathrm{d}\Theta} \\ \dfrac{\mathrm{d}\mathsf{L}_f}{\mathrm{d}\Theta} - \dfrac{\partial \mathsf{L}_f}{\partial \beta_\mathrm{t}} \left[\dfrac{\partial \mathsf{L}_\beta}{\partial \beta_\mathrm{t}}\right]^{-1} \dfrac{\mathrm{d}\mathsf{L}_\beta}{\mathrm{d}\Theta} \end{Bmatrix} \tag{6.155}$$

There are several possibilities to determine the required derivatives $\partial \boldsymbol{\mathsf{L}}/\partial \mathbf{q}$, $\partial \boldsymbol{\mathsf{L}}/\partial \boldsymbol{\mathsf{C}}$ and $\partial \boldsymbol{\mathsf{L}}/\partial \Theta$. For example, it is possible to apply analytical, numerical or automatic differentiation. For the analytical calculation of the consistent tangent operator, one has to compute the Gateaux derivative of the stress with respect to the strain increment, see [Braudel et al., 1986] and [Hartmann et al., 1997]. This can lead to a time-consuming derivation and implementation. It can also be tedious and error-prone. Due to the high effort of analytical manual computations, an alternative could be seen in an approach based on finite differences. This, however, can lead to a significant slowdown or even failure as a result of truncation errors. With the help of automatic (also known as *algorithmic*) differentiation, derivatives (AD) can be computed efficiently and accurately, see the works of Griewank and Walther [2008] and Naumann [2012] as well for further information about AD. The tangent is computed with machine accuracy and truncation errors are avoided.

In [Korelc, 2002; Korelc, 2009], use is made of symbolic programs such as Mathematica [Wolfram, 2003]. Korelc developed a program that automatically generates suitable element formulations, stress algorithms and tangent computations on the basis of Mathematica and the offered program itself. The program often yields very efficient implementations. Unfortunately, the approach has the disadvantage that one has to purchase the program and to become accustomed to its programming language.

In this work, an alternative is proposed – using Automatic Differentiation (AD), here by applying OpenAD, see [Utke et al., 2008]. In this case, a program translates the Fortran code of the programmed function into a new code that contains the derivative or the entire functional matrix in the case of multi-dimensional functions. Thus, only the functions, e.g. the stress algorithm, need to be provided. The resulting code of the “consistent tangent” is generated automatically.

A different robust numerical calculation procedure for the tangent operators is reported in [Tanaka et al., 2014]. A comparison of analytical, numerical and Automatic Differentiation applied to non-linear finite elements can be found in [Rothe and Hartmann, 2014]. For the sake of simplicity, this work focuses on central finite differences.

7 Numerical Simulations

In this chapter, the thermo-electro-mechanical numerical simulations of the FAST-process are investigated and compared to experiments. All simulations are performed within the commercial finite element program Abaqus. The unit system used in all Abaqus simulations can be found in App. 7. In a first step, different element types and spatial discretizations are compared in order to choose an appropriate finite element mesh with a small error. The second step is to analyze the time integration and the time-step control and to determine appropriate control parameters. Afterwards, simulations of the graphite tool system without any powder are performed. The aim of these simulations is to compute the temperature distribution and to obtain a better understanding of the various modeling parameters and their influence on the process simulation. In addition, the simulated temperatures at the thermocouple position and the pyrometer measurement point are compared to experimental data. Then, based on this information, the numerical model is discussed. Furthermore, a PID-controller is introduced and implemented into Abaqus for the temperature control at the thermocouple position. This controller changes the current boundary condition in such a way that it follows a prescribed temperature path. Then, as the current does not have to be taken from experiments anymore, it is possible to make predictions based on the Abaqus model.

In the second part of this chapter, the numerical simulations of the FAST-process are performed. For this purpose, the developed material model in Chap. 4 is implemented into Abaqus. In these simulations, the fully coupled thermo-electro-mechanical sintering process of the copper powder at finite strains is treated. These simulations render the temperature as well as the relative density distribution inside the powder.

7.1 Simulation of Experiments without Powder

The following simulations are performed to obtain a better understanding of the graphite tool system, see Fig. 2.5, especially focusing on the simulated temperature field. At first, the boundary conditions are explained. Subsequently, a mesh convergence study for choosing an appropriate mesh is performed and the influence of the time integration parameters on the simulation is studied. Afterwards, a parameter study is carried out in Sect. 7.1.4. In this study, the model complexity will be increased step by step, analyzing whether the simulation is capable to predict the temperature at certain measurement points. Furthermore, a sensitivity analysis serves to investigate the influence of the convection coefficient used for the modeling of the water cooling as well as the thermal and electric contact resistance on the temperature distribution. In these simulations, the measured current is applied as a boundary condition. Due to this reason, the simulations are limited to reproduce existing experiments. In order to make predictions, a PID-controller is implemented into the finite element program. With this controller, the prescribed temperature at the thermocouple position can be achieved by controlling the current.

7.1.1 Boundary Conditions

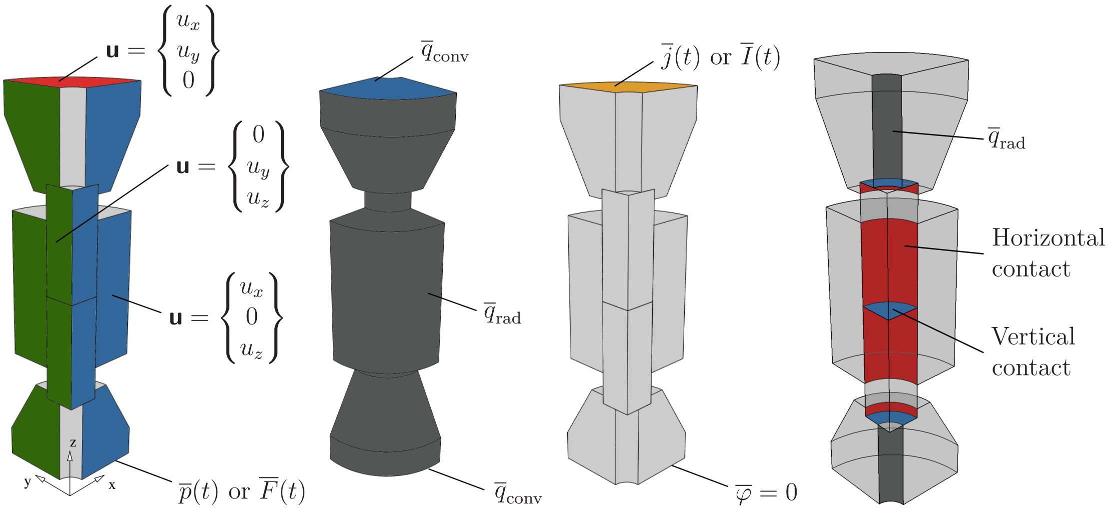

(a) Mechanical field (b) Thermal field (c) Electrical field (d) Contact surfaces and Radiation

Figure 7.1: Boundary conditions

The geometry of the graphite tool system is shown in Fig. 2.6. Due to the axial symmetry, only one-fourth is modeled. In Abaqus, there are no axisymmetric elements available for the three-field coupled problem. Therefore, volume (brick) elements are used.

It is necessary to prescribe boundary conditions for the three different fields – namely the mechanical, thermal and electrical field. The boundary conditions of the mechanical field are depicted in Fig. 7.1a. The bottom surface is loaded with a time-dependent pressure $\overline{p}(t)$ or force $\overline{F}(t)$, whereas the upper surface is fixed. Additionally, symmetry boundary conditions are applied.

The water cooling inside the FAST-machine is modeled by convection at the top and the bottom surface of the tool system, see Fig. 7.1b. Radiation occurs on the outer surfaces, see Fig. 7.1b and Fig. 7.1d. The convection and radiation are modeled by

$$\overline{q}_{\mathrm{conv}} = h_{\mathrm{c}}(\Theta_{\mathrm{s}} - \Theta_{\mathrm{f}}), \qquad \overline{q}_{\mathrm{rad}} = \sigma\epsilon(\Theta_{\mathrm{s}}^4 - \Theta_{\infty}^4), \tag{7.1}$$

where Θ_{s} is the surface temperature, Θ_{f} the water, Θ_{∞} the chamber temperature and h_{c} the heat transfer coefficient. The water temperature in the FAST-machine is assumed to be $\Theta_{\mathrm{f}} = 25\,°\mathrm{C}$. The chamber temperature may change during the process, but the chamber walls are cooled. Thus, a constant chamber temperature of $\Theta_{\infty} = 25\,°\mathrm{C}$ is assumed. σ denotes the Stefan Boltzmann constant and $\epsilon = 0.8$ is the emissivity, which is taken from [Zavaliangos et al., 2004].

The boundary conditions of the electrical field are shown in Fig. 7.1c. At the top surface, the electric current density $\overline{j}(t)$ or the current $\overline{I}(t)$ is prescribed as a function of time. At the bottom surface, the electrical potential is set to zero.

Furthermore, contact resistances are present due to the non-perfect contact between the graphite punch, the die and the cone part. There are two different kinds of resistances: the thermal and the electrical contact resistance. These resistances lead to a temperature and voltage drop at the interfaces, as illustrated in Fig. 7.2. Moreover, heat is produced at the interfaces, due to the electrical contact resistance. The incorporation of the resistances in Abaqus is explained subsequently.

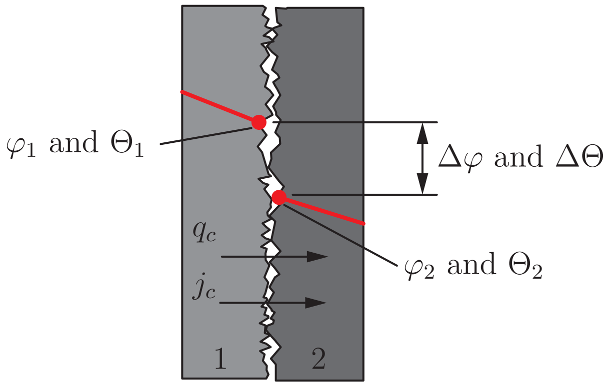

Figure 7.2: Temperature and voltage drop at interface due to contact resistances

In Abaqus, the heat conduction q_c as well as the electric current density flow j_c between two surfaces are modeled by

$$q_c = \kappa_{C,\mathrm{th}}(p)(\Theta_1 - \Theta_2), \qquad j_c = \kappa_{C,\mathrm{el}}(p)(\varphi_1 - \varphi_2), \tag{7.2}$$

where Θ_1 or φ_1 and Θ_2 or φ_2 are the temperatures or electrical potentials of the points on the surfaces, see Fig. 7.2. $\kappa_{C,\mathrm{th}}$ is the thermal contact conductance and $\kappa_{C,\mathrm{el}}$ denotes the electrical contact conductance. Both quantities can depend on the contact pressure p.

The heat due to the electrical resistance at the interfaces is calculated by

$$q_e = \kappa_{C,\mathrm{el}}(p)(\varphi_1 - \varphi_2)^2 = \kappa_{C,\mathrm{el}}(p)\Delta\varphi^2. \tag{7.3}$$

7.1.2 Mesh Convergence Study

For the finite element simulations, an adequate mesh with a small error is desired. Therefore, a mesh convergence study is performed to compare two different element types in Abaqus. The investigated elements are a linear eight-noded (Q3D8) and a quadratic twenty-noded (Q3D20) hexahedral element. Different spatial discretizations are investigated according to the resulting error in the temperature and the electrical potential. As the error in the displacements is not in the focus of these simulations, it is not investigated. Four different meshes are investigated for each element type, see Tab. 7.1 and Fig. 7.3. The reference solution is performed with a mesh consisting of 14 739 quadratic elements and a total number of degrees of freedom, $n_\mathrm{dof} = 213\,546$, see Fig. 7.3d. For the pressure and the electric current density, the following boundary conditions are used: The pressure $\overline{p}(t)$ is raised linearly from 0 MPa to 10 MPa in 1000 s, whereas the current density

Table 7.1: Number of degrees of freedom n_dof and number of elements n_e for different spatial discretizations

	Q3D8				Q3D20			
	M1	M2	M3	M4	M5	M6	M7	M8
n_e	3168	5501	12 819	41 644	1356	2399	3805	6598
n_dof	21 705	35 965	78 810	240 360	21 875	35 117	57 402	96 319

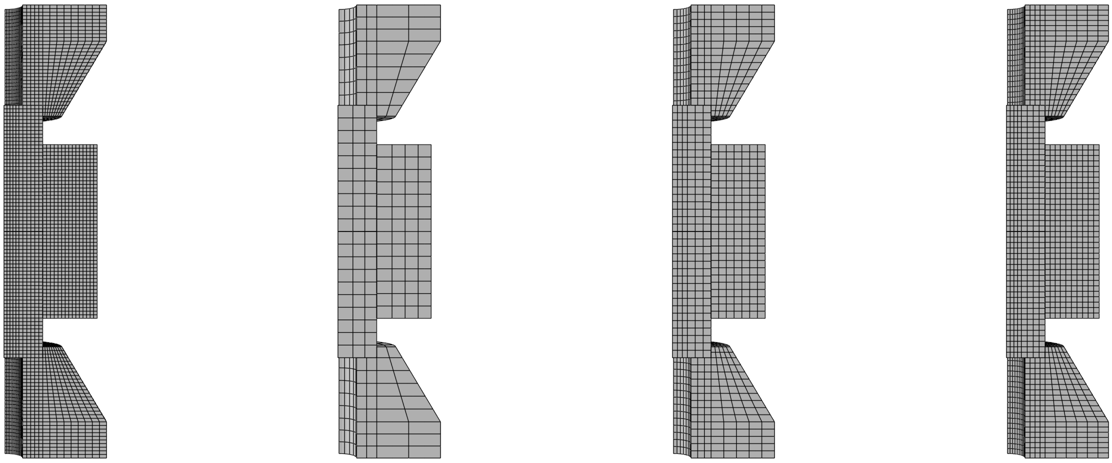

(a) Mesh M4

(b) Mesh M5

(c) Mesh M8

(d) Reference Mesh

Figure 7.3: Spatial discretizations

$\bar{j}(t)$ is increased linearly from $0\,\mathrm{A\,m^{-2}}$ to $4 \times 10^5\,\mathrm{A\,m^{-2}}$ in 1000 s. For the time integration, the backward Euler method is used with a constant time step-size of 10 s (100 time-steps). For the graphite material, a linear thermo-elastic behavior is assumed. The model parameters are specified in Tab. 7.2, where E denotes the Young's modulus, ν the Poisson ratio, η the friction coefficient, h_c the heat transfer coefficient for convection, ϵ the emissivity, ρ the density, α_Θ the thermal expansion coefficient and Θ_0 the initial temperature. For the heat capacity $c_\mathrm{p}(\Theta)$, the thermal $\kappa_\mathrm{th}(\Theta)$ and the electrical conductivity $\kappa_\mathrm{el}(\Theta)$, the identified functions from Sect. 5.5.2 are used.

Table 7.2: Parameters used in the mesh and time study

E MPa	ν -	η -	h_c $\mathrm{W\,m^{-2}\,K^{-1}}$	ϵ -	ρ $\mathrm{kg\,m^{-3}}$	α_Θ $\mathrm{K^{-1}}$	Θ_0 °C
11500	0.2	0.1	880	0.8	1850	4.55×10^{-6}	25

For the comparison of the eight different meshes, the error of the temperature and the electrical potential in a specific node at the end of the simulation are computed by

$$\mathrm{relerr}_\Theta = \frac{|\Theta^\mathrm{TC}(t_\mathrm{end}) - \Theta^\mathrm{TC}_\mathrm{ref}(t_\mathrm{end})|}{\Theta^\mathrm{TC}_\mathrm{ref}(t_\mathrm{end})} \times 100, \qquad \mathrm{relerr}_\varphi = \frac{|\varphi^\mathrm{Pyro}(t_\mathrm{end}) - \varphi^\mathrm{Pyro}_\mathrm{ref}(t_\mathrm{end})|}{\varphi^\mathrm{Pyro}_\mathrm{ref}(t_\mathrm{end})} \times 100, \tag{7.4}$$

with $\Theta^\mathrm{TC}(t_\mathrm{end})$ as the temperature at the thermocouple position at the end of the simulation. $\Theta^\mathrm{TC}_\mathrm{ref}(t_\mathrm{end})$ is the temperature at the same position for the simulation with the reference mesh. The error of the electrical potential is computed with the potential at the pyrometer measurement point $\varphi^\mathrm{Pyro}(t_\mathrm{end})$ at the end of the simulation, while $\varphi^\mathrm{Pyro}_\mathrm{ref}(t_\mathrm{end})$ denotes the reference solution. The position of the thermocouple and the pyrometer measurement point is shown in Fig. 7.11a.

Fig. 7.4 shows the computed relative error in % over the number of degrees of freedom for the entire mesh. It can be seen that the error in the temperature reduces slightly for the linear elements, whereas the error for the quadratic elements shows a large decrease with an increasing number of degrees of freedom. As can be seen in Fig. 7.4b, the error of the electric potential remains nearly constant. In contrast, the error of the quadratic elements increases at first – and then decreases again. The mesh M8 with quadratic elements shows the best results, with error values of less than 1% for the temperature and less than 0.1% for the electrical potential. Thus, this mesh is used for all simulations of the graphite system.

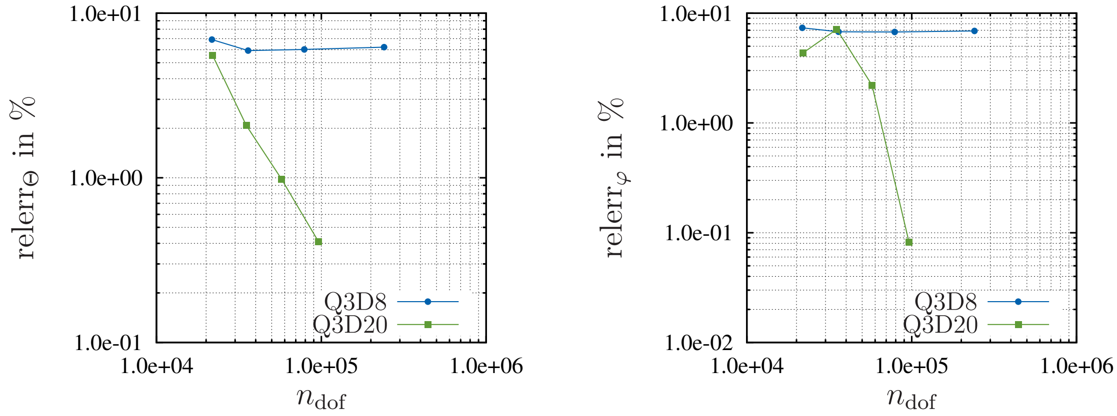

(a) Error of temperature over degrees of freedom at thermocouple position

(b) Error of electrical potential over degree of freedom at pyrometer measurement point

Figure 7.4: Comparison of a linear hexahedral (Q3D8) and a quadratic hexahedral element (Q3D20) in Abaqus

7.1.3 Time Integration

Apart from the spatial discretization, the time integration is important for the accuracy and the overall computational time too. Therefore, the following passage focuses on the step-size control of Abaqus with the backward Euler method. The same boundary conditions as in the previous section are applied, also using the mesh M8. A reference solution with $\Delta t = 1\,\mathrm{s}$ (1000 steps) is performed. The results are shown in Fig. 7.5a (for the electrical potential) and in Fig. 7.5b (for the temperature). This reference solution is compared to simulations with a controlled time-step. In Abaqus, one has to prescribe the maximum temperature change and the minimum and maximum time step-size Δt. The minimum step-size is set to $\Delta t_\mathrm{min} = 1 \times 10^{-4}\,\mathrm{s}$ and the maximum temperature change is set to $10\,^\circ\mathrm{C}$ per time-step. Two different maximum step-sizes are investigated, $\Delta t_\mathrm{max} = 100\,\mathrm{s}$ and $\Delta t_\mathrm{max} = 25\,\mathrm{s}$. The computation with a maximal step-size of $\Delta t_\mathrm{max} = 100\,\mathrm{s}$ shows a kink in the potential over the time, see Fig. 7.5a, which cannot be observed in the reference solution. The simulation with $\Delta t_\mathrm{max} = 25\,\mathrm{s}$ shows a difference to the reference solution below 300 s, but a good agreement after that and no kink. The temperature is shown in Fig. 7.5b. Here, the different solutions show a good agreement with the reference solution.

The time-step over the time is shown in Fig. 7.6. At the beginning of the simulation using $\Delta t_\mathrm{max} = 100\,\mathrm{s}$, the time-step grows up to 70 s and decreases again after that. This large time-step is probably what causes the kink in the solution. In the simulation with $\Delta t_\mathrm{max} = 25\,\mathrm{s}$, the time-step is limited, showing a plateau at the beginning and the same decreasing behavior after that. In the following simulations, the maximum time-step is set to $\Delta t_\mathrm{max} = 25\,\mathrm{s}$.

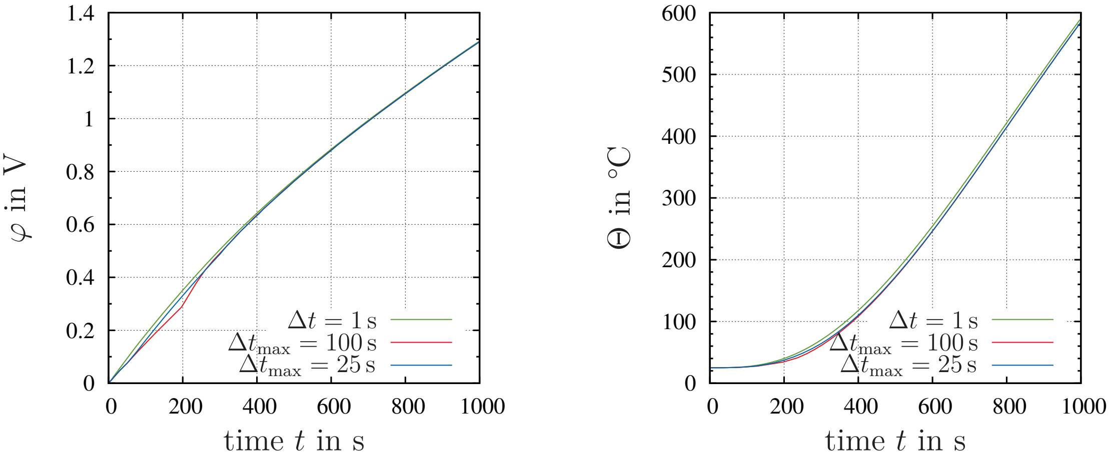

(a) Electrical potential over time at pyrometer measurement point

(b) Temperature over time at thermocouple position

Figure 7.5: Comparison of simulations with constant time-step and controlled time-step

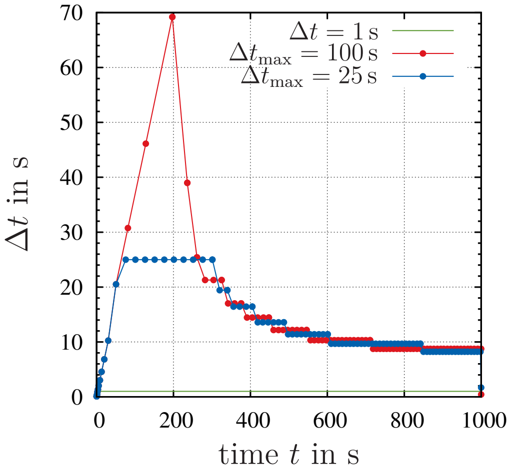

Figure 7.6: Time-step over time

7.1.4 Parameter Study

Here, the aim is to study the influence of the thermo-electrical properties as well as the thermal and electrical contact resistance on the temperature evolution. For this reason, data of a FAST-experiment without any powder is used. The measured current, as shown in Fig. 7.7a, is applied as a boundary condition. The applied axial force is shown in Fig. 7.7b. The different investigated parameters are defined in Tab. 7.3. The model complexity is increased step by step. In the first set, a constant heat capacity, thermal and electrical conductivity are chosen. The values represent the parameters at room temperature, see Sect. 5.5.2. In the second set, the thermal and electrical contact resistance is taken into account. The values are taken from [Zavaliangos et al., 2004]. In the work of Zavaliangos et al. [2004], the resistance is separated into a vertical and horizontal part, where the values are given by $\kappa^{\mathrm{H}}_{C,\mathrm{th,GG}} = 1.32 \times 10^3\,\mathrm{W\,m^{-2}\,K^{-1}}$ as the horizontal, $\kappa^{\mathrm{V}}_{C,\mathrm{th,GG}} = 2.4 \times 10^3\,\mathrm{W\,m^{-2}\,K^{-1}}$ as the vertical thermal conductance as well as $\kappa^{\mathrm{H}}_{C,\mathrm{el,GG}} = 7.5 \times 10^6\,\mathrm{S\,m^{-2}}$ as the horizontal and $\kappa^{\mathrm{V}}_{C,\mathrm{el,GG}} = 1.25 \times 10^7\,\mathrm{S\,m^{-2}}$ as the vertical electrical contact conductance. In the third set, the identified temperature-dependent functions for the graphite material $c_\mathrm{p}(\Theta)$, $\kappa_\mathrm{th}(\Theta)$ and $\kappa_\mathrm{el}(\Theta)$ are used, see Sect. 5.5.2. The electrical resistance is added in set 4, and the thermal resistance is included additionally in set 5. Further, it is necessary to prescribe the electrical as well as the thermal contact conductance in the thermo-electro-mechanical contact simulations. Therefore, the thermal contact conductance $\kappa^{\mathrm{H}}_{C,\mathrm{th,GG}}$ and $\kappa^{\mathrm{V}}_{C,\mathrm{th,GG}}$ is set to $1 \times 10^6\,\mathrm{W\,m^{-2}\,K^{-1}}$ for the sets 1, 3 and 4. It can be regarded as a perfect contact. The electrical contact conductance $\kappa^{\mathrm{H}}_{C,\mathrm{el,GG}}$ and $\kappa^{\mathrm{V}}_{C,\mathrm{el,GG}}$ is set to $1 \times 10^{10}\,\mathrm{S\,m^{-2}}$ in set 1 and 3.

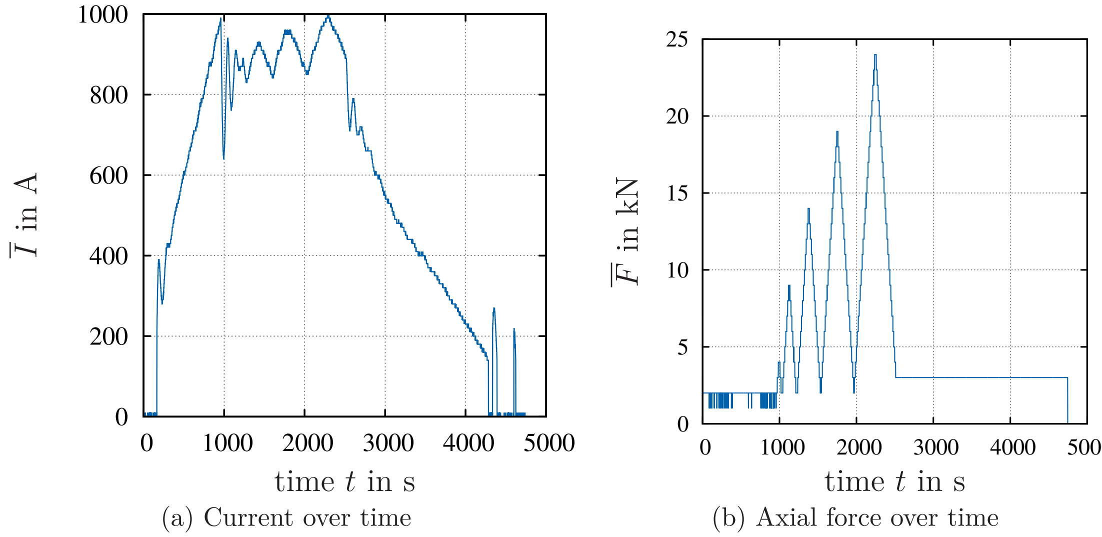

(a) Current over time

(b) Axial force over time

Figure 7.7: Prescribed current $\overline{I}$ and prescribed axial force $\overline{F}$

In Sect. 2.8, the electrical resistance between graphite and graphite is measured as a function of the applied pressure. For the use in Abaqus, the thermal contact conductance is required – and a power function is fitted to the experimental data, see Sect. 5.5.3. In set 6, the fitted function $\kappa_{C,\mathrm{el,GG6}}$ is used.

Table 7.3: Definition of sets

Set	Thermal Conductivity $\mathrm{W\,m^{-1}\,K^{-1}}$	Heat Capacity $\mathrm{J\,kg^{-1}\,K^{-1}}$	Electrical Conductivity $\mathrm{S\,m^{-1}}$	Thermal Resistance $\mathrm{W\,m^{-2}\,K^{-1}}$	Electrical Resistance $\mathrm{S\,m^{-2}}$
1	100	896	8.45×10^4	-	-
2	100	896	8.45×10^4	$\kappa^{\mathrm{H}}_{C,\mathrm{th,GG}}$ $\kappa^{\mathrm{V}}_{C,\mathrm{th,GG}}$	$\kappa^{\mathrm{H}}_{C,\mathrm{el,GG}}$ $\kappa^{\mathrm{V}}_{C,\mathrm{el,GG}}$
3	$\kappa_{\mathrm{th}}(\Theta)$	$c_p(\Theta)$	$\kappa_{\mathrm{el}}(\Theta)$	-	-
4	$\kappa_{\mathrm{th}}(\Theta)$	$c_p(\Theta)$	$\kappa_{\mathrm{el}}(\Theta)$	-	$\kappa^{\mathrm{H}}_{C,\mathrm{el,GG}}$ $\kappa^{\mathrm{V}}_{C,\mathrm{el,GG}}$
5	$\kappa_{\mathrm{th}}(\Theta)$	$c_p(\Theta)$	$\kappa_{\mathrm{el}}(\Theta)$	$\kappa^{\mathrm{H}}_{C,\mathrm{th,GG}}$ $\kappa^{\mathrm{V}}_{C,\mathrm{th,GG}}$	$\kappa^{\mathrm{H}}_{C,\mathrm{el,GG}}$ $\kappa^{\mathrm{V}}_{C,\mathrm{el,GG}}$
6	$\kappa_{\mathrm{th}}(\Theta)$	$c_p(\Theta)$	$\kappa_{\mathrm{el}}(\Theta)$	$\kappa^{\mathrm{H}}_{C,\mathrm{th,GG}}$ $\kappa^{\mathrm{V}}_{C,\mathrm{th,GG}}$	$\kappa_{C,\mathrm{el,GG6}}(p)$

The temperature is measured at two positions in the experiment, see Fig. 7.11a. These positions are the thermocouple position and the pyrometer measurement point. A simulation is performed for each set defined in Tab. 7.3. The simulated temperature at the thermocouple position is compared to the temperature measured in the experiment in Fig. 7.8a. The simulated temperature of set 1 shows a lower heating rate than the measured temperature. At 1000 s, the simulated temperature is approximately 500 °C in contrast to the measured temperature of 700 °C. In the following, the simulated temperature decreases to below 500 °C and shows an oscillating behavior, which is probably due to the oscillating prescribed current, Fig. 7.7a. The simulated temperature at the pyrometer measurement point, see Fig. 7.8b, shows a large deviation to the temperature in the experiment. For the second set, the thermal and electrical resistance is taken into account. In Fig. 7.8a, the simulation overestimates the experimental temperature. The temperature at the pyrometer position is overestimated as well, Fig. 7.7a. The higher simulated temperature can be connected to the resistances. On the one hand, the electrical resistances lead to higher temperatures at the interfaces – while, on the other hand, there are thermal barriers due to the thermal resistances that lead to temperature differences between the different graphite parts. This shows that the temperature field is strongly influenced by the contact resistance.

In the third set, the measured temperature-dependent heat capacity, thermal conductivity and electrical conductivity from Sect. 5.5.2 are used, and perfect contacts

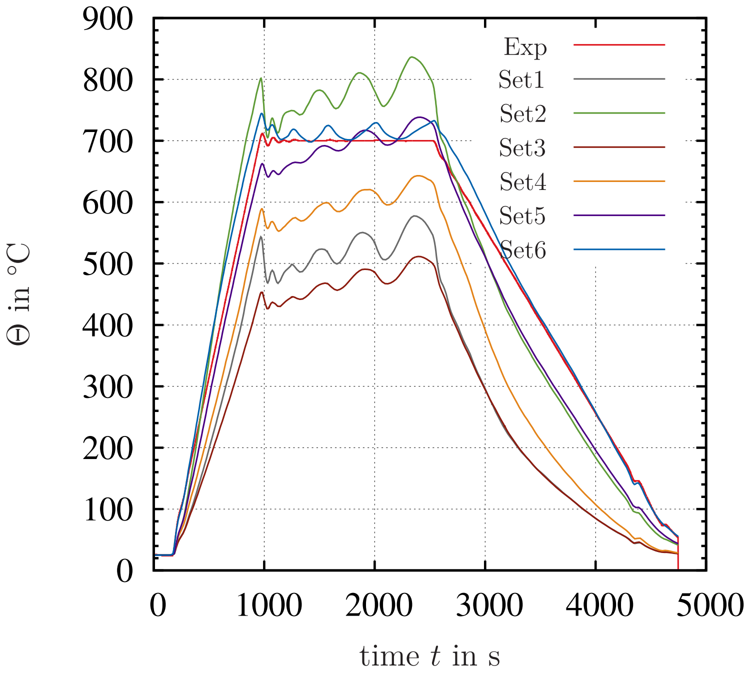

(a) Thermocoupe position

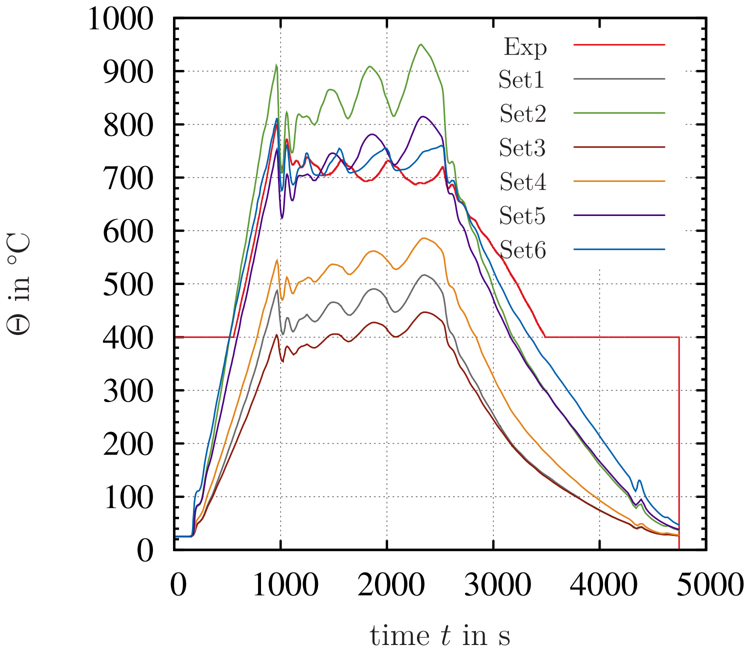

(b) Pyrometer measurement point

Figure 7.8: Temperature evolution at the thermocouple position and the pyrometer measurement point for the different sets defined in Tab. 7.3

are assumed. The simulated temperature curves in Fig. 7.8a and Fig. 7.8b for this set of parameters have the lowest temperature of all the sets under consideration. Taking into account the electrical resistance in set 4 leads to a higher temperature and a smaller deviation to the measured temperature. If, in set 5, the thermal resistance is added too, the temperature coincides very well with the measured temperature during the heating phase in Fig. 7.8a and Fig. 7.8b. The simulated temperature for set 5 at the thermocouple position, see Fig. 7.8a, shows a difference at 1000 s of approximately 50 °C and an increasing oscillating behaviour after that, whereas the experimental temperature remains nearly constant at 700 °C. The cooling rate between the experimental temperature and the simulated temperature for set 5 shows a deviation. In set 6, the measured pressure-dependent electrical contact resistance is considered. The simulated temperature for this set of parameters shows the best agreement with the experimental data.

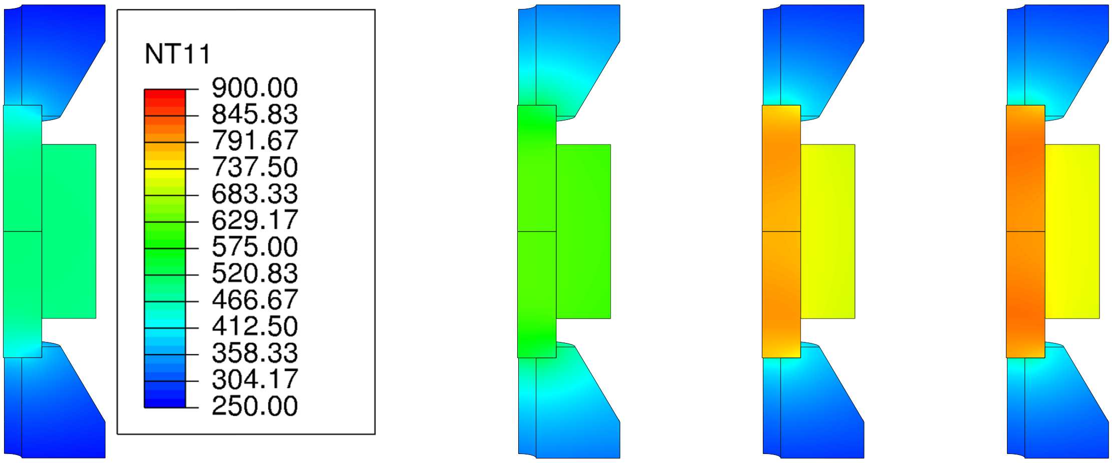

(a) Set 3 $t = 2000\,\mathrm{s}$

(b) Set 4 $t = 2000\,\mathrm{s}$

(c) Set 5 $t = 2009\,\mathrm{s}$

(d) Set 6 $t = 2009\,\mathrm{s}$

Figure 7.9: Temperature distribution for different sets

The temperature distributions for set 3-6 around $t = 2000\,\mathrm{s}$ are depicted in Fig. 7.9. For set 3, it can be observed that the temperature is nearly the same in the punches and the die. For set 4, where the electrical resistance is added, this leads to a higher temperature in this region. Still, the temperature can be assumed as homogeneous. If the thermal resistance is considered, which is done in set 5 and set 6, an inhomogeneous temperature distribution is observed between the punches and the die. Due to the small punch area, the highest electrical resistance can be observed in these parts. This can be proved by the dissipated energy, as shown in Fig. 7.10. Most of the energy is dissipated into heat in the punch region, see Fig. 7.10.

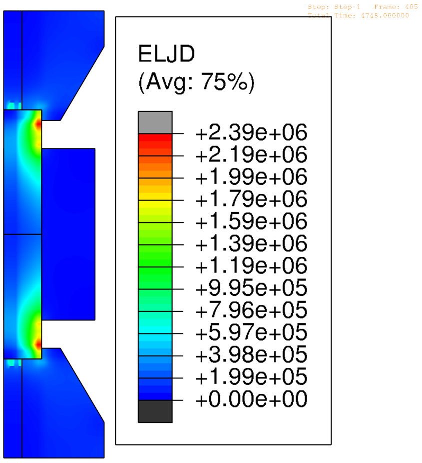

Figure 7.10: Total electrical energy dissipated into heat due to flow of current at 4748 s

Furthermore, the thermal resistance creates a thermal barrier so that the heat flux between the interfaces is not perfect anymore. The heat in the tool system is produced by Joule heating, which volumetrically heats the parts. The thermal resistance leads to a reduced heat transport to the water cooling. As a result, the punches show a higher temperature than the cone part or the die.

In summary, it can be stated that the contact resistances play a major role for the correct temperature distribution. Furthermore, the temperature-dependent material properties – such as the heat capacity, the thermal and the electrical conductivity – are important to obtain a better agreement with the experiments.

For a deeper study of the temperature and electrical distribution, two paths are defined in Fig. 7.11b. The temperature along the horizontal path is shown in Fig. 7.12a around 2000 s. The temperature over the radius is nearly constant for set 3 and 4, which can be explained by the missing thermal resistance. The temperature for set 4 is higher due to the electrical contact resistance. Set 5 and 6 show a jump in temperature between the punch and the die due to the thermal resistance.

Fig. 7.12b illustrated the temperature versus the z-coordinate around 2000 s. Again, the temperature for set 3 and 4 shows a smooth transition at the interfaces between the cone and the punches. In contrast, the temperature for set 5 and 6 shows a large jump in the cone-punch interface. Additionally, the temperature is symmetric according to the symmetry plane.

The magnitude of the electrical current density is shown in Fig. 7.13a for the horizontal path around 2000 s. For set 3, where a perfect contact is assumed, no jump at the interface can be observed. For set 4 and 5, the jump at the interface between the die and the punch is small. For set 6, however, the magnitude of the electrical current density shows a large jump from approximately 550 mA mm^{-2} to

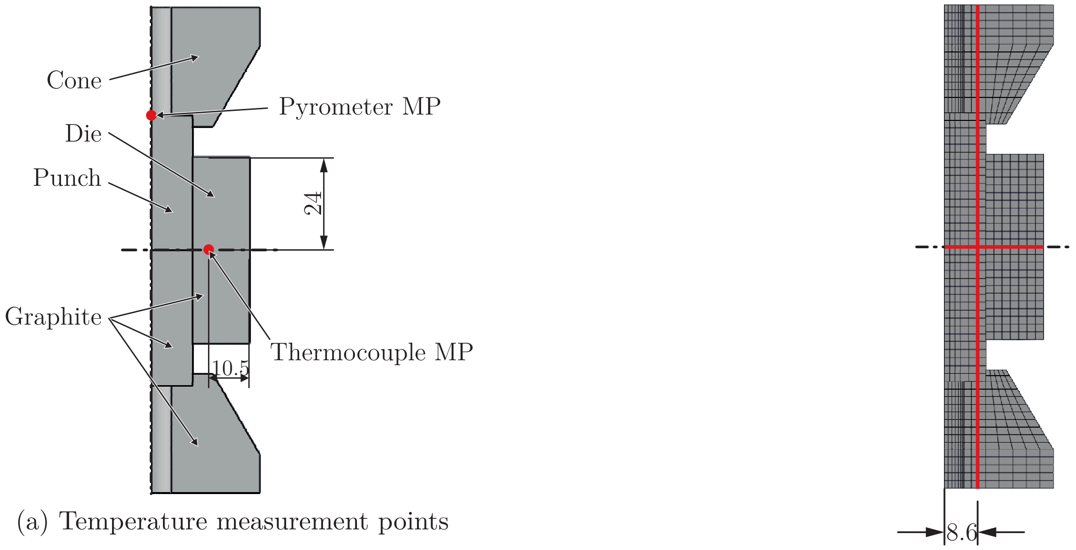

(a) Temperature measurement points

(b) Path definition

Figure 7.11: Temperature measurement points and path definition for the graphite tool system

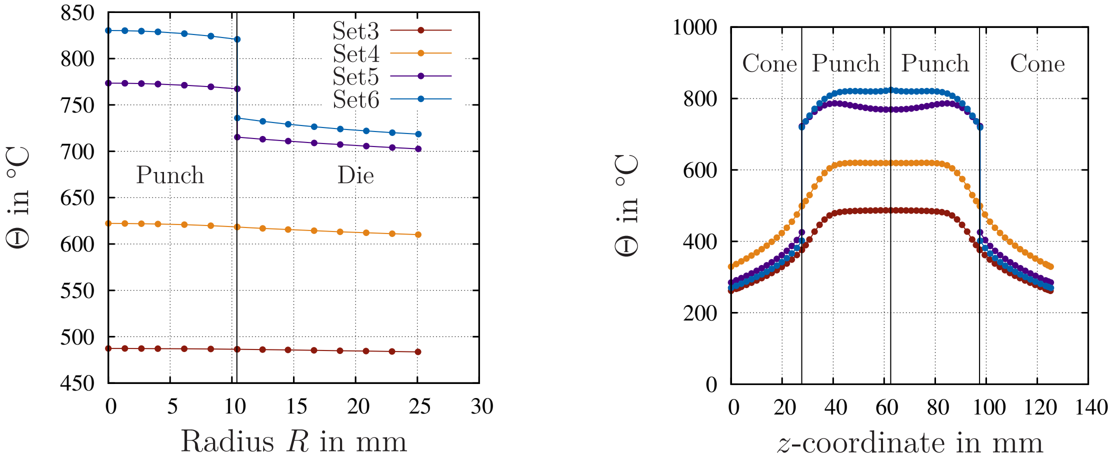

(a) Temperature vs. radius

(b) Temperature vs. z-coordinate

Figure 7.12: Temperature along the paths defined in Fig. 7.11b for different sets

920 mA mm^{-2}. For the vertical path, the magnitude of the electrical current density is plotted in Fig. 7.13b around 2000 s. The highest values appear in the punches near to the punch-cone interface. The values drop down towards the middle and have a sink at the punch-punch interface.

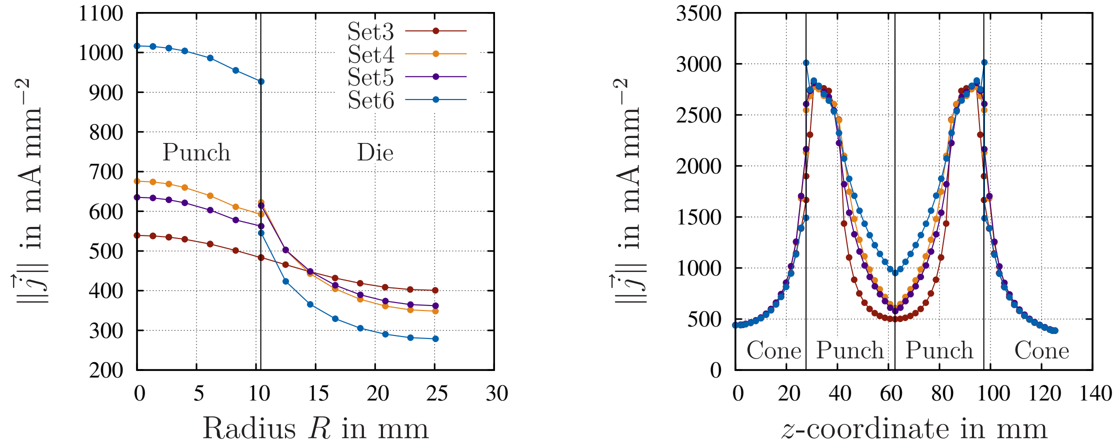

(a) Magnitude of electrical current density vs. radius

(b) Magnitude of electrical current density vs. z-coordinate

Figure 7.13: Magnitude of electrical current density along the paths defined in Fig. 7.11b for different sets

7.1.5 Sensitivity Analysis

This analysis focuses on the influence of the convection coefficient, the thermal as well as the electric contact resistance parameters on the temperature evolution in the thermocouple and at the pyrometer measurement point. All performed simulations are based on the parameters used for set 6, see Sect. 7.1.4.

Convection Study

The water cooling in the FAST-machine is modeled by convection. The convection coefficient $h_c = 880\,\mathrm{W\,m^{-2}\,K^{-1}}$ is taken from [Vanmeensel et al., 2005], where the temperature distribution of a FAST-machine produced by FCT is modeled. The experiments in this work are performed with a machine from the same company, a FCT HP D5, see Sect. 2.2.

The purpose of this study is to check the validity of the chosen coefficient and the influence on the temperature evolution. The investigated convection coefficients are: $300\,\mathrm{W\,m^{-2}\,K^{-1}}$, $500\,\mathrm{W\,m^{-2}\,K^{-1}}$, $700\,\mathrm{W\,m^{-2}\,K^{-1}}$ and $1000\,\mathrm{W\,m^{-2}\,K^{-1}}$. In Fig. 7.14a, the temperature at the thermocouple position is plotted over the time. It is found that a lower convection coefficient leads to a higher temperature and to a larger deviation to the experimental temperature curve. At the pyrometer measurement position, the temperature evolution shows a larger deviation for the different convection coefficients. In conclusion, the chosen convection coefficient $h_c = 880\,\mathrm{W\,m^{-2}\,K^{-1}}$ can be regarded as appropriate for the simulations.

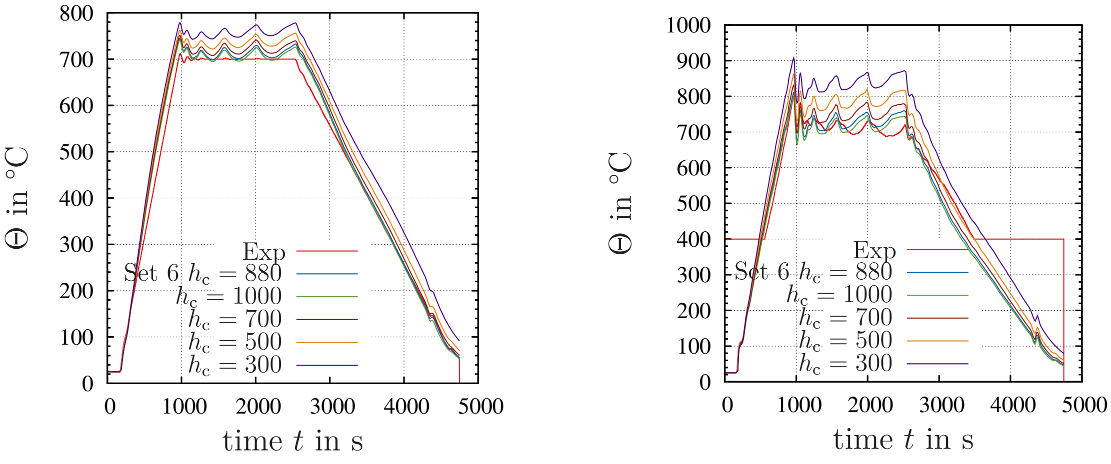

(a) Thermocouple position

(b) Pyrometer measurement point

Figure 7.14: Influence of convection coefficient on the temperature evolution

Thermal Contact Resistance Parameter Study

For the thermal contact conductance, there are no measurements for the graphite-graphite contact. For this reason, the parameters for the horizontal and vertical thermal contact resistance are taken from Zavaliangos et al. [2004]. Here, the aim is to investigate the fundamental influence on the temperature field. For this purpose, the same parameters are used for the vertical and the horizontal thermal conductances. The following thermal conductances are used: $300\,\mathrm{S\,m^{-2}}$, $500\,\mathrm{S\,m^{-2}}$, $700\,\mathrm{S\,m^{-2}}$ and $1000\,\mathrm{S\,m^{-2}}$. A higher thermal contact conductance leads to an overheating at the thermocouple position at 1000 s in Fig. 7.15a. Subsequently, the temperature shows an oscillating behavior with a higher thermal contact conductance, where higher conductances lead to increased oscillations. At the pyrometer measurement point, the temperature is strongly influenced by the thermal contact conductance, while the maximum temperature difference between the different curves is approximately 300 °C, see Fig. 7.15b. As mentioned before, the thermal contact conditions are important for the simulation of the correct temperature distribution and lead to different temperatures in the graphite parts.

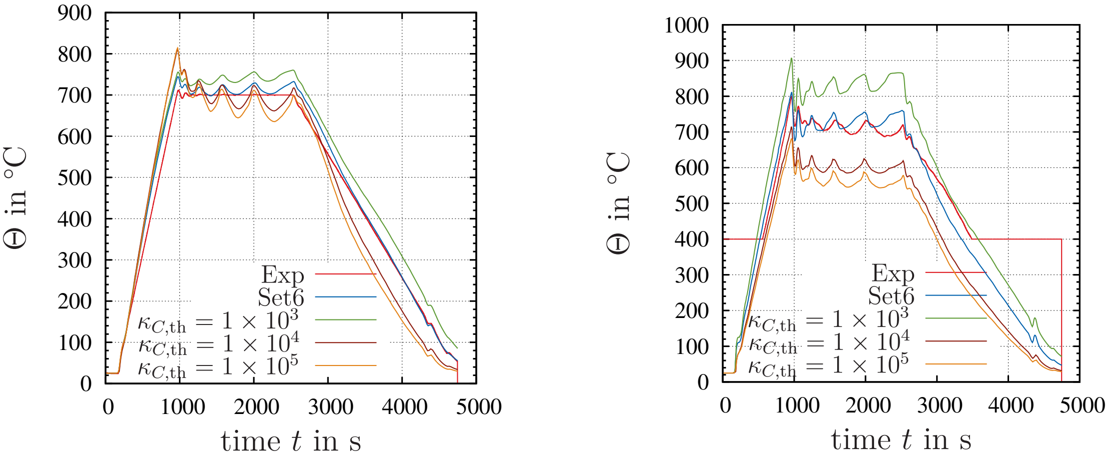

(a) Thermocouple position (b) Pyrometer measurement point

Figure 7.15: Temperature evolution for different thermal contact conductances

Electrical Contact Resistance Parameter Study

The electrical contact resistance produces heat at the interfaces and, accordingly, increases the interface temperature. In Sect. 5.5.3, the electrical contact conductance was derived out of the experiments in Sect. 2.8. Due to the scatter in the experiments, different functions for the pressure-dependent electrical contact conductance were derived in Sect. 5.5.3. As the influence of these different functions on the temperature evolution is to be analyzed here, Fig. 7.16 shows the temperature evolution at the thermocouple position and the pyrometer measurement point.

The different functions mainly influence the temperature evolution between 1000 s and 3000 s, where the influence at the pyrometer measurement point is larger than at the thermocouple position. In summary, the simulated temperature with $\kappa_{C,\mathrm{el,GG6}}$ agrees well with the experimental temperature. Therefore, this function is used in the following sintering experiments.

7.1.6 PID-Controller

One possibility to prescribe the boundary conditions of the simulation is to apply values for the current that are taken from an experiment. This is done in the parameter study, see Sect. 7.1.4 and Fig. 7.7a. The current in the FAST-machine is not prescribed. Rather, the process is temperature-controlled by placing a thermocouple into a borehole in the die, see Fig. 7.11a for the thermocouple position. The temperature at this position is prescribed – and a PID-controller serves to control the current in the machine. In order to make predictions instead of relying on the measured current, a PID-controller is implemented into Abaqus for the simulations. A PID-controller is used also in the work of Munoz and Anselmi-

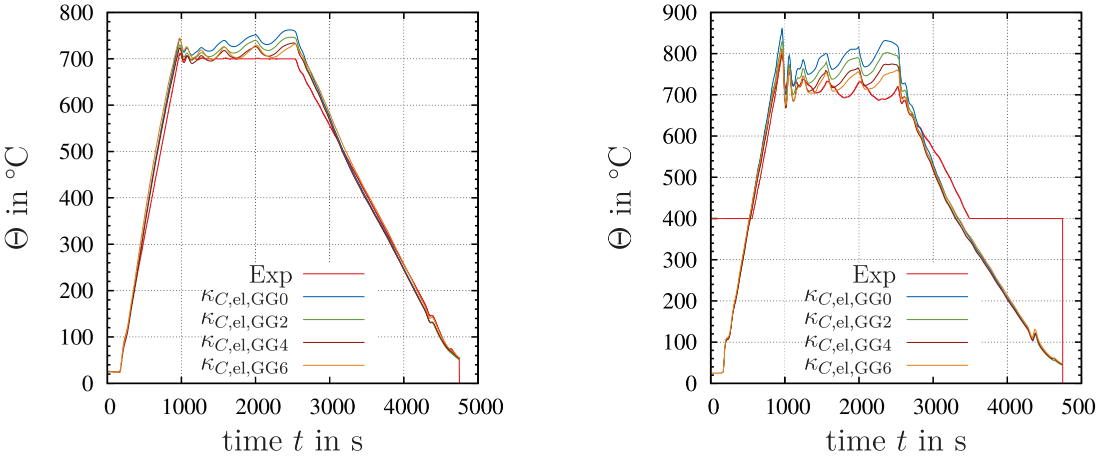

(a) Thermocouple position

(b) Pyrometer measurement point

Figure 7.16: Temperature evolution for different electrical contact conductances

Tamburini [2010] and Mondalek et al. [2011]. The implementation aspects and the theory are explained in App. 8. Except for the boundary condition of the electrical field, the parameters of set 6 and the same conditions as in the parameter study are used. Here, the temperature at the thermocouple position is prescribed and the controller changes the current. The three controller parameters K_P, K_I, K_D identified by this experiment are listed in Tab. 7.4. The measured current over the time in the experiment is compared to the computed current by the PID-controller in the simulation in Fig. 7.17b. The temperature in the thermocouple position over the time is plotted in Fig. 7.17a. A very good agreement between the simulated and the measured current can be observed. Also, the controlled temperature agrees very well with the prescribed temperature. Between 1000 s and 2500 s, the simulated temperature shows a higher but acceptable oscillation compared to the experiment.

The temperature at the pyrometer measurement position is shown in Fig. 7.18 for the experiment and the simulation. During the heating and cooling phase, the simulated temperature agrees well with the temperature of the experiment. The maximum temperature in the simulation is lower than the experimental temperature. Between 1000 s to 2500 s, the oscillating behavior of the temperature in the simulation differs from the behavior in the experiment, which can be explained by the uncertainties in the contact conditions. Nevertheless, the deviation is in an acceptable range.

For validation purposes, an experiment with $\Theta_c = 600\,^\circ\mathrm{C}$ is simulated in order to test the PID-controller. Fig. 7.19a shows the temperature at the thermocouple position in the simulation and the experiment. The simulated temperature shows a larger oscillation after 1000 s, but still coincides well with the experimental

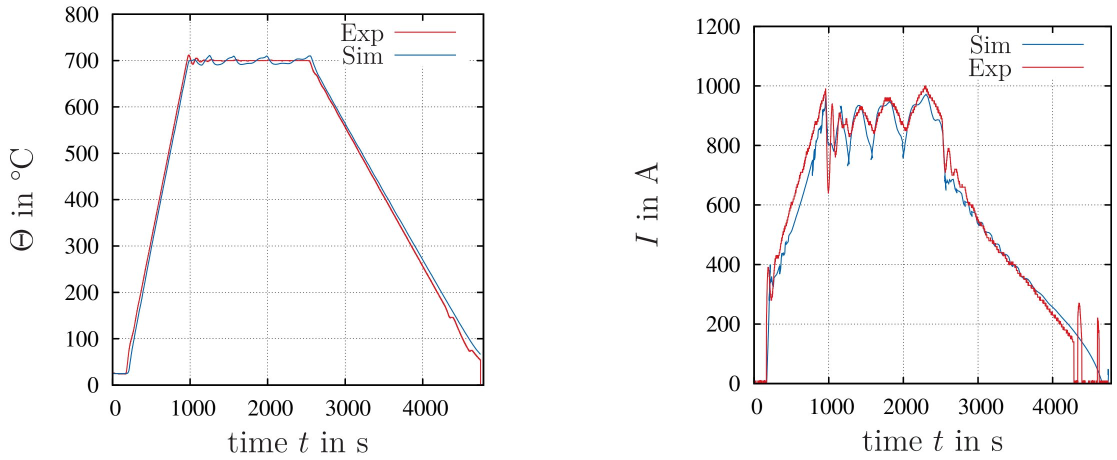

(a) Comparison of temperature in the experiment and in the simulation

(b) Comparison between controlled current from experiment and the simulation

Figure 7.17: Graphite experiment used for the identification of the PID-controller parameters

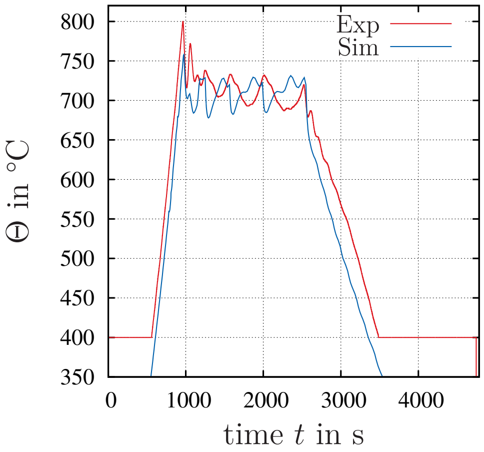

Figure 7.18: Temperature evolution at pyrometer position for the controller identification experiment

Table 7.4: PID-controller parameters identified with Exp. 7.17

K_P A °C^{-1}	K_I A °C^{-1} s^{-1}	K_D A s °C^{-1}
4.00	0.02	6.00

temperature. The current shown in Fig. 7.19b oscillates more in the experiment than in the simulation – especially after 2500 s.

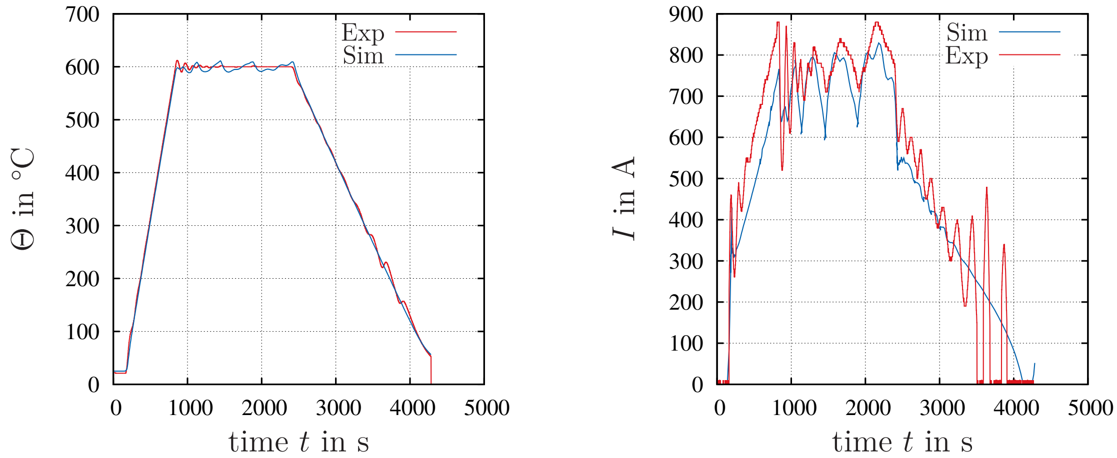

(a) Temperature at the thermocouple position

(b) Current, controlled by the PID-controller

Figure 7.19: Simulation of an experiment with $\Theta_c = 600\,^{\circ}\mathrm{C}$

In summary, the PID-controller works quite well and offers the possibility to directly prescribe the temperature in the thermocouple position. Hence, it is possible to make predictions, and the simulated conditions are closer to the actual conditions in the experiment.

7.2 Simulation of Sintering Experiments

The following section focuses on a simulation of the fully coupled thermo-electro-mechanical sintering at finite strains. For this purpose, two materials have to be considered. These are the copper powder, which is sintered, and the graphite material, which is used for the tool system. The finite element simulations are performed with the commercial program Abaqus. For this reason, the material model for the copper powder, see Tab. 4.3, is implemented via a user subroutine in Abaqus. During the sintering process, the powder is compressed from approximately 12 mm to 5 mm. Due to these large deformations, it is necessary to perform contact simulations at large strains. Furthermore, the thermal and electrical resistances at the interfaces are crucial to match the conditions in the real process, see Sect. 7.1.4, and thus have to be incorporated in the simulation.

First of all, the boundary conditions and the parameters used in the simulation are described – followed by the simulation of an instationary creep experiment that was not used for the parameter identification. In this experiment, the heating rate is

$\dot{\Theta} = 50\,°\mathrm{C\,min}^{-1}$. In the second simulation, an instationary creep experiment with a heating rate of $\dot{\Theta} = 200\,°\mathrm{C\,min}^{-1}$ is investigated. For the last simulation, a creep experiment with a dwell time of 2 h is chosen, which was used for the parameter identification.

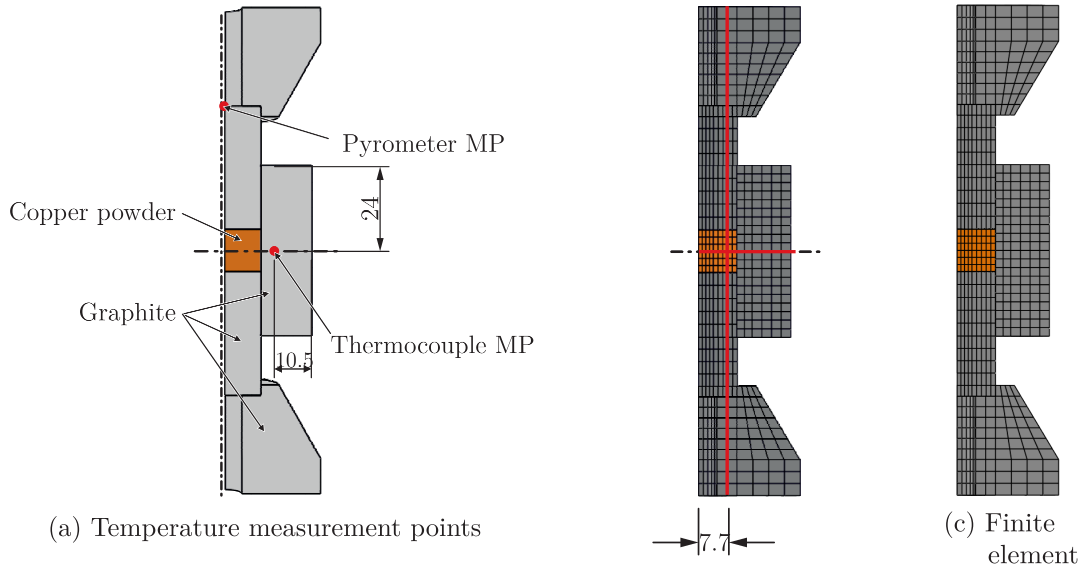

(a) Temperature measurement points

(b) Path definition

(c) Finite element mesh

Figure 7.20: Set-up and temperature measurement points for the FAST tool system

Fig. 7.20 shows the graphite tool system with the copper powder. The FAST-machine features two temperature measurement points. The temperature, which is measured at the thermocouple, is used as a basis to control the current. In addition, the temperature at the upper punch is measured by a pyrometer. The PID-controller introduced in the previous section is used in these simulations too. Therefore, the temperature at the thermocouple is used as the desired value for the controller. The temperature at the pyrometer is used for comparison.

Fig. 7.20c shows the mesh used in the sintering simulations. According to the Abaqus manual, linear elements are more suitable than quadratic elements when it comes to contact simulations. No convergence could be obtained with a mesh consisting of quadratic hexahedral elements (Q3D20). Hence, linear brick elements are used in the simulation. The mesh contains $n_\mathrm{e} = 3627$ linear hexahedral elements (Q3D8) and a total number of unknowns $n_\mathrm{dof} = 24590$.

7.2.1 Boundary Conditions

The geometry of the graphite tool system is shown in Fig. 2.6. Due to the axisymmetry, only one-fourth is modeled. Due to the fact that the lower punch moves

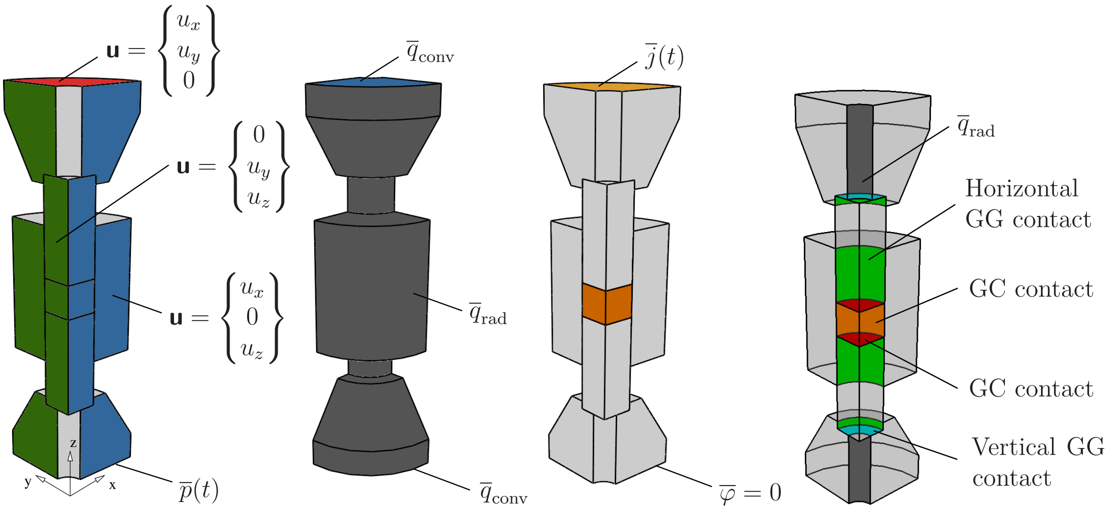

(a) Mechanical field (b) Thermal field (c) Electrical field (d) Contact surfaces and radiation

Figure 7.21: Boundary conditions

during the process and the upper punch is fixed, there is no further symmetry in the horizontal plane.

For the multi-field simulation, various boundary conditions have to be applied. The mechanical boundary conditions are shown in Fig. 7.21a. Symmetry boundary conditions are used for the side surfaces. The top surface is fixed, whereas a force is applied over the time at the bottom surface. As in the experimental set-up, the die is not fixed and can therefore move in vertical/axial direction.

The water cooling for the FAST tool system is modeled by convection at the top and the bottom surface, see Fig. 7.21b. Due to the vacuum chamber, radiation only takes place at the outer surfaces, Fig. 7.21b. The convection and radiation is modeled by Eq. (7.1). The temperature of the water in the cooling circuit is assumed to be $\Theta_\mathrm{f} = 25\,^\circ\mathrm{C}$. The convection coefficient $h_\mathrm{c} = 880\,\mathrm{W\,m^{-2}\,K^{-1}}$ is taken from [Vanmeensel et al., 2005], where a FAST-machine from the same manufacturer is modeled. A constant chamber temperature of $\Theta_\infty = 25\,^\circ\mathrm{C}$ is used as a first attempt. σ denotes the Stefan Boltzmann constant and $\epsilon = 0.8$ the emissivity for graphite, which is taken from [Zavaliangos et al., 2004]. The initial temperature for the FAST-tool system with the powder is set to $25\,^\circ\mathrm{C}$.

For the electrical field, the current at the top surface is prescribed by the PID-controller, see Fig. 7.21c. At the bottom surface, the electrical potential is set to zero.

Furthermore, two different contact pairs are present in the model. The graphite-graphite contact and the graphite-powder contact conditions have to be inserted. The electrical contact conductance is identified in Sect. 5.5.3 out of the experiments in Sect. 2.8 for the graphite-graphite contact $\kappa_{C,\mathrm{el},\mathrm{GG6}}(p)$ and the graphite-copper contact $\kappa_{C,\mathrm{el},\mathrm{GC6}}(p)$. The contact conductances depend on the applied pressure p. For the thermal contact conductance between graphite and graphite, the according values are taken from Zavaliangos et al. [2004]. In this work, the contact conductance is separated into a vertical and horizontal part, where the values are given by $\kappa^{\mathrm{H}}_{C,\mathrm{th},\mathrm{GG}} = 1.32 \times 10^3\,\mathrm{W\,m^{-2}\,K^{-1}}$ as the horizontal, $\kappa^{\mathrm{V}}_{C,\mathrm{th},\mathrm{GG}} = 2.4 \times 10^3\,\mathrm{W\,m^{-2}\,K^{-1}}$ as the vertical thermal conductance. There are no values available for the graphite-copper contact, which is the reason for the use of the thermal contact conductance $\kappa_{C,\mathrm{th},\mathrm{CC}}(p)$ for copper-copper contact as a first attempt. The data from the publication of Rao et al. [2004] is used, and a power function is fitted to this data in Sect. 5.5.4. The according contact conductances are summarized in Tab. 7.5. For the mechanical contact, the simulation is based on a friction coefficient of $\eta = 0.1$ – and a finite sliding node-to-surface formulation is chosen for the contact discretization. For the curved surfaces, a smoothing technique offered in Abaqus is used for the simulations. Furthermore, the tolerance for the slave surface adjustment is chosen to be 0.01. The relative density dependence of the thermal and electrical conductivity can be incorporated via a user defined field. Therefore, the relative density is set as a field variable. The maximum number of equilibrium iterations is increased from 5 to 25.

Table 7.5: Contact parameters used in the sintering simulations

	$\kappa_{C,\mathrm{el}}$ $\mathrm{S\,m^{-2}}$	$\kappa_{C,\mathrm{th}}$ $\mathrm{W\,m^{-2}\,K^{-1}}$	$\kappa_{C,\mathrm{th}}$ $\mathrm{W\,m^{-2}\,K^{-1}}$
Graphite-Graphite contact	$\kappa_{C,\mathrm{el},\mathrm{GG6}}(p)$	$\kappa^{\mathrm{H}}_{C,\mathrm{th},\mathrm{GG}} = 1.32 \times 10^3$	$\kappa^{\mathrm{V}}_{C,\mathrm{th},\mathrm{GG}} = 2.40 \times 10^3$
Graphite-Copper contact	$\kappa_{C,\mathrm{el},\mathrm{GC6}}(p)$	$\kappa_{C,\mathrm{th},\mathrm{CC}}(p)$	$\kappa_{C,\mathrm{th},\mathrm{CC}}(p)$

Moreover, two materials have to be considered. The copper powder is characterized by the constitutive model developed in Chap. 4. The identified material parameters are listed in Tab. 5.5. For the thermal field, the temperature-dependent heat capacity $c_{\mathrm{p}}(\Theta)$ and the temperature as well as relative density-dependent thermal conductivity $\kappa_{\mathrm{th}}(\rho_{\mathrm{rel}}, \Theta)$ are incorporated. The electrical conductivity $\kappa_{\mathrm{el}}(\rho_{\mathrm{rel}}, \Theta)$ of the copper powder is a function of the temperature and the relative density as well. All functions determined by the experiments are reported in Sect. 5.5.

The second material to be characterized is graphite R8510, produced by the SGL Carbon GmbH. For this material, a thermo-elastic behavior is assumed. The Young's modulus is given by $E = 11\,500\,\mathrm{MPa}$ and the Poisson ratio reads $\nu = 0.2$. Graphite has a density of $1850\,\mathrm{kg\,m^{-3}}$. The identified thermal expansion coefficient is defined by $\alpha_\Theta = 4.55 \times 10^{-6}\,\mathrm{K}^{-1}$, see Sect. 5.5.2. For the thermal and the electrical field, the temperature-dependent heat capacity $c_\mathrm{p}(\Theta)$, the thermal $\kappa_\mathrm{th}(\Theta)$ as well as the electrical conductivity $\kappa_\mathrm{el}(\Theta)$ are incorporated in the finite element model. These functions are fitted to the experiments in Sect. 5.5.2.

7.2.2 Instationary Creep Simulation with $\dot{\Theta} = 50\,°\mathrm{C}\,\mathrm{min}^{-1}$

First, an instationary creep experiment, which was not used for the identification of the constitutive model, is simulated. The loading conditions are shown in Fig. 7.22. The force is applied up to the constant value of approximately 24.5 kN. Subsequently, the temperature is raised up to 560 °C with a heating rate of $\dot{\Theta} = 50\,°\mathrm{C}\,\mathrm{min}^{-1}$. The temperature path from the experiment is used as the desired value for the PID-controller. As can be seen in Fig. 7.22b, the simulated temperature shows a good agreement with the experimental temperature. Thus, the PID-controller apparently works well for the sintering experiments too. The simulated temperature at the pyrometer measurement point is shown in Fig. 7.23a. The pyrometer in the FAST-machine measures temperatures above 400 °C. The simulated temperature matches the experiment perfectly. As can be seen in Fig. 7.23b, the current that is governed by the PID-controller shows an oscillating behavior between 400 s and 800 s. This can be explained by the various non-linearities in the model, which originate from the contact conditions as well as the materials.

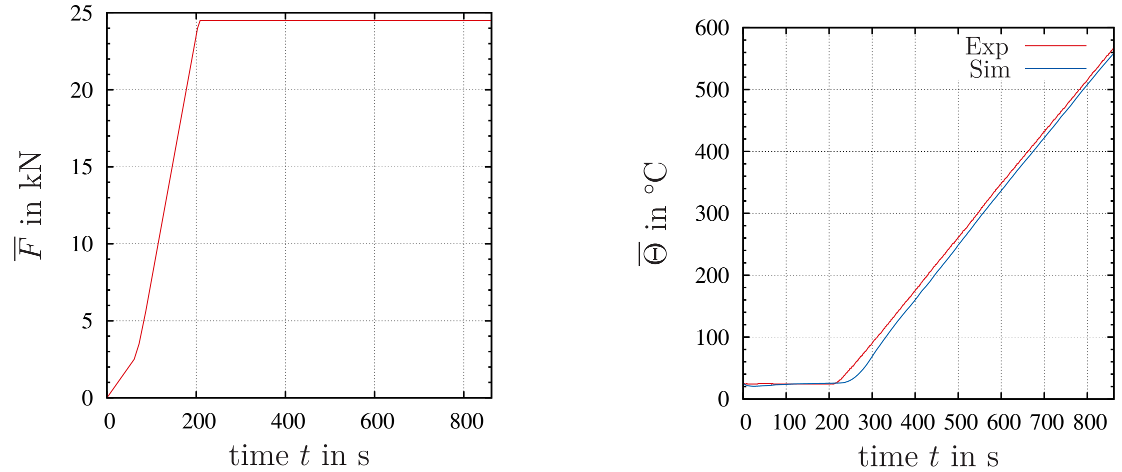

(a) Applied axial force

(b) Prescribed temperature at the thermocouple position

Figure 7.22: Prescribed axial force $\overline{F}$ and temperature $\overline{\Theta}$

The temperature distribution for the whole FAST-tool system, including the powder, is shown for different times in Fig. 7.24. At 200 s, there is no heating – and the temperature is homogeneously distributed given by 25 °C, see Fig. 7.24a.

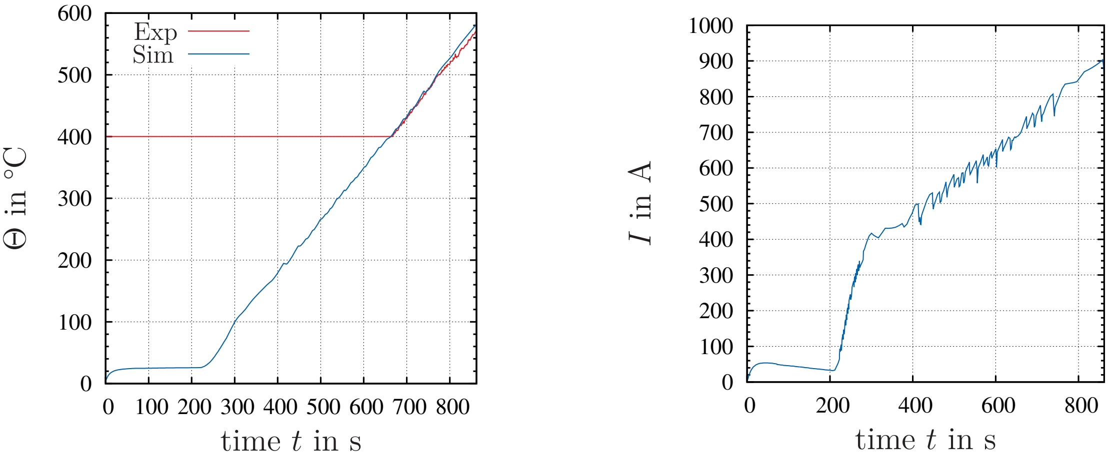

(a) Simulated temperature at the pyrometer measurement point

(b) Computed current by the PID-controller

Figure 7.23: Temperature at pyrometer measurement point and controller current

Subsequently, the current is applied, see Fig. 7.23b, and the temperature increases especially in the punches and the die at 398 s. The cone parts are cooler because of the water cooling. In addition, the contact resistances lead to different temperature distributions between the parts, see Sect. 7.1.4. The temperature distribution at 600 s is homogeneous in the punches, the die and the powder. At the end of the sintering simulation, at 862 s, the punches and the powder have the highest temperature. The die is cooler than the punches, which can be explained by the radiation over the surface and the thermal resistance at the interfaces between the punch and the die.

For a deeper study, the temperature is plotted over a horizontal and a vertical path defined in Fig. 7.20b. The temperature over the radius is plotted in Fig. 7.25a. There is no large temperature gradient between the copper powder and the graphite die to be observed during the process. Thus, the temperature measured at the thermocouple position represents the powder temperature for this FAST set-up with copper powder. In contrast, the temperature along the axial/z-direction shows a big difference between the cone, the punch and the powder (P). At 200 s, where no heating took place, the temperature is 25 °C. The temperature increases during the process, and the highest temperature is always found in the punches. Furthermore, the temperature is approximately symmetric, although the lower punch and cone are moving and the upper part is fixed. The cone parts are much cooler than the rest of the tool system. At the end of the process, the difference is about 300 °C, which can be explained by the contact resistances and the connection to the remaining system. The thermal resistance creates a barrier for the heat transport, and the heat flux is low due to the fact that the contact area between the punch and the cone part is fairly small. The powder region is a heat sink over the axial direction, and the

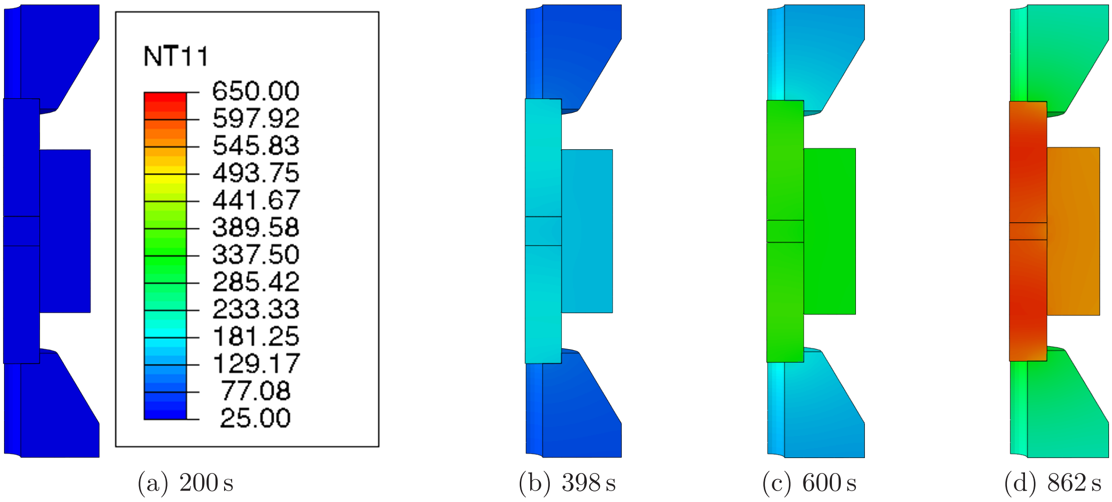

(a) 200 s (b) 398 s (c) 600 s (d) 862 s

Figure 7.24: Simulated temperature distribution at different times

temperature is lower than in the punch area. This can be explained by the electrical energy[1] dissipated into heat, as shown in Fig. 7.26. Most of the energy is dissipated in the punch and the cone area. In contrast, only little energy is dissipated in the die and the powder. The punch has the smallest area and, accordingly, the highest resistance. Other than that, copper is a good conductor and has a low resistance.

The relative density is an appropriate measure to evaluate the stage of sintering. Therefore, it is of interest to understand the relative density distribution in the powder region and to determine whether there are any gradients. Furthermore, the question is whether the powder is fully sintered and what the value of relative density is at the end of the process. The relative density distribution for different simulation times is shown in Fig. 7.27. At the beginning of the process, the relative density is approximately 0.4 – increasing up to approximately 1 at the end. During the whole process, the relative density is homogeneous inside the powder region. Also, one can observe the decreasing height, which is around 12 mm at the beginning and 5 mm at the end. The relative density over the time is shown in Fig. 7.28. The simulated relative density is in good agreement with the relative density from the experiment. For a better understanding of the relative density evolution, it is plotted together with the axial force and the temperature at the thermocouple position in Fig. 7.29. First, the force is increased, followed by an increase in relative density from 0.41 to 0.6. Subsequently, the temperature is raised. Here, the relative density remains nearly constant because the temperature is below the sintering temperature $\Theta_S = 151.36\,^\circ\mathrm{C}$. For higher temperatures above this value, the relative density increases up to approximately 1.

---

[1] The energy is given in $\mathrm{t\,mm^2\,s^{-2}}$ according to the unit system defined in Tab. 3. The energy in Joule can be obtained by dividing the values by 1000.

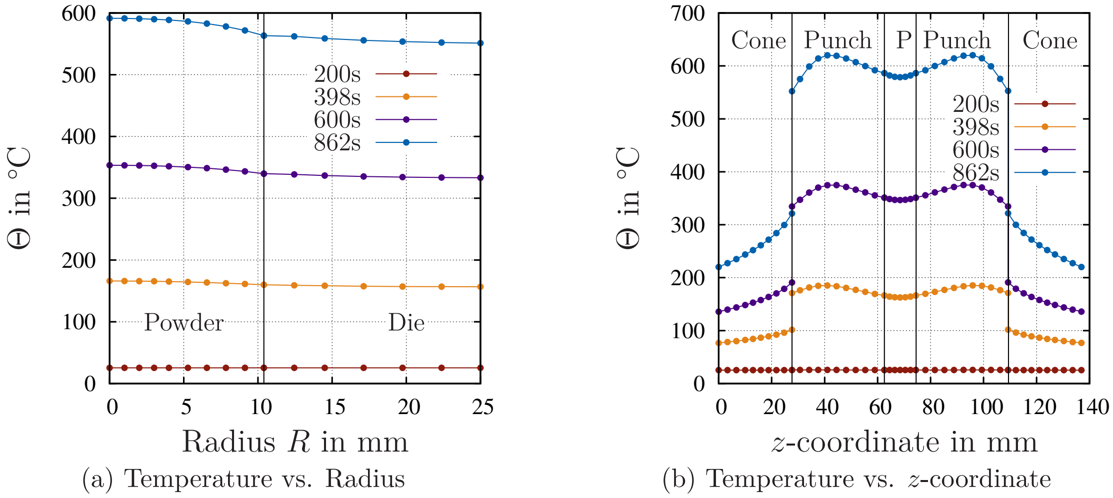

(a) Temperature vs. Radius (b) Temperature vs. z-coordinate

Figure 7.25: Temperature along different paths defined in Fig. 7.20b at different simulation times

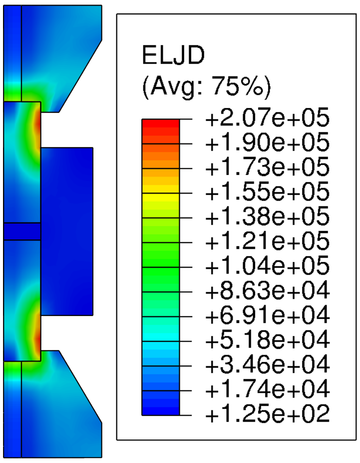

Figure 7.26: Total electrical energy dissipated into heat due to flow of current at 862 s

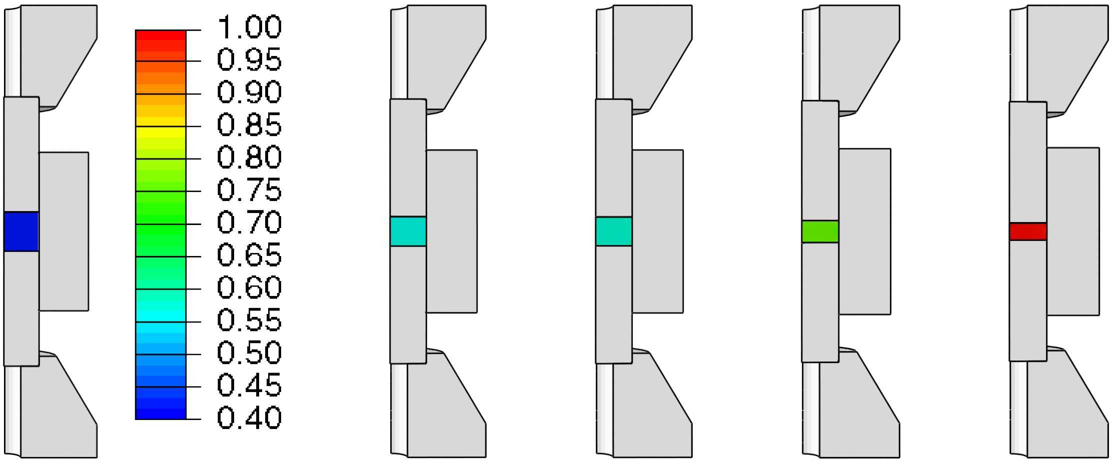

(a) 0 s (b) 200 s (c) 398 s (d) 600 s (e) 862 s

Figure 7.27: Relative density distribution at different times

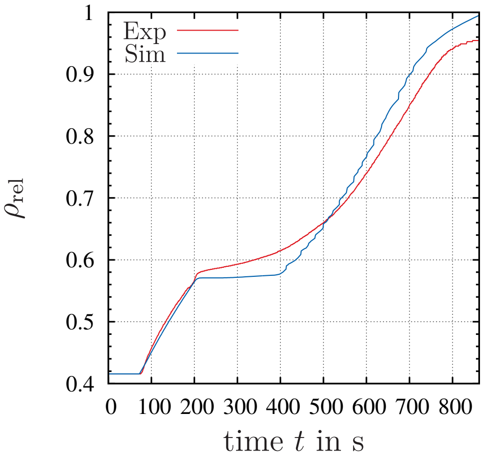

Figure 7.28: Relative density vs. time

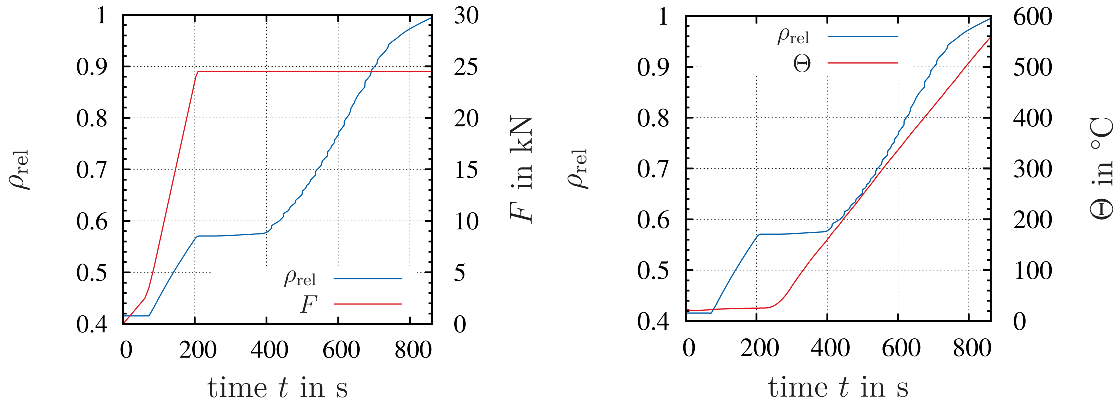

(a) Applied axial force and relative density vs. time

(b) Temperature at thermocouple position and relative density vs. time

Figure 7.29: Relative density, axial force and temperature over the time

7.2.3 Instationary Creep Simulation with $\dot{\Theta} = 200\,°\mathrm{C}\,\mathrm{min}^{-1}$

In the second sintering simulation, another instationary creep experiment is investigated – but with a higher heating rate of about $\dot{\Theta} = 200\,°\mathrm{C}\,\mathrm{min}^{-1}$. This experiment was again not utilized in the identification procedure for the constitutive model in Chap. 5. First, the force is raised up to 25 kN, followed by an increase in temperature, see Fig. 7.30. The temperature in the simulation has an offset towards the experimental desired temperature, meaning that the controlled system cannot follow the prescribed temperature due to the high heating rate. The simulated temperature at the pyrometer measurement point coincides well with the temperature in the experiment, see Fig. 7.31a. The relative density in the powder region is again homogeneous in the simulations and shown versus the time in Fig. 7.31b. For the cold compaction, the relative density in the simulation agrees perfectly with the density from the experiment. Afterwards, the simulated relative density remains constant while the relative density in the experiment still increases. For time values higher than 300 s, the deviation becomes smaller. Also, there is a very good agreement between the simulation and the experiment. This FAST sintering experiment and its simulation is of interest to save production time and to accelerate the process of sintering. The developed model represents a suitable approach to conduct detailed sintering experiments with high heating.

7.2.4 Creep Simulation

It turns out that the creep behavior of the copper powder at elevated temperatures largely contributes to the increase of the relative density, as can be observed in the experiments in Sect. 2.5.4. As it is important to incorporate this effect in the

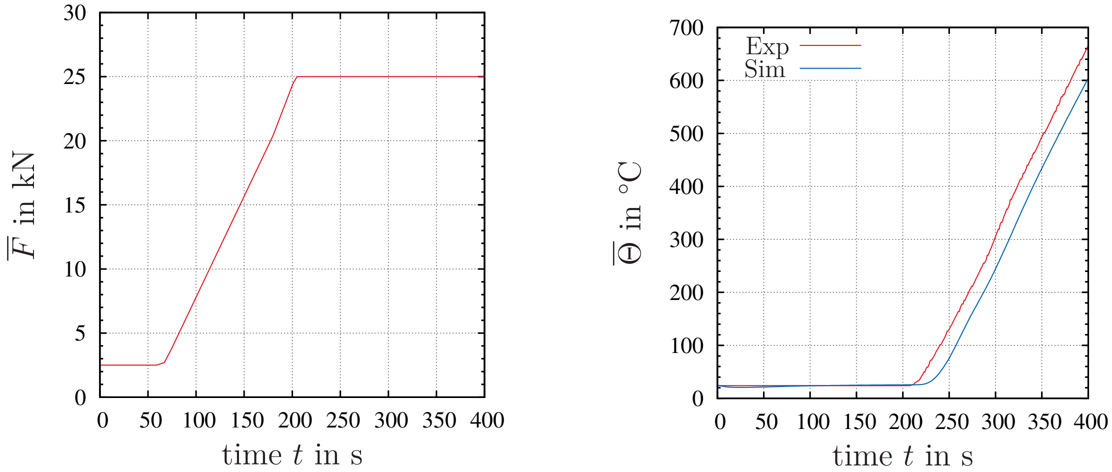

(a) Applied axial force

(b) Prescribed temperature at the thermocouple position

Figure 7.30: Prescribed axial force $\overline{F}$ and temperature $\overline{\Theta}$ for the instationary creep simulation with $\dot{\Theta} = 200\,°\mathrm{C\,min^{-1}}$

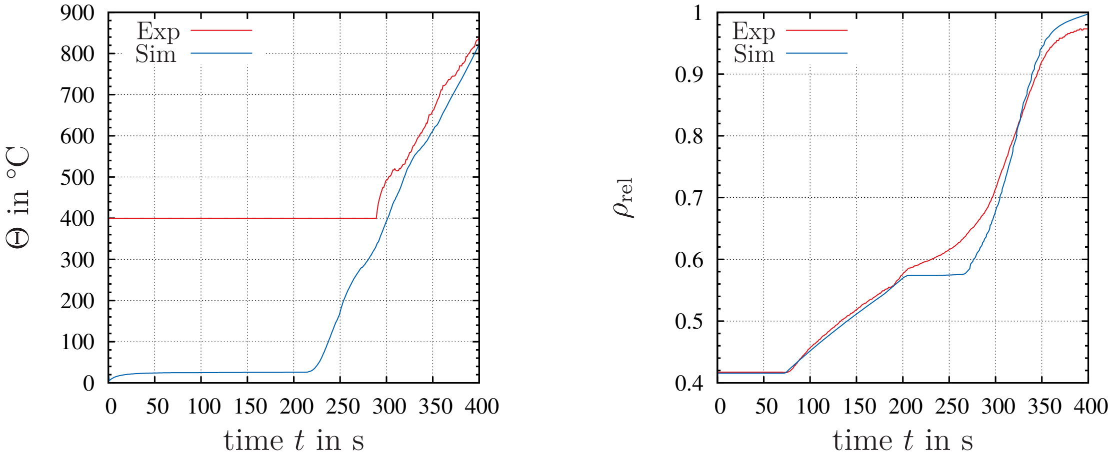

(a) Simulated temperature at the pyrometer measurement point

(b) Relative density vs. time

Figure 7.31: Temperature at pyrometer measurement point and relative density over time for the instationary creep simulation with $\dot{\Theta} = 200\,°\mathrm{C\,min^{-1}}$

model, the simulation performed in this chapter demonstrates that the model is suitable for creep experiments with a holding time of 2 h. The loading conditions are shown in Fig. 7.32. In this simulation, first the temperature is increased up to the constant value of 300 °C. Afterwards, the axial force is increased up to approximately 24.5 kN where it is held constant for 2 h. The simulated temperature in Fig. 7.32b shows a very good agreement with the temperature in the experiment. Thus, the PID-controller works quite well for this simulation. The controlled current, as shown in Fig. 7.33a, exhibits an oscillating behavior during the loading period and remains nearly constant afterwards. The relative density over the time is plotted in Fig. 7.33b, showing a perfect agreement during the loading period and an acceptable agreement during the creep period.

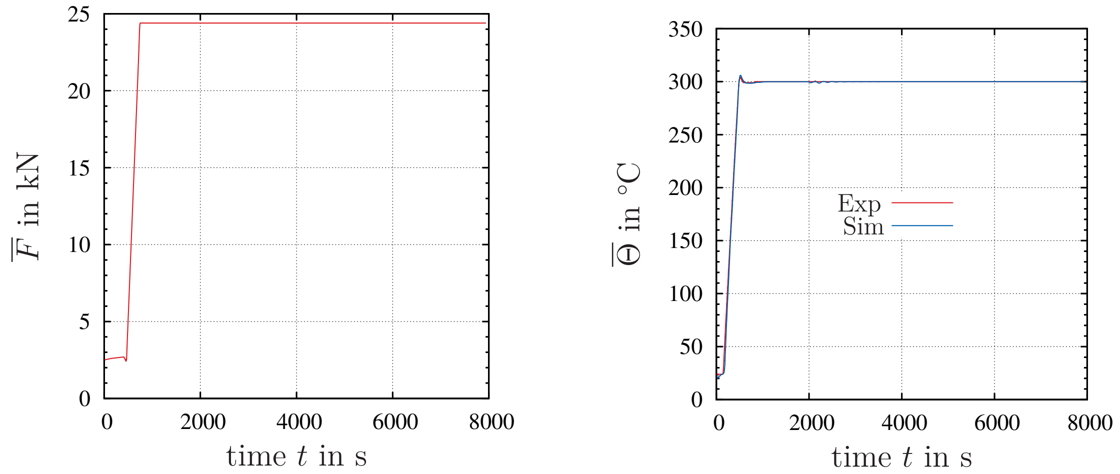

(a) Applied axial force

(b) Prescribed temperature at the thermocouple position

Figure 7.32: Prescribed axial force $\overline{F}$ and temperature $\overline{\Theta}$ for the creep simulation at 300 °C

7.3 Summary

The underlying physical problem of the FAST-process is a coupled multi-field problem involving the electrical, thermal and mechanical field. In addition, the thermal, electrical and mechanical contact conditions have to be incorporated. This complex problem is studied starting with the graphite tool system without any powder. The performed parameter study reveals the significance of the contact conditions as well as the temperature-dependent heat capacity, the thermal and the electrical conductivity. To determine the correct temperature, it is especially the incorporation of the thermal and electrical contact resistance that is of main

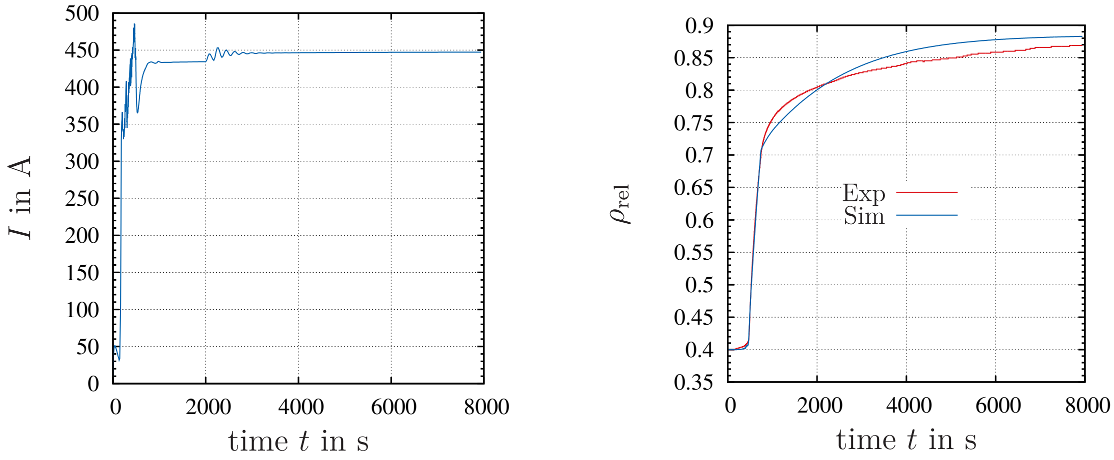

(a) Computed current by the PID-controller (b) Relative density vs. time

Figure 7.33: Temperature at pyrometer measurement point and controlled current for the creep simulation at 300 °C

importance. This is emphasized by the sensitivity analysis, which confirms the significant effect of the thermal contact resistance on the temperature at the pyrometer measurement point. A further possibility for improvement would be the measurement of the thermal contact conductance for the graphite-graphite and the graphite-copper contact depending on the contact pressure.

In order to make predictions, a PID-controller is implemented into Abaqus. Otherwise, it would only be possible to perform simulations by drawing on current values from conducted experiments. The current that is controlled by means of the PID-controller shows a very good agreement with the current from the experiments. Apart from that, the controller is also used for the sintering simulations in which the fully coupled thermo-electro-mechanical sintering process of the copper powder at finite strains is treated. The finite element simulations show a good agreement with the experiments. The model is capable to reproduce the sintering process. Furthermore, the simulation delivers a greater insight into the FAST-process because it enables to examine an entire temperature field instead of having to depend on only a few measuring points in actual experiments. Further, it is possible to analyze the homogeneity of the temperature field as well as the relative density. According to the simulations in this work, the copper powder showed no large gradients – which is probably related to the good thermal and electrical conductivity of copper. As a result, the finite element model including the constitutive model for the copper powder can be seen as a tool to improve and to understand the FAST-process in its details.

8 Conclusions and Outlook

The focus of this thesis lies on the development of a numerical model to simulate the FAST-process, which is a new production process for the sintering of powders. The sintering experiments are performed inside a closed vacuum chamber, and the temperature is measured by a thermocouple or a pyrometer – whereby the actual temperature distribution in the powder is not known. Moreover, it is of interest to minimize the sintering time and to ensure a homogeneous distribution of the thermal, the mechanical as well as the electrical field, leading to a sintering product with homogeneous properties. Therefore, an essential goal is to gain a deeper insight into the process by means of numerical simulations. With these simulations at hand, it is possible to predict the temperature during the process, the relative density as well as the shape of the powder product. However, primarily due to the underlying thermo-electro-mechanical problem, the modeling process is a complex and challenging task.

Chapter 2 focuses on a description of the experiments, starting with an investigation of the material behavior of copper powder. Various experiments are conducted for that purpose. The FAST experiments are performed at the group of our research collaborator, Prof. Frage, while the specifics of the loading paths are defined by our group. Monotonic sintering experiments at different temperature levels serve to investigate the rate dependence, and the force-rate as well as the temperature-rate dependence are studied. It turns out that the copper powder is dependent on the force-rate, but it shows no significant temperature-rate dependence. Instead, the creep experiments reveal that the creep behavior has significant influence on the sintering of the powder. The dilatometer experiments show a negligible volumetric deformation for free sintering without any applied force. An increasing yield stress with increasing relative density is discovered by tensile tests with sintered specimens.

Unfortunately, the radial stresses of the powder cannot be measured inside the FAST-machine during the sintering process. For this reason, cold compaction experiments with applied strain gauges are performed to get an information about the radial stresses. Based on the experiments, it is possible to make assumptions for the computation of the radial stresses.

For the numerical simulation the thermo-electrical properties for the copper powder as well as for the graphite material are required. The specific heat capacity in dependence of the temperature is determined for both the graphite material as well as the copper powder. The electrical and the thermal conductivity for the copper powder depend on the temperature and also on the relative density. These properties are determined for the graphite material as well.

Furthermore, the electrical contact resistance, which arises due to the surface roughness between the parts in contact, is measured for the graphite-graphite and the graphite-copper contact.

In Chapter 3, the fundamentals of Continuum Mechanics are introduced in order to provide a basis for the underlying thermo-electro-mechanical problem. A phenomenological material model for the copper powder is formulated with the help of Continuum Mechanics in Chapter 4. Here, the work of Bier [2008] serves as an important basis for this model – see also [Bier and Hartmann, 2006], where a new pressure dependent yield function is developed to address the cold compaction of metal powders. The respective convex single surface yield function is also used in this work, but modified in regard of its evolution. The constitutive model developed in this work is based on a multiplicative decomposition of the deformation gradient into an elastic, thermal, plastic and a creep part. A thermo-dynamically consistent compressible thermo-viscoplasticity model is obtained with the help of the Clausius-Duhem inequality. The evolution equations describing the yield surface are derived from this inequality with proposed free energy functions. In the compression range, the yield function evolves according to the kinematic and isotropic hardening variables. Moreover, the powder turns into a solid material during the sintering process, and the evolution of the tensile yield stress is included in the model by a tensile hardening variable. As a limit case, the von Mises yield function is reached. Creep consolidation is one main effect that leads to sintering. This creep behavior is mainly related to the change of relative density and, accordingly, to the change of volume. Hence, a new volumetric creep flow rule is proposed. Furthermore, an associative flow rule is used for the plastic part. The temperature dependence of the copper powder is incorporated by an exponential decrease of the yield function with increasing temperature. The final constitutive model has to be adapted to the experiments, which is done in Chapter 5. In the parameter identification procedure, the three-dimensional material model is reduced to a homogeneous constrained compression case – and a least-square method serves to minimize the residuals between the material model response and the experimental data, leading to the identified parameters.

Modeling the sintering process includes the numerical solution of the thermo-electro-mechanical problem. Starting from the variational forms of the balance relations, a spatial discretization with isoparametric finite elements is performed in a second step, leading to a differential-algebraic equation system. The differential part stems from the evolution equations, from the flow rules for the internal variables and the time-dependent thermal field. The algebraic part originates from the quasistatic balance of linear momentum and the stationary electrical charge equation. This DAE-system is solved with the backward Euler method in the temporal domain. The resulting nonlinear equation systems are solved with the Multilevel-Newton algorithm in each time step.

The last chapter addresses fully coupled thermo-electro-mechanical numerical simulations of the FAST-process with the help of Abaqus. For this purpose, the developed compressible finite strain thermo-viscoplasticity is implemented in Abaqus via a user subroutine. First, the complex problem is considered for a graphite tool system without any powder. The performed parameter study reveals the significance of the contact conditions as well as the temperature-dependent heat capacity as well as the thermal and electrical conductivity. It is especially the incorporation of the thermal and electrical contact resistance that is of main importance to retrieve the correct temperature. In order to make predictions, a PID-controller is implemented into Abaqus. Without this controller, it would only be possible to draw on current values taken from conducted experiments to define the boundary conditions of the simulations. The current that is controlled by the PID-controller shows a very good agreement with the current from the experiments. These simulations reproduce the fully coupled thermo-electro-mechanical sintering process of the copper powder at finite strains, revealing the temperature as well as the stress distribution inside the powder and the relative density evolution. The finite element simulations are in a good agreement with the experiments, and the model is capable of reproducing the sintering process. As a result, the finite element model including the constitutive model for the copper powder can be seen as a tool to improve and to understand the FAST-process in its details.

A further improvement for the constitutive model would be to incorporate the microstructure evolution, which should be considered in future work. Another aspect would be to measure the radial stresses of the powder material during sintering. For a better material characterization, triaxial tests would be desirable – which are, however, difficult to perform because of the thermo-electro-mechanical sintering process at high mechanical loads. Moreover, the elasticity parameters can be assumed as process-dependent, meaning that they would have to adapt to the relative density or, respectively, the sintering variables. Another approach would be to investigate steel powder instead of copper powder and to adapt the constitutive model to steel, which is used for many industrial products. Beyond that, the mechanical behavior of the graphite material could be investigated in order to develop a more sophisticated model for graphite. A further aspect to improve the finite element model would be the measurement of the pressure-dependent thermal contact conductance of the graphite-graphite as well as the copper-graphite contact. Moreover, the reflection of the radiative heat transport between the graphite surfaces itself and between the chamber walls should be addressed in future work.

Appendix

1 Electromagnetic Energy

The magnetic and the electric energy are given by

$$W_{\mathrm{magn}} = \frac{1}{2} \int\limits_v \vec{B} \cdot \vec{H} \, \mathrm{d}v, \qquad W_{\mathrm{el}} = \frac{1}{2} \int\limits_v \vec{E} \cdot \vec{D} \, \mathrm{d}v \tag{1}$$

according to [Klingbeil, 2010]. The time derivative of the magnetic energy reads

$$\dot{W}_{\mathrm{magn}} = \frac{1}{2} \frac{\mathrm{d}}{\mathrm{d}t} \int\limits_v \vec{B} \cdot \vec{H} \, \mathrm{d}v = \frac{1}{2} \int\limits_v \left(\dot{\vec{B}} \cdot \vec{H} + \vec{B} \cdot \dot{\vec{H}} \right) \mathrm{d}v. \tag{2}$$

Using the linear material relation $\vec{B} = \mu \vec{H}$ with the permeability coefficient μ, equation Eq. (2) can be written as

$$\dot{W}_{\mathrm{magn}} = \frac{1}{2} \int\limits_v \left(\mu \dot{\vec{H}} \cdot \vec{H} + \mu \vec{H} \cdot \dot{\vec{H}} \right) \mathrm{d}v = \int\limits_v \left(\mu \dot{\vec{H}} \cdot \vec{H} \right) \mathrm{d}v = \int\limits_v \left(\dot{\vec{B}} \cdot \vec{H} \right) \mathrm{d}v. \tag{3}$$

The electric energy is given by

$$W_{\mathrm{el}} = \frac{1}{2} \int\limits_v \vec{E} \cdot \vec{D} \, \mathrm{d}v. \tag{4}$$

With the linear material model $\vec{D} = \epsilon \vec{E}$, where ϵ denotes the dielectric coefficient, the electric power can be formulated as

$$\dot{W}_{\mathrm{el}} = \int\limits_v \vec{E} \cdot \dot{\vec{D}} \, \mathrm{d}v. \tag{5}$$

Thus, according to [Klingbeil, 2010], the power can be written as

$$P = \int\limits_a \vec{S} \cdot \mathrm{d}\vec{a} = -\dot{W}_{\mathrm{el}} - \dot{W}_{\mathrm{magn}} - P_{\mathrm{heat}}. \tag{6}$$

With this equation, the power flow inside a volume can be connected to the temporal change of the electrical energy W_{el} and the magnetic energy W_{magn}. The remaining part is transferred into heat.

2 Arguments for the Steady-State Charge Equation

This section provides arguments for neglecting the time dependence of the charge equation. The procedure is reported in [Zohdi, 2014]. This means that if $\dot{\rho}_\varphi = 0$, $\operatorname{div} \vec{j} = 0$ holds. By using the constitutive relations $\vec{j} = \kappa_{\mathrm{el}} \vec{E}$ and $\vec{D} = \epsilon \vec{E}$ as well as Gauss's law (3.69), the divergence of the electric current density can be formulated as

$$\operatorname{div} \vec{j} = \kappa_{\mathrm{el}} \operatorname{div} \vec{E} = \frac{\kappa_{\mathrm{el}}}{\epsilon} \operatorname{div} \vec{D} = \frac{\kappa_{\mathrm{el}}}{\epsilon} \rho_\varphi, \tag{7}$$

with the constant material parameters κ_{el} and ϵ. Inserting this equation into the charge equation (3.72) leads to

$$\dot{\rho}_\varphi = -\frac{\kappa_{\mathrm{el}}}{\epsilon} \rho_\varphi. \tag{8}$$

This initial value problem is a homogenous first order linear differential equation – and its solution, see [Meyberg and Vachenauer, 2001], reads

$$\rho_\varphi(t) = \rho_\varphi(t_0) \exp\left(-\frac{\kappa_{\mathrm{el}}}{\epsilon}(t - t_0)\right) \tag{9}$$

Computing the time derivative yields

$$\dot{\rho}_\varphi = -\frac{\kappa_{\mathrm{el}}}{\epsilon} \exp\left(-\frac{\kappa_{\mathrm{el}}}{\epsilon}(t - t_0)\right). \tag{10}$$

The electrical conductivity for copper is approximately $\kappa_{\mathrm{el}} = 6 \times 10^7 \,\mathrm{A\,V^{-1}\,m}$. The ratio $\kappa_{\mathrm{el}}/\epsilon$ is very large for metals. In this case, the charge density rate $\dot{\rho}_\varphi = -\frac{\kappa_{\mathrm{el}}}{\epsilon} \exp\left(-\frac{\kappa_{\mathrm{el}}}{\epsilon}(t - t_0)\right) \approx 0$ can be assumed as zero. For small time values, the charge density rate can be non-zero, but with an exponential decrease. As the experiments presented in this work take minutes or hours, the charge density rate can be neglected. Additionally, it is shown in [Klingbeil, 2010, p. 75] that the charge density rate can be neglected in metal conductors.

Compared to the mechanical deformations, the propagation of electricity is considered to be instantaneous. Additionally, a non-pulsed direct current is used in all the sintering experiments.

3 Load Cases for the Characterization of the Yield Function

Fig. 4.5 shows the different load cases in the I_1-J_2-plane.

Simple Shear

The deformation gradient and the stress tensor for simple shear reads

$$\mathbf{F} = \begin{bmatrix} 1 & \lambda & 0 \\ 0 & 1 & 0 \\ 0 & 0 & 1 \end{bmatrix}, \quad \mathbf{C} = \begin{bmatrix} 1 & \lambda & 0 \\ \lambda & \lambda^2 + 1 & 0 \\ 0 & 0 & 1 \end{bmatrix}, \quad \mathbf{T} = \begin{bmatrix} 0 & \tau & 0 \\ \tau & 0 & 0 \\ 0 & 0 & 0 \end{bmatrix}. \tag{11}$$

For this loading case, the first invariant is zero because no volume change occurs. Only the stress deviator is present

$$\mathrm{I}_1 = \operatorname{tr}\mathbf{T} = 0, \qquad \mathrm{J}_2 = \frac{1}{2}\mathbf{T}^{\mathrm{D}} \cdot \mathbf{T}^{\mathrm{D}} = \tau^2. \tag{12}$$

Uniaxial Tension

For the uniaxial tensile loading with loading in x-direction, the quantities are given by

$$\mathbf{F} = \begin{bmatrix} \lambda & 0 & 0 \\ 0 & \lambda_l & 0 \\ 0 & 0 & \lambda_l \end{bmatrix}, \quad \mathbf{C} = \begin{bmatrix} \lambda^2 & 0 & 0 \\ 0 & \lambda_l^2 & 0 \\ 0 & 0 & \lambda_l^2 \end{bmatrix}, \quad \mathbf{T} = \begin{bmatrix} \sigma_{\text{axial}} & 0 & 0 \\ 0 & 0 & 0 \\ 0 & 0 & 0 \end{bmatrix} \tag{13}$$

The stress deviator reads

$$\mathbf{T}^{\mathrm{D}} = \begin{bmatrix} \frac{2}{3}\sigma_{\text{axial}} & 0 & 0 \\ 0 & -\frac{1}{3}\sigma_{\text{axial}} & 0 \\ 0 & 0 & -\frac{1}{3}\sigma_{\text{axial}} \end{bmatrix} \tag{14}$$

leading to the invariants

$$\mathrm{I}_1 = \operatorname{tr}\mathbf{T} = \sigma_{\text{axial}}, \quad \mathrm{J}_2 = \frac{1}{2}\mathbf{T}^{\mathrm{D}} \cdot \mathbf{T}^{\mathrm{D}} = \frac{1}{3}\sigma_{\text{axial}}^2. \tag{15}$$

Uniaxial Laterally Constrained Compression

The sintering experiments can be seen as uniaxial constrained compression experiments, where the die deformation is negligible and the main deformation is in axial/z-direction. In this case, axial and radial stresses occur. The stress state is derived in App. 4.

$$\mathbf{F} = \begin{bmatrix} 1 & 0 & 0 \\ 0 & 1 & 0 \\ 0 & 0 & \lambda \end{bmatrix}, \quad \mathbf{C} = \begin{bmatrix} 1 & 0 & 0 \\ 0 & 1 & 0 \\ 0 & 0 & \lambda^2 \end{bmatrix}, \quad \mathbf{T} = \begin{bmatrix} \sigma_{\text{radial}} & 0 & 0 \\ 0 & \sigma_{\text{radial}} & 0 \\ 0 & 0 & \sigma_{\text{axial}} \end{bmatrix} \tag{16}$$

The stress deviator is given by

$$\mathbf{T}^{\mathrm{D}} = \begin{bmatrix} \frac{2}{3}\sigma_{\mathrm{axial}} - \frac{2}{3}\sigma_{\mathrm{radial}} & 0 & 0 \\ 0 & -\frac{1}{3}\sigma_{\mathrm{axial}} + \frac{1}{3}\sigma_{\mathrm{radial}} & 0 \\ 0 & 0 & -\frac{1}{3}\sigma_{\mathrm{axial}} + \frac{1}{3}\sigma_{\mathrm{radial}} \end{bmatrix}. \tag{17}$$

The invariants can be calculated by

$$\mathrm{I}_1 = \operatorname{tr}\mathbf{T} = \sigma_{\mathrm{axial}} + 2\sigma_{\mathrm{radial}}, \qquad \mathrm{J}_2 = \frac{1}{2}\mathbf{T}^{\mathrm{D}} \cdot \mathbf{T}^{\mathrm{D}} = \frac{1}{3}\left(\sigma_{\mathrm{axial}} - \sigma_{\mathrm{radial}}\right)^2. \tag{18}$$

Hydrostatic Compression

For the hydrostatic compression, the pressure and the deformation is the same in all directions.

$$\mathbf{F} = \begin{bmatrix} \lambda & 0 & 0 \\ 0 & \lambda & 0 \\ 0 & 0 & \lambda \end{bmatrix}, \quad \mathbf{C} = \begin{bmatrix} \lambda^2 & 0 & 0 \\ 0 & \lambda^2 & 0 \\ 0 & 0 & \lambda^2 \end{bmatrix}, \quad \mathbf{T} = \begin{bmatrix} -p & 0 & 0 \\ 0 & -p & 0 \\ 0 & 0 & -p \end{bmatrix} \tag{19}$$

In this case, only volumetric deformations occur, and the second stress deviator invariant is zero

$$\mathrm{I}_1 = \operatorname{tr}\mathbf{T} = -3p, \qquad \mathrm{J}_2 = \frac{1}{2}\mathbf{T}^{\mathrm{D}} \cdot \mathbf{T}^{\mathrm{D}} = 0. \tag{20}$$

4 Stress State of Uniaxial Laterally Constrained Compression

The equilibrium condition neglecting the body forces reads

$$\operatorname{div}\mathbf{T} = 0. \tag{21}$$

The balance of angular momentum leads to a symmetry of the stress tensor, $\mathbf{T} = \mathbf{T}^{\mathrm{T}}$. The stress tensor in a cylindrical coordinate system, see Fig. 1, is defined by

$$\mathbf{T} = \begin{bmatrix} \sigma_{rr} & \sigma_{r\phi} & \sigma_{rz} \\ \sigma_{r\phi} & \sigma_{\phi\phi} & \sigma_{\phi z} \\ \sigma_{rz} & \sigma_{\phi z} & \sigma_{zz} \end{bmatrix} \vec{e}_i \otimes \vec{e}_j \tag{22}$$

If this is inserted into the equilibrium condition, it yields

$$\frac{\partial \sigma_{rr}}{\partial r} + \frac{1}{r}\frac{\partial \sigma_{r\phi}}{\partial \phi} + \frac{\partial \sigma_{rz}}{\partial z} + \frac{\sigma_{rr} - \sigma_{\phi\phi}}{r} = 0 \tag{23}$$

$$\frac{\partial \sigma_{r\phi}}{\partial r} + \frac{1}{r}\frac{\partial \sigma_{\phi\phi}}{\partial \phi} + \frac{\partial \sigma_{\phi z}}{\partial z} + 2\frac{\sigma_{r\phi}}{r} = 0 \tag{24}$$

$$\frac{\partial \sigma_{rz}}{\partial r} + \frac{1}{r}\frac{\partial \sigma_{\phi z}}{\partial \phi} + \frac{\partial \sigma_{zz}}{\partial z} + \frac{\sigma_{rz}}{r} = 0 \tag{25}$$

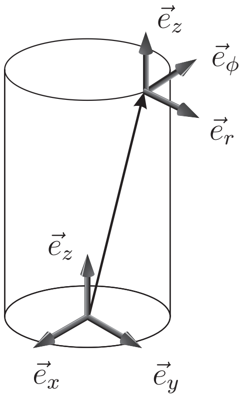

Figure 1: Cylindrical coordinate system

The powder compaction is performed in a cylindrical die – and due to the axial symmetry, the stresses are independent of the angle ϕ

$$\frac{\partial}{\partial \phi} = 0. \tag{26}$$

Furthermore, it is assumed that the stresses are constant over the height and do not depend on the z-coordinate. Thus, the stresses only depend on the radius r and simplify to

$$\frac{\partial \sigma_{rr}}{\partial r} + \frac{\sigma_{rr} - \sigma_{\phi\phi}}{r} = 0 \tag{27}$$

$$\frac{\partial \sigma_{r\phi}}{\partial r} + 2\frac{\sigma_{r\phi}}{r} = 0 \tag{28}$$

$$\frac{\partial \sigma_{rz}}{\partial r} + \frac{\sigma_{rz}}{r} = 0 \tag{29}$$

It is assumed that the powder compaction is a homogeneous deformation and that the radial stress is constant over the radius, leading to

$$\sigma_{\phi\phi} = \sigma_{rr} \tag{30}$$

Furthermore, it is assumed that no shear stresses occur in the powder compaction. The final stress tensor with $\sigma_{\text{radial}} = \sigma_{rr}$ and $\sigma_{\text{axial}} = \sigma_{zz}$ reads

$$\mathbf{T} = \begin{bmatrix} \sigma_{\text{radial}} & 0 & 0 \\ 0 & \sigma_{\text{radial}} & 0 \\ 0 & 0 & \sigma_{\text{axial}} \end{bmatrix} \tag{31}$$

5 Isothermal Compressible Viscoplasticity

The isothermal compressible viscoplasticity for the cold compaction of metal powders is based on the multiplicative decomposition of the deformation gradient into an elastic and a plastic part $\mathbf{F} = \hat{\mathbf{F}}_\mathrm{e}\mathbf{F}_\mathrm{p}$, see also [Bier and Hartmann, 2006] and [Bier, 2008]. This work draws on a different elasticity relation and internal variables as well as evolution equations. Instead of the ellipse aspect ratio α, the height k is used for the isotropic hardening behavior. In this case, k can be connected to the yield stress in the von Mises plasticity. Additionally, the hydrostatic kinematic hardening is modified to incorporate the vanishing deformation at $\rho_\mathrm{rel} = 1.0$. The same yield function as in the work of Bier [2008] is used, and the flow rule remains unchanged.

The elastic free energy is given by

$$\rho_0\psi_\mathrm{e}(\overline{\hat{\mathbf{C}}}_\mathrm{e}) = U(J_\mathrm{e}) + v(\mathrm{I}_{\bar{\mathrm{e}}}) \tag{32}$$

with the volumetric and isochoric parts

$$U(J_\mathrm{e}) = \frac{K}{50}\left(J_\mathrm{e}^5 + J_\mathrm{e}^{-5} - 2\right), \quad \text{and} \quad v(\mathrm{I}_{\bar{\mathrm{e}}}) = \frac{G}{2}\left(\mathrm{I}_{\bar{\mathrm{e}}} - 3\right), \tag{33}$$

The isochoric part is a Neo-Hooke type, and the volumetric part is proposed by Hartmann and Neff [2003]. For the isotropic hardening, a quadratic approach is chosen

$$\rho_0\psi_\mathrm{i}(r_\mathrm{i}) = \frac{1}{2}\gamma_k r_\mathrm{i}^2. \tag{34}$$

The kinematic part of the free energy is defined by

$$\rho_0\psi_\mathrm{k}(r_\mathrm{v}) = \frac{a_\xi}{b_\xi}e^{-b_\xi r_\mathrm{v}} - \frac{c_\xi}{2}r_\mathrm{v}^2 + \ln(e^{r_\mathrm{v}} - \rho_\mathrm{rel}). \tag{35}$$

The final material model is summarized in Tab. 1, formulated with quantities relative to the intermediate configuration and with quantities relative to the reference configuration in Tab. 2.

6 Matrix Representation

The strain displacement matrix reads

$$\tilde{\mathbf{B}}_a = \begin{bmatrix} F_{11}N_{a,X} & F_{21}N_{a,X} & F_{31}N_{a,X} \\ F_{12}N_{a,Y} & F_{22}N_{a,Y} & F_{32}N_{a,Y} \\ F_{13}N_{a,Z} & F_{23}N_{a,Z} & F_{33}N_{a,Z} \\ F_{11}N_{a,Y} + F_{12}N_{a,X} & F_{21}N_{a,Y} + F_{22}N_{a,X} & F_{31}N_{a,Y} + F_{32}N_{a,X} \\ F_{12}N_{a,Z} + F_{13}N_{a,Y} & F_{22}N_{a,Z} + F_{23}N_{a,Y} & F_{32}N_{a,Z} + F_{33}N_{a,Y} \\ F_{13}N_{a,X} + F_{11}N_{a,Z} & F_{23}N_{a,X} + F_{21}N_{a,Z} & F_{33}N_{a,X} + F_{31}N_{a,Z} \end{bmatrix} \tag{36}$$

with the index $a = 1, \ldots, n_\mathrm{en}$ ranging from 1 up to the number of nodes per element n_en. For further information, see [Hartmann, 2003].

Table 1: Summary of constitutive model formulated with quantities relative to the intermediate configuration

	Elasticity	Viscoplasticity
Loading condition	$\hat{F} < 0$	$\hat{F} \geq 0$
Strain energy	$\psi = \psi\big(\hat{\boldsymbol{\Gamma}}_{\mathrm{e}}, r_{\mathrm{i}}, r_{\mathrm{v}}\big) = \psi_{\mathrm{e}}\big(\hat{\boldsymbol{\Gamma}}_{\mathrm{e}}\big) + \psi_{\mathrm{k}}\big(r_{\mathrm{v}}\big) + \psi_{\mathrm{i}}\big(r_{\mathrm{i}}\big)$	
Elasticity relation	$\hat{\mathbf{P}} = \frac{K}{10}\left(J_{\mathrm{e}}^{5} - J_{\mathrm{e}}^{-5}\right)\mathbf{1} + G J_{\mathrm{e}}^{-2/3}\left(\hat{\mathbf{C}}_{\mathrm{e}} - \frac{1}{3}\left(\mathrm{tr}\,\hat{\mathbf{C}}_{\mathrm{e}}\right)\mathbf{1}\right)$	
Flow rule	$\overset{\triangle}{\hat{\boldsymbol{\Gamma}}}_{\mathrm{p}} = 0$	$\overset{\triangle}{\hat{\boldsymbol{\Gamma}}}_{\mathrm{p}} = \Lambda \dfrac{\partial F}{\partial \hat{\mathbf{P}}} = \Lambda \left(\dfrac{\partial F}{\partial \mathrm{I}_1}\mathbf{1} + \dfrac{\partial F}{\partial \mathrm{J}_2}\hat{\mathbf{P}}^{\mathrm{D}} \right)$
Isotropic hardening	$\dot{k}_{\mathrm{M}} = 0$	$\dot{k}_{\mathrm{M}} = \Lambda \dfrac{\gamma}{k_{\mathrm{M}}}\hat{\mathbf{P}} \cdot \dfrac{\partial F}{\partial \hat{\mathbf{P}}} - \Lambda \chi \beta k_{\mathrm{M}}$
Hydrostatic kin. hard.	$\xi_{\mathrm{M}} = -a_{\xi} e^{-b_{\xi} r_{\mathrm{v}}} + c_{\xi} r_{\mathrm{v}} - \dfrac{1}{1 - \rho_{\mathrm{rel}}}$	
Abbrev.	$\mathrm{I}_1 = \mathrm{tr}\,\hat{\mathbf{P}},\ \mathrm{J}_2 = \frac{1}{2}\hat{\mathbf{P}}^{\mathrm{D}} \cdot \hat{\mathbf{P}}^{\mathrm{D}},\ J_{\mathrm{e}} = (\det \mathbf{C}_{\mathrm{e}})^{\frac{1}{2}}$ $r_{\mathrm{v}} = \ln(\det \mathbf{C} / \det \mathbf{C}_{\mathrm{e}})/2, \quad \Lambda = \left\langle \hat{F}/\sigma_0 \right\rangle^{m} / \eta$	

Table 2: Summary of constitutive model formulated with quantities relative to the reference configuration

	Elasticity	Viscoplasticity
Loading condition	$\hat{F} < 0$	$\hat{F} \geq 0$
Elasticity relation	$\tilde{\mathbf{T}} = \frac{K}{10}\left(J_{\mathrm{e}}^{5} - J_{\mathrm{e}}^{-5}\right)\mathbf{C}^{-1} + G J_{\mathrm{e}}^{-2/3}\left(\mathbf{C}_{\mathrm{p}}^{-1} - \frac{1}{3}\,\mathrm{tr}(\mathbf{C}_{\mathrm{p}}^{-1}\mathbf{C})\mathbf{C}^{-1}\right)$	
Flow rule	$\dot{\mathbf{C}}_{\mathrm{p}} = \mathbf{0}$	$\dot{\mathbf{C}}_{\mathrm{p}} = \Lambda 2 \left(\dfrac{\partial \hat{F}}{\partial \mathrm{I}_1}\mathbf{I} + \dfrac{\partial \hat{F}}{\partial \mathrm{J}_2}(\mathbf{C}\tilde{\mathbf{T}} - (\mathrm{I}_1/3)\mathbf{I}) \right) \mathbf{C}_{\mathrm{p}}$
Isotropic hardening	$\dot{k}_{\mathrm{M}} = 0$	$\dot{k}_{\mathrm{M}} = \Lambda \dfrac{\gamma}{k} \left(\dfrac{\partial F}{\partial \mathrm{I}_1}\mathrm{I}_1 + 2\dfrac{\partial F}{\partial \mathrm{J}_2}\mathrm{J}_2 \right) - \Lambda \chi \beta k_{\mathrm{M}}$
Hydrostatic kin. hard.	$\xi_{\mathrm{M}} = -a_{\xi} e^{-b_{\xi} r_{\mathrm{v}}} + c_{\xi} r_{\mathrm{v}} - \dfrac{1}{1 - \rho_{\mathrm{rel}}}$	
Abbrev.	$\mathrm{I}_1 = \mathrm{tr}(\tilde{\mathbf{T}}\mathbf{C}),\ \mathrm{J}_2 = (\mathbf{C}\tilde{\mathbf{T}} \cdot \tilde{\mathbf{T}}\mathbf{C} - \mathrm{I}_1^2/3)/2,\ J_e = ((\det \mathbf{C})/(\det \mathbf{C}_{\mathrm{p}}))^{1/2}$ $r_{\mathrm{v}} = \ln(\det \mathbf{C}_{\mathrm{p}})/2, \quad \Lambda = \left\langle \hat{F}/\sigma_0 \right\rangle^{r_{\mathrm{v}}} / \eta$ $\chi = \sqrt{3 \left(\dfrac{\partial \tilde{F}}{\partial \hat{\mathrm{I}}_{1\mathrm{i}}} \right)^2 + 2\hat{\mathrm{J}}_{2\mathrm{i}} \left(\dfrac{\partial \tilde{F}}{\partial \hat{\mathrm{J}}_{2\mathrm{i}}} \right)^2}$	

For the transformation of the second Piola Kirchhoff stress tensor into the weighted Cauchy stresses in matrix representation, $\mathsf{\mathbf{S}}^{\mathrm{e}} = \mathsf{\mathbf{F}}^{\mathrm{e}}_{23}\tilde{\mathsf{\mathbf{T}}}^{\mathrm{e}}$ the tensor $[\mathbf{F} \otimes \mathbf{F}]^{\mathrm{T}_{23}}$ in matrix representation reads, see [Hartmann, 2003],

$$\mathsf{\mathbf{F}}^{\mathrm{e}}_{23} = \begin{bmatrix} \mathrm{F}_{11}\mathrm{F}_{11} & \mathrm{F}_{12}\mathrm{F}_{12} & \mathrm{F}_{13}\mathrm{F}_{13} & 2\mathrm{F}_{11}\mathrm{F}_{12} & 2\mathrm{F}_{12}\mathrm{F}_{13} & 2\mathrm{F}_{13}\mathrm{F}_{11} \\ \mathrm{F}_{21}\mathrm{F}_{21} & \mathrm{F}_{22}\mathrm{F}_{22} & \mathrm{F}_{23}\mathrm{F}_{23} & 2\mathrm{F}_{21}\mathrm{F}_{22} & 2\mathrm{F}_{22}\mathrm{F}_{23} & 2\mathrm{F}_{23}\mathrm{F}_{21} \\ \mathrm{F}_{31}\mathrm{F}_{31} & \mathrm{F}_{32}\mathrm{F}_{32} & \mathrm{F}_{33}\mathrm{F}_{33} & 2\mathrm{F}_{31}\mathrm{F}_{32} & 2\mathrm{F}_{32}\mathrm{F}_{33} & 2\mathrm{F}_{33}\mathrm{F}_{31} \\ \mathrm{F}_{11}\mathrm{F}_{21} & \mathrm{F}_{12}\mathrm{F}_{22} & \mathrm{F}_{13}\mathrm{F}_{23} & \mathrm{F}_{11}\mathrm{F}_{22} + \mathrm{F}_{12}\mathrm{F}_{21} & \mathrm{F}_{12}\mathrm{F}_{23} + \mathrm{F}_{13}\mathrm{F}_{22} & \mathrm{F}_{13}\mathrm{F}_{21} + \mathrm{F}_{11}\mathrm{F}_{23} \\ \mathrm{F}_{21}\mathrm{F}_{31} & \mathrm{F}_{22}\mathrm{F}_{32} & \mathrm{F}_{23}\mathrm{F}_{33} & \mathrm{F}_{21}\mathrm{F}_{32} + \mathrm{F}_{22}\mathrm{F}_{31} & \mathrm{F}_{22}\mathrm{F}_{33} + \mathrm{F}_{23}\mathrm{F}_{32} & \mathrm{F}_{23}\mathrm{F}_{31} + \mathrm{F}_{21}\mathrm{F}_{33} \\ \mathrm{F}_{31}\mathrm{F}_{11} & \mathrm{F}_{32}\mathrm{F}_{12} & \mathrm{F}_{33}\mathrm{F}_{13} & \mathrm{F}_{31}\mathrm{F}_{12} + \mathrm{F}_{32}\mathrm{F}_{11} & \mathrm{F}_{32}\mathrm{F}_{13} + \mathrm{F}_{33}\mathrm{F}_{12} & \mathrm{F}_{33}\mathrm{F}_{11} + \mathrm{F}_{31}\mathrm{F}_{13} \end{bmatrix} \tag{37}$$

7 Unit System

In Abaqus, there are no predefined units. The user has to make sure that the quantities are self-consistent. This means that a consistent unit system for the material parameters as well as for the geometry has to be considered. The SI-unit system consists out of seven basis units. These are: m, kg, s, A, K, mol, cd. With these basis units, all other physical units can be derived in a consistent manner. Here, five basis units for the thermo-electro-mechanical simulations are used – which are: mm, t, s, K and mA. This leads to the stress in MPa, which is commonly used in engineering. The conversion from the SI unit system into the mm, t, s, K, mA-system for the used quantities is shown in Tab. 3.

Table 3: Unit system

Measure	**Dim**	**SI**	**Factor**	**Units**
Length	L	m	10^3	**mm**
Mass	M	kg	10^{-3}	**t**
Time	T	s	1	**s**
Temperature	Θ	K	1	**K**
Electric current	I	A	10^3	**mA**
Density	$\mathrm{M/L^3}$	$\mathrm{kg\,m^{-3}}$	10^{-12}	$\mathrm{t\,mm^{-3}}$
Force	$\mathrm{ML/T^2}$	N	1	$\mathrm{t\,mm\,s^{-2}} \mathrel{\widehat{=}} \mathrm{N}$
Stress	$\mathrm{M/L\ T^2}$	Pa	10^{-6}	$\mathrm{t\,mm^{-1}\,s^{-2}} \mathrel{\widehat{=}} \mathrm{MPa}$
Energy	$\mathrm{ML^2/T^2}$	J	10^3	$\mathrm{t\,mm^2\,s^{-2}}$
Power	$\mathrm{ML^2/T^3}$	W	10^3	$\mathrm{t\,mm^2\,s^{-3}}$
Voltage	$\mathrm{ML^2/T^3I}$	V	1	$\mathrm{t\,mm\,s^{-3}\,mA^{-1}} \mathrel{\widehat{=}} \mathrm{V}$
Heat capacity	$\mathrm{L^2/T^2\Theta}$	$\mathrm{J\,kg^{-1}\,K^{-1}}$	10^6	$\mathrm{mm^2\,s^{-2}\,K^{-1}}$
Thermal conductivity	$\mathrm{ML/T^3\Theta}$	$\mathrm{W\,m^{-1}\,K^{-1}}$	1	$\mathrm{t\,mm\,s^{-3}\,K^{-1}}$
Thermal contact conductance	$\mathrm{M/T^3\Theta}$	$\mathrm{W\,m^{-2}\,K^{-1}}$	10^{-3}	$\mathrm{t\,s^{-3}\,K^{-1}}$
Electrical conductivity	$\mathrm{T^3I^2/ML^3}$	$\mathrm{S\,m^{-1}}$	1	$\mathrm{mA\,V^{-1}\,mm^{-1}}$
Electric contact conductance	$\mathrm{T^3I^2/ML^4}$	$\mathrm{S\,m^{-2}}$	10^{-3}	$\mathrm{mA\,V^{-1}\,mm^{-2}}$
Heat transfer coefficient	$\mathrm{M/T^3\Theta}$	$\mathrm{W\,m^{-2}\,K^{-1}}$	10^{-3}	$\mathrm{t\,s^{-3}\,K^{-1}}$
Current density	$\mathrm{I/L^2}$	$\mathrm{A\,m^{-2}}$	10^{-3}	$\mathrm{mA\,mm^{-1}}$
Stefan-Boltzmann constant	$\mathrm{M/T^3\Theta^4}$	$\mathrm{W\,m^{-2}\,K^{-4}}$	10^{-3}	$\mathrm{t\,s^{-3}\,K^{-4}}$

8 PID-Controller

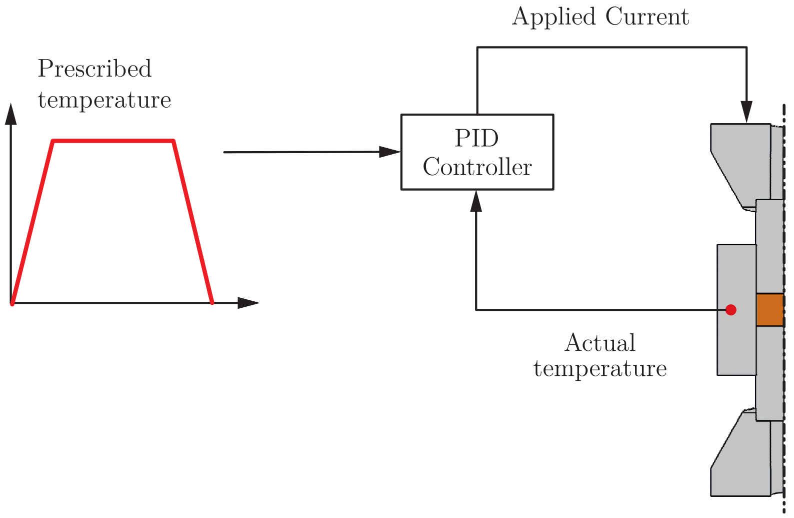

Figure 2: Temperature control loop inside the FAST-machine

The sintering process in the FAST-machine is temperature-controlled. In the experiments in Chapter 2, a thermocouple (placed in a borehole in the graphite die) is used for the temperature measurement. At this measurement point, the temperature $\overline{\Theta}_{\mathrm{TC}}(t)$ is prescribed, and a proportional-integral-derivative (PID) controller inside the machine serves to adapt the applied current according to the prescribed temperature path. The idea is to implement a PID-controller into Abaqus too, as a prerequisite to make predictions. Without a controller, it would only be possible to prescribe the measured current drawing on experiments, and these values would have to suffice to determine the current as a boundary condition for the simulation. For any predictions, it is of interest to prescribe the temperature in the same manner as in the FAST-machine. PID-controllers are also used in the context of FAST-processes in the work of Munoz and Anselmi-Tamburini [2010] and Mondalek et al. [2011]. The general control theory can be found e.g. in [Lutz and Wendt, 2007], [Lunze, 2012] and [Unbehauen, 2008]. Fig. 3 shows the closed loop control, where $\overline{\Theta}_{\mathrm{TC}}(t)$ is the set value over the time. The actual temperature at the thermocouple position in the simulation is given by $\Theta_{\mathrm{TC,actual}}(t)$. The control

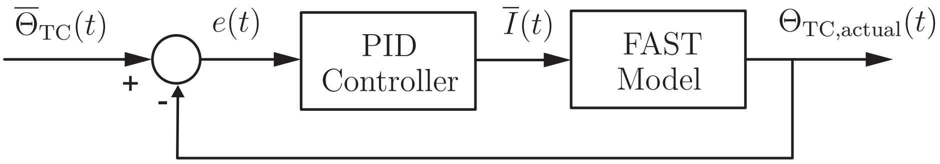

Figure 3: Closed loop control

deviation $e(t) := \overline{\Theta}_{\mathrm{TC}}(t) - \Theta_{\mathrm{TC,actual}}(t)$ can be calculated out of these two quantities. With the help of the controller, the current or, respectively, the current density[1] is computed and applied as a boundary condition in the FAST model. Due to the loop control, the deviation between the actual and the set value is permanently computed and reduced. In this work, a PID-controller is chosen. It is given by

$$\overline{I}(t) = K_P e(t) + K_I \int_0^t e(\tau)\,\mathrm{d}\tau + K_D \dot{e}(t). \tag{38}$$

The control parameters are K_P for the proportional, K_I for the integral and K_D for the differential part. The identified parameters can be found in Tab. 7.4. For the implementation into Abaqus, Eq. (38) is discretized. The equations can be found in the work of Lutz and Wendt [2007]. The integral can be approximated by the trapezoidal rule, and the time derivative is replaced by backward differences

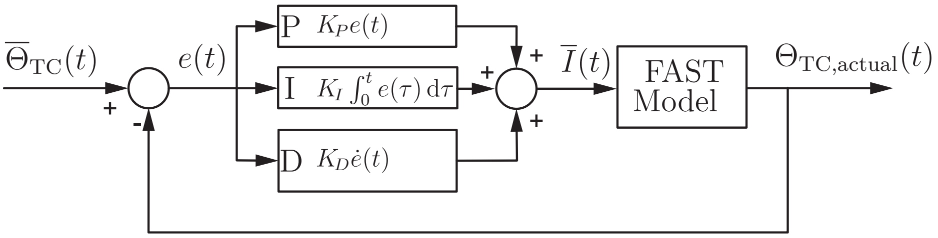

Figure 4: Closed loop control with PID-controller

$$\int_0^t e(\tau)\,\mathrm{d}\tau \approx \frac{1}{2}\sum_{i=1}^{n} \Delta t_i \left(e_i + e_{i-1}\right), \qquad \dot{e}(t) \approx \frac{e_n - e_{n-1}}{\Delta t_n} \tag{39}$$

Inserting these approximations into Eq. (38) yields

$$\overline{I}_n = K_P e_n + \frac{1}{2} K_I \sum_{i=1}^{n} \Delta t_i (e_i + e_{i-1}) + \frac{K_D}{\Delta t_n}(e_n - e_{n-1}) \tag{40}$$

In the same way, the current $\overline{I}_{n-1}$ at the previous time can be determined

$$\overline{I}_{n-1} = K_P e_{n-1} + \frac{1}{2} K_I \sum_{i=1}^{n-1} \Delta t_i (e_i + e_{i-1}) + \frac{K_D}{\Delta t_{n-1}}(e_{n-1} - e_{n-2}) \tag{41}$$

---

[1] The current density is applied as the boundary condition in the simulation, see Fig. 7.1c and Fig. 7.21c. The current density can be calculated by the current divided by the area.

In order to minimize the computational effort and save memory, the new current will be computed by the current from the last time step and the difference. The current at t_n can be calculated by

$$\overline{I}_n = \overline{I}_{n-1} + \Delta\overline{I}_n \qquad \Leftrightarrow \qquad \Delta\overline{I}_n = \overline{I}_n - \overline{I}_{n-1} \tag{42}$$

Thus, the current increment $\Delta\overline{I}_n$ can be obtained by

$$\begin{aligned}\Delta\overline{I}_n = K_P(e_n - e_{n-1}) + \frac{1}{2}K_I\Delta t_n(e_n + e_{n-1}) + \\ + K_D\left(\frac{e_n}{\Delta t_n} - e_{n-1}\left(\frac{1}{\Delta t_n} + \frac{1}{\Delta t_{n-1}}\right) + \frac{e_{n-2}}{\Delta t_{n-1}}\right).\end{aligned} \tag{43}$$

The current used as a boundary condition in order to follow the temperature is given by

$$\begin{aligned}\overline{I}_n = \overline{I}_{n-1} + K_P(e_n - e_{n-1}) + \frac{1}{2}K_I\Delta t_n(e_n + e_{n-1}) + \\ + K_D\left(\frac{e_n}{\Delta t_n} - e_{n-1}\left(\frac{1}{\Delta t_n} + \frac{1}{\Delta t_{n-1}}\right) + \frac{e_{n-2}}{\Delta t_{n-1}}\right).\end{aligned} \tag{44}$$

Here, the advantage is that only the previous values $\overline{I}_{n-1}$, e_{n-1} and e_{n-2} have to be saved for the sum – not the entire history, as in Eq. (40). Rearranging leads to

$$\begin{aligned}\overline{I}_n = \overline{I}_{n-1} + \left[K_P + \frac{1}{2}K_I\Delta t_n + \frac{K_D}{\Delta t_n}\right]e_n + \\ + \left[-K_P + \frac{1}{2}K_I\Delta t_n - K_D\left(\frac{1}{\Delta t_n} + \frac{1}{\Delta t_{n-1}}\right)\right]e_{n-1} + \frac{K_D}{\Delta t_{n-1}}e_{n-2}\end{aligned} \tag{45}$$

$$\overline{I}_n = \overline{I}_{n-1} + b_0 e_n + b_1 e_{n-1} + b_2 e_{n-2} \tag{46}$$

with

$$b_0 := K_P + \frac{1}{2}K_I\Delta t_n + \frac{K_D}{\Delta t_n} \tag{47}$$

$$b_1 := -K_P + \frac{1}{2}K_I\Delta t_n - K_D\left(\frac{1}{\Delta t_n} + \frac{1}{\Delta t_{n-1}}\right), \qquad b_2 := \frac{K_D}{\Delta t_{n-1}} \tag{48}$$

For the practical implementation, the controller output has to be limited according to the machine properties. The maximum applied current for the used FAST-machine, see Tab. 2.1, is 5500 A. This is set as an upper limit for the applied current. The lower limit is set to zero and no negative values are allowed.

List of Symbols

The notation used in this work is defined in the following manner: geometrical vectors are symbolized by $\vec{a}$, second order tensors $\mathbf{A}$ by bold-faced Roman letters. Furthermore, matrices at global level are denoted by bold-faced italic letters $\boldsymbol{A}$ and matrices on local level are given by bold-faced Roman letters $\mathbf{A}$. Local level in the sense of finite elements means the element level. Global matrices are quantities related to the whole domain.

Acronyms

Symbol	Description	Page
AC	alternating current	2
DAE	differential-algebraic equations	169
DC	direct current	2
DSC	differential scanning calorimetry	51
ECAS	Electric Current Activated/Assisted Sintering	4
FAST	Field Assisted Sintering Technology	iii, 4
HIP	hot isostatic pressing	iii
MLNA	Multilevel-Newton algorithm	9, 169
MOL	method of lines	169
ODE	ordinary differential equation	127
PECS	Pulsed Electric-Current Sintering	4
PID controller	proportional-integral-derivative controller	2, 6
SPS	Spark Plasma Sintering	4

2nd order tensors

Symbol	Description	Page
$\mathbf{A}$	Almansi strain tensor	69
$\mathbf{B}$	Left Cauchy-Green tensor	67
$\mathbf{C}_\mathrm{c}$	Creep right Cauchy-Green strain tensor	108
$\check{\mathbf{C}}_\mathrm{e}$	Elastic right Cauchy-Green strain tensor	113
$\mathbf{C}_\mathrm{i}$	Inelastic right Cauchy-Green strain tensor	108

Symbol	Description	Page
$\mathbf{C}$	Right Cauchy-Green tensor	67
$\mathbf{D}$	Strain rate tensor	70
$\mathbf{E}$	Green strain tensor	68
$\mathbf{E}_{\mathrm{c}}$	Creep part of Green strain tensor	108
$\mathbf{E}_{\mathrm{e}}$	Elastic part of Green strain tensor	108
$\mathbf{E}_{\mathrm{p}}$	Plastic part of Green strain tensor	108
$\mathbf{E}_{\Theta}$	Thermal part of Green strain tensor	108
$\delta\mathbf{E}$	Virtual Green strain tensor	176
$\mathbf{F}$	Deformation gradient	66
$\mathbf{F}_{\mathrm{c}}$	Creep part of deformation gradient	106
$\breve{\mathbf{F}}_{\mathrm{e}}$	Elastic part of deformation gradient	106
$\mathbf{F}_{\mathrm{i}}$	Inelastic part of deformation gradient	106
$\check{\mathbf{F}}_{\mathrm{p}}$	Plastic part of deformation gradient	106
$\mathbf{F}_{\mathrm{r}}$	Reversible part of deformation gradient	106
$\hat{\mathbf{F}}_{\Theta}$	Thermal part of deformation gradient	106
$\check{\mathbf{\Gamma}}$	Strain tensor in intermediate configuration $\check{\boldsymbol{\chi}}_t$	108
$\hat{\boldsymbol{\varepsilon}}$	Strain tensor in intermediate configuration $\hat{\boldsymbol{\chi}}_t$	112
$\breve{\boldsymbol{\gamma}}$	Strain tensor in intermediate configuration $\breve{\boldsymbol{\chi}}_t$	113
$\boldsymbol{\kappa}_{\mathrm{el}}^{\mathrm{R}}$	Electrical conductivity formulated in the reference configuration	136
$\boldsymbol{\kappa}_{\mathrm{th}}^{\mathrm{R}}$	Thermal conductivity formulated in the reference configuration	136
$\mathbf{L}$	Spatial velocity gradient	69
$\mathbf{L}_{\mathrm{c}}$	Creep velocity gradient	112
$\mathbf{L}_{\Theta\mathrm{pc}}$	Thermal-inelastic velocity gradient	113
$\hat{\mathbf{P}}$	Mandel stress tensor in plastic configuration	118
$\mathbf{R}$	Rotation tensor of polar composition of $\mathbf{F}$	67
$\mathbf{S}$	Weighted Cauchy stress tensor	71
$\mathbf{T}$	Cauchy stress tensor	70
$\mathbf{T}_{\mathrm{R}}$	First Piola-Kirchhoff stress tensor	71, 175
$\tilde{\mathbf{T}}$	Second Piola-Kirchhoff stress tensor	71
$\mathbf{U}$	Right stretch tensor	67
$\mathbf{V}$	Left stretch tensor	67
$\mathbf{W}$	Spin or vorcity tensor	70

Scalars

Symbol	Description	Page
A_1	(Abbreviation) parameter in yield function	98

Symbol	**Description**	**Page**
A_2	(Abbreviation) parameter in yield function	98
A_3	(Abbreviation) parameter in yield function	98
A_c	Creep material parameter	131
A_0	Cross section area of the powder compact	21
α_T	Diffusivity	52
α_Θ	Coefficient of linear thermal expansion	113
a_ξ	Material parameter connected to the hydrostatic kinematic hardening	124
b_ξ	Material parameter connected to the hydrostatic kinematic hardening	124
c_β	Material parameter connected to the sintering variable β_t	127
c	Interpolation parameter that controls the sharpness at the intersection point	99
c_∞	Creep material parameter	131
c_ξ	Material parameter connected to the hydrostatic kinematic hardening	124
E	Young's modulus	22
$\varepsilon_{\varphi\varphi}$	Circumferential strains	19
$\varepsilon_{\varphi\varphi}^{\mathrm{powder}}$	Powder induced circumferential strains	19
$\varepsilon_{\varphi\varphi}^{\mathrm{punch}}$	Punch induced circumferential strains	19
ε_Θ	Thermal strain	45
U	Volumetric part of elastic free energy ψ_e	129
v	Isochoric part of elastic free energy ψ_e	129
f_c	Creep variable	130
f_1	Ellipse yield function	97
f_2	Exponential yield function	98
f_k	Exponential temperature dependence for yield function parameter k	101
f_ξ	Exponential temperature dependence for yield function parameter ξ	101
$\tilde{F}$	Single surface yield function	100
G	Shear modulus	129
g_1	Reformulated ellipse yield function	99
g_2	Reformulated exponential yield function	99
w_l	Weighting factor of numerical quadrature rule	185
Λ	Plastic multiplier	121

Symbol	**Description**	**Page**
ρ	Density in the current configuration	21, 73
ρ_{rel}	Relative density in the current configuration	21
Q_{el}	Total charge over the volume	76
ρ_0	Density in the reference configuration	73
$\rho_{0,\mathrm{rel}}$	Relative density in the reference configuration	119
h	Current height of the powder	21
h_{c}	Heat transfer coefficient	172
H_0	Initial height of the powder	21
I	Electric current	53, 77
I_1	First invariant of stress tensor $\mathbf{T}$	93
β_k	Material parameter connected to the isotropic hardening	126
$\check{\mathrm{I}}_{1\mathrm{c}}$	First invariant of stress tensor $\check{\mathbf{S}}$	123
γ_k	Material parameter connected to the isotropic hardening	126
$\hat{\mathrm{I}}_{1\mathrm{i}}$	First invariant of stress tensor $\hat{\mathbf{S}}$	121
I_0	Intersection point of yield function with the hydrostatic axis in tensile direction for isothermal conditions	104
I_{t}	Intersection point of yield function with hydrostatic axis I_1	97
J_2	Second invariant of stress deviator $\mathbf{T}^{\mathrm{D}}$	93
$\hat{\mathrm{J}}_{2\mathrm{i}}$	Second invariant of stress deviator $\hat{\mathbf{S}}^{\mathrm{D}}$	121
K	Bulk modulus	129
$\kappa_{C,\mathrm{el},\mathrm{GC}}$	Electrical contact conductance for graphite-copper contact	164
$\kappa_{C,\mathrm{el},\mathrm{GG}}$	Electrical contact conductance for graphite-graphite contact	164
$\kappa_{C,\mathrm{th},\mathrm{CC}}$	Thermal contact conductance for copper-copper contact	167
κ_{el}	Electrical conductivity	53, 136
k	Height of the ellipse function	97
k_{M}	Mechanical part of isotropic hardening variable	101
κ_{th}	Thermal conductivity	51, 136
λ	Stretch	21
N_a	Shape function connected to node a	180

Symbol	**Description**	**Page**
n_e	Number of finite elements of given mesh	22, 180
n_eq	Number of equations/unknowns	22
n_Q	Number of internal variables of complete structure	185
$n_{\varphi\mathrm{a}}$	Number of electrical potential degrees of freedom of the entire mesh	183
n^e_φ	Number of electrical potential element degrees of freedom	183
$n_{\varphi\mathrm{p}}$	Number of prescribed electrical potential degrees of freedom	183
$n_{\varphi\mathrm{u}}$	Number of unknown electrical potential degrees of freedom	183
$n_{\Theta\mathrm{a}}$	Number of temperature degrees of freedom of the entire mesh	183
n^e_Θ	Number of temperature element degrees of freedom	183
$n_{\Theta\mathrm{p}}$	Number of prescribed temperature degrees of freedom	183
$n_{\Theta\mathrm{u}}$	Number of unknown temperature degrees of freedom	183
n_ua	Number of displacement degrees of freedom of the entire mesh	183
n^e_u	Number of displacement element degrees of freedom	183
n_up	Number of prescribed displacement degrees of freedom	183
n_uu	Number of unknown displacement degrees of freedom	183
ψ	Helmholtz free energy	83
α_k	Parameter of radial stress computation model	32
C	Parameter of radial stress computation model	32
c_1	Parameter of radial stress computation model	31
c_2	Parameter of radial stress computation model	31
c_3	Parameter of radial stress computation model	31
ψ_e	Elastic part of free energy	115
P_elec	Electrical power	82
$\delta\varphi$	Virtual electric potential	177
ψ_i	Part of free energy connected to isotropic hardening	115

Symbol	**Description**	**Page**
ψ_k	Part of free energy connected to hydrostatic kinematic hardening	115
k_∞	Parameter of radial stress computation model	32
P_mech	Power of external forces	82
ψ_i	Plastic part of free energy	115
ψ_t	Part of free energy connected to hydrostatic tensile hardening	115
ψ_Θ	Thermal part of free energy	115
Q	Resultant heat supply	82
$\overline{q}_\mathrm{con}$	Convective heat flux	172
q_el	Electrical charge	75
$\overline{q}_\mathrm{rad}$	Radiative heat flux	172
q_t	Test charge	75
$R_\mathrm{Rad/Ax}$	Radial-axial stress ratio	30
R_contact	Contact resistance	60
R^2	Coefficient of determination	48, 144
c_p	Specific heat capacity	51
ρ_solid	Density of the pore free bulk material	21
ρ_Copper	Density of copper	53
e	Specific internal energy	81
r_el	Electrical energy dissipated into heat	138
ρ_φ	Charge density	76, 78
n_en	Number of nodes per element	180, 183
r	Parameter of yield function	98
r	Thermal energy production due to radiation or internal processes	82
s	Specific entropy	83
R_total	Total resistance	60
r_v	Internal variable coupled to the inelastic volume deformation	115
s_Θ	Temperature arclength	31
σ_radial	Radial stress	22
Θ_0	Initial temperature	114
b_t	Material parameter connected to the hydrostatic tensile stress hardening	127
Θ	Temperature	1

Symbol	**Description**	**Page**
Θ_{f}	Absolute temperature of surrounding fluid	172
t	Time	65
Θ_S	Sintering temperature, material parameter	101
m_k	Material parameter in yield function describing the temperature shrinkage for k	101
m_ξ	Material parameter in yield function describing the temperature shrinkage for ξ	101
$\delta\Theta$	Virtual temperature	176
U	Voltage	53, 76
$u_{\mathrm{axial}}^{\mathrm{powder}}$	Axial powder displacement	19
u_{axial}	Axial punch displacement	19
$u_{\mathrm{axial}}^{\mathrm{system}}$	Axial displacement due to system compliance	19
α	Aspect ratio of the ellipse function	97
f_t	Decoupling (function) between kinematic and tensile hardening	104
ξ	Center of the ellipse function	97
ξ_{M}	Mechanical part of hydrostatic kinematic hardening variable	101

Vectors

Symbol	**Description**	**Page**
$\vec{E}$	Electrical field	53, 75
$\vec{B}$	Magnetic field or magnetic field density	78
$\vec{\boldsymbol{\chi}}_{\mathrm{R}}$	Motion of material body	65
$\vec{D}$	Electric displacement field or electric induction	78
$\vec{H}$	Magnetic field intensity	78
$\vec{j}$	Electrical current density	53, 72
$\vec{k}$	Body force density in the current configuration	73
$\mathrm{d}\vec{A}$	Material surface element in the reference configuration	66
$\mathrm{d}\vec{a}$	Material surface element in the current configuration	66
$\vec{e}_i$	Cartesian base vectors in the current configuration	65
$\vec{E}_k$	Cartesian base vectors in the reference configuration	65
$\vec{n}_{\mathrm{R}}$	Unit normal vector in the reference configuration	71
$\vec{n}$	Unit normal vector in the current configuration	71

Symbol	Description	Page
$\vec{q}$	Cauchy heat flux vector	72, 133
$\vec{t}$	Cauchy stress vector	70
$\vec{v}$	Velocity vector	69
$\vec{S}$	Poynting vector	79
$\vec{u}$	Displacement of material point	65
$\delta\vec{u}$	Virtual displacement	175

Matrices

Symbol	Description	Page
$\delta\mathbf{E}$	$\in \mathbb{R}^6$, Virtual strain tensor in matrix notation	183
$\boldsymbol{G}_\varphi$	Nonlinear equations (electrical part of DAE-system)	191
$\boldsymbol{g}_\varphi$	Discretized stationary electrical charge equation	188
$\boldsymbol{L}_\mathrm{q}$	Nonlinear equations (differential part of DAE-system)	191
$\boldsymbol{G}_\mathrm{u}$	Nonlinear equations (mechanical part of DAE-system)	191
$\boldsymbol{G}_\Theta$	Nonlinear equations (thermal part of DAE-system)	191
$\boldsymbol{g}_\mathrm{u}$	Discretized principle of virtual displacements	184
$\mathbf{\Phi}$	$\in \mathbb{R}^{n_{\varphi\mathrm{u}}}$, Vector of unknown nodal electric potentials	183
$\mathbf{\Phi}_\mathrm{a}$	$\in \mathbb{R}^{n_{\varphi\mathrm{a}}}$, Electrical potential degree of freedom of the entire mesh	183
$\overline{\mathbf{\Phi}}$	$\in \mathbb{R}^{n_{\varphi\mathrm{p}}}$, Vector of prescribed nodal electric potentials	183
$\mathbf{q}$	$\in \mathbb{R}^{n_\mathrm{q}}$, Internal variables at a Gauss point	186
$\boldsymbol{q}$	$\in \mathbb{R}^{n_\mathrm{Q}}$, Internal variables of the whole structure	186
$\boldsymbol{r}$	Evolution equation functions	186
$\mathbf{\Theta}$	$\in \mathbb{R}^{n_{\Theta\mathrm{u}}}$, Vector of unknown nodal temperatures	183
$\mathbf{\Theta}_\mathrm{a}$	$\in \mathbb{R}^{n_{\Theta\mathrm{a}}}$, Temperature degree of freedom of the entire mesh	183
$\overline{\mathbf{\Theta}}$	$\in \mathbb{R}^{n_{\Theta\mathrm{p}}}$, Vector of prescribed nodal temperatures	183
$\boldsymbol{u}$	$\in \mathbb{R}^{n_\mathrm{uu}}$, Vector of unknown nodal displacements	183
$\boldsymbol{u}_\mathrm{a}$	$\in \mathbb{R}^{n_\mathrm{ua}}$, Displacement degree of freedom of the entire mesh	183

Symbol	**Description**	**Page**
$\overline{\boldsymbol{u}}$	$\in \mathbb{R}^{n_{\mathrm{up}}}$, Vector of prescribed nodal displacements	183
$\overline{\boldsymbol{Z}}^{\mathrm{e}}_{\mathrm{u}}$	$\in \mathbb{R}^{n^{e}_{\varphi} \times n_{\varphi\mathrm{p}}}$, Incidence matrix for the prescribed electrical potential degree of freedom	183
$\boldsymbol{Z}^{\mathrm{e}}_{\varphi}$	$\in \mathbb{R}^{n^{e}_{\varphi} \times n_{\varphi\mathrm{u}}}$, Incidence matrix for the unknown electrical potential degree of freedom	183
$\overline{\boldsymbol{Z}}^{\mathrm{e}}_{\Theta}$	$\in \mathbb{R}^{n^{e}_{\Theta} \times n_{\Theta\mathrm{p}}}$, Incidence matrix for the prescribed temperature degree of freedom	183
$\boldsymbol{Z}^{\mathrm{e}}_{\Theta}$	$\in \mathbb{R}^{n^{e}_{\Theta} \times n_{\Theta\mathrm{u}}}$, Incidence matrix for the unknown temperature degree of freedom	183
$\overline{\boldsymbol{Z}}^{\mathrm{e}}_{\mathrm{u}}$	$\in \mathbb{R}^{n^{e}_{\mathrm{u}} \times n_{\mathrm{up}}}$, Incidence matrix for the prescribed displacement degree of freedom	183
$\boldsymbol{Z}^{\mathrm{e}}_{\mathrm{u}}$	$\in \mathbb{R}^{n^{e}_{\mathrm{u}} \times n_{\mathrm{uu}}}$, Incidence matrix for the unknown displacement degree of freedom	183
$\boldsymbol{\kappa}^{*}$	Identified material parameters	141
$\boldsymbol{\kappa}$	Vector containing the material parameters	141
$\mathbf{B}^{\mathrm{e}}_{\mathrm{u}}$	$\in \mathbb{R}^{6 \times 3n^{e}_{\mathrm{u}}}$, Strain displacement matrix on element level with respect to the current configuration	184
$\mathbf{B}^{\mathrm{e}}_{\mathrm{u}a}$	$\in \mathbb{R}^{6 \times 3}$, Strain displacement matrix on element level for node a	184
$\mathbf{B}^{\mathrm{e}}_{\varphi}$	$\in \mathbb{R}^{3 \times n^{e}_{\varphi}}$, Potential-gradient matrix on element level	188
$\mathbf{B}^{\mathrm{e}}_{\varphi a}$	$\in \mathbb{R}^{3 \times 1}$, Potential-gradient matrix on element level for node a	188
$\tilde{\mathbf{B}}^{\mathrm{e}}_{\mathrm{u}}$	$\in \mathbb{R}^{6 \times 3n^{e}_{\mathrm{u}}}$, Strain displacement matrix on element level with respect to the reference configuration	184
$\mathbf{B}^{\mathrm{e}}_{\Theta a}$	$\in \mathbb{R}^{3 \times 1}$, Temperature-gradient matrix on element level for node a	186
$\mathbf{B}^{\mathrm{e}}_{\Theta}$	$\in \mathbb{R}^{3 \times n^{e}_{\Theta}}$, Temperature-gradient matrix on element level	186
$\mathbf{R}$	Correlation matrix	143
$\mathbf{J}^{e}$	Jacobian matrix of transformation from parametric $\boldsymbol{\xi}$-space into the initial configuration	181
$\mathbf{j}^{e}$	Jacobian matrix of transformation from parametric $\boldsymbol{\xi}$-space into the current configuration	182

Symbol	Description	Page
$\tilde{\mathbf{T}}$	$\in \mathbb{R}^6$, second Piola Kirchoff stress tensor in matrix notation	183
$\boldsymbol{\xi}_l$	Quadrature point of numerical integration rule	185
$\boldsymbol{\xi}$	Local coordinates	181

Miscellaneous

Symbol	Description	Page
$\boldsymbol{\chi}_t$	Current configuration of material body	65
$\boldsymbol{\chi}$	Arbitrary configuration of material body	64
$\check{\boldsymbol{\chi}}_t$	Creep intermediate configuration of material body	106
$\hat{\boldsymbol{\chi}}_t$	Inelastic intermediate configuration of material body	106
$\breve{\boldsymbol{\chi}}_t$	Thermal intermediate configuration of material body	106
π_φ	Weak form of electric field equation	178
π_Θ	Weak form of heat conduction	178
π_{u}	Weak form of moment of momentum	178
$\mathcal{B}$	Material body	64
$\mathrm{d}V$	Material volume element in the reference configuration	66
$\mathrm{d}v$	Material volume element in the current configuration	66
$\mathrm{d}\vec{X}$	Material line element in the reference configuration	66
$\mathrm{d}\vec{x}$	Material line element in the current configuration	66
$\mathcal{P}$	Material point or particle	64
$\mathbb{R}$	Set of real numbers	64
$\mathcal{V}_\varphi$	Set of electrical potential test functions, variations	177
$\mathcal{V}_\Theta$	Set of temperature test functions, variations	176
$\boldsymbol{\mathcal{V}}_u$	Set of displacement test functions, variations	175

Mathematical Operators

Symbol	Description	Page
$\vec{a} \times \vec{b}$	Cross product	
$f'(x)$	Derivative of f with respect to x	
$\frac{\partial y}{\partial x}$	Partial derivative of y with respect to x	
$\frac{\mathrm{d}y}{\mathrm{d}x}$	Total derivative of y with respect to x	

Symbol	**Description**	**Page**
$\otimes$	Dyadic product	
$\mathbf{A}^{\mathrm{D}}$	Deviator of a tensor	
Grad	Gradient with respect to coordinates in the reference configuration	
$\mathbf{A} \cdot \mathbf{B}$	Inner product between two second order tensors	
$\mathbf{A}^{-1}$	Inverse of a tensor	
$\langle x \rangle$	Macaulay brackets	
$\dot{\mathbf{A}}$	Material time derivative	
Div	Divergence operator with respect to material coordinates	
div	Divergence operator with respect to spatial coordinates	
$\mathbf{A}^{\mathrm{T}}$	Transpose of a tensor	

Bibliography

Abbo, A. J. and S. W. Sloan [1995]. "A smooth hyperbolic approximation to the Mohr-Coulomb yield criterion". In: *Computers & Structures* 54.3, pp. 427–441. DOI: `10.1016/0045-7949(94)00339-5` [see p. 100].

Abou-Chedid, G. V. [1993]. "Experimental yield surface studies for the compaction of metal powder". PhD thesis. Massachusetts Institute of Technology. URL: `http://hdl.handle.net/1721.1/12469` [see p. 96].

Altenbach, J. and H. Altenbach [1994]. *Einführung in die Kontinuumsmechanik.* Stuttgart: Teubner [see pp. 63, 85].

Anselmi-Tamburini, U., S. Gennari, J. E. Garay, and Z. A. Munir [2005]. "Fundamental investigations on the spark plasma sintering/synthesis process II. Modeling of current and temperature distributions". In: *Materials Science and Engineering* A 394, pp. 139–148. DOI: `10.1016/j.msea.2004.11.019` [see p. 5].

Antou, G., G. Mathieu, G. Trolliard, and A. Maitre [2009]. "Spark plasma sintering of zirconium carbide and oxycarbide: Finite element modeling of current density, temperature, and stress distributions". In: *Journal of Materials Research* 24, pp. 404–412. DOI: `10.1557/JMR.2009.0039` [see p. 6].

Armero, F. and A. Perez-Foguet [2002]. "On the formulation of closest-point projection algorithms in elastoplasticity–part I: The variational structure". In: *International Journal for Numerical Methods in Engineering* 53, pp. 331–374. DOI: `10.1002/nme.278` [see p. 196].

Armero, F. and J. C. Simo [1992]. "A new unconditionally stable fractional step method for non-linear coupled thermomechanical problems". In: *International Journal for Numerical Methods in Engineering* 35.4, pp. 737–766. DOI: `10.1002/nme.1620350408` [see p. 179].

Arnold, M. and K. Frischmuth [1998]. "Solving problems with unilateral constraints by DAE methods". In: *Mathematics and Computers in Simulation* 47, pp. 47–67. DOI: `10.1016/S0378-4754(98)00118-9` [see pp. 96, 98].

Bathe, K.-J. [1996]. *Finite Element Procedures.* New Jersey: Prentice Hall [see p. 180].

Bergmann, W. [2003]. *Werkstofftechnik.* Hanser-Studien-Bücher Teil 1. Hanser [see p. 48].

Bier, W. [2008]. "A Constitutive Model for Metal Powder and its Numerical Treatment using Finite Elements". PhD thesis. Universität Kassel. URL: `http://nbn-resolving.de/urn:nbn:de:hebis:34-2008061221983` [see pp. 93, 100–101, 115–116, 119, 146, 236, 244].

Bier, W., M. P. Dariel, N. Frage, S. Hartmann, and O. Michailov [2007]. “Die compaction of copper powder designed for material parameter identification”. In: *International Journal of Mechanical Science* 49, pp. 766–777. DOI: `10.1016/j.ijmecsci.2006.09.026` [see pp. 18, 30–31].

Bier, W. and S. Hartmann [2006]. “A finite strain constitutive model for metal powder compaction using a unique and convex single surface yield function”. In: *European Journal of Mechanics, Series A/solids* 25, pp. 1009–1030. DOI: `10.1016/j.euromechsol.2006.01.002` [see pp. 89, 93, 96–100, 115–116, 119, 236, 244].

Birken, P., K. J. Quint, S. Hartmann, and A. Meister [2010]. “A time-adaptive fluid-structure interaction method for thermal coupling”. In: *Computing and Visualization in Science* 13.7, pp. 331–340. DOI: `10.1007/s00791-010-0150-4` [see pp. 172, 189].

Brandt, J. [1998]. “FE-simulation of compaction and solid state sintering of cemented carbides”. In: *Mechanics of Cohesive-frictional Materials* 3.1, pp. 181–205. DOI: `10.1002/(SICI)1099-1484(199804)3:2<181::AID-CFM47>3.0.CO;2-H` [see p. 90].

Brandt, N., S. Chudinov, and Y. Ponomarev [2012]. *Semimetals: 1. Graphite and its Compounds*. Modern Problems in Condensed Matter Sciences. Elsevier Science [see p. 56].

Braudel, H., M. Abouaf, and J. Chenot [1986]. “An implicit and incremental formulation for the solution of elastoplastic problems by the finite element method”. In: *Computers and Structures* 22.5, pp. 801–814. DOI: `http://dx.doi.org/10.1016/0045-7949(86)90269-5` [see p. 200].

Brown, S. and G. Abou-Chedid [1994]. “Yield behavior of metal powder assemblages”. In: *Journal of the Mechanics and Physics of Solids* 42.3, pp. 383–399. DOI: `10.1016/0022-5096(94)90024-8` [see p. 31].

Carnavas, P. C. [1996]. “The effect of particle morphology on metal powder compaction”. PhD thesis. University of Queensland [see pp. 30–31, 48, 144, 146, 159].

Casey, J. [1985]. “Approximate kinematical relations in plasticity”. In: *International Journal of Solids and Structures* 21.7, pp. 671–682. DOI: `10.1016/0020-7683(85)90071-X` [see p. 120].

Chaboche, J. L. [2008]. “A review of some plasticity and viscoplasticity constitutive theories”. In: *International Journal of Plasticity* 24.10, pp. 1642–1693. DOI: `10.1016/j.ijplas.2008.03.009` [see p. 96].

Cincotti, A., A. M. Locci, R. Orru, and G. Cao [2007]. “Modeling of SPS apparatus: Temperature, current and strain distribution with no powders”. In: *AIChE journal* 53.3, pp. 703–719. DOI: `10.1002/aic.11102` [see p. 5].

Cocks, A. C. F. and I. C. Sinka [2007]. “Constitutive modelling of powder compaction I. Theoretical concepts”. In: *Mechanics of Materials* 39, pp. 392–403. DOI: `10.1016/j.mechmat.2006.09.003` [see p. 93].

Brandt, S. [1999]. *Datenanalyse.* 4nd. Heidelberg, Berlin: Spektrum, Akademischer Verlag [see p. 143].

Demkowicz, L. [2006]. *Computing with hp-Adaptive Finite Elements: Volume 1 One and Two Dimensional Elliptic and Maxwell Problems.* Chapman & Hall/CRC Applied Mathematics & Nonlinear Science. Taylor & Francis [see p. 179].

Demkowicz, L. [2008]. *Frontiers: Three Dimensional Elliptic and Maxwell Problems with Applications.* Computing with hp-adaptive finite elements / Leszek Demkowicz. Chapman & Hall/CRC [see p. 179].

Dhatt, G. and G. Touzot [1985]. *The Finite Element Method Displayed.* Chichester: John Wiley & Sons Ltd, England [see p. 185].

DiMaggio, F. and I. Sandler [1971]. "Material Model for Granular Soils". eng. In: *Journal of the Engineering Mechanics Division* 97.3, pp. 935–950 [see p. 96].

Düster, A. [2001]. "High order finite elements for three-dimensional, thin-walled nonlinear continua". PhD thesis. Lehrstuhl für Bauinformatik, Fakultät für Bauingenieur- und Vermessungswesen, Technische Universität München [see p. 177].

Düster, A., H. Bröker, and E. Rank [2001]. "The p-version of the finite element method for three-dimensional curved thin walled structures". In: *International Journal for Numerical Methods in Engineering* 52, pp. 673–703. DOI: `10.1002/nme.222` [see p. 177].

Düster, A., S. Hartmann, and E. Rank [2003]. "p-FEM applied to finite isotropic hyperelastic bodies". In: *Computer Methods in Applied Mechanics and Engineering* 192, pp. 5147–5166. DOI: `10.1016/j.cma.2003.07.003` [see p. 177].

Düster, A., A. Niggl, V. Nübel, and E. Rank [2002]. "A Numerical Investigation of High-Order Finite Elements for Problems of Elastoplasticity". In: *Journal of Scientific Computing* 17, pp. 397–404. DOI: `10.1023/A:1015189706770` [see p. 177].

Düster, A. and E. Rank [2001]. "The p-version of the finite element method compared to an adaptive h-version for the deformation theory of plasticity". In: *Computer Methods in Applied Mechanics and Engineering* 190, pp. 1925–1935. DOI: `10.1016/S0045-7825(00)00215-2` [see p. 177].

Düster, A. and E. Rank [2002]. "A p-version finite element approach for two- and three-dimensional problems of the J_2 flow theory with non-linear isotropic hardening". In: *International Journal for Numerical Methods in Engineering* 53, pp. 49–63 [see p. 177].

Ehlers, W. [1995]. "A single-surface yield function for geomaterials". English. In: *Archive of Applied Mechanics* 65.4, pp. 246–259. DOI: `10.1007/BF00805464` [see p. 101].

Ellsiepen, P. and S. Hartmann [2001]. "Remarks on the interpretation of current non-linear finite element analyses as differential-algebraic equations". In: *International Journal for Numerical Methods in Engineering* 51, pp. 679–707. DOI: `10.1002/nme.179` [see p. 189].

Erbts, P. and A. Düster [2012]. “Accelerated staggered coupling schemes for problems of thermoelasticity at finite strains”. In: *Computers and Mathematics with Applications* 64, pp. 2408–2430. DOI: `10.1016/j.camwa.2012.05.010` [see p. 179].

Erbts, P., S. Hartmann, and A. Düster [2014]. “A partitioned solution approach for electro-thermo-mechanical problems”. In: *Archive of Applied Mechanics*. accepted for publication [see p. 179].

Erbts, P., S. Rothe, A. Düster, and S. Hartmann [2012]. “Coupling Algorithms for Small Strain Thermo-Viscoplasticity: Monolithic vs. Partitioned Approach”. In: *Proceedings of the 1st International Conference on Thermo-Mechanically Graded Materials*. Ed. by H.-P. Heim, D. Biermann, and J. Maier. Verlag Wissenschaftliche Scripten, Auerbach, pp. 81–86 [see p. 179].

Eringen, A. and G. Maugin [1990]. *Electrodynamics of Continua: Foundations and solid media.* Springer-Verlag [see pp. 63, 74, 81].

Farhat, C., K. C. Park, and Y. Dubois-Pelerin [1991]. “An unconditionally stable staggered algorithm for transient finite element analysis of coupled thermoelastic problems”. In: *Computer Methods in Applied Mechanics and Engineering* 85.85, pp. 349–365. DOI: `10.1016/0045-7825(91)90102-C` [see p. 179].

Fleck, N. [1995]. “On the cold compaction of powders”. In: *Journal of the Mechanics and Physics of Solids* 43.9, pp. 1409–1431. DOI: `10.1016/0022-5096(95)00039-L` [see p. 93].

Frei, J. M., U. Anselmi-Tamburini, and Z. A. Munir [2007]. “Current effects on neck growth in the sintering of copper spheres to copper plates by the pulsed electric current method”. In: *Journal of applied physics* 101, p. 114914. DOI: `10.1063/1.2743885` [see p. 12].

Fried, E. and M. J. Kelley [1966]. “Thermal conductance of metallic contacts in a vacuum.” en. In: *Progress in Astronautics and Aeronautics vol 18: Thermophysics and Temperature Control of Spacecraft and Entry Vehicle*, p. 697. URL: `http://ntrs.nasa.gov/search.jsp?R=19670034338` [see p. 167].

Frischkorn, J. and S. Reese [2011]. “Modelling and simulation of process-integrated powder coating by radial axial rolling of rings”. In: *Archive of Applied Mechanics* 82.2, pp. 243–259. DOI: `10.1007/s00419-011-0553-9` [see pp. 89–90, 120–121].

Fritzen, P. [1997]. “Numerische Behandlung nichtlinearer Probleme der Elastizitäts- und Plastizitätstheorie”. PhD thesis. Technische Universität Darmstadt [see pp. 170, 189].

Gan, Y. [2008]. “Thermo-Mechanics of Pebble Beds in Fusion Blankets”. PhD thesis. Universität Karlsruhe. URL: `http://nbn-resolving.de/urn:nbn:de:0005-074552` [see p. 123].

Gan, Y. and M. Kamlah [2007]. “Identification of material parameters of a thermo-mechanical model for pebble beds in fusion blankets”. In: *Fusion Engineering and Design* 82.2, pp. 189–206. DOI: `10.1016/j.fusengdes.2006.09.005` [see p. 123].

Garay, J. [2010]. “Current-Activated, Pressure-Assisted Densification of Materials”. In: *Annual Review of Materials Research* 40.1, pp. 445–468. DOI: `10.1146/annurev-matsci-070909-104433` [see p. 4].

Giuntini, D., E. Olevsky, C. Garcia-Cardona, A. Maximenko, M. Yurlova, C. Haines, D. Martin, and D. Kapoor [2013]. “Localized Overheating Phenomena and Optimization of Spark-Plasma Sintering Tooling Design”. In: *Materials* 6.7, pp. 2612–2632. DOI: `10.3390/ma6072612` [see p. 7].

Grasso, S., Y. Sakka, and G. Maizza [2009]. “Electric current activated/assisted sintering (ECAS): a review of patents 1906–2008”. In: *Science and Technology of Advanced Materials* 10.5, p. 053001. DOI: `10.1088/1468-6996/10/5/053001` [see p. 4].

Griewank, A. and A. Walther [2008]. *Evaluating Derivatives: Principles and Techniques of Algorithmic Differentiation.* Philadelphia: SIAM Society for Industrial and Applied Mathematics [see p. 200].

Griffiths, D. [2011]. *Elektrodynamik.* Pearson Studium [see pp. 74–75].

Guillon, O., J. Gonzalez-Julian, B. Dargatz, T. Kessel, G. Schierning, J. Räthel, and M. Herrmann [2014]. “Field-Assisted Sintering Technology/Spark Plasma Sintering: Mechanisms, Materials, and Technology Developments”. In: *Advanced Engineering Materials*, n/a–n/a. DOI: `10.1002/adem.201300409` [see p. 4].

Hairer, E. and G. Wanner [2002]. *Solving Ordinary Differential Equations II: Stiff and Differential-Algebraic Problems.* Berlin: Springer [see p. 190].

Hamkar, A.-W. [2013]. “Eine iterationsfreie Finite-Elemente Methode im Rahmen der finiten Thermoviskoelastizität”. PhD-thesis, Report No. 1/2013. Clausthal-Zellerfeld: Institute of Applied Mechanics, Clausthal University of Technology. URL: `http://nbn-resolving.de/urn:nbn:de:gbv:104-1116208` [see pp. 184, 186, 189].

Hamkar, A.-W., S. Hartmann, and J. Rang [2012]. “A stiffly accurate Rosenbrock-type method of order 2 applied to FE-analyses in finite strain viscoelasticity”. In: *Applied Numerical Mathematics* 62.12, pp. 1837–1848. DOI: `10.1016/j.apnum.2012.08.001` [see p. 189].

Hartmann, S. [2003]. “Finite-Elemente Berechnung inelastischer Kontinua: Interpretation als Algebro-Differentialgleichungssysteme”. Habilitation. University of Kassel, Institute of Mechanics. URL: `http://nbn-resolving.de/urn:nbn:de:hebis:34-2007060618581` [see pp. 184, 186, 196, 244, 246].

Hartmann, S. [2005]. “A remark on the application of the Newton-Raphson method in non-linear finite element analysis”. In: *Computational Mechanics* 36.2, pp. 100–116. DOI: `10.1007/s00466-004-0630-9` [see pp. 183, 186, 190–192].

Hartmann, S. [2012]. *Comparison of the multiplicative decompositions* $\mathbf{F} = \mathbf{F}_\Theta \mathbf{F}_m$ *and* $\mathbf{F} = \mathbf{F}_m \mathbf{F}_\Theta$ *in finite strain thermo-elasticity.* Technical Report Series Fac3-12-01. Clausthal University of Technology (Germany): Faculty of Mathematics/Computer Sciences and Mechanical Engineering. URL: `http://www.`

`fakultaeten.tu-clausthal.de/fileadmin/fakultaet3/Technical_Reports/TR_FAC3-1201.pdf` [see p. 108].

Hartmann, S. and W. Bier [2008]. “High-order time integration applied to metal powder plasticity”. In: *International Journal of Plasticity* 24.1, pp. 17–54. DOI: `10.1016/j.ijplas.2007.01.014` [see pp. 189, 196].

Hartmann, S. and A.-W. Hamkar [2010]. “Rosenbrock-type methods applied to finite element computations within finite strain viscoelasticity”. In: *Computer Methods in Applied Mechanics and Engineering* 199.23–24, pp. 1455–1470. DOI: `10.1016/j.cma.2009.12.011` [see pp. 183, 189].

Hartmann, S. and P. Haupt [1993]. “Stress computation and consistent tangent operator using non-linear kinematic hardening models”. In: *International Journal for Numerical Methods in Engineering* 36, pp. 3801–3814. DOI: `10.1002/nme.1620362204` [see p. 195].

Hartmann, S., D. Kuhl, and K. J. Quint [2009a]. “Time-Adaptive Computation of Finite Strain Thermoviscoplastic Structures”. In: *Functionally Graded Materials in Industrial Mass Production.* Ed. by K. Steinhoff, K.-J. Maier, and B. Svendsen. Verlag Wissenschaftliche Scripten, Auerbach. Chap. 4.1, pp. 269–282 [see p. 189].

Hartmann, S., G. Lührs, and P. Haupt [1997]. “An efficient stress algorithm with applications in viscoplasticity and plasticity”. In: *International Journal for Numerical Methods in Engineering* 40, pp. 991–1013. DOI: `10.1002/(SICI)1097-0207(19970330)40:6<991::AID-NME98>3.0.CO;2-H` [see pp. 195, 200].

Hartmann, S., A. Meister, P. Birken, and K. J. Quint [2009b]. “Thermal Fluid-Structure-Interaction of Cooling Processes in Steel Forming”. In: *Functionally Graded Materials in Industrial Mass Production.* Ed. by K. Steinhoff, K.-J. Maier, and B. Svendsen. Verlag Wissenschaftliche Scripten, Auerbach. Chap. 4.2, pp. 283–292 [see p. 172].

Hartmann, S. and P. Neff [2003]. “Polyconvexity of generalized polynomial-type hyperelastic strain energy functions for near-incompressibility”. In: *International Journal of Solids and Structures* 40.11, pp. 2767–2791. DOI: `10.1016/S0020-7683(03)00086-6` [see pp. 129, 244].

Hartmann, S., K. J. Quint, and M. Arnold [2008a]. “On plastic incompressibility within time-adaptive finite elements combined with projection techniques”. In: *Computer Methods in Applied Mechanics and Engineering* 198.2, pp. 178–193. DOI: `10.1016/j.cma.2008.06.011` [see p. 189].

Hartmann, S., K. J. Quint, and A.-W. Hamkar [2008b]. “Displacement control in time-adaptive non-linear finite-element analysis”. In: *Journal of Applied Mathematics and Mechanics* 88.5, pp. 342–364. DOI: `10.1002/zamm.200800002` [see p. 189].

Hartmann, S., S. Rothe, and N. Frage [2013]. “Electro-Thermo-Elastic Simulation of Graphite Tools Used in SPS Processes”. In: *Generalized Continua as Models of Materials.* Ed. by H. Altenbach, S. Forest, and A. Krivtsov. Vol. 22. Advanced

Structured Materials. Berlin: Springer, pp. 143–161. DOI: `10.1007/978-3-642-36394-8_8` [see p. 6].

Hartmann, S. and S. Rothe [2013]. “A Rigorous Application of the Method of Vertical Lines to Coupled Systems in Finite Element Analysis”. In: *Recent Developments in the Numerics of Nonlinear Hyperbolic Conservation Laws.* Ed. by R. Ansorge, H. Bijl, A. Meister, and T. Sonar. Vol. 120. Notes on Numerical Fluid Mechanics and Multidisciplinary Design. Springer Berlin / Heidelberg, pp. 161–175. DOI: `10.1007/978-3-642-33221-0_10` [see p. 189].

Haupt, P. [2002]. *Continuum Mechanics and Theory of Materials.* Berlin: Springer, 2nd edition [see pp. 63, 66–68, 70, 72–74, 83–88, 121, 137, 140].

Haupt, P. and C. Taskmakis [1996]. “Stress tensors associated with deformation tensors via duality”. In: *Archives of Mechanics* 48, pp. 347–384. URL: `http://www.ippt.pan.pl/Repository/am-v48-no2-pp347-384.pdf` [see p. 87].

Haupt, P. and C. Tsakmakis [1989]. “On the application of dual variables in continuum mechanics”. In: *Journal of Continuum Mechanics and Thermodynamics* 1, pp. 165–196. DOI: `10.1007/BF01171378` [see pp. 86, 88].

Heimes, T. [2005]. “Finite Thermoinelastizität: Experimente, Materialmodellierung und Implementierung in die FEM am Beispiel einer technischen Gummimischung”. PhD thesis. Universität der Bundeswehr München [see p. 138].

Heisserer, U., S. Hartmann, A. Düster, W. Bier, Z. Yosibash, and E. Rank [2008]. “p-FEM for finite deformation powder compaction”. In: *Computer Methods in Applied Mechanics and Engineering* 197, pp. 727–740. DOI: `10.1016/j.cma.2007.09.001` [see p. 177].

Helm, D. [2001]. “Formgedächtnislegierungen: Experimentelle Untersuchung, phänomenologische Modellierung und numerische Simulation der thermomechanischen Materialeigenschaften”. PhD thesis. Institut für Mechanik, Universität Kassel. URL: `http://nbn-resolving.de/urn:nbn:de:hebis:34-2007062718775` [see p. 136].

Hofer, D. and M. Kamlah [2005]. “Drucker–Prager–Cap creep modelling of pebble beds in fusion blankets”. In: *Fusion Engineering and Design* 73.2-4, pp. 105–117. DOI: `10.1016/j.fusengdes.2005.02.002` [see p. 123].

Höhne, G., W. F. Hemminger, and H.-J. Flammersheim [2003]. *Differential Scanning Calorimetry.* Berlin: Springer [see p. 51].

Holm, R. [1999]. *Electric contacts: theory and applications.* Springer [see p. 59].

Holzapfel, G. A. [2000]. *Nonlinear Solid Mechanics.* Chichester: Wiley & Sons [see pp. 63, 65, 70, 83, 85].

Hoyer, W. and J. W. Schmidt [1984]. “Newton-Type Decomposition Methods for Equations Arising in Network Analysis”. In: *ZAMM Zeitschrift für Angewandte Mathematik und Mechanik* 64, pp. 397–405. DOI: `10.1002/zamm.19840640904` [see p. 191].

Hughes, T. J. R. [2000]. *The Finite Element Method: Linear Static and Dynamic Finite Element Analysis.* Mineola, NY: Dover Publications [see pp. 180, 183].

Hulbert, D. M., A. Anders, J. Andersson, E. J. Lavernia, and A. K. Mukherjee [2009]. "A discussion on the absence of plasma in spark plasma sintering". In: *Scripta Materialia* 60.10, pp. 835–838. DOI: `10.1016/j.scriptamat.2008.12.059` [see p. 11].

Hutter, K. and K. Jöhnk [2004]. *Continuum Methods of Physical Modeling. Continuum Mechanics, Dimensional Analysis, Turbulence.* Berlin: Springer [see pp. 63, 85].

Incropera, F. P., D. P. Dewitt, T. L. Bergman, and A. S. Lavine [2007]. *Fundamentals of Heat and Mass Transfer.* 6th. Hoboken, NJ: John Wiley & Sons [see p. 171].

Tarantola, A. [2005]. *Inverse Problem Theory and Methods for Model Parameter Estimation.* Philadelphia: SIAM Society for Industrial and Applied Mathematics [see p. 143].

Jäger, H. et al. [2000]. "Carbon, 4. Industrial Carbons". In: *Ullmann's Encyclopedia of Industrial Chemistry.* Wiley-VCH Verlag GmbH & Co. KGaA. DOI: `10.1002/14356007.n05_n03` [see pp. 13, 56].

Jansohn, W. [1997]. "Formulierung und Integration von Stoffgesetzen zur Beschreibung großer Deformationen in der Thermoplastizität und -viskoplastizität". PhD thesis. Forschungszentrum Karlsruhe, Institut für Materialforschung. URL: `http://gso.gbv.de/DB=2.1/PPNSET?PPN=238603970` [see p. 138].

Jeltsch-Fricker, R. [2007]. *Variationsrechnung.* Skript zur Vorlesung in den Technikstudiengängen der Universität Kassel [see p. 175].

Jeong, M.-S., J.-H. Yoo, S.-H. Rhim, S.-K. Lee, and S.-I. Oh [2012]. "A unified model for compaction and sintering behavior of powder processing". In: *Finite Elements in Analysis and Design* 53, pp. 56–62. DOI: `10.1016/j.finel.2011.08.011` [see p. 90].

Kamlah, M. [2000]. *Zur Modellierung von nichtlinearen elektromechanischen Koppelphänomenen in Piezokeramiken.* Habilitationsschrift. Habilitation [see p. 74].

Kebriaei, R., J. Frischkorn, S. Reese, T. Husmann, H. Meier, H. Moll, and W. Theisen [2013]. "Numerical modelling of powder metallurgical coatings on ring-shaped parts integrated with ring rolling". In: *Journal of Materials Processing Technology* 213, pp. 2015–2032. DOI: `10.1016/j.jmatprotec.2013.05.023` [see pp. 89, 120].

Khoei, A., Z. Molaeinia, and S. Keshavarz [2013]. "Modeling of hot isostatic pressing of metal powder with temperature–dependent cap plasticity model". In: *International Journal of Material Forming* 6.3, pp. 363–376. DOI: `10.1007/s12289-012-1091-x` [see p. 90].

Kieback, B. and J. Trapp [2011]. "Grundlegende Prozesse beim Spark-Plasma-Sintern". In: *Pulvermetallurgie in Wissenschaft und Praxis.* 27th ed. Heimdall Verlag, pp. 47–75. URL: `http://publica.fraunhofer.de/dokumente/N-213974.html` [see p. 12].

Klingbeil, H. [2010]. *Elektromagnetische Feldtheorie: Ein Lehr- und Übungsbuch.* Vieweg+Teubner Verlag [see pp. 74, 76, 79–80, 239–240].

Klinger, J. [2013]. “Messung temperaturabhängiger, spezifischer elektrischer Widerstände poröser und geschichteter Sinterproben”. MA thesis. Ruhr-Universität Bochum [see pp. 54, 59].

Korelc, J. [2002]. “Multi-language and Multi-environment Generation of Nonlinear Finite Element Codes”. In: *Engineering with Computers* 18.4, pp. 312–327. DOI: `10.1007/s003660200028` [see p. 200].

Korelc, J. [2009]. “Automation of primal and sensitivity analysis of transient coupled problems”. In: *Computational Mechanics* 44.5, pp. 631–649. DOI: `10.1007/s00466-009-0395-2` [see p. 200].

Kraft, T. and H. Riedel [2004]. “Numerical simulation of solid state sintering; model and application”. In: *Journal of the European Ceramic Society* 24, pp. 345–361. DOI: `10.1016/S0955-2219(03)00222-X` [see p. 90].

Krämer, S., S. Rothe, and S. Hartmann [2015]. “Homogeneous stress-strain states computed by 3D-stress algorithms of FE-codes: application to material parameter identification”. In: *Engineering with Computers* 31.1, pp. 141–159. DOI: `10.1007/s00366-013-0337-7` [see pp. 140–141].

Krautkrämer, J. and H. Krautkrämer [1990]. *Ultrasonic Testing of Materials.* Springer-Verlag, pp. 13–14 [see p. 22].

Kreisselmeier, G. and R. Steinhauser [1979]. “Systematische Auslegung von Reglern durch Optimierung eines vektoriellen Gütekriteriums”. In: *Regelungstechnik* 3, pp. 76–79 [see pp. 96, 98].

Kreißig, R., U. Benedix, and U.-J. Görke [2001]. “Statistical aspects of the identification of material parameters for elasto-plastic models”. In: *Archive of Applied Mechanics* 71, pp. 123–134. DOI: `10.1007/s004190000106` [see p. 143].

Kuhn, H. A. and C. L. Downey [1971]. “Deformation characteristics and plasticity theory of sintered powder materials”. In: *Int. J. Powder Metall.* 7.1, pp. 15–25 [see pp. 30, 96].

Kulkarni, D. V., D. Tortorelli, and M. Wallin [2007]. “A Newton-Schur alternative to the consistent tangent approach in computational plasticity”. In: *Computer Methods in Applied Mechanics and Engineering* 196, pp. 1169–1177. DOI: `10.1016/j.cma.2006.06.013` [see p. 191].

Lagarias, J., J. Reeds, M. Wright, and P. Wright [1998]. “Convergence Properties of the Nelder–Mead Simplex Method in Low Dimensions”. In: *SIAM Journal on Optimization* 9.1, pp. 112–147. DOI: `10.1137/S1052623496303470` [see p. 48].

Landau, L. D., E. M. Lifshits, and Pitaevskii [2008]. *Electrodynamics of continuous media.* 2nd ed. Amsterdam: Elsevier, p. 460 [see pp. 74, 138].

Lee, E. H. [1969]. “Elastic-Plastic Deformation at Finite Strains”. In: *Journal of Applied Mechanics* 36, pp. 1–6. DOI: `10.1115/1.3564580` [see p. 106].

Lemaitre, J. and J. Chaboche [2010]. *Mechanics of Solid Materials.* Cambridge University Press [see p. 48].

Lide, D. R. and W. Haynes [2009]. *CRC Handbook of Chemistry and Physics, 90th Edition.* CRC Handbook of Chemistry and Physics. Taylor & Francis [see p. 51].

Lindner, H. [1978]. *Grundriß der Festkörperphysik.* Viewegs Fachbücher der Technik. Vieweg Verlag, Friedr, & Sohn Verlagsgesellschaft mbH [see pp. 53, 55].

Lion, A. [2000]. “Constitutive modelling in finite thermoviscoplasticity: a physical approach based on nonlinear rheological models”. In: *International Journal of Plasticity* 16, pp. 469–494. DOI: `10.1016/S0749-6419(99)00038-8` [see p. 108].

Lu, S. C. H. and K. S. Pister [1975]. “Decomposition of deformation and representation of the free energy function for isotropic thermoelastic solids”. In: *International Journal of Solids and Structures* 11.7–8, pp. 927–934. DOI: `10.1016/0020-7683(75)90015-3` [see p. 106].

Lubliner, J. [2008]. *Plasticity Theory.* Mineola, NY: Dover Publications [see pp. 91, 100, 120].

Luenberger, D. and Y. Ye [2008]. *Linear and Nonlinear Programming.* International Series in Operations Research & Management Science. Springer [see p. 124].

Lührs, G., S. Hartmann, and P. Haupt [1997]. “On the numerical treatment of finite deformations in elastoviscoplasticity”. In: *Computer Methods in Applied Mechanics and Engineering* 144, pp. 1–21. DOI: `10.1016/S0045-7825(96)01163-2` [see p. 195].

Lunze, J. [2012]. *Automatisierungstechnik.* 3., überarb. Aufl. München: Oldenbourg [see p. 248].

Lutz, H. and W. Wendt [2007]. *Taschenbuch der Regelungstechnik: mit MATLAB und Simulink.* Harri Deutsch [see pp. 248–249].

Mähler, L., M. Ekh, and K. Runesson [2001]. “A class of thermo-hyperelastic-viscoplastic models for porous materials: theory and numerics”. In: *International Journal of Plasticity* 17, pp. 934–969. DOI: `10.1016/S0749-6419(00)00048-6` [see pp. 89, 108].

Mähler, L. and K. Runesson [2000]. “Modelling of solid-phase sintering of hardmetal using a mesomechanics approach”. In: *Mechanics of Cohesive-Frictional Materials* 5, pp. 653–671. DOI: `10.1002/1099-1484(200011)5:8<653::AID-CFM111>3.0.CO;2-A` [see pp. 89, 120–121].

Mähler, L. and K. Runesson [2003]. “Constitutive Modeling of Cold Compaction and Sintering of Hardmetal”. In: *Journal of Engineering Materials and Technology* 125.2, pp. 191–199. DOI: `10.1115/1.1491576` [see pp. 89–90, 101, 120–121].

Maizza, G., S. Grasso, Y. Sakka, T. Noda, and O. Ohashi [2007]. “Relation between microstructure, properties and spark plasma sintering (SPS) parameters of pure ultrafine WC powder”. In: *Science and Technology of Advanced Materials* 8.7-8, pp. 644–654. DOI: `10.1016/j.stam.2007.09.002` [see p. 6].

Martin, C., D. Bouvard, and S. Shima [2003]. “Study of particle rearrangement during powder compaction by the Discrete Element Method”. In: *Journal of the Mechanics and Physics of Solids* 51.4, pp. 667–693. DOI: `10.1016/S0022-5096(02)00101-1` [see p. 33].

McWilliams, B. [2008]. “Numerical Simulation of Electric Field Assisted Sintering”. PhD thesis. Drexel University [see p. 6].

McWilliams, B. and A. Zavaliangos [2008]. “Multi-phenomena simulation of electric field assisted sintering”. In: *Journal of Materials and Science* 43, pp. 5031–5035 [see p. 6].

Meyberg, K. and P. Vachenauer [2001]. *Höhere Mathematik 2.* 4th. Springer Berlin Heidelberg [see p. 240].

Miehe, C. [1988]. “Zur numerischen Behandlung thermomechanischer Prozesse”. PhD thesis. Universität Hannover [see p. 108].

Miehe, C. [1995a]. “A theory of large-strain isotropic thermoplacticity based on metric transformation tensors”. In: *Archive of Applied Mechanics* 66, pp. 45–64. DOI: `10.1007/BF00786688` [see p. 179].

Miehe, C. [1995b]. “Entropic thermoelasticity at finite strains: Aspects of the formulation and numerical implementation”. In: *Computer Methods in Applied Mechanics and Engineering* 120, pp. 243–269. DOI: `10.1016/0045-7825(94)00057-T` [see p. 179].

Mondalek, P. [2012]. “Numerical modeling of the spark plasma sintering process”. PhD thesis. MINES ParisTech [see p. 7].

Mondalek, P., L. Silva, and M. Bellet [2011]. “A Numerical Model for Powder Densification by SPS Technique”. In: *Advanced Engineering Materials* 13.7, pp. 587–593. DOI: `10.1002/adem.201000340` [see pp. 7, 90, 219, 248].

Montes, J. M., J. A. Rodriguez, and E. J. Herrera [2003]. “Thermal and electrical conductivities of sintered powder compacts”. In: *Powder Metallurgy* 46, pp. 251–256. DOI: `10.1179/003258903225008544` [see p. 136].

Munir, Z. A., D. V. Quach, and M. Ohyanagi [2011]. “Electric Current Activation of Sintering: A Review of the Pulsed Electric Current Sintering Process”. In: *Journal of the American Ceramic Society* 94.1, pp. 1–19. DOI: `10.1111/j.1551-2916.2010.04210.x` [see p. 4].

Munoz, S. and U. Anselmi-Tamburini [2010]. “Temperature and stress fields evolution during spark plasma sintering processes”. In: *Journal of Material Science* 45, pp. 6528–6539 [see pp. 6, 218, 248].

Muñoz, S. and U. Anselmi-Tamburini [2012]. “Parametric investigation of temperature distribution in field activated sintering apparatus”. In: *The International Journal of Advanced Manufacturing Technology.* DOI: `10.1007/s00170-012-4155-7` [see p. 5].

Naumann, U. [2012]. *The Art of Differentiating Computer Programs: An Introduction to Algorithmic Differentiation.* SIAM Society for Industrial and Applied Mathematics [see p. 200].

Naumenko, K. [2006]. “Modeling of High-Temperature Creep for Structural Analysis Applications”. PhD thesis. Universität Halle-Wittenberg. URL: `http://sundoc.bibliothek.uni-halle.de/habil-online/06/06H055/habil.pdf` [see p. 123].

Naumenko, K., H. Altenbach, and Y. Gorash [2009]. “Creep analysis with a stress range dependent constitutive model”. In: *Archive of Applied Mechanics* 79.6-7, pp. 619–630. DOI: `10.1007/s00419-008-0287-5` [see p. 123].

Nelder, J. and R. Mead [1965]. “A Simplex Method for Function Minimization”. In: *Computer journal* 7.4, pp. 308–313. DOI: `10.1093/comjnl/7.4.308` [see p. 48].

Netz, T. [2013]. “High-order space and time discretization scheme applied to problems of finite thermo-viscoelasticity”. PhD-thesis, Report No. 3/2013. Clausthal-Zellerfeld: Institute of Applied Mechanics, Clausthal University of Technology. URL: `http://nbn-resolving.de/urn:nbn:de:gbv:104-1116793` [see pp. 177, 189].

Netz, T., A. Düster, and S. Hartmann [2013a]. “High-order finite elements compared to low-order mixed element formulations”. In: *Journal of Applied Mathematics and Mechanics* 93, pp. 163–176. DOI: `10.1002/zamm.201200040` [see p. 177].

Netz, T., A.-W. Hamkar, and S. Hartmann [2013b]. “High-order quasi-static finite element computations in space and time with application to finite strain viscoelasticity”. In: *Computers and Mathematics with Applications* 66, pp. 441–459. DOI: `10.1016/j.camwa.2013.05.022` [see p. 189].

Neumüller, O. [1972]. *Römpps Chemie-Lexikon: Cm-G.* Bd. 2. Franckh [see p. 56].

Öhman, M., K. Runesson, and F. Larsson [2012]. “Computational Mesoscale Modeling and Homogenization of Liquid-Phase Sintering of Particle Agglomerates”. In: *Technische Mechanik* 32.2-5, pp. 463–483. URL: `http://www.ovgu.de/ifme/zeitschrift_tm/2012_Heft2_5/33_Oehman.pdf` [see p. 90].

Öhman, M., F. Larsson, and K. Runesson [2013]. “Computational homogenization of liquid-phase sintering with seamless transition from macroscopic compressibility to incompressibility”. In: *Computer Methods in Applied Mechanics and Engineering* 266, pp. 219–228. DOI: `10.1016/j.cma.2013.07.006` [see p. 90].

Oldenhuis, R. [2009]. *optimize (non)linear (in)equality constrained functions with FMINSEARCH.* Download 08.06.2013. URL: `http://www.mathworks.com/matlabcentral/fileexchange/24298-optimize` [see p. 48].

Olevsky, E. A., C. Garcia-Cardona, W. L. Bradbury, C. D. Haines, D. G. Martin, and D. Kapoor [2012a]. “Fundamental Aspects of Spark Plasma Sintering: II. Finite Element Analysis of Scalability”. In: *Journal of the American Ceramic Society* 95.8, pp. 2414–2422. DOI: `10.1111/j.1551-2916.2012.05096.x` [see pp. 6–7].

Olevsky, E. A., W. L. Bradbury, C. D. Haines, D. G. Martin, and D. Kapoor [2012b]. “Fundamental Aspects of Spark Plasma Sintering: I. Experimental Analysis of Scalability”. In: *Journal of the American Ceramic Society* 95.8. Ed. by S.-J. Kang, pp. 2406–2413. DOI: `10.1111/j.1551-2916.2012.05203.x` [see p. 1].

Oliver, J., J. A. Hernandez, J. C. Cante, and R. Weyler [2010]. “Numerical modeling of crack formation in powder forming processes”. In: *International Journal of Solids and Structures* 48, pp. 292–316 [see p. 121].

Oliver, J., S. Oller, and J. Cante [1996]. “A plasticity model for simulation of industrial powder compaction processes”. In: *International Journal of Solids and Structures* 33.20-22, pp. 3161–3178. DOI: `10.1016/0020-7683(95)00249-9` [see p. 93].

Palma, R., J. L. Pérez-Aparicio, and R. L. Taylor [2012]. "Non-linear finite element formulation applied to thermoelectric materials under hyperbolic heat conduction model". In: *Comput. Methods Appl. Mech. Engrg.* 213-216, pp. 93–103. DOI: `10.1016/j.cma.2011.11.011` [see p. 179].

Pavia, A., L. Durand, F. Ajustron, V. Bley, G. Chevallier, a. Peigney, and C. Estournès [2013]. "Electro-thermal measurements and finite element method simulations of a spark plasma sintering device". In: *Journal of Materials Processing Technology* 213.8, pp. 1327–1336. DOI: `10.1016/j.jmatprotec.2013.02.003` [see p. 5].

Pérez-Aparicio, J. L., R. Palma, and R. L. Taylor [2012]. "Finite element analysis and material sensitivity of Peltier thermoelectric cells coolers". In: *International Journal of Heat and Mass Transfer* 55, pp. 1363–1374. DOI: `10.1016/j.ijheatmasstransfer.2011.08.031` [see p. 179].

Pérez-Aparicio, J. L., R. L. Taylor, and D. Gavela [2006]. "Finite Element Analysis of Nonlinear Fully Coupled Thermoelectric Materials". In: *Computational Mechanics* 40.1, pp. 35–45. DOI: `10.1007/s00466-006-0080-7` [see p. 179].

Pérez-Foguet, A. and F. Armero [2002]. "On the formulation of closest-point projection algorithms in elastoplasticity—part II: Globally convergent schemes". In: *International Journal for Numerical Methods in Engineering* 53.2, pp. 331–374. DOI: `10.1002/nme.279` [see p. 196].

Pizette, P., C. Martin, G. Delette, P. Sornay, and F. Sans [2010]. "Compaction of aggregated ceramic powders: From contact laws to fracture and yield surfaces". In: *Powder Technology* 198.2, pp. 240–250. DOI: `10.1016/j.powtec.2009.11.013` [see p. 34].

Quach, D. V., J. R. Groza, A. Zavaliangos, and U. Anselmi-Tamburini [2010]. "Fundamentals and applications of field/current assisted sintering". In: *Sintering of advanced materials.* Woodhead Publishing Series in Metals and Surface Engineering No. 35, pp. 249–273. DOI: `10.1533/9781845699949.2.249` [see p. 4].

Quint, K. J. [2012]. "Thermomechanically Coupled Processes for Functionally Graded Materials: Experiments, Modelling, and Finite Element Analysis using High-Order DIRK-Methods". PhD-thesis, Report No. 2/2012. Clausthal-Zellerfeld: Institute of Applied Mechanics, Clausthal University of Technology. URL: `http://nbn-resolving.de/urn:nbn:de:gbv:104-1109284` [see pp. 67, 108, 121, 180–181, 189, 192].

Quint, K. J., S. Hartmann, S. Rothe, N. Saba, and K. Steinhoff [2011]. "Experimental validation of high-order time-integration for non-linear heat transfer problems". In: *Computational Mechanics* 48, pp. 81–96. DOI: `10.1007/s00466-011-0572-y` [see pp. 179, 189].

Rabbat, N. B. G., A. L. Sangiovanni-Vincentelli, and H. Y. Hsieh [1979]. "A multilevel Newton algorithm with macromodeling and latency for the analysis of large-scale nonlinear circuits in the time domain". In: *Circuits and Systems, IEEE*

Transactions on 26.9, pp. 733–740. DOI: 10.1109/TCS.1979.1084693 [see pp. 190–191].

Rao, V. V., K. Bapurao, J. Nagaraju, and M. V. K. Murthy [2004]. "Instrumentation to measure thermal contact resistance". In: *Measurement Science and Technology* 15.1, p. 275. URL: http://stacks.iop.org/0957-0233/15/i=1/a=040 [see pp. 167, 224].

Räthel, J., M. Herrmann, and W. Beckert [2009]. "Temperature distribution for electrically conductive and non-conductive materials during Field Assisted Sintering (FAST)". In: *Journal of the European Ceramic Society* 29, pp. 1419–1425. DOI: 10.1016/j.jeurceramsoc.2008.09.015 [see p. 5].

Reid, C. R. and R. G. Oakberg [1990]. "A continuum theory for the mechanical response of materials to the thermodynamic stress of sintering". In: *Mechanics of Materials* 10.3, pp. 203–213. DOI: 10.1016/0167-6636(90)90043-F [see p. 89].

Riedel, H., T. Kraft, M. Reiterer, and U. Janosovits [2003]. "Finite element simulation of cold isostatic pressing and sintering of SiC components". In: *Ceramics International* 30, pp. 177–183. DOI: 10.1016/S0272-8842(03)00086-5 [see p. 93].

Rösler, J., H. Harders, and M. Bäker [2008]. *Mechanisches Verhalten der Werkstoffe.* 3. Vieweg+Teubner [see pp. 53, 100–101].

Rothe, S., A.-W. Hamkar, K. J. Quint, and S. Hartmann [2012]. "Comparison of diagonal-implicit, linear-implicit and half-explicit Runge-Kutta methods in non-linear finite element analyses". In: *Archive of Applied Mechanics* 82.8, pp. 1057–1074. DOI: 10.1007/s00419-012-0617-5 [see p. 189].

Rothe, S. and S. Hartmann [2014]. "Automatic Differentiation for Stress and Consistent Tangent Computation". In: *Archive of Applied Mechanics*, pp. 1–23. DOI: 10.1007/s00419-014-0939-6 [see p. 201].

Rothe, S., J. H. Schmidt, and S. Hartmann [2014]. "Analytical and numerical treatment of electro-thermo-mechanical coupling". In: *Archive of Applied Mechanics*, pp. 1–20. DOI: 10.1007/s00419-014-0948-5 [see pp. 6, 179].

Schiesser, W. E. [1991]. *The Numerical Method of Lines: Integration of Partial Differential Equations.* San Diego, CA: Academic Press Inc [see p. 177].

Schiesser, W. E. and G. W. Griffiths [2009]. *A Compendium of Partial Differential Equation Models: Method of Lines Analysis with Matlab.* New York, NY: Cambridge University Press [see p. 177].

Schwarz, H. R. and N. Köckler [2004]. *Numerische Mathematik.* Stuttgart: Teubner [see pp. 182, 185].

SGL Carbon GmbH [2014]. *Ringsdorff Isostatic Graphite Grade R8510.* Tech. rep. Download 18.04.2014. URL: http://www.sglgroup.com/cms/_common/downloads/products/product-groups/gs/special_page3/RINGSDORFF_TDS-8510_v1_e_korr01.pdf [see pp. 22, 56, 58].

Shima, S. and M. Oyane [1976]. “Plasticity theory for porous metals”. In: *International Journal of Mechanical Sciences* 18.6, pp. 285–291. DOI: `10.1016/0020-7403(76)90030-8` [see p. 96].

Shinagawa, K. [1996]. “Finite element simulation of sintering process: Microscopic modelling of powder compacts and constitutive equation for sintering”. In: *JSME international journal. Series A, mechanics and material engineering* [see p. 90].

Simo, J. C. and T. J. R. Hughes [2000]. *Computational Inelasticity.* Berlin: Springer [see pp. 129, 195].

Simo, J. C. and R. L. Taylor [1985]. “Consistent tangent operators for rate-independent elastoplasticity”. In: *Computer Methods in Applied Mechanics and Engineering* 48.1, pp. 101–118. DOI: `10.1016/0045-7825(85)90070-2` [see p. 192].

Simo, J. C., R. L. Taylor, and P. Wriggers [1991]. “A note on finite-element implementation of pressure boundary loading”. In: *Communications in Applied Numerical Methods* 7.7, pp. 513–525. DOI: `10.1002/cnm.1630070703` [see p. 179].

Sinka, I. C. [2007]. “Modelling powder compaction”. In: *Kona* 25, pp. 4–22. URL: `http://www.kona.or.jp/jp/journal/pdf/2007.pdf` [see p. 93].

Sinka, I. and A. Cocks [2007]. “Constitutive modelling of powder compaction – II. Evaluation of material data”. In: *Mechanics of Materials* 39.4, pp. 404–416. DOI: `10.1016/j.mechmat.2006.09.002` [see p. 93].

Song, Y., Y. Li, Z. Zhou, Y. Lai, and Y. Ye [2011]. “A multi-field coupled FEM model for one-step-forming process of spark plasma sintering considering local densification of powder material”. In: *Journal of Material Science* 46, pp. 5645–5656. DOI: `10.1007/s10853-011-5515-7` [see p. 6].

Svoboda, J., H. Riedel, and R. Gaebel [1996]. “A model for liquid phase sintering”. In: *Acta materialia* 44.8, pp. 3215–3226. DOI: `10.1016/1359-6454(95)00440-8` [see p. 90].

Szabó, B. and I. Babuška [1991]. *Finite Element Analysis.* New York: John Wiley & Sons [see p. 177].

Szabo, B., A. Düster, and E. Rank [2004]. “The p-version of the Finite Element Method”. In: *Encyclopedia of Computational Mechanics.* John Wiley & Sons. Chap. 5, pp. 119–139. DOI: `10.1002/0470091355.ecm003g` [see p. 177].

Tanaka, M., M. Fujikawa, D. Balzani, and J. Schröder [2014]. “Robust numerical calculation of tangent moduli at finite strains based on complex-step derivative approximation and its application to localization analysis”. In: *Computer Methods in Applied Mechanics and Engineering* 269, pp. 454–470. DOI: `10.1016/j.cma.2013.11.005` [see p. 201].

Tiwari, D., B. Basu, and K. Biswas [2009]. “Simulation of thermal and electric field evolution during spark plasma sintering”. In: *Ceramics International* 35, pp. 699–708. DOI: `10.1016/j.ceramint.2008.02.013` [see p. 5].

Touloukian, Y. [1970]. *Thermophysical Properties of Matter: Thermal conductivity; nonmetallic liquids and gases, by Y. S. Touloukian, P. E. Liley, and S. C. Saxena.* The TPRC data series. IFI/Plenum [see p. 51].

Truesdell, C. A. and W. Noll [2004]. *The Non-Linear Field Theories of Mechanics.* Berlin: Springer [see p. 84].

Unbehauen, H. [2008]. *Regelungstechnik I.* 15., überarbeitete und erweiterte Auflage. Wiesbaden: Vieweg+Teubner Verlag / GWV Fachverlage GmbH Wiesbaden [see p. 248].

Utke, J., U. Naumann, M. Fagan, N. Tallent, M. Strout, P. Heimbach, C. Hill, and C. Wunsch [2008]. “OpenAD/F: A Modular, Open-Source Tool for Automatic Differentiation of Fortran Codes”. In: *ACM Transactions on Mathematical Software* 34.4, pp. 1–34. DOI: `10.1145/1377596.1377598` [see p. 201].

Vanherck, T., G. Jean, M. Gonon, J. Lobry, and F. Cambier [2013]. “Spark Plasma Sintering: Homogenization of the Compact Temperature Field for Non Conductive Materials”. In: *International Journal of Applied Ceramic Technology* 12, n/a–n/a. DOI: `10.1111/ijac.12187` [see p. 5].

Vanmeensel, K., A. Laptev, J. Hennicke, J. Vleugels, and O. der Biest [2005]. “Modelling of the temperature distribution during field assisted sintering”. In: *Acta Materialia* 53, pp. 4379–4388. DOI: `10.1016/j.actamat.2005.05.042` [see pp. 5, 216, 223].

Wang, C., L. Cheng, and Z. Zhao [2010]. “FEM analysis of the temperature and stress distribution in spark plasma sintering: Modelling and experimental validation”. In: *Computational Materials Science* 49.2, pp. 351–362. DOI: `10.1016/j.commatsci.2010.05.021` [see p. 6].

Wang, J. [1984]. “Young’s modulus of porous materials”. In: *Journal of Materials Science* 19.3, pp. 801–808. DOI: `10.1007/BF00540451` [see p. 48].

Wang, X., S. R. Casolco, G. Xu, and J. E. Garay [2007]. “Finite element modeling of electric current-activated sintering: The effect of coupled electrical potential, temperature and stress”. In: *Acta Materialia* 55, pp. 3611–3622. DOI: `10.1016/j.actamat.2007.02.022` [see p. 6].

Wittekindt, J. [1991]. “Die numerische Lösung von Anfangs-Randwertproblemen zur Beschreibung inelastischen Werkstoffverhaltens”. PhD thesis. Technische Hochschule Darmstadt [see p. 189].

Wolff, C., S. Mercier, H. Couque, and A. Molinari [2012]. “Modeling of conventional hot compaction and Spark Plasma Sintering based on modified micromechanical models of porous materials”. In: *Mechanics of Materials* 49, pp. 72–91. DOI: `10.1016/j.mechmat.2011.12.002` [see pp. 6–7, 90].

Wolfram, S. [2003]. *The Mathematica Book.* 5th ed. Wolfram Media, Incorporated [see p. 200].

Workman, G. L., D. Kishoni, and P. O. Moore [2007]. *Nondestructive Testing Handbook: Ultrasonic Testing.* Nondestructive testing handbook. American Society for Nondestructive Testing, pp. 319–321 [see p. 22].

Wriggers, P. [2009]. *Nonlinear Finite Element Methods.* Berlin: Springer [see pp. 180, 183].

Zavaliangos, A., J. Zhang, M. Krammer, and J. R. Groza [2004]. “Temperature evolution during field activated sintering”. In: *Materials Science and Engineering* 379, pp. 218–228. DOI: `10.1016/j.msea.2004.01.052` [see pp. 4, 164, 205, 210, 217, 223–224].

Zienkiewicz, O. C. and R. L. Taylor [2005]. *The Finite Element Method: Its Basis and Fundamentals.* 6th ed. Burlington, MA: Butterworth-Heinemann [see p. 180].

Zohdi, T. I. [2010]. “Simulation of coupled microscale multiphysical-fields in particulate-doped dielectrics with staggered adaptive FDTD”. In: *Computer Methods in Applied Mechanics and Engineering* 199.49-52, pp. 3250–3269. DOI: `10.1016/j.cma.2010.06.032` [see p. 5].

Zohdi, T. I. [2012a]. “Estimation of electrical heating load-shares for sintering of powder mixtures”. In: *Proceedings of the Royal Society A: Mathematical, Physical and Engineering Sciences* 468.2144, pp. 2174–2190. DOI: `10.1098/rspa.2011.0755` [see p. 5].

Zohdi, T. I. [2014]. “A direct particle-based computational framework for electrically enhanced thermo-mechanical sintering of powdered materials”. In: *Mathematics and Mechanics of Solids* 19.1, pp. 93–113. DOI: `10.1177/1081286513505472` [see pp. 6, 240].

Zohdi, T. I. [2012b]. *Electromagnetic Properties of Multiphase Dielectrics: A Primer on Modeling, Theory and Computation.* Vol. 64. Springer [see pp. 75–76, 138].

List of Publications

[1] P. Erbts, S. Rothe, A. Düster, and S. Hartmann. “Coupling Algorithms for Small Strain Thermo-Viscoplasticity: Monolithic vs. Partitioned Approach”. In: *Proceedings of the 1st International Conference on Thermo-Mechanically Graded Materials*. Ed. by H.-P. Heim, D. Biermann, and J. Maier. Verlag Wissenschaftliche Scripten, Auerbach, 2012, pp. 81–86.

[2] P. Erbts, S. Rothe, A. Düster, and S. Hartmann. “Energy conserving data transfer in the partitioned treatment of thermo-viscoplastic problems”. In: *PAMM*. 2013. DOI: `10.1002/pamm.201310101`.

[3] S. Hartmann, S. Rothe, and N. Frage. “Aspekte der Simulation von Kompaktierungsvorgängen an Pulvermaterialien”. In: *Pulvermetallurgie - zukunftsweisend vom Rohstoff bis zur Anwendung, Pulvermetallurgie in Wissenschaft und Praxis*. Ed. by H. KOLASKA. 28. Heimdall Verlag, Dortmund, 2012, pp. 127–142.

[4] S. Hartmann, S. Rothe, and N. Frage. “Electro-Thermo-Elastic Simulation of Graphite Tools Used in SPS Processes”. In: *Generalized Continua as Models of Materials*. Ed. by H. Altenbach, S. Forest, and A. Krivtsov. Vol. 22. Advanced Structured Materials. Berlin: Springer, 2013, pp. 143–161. DOI: `10.1007/978-3-642-36394-8_8`.

[5] S. Hartmann and S. Rothe. “A Rigorous Application of the Method of Vertical Lines to Coupled Systems in Finite Element Analysis”. In: *Recent Developments in the Numerics of Nonlinear Hyperbolic Conservation Laws*. Ed. by R. Ansorge, H. Bijl, A. Meister, and T. Sonar. Vol. 120. Notes on Numerical Fluid Mechanics and Multidisciplinary Design. Springer Berlin / Heidelberg, 2013, pp. 161–175. DOI: `10.1007/978-3-642-33221-0_10`.

[6] S. Krämer, S. Rothe, and S. Hartmann. “Homogeneous stress-strain states computed by 3D-stress algorithms of FE-codes: application to material parameter identification”. In: *Engineering with Computers* 31.1 [2015], pp. 141–159. DOI: `10.1007/s00366-013-0337-7`.

[7] S. Krämer, S. Rothe, and S. Hartmann. “Material parameter identification using model reduction to uniaxial tensile test”. In: *PAMM* 12.1 [2012], pp. 315–316. DOI: `10.1002/pamm.201210147`.

[8] K. J. Quint, S. Hartmann, S. Rothe, N. Saba, and K. Steinhoff. “Experimental validation of high-order time-integration for non-linear heat transfer problems”. In: *Computational Mechanics* 48 [2011], pp. 81–96. DOI: `10.1007/s00466-011-0572-y`.

[9] S. Rothe, A.-W. Hamkar, K. J. Quint, and S. Hartmann. “Comparison of diagonal-implicit, linear-implicit and half-explicit Runge-Kutta methods in non-linear finite element analyses”. In: *Archive of Applied Mechanics* 82.8 [2012], pp. 1057–1074. DOI: `10.1007/s00419-012-0617-5`.

[10] S. Rothe and S. Hartmann. “Automatic Differentiation for Stress and Consistent Tangent Computation”. In: *Archive of Applied Mechanics* [2014], pp. 1–23. DOI: `10.1007/s00419-014-0939-6`.

[11] S. Rothe, J. H. Schmidt, and S. Hartmann. “Analytical and numerical treatment of electro-thermo-mechanical coupling”. In: *Archive of Applied Mechanics* [2014], pp. 1–20. DOI: `10.1007/s00419-014-0948-5`.

[12] S. Rothe and S. Hartmann. “Accelerating constitutive modeling by automatic tangent generation”. In: *PAMM* 12.1 [2012], pp. 313–314. DOI: `10.1002/pamm.201210146`.

[13] S. Rothe and S. Hartmann. “Powder compaction. Experiments, modeling and simulation”. In: *PAMM* 14.1 [2014], pp. 457–458. DOI: `10.1002/pamm.201410216`.

[14] S. Rothe, S. Hartmann, A.-W. Hamkar, and K. Quint. “A comparison of time adaptive integration methods for small and large strain viscoelasticity”. In: *PAMM* 11.1 [2011], pp. 263–264. DOI: `10.1002/pamm.201110123`.

Steffen Rothe

Curriculum Vitae

Personal Data

Date of birth	April 13, 1985
Place of birth	Kassel
Nationality	German

Professional Experience

07/2010–08/2014	**Research Assistant**, *Clausthal University of Technology*, Clausthal-Zellerfeld.
10/2008–03/2009	**Intern**, *Volkswagen AG*, Wolfsburg. FEM-simulation division for the car steering/chassis development
2007–2009	**Student Research Assistant**, *Institute of Mechanics, University of Kassel*, Participation in the Collaborative Research Project Transregio 30: Time-Adaptive Computation of Finite Thermoviscoplastic Structures. FEM computations and development of FORTRAN programs
10/2005–06/2010	**Cooperative Studies**, *Volkswagen AG in cooperation with the University of Kassel*.
09/2004–05/2005	**Civilian service**, *youth education facility "Stadtteilzentrum Baunsberg"*, Baunatal.

Education

07/2010–08/2014	**Phd Student**, *Clausthal University of Technology*. Research Topic: Electro-thermo-mechanical modeling of Field Assisted Sintering Technology using high-order finite elements validated by experiments, founded by the DFG (German Research Foundation)
08/2005–06/2010	**Diploma Student of Mechanical Engineering**, *University of Kassel, Main focus on FEM, Continuum Mechanics and Numerics*, Diploma thesis II (equivalent to Master thesis), title: *Time-adaptive finite element computations of thermal processes for the production of functionally graded structures*, Diploma thesis I (equivalent to Bachelor thesis), title: *Life time prediction of thermomechanically loaded exhaust systems on the basis of finite element computations (in cooperation with Volkswagen)*.
08/2005–02/2008	**Technical apprenticeship as an industrial mechanic**, *Volkswagen AG*, Kassel.
2005–2008	**Vocational school**, *Herwig-Blankertz-Schule*, Wolfhagen.
1995–2004	**Secondary school**, *Georg-Christoph-Lichtenberg-Schule*, Kassel.
1991–1995	**Elementary school**, *Brüder-Grimm-Grundschule*, Baunatal.